INVESTIGATION OF PITTING CORROSION OF CARBON STEEL IN SWEET AND SOUR OILFIELD CORROSION CONDITIONS: A PARAMETRIC STUDY

Frederick Oritseweneye Pessu

Submitted in accordance with the requirements for the degree of

Doctor of Philosophy

The University of Leeds

Institute of Functional Surfaces

School of Mechanical engineering

June 2015

The candidate confirms that the work submitted is his own and that appropriate credit has been given where reference has been made to the work of others.

Acknowledgements

All of my thanks and acknowledgments are to the name of the most High and Almighty God for the gifts of life, mercy, love, grace, strength, motivation and wisdom to have come this far in all of my endeavor and most importantly to the end of this phase of my personal development.

I would like to express my profound gratitude to Professor Anne Neville for her constant supervision, guidance, support and encouragement. Her unique leadership, motivation, insights and passion for science and engineering were the driving force behind the success of this research work. I am very grateful for the support of my co-supervisor Dr. Richard James Barker for his invaluable day-to-day advice and support. Hi Rick, we did it!!!

I wish to express my gratitude to the Niger-Delta Development Commission (NDDC), Nigeria and University of Leeds, United Kingdom for funding this research.

To all past and present members; students and staff of iFS research institute, university Leeds, I say thank you. The success in my research would not be complete without your supports, friendship and discussions. Special thanks goes to; Mohammed Ismail, Juan, Laura, Ikechuckwu, Sunday, Doris, Farnaz, Zahra, Wassim, Leo, Ali G, Moshen, Bello and Lukeman. Thank you to; Ron Celier, Andrew, Michael Huggan, Fiona Slade, Dr. T. Charpentier, Dr. C. Wang, Alice Mackay for creating an efficient research environment. Special thanks to Adrian Eagles, Michael Ward and Stuart Micklethwaite.

I would like to use this opportunity to thank my mentors; Professor Lucky Akaruese and Hon. Daniel Reyenieju, member, Nigerian federal house of representative, for their support. I am thankful to some friends for their time, support and for coping with me when I am lost in research; Mrs. Nora Chinawa, Mrs. Eneyi Kpokiri, Jeffery Umukoro, Nmgbede Agada, Adeolu and Mrs. Adebukola Adegbulugbe, Kosi Itodo, Pst. and Pst.(Mrs). Ralph Ibiyeye, Stella Momanyi, Mrs. Sophie Sasime, Peace, Kwinba, Ugohinyere, Temitola Ojo, Powei Lopkobiri, Adah Juliet, Kelechi, the family of late Prince Benjamin Fregene and AFC Horsforth.

I would finally like to express my profound appreciation and dedicate this work to my Mother, Mercy Pessu, my Father, Oritsweyinmi Pessu and my sister, Toritseju Pessu and my aunt; Edith Ogharaerumi. To my mother and sister for their endless prayers, love, patience and support throughout my studies and my dad for always being there. God bless you and keep you all for me…Amen!!!

..*“Studies are over for now…but the journey of life is only taking a turn into a new road……”*

Abstract

The challenges in managing localised corrosion failures in oilfields are large. In environments containing both CO_2 and H_2S gas, pitting corrosion of carbon steel is considered to be a common occurrence and particularly complex. The consequences of pitting corrosion failures are usually severe in terms of the health and safety or the environment as well as economic cost to the operators.

The actual mechanisms and sequence of electrochemical activities for pitting corrosion in these environments is still not fully understood. The film formation characteristics and morphology in CO_2 and H_2S-containing systems are also known to influence the general and pitting corrosion behavior of carbon steel. However, questions still remain as to how different oilfield process parameters such as temperature, chloride ion concentration, in-situ pH of corrosion environment and the combined presence of CO_2 and H_2S gas could be influencing the corrosion kinetics and pitting corrosion process; pit initiation and pit propagation of carbon steel materials exposed to oilfield corrosion environments.

A comprehensive and systematic investigation of the pitting corrosion behaviour of X65 carbon steel in sweet and sour corrosion environment has been carried out using a combination of electrochemical techniques and a robust set of post-experiment surface analysis techniques. The results confirms the notion that pitting corrosion process of carbon steel is very different from pitting corrosion in passive alloys and that the evolution of pitting corrosion of active materials in sweet and sour corrosion environments is governed by; the uniform corrosion contribution, the local environments; corrosion products and active ionic species and environmental parameters.

In sour corrosion environments, pitting corrosion characterisation using the NPFLEX 3D interferometer and extensive analysis of corrosion product morphologies using the transmission electron microscope was able to show that FeS corrosion product formation occurs faster than $FeCO_3$ in H_2S-CO_2-containing corrosion system leading to pit initiation and also that in scenarios where competitive precipitation of $FeCO_3$ and FeS is likely, the risk of pitting corrosion is increased.

Table of contents

List of figures

List of tables

Chapter 1. Introduction

Corrosion of materials is an inevitable process that completes a natural cycle for thermodynamically unstable metals. These metals become thermodynamically unstable by virtue of the extractive metallurgical processes employed to separate the pure metals from their ore [1]. Metal deterioration by corrosion is a consequence of an electrochemical interaction between these unstable metals, and their environments in a system of electron and charge transfer via an electrical circuit model [1, 2]. Since the requisite for electrochemical interaction between metals and their environment is a readily available electron sink to complete the circuit of charge transfer process from metals to their environment, it can therefore be inferred that electrochemical deterioration of metals in oilfield environments is driven by a combination of the thermodynamic instability of substrate metal and the nature and chemical potential of electrochemically active species that are ever present in oilfields [3, 4].

1.1 The cost of corrosion

The overall impact of corrosion transcends every aspect of the industrial economic space that employs the use of one form of metallic component or the other. On a general note and for clearer perspective, the annual cost of corrosion has been put globally at 3-4% of total Gross Domestic Product (GDP) of industrialised nations (about $1.8 trillion) [5]. According to the 2002 cost of corrosion study by Gerhardus et.al [6] (on behalf of the US Federal Highway Administration (FHWA)), the total annual cost of corrosion to a $8.79 trillion US economy is about $276 billion or 3.1% of her GDP [5, 6] and was expected to have exceed an initially forecasted total cost of $1.00 trillion by 2013 [7]. The annual cost of corrosion to US oil and gas exploration and production operations was also put at $1.4 billion (about 8% of total cost of corrosion in production and manufacturing sector of the US economy) [6]. This is as shown in Figure 1-1.

Corrosion is always going to be an ever present problem of the oil and gas industry. However, unlike the impacts of natural disasters, the consequences of corrosion can be significantly managed, but at a cost. Such costs would be incurred through the development and effective application of innovative technologies, engaging industry best practices when applying long-proven technologies, understanding the science and prevention of corrosion through worldwide knowledge sharing mechanisms between individuals and professional societies. Appreciation of the role of research and development (R&D) in areas such as materials development and selection, innovative surface protection systems, and condition based monitoring using sensors

and remote data collection methods could be a worthy investment. Optimal harmonization of these strategies could significantly help reduce the cost of corrosion by up to 25-30% of the total annual cost of corrosion in the U.S economy alone according to Schmitt *et al* [5] and Gerhardus *et al* [6].

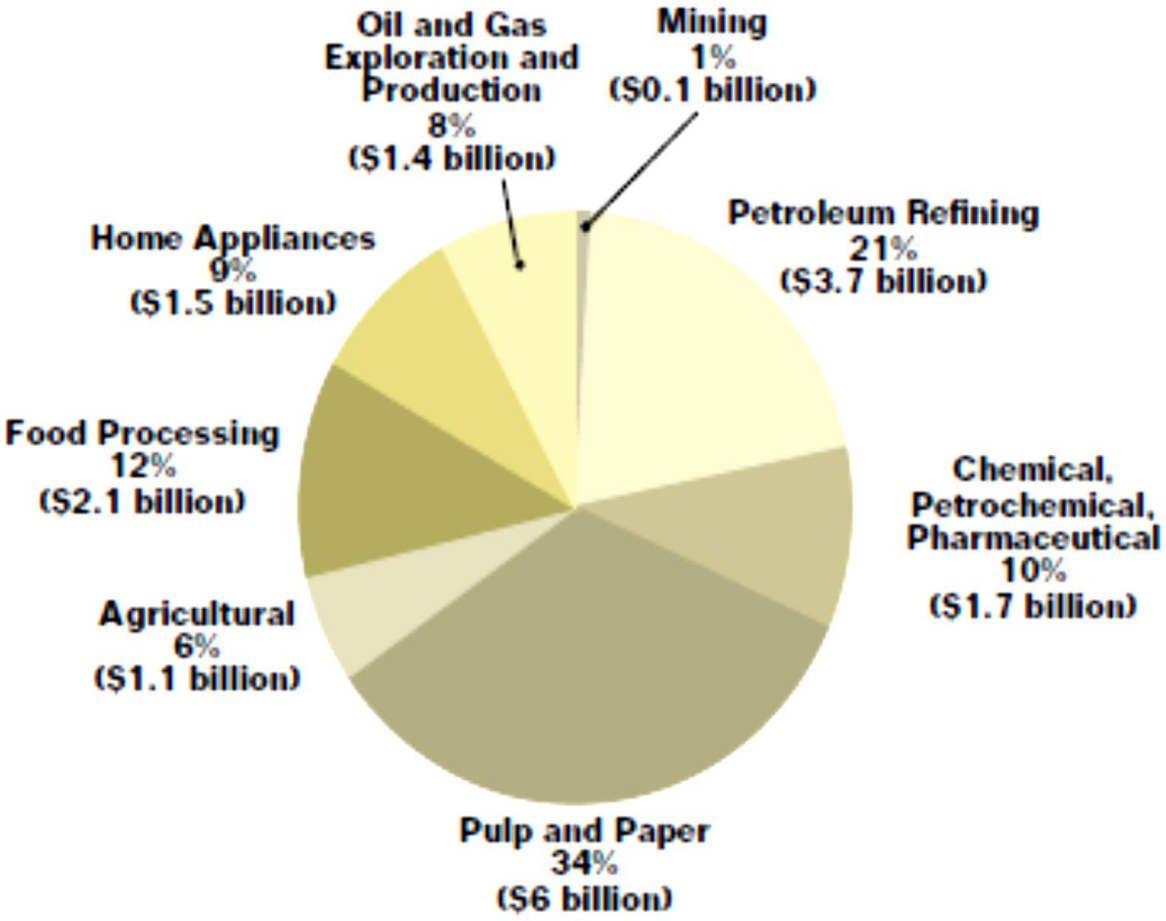

Figure 1-1 A breakdown of annual cost of corrosion in production and manufacturing sector of the US economy [6].

1.2 The problem of oilfield corrosion

In the oil and gas industry, corrosion-related failures have been reported to constitute over 25% of total safety incidents [8, 9]. The problem of corrosion in oilfield environments is predominantly associated with the presence of dissolved acidic gases in reservoir brine; CO_2 (sweet corrosion) and H_2S (sour corrosion) gases, other associated reservoir constituents and some as-manufactured defects on metallic components [3, 9-14]. A statistical breakdown of oilfield corrosion related failures are shown in Table 1-1.

Table 1-1 Cause of corrosion-related failure in petroleum-related industries [8]

Type of failure	Total failure (%)
CO_2 related	28
H_2S related	18
Preferential weld	18
Pitting	12
Erosion corrosion	9
Galvanic	6
Crevice	3
Impingement	3
Stress corrosion	3

The impacts of oilfield corrosion-related failures are often relatively wide, ranging from;

- Unfavourable economics of oil and gas production such as effects on capital expenditures (CAPEX) and operating expenditures (OPEX). CAPEX involves costs incurred at the project design stage, representing additional capital outlay on preventing, minimising, or controlling corrosion in comparison to the expenditure that would have been required if corrosion did not exist.
- Loss of oilfield facility integrity
- Loss production and loss containment
- Challenging and difficult conditions of operation
- Health and Safety and Environment (HSE) constraints and the adverse ripple effects on the overall survival of the ecosystem [8, 9, 15-17].

The above-mentioned impacts and risks of oilfield corrosion failures are currently being aggravated in oil and gas production environments by the constraints of increased pressures on production, aging of oilfields [18], increase in the price of oil and gas, increased search and shift of oilfield production environment to harsher conditions of high temperature and pressures, increased H_2S content and reservoir souring. Reservoir souring is usually related to enhanced microbial activities (SRB's) during sea-water re-injection operations [4, 9, 13, 19-26]. Carbon steel remains a widely used material for pipelines used for transportation of oilfield produced

fluids (oil, gas, and water, CO_2, H_2S and other associated reservoir constituents) over hundreds of kilometres in length from offshore platforms to onshore refineries as shown in Figure 1-2

Carbon steel materials are commonly the preferred choice because they are relatively cheap [9]. However, this becomes a significant factor with respect to the risk of corrosion because of the poor corrosion resistance carbon steel materials. This is mainly because they are readily available in volumes required and with well-developed technologies to ease the challenge of tailoring these materials to meet many of the mechanical, structural, and fabrication requirements [9].

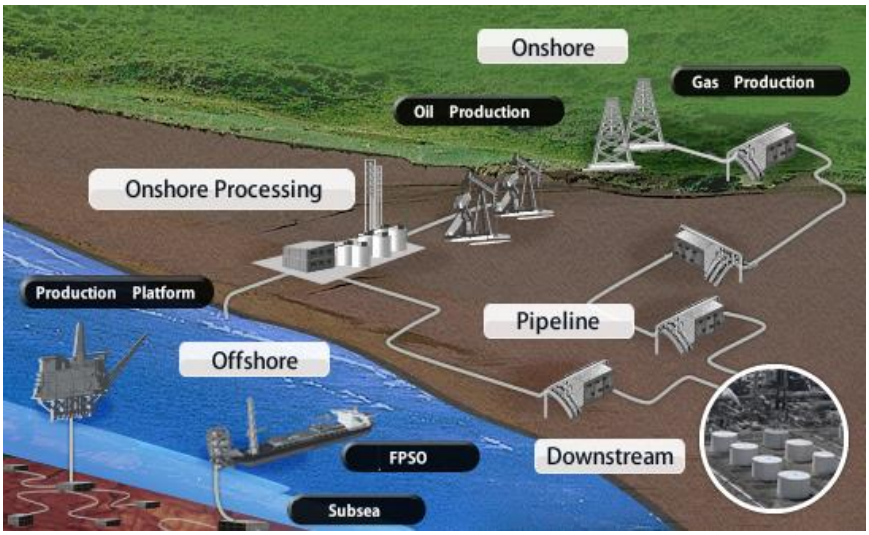

Figure 1-2 Schematic illustration of carbon steel pipeline used for transporting oilfield produced fluids from offshore platform to onshore refining facilities

1.3 Sweet and sour corrosion in the oilfield environment

The current scenarios of corrosion in oilfields is such that a complex material degradation mechanism of pipeline steel is currently being manifested by an operation environment containing both CO_2 and H_2S gases dissolved in reservoir brine [27]. A reservoir that is formally saturated with just CO_2 gas and dominated by CO_2 corrosion may likely contain increasing amount of H_2S gas with aging especially with the enhanced microbial activities of sulphate reducing bacteria (SRB) during the process of enhanced oil recovery and with the use of water injection [28]. Hence, the need to define the boundaries between CO_2 and H_2S dominated reservoirs. The term sweet corrosion is often used to describe oilfield environments containing either 100% CO_2 or an insignificant amount of H_2S gas, such that the corrosion reaction process is controlled by the formation of carbonic acid (H_2CO_3). The term "sour service condition" has often been used to describe oilfield environment containing H_2S gas beyond a

pre-defined threshold and in variable ratio with CO_2 gas [9, 27, 29]. In this case, the corrosion reaction is influenced by the formation of carbonic acid and aqueous hydrogen sulphide (from the dissolution of CO_2 and H_2S gases respectively). The corrosion damage mechanisms often experienced in oilfields are dominated by, but not limited to general and localised corrosion or pitting [15, 30-32]. Localised corrosion or pitting is usually associated with presence of both CO_2 and H_2S gas. However, this type of corrosion attack in both pure CO_2 and CO_2-H_2S saturated environment is such that it is strongly influenced by the presence of both CO_2 and H_2S gas in oilfield production environments. These modes of corrosion failure are presently of significant concern to the oil and gas industry as well as the research community. This is because it is difficult to predict the dominant nature and risks of the related failures (especially in carbon steels) and the fact that there is still no clear fundamental understanding of localised/pitting corrosion mechanisms of carbon steels in both CO_2 and H_2S-containing conditions.

1.4 Statement of research problem

Sweet and sour corrosion conditions in oilfield environments are often characterised by the relative concentration of H_2S and CO_2 gas in the reservoir. A significant concentration of H_2S gas and in combination with CO_2 gas in the reservoir [14, 22, 28], especially at relatively low to moderate concentrations ($0.3kPa \approx 0.05psia$) of H_2S [28] is usually considered as sour (according to the NACE MR0175/ISO 15156 standard). The morphologies of localised pitting of carbon steels in CO_2 and CO_2-H_2S containing systems is considered complex because of the insidious manifestation of pitting corrosion and the combined electrochemical activities of H_2S and CO_2 dissolved gases. Hence, carbon steel components are likely to be predisposed to variable forms of corrosion damage (most commonly uniform and localised/pitting corrosion) in sweet and sour oilfield service conditions. Some of the established challenges related to localised/pitting corrosion of carbon steel in "sweet" and "sour" service conditions are associated with the following;

- The mechanisms of localised corrosion of carbon steel in CO2 and H2S environment is not clearly understood
- The aforementioned complexity in the nature of localised corrosion is also dependent on a wide range of physical and environmental factors.
- The likely transition from general to localised corrosion.
- The protectiveness of iron carbonate

- The influence of the complex kinetics and composition of corrosion products ($FeCO_3$, FeS) deposited on pipeline steel in H_2S/CO_2 systems [33, 34].
- The kinetics of iron sulphide formation,
- The complex chemistry and protectiveness of iron sulphides

1.5 Pitting corrosion of carbon steel in sweet and sour conditions

It has been suggested that localised or pitting corrosion of carbon steel in CO_2 and CO_2-H_2S containing environments is often related to the formation of, and/or breakdown of (non-protective and protective respectively) $FeCO_3$ films and formation of semi-protective iron sulphide (Fe_xS_y) film respectively. It has been hypothesised that localised or pitting corrosion in CO_2 and CO_2-H_2S containing environments occurs in a similar frame to the classical pitting corrosion defined by Papavinasam *et al* [33] as; *"formation of a passive film on the metal surface, initiation of pits at localised regions on the metal surface where film breakdown occurs, followed by pit initiation and propagation and eventual failure".* While $FeCO_3$ is the main corrosion products formed in sweet (CO_2) corrosion environments, Fe_xS_y films forms in sour corrosion environments along with $FeCO_3$ for a CO_2-H_2S gas system. Fe_xS_y films formed in sour environment could take complex and different thermodynamic forms which are dependent on H_2S concentration, *in-situ* pH, temperature and exposure time. It has also been suggested that the kinetics and severity of pitting corrosion in sour conditions could be controlled by the nature of corrosion product film ($FeS/FeCO_3$) in terms of its chemistry and morphology [18, 34-37].

During corrosion reactions of carbon steel in sweet environments, the localised breakdown of protective iron carbonate film ($FeCO_3$) [33, 38] and/or the non-uniform deposition of iron carbonate film ($FeCO_3$) or formation of a non-protective form of iron carbonate film ($FeCO_3$) [38] could be the precursor to pitting corrosion. On the other hand, the intrinsic transition from one thermodynamic state from one form of Fe_xS_y corrosion product to other forms of Fe_xS_y could be causing film rupture and breakdown in H_2S containing environment [18, 34, 39]. Iron sulphide film rupture and/or breakdown of $FeCO_3$ film may be occurring along with the tendency for chloride ions to undermine the integrity of corrosion product films and promote localised areas for pit initiation and propagation [40, 41]. In addition to these envisaged aspects of sweet and sour corrosion, is a great deal about this subject that is not known to the oil and gas industry and research community. For example, there are currently no generally accepted prediction algorithms for any form of H_2S corrosion, as well as pitting corrosion in CO_2 and CO_2-H_2S containing environments. There exist a number of unknowns about the corrosion

reaction mechanisms that may lead to metal degradation and pitting (especially in H_2S containing environments). There is also the lack of in-depth understanding of iron sulphide evolution from one thermodynamic state to another and influences the mechanisms of pit initiation and propagation. The role of the constituent acidic gases (CO_2 and H_2S) as well as the associated corrosion products on localised or pitting corrosion mechanisms of pipeline steel is yet to be established, the impact of changing temperature, *in-situ* pH and chloride ion on pitting corrosion in both sweet and sour corrosion environments is also yet to be established, as well as unanswered questions regarding the role of $FeCO_3$ precipitation kinetics and FeS corrosion film breakdown as a precursor for pit initiation in both sweet and sour environments. There is still only little knowledge of the contribution of galvanic effects from corrosion products and electronically conductive FeS films to pit growth, during localised corrosion/pitting of carbon steel [24, 39, 42].

1.6 Objectives and scope of research

This research aims to provide an in-depth scientific understanding of localised/pitting corrosion of carbon steel materials in both sweet and sour service conditions. This is done by conducting a careful and systematic parametric study which integrates electrochemical measurements and advanced surface analysis.

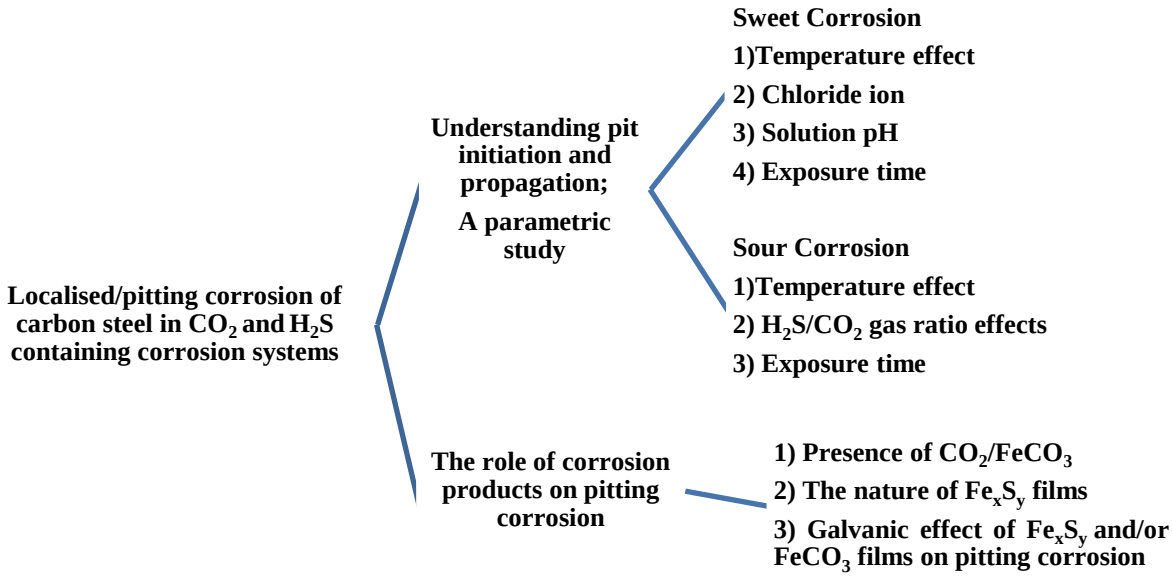

Figure 1-3 A summary of the scope of this research project

This research work also aims to address some of the unanswered questions related to H_2S-induced corrosion failures currently encountered in the oil and gas industry. Figure 1-3 shows a breakdown of the scope of this research project that would help towards improving the

fundamental understanding of localised or pitting corrosion in CO_2 and CO_2-H_2S containing environments. This aims to provide useful real-time experimental data for empirical calibration of existing corrosion prediction models for both sweet and sour corrosion and subsequently aiding accurate prediction of probability and consequences of H_2S/CO_2 corrosion related failures in oilfields.

The scope of this research work will focus on achieving the following objectives;

1. **To improve the understanding of pit initiation and pit propagation;** this is aimed at unravelling useful information about localised/pitting corrosion of carbon steel materials in a both CO_2 and CO_2-H_2S containing environments using a robust corrosion damage characterisation framework. This will be based on a parametric study that explores key factors such as temperature, H_2S/CO_2 and H_2S/N_2 gas mixtures, chloride ion content, *in-situ* pH of the bulk solution as well as exposure time. This part of the research work will also look to explore how these parameters will independently or synergistically influence the nature and chemistry of corrosion products in CO_2 and CO_2-H_2S containing systems.
2. **To investigate the role of corrosion products;** the aim is to explore the role of $FeCO_3$ and the mutual roles of $FeCO_3/Fe_xS_y$ corrosion products on pit initiation and propagation in sweet and sour corrosion environments. This will include establishing the effect of the difference in the kinetics of $FeCO_3/Fe_xS_y$ deposition on localised or pitting corrosion of carbon steel in H_2S/CO_2 containing environments.
3. **To establish the galvanic effect of iron sulphides and/or $FeCO_3$ films,** on overall pitting corrosion of substrate metal. This includes establishing the role of $FeCO_3$ and $FeCO_3/Fe_xS_y$ or Fe_xS_y on pit growth rate.

As a long-term objective of this study is the drive towards developing a comprehensive understanding with a mechanistic viewpoint with respect to pitting corrosion in sweet and sour service conditions. This objective is inspired by the need to accurately predict the probability and consequences of corrosion failures associated with pitting in sweet and sour oilfield environments as a function of process parameters.

1.7 Outline of thesis

The thesis is presented in 12 chapters

Chapter 2 discusses some of the key theories of electrochemistry and corrosion reactions, some aspects of the kinetics and thermodynamics of corrosion process that are relevant for a strong appreciation of the corrosion behavior of a metal substrate in contact with an active

environment. There is also a brief discussion of the forms of corrosion with emphasis on localised and pitting corrosion.

Chapter 3 discusses a review of relevant literature on corrosion in sweet environments. The reviews are related to the mechanism of sweet corrosion, the most common forms of corrosion damages with emphasis on localised corrosion, the kinetics and thermodynamics of iron carbonate corrosion product formation, the effect of operating parameters on corrosion of carbon steel in sweet environments, and a summary of current research status with a focus on pitting corrosion.

Chapter 4 discusses a review of relevant literature on corrosion in sour environments. The reviews are related to the mechanism of sour corrosion, the nature of sour corrosion damages with emphasis on pitting corrosion, the kinetics and thermodynamics of iron sulphide corrosion product formation, the effect of operating parameters on corrosion of carbon steel in sour environments, and a summary of current research status with a focus on pitting corrosion in sour corrosion environment.

Chapter 5 describes the test set-up for sweet and sour corrosion testing, designs for bubble cell and test sample holder, sample preparation, details of experiment conditions and materials, electrochemical techniques and post-experiment surface analysis techniques used in this project. Health and safety measures put in place and a comprehensive sour corrosion test protocol are also discussed.

Chapter 6 describes presents and describes the experimental results from pitting corrosion studies of carbon steel in CO_2 corrosion environment. The focus of this study is on the effect of temperature The concept of total metal penetration for characterising pitting corrosion damage is also applied and discussed in this chapter, as well as the relevant post-experiment analysis employed.

Chapter 7 describes presents and describes the experimental results from pitting corrosion studies of carbon steel in CO_2 corrosion environment. The focus of this study is on the effect of ionic strength/chloride ion concentration as part of the ionic component of the corrosion environment on iron carbonate corrosion product formation but with emphasis on pit initiation and propagation. The synergy between chloride ion and temperature on localised or pitting corrosion; pit initiation and propagation is discussed in this chapter.

Chapter 8 describes presents and describes the experimental results from pitting corrosion studies of carbon steel in CO_2 corrosion environment. The focus of this study is on the effect of pH of the corrosion environment on iron carbonate corrosion product formation but with emphasis on pit initiation and propagation.

Chapter 9 describes the experimental results from pitting corrosion studies focused on the early stages of corrosion of carbon steel in sour corrosion environment. This section discusses sour corrosion kinetics, the formation of iron sulphide films and pitting corrosion initiation in an un-buffered sour corrosion environment. Emphasis will be placed on the effect of temperature and acid gas composition. There will also be detailed discussion of the pitting corrosion initiation mechanisms as influenced by temperature and H_2S/CO_2 gas composition as well as the distinct roles of $FeCO_3$ and or Fe_xS_y corrosion product layer.

Chapter 10 describes the experimental results from pitting corrosion studies focused on the long-term corrosion behaviour of carbon steel in sour corrosion environment. This discusses sour corrosion kinetics, the formation of iron sulphide films and pitting corrosion process in an un-buffered sour corrosion environment. Emphasis will be placed on the effect of temperature and acid gas composition. There will also be detailed discussion of the pitting corrosion mechanisms as influenced by temperature and H_2S/CO_2 gas composition as well as the distinct roles of $FeCO_3$ and or Fe_xS_y corrosion product layer.

Chapter 11 presents a summarised discussion on the experimental results and the key findings described in chapter 6, and 7 with the backing of the literature and with emphasis on the relevance of this study. The main sections of this chapter will based on the effect of operating parameters; temperature, chloride ion concentration and *in-situ* pH on pitting corrosion in sweet environments, and the effect of temperature and H_2S/CO_2 gas combination on pitting corrosion of carbon steel in H_2S containing environment.

Chapter 12 presents the conclusions derived from this study with emphasis on the contribution of this work to the knowledge base of the research community. This chapter also highlights the industrial application of this work, with mention of possible future study for a better understanding of this subject area.

Chapter 2. Fundamental theory of corrosion and oilfield corrosion

This chapter presents some of the key theories and scientific concepts that govern electrochemical corrosion reactions, with emphasis on the thermodynamics and kinetic aspects of corrosion of metallic substrates. Relevant electrochemistry techniques that help to provide a strong appreciation and clear interpretation of the corrosion behaviour of materials are also discussed in this chapter. Finally, this chapter introduces some concepts on corrosion in oilfield environments.

2.1 Thermodynamics and kinetics of corrosion

The scientific theories that govern the thermodynamic aspects of corrosion are usually related to the energy flow and energy balance in an electrochemical system. The flow of energy and energy balance defines the spontaneity for the corrosion reactions to occurs, while the kinetics of corrosion is related to the rate at which corrosion reactions and substrate metal degradation occurs. The most relevant of these scientific concepts and theories with respect to electrochemical corrosion of material include;

- Electrical Double Layer (EDL) and corrosion
- Free energy of corrosion reactions and relationship to Nernst equation
- Electrochemical cell and electrode potential
- Open circuit potential
- Polarisation and corrosion kinetics
- Corrosion kinetics; Electrical double layer/Over-potential/corrosion current relationship
- Linear Polarisation Resistance (LPR)
- Tafel polarisation
- Electrochemical Impedance Spectroscopy (EIS)
- Galvanic cell and galvanic corrosion

These are briefly described in the following sections.

2.1.1 Electrical Double Layer (EDL) and corrosion

Once a metal comes in contact with an electrochemically active environment (usually an electrolyte), an electrochemical corrosion cell is created that involves transfer of charge. The EDL is a phenomenon that occurs in an electrochemical environment as a state of redox equilibrium in charge transfer as metals lose electrons to a suitable electrolyte. This is attained

after an initial loss of electrons from the lattice structure of a metal, leaving the near surface with a residual negative charge. The metal surface forms an electrostatic field of hydrated positively charged cations held to the negatively polar ends of H_2O molecules from the electrolyte by an electrostatic force of attraction between counter-ions. This tends to shield the charged metal surface, manifesting as an ionic structure held in an electronic balance by electrostatic attraction with the solvated cations at the near surface of the metal. The hydrated positively charged cations are also in electrostatic attraction with the negatively charged end of polar H_2O molecules but with the tendency to diffuse away by a repulsive force. This electronic charge transfer equilibrium acts to prevent further dissolution of metal provided there are no other complex reactions taking place and no external electrical current are allowed into the system to control the kinetics of electrochemical activity at the surface.

However, the presence of other chemically active species like CO_3^{2-} from dissolved CO_2, HS^- from dissolved H_2S, etc, would act to distort such equilibrium and enhances loss of ions from the metal in an attempt to attain prior state of charge transfer equilibrium. This causes metal to continuously lose electrons and becoming the natural driving force for electrochemical corrosion processes to proceed unhindered. This is shown schematically in Figure 2-1[43, 44]

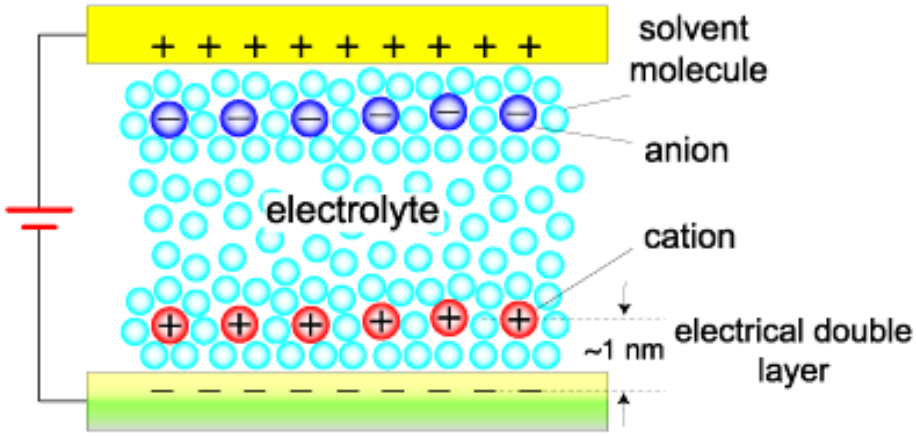

Figure 2-1 A simplified schematic representation of the Electrical Double Layer (EDL)

2.1.2 Free energy of corrosion reactions and the Nernst equation

In the EDL scenario described, there is a relative tendency for transfer of ions (within electrolyte) or electrons through metal from the metal/electrolyte-solution system in the direction of either the electrolyte phase or the metal lattice. This behaviour is however dependent on the electrochemical free energy often defined as the Gibb's free energy per unit ion or simply the activation energy. Therefore, at the state of charge transfer equilibrium as

inferred from the EDL analogy, the first law of thermodynamics can be used to describe this state of equilibrium in terms of the Gibbs free energy ($\Delta G_{Reaction}$) and number of charge transferred ($-nFE_{Cell}$) [43, 45], and it states that;

"At equilibrium, the Gibb's free energy or electrochemical free energy, which is the driving force for the transfer of electrons from the metal to the solution, is exactly balanced by the electrochemical potential difference which is the driving force for attracting the ions back to the metal crystals"

Mathematically,

$$\Delta \boldsymbol{G}^{\circ} = -\boldsymbol{nFE}^{\circ}_{\boldsymbol{Cell}} \quad 2.1$$

Hence, the following could be deduced as the thermodynamic conditions for electrochemical corrosion to occur:

If E_{cell} *is* > 0, *then* $\Delta G_{reaction} < 0$ *and loss of ions and corrosion becomes spontaneous.*

If E_{cell} *is* < 0, *then* $\Delta G_{reaction} > 0$ *and the loss of electron and corrosion becomes non-spontaneous[45]*

The Vant Hoff's reaction isotherm gives the relationship between Gibb's free energy and the concentration of chemically active species of the electrolyte at constant temperature as,

$$\boldsymbol{G} = \Delta \boldsymbol{G}^{\circ} + \boldsymbol{RTlnQ} \quad 2.2 \text{ [46]}$$

Where Q is the activity quotient corresponding to the Gibb's free energy change of the system,

R is universal gas constant, given as 8.31451 J K^{-1} mol^{-1} or 8.31451 x 10^{-2} L $barK^{-1}$ mol^{-1}

ΔG° is the equilibrium free energy change. $\Delta \boldsymbol{G}^{\circ} = -\boldsymbol{nFE}^{\circ}_{\boldsymbol{Cell}}$

ΔG is the free energy change for the system. $\Delta \boldsymbol{G} = -\boldsymbol{nFE}_{\boldsymbol{Cell}}$

Further simplification gives

$$\boldsymbol{E}_{\boldsymbol{Cell}} = \boldsymbol{E}^{\circ}_{\boldsymbol{Cell}} - \frac{\boldsymbol{RTlnQ}}{\boldsymbol{nF}} \quad 2.3$$

Eq. 2.3 is known as the **Nernst Equation.**

Thus, for a corrosion process described by the redox reaction $\boldsymbol{Fe + M^{2+} \rightarrow Fe^{2+} + M}$

$$\boldsymbol{Q = \frac{[Fe^{2+}]\,[M]}{[Fe]\,[M^{2+}]}} \qquad 2.4$$

And $F = 96500$ (Colombes/mole of electrons) (From Eq. 2.1) is known as Faraday's constant.

Finally, the Nernst equation is written as;

$$\boldsymbol{E_{Cell} = E^{\circ}_{Cell} - \frac{RTln}{nF}\frac{[Fe^{2+}]\,[M]}{[Fe]\,[M^{2+}]}} \qquad 2.5 \text{ [44, 45]}$$

Where, $\left|-\frac{RTln}{nF}\frac{[Fe^{2+}]\,[M]}{[Fe]\,[M^{2+}]}\right|$ = is the magnitude of deviation from equilibrium redox state.

2.1.3 Electrochemical cell and electrode Potential

The corrosion interaction of metals with an electrochemically active environment can simply be modelled as an electrochemical cell composed of two electrodes each of different half cells reactions interacting across a conducting electrolyte. The half cells are described as oxidation and reduction half cells. Oxidation half cells occurs at anodic sites and involves the loss of electrons from the substrate metal to electrochemically active species in the electrolyte, while reduction half cells involve the build-up or gain of electrons and occurs at the cathodic sites. As an example; for the corrosion of steel (Fe) in any environment, these reactions could be represented as:

Oxidation Half-cell reaction ***(Anodic)****;* $Fe \rightarrow Fe^{2+} + 2e^{-}$

Reduction Half-cell reaction ***(Cathodic)****;* $M^{2+} + 2e^{-} \rightarrow M$

Where M denotes anions from any corrosion media undergoing reduction reaction [45].

Electrode potential is the potential difference or energy per unit charge of an electrode in electrical contact with an electrolyte. It is usually designated as E and is measured relative to reference electrodes e.g., Standard Hydrogen Electrode (S.H.E) [44, 45].

2.1.4 Open circuit potential (OCP)

Open circuit potential (OCP) is the measured natural electrode potential difference between the two electrodes half-cells of an electrochemical cell. It is the potential of an electrode relative to

the reference standard electrode when no potential or current driving force is being applied to the cell. It is the potential that defines a state of redox equilibrium between electrodes in electrical contact with an electrolyte. It is often termed the free corrosion potential of a metal [43, 47].

2.1.5 Polarisation and corrosion kinetics

The concept of polarisation is strongly related to the kinetics of electrochemical corrosion. It is an electrochemical phenomenon that measures the deviation from equilibrium electrode reaction (see Eq. 2.5) of a corrosion cell by the passage of electric current, to induce a change in electrode potential E_{Cell} from equilibrium (E°_{Cell}). The magnitude of deviation in electrode potential difference from equilibrium condition is termed as over-potential and is employed to drive corrosion reactions. There are three types of polarisation phenomenon occurring independently or simultaneously when a metal substrate interact with its environment; activation polarisation (η_{Act}), describes charge transfer controlled kinetics of corrosion of a substrate metal, concentration polarisation (η_{Conc}) describes mass transfer limitation to corrosion kinetics, and resistance polarisation (iR), describes the ohmic or potential drop due to either the high resistivity of the electrolyte surrounding the electrode or an insulation effect of the film on the electrode surface formed by the reaction products [43-45]. Thus, the total polarization that influences the kinetics of corrosion is given as;

$$\boldsymbol{Total\ polarisation\ (\eta_{Total}) = \eta_{Act} + \eta_{Conc} + iR} \qquad 2.6\ [2]$$

In the course of this work, linear polarisation and Tafel polarization techniques will be explored [47]. These techniques can only be fully appreciated by establishing the relationship between the redox equilibrium, over-potential and corrosion rate of metals in an electrochemically active environment. This is briefly discussed in subsequent sections.

2.1.6 Corrosion kinetics; electrical double layer/over-potential/corrosion current relationship

As discussed in section 2.1.1, the EDL represents a state of redox equilibrium. At this state, the rate of anodic reaction equals the rate of cathodic reaction. Hence, according to the Nernst equation (Eq. 2.5), a more negative electrode potential than the equilibrium potential implies a thermodynamic tendency for cathodic half-cell reaction to occur spontaneously, creating a negative over-potential ($E - E_{redox}$). The anodic reaction will be thermodynamically favoured

by a positive over-potential ($E - E_{redox}$) due to a more positive electrode potential. From the foregoing, it can be implied that the rate of corrosion reaction is the result of a distortion of redox equilibrium at the EDL due to either induced over-potential or the presence of more chemically active species at the metal-electrolyte interface. The resulting deviation is measured in terms of a net current density (i_{net}), defined as the difference between current density due to anodic (i_{ox}) and cathodic(i_{red}) processes [43, 47]. (i_{ox}) and (i_{red}) are both dependent on over-potential ($E - E_{redox}$) and exchange current density (i_o) according to Eqns. 2.7 and 2.8.

$$i_{ox} = i_o e^{[\alpha_a nF((E-E_{redox})/RT)]} \quad 2.7$$

$$i_{red} = i_o e^{[\alpha_c nF((E-E_{redox})/RT)]} \quad 2.8$$

If at equilibrium, $i_{ox} - i_{red} = 0$

Therefore for a single non-equilibrium charge transfer controlled redox reaction,

$$i_{net} = i_{ox} - i_{red} = \quad 2.9 \text{ [47]}$$

$$i_o e^{[\alpha_a nF((E-E_{redox})/RT)]} - i_o e^{[\alpha_c nF((E-E_{redox})/RT)]}$$

This is known as the Butler-Volmer equation for electrochemical corrosion kinetics. α represents charge or ion transfer coefficient. Eq. 2.9 is the current density measured during a polarisation experiment involving unit charge transfer controlled anodic and cathodic reaction and can be re-written as;

$$i_{net} = i_{corr} e^{[\alpha_a nF((E-E_{corr})/RT)]} - i_{corr} e^{[\alpha_c nF((E-E_{corr})/RT)]} \quad 2.10$$

i_{corr} and E_{corr} represents the corrosion rate and free corroding potential at equilibrium without any external current. The electrochemical implication of Eq. 2.10 is illustrated in Figure 2-2.

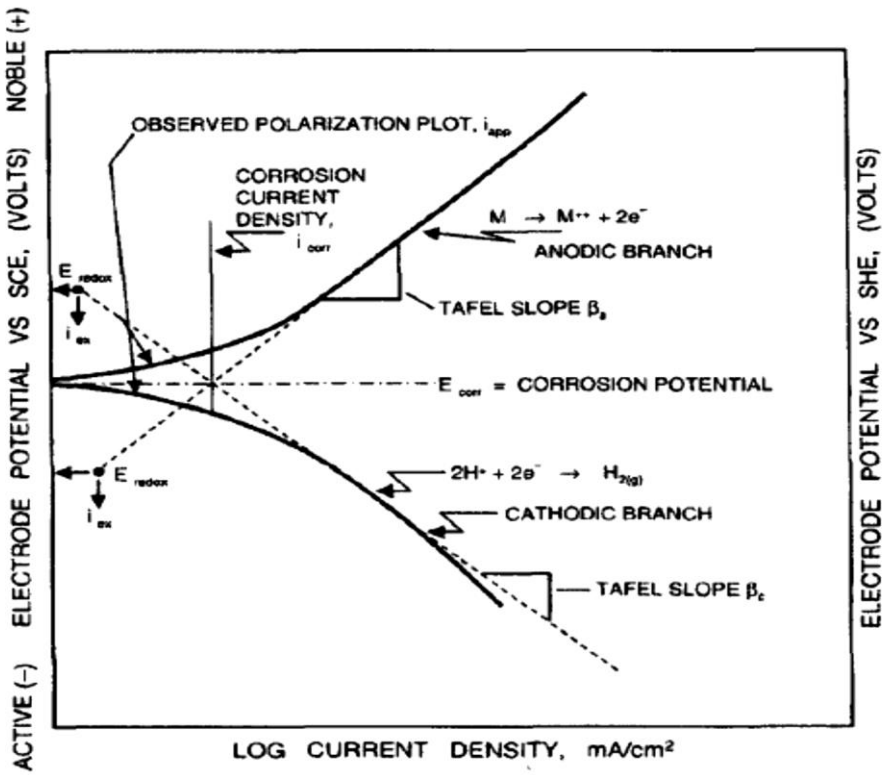

Figure 2-2 Application of the mixed potential theory showing the potential-current density relationship for a corroding system consisting of a single charge transfer controlled anodic and cathodic reactions[47].

During polarisation experiments, the redox equilibrium is distorted and this also affects the capacitive tendency of the EDL at the interface such that the modified Butler-Volmer equation changes from;

$$i_{net} = i_{corr} 2.030n(E - E_{redox}) \left[\frac{\alpha_a F}{RT} - \frac{\alpha_c F}{RT}\right] \quad 2.11$$

to;

$$= i_{net} = i_{corr} 2.030n(E - E_{redox}) \left[\frac{\alpha_a F}{RT} - \frac{\alpha_c F}{RT}\right] + C\frac{\partial E}{\partial t} \quad 2.12$$

Where n is the number of transferred electrons, while $C\ and \frac{\partial E}{\partial t}$ represent the interfacial capacitance associated with the EDL and the scan rate of applied over-potential during polarisation experiments respectively. Application of the polarisation techniques are discussed in the sections 2.1.7 and 2.1.8.

2.1.7 Tafel polarisation

Tafel polarisation is an electrochemical technique that logs non-equilibrium potential and current response of a corrosion cell in a potential-current plot. The current response is usually

plotted on a logarithm scale. Tafel polarisation technique is usually applied for understanding the anodic and cathodic behaviour of a substrate metal in contact with a corrosive environment. Tafel polarisation technique is also used to estimate the Tafel slopes ($\beta_a \; and \; \beta_c$) (shown in Figure. 2.2) by polarising a working electrode (substrate metal) in both the anodic and cathodic direction within an over-potential range of ± 250mV about the open circuit potential of the substrate metal in an electrolyte. The Tafel (β_a and β_c) slopes represents the slopes of the anodic and cathodic reaction lines respectively and over a range of potential within which i_{net} varies linearly with $E - E_{redox}$ or $E - E_{corr}$. The over-potential range of ±5-10mV off E_{corr} [47] is considered to represent the linear regions of anodic and cathodic process, from which the Tafel slopes are estimated and used to calculate the Stern-Geary constant according to the Eq.2.13. Tafel slopes are used in this work to calculate corrosion rate and also serve as a useful tool for quickly assessing the effect of the variable experimental parameters on the corrosion process.

$$\text{Stern-Geary constant} \;\; = B = \frac{1}{2.303}\left[\frac{1}{\beta_a} - \frac{1}{\beta_c}\right]^{-1} \qquad 2.13[47].$$

2.1.8 Linear polarisation resistance

Linear polarisation technique applies very small over-potential ($E - E_{corr}$) from the open circuit potential of a corrosion system for both anodic and cathodic reaction process. The applied over-potential (ΔE) used in this technique ususally ranges up to a maximum of ±20mV about the OCP. This small over-potential represents a range upon which the Stern-Geary linear approximation of the Butler-Volmer equation (Eq. 2.9-2.12) is based and a potential-current density relationship is generated and used for evaluating the charge transfer controlled corrosion rate of the system [44, 47]. Because the primary aim of using this technique is to measure the steady state corrosion rate i_{corr} and potential E_{corr} of corrosion systems, the term $C\frac{\partial E}{\partial t}$ is assumed to approach zero at a constant voltage scan rate.

Therefore, If $\frac{\alpha_a nF}{RT} = \frac{1}{\beta_a}$ and $\frac{\alpha_c nF}{RT} = \frac{1}{\beta_c}$, the Stern-Geary linear approximation is given as;

$$i_{net} = 2.030\, i_{corr}(\Delta E)\left[\frac{1}{\beta_a} - \frac{1}{\beta_c}\right] \qquad 2.13$$

Referring to Figure 2.2, the Tafel slope for cathodic reaction is negative; therefore Eq. 2.12 is written as;

$$i_{net} = 2.030\, i_{corr}(\Delta E)\left[\frac{1}{\beta_a} + \frac{1}{\beta_c}\right] \qquad 2.14[48]$$

And $$i_{corr} = \frac{i_{net}}{2.303\Delta E}\left[\frac{1}{\beta_a} + \frac{1}{\beta_c}\right]^{-1} \quad 2.15$$

Where $\beta_a \; and \; \beta_c$ are known as Tafel constants with units in mV/decade and they are characteristics of anodic and cathodic reactions respectively.

According to ohms law, $R \equiv \frac{E}{I}$ where R is the resistance to charge transfer. Therefore for very small over-potential, such that $\boldsymbol{\Delta E \rightarrow 0}$**,** Eq. 2.15 can be written as;

$$\frac{i_{net_{\Delta E \rightarrow 0}}}{\Delta E} = \frac{1}{R_p} \quad 2.16$$

Where, R_p is the linear polarisation resistance in Ωcm^2

$i_{net_{\Delta E \rightarrow 0}} \; and \; \Delta E$ are the measured potential - current density data during polarisation experiments.

i_{corr} is the desired corrosion rate,

And Stern-Geary co-efficient is already defined in Eq. 2.13

Therefore,

$$i_{corr} = \frac{1}{2.303R_p}\left[\frac{1}{\beta_a} + \frac{1}{\beta_c}\right]^{-1} = \frac{B}{R_p} \quad 2.17$$

Corrosion rate is converted to cm/s and then mm/yr by a factor of 3.17×10^{-9}. using the Faraday's relation;

$$CR(^{cm}/_{S}) = \frac{i_{corr}A_w}{nF\rho} \quad 2.18$$

CR (cm/s) is converted to CR (mm/yr.) = corrosion rate,

$n =$ no of transferred electrons

$A_w =$ Molecular weight

$\rho =$ Density of corroding metal respectively,

$F =$Faraday's constant at 96500 (Colombes/mole of electrons).

Linear polarisation technique provides a straightforward means of interpretation of corrosion rate measurements. In application, the range of over-potential is limited up to a maximum of $\pm 30mV$ about the OCP within which the $E - \log i_{net}$ plot remains significantly linear and the Stern Geary approximation remains valid. [47]

2.1.9 Electrochemical Impedance Spectroscopy (EIS)

Electrochemical Impedance Spectroscopy, also known as AC impedance is an electrochemical test technique used for characterising and defining the dynamics of a corrosion process. It exploits the concepts of measuring electrical responses to non-linear excitation in potential signal to help unravel complex non-linear corrosion process at corrosion interface (EDL) [49]. The electrochemical impedance (Z) is the resistance response of a corrosion system to an applied AC potential signal that is strongly frequency dependent. A small AC potential signal of between ~ 1-20mV over a range of frequencies from ~100,000 – 0.001 Hz is applied to create a resultant complex pseudo-linear current response [2, 47, 49]. The resulting current response is sinusoidal and usually out of phase with the potential signal by an amount (φ) and also inversely proportional to the impedance of the corrosion interface [47]. This is depicted in Figure 2-3.

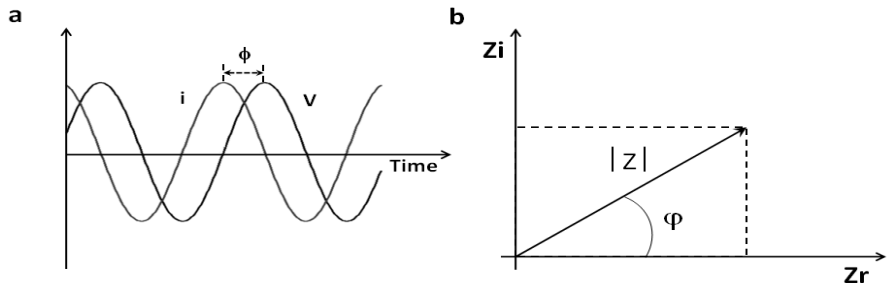

Figure 2-3 (a) Phase lag of (φ) between applied AC potential signal (V) and current response (i), (b) The real and imaginary component of measured impedance from EIS measurements.

In the classical circuit theory system, the concept of resistance is used to describe the ability of an electrical circuit to resist the flow of electrical current. It is given as;

$$R \equiv \frac{E}{I} \quad \text{(Ohm's Law)} \tag{2.19}$$

Where, R = Circuit resistance (Ohms),

E = Voltage (V) and

I = Current (A).

However, the concept of Impedance ($Z = f(\omega)$) in corrosion studies is a characteristic of the corrosion interface that takes into consideration other electrical properties; resistance and reactance (inductance, and capacitance) within the corrosion interface. The relationship between applied AC potential and current response is as follows;

The AC potential signal used in EIS is time dependent and represented mathematically as;

$$E_t = E_o \sin(\omega t) \quad 2.20$$

Where E_t the potential at time t is, E_o is the amplitude of the applied signal and ω is the radial frequency.

The current response signal I_t is shifted in phase by φ and is represented as;

$$I_t = I_o \sin(\omega t + \varphi) \quad 2.21$$

Thus the Impedance based on ohm's law that also accounts for the complex and non-linear nature of the corrosion process is obtained as follows;

$$Z(\omega) = \frac{E(\omega)}{i(\omega)} = \frac{E_t}{I_t} = \frac{E_o \sin(\omega t)}{I_o \sin(\omega t + \varphi)} \quad 2.22$$

$Z(\omega)$ is a complex-value vector with real and imaginary component and represented by the Euler's relation;

$$Z(\omega) = \frac{E(\omega)}{i(\omega)} = \frac{E_t}{I_t} = Z'(\omega) + jZ''(\omega) = Z\cos\varphi + Z\sin\varphi \quad 2.23$$

Where,

$Z'(\omega) = Z\cos\varphi$ is the real component and

$jZ''(\omega) = Z\sin\varphi$ is the imaginary component

The magnitude of electrochemical impedance $[Z(\omega)]$ is a fundamental characteristic of the corrosion system it describes. Thus, knowledge of the corrosion system enables the determination of electrical circuit model describing such systems. The non-linear electrochemical responses obtained during EIS measurements are displayed in a Nyquist format as shown in Figure 2-5 [2, 47, 49]. The Nyquist plot of Figure 2-5 represent the simple equivalent circuit model shown in Figure 2-4 for an EIS measurement of a corrosion interface (EDL) (that acts as a charge capacitor, possessing a tendency for metal to resist flow of electrons across the interface), and with an electrolyte having a solution resistance (R_S) [43, 44]. The sum of electrolyte resistance (R_S) and charge transfer resistance (R_{ct}) is equal to the magnitude of R of the semi-circle along the x-axis in Figure 2-5 [47]

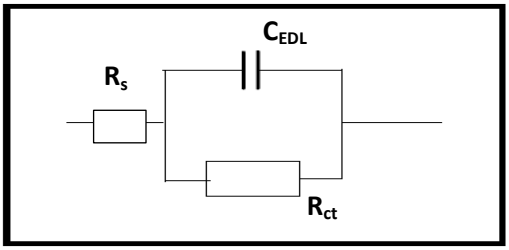

Figure 2-4 Simplified Equivalent circuit for the EDL of a corroding surface [49]

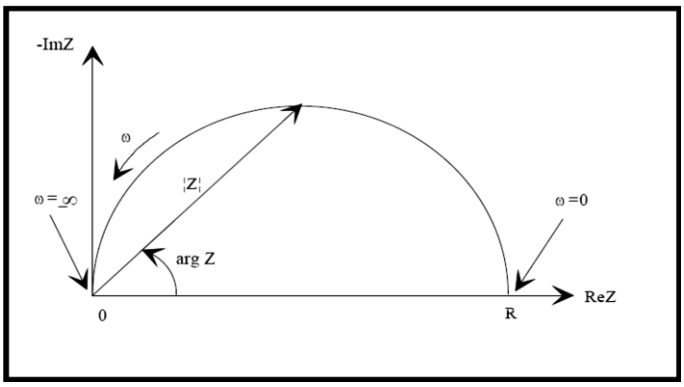

Figure 2-5 Nyquist Plot for the simple corroding surface represented in Figure 2-4[49]

2.1.10 Galvanic cell and galvanic corrosion

A Galvanic cell is an electrochemical system consisting of two metals with different electrode potentials in electrical contact with an electrolyte such that the potential difference between the two metals becomes the source of Gibb's free energy that drives the transfer of elections from one of the metal to the other [43, 45]. **Galvanic corrosion** is a type of electrochemical degradation resulting from the direct or indirect coupling of dissimilar metallic component and/or alloys, both of which are in direct contact with a common electrolyte. The consequence of this is that the rate of material loss is increased for the most electrochemically active metal in the couple while the material loss rate for the most noble metal is supressed. Galvanic corrosion occurs as a result of significant difference in the electrode potential of the two metals of the galvanic corrosion cell in contact with the electrolyte and often leads to the preferential dissolution of the material with the more negative potential [43, 47, 50].

2.1.10.1 Mixed potential theory

An attempt that aims to accurately predict and or estimate the galvanic corrosion rate of two electronically dissimilar metals in a galvanic corrosion set-up will have to take into consideration the Evans diagram of both metals. The analytical tool that enables this is called the mixed potential theory and can be shown for a zinc/Iron couple of similar surface area in an acidic media in Figure 2-6

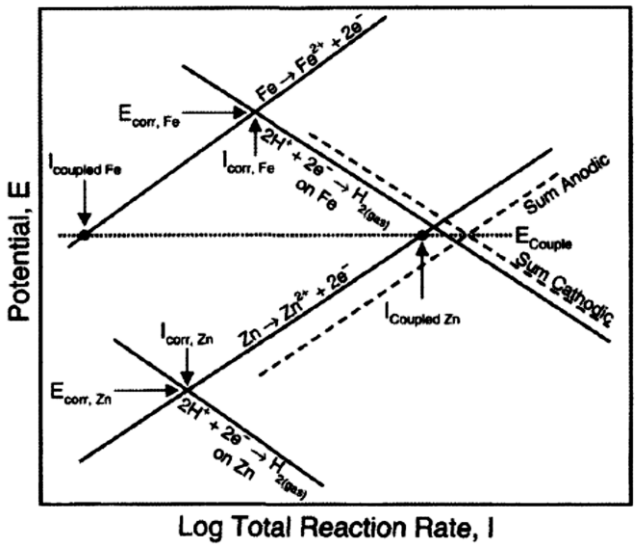

Figure 2-6 Potential-current relationship for a the case of a galvanic couple between iron and zinc [47]

Zinc (with the more negative potential $E_{cor,\ Zn}$) will corrode uncoupled at $I_{corr,Zn}$ but will corrode in the galvanic couple at a galvanic current $I_{coupled,,Zn}$. While iron which is now the cathode in the galvanic cell will corrode uncoupled at $I_{corr,Fe}$ and protected in the couple at $I_{coupled,Fe.}$ The sum of anodic and cathodic reaction lines is shifted to the right of the Evans diagram as shown in Figure 2-6 and the intersection of this line represents the charge balance effect of the galvanic cell and the potential defines the mixed potential of the galvanic couple. $I_{coupled,,Zn}$ is the corrosion rate of the anode (the most active metal of the couple) of the galvanic couple while $I_{coupled,Fe}$ is the cathodic protection current for the most noble metal in the couple and is usually lesser than the uncouple corrosion rate of the noble metal. The increase in corrosion rate of the electrochemically more active metal in the uncoupled state to that in the galvanic couple is defined as the galvanic corrosion rate.

2.1.11 Factors influencing the corrosion of metallic components of a galvanic cell

As shown in Figure 2-6, a galvanic couple will usually comprise of four reaction lines, each of which represents the anodic and cathodic reaction of the individual metals in the couple. Thus, any environmental factor that can influence the tendency for and rate of corrosion of a single metal will also have the tendency to control the overall corrosion behaviour of a galvanic corrosion system. Some of these parameters may include, temperature, flow effects, ionic strength of electrolyte, pH, etc.[47]. However, there are some other factors that are also very important to the galvanic corrosion behaviour of a coupled system. These include; anode:

cathode ratio, the strength of electrolyte, position of metals in the galvanic series and the distance and geometry effects from the coupled metal of the galvanic cell [43, 47, 51].

***Position of metals in the galvanic series*:** From a thermodynamic perspective, the difference in electrode potential of dissimilar metals in the galvanic cell is the source of the Gibb's free energy that drives the flow of electrons from the more active metal to the most noble metal [43, 45]. Thus, the farther apart the two metals are on the galvanic series, the more the magnitude of the potential difference between the metals and galvanic corrosion rate of the most active metal as well as protection rate for the most noble metal [2, 43, 47].

Ionic strength and/or conductivity of electrolyte: Like in every other form of corrosion degradation process, the ionic strength of the corroding environment surrounding the metals of the galvanic couple must be significantly considered along with other factors. This is because the ionic strength of corrosion environments significantly influences the resistivity of the solution and the nature of the cathodic reaction lines of the individual metals [43, 47].

Anode: cathode ratio: The effect of anode to cathode ratio on galvanic corrosion cannot be underestimated. Since the potential difference of the coupled cell induces the current that flows through the galvanic cell, it is therefore evident that the current density of either of the anodic or cathodic reaction would control the corrosion kinetics. The total galvanic current *I*, defined as the summation of the effects of current flow from the anode to the cathode, would therefore be considered independent of the relative area of cathodic and anodic surfaces. From Figure 2-7, it has be seen that galvanic corrosion rate increases with increase in area ratio of cathode to anode [43, 44, 47].

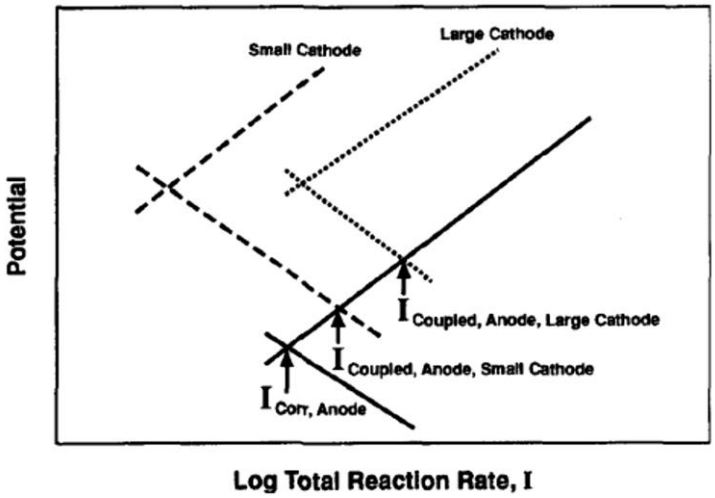

Figure 2-7 Effect of cathodic area on a galvanic corrosion cell [47]

2.2 Corrosion in an oilfield environment

Oilfield environments are naturally corrosive [3], comprising of a wide range of dissolved ions as corrosive species and may lead to manifestation of different forms of corrosion damage of oilfield production facilities [9]. The most common mechanisms of corrosion related failures encountered in the oil and gas industry are associated with the presence of CO_2 and H_2S [8, 9] and their derivatives, and constitute almost 58% of total corrosion related failures in the industry [8]. CO_2 and H_2S related corrosion failures are generally manifested in any one of the following mechanisms of corrosion discussed in section 2.2.1. There are also other forms of corrosion not mentioned here that are specific to the chemistry of certain corrosion environment.

CO_2 or carbonic acid (H_2CO_3) corrosion: is known to manifest in oil and gas production systems in the form of general corrosion, and other forms of localised corrosion. The later includes; pitting corrosion, mesa-type attack, and flow induced localised corrosion [9]. These corrosion damage mechanism are strongly linked with a wide range of environmental parameters; CO_2 partial pressure, pH, temperature, fluid velocity, nature of iron carbonate films, etc. [9]

H_2S corrosion and associated failures: generally, sour corrosion-related failures of oilfield facilities are often in the form of general corrosion but become easily dominated by unpredictable local failures; occurring as brittle fractures after initiation and propagation of cracks, and the initiation and propagation of localised pits in oilfield components [25, 52-54]. The brittle fracture form of sour corrosion failure is associated with an enhanced absorption of hydrogen atoms into pipeline steels, while the localised pitting tendency of metals in sour conditions are strongly linked to the thermodynamics, kinetics and nature of iron sulphide film formed [24, 25, 54, 55]. Corrosion damages resulting from exposure of pipeline facilities to wet hydrogen sulphide (H_2S) can be grouped into four principal categories;

1) Hydrogen internal pressure and embrittlement effects.
2) Stress corrosion cracking (SCC) and Sulphide Stress Corrosion Cracking (SSCC)
3) Localised pitting corrosion
4) Other damages associated with sour conditions containing other acidic salts; chlorides, cyanides, etc [15, 25, 56, 57].

2.2.1 Forms of oilfield corrosion failures

General corrosion characterises a uniform material degradation across the surface area of the corroding steel exposed to brine [33, 47]. This type of corrosion phenomenon is hinged on the fact that the active corrosion area on the surface of the exposed metal is evenly distributed over the surface throughout the duration of exposure. General corrosion can be easily predicted and managed because the uniform thinning of metal thickness without any local pits. General corrosion damage can be quantified by either of gravimetric or electrochemical techniques. Gravimetric/weight loss method averages the corrosion rate over the surface of the corroding metal and provides a qualitative evaluation of the corrosion damage. Electrochemical technique such as linear polarization provides an instantaneous and time dependent average of material loss rate [47]. Further numerical analytical tools would be required to quantify the average corrosion losses in weight over the duration of exposure time with linear polarisation technique.

Localised and pitting corrosion is a devastating and insidious material degradation process with relatively rapid penetration rate in small and discreet areas on the surface of corroding metals, while a large majority of the surface remains virtually unaffected [33, 47, 58, 59]. It often manifests as deep hollow voids and shallow undercut that are more destructive than general corrosion. When interconnected, these discrete areas pose a disastrous direct impact on the integrity and service life of materials [58, 59]. Localised and pitting corrosion is favoured when portions of corroding metal losses their passivity and corrode rapidly. Passivity in the case of carbon steel in oilfield application may never be attained but could be related to the formation of protective corrosion products; for example, Fe_3O_4, $FeCO_3$ and FeS. However, pitting corrosion is initiated with localised loss of protection from these films, which could often be induced by mechanical breakdown or damages by chemical dissolution (e.g. mineral acids) from the presence of acidic anions (e.g. chlorides), external stress effects during installation, internal stress build-up in solid corrosion films, solids impingement in operation, and some as manufactured micro-structural phase heterogeneity [47, 58, 59] etc.

Mesa attack is a form of localised corrosion often associated with the instability of iron carbonate corrosion products. It has been attributed to local acidification and manifests as large flat-bottom steps with sharp edges [9]. Corrosion damage in these locations is well in excess of the surrounding areas. Mesa type attack occurs in low to medium flow conditions where iron carbonate film formed is unable to withstand the operating low flow regime [9]. Mesa type

attack in corrosion may also start with pitting and develops when several pits are growing together [60]. This type of localised corrosion can also develop underneath an iron carbonate film during CO_2 corrosion of carbon steel [61]. Figure 2-8 show examples of the three main form of corrosion attack in oilfield environments that are associated with the presence of H_2S-CO_2 in reservoir brine.

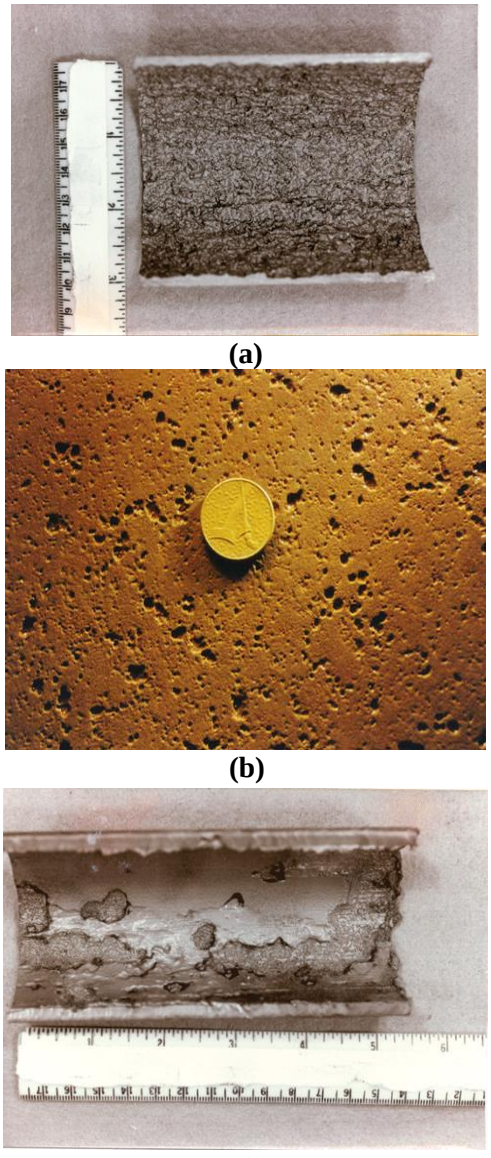

Figure 2-8 a) General corrosion damage [62] b) pitting corrosion damages [63] and c) mesa-type attack [64]

2.3 Pitting corrosion

Pitting corrosion is the most common form of localised corrosion attack on oilfield materials and constitutes a very serious material degradation mechanism because of the very rapid,

insidious and unpredictable nature by which confined points, small areas (that often take the form of small cavities) on metals sections becomes perforated [65, 66]. Occurrence of pitting corrosion in the oilfields can be manifested as follows;

1) Pitting in materials is triggered by the creation of local anodes at regions of local breakdown of oxide films, usually caused by either of chemical or mechanical mechanisms without immediate re-passivation or formation of non-passivating carbonaceous corrosion products [67-69]. The later applies to active materials.
2) Local anodes are active part of a local electrolytic cell that also has the surrounding passive areas of the metal/corrosion products acting as the cathodes [65].The potential difference between these sites accounts for significant current flow with rapid corrosion of local anodes [65]
3) Pitting corrosion most commonly occurs in passivating metals and corrosion resistant alloys exposed to aggressive environment [65, 66, 68].
4) Pitting corrosion is not entirely limited to corrosion resistance alloys as it also often occurs in non-passivating metals and in certain heterogeneous corrosive media, some of which occurs at areas of breaks in carbonaceous films deposited on metal surface [65, 68].
5) Pitting corrosion of metallic sections does manifests in various forms; these are shown.

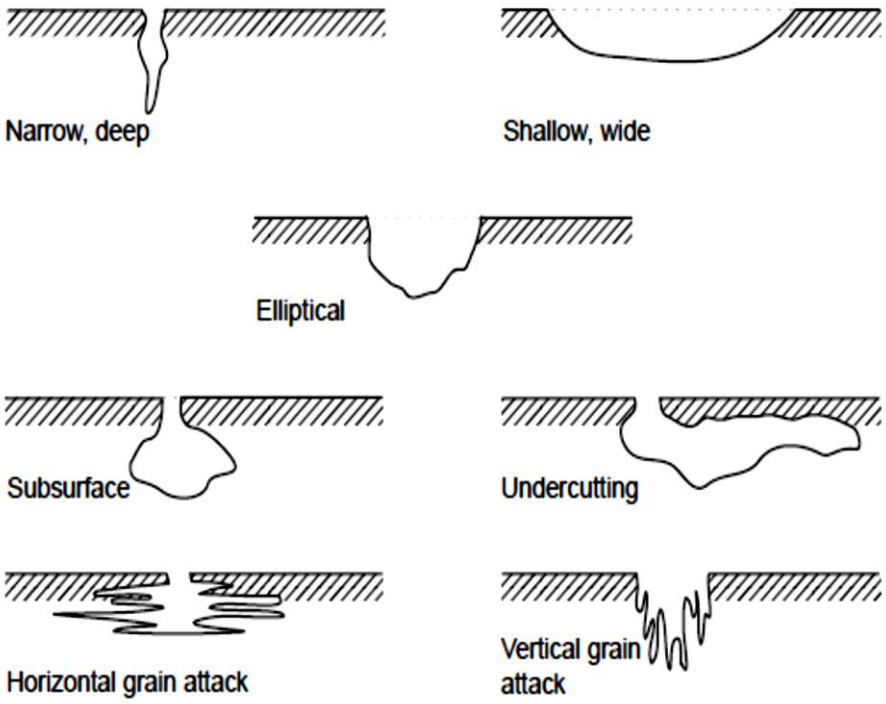

Figure 2-9 The different possible shapes of pitting corrosion damage [65, 66, 70].

Pits can also manifest as widely scattered and very dense pits (where it tend to overlap), with pit density being the number of pits per unit area [7]. It is assumed that the penetration rate of pits decreases with increase in pit density because adjacent anodic sites have to share a common cathodic site [66], such that the distinction between dense pitting and irregular general corrosion remained arbitrary. This may undoubtedly be the case with pitting corrosion in active materials like carbon steel.

2.3.1 Stages of pitting corrosion process

The classical process of pitting corrosion is usually modelled around passivating alloys such as stainless steels and other corrosion resistance alloys (CRA's). It is broadly seen in the context of the following sequence of **events;**

a) ***Initiation or nucleation of pits*;** this encompasses breakdown of passive films/carbonaceous corrosion products.
b) ***Pit growth or pit propagation process*;** under the pit growth stage is a metastable pit growth that could be seen as a transition between pit initiation and stable pit growth.
c) ***Re-passivation of pits*** is possible in some materials (especially passive materials) and also depending on environmental parameters; like pH, temperature, and solution chemistry [65, 69, 71].

Note that propagation or growth of pits can also be divided into two stages; the early stage pit growth corresponding to free metal dissolution and the later stage pit growth which is stabilized by the precipitation of corrosion films and potential drop within the growing cavities [5]. There is also the additional two stages of pit termination (where some pits stops growing and become dormant) while others may re-initiate [66]

2.3.2 Pit Initiation

The main requisites for pit initiation or nucleation of pits is the breakdown of passive oxide films (in the case of passivating metals) or presence of local discontinuities of corrosion products (in the case of active materials) in aggressive environments [65, 68, 69]

Halides and most especially chlorides have been identified as the most aggressive anions that promote pit initiation by penetrating local cavities created as a result of breakdown of passive oxide films [65, 68, 69].The actual mechanism of passive .oxide-films breakdown has been suggested to be either of the penetration mechanism, adsorption mechanism or the film-

breaking mechanism [69],

The film breaking mechanism appears the most likely as it can clearly be linked to the mechanical stress build-up, defined as the Pilling-Bedworth ratio [69], which measure of the fraction of corroded iron that is captured in the oxide film corrosion layer and defined as the ratio of the volume of the metal corrosion product to the consumed metal volume

Note also that this mechanism of film breakdown and pit initiation can be applied to non-passivating metallic alloys like carbon steel in oilfield environment and is most likely influenced by changes in the environment [38, 72, 73]

2.3.3 Pit Propagation

Once pits have been initiated in passivating alloys such as corrosion resistant alloys, they tend to grow in a self-sustaining for passivating alloys, autocatalytic chain reaction at local cavities depending on the discrete environment within these cavities[65]. The advent of such autocatalytic chain reactions at locally formed cavities, (often initiated by aggressive anions [65]) prevents the re-passivation of pits [68, 69] leading to further pit growth. This process of pit growth is thought to be a continuous process of metal dissolution by a series of uncontrolled chemical/electrochemical activities at already formed pits that ensures that a high acidity level is maintained in these cavities [65]. Aggressive anions like chloride ions, increases dissolution of metals to metallic ions ($M^{n+)}$ within already formed pits by reaction with chloride ions (Cl^-) in other to attain prior redox equilibrium. Hydrolysis of resultant metallic halide within the cavities produces free acids that lowers local pH significantly and promotes pit penetration process [65].

$$M^+_{(aq)} + Cl^-_{(aq)} \rightarrow MCl_{(aq)} \quad 2.24$$

$$MCl_{(aq)} + H_2O_{(aq)} \rightarrow MOH_{(aq)} + HCl_{(aq)} \quad 2.25$$

The rate of pit propagation will tend to increase when the anodic and cathodic sites of the corroding metal become acidic and alkaline respectively according to Eq.2.24 and 2.25 [65, 66]. The extent of pitting can also be linked to the chemical composition and microstructure of the material, temperature, duration of attack, chemistry of electrolyte and local solution conditions [67]. This is because pits in passivating alloys like stainless steels tend to be much deeper than pits in active metals like carbon steels and pits may grow extensively in stainless steels in chloride containing aerated environments than in de-aerated environments [68]. A pit may also terminate (dormant pit) when there is an internal resistance to local cell by deposition of

corrosion products above these pits. Pits propagation may also be retarded when cavities become dried out and may re-initiate once these cavities become rewetted [66]

2.4 Pit identification

Pit identification and characterisation is very important for accurate evaluation of the extent of pitting corrosion damage. Pit identification can be carried out by a number of methods. This includes

1) Visual examination,
2) Metallographic examination and
3) Non-destructive inspections [65, 67, 70].

However, inspection and characterization of the extent of pitting corrosion damage in laboratories and in field applications has proven to be a very challenging endeavour because of the need to establish the shape and general morphology of pits, to establish their surface dimensions, shapes and density [67].

One of such challenges with pit identification is with determining the deepest pits on an exposed surface as it is usually the first to perforate [67]. It is also important to note that the maximum pit depth found on a test sample is related to the percentage of the structure inspected [66]. Thus finding the deepest actual pit requires detail inspection of whole surface and probability of achieving this decrease as the surface area of the metal structure decreases. Based on this ambiguity in identification of pits, a rather qualitative approach describes pitting as;

1. Light when at a depth of 0.025 mm (25 um) maximum and
2. Moderate pitting is viewed as potentially 0.25 mm (250 um) and notes this type of damage is usually removed by "extensive mechanical sanding" [67]

2.4.1.1 Evaluation of extent of pitting corrosion damage

1. **Metal loss measurement** can be useful a technique but it is usually not considered the best technique for measuring the extent of pitting corrosion damage [70].
2. This is mainly because mass loss can only provide information about total metal loss due to pitting corrosion and not about the depth of penetration and penetration rate, especially when the contribution of general corrosion dominates the damage mechanisms.
3. Hence pitting corrosion rate from mass loss is often considered misleading [70].
4. **Pit depth measurement** which is the most critical and important of parameters for assessing the extent pitting corrosion damage [67], can be evaluated by destructive

techniques like; sectioning, machining, micrometre gauge and non-destructive technique like microscopic methods employing most notably white light interference microscopy [67, 70] (an advanced form of which is used in this research work).

2.4.1.2 Characterisation of pitting corrosion damage

Characterisation of pitting can be done in several ways: some are qualitative like the standard charts shown in Figure 2-10. Standard charts rates pits in terms of pits density (number of pits per unit area (pits per square meter) in column "A"), average size of pits (column "B") and average depth of pits (column "C") [66, 67, 70].

However, because maximum values like "Maximum pit depth" are usually more important for pitting corrosion study than average value, the standard charts rating method is usually not justified [70].

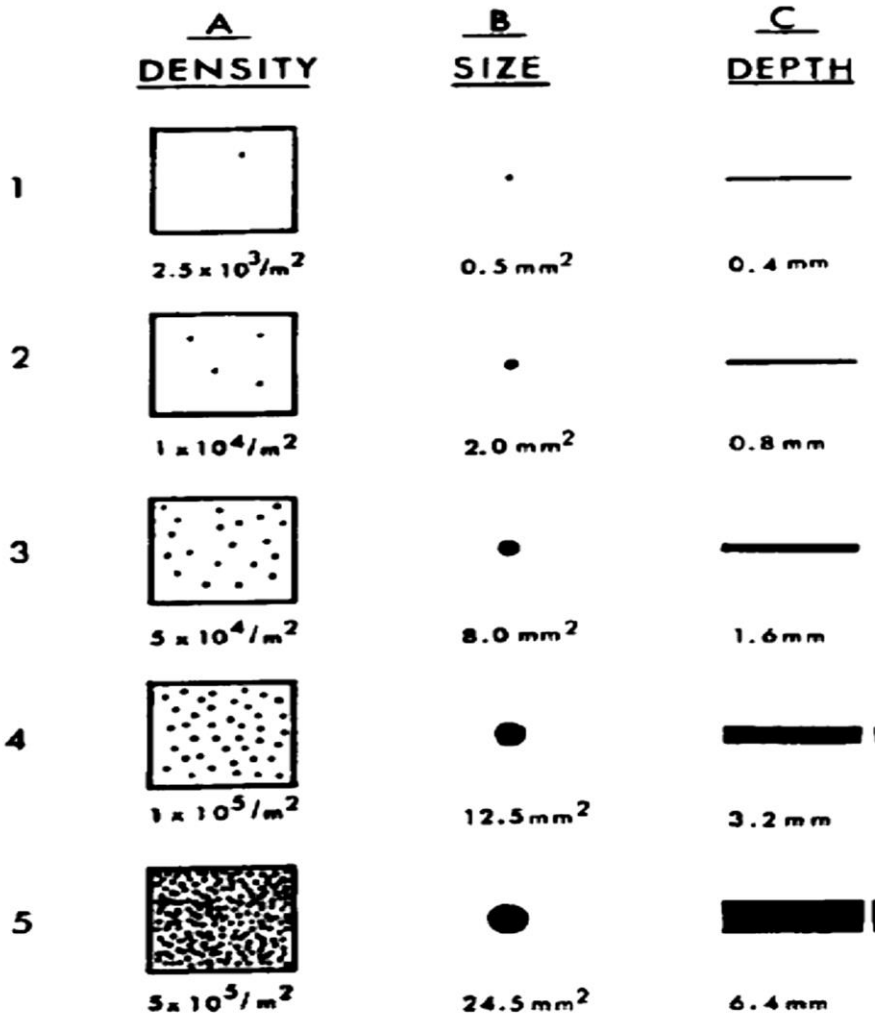

Figure 2-10 Pit ratings as applied in the standard charts [66, 67, 70]

Other very important useful methods of evaluating pitting corrosion damage include;

- Metal penetration which is expressed in terms of maximum pith depth or average of the 10 deepest pits and most preferably both.

- Metal penetration can also be expressed in terms of pitting factor defined as the ratio of the deepest metal penetration to the average metal penetration, determined by weight loss. Pitting factor of one represent uniform corrosion and the lager the number the deeper the penetration [1, 6].

$$Pitting\ factor\ (P_f) = \frac{Deepest\ metal\ penetration}{Average\ metal\ penetration\ from\ mass\ loss} \qquad 2.26$$

However, because of the misleading nature of mass loss measurement for characterising pitting corrosion this evaluation method appears less reliable.

From the foregoing it very apparent that metal penetration/pit penetration rate measurement combined with a statistical approach is the most viable and effective method for evaluating and characterising pitting corrosion damage in oilfield environments.

Chapter 3. Literature review: Sweet (CO_2) corrosion

3.1 Definition of concepts: Sweet (CO_2) corrosion

In real oilfield scenarios, the corrosion chemistry in sweet and sour environment is usually controlled by the nature of the brine phase and the relative concentration of H_2S and CO_2 gas. Sweet (CO_2) corrosion environment is characterised by the presence of mainly CO_2, but with insignificant amounts of H_2S; usually at H_2S partial pressure $\leq$ 0.3kPa according to NACE MR0175/ISO 15156[15]. The corrosion process is therefore dominated by chemical processes associated mainly with CO_2 gas dissolution and reduction reactions. This chapter discusses the relevant environmental factors (including CO_2 partial pressures) that have been shown in the literature to significantly influence the corrosion behaviour of carbon steel in CO_2-containing oilfield environments (with emphasis on pitting corrosion). These parameters include; temperature, *in-situ* pH, solution chemistry (presence of dissolved chlorides) and supersaturation, metallurgical and mechanical variables; as-manufactured defects, etc.

3.2 Mechanism of CO_2 corrosion

Dry and pure CO_2 is usually not corrosive but readily dissolves in water phase, producing a weak carbonic acid. However, the oilfield corrosion environment does not often provide scenarios where CO_2 gas is always in a dry form. CO_2 gas is usually naturally present in oil and gas reservoirs and readily dissolves in oilfield produced fluids [9]. It is also often injected into oilfield reservoirs during enhanced oil recovery and sometimes with treated seawater [74]. The dissolution of CO_2 gas in reservoir produced water creates aqueous as H_2CO_3 as the agent of corrosion [9, 75]. Generally, when dissolved in water, CO_2 is hydrolysed to form carbonic acid (H_2CO_3) according to Eq.3.1. H_2CO_3 is diprotic and usually dissociates via a two-step process according to Eq. 3.2 and 3.3[76].

$$CO_{2\,(g)} + H_2O \leftrightarrow H_2CO_{3\,(aq)} \quad 3.1$$

$$H_2CO_{3\,(aq)} \leftrightarrow H^+_{(aq)} + HCO_3^-{}_{(aq)} \quad 3.2$$

$$HCO_3^-{}_{(aq)} \leftrightarrow \quad H^+_{(aq)} + CO_3^{2-}{}_{(aq)} \quad 3.3$$

The mechanism of corrosion of carbon steel in CO_2 containing environment is very complex. Some complexities have been that carbonic acid can be more corrosive than a completely dissociated acid of the same pH [77]. Dugstad [78] also stated that the term "CO_2 corrosion" and the effect of CO_2 is not related to solely one mechanism. Hence the need to understand the various range of electrochemical, chemical and mass transport processes that occurs

simultaneously at the interface of the corroding steel in an electrolyte. Some of the other electrochemical and chemical processes in practical CO_2 corrosion situations are also known to be related to a large number of other chemical species present in oilfield environments. For instance, some of the complexities in the mechanism of CO_2 corrosion have been related to chemical and electrochemical reactions that include; water dissociation and reduction, H^+ reduction and hydrogen evolution as well as iron carbonate formation [76, 79]. These reactions all contribute to the cathodic reaction mechanism and total cathodic current but with varying sensitivities to changes in the fluid properties [9, 77] (temperature, pressure, brine chemistry) and flow conditions (velocity, flow regime) [9], making the CO_2 corrosion process incredibly complex in most instances. A brief discussion on the possible reaction steps involved in the cathodic and anodic reactions of carbon steel in CO_2 corrosion systems.

3.2.1 Cathodic reactions

Carbonic acid is usually a weak acid when compared to mineral acids and thus, does not dissociate completely. Kermani and Morshed [9] had summarised the cathodic reaction of carbon steel in CO_2 containing environment as;

$$CO_2 + H_2O \leftrightarrow CO_2 - H_2O \equiv H_2CO_3 \leftrightarrow H^+ + H_2CO_3^- \qquad 3.4$$

According to Eq.3.4, it is assumed that H_2CO_3 behaves as a source of proton for reduction at the steel surface, while the hydration of CO_2 to H_2CO_3 is considered the Rate-Determining Steps (RDS). The simplified cathodic reaction of Eq. 3.4 does not reflect the inherent complexities in the Rate-Determining Steps (RDS) of the cathodic reaction. De Waard and Milliams [77], on one hand had hypothesised that H_2CO_3 is directly reduced at the steel surface according to the following reactions;

$$H_2CO_3 + e^- \xrightarrow{RDS} H + HCO_3^- \qquad 3.5$$

$$HCO_3^- + H^+ \leftrightarrow H_2CO_3 \qquad 3.6$$

It was suggested from experiments by De Waard and Milliams [77], that the measured corrosion rate correlates with the concentration of undissociated H_2CO_3, rather than that of dissociated H_2CO_3 which influences the solution pH. Reaction step 3.5 was considered the rate-determining step because reaction step 3.6 and the subsequent combination of H atoms to H_2 were envisaged to be too fast to be the rate-determining step.

On the other hand, Ogundele and White [80] suggested that the cathodic reaction in CO_2 corrosion of steel is governed by the direct reduction of HCO_3^- at the steel surface according to the following reactions;

$$HCO_3^- + e^- \xrightarrow{RDS} H_{ads} + CO_3^{2-} \quad 3.7$$

$$HCO_3^- + H_{ads} + e^- \rightarrow H_2 + CO_3^{2-} \quad 3.8$$

It was suggested that the change in cathodic Tafel slope from ≈|120mV| in synthetic brine without HCO_3^- to ≈ |365mV| in the presence of HCO_3^- is an indication of the effect of HCO_3^- reduction to total cathodic current with the proposition that reactions 3.7 is the rate-determining step of the cathodic reaction in CO_2 corrosion environment.

It has also been proposed by Schwenk and Korros that the cathodic reaction of hydrogen-evolution results from H_2CO_3 simply acting as H^+ reservoir in the dissociated form [9]. This reaction process is described by the following reaction;

$$H_2CO_3^- : H^+ + e^- \rightarrow H \quad 3.9(a)$$

$$\text{and } 2H \rightarrow H_2 \quad 3.9(b)$$

The abovementioned cathodic reactions as proposed by the different authors does suggest a significant influence of the concentration and mass transport of dissolved CO_2 species on the corrosion reactions and subsequently, corrosion rate of carbon steel materials in these systems. The complex interactions from other dissolved specie present in media can also contribute to the cathodic reactions [9], hence the need for characterisation of solution chemistry with respect to CO_2 dissolution and the buffering capacity of water constituents.

3.2.2 Anodic reactions

Carbon steel is divalent and the anodic dissolution of iron of carbon steel in acidic corrosion medium has often described by the generic reaction;

$$Fe \rightarrow Fe^{2+} + 2e^- \quad 3.10$$

Extensive studies by several researchers have helped develop several multi-step mechanisms to explain the anodic dissolution reaction of Fe of carbon steel. Studies by Bockris *et al* [81] in d-oxygenated acid solutions reported evidence of pH-dependent multi-step mechanism of iron dissolution according to the reactions;

$$Fe + OH^- \rightarrow FeOH_{ads} + e^- \quad 3.11$$

$$FeOH_{ads} \xrightarrow{RDS} FeOH^{+} + e^{-} \quad 3.12$$

$$FeOH^{+} \rightarrow Fe^{2+} + OH^{-} \quad 3.13$$

According to Bockris *et al* [81], the anodic dissolution of rate at constant potential is inversely proportional to the H^+ and hence pH of the environment and $FeOH_{ads}$ is considered as an intermediate specie rather than as a catalyst as proposed by other authors [82].

It is also important to note that there is difference in the kinetics of iron dissolution between CO_2 solutions and strong acids as. Detailed explanation of this disparity was presented by Nesic [83]. It was suggested that the effect of the presence of CO_2 gas is associated with carbonic acid specie acting as chemical ligands and catalysing the dissolution of iron. Nesic [83] assumed that the ligand Fe_L (which denotes the complex Fe-CO_2) forms as an adsorbed species at the electrode surface and catalyses the dissolution of iron. The following reactions described the anodic dissolution model proposed by Nesic [83].

$$Fe + CO_2 \leftrightarrow Fe_L \quad 3.14$$

$$Fe_L + H_2O \leftrightarrow Fe_LOH_{ads} + H^{+} + e^{-} \quad 3.15$$

$$Fe_LOH_{ads} \xrightarrow{RDS} Fe_LOH^{+}_{ads} + e^{-} \quad 3.16$$

$$Fe_LOH^{+}_{ads} + H_2O \leftrightarrow Fe_L(OH)_{2ads} + H^{+} \quad 3.17$$

$$Fe_L(OH)_{2ads} \leftrightarrow Fe_L(OH)_{2sol} \quad 3.18$$

$$Fe_L(OH)_{2sol} + 2H^{+} \leftrightarrow Fe^{2+} + CO_2 + 2H_2O \quad 3.19$$

Ogundele and White [80], had also tried to explain the mechanism of anodic dissolution of Fe of carbon steel from the point of view of thermodynamic stability. It was proposed that the formation of iron carbonate ($FeCO_3$) and magnetite (Fe_3O_4) was more stable compound and favoured to form via the following reactions;

$$Fe + H_2CO_3^{-} \rightarrow FeCO_3 + H^{+} + 2e^{-} \quad 3.20$$

$$Fe + CO_3^{2-} \rightarrow FeCO_3 + 2e^{-} \quad 3.21$$

$$3Fe + 4H_2O \rightarrow Fe_3O_4 + 8H^+ + 8e^- \quad 3.22$$

$$3FeCO_3 + 4H_2O \rightarrow Fe_3O_4 + 3H_2CO_3^- + 5H^+ + 2e^- \quad 3.23$$

It is therefore important to note that while these proposed reaction mechanisms for anodic dissolution of Fe may be different, it is evident that all reaction mechanisms proceed in a manner consistent with the generic reaction of Eq. 3.10 for converstion of Fe to Fe^{2+}. Hence, from the proposed cathodic and anodic reaction mechanisms by other researchers, the overall mechanism of CO_2 corrosion of carbon steel that that includes hydrogen evolution can be summarized as follows;

Anodic reaction;

$$Fe \rightarrow Fe^{2+} + 2e^- \quad 3.24$$

Cathodic reaction;

$$H_2CO_3 + 2e^- \leftrightarrow CO_3^{2-} + H_{2\,(g)} \uparrow \quad 3.25$$

$$Fe + H_2CO_3 + 2e^- \leftrightarrow Fe^{2+} + CO_3^{2-} + 2e^- + H_{2\,(g)} \uparrow \quad 3.26$$

$$Fe + H_2CO_3 \leftrightarrow FeCO_3 \downarrow + H_{2\,(g)} \uparrow \text{ ($FeCO_3$ film formation)} \quad 3.27$$

The anodic reaction and hence overall CO_2 corrosion reaction in Eq. 3.27 often results in the formation of iron carbonate films. Iron carbonate corrosion product has been found to be protective against CO_2 corrosion depending on some other environmental factors [9, 76, 84, 85].

3.3 Corrosion product films in CO_2 corrosion of carbon steel

Any assumptions that iron carbonate is the sole corrosion product that may be encountered in CO_2 corrosion of carbon steel may be misleading. This is because the generic CO_2 corrosion reaction mechanism described by Eq.3.25-3.27 does not reflect the other possible corrosion products that have direct influence on the overall corrosion mechanism as well as the corrosion damage morphology in these systems. However, these other possible corrosion products will be dependent on other environmental parameters as would be discussed in this section of the literature review. The following sub-sections provide detail regarding a number of surface films that have been identified and/or observed in either the field or laboratory experiments on carbon steel in CO_2-containing environments. It was deemed useful to highlight the variety of films encountered and identify the conditions under which their formation is most prevalent, along

with the mechanisms by which they are generated. This review focuses on publications which observed the formation of three main classes of film:

1) iron carbide (Fe_3C)
2) iron carbonate ($FeCO_3$) and
3) magnetite (Fe_3O_4)

3.3.1 Iron carbide (Fe_3C)

Iron carbide (Fe_3C) is a commonly encountered corrosion product layer on the surfaces of carbon steel subjected to CO_2 corrosion and has been observed as a porous network revealed on steels with a carbon content in excess of 0.15% [9, 86]. Fe_3C is not a 'corrosion product' as it already exists as part of the steel microstructure and its quantity within the material increases in conjunction with its carbon content of the steel [86]. An Fe_3C network is revealed on the steel surface as a result of the anodic dissolution of the α-ferrite phase in the steel microstructure, leaving behind an uncorroded network of empty cementite on the surface of steel [9, 86, 87]. Fe_3C film can be fragile, porous and consequently, very susceptible to flow conditions. However, studies have also shown that this layer can produce a very tough network in acidic solutions [9].

It has been suggested that empty cementite (Fe_3C) network is capable of acting as an electronic conductor which is able to accelerate the corrosion rate of carbon steel by inducing a galvanic effect on the surface and acting as a favourable cathodic site for hydrogen evolution [9, 86, 88]. Fe_3C is capable of increasing corrosion rate by a factor of 3 to 10 in some instances by playing a number of roles including galvanic coupling and/or creation of micro-galvanic corrosion cell on steel surfaces[9, 86, 88], as well as internal acidification of anodic regions within the layer [9, 88].

Farelas *et al* [86] conducted experiments on C1018 carbon steel using a flow cell in 3 wt.% NaCl at a fluid velocity of 0.5 $ms^{-}1$, temperature of 80°C and a pH of 6. Over the first 20 hours of exposure to the test solution at a velocity of 0.5 m/s, corrosion rate increased from 3 mm/year to 6.2 ± 0.1 mm/year. The significant increase in corrosion rate was attributed to the modification of the corrosion interface as a result of evolution of Fe_3C from the selective dissolution of the α-ferrite phase in the steel microstructure. Fe_3C formed in such circumstances become preferential cathodic sites with a lower over-potential for hydrogen evolution [9, 88].

Despite Fe_3C serving to significantly increase the dissolution of steel, research has also indicated that the development of the network can possess some beneficial effects. Al-Hassan *et al* [89] stated that Fe_3C was capable of acting as a substrate for $FeCO_3$ precipitation, anchoring the scale down and protecting it from removal via local shear stresses. This was believed to significantly reduce the likelihood of localised corrosion. Kermani and Morshed [9] suggested that the formation of Fe_3C can result in an enrichment of Fe^{2+} at the steel surface. Such a process would increase the local supersaturation of ferrous ions at the surface and potentially aid in the formation of a protective $FeCO_3$ layer. However, in cases where there is significant corrosion leading to Fe_3C formation and preceding supersaturation, the local acidification effect of Fe_3C is thought to undermine the potential protective properties of $FeCO_3$ corrosion products [88].

In general, Fe_3C has an overall contrasting role on corrosion kinetics, depending on its formation and the local environment. From the foregoing, changes in environmental parameters in CO_2 corrosion systems may influence development a porous Fe_3C layer.

3.3.2 Iron carbonate formation ($FeCO_3$)

With reference to Eqns. 3.24-3.27, iron carbonate corrosion product ($FeCO_3$) is one of the most important films usually formed on carbon steel in CO_2 environments. From the perspective of corrosion mitigation, it is capable of dramatically influencing the corrosion kinetics of the underlying steel via it precipitation onto the steel surface [9, 87, 90]. $FeCO_3$ crystals of cubic morphology has the ability to hinder the reaction process by blocking active sites on the steel surface and acting as a diffusion barrier to electrochemically active species, and reducing the diffusion fluxes of the species involved in the corrosion process [9]. The protectiveness of the film is influenced by several environmental factors such as temperature, pH, partial pressure of CO_2 etc [9].

Iron carbonate film formation process is like every other chemical reaction process dependent on the thermodynamics and kinetics of $FeCO_3$ precipitation process. In this case, supersaturation is one of the most important phenomena in $FeCO_3$ growth process that also influences its morphology [9, 87]. A thermodynamic equilibrium constant (K_{sp}) for the reaction of Eq.3.26 to proceed is usually defined as;

$$K_{sp} = [Fe^{2+}] [CO_3^{2}] \qquad 3.28$$

Where; K_{sp} is the solubility limit for the formation of $FeCO_3$ (Eq.3.26 and 3.27).

Eq.3.8 defines a controlling concentration threshold of Fe^{2+} and CO_3^{2-} needed for the formation of $FeCO_3$ during corrosion of carbon steel in CO_2 environment.

Practical CO_2 corrosion environment usually contains several species in solution and thus influences the cathodic reaction [76], making it very pertinent to characterise the corroding solution chemistry with respect to dissolved CO_2 since it influences the solution pH along with the other radicals constituting the water chemistry. Hence, the ionic concentration amongst other factors will significantly influence the thermodynamics and kinetics of CO_2 corrosion and $FeCO_3$ films formation [84]. The effect of these factors would be reviewed in subsequent sections.

3.3.3 Magnetite (Fe_3O_4)

It has been indicated that in addition to the generation of a $FeCO_3$ as a corrosion product, Fe_3O_4 can also form onto steel surface as a corrosion product. It has also been suggested from thermodynamic analysis that $FeCO_3$ and Fe_3O_4 are more stable compounds under certain experimental conditions to be formed as corrosion product during corrosion of steel in CO_2 environment [80]. The formation of Fe_3O_4 in CO_2 corrosion environment is thought to be favoured by the reactions;

$$3Fe + 4H_2O = Fe_3O_4 + 8H^+ + 8e^- \quad 3.29$$

$$3FeCO_3 + 4H_2O = Fe_3O_4 + 3HCO_3^- + 5H^+ + 2e^- \quad 3.30$$

There have been reports of steel surface entering into a pseudo-passive state, once Fe_3O_4 is formed, facilitating further corrosion protection. The pseudo-passivation process results in a significant ennoblement of OCP of the steel surface (a rise of between 400 and 800 mV increase in some instances [91]). It was postulated by Han *et al* [91], that the formation of the pseudo-passive film could establish galvanic cells on the carbon steel between the film covered passive area (acting as a cathode) and the actively corroding bare steel (forming the anode). This could help to explain the mechanism of localized attack in some environments, with the passive film acting as a large cathode to accelerate attack at localized bare regions of the steel surface.

An analysis by Han *et al* [92] involving the implementation of Grazing Incidence X-ray Diffraction (GIXRD) and TEM suggested that the film was composed of magnetite (Fe_3O_4). According to Han *et al* [92], the tendency for formation of magnetite via Eq.3.29 is influenced

by a critical pH. Han *et al* [91], also showed through the implementation of a simulation package that the formation of $FeCO_3$ was able to change the local electrolyte condition at the steel surface, beneath the film. By modelling a protective $FeCO_3$ film, Han *et al* [91] demonstrated that the pH value at the surface of the steel can be significantly higher than that in the bulk solution, making pseudo-passivation (potentially by the presence of Fe_3O_4) more favourable. For a bulk solution pH of 6.6, a surface pH of ~7.3 was predicted. The pseudo-passivation process was only deemed to be possible above a certain local pH. Han *et al* [91] concluded that the presence of an $FeCO_3$ layer was capable of inducing the formation of the pseudo-passive film at a lower bulk solution pH because of the ability to raise the surface pH to induce pseudo-passivation.

3.4 Key factors affecting thermodynamics and kinetics of CO_2 corrosion and iron carbonate film formation

The mechanism of CO_2 corrosion, iron carbonate formation, CO_2 induced localised corrosion and pitting cannot be fully understood without considering the most relevant parameters that can independently and collectively influence the thermodynamics and kinetics of iron carbonate films formation as linked to the mechanism of CO_2 corrosion and pit initiation and propagation in CO_2 saturated systems. Works by other researchers on this subject area are reviewed in this section. The most relevant environmental parameters include but not limited to the following;

- Supersaturation of solution and gas solubility
- Partial pressure of CO_2 gas
- In-situ pH
- Chloride ion concentration/ionic strength
- Temperature [9].

3.4.1 Solution Chemistry, Gas Solubility and Solution Saturation Index

The concentration of Fe^{2+} and CO_3^{2-} made available in solution by the corrosion of carbon steel is very important for defining the nature of iron carbonate films (referring to Eqns 3.25-3.27). As carbon steel corrodes, Fe is oxidized to Fe^{2+} as the anode while H_2CO_3 is reduced to CO_3^{2-} as the cathodic reaction at the surface of the metal. This increases the concentration of Fe^{2+} and CO_3^{2-} in the bulk solution until the solubility limit defined by Eq. 3.28 is exceeded, leading to solution supersaturation and precipitation of $FeCO_3$ [9].

Saturation Index (SI) measures the tendency to form precipitates of dissolved ions in the bulk of the solution and is defined as the logarithm ratio of the ionic product and solubility limit.

$$SI = \log\left(\frac{[\mathbf{Fe^{2+}}]\,[\mathbf{CO_3^{2-}}]}{K_{sp_{FeCO_3}}}\right) \quad 3.31$$

Where Ionic Product (product of non-equilibrium ionic concentration of species in solution) **(IP) = $[Fe^{2+}]$ $[CO_3^{2-}]$** in solution at any time, and K_{sp}= **$[Fe^{2+}]$ $[CO_3^{2-}]$** at equilibrium [9].

Therefore, at saturation, IP = K_{sp} and SI = 0, at undersaturation, IP < $K_{sp\ and}$ SI < 0.

From a thermodynamic standpoint, supersaturation (S) is the driving force for precipitation of $FeCO_3$. The extent of dissolved species in the bulk solution (Fe^{2+} and CO_3^{2-}) is influenced by the rate of loss of ferrous ions into the bulk solution. The amount of these ions in the bulk phase is characterized by the term *"saturation index (SI)"*. While a very large positive value of SI does not always guarantee the formation of $FeCO_3$ films, it provides a useful thermodynamic perspective for the formation of $FeCO_3$ films. Typically, a high degree of supersaturation is required in the bulk solution to obtain appreciable levels of $FeCO_3$ precipitation onto the steel surface[78]. Supersaturation (S) is defined as:

$$S = \frac{[Fe^{2+}][CO_3^{2-}]}{K_{sp}} \quad 3.32$$

Where $[Fe^{2+}]$ and $[CO_3^{2-}]$ are the concentrations of ferrous and carbonate ions, respectively. K_{sp} has been defined as the equilibrium solubility product for $FeCO_3$, which is a function of ionic strength and temperature [84]. Supersaturation is attained when IP> K_{sp} and SI > 0 or S > 1. The nucleation of $FeCO_3$ is initiated. Although nuclei formation is possible at S > 1, its kinetics increases rapidly only when a critical supersaturation is exceeded [93]. The kinetics of $FeCO_3$ scale formation also depends on other parameters. According to Dugstad [87], a positive Saturation Index for carbon steel in a CO_2 saturated environment is very necessary amongst other factors to enhance formation of protective iron carbonate films. This is also dependent on the initial corrosion rate of carbon steel which provides the Fe^{2+} ions required for supersaturation of diffusion boundary layer between the metal surface and the bulk solution (EDL) [94]. This process of gradual pile-up of Fe^{2+} and bicarbonate ions on the surface of steels as a precursor to $FeCO_3$ precipitation has been illustrated by experimental results at 80ºC given in Figure 3-1.

In principle, there exist two steps involved in the precipitation processes; nucleation and particle growth. The assumption is made that these two processes are related to the relative supersaturation (S_R):

$$S_R = \frac{Q - Q_{eq}}{Q_{eq}} = S - 1 \qquad 3.33$$

Where Q is the concentration of the solute, Q_{eq} is the equilibrium solubility and S is the supersaturation.

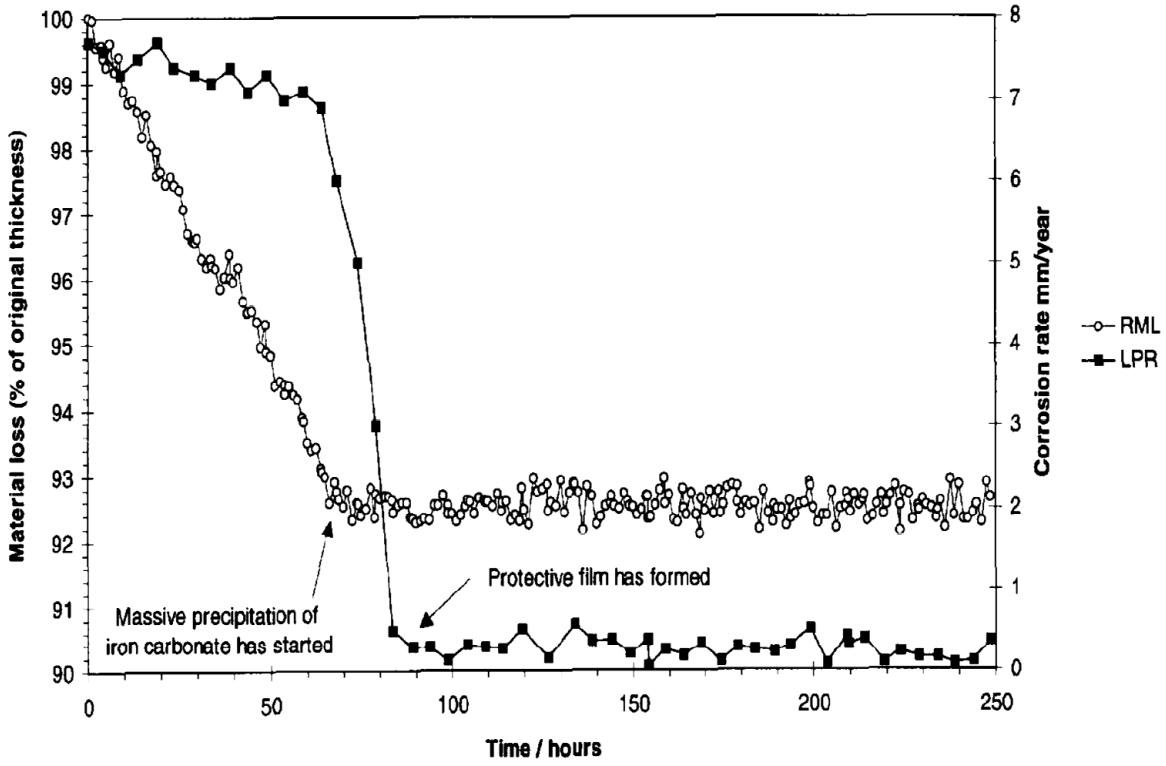

Figure 3-1 Material loss on carbon steel in CO_2 environment as a function of time measured with radioactive material loss technique (RML) and linear polarisation technique (LPR) [87].

It is assumed that the rate of both nucleation and particle growth is related to the relative supersaturation (S_R). The rate of nucleation is believed to increase exponentially with relative supersaturation, whilst particle growth varies linearly with S_R. Consequently, particle growth should occur at low relative supersaturation. Conversely, when relative supersaturation is high, particle growth is prevented and a nan-ocrystalline or even amorphous form of $FeCO_3$ can develop [93]. The later form of iron carbonate has been reported by some authors as the precursor for pitting corrosion in CO_2 corrosion environment [95].

The critical part of the film formation process is the initiation. If the temperature and the supersaturation in the bulk solution are high, significant precipitation will take place and a protective iron carbonate film will form. Dugstad [78] stated that at temperatures below 40°C, a lower precipitation rate is established and the relative supersaturation can become very high, which is likely to lead to a porous film, which is loosely adherent, lacks crystallinity and is less protective than at higher temperatures leading to the potential risk of localised corrosion (pitting inclusive) [9]. At higher temperatures, the precipitation rate is faster and relative supersaturation is low, leading to dense crystalline form of $FeCO_3$, offering good protection

Hence, the concentration and supersaturation of the bulk solution at any time during the corrosion of carbon steel, influences the rate of precipitation and protectiveness of iron carbonate film. The effect of which determines the extent to which pitting corrosion is likely to occur in CO_2 dominated corrosion systems.

3.4.2 Effect of CO_2 partial pressure

The role of CO_2 partial pressure on corrosion rate and subsequent precipitation of $FeCO_3$ is often related to the solution pH. Referring reactions given by Eq. 3.1-3.3, the hydrolysis of CO_2 precedes the formation of the diprotic carbonic acid H_2CO_3, which is the chief agent of CO_2 corrosion. The influence of CO_2 partial pressure on corrosion behaviour of carbon steel can also be correlated on its influence on the pH of the solution [9, 77]. Carbonic acid is considered a weak acid and hence dissociates in two steps as given by reactions in Eqns. 3.1-3.3. Therefore, it follows that the dissociation constant K for carbonic acid can be written as [77];

$$(H^+)^2 = K\,(H_2CO_3) \qquad 3.34$$

A relationship between CO_2 partial pressure and solution pH was established by De Waard and Milliams [77], on the assumption of Henry's law approximation. According to Henry's law, the concentration of carbonic acid (dissolved form of CO_2) is directly proportional to the partial pressure of CO_2 gas. Hence, the relation;

$$pH = -{}^{1}/_{2} \log P_{CO_2} + k \qquad 3.35$$

where, k incorporates Henry's constant (H) and dissociation constant (K) as $-{}^{1}/_{2} \log HK$.

De waard and Milliams [77] were also able to establish a direct relationship between corrosion rate of carbon steel and CO_2 partial pressure at different temperature. It was concluded that

corrosion rate increases with CO_2 partial pressure based on experiments on X65 carbon steel exposed to a 0.1% NaCl solution saturated with CO_2 by De waard and Milliams [77]. This is provided in Figure 3-2. From the results shown in Figure 3.2, the following relation was developed by De waard and Milliams [77];

$$\log i_c = {}^{1}/_{2}\, A \log P_{CO_2} + B' \qquad 3.36$$

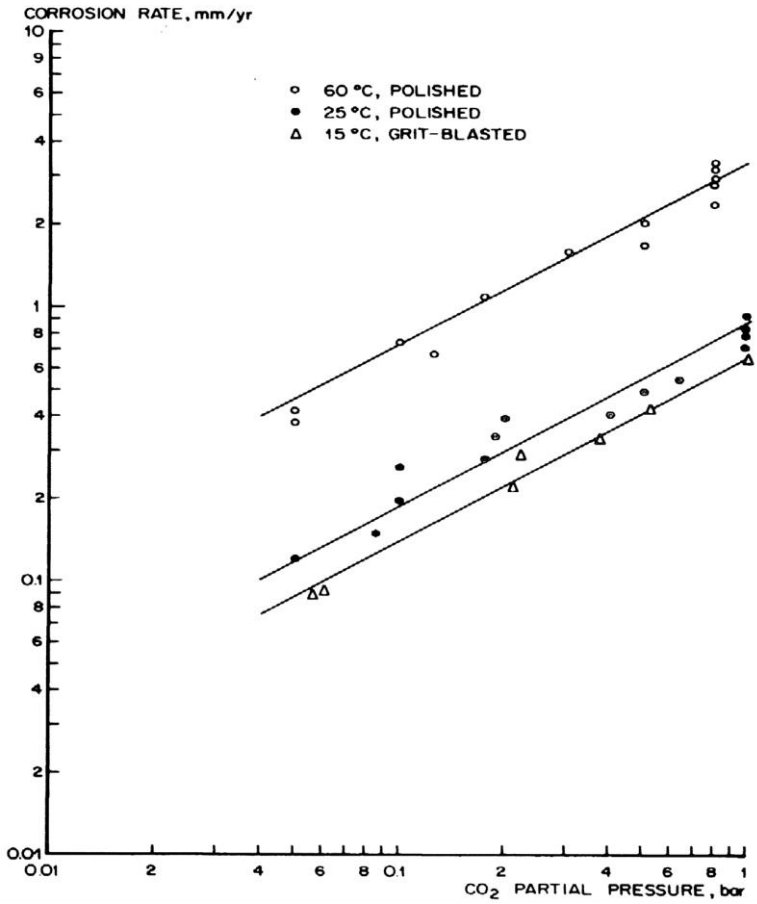

Figure 3-2 The influence of CO_2 partial pressure and temperature on the corrosion rate of carbon steel [77].

Eq. 3.34 -3.36 clearly depicts a correlation between CO_2 partial pressure, solution pH and corrosion rate of carbon steel materials. However, a majority of pH calculations and corrosion rate predictions based on this relationship do not often take into account the complexities in the brine chemistry and especially in the presence of $CaCO_3$ [9, 96]. It is also important to note that with increasing CO_2 gas pressure comes with the non-ideality of the gas phase playing a much more significant role in the whole corrosion process [9, 96]. Hence, CO_2 partial pressure is replaced with CO_2 fugacity (f_{CO_2}). It has also been suggested that carbonic acid may be acting

as a reservoir for H^+ over and above that determined by –log $[H^+]$. This has been attributed to the fact that H_2CO_3 does not dissociate completely and hence may be more corrosive than mineral acids at the same solution pH [9].

In terms of the effect of CO_2 partial pressure on formation of iron carbonate, it would be expected that increased rate of corrosion as a result of increasing CO_2 partial pressure will imply increase Fe^{2+} and CO_3^{2-} ions in solution, leading to solution supersaturation for $FeCO_3$ formation over time and depending on other factors. However, De Waard *et al* [97] had reported that increasing CO_2 partial pressure reduces the scaling temperature at which protective $FeCO_3$ corrosion scale is likely to formed from Fe^{2+} and CO_3^{2-} ions in solution.

From the foregoing, increasing the partial pressure of CO_2 gas is likely to increase the tendency for protective iron carbonate film to form during corrosion of carbon steel, depending on local pH and Fe^{2+} concentration. It also reduces the threshold for such corrosion films to be formed, while becoming a key determinant of the propensity for pitting corrosion or other forms of localise corrosion to occur, since these forms of corrosion are directly linked to the protectiveness of $FeCO_3$ corrosion product layer.

3.4.3 Effect of temperature

The effect of temperature on the thermodynamics and kinetics of CO_2 corrosion and iron carbonate formation is correlated to its influence on the aggressiveness of the corrosion media and the solubility limit (K_{sp}) of iron carbonate. Temperature has been identified to influence electrochemical corrosion and kinetics of corrosion film formation at metal – brine interface of steel by increasing the kinetics of corrosion with increasing temperature [77, 98], changing brine phase behaviour with changes in temperature, increasing the aggressiveness of chloride ions in aqueous solutions with increasing temperature by thermal activation [40] and increase in the tendency for iron carbonate to precipitate out of solution with increasing temperature [9, 40]. Experiments conducted by De Waard and Milliams [77] on carbon steel in a CO_2 corrosion environment up to 80ºC, show that corrosion rate increases gradually with increase temperature from 0.4mm/yr at 5.5ºC to 5.7mm/yr at 80ºC. In the same study, the effect of temperature on CO_2 gas solubility and dissociation was accounted for in terms of measured pH as a function of temperature at a total pressure of 1 bar as shown in Figure 3-3(a). The results gave a linear relationship between pH and temperature in CO_2 corrosion environment.

Temperature is also known to strongly affect the nature, characteristics, and morphology of corrosion films [9, 87]. Several authors [77, 87] have observed that at temperatures in excess of 80ºC, the solubility limit for the formation of $FeCO_3$ is reduced, leading to high superasturation and $FeCO_3$ precipitation. Sun *et al* [84] and Dugstad [87] have shown from a unified model and experimental results respectively that temperature of about 80ºC is the likely tipping point in terms of the effect of temperature on the solubility limit K_{sp} for $FeCO_3$ .This temperature has been defined as the "scaling temperature" in the De waard 1991 CO_2 corrosion model for wet natural gas pipelines [97]. The scaling temperature has been shown in Figure 3-3(b) to vary with changing CO_2 partial pressure. It has also been reported to increase with fluid velocity and decrease with increase pH [97].

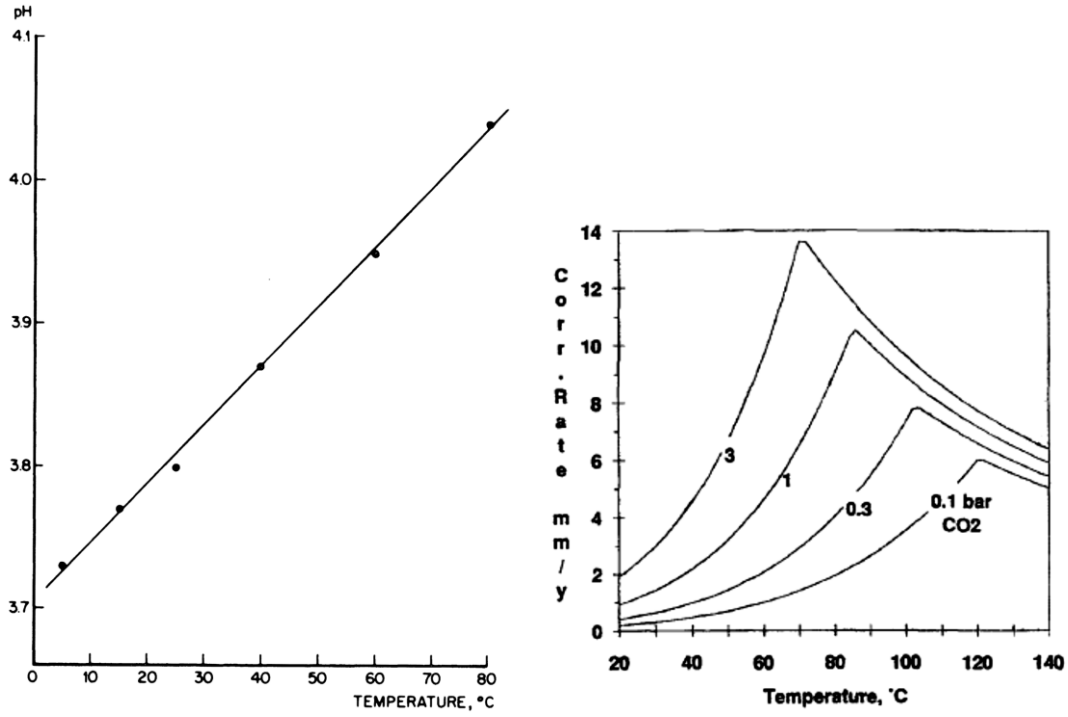

(a) (b)

Figure 3-3 a) Effect of temperature on pH at 1bar CO_2 (corrected for water vapour) [77] and b) Effect of high-temperature corrosion product film calculated with scale factor [97].

At temperatures lower than the scaling temperature, CO_2 corrosion rate was also reported to increase due to the high solubility for $FeCO_3$ formation [9, 99]. Dugstad [87] also stated that at various supersaturations, there was no appreciable film growth at temperatures less than 60-70℃ (especially at low supersaturation) which may increase the tendency and rate of localised corrosion (pitting and mesa attack). This is because corrosion products formed at such temperature ranges are likely to have poor adherence, compactness and protectiveness than film formed at temperature ≥80ºC [9, 87].

3.4.4 Effect of solution pH

The rate of electrochemical degradation of carbon steel pipe in a CO_2 saturated environment and nature of iron carbonate film is strongly influenced by the level of acidification of corroding medium (solution pH) by the dissolved species. The ionic strength of solution also influences its acidity by modifying the solution pH [9, 84]. Increasing pH is known to reduce the rate of cathodic reduction of H^+ and thus, significantly reduces the rate of anodic dissolution of iron [100]. This has been explored by several researchers as a means of mitigating corrosion rate of wet gas carrying gas pipelines in a technique known as pH-stabilisation [100, 101]. PH-stabilisation technique is based on the addition of alkaline chemicals (e.g. NaOH or methyldiethanolamine, MDEA) to corrosive media in order to increase pH of the glycol/water mixture and thus improve the protective properties of the corrosion films [101, 102]. Nyborg [100], stated that at significantly higher pH, corrosion rates below 0.1mm/year have been achieved, even with CO_2 partial pressures higher than 10bar. The reduction in corrosion rate at higher pH in ranges of about 6-7 was attributed to the enhanced precipitation of protective corrosion product films ($FeCO_3$) on the steel surface [100, 102].

It was also observed that in a multi-phase flow loop system, increasing solution pH to above 6.2 decreases corrosion rate significantly [9, 99]. Low pH increases the oxidizing power of H^+ in solution which may be markedly underestimated because of the partial dissociation of carbonic acid [9]. According to Crolet and Bonis [96] , there may be local partial re-association of HCO_3^- to increase the limiting diffusion current density for cathodic reaction, and causing the media to be more corrosive than mineral acid of at the same pH. Nesic *et al* [103], observed a decrease in the limiting diffusion current density of St52 steel by a factor of ≈ 3 by increasing the solution pH from 4 to 5 in a CO_2 saturated corrosion environment containing 3.5wt.% of NaCl, at a rotating speed of 1000rpm and at temperature of 20ºC. This is shown in Figure 3-4.

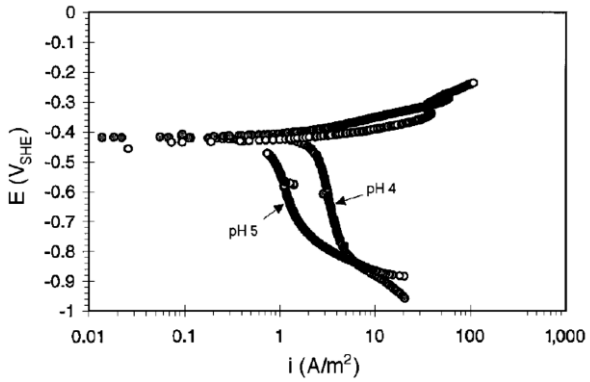

Figure 3-4 pH effect in CO_2 solution, water + 3% NaCl, PCO_2 = 1 bar (100 kPa), t = 20°C, 1,000 rpm, and t = 1.7 Pa, Re = 5,235, and St52 steel

The main reason for this threefold difference in limiting current density was attributed to the complex reactions contributing to the total cathodic current at different conditions [76, 79, 103]. The direct effect of pH on the anodic dissolution reaction was observed to be insignificant. The results by Nesic *et al* [103] does show that at low pH (< 4), the dominant cathodic reaction process in CO_2 systems is the cathodic reduction of H^+ because of its high concentration. At intermediate concentrations (4 < pH < 6), a new cathodic reaction becomes important in addition to the reduction of H^+ [77, 103]. This is the direct reduction of H_2CO_3 [77, 103].

In terms of the formation of $FeCO_3$ film, it has been reported that the solubility of Fe^{2+} is reduced by 5 times on increasing the pH from 4 to 5 and a further 100 times reduction is achieved by increasing the pH from 5 to 6 [9]. This can correspond to higher supersaturation and precipitation of $FeCO_3$. Under certain conditions, solution constituents, such as bicarbonate ions can also buffer the pH, leading to precipitation of $FeCO_3$ and reducing corrosion rate. While the debate on the exact defining temperature for formation of $FeCO_3$ continues, Videm and Dugstad [104] reported that a pH of 6.0 enables good protection of the steel surface due to the presence of $FeCO_3$ films even at room temperature.

From the foregoing, pH can be seen as a very important factor in $FeCO_3$ formation given its ability to strongly influence the solubility of $FeCO_3$. Thus, saturation of a saline solution could be expected with only a fraction of a ppm when the system pH is in the range of 6-7.5, making precipitation of $FeCO_3$ very favourable in such environments, especially at high temperature. Reduction in K_{sp} with increasing pH implies a largely positive SI (Eq. 3.31) and hence a very high supersaturation and tendency for $FeCO_3$ precipitation. This also implies that reducing the pH also increases the solubility limit of iron carbonate films leading to possible re-dissolution of already formed films and hence resulting in the initiation of localised and pitting corrosion of carbon steel [61]. In other instances where dissolution of iron precedes supersaturation and formation of $FeCO_3$, it is expected that at low pH, corrosion product formed is like to be un-protective leading to pit initiation and propagation [88]. These behaviours could be because the pH of the bulk solution and localised pits is very much dependent on the chemistry of solution in both the bulk solution and pits [58, 59] .

3.4.5 Chloride ion concentration/ionic strength

The mechanism of CO_2 corrosion is known to be dependent on many interrelated physicochemical factors whose interactions with steel in CO_2 environment is considered very important [105]. Water chemistry is considered one of the most influential parameter affecting

CO_2 corrosion. Oilfield produced water is usually characterised by a high amount of dissolved salts amongst other ions [83]. One of such ion is the dissolved chloride ion concentration [40, 83, 106], whose potential effect on accelerating corrosion reactions [105], as well as on localised and pitting corrosion of stainless steel materials are widely recognised [106].

Fundamentally, chloride ion has been regarded as aggressive agent of corrosion capable of destabilising corrosion product layers, leading to initiation of localised corrosion of carbon steel in CO_2 containing environment [40, 105, 107]. Yap and Srinivasan [40] also stated that corrosion rate increases with increase in chloride ion over a range of 10,000ppm to 100,000ppm in a deaerated production environment. However, recent studies on the actual effect of chloride ion on corrosion of carbon steel have offered conflicting viewpoints. Experiments by Luo and Singh [108] on carbon steel in simulated fuel-grade-ethanol (SFGE) show a decrease in corrosion potential and increase in corrosion rate with increasing chloride ion from 0 to 160 mg/L of NaCl. Post-test characterisation also showed a decrease in the pit density that was attributed to the fast uniform corrosion with some pit growth coalescence. The findings of Luo and Singh [108] was found to be consistent with observations by Papavinasam *et al* [38]. Experiments by Papavinasam *et al* [38] was however focused on pitting rate.

On the other hand, experiments by Jiang *et al* [109] at 80ºC and Fang *et al* [18] at 25ºC both concluded that corrosion rate and hence pitting corrosion rate decreases with increasing chloride ion concentration. However, Fang *et al* [18] also suggested that the presence of chlorides is an indication of an increase in solution conductivity and ionic strength, but stops short of a possible effect on the general corrosion rate. Experiments by Schmitt and Feinen [110] presents a rather interesting perspective to suggest that chloride seems to inhibit pitting corrosion at low concentrations in the order of 10^{-4}M However at higher concentrations, it was concluded that the chloride ion acts as an mobile anion which stabilises local anodes due to transfer of negative charges to anodic sites. Thus the later effect appears to be overriding inhibiting effects due to chloride adsorption at the corroding surface.

The above-mentioned controversial viewpoints of the effect of chloride on CO_2 corrosion of carbon steel have remained unanswered in recent years. However research by Eliyan *et al* [105] has help to provide useful explanation to some of the points raised. Eliyan *et al* [105] presented results over a chloride concentration range of (0-80mg/L of NaCl) that shows that corrosion rate increases with chloride ion up to a certain threshold after which reduces with increasing chloride ion. Such a threshold was higher at 90ºC than at 20ºC. The corrosion potential was also

observed to be lesser at 90ºC than at 20ºC with increasing chloride content. This suggests the influence of chloride ion on the aggressiveness of electrolyte and the extent to which it is influenced by temperature.

While the effect of cholride conentration on susceptibility of carbon steel materials to localised corrosion has been well recognised, the mechanism by which this effect is manifested has also remanined elusive. It has often been suggested that chloride would destabilised already formed film [40]. However, there have been little mention of its impact on the thermodynamics and kinetics of iron carbonate film formation. Sun *et al* [84] developed a unified model that shows the relationship between solubility limits of $FeCO_3$ and ionic strength and temperautre. Ionic strength in this context can be related to chloride ion concentration in a simple brine chemistry. The unified eqution is given as;

$$\log K_{sp\ (FeCO_3)} = -59.3498 - 0.041377T_K - \frac{2.1963}{T_K} + 24.5724 \log T_K + 2.518I^{0.5} - 0.657I \text{ [84]} \qquad 3.37$$

Where,$K_{sp\ (FeCO_3)}$, T_K and I are the solubility limit of $FeCO_3$, temperature in Kelvin and ionic strength of solution respectively.

Eq. 3.37 was shown to correlate well with experimental data at room temperature and suggest an increase in $FeCO_3$ solubility limit with ionic strength up to a certain value after which it remained unchanged. This relationship is shown in Figure 3-5. it is important to note that increasing solubility limit of $FeCO_3$ implies that supersaturation is unlikely to occur leading to formation of non-protective form of iron carbonate films. This has already been highlighted as the precusor to pit initionand propagation.

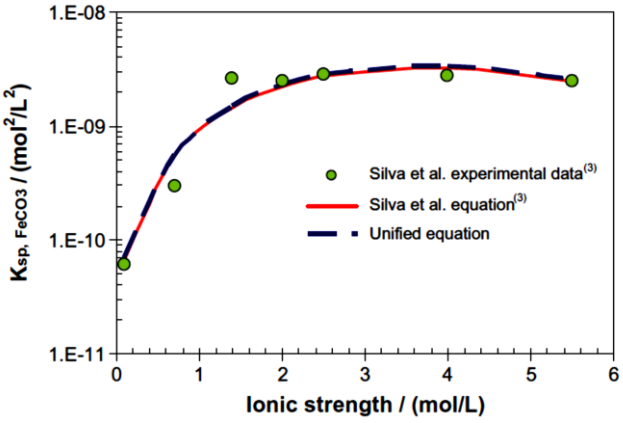

Figure 3-5 The experimental and calculated solubility of iron carbonate vs. ionic strength at room temperature [84].

3.5 The kinetics of iron carbonate crystallisation

The concept of iron carbonate formation had previously been discussed in this chapter. It is quite evident that the driving force for precipitation of $FeCO_3$ is the supersaturation (S) (see Eq. 3.32) of $FeCO_3$ and that a high degree of supersaturation is required in the bulk solution to obtain appreciable levels of $FeCO_3$ precipitation onto the steel surface [78]. In principle, there exist two steps involved in the precipitation processes once supersaturation is attained; nucleation and particle growth [78, 93]. The assumption is made that these two processes are related to the relative supersaturation (S_R):

$$S_R = \frac{Q - Q_{eq}}{Q_{eq}} = S - 1 \qquad 3.38$$

Where Q is the concentration of the solute and Q_{eq} is the equilibrium solubility.

It is assumed that the rate of both nucleation and particle growth is related to the relative supersaturation (S_R). The rate of nucleation is believed to increase exponentially with relative supersaturation (S_R), whilst particle growth varies linearly with relative supersaturation (S_R) [78]. Consequently, it is expected that $FeCO_3$ particle growth should occur at low relative supersaturation. However, when relative supersaturation is high, the exponentially increased nucleation rate will far exceed the linearly increased particle growth rate, thereby preventing particle growth and leading to the formation of nanocrystalline or even non-crystalline or amorphous form of $FeCO_3$ to develop [93].

It has also been stated that although nucleation of $FeCO_3$ is possible at $S > 1$, its rate increases rapidly only when a critical supersaturation S_c is exceeded [93]. This critical supersaturation S_c and hence the propensity for formation of crystalline form of $FeCO_3$ film has been shown from experiments by Guo *et al* [93] to be strongly influenced by solution pH. Guo *et al* [93] concluded that the non-crystalline $FeCO_3$ will form if the pH is decreased and that there must be a critical pH value above which the amorphous $FeCO_3$ which forms as a result of extended nucleation will be dominated by growth of larger sized crystals of $FeCO_3$. Figure 3-6 summarises the effect of different morphologies of $FeCO_3$ on the corrosion behaviour of steel in CO_2 environment.

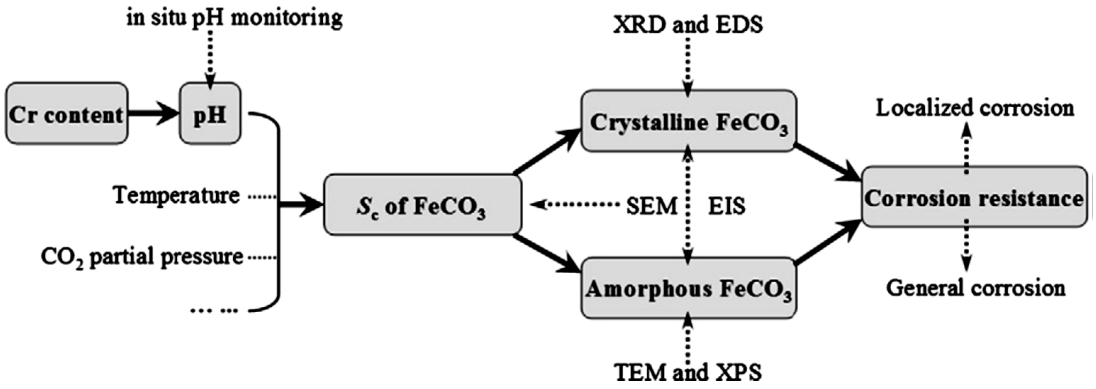

Figure 3-6 The CO_2 corrosion resistance mechanism for low Cr alloy steel [93].

3.6 Pitting corrosion of carbon steel in CO_2 saturated environments

Pitting is considered one of the main causes of corrosion failures in oilfields and contributing about 12% of oil and gas asset failures [8]. In oilfield corrosion environments, incidences of pitting corrosion are fundamentally associated with passive alloys such as stainless steel materials [106, 111]. Its mechanism is well understood and revolves around the localised breakdown of the passive oxide film, leading to pit initiation, metastable pit growth due to localised aggressive environment and stable propagation [111]. Initiation of pitting in passive materials is understood to start at areas of sulphide inclusions [112-114]. Sulphide inclusions are usually not covered by passive oxides and are less noble than the surrounding passive surface, hence preferentially dissolves and becomes the nucleation sites for pit initiation [112]. However, what remains unclear is the actual mechanism(s) of pitting corrosion in cases of non-passivating materials such as carbon steel in oilfield environment (often saturated with CO_2 and/or H_2S gas) [9, 38, 68]. Although, sulphide inclusions have also been associated with pit initiation in carbon steels, it revolves around the areas of sulphide inclusions being more noble than the surrounding steel matrix that becomes preferentially more anodic [112, 114]. Preferential dissolution of the surrounding steel matrix means that the sulphide inclusions may become undermined and falls away, leading to initiation of micropits that usually stops growing [112]. In the context of pitting corrosion of carbon steel in CO_2-containing environments, pit initiation may not be far from the above-mentioned scenario and in addition to the role of preferential dissolution of ferrite phase from steels [88]. However, the mechanism of pitting corrosion beyond the initiation stage still remains vague and is currently a subject of extensive discussion within the research communities. Nonetheless, the general consensus on the mechanism of pitting corrosion of carbon steel materials in CO_2 containing environments have

often been adapted from the mechanism of pitting in passive materials to involve the following stages;

1) Formation of protective corrosion product layers ($FeCO_3$ and FeS) due to corrosion of metal exposed to the environment.
2) Localised breakdown or removal of protective corrosion product layers
3) Anodic dissolution of materials at localised regions with breakdown of protective corrosion products layers with respect to the rest of the film covered surface (which becomes sites preferential sites for cathodic reactions.
4) Pitting growth at localised anodic areas will continue due to anodic dissolution at sufficient rate, such that reformation of the protective corrosion product layer becomes unattainable [38].

However, it is worth noting that in passive alloys, the pit is usually the anode while the surrounding oxide covered areas are the cathodes. On the other hand, for open pits in active materials like carbon steels, it is likely that the base of an active pit is the anode while different sites on the surrounding walls of the pits could be acting as the cathode. This is probable because pitting on an active site may not necessarily prevent electrochemical activities at other sites at the same surface; at anodic and cathodic reaction sites. Papavinasam *et al* [38] also stated that for cases where $FeCO_3$ corrosion product layers do not form, then the corrosion rate will be uniform and corrosion damage morphology will be general corrosion. But it is expected that if an intact and protective $FeCO_3$ corrosion layer forms, the corrosion rate will decrease to a negligible value. However, Crolet *et al* [88], suggested a slightly contrasting viewpoint that when the formation of protective iron carbonate layer is unattainable from the start of corrosion process at almost zero saturation, uniform corrosion will occur but may gradually progresses to localised or pitting corrosion due to the formation of non-protective $FeCO_3$ corrosion layers. Such corrosion scenario have been explored by several authors [93, 95] for corrosion of carbon steel in different brine saturated with CO_2. Both authors observed pitting corrosion in situations where the $FeCO_3$ corrosion product layers were non-crystalline and non-protective. The formation of non-crystalline and non-protective $FeCO_3$ these research works was attributed to the low initial saturation of the solution as a result of the low starting pH of the corrosion media. The views on pitting corrosion of carbon steel in sweet environments as discussed in this section do suggest that a convincing conclusion on this subject is still beyond the reach of the research community.

3.7 Summary of literature review: CO_2 corrosion and CO_2 induced pitting corrosion

CO_2 corrosion and CO_2 induced localised and pitting corrosion has been shown from this review to be strongly linked to the formation of iron carbonate films. CO_2 corrosion reaction of carbon steel leads to the production of CO_3^{2-} and Fe^{2+} in the bulk solution. The availability of these ions strongly determines the tendency and to a lesser extent, the kinetics of iron carbonate film formation on the surface of the corroding steel, often defined in terms of saturation index of solution. However, the nature; protectiveness, stability, adherence, coverage and chemistry of the deposited iron carbonate films are strongly linked to the kinetics of corrosion reactions and the kinetics of its deposition on the metal surface. These kinetics aspect of corrosion reaction and iron carbonate formation is however, also dependent on other such factors like CO_2 partial pressure, solution pH, chloride ion concentration and temperature. The impact of which determines the integrity and stability of deposited films and the likelihood of initiation and propagation of localised pits. Pitting in CO_2 saturated environments usually results from the formation of poorly protective and stable iron carbonate films, such that there exist discrete areas corroding faster than at the rest of the steel surface. This leads to preferential material loss by corrosion, influenced by some localised galvanic cell on steel surface. The presence of chloride ions has been shown in this review to have variable influence on the electrochemical process steel surfaces as well as the damage from pitting corrosion.

The literature review has also shown that increasing the partial pressure of CO_2 gas is likely to increase the tendency for protective iron carbonate film to form during corrosion of carbon steel, depending on local pH and Fe^{2+} concentration. It is also important to note that in systems where supersaturation is expect from the anodic dissolution reaction of steel, CO_2 partial pressure influence on the environment becomes very crucial. CO_2 partial pressure also influences the threshold for such corrosion films to be formed in terms scaling temperature. In the later aspect, CO_2 partial pressure may become a key determinant of the propensity for pitting corrosion or other forms of localise corrosion to occur, since these forms of corrosion are directly linked to the protectiveness of $FeCO_3$ corrosion product layer.

The temperature effect on corrosion pitting corrosion in CO_2 containing corrosion environment can therefore be correlated on its impact on the rate of increase in aggressiveness of chloride ions present in brines by thermal activation, the impact of the rate of electrochemical activation of substrate metal to lose more Fe^{2+} and how much it could promote or deter the precipitation of protective iron carbonate films. While it has been generally accepted that temperatures in excess

of 70-90ºC may promote protective iron carbonate films that acts to protect against localised corrosion, other environmental variables like pH, solution chemistry, and ionic strength may also have some significant influence on the integrity of iron carbonate films, especially at lower temperatures where the corrosion product is likely to be non-protective. It is still unclear how changing temperature may influence the pitting corrosion behavior of carbon steel in CO_2 corrosion environments. This hypothesis will to be fully explored and would form an important part of this research project.

The effect of pH on corrosion and pitting corrosion in CO_2 containing environment is modelled around its influence of H^+ reduction and effects on formation of $FeCO_3$ corrosion products. Higher pH suppresses H^+ reduction reaction contribution to the limiting cathodic current density and reduces corrosion rate of steel in these conditions. On the effect of pH on the formation of $FeCO_3$ corrosion layer, a pH of 6-7 enhances the formation protective and crystalline $FeCO_3$ film with corrosion rate down to 0.1mm/yr. However, there has been limited investigation on the propensity for pitting to occur even in these conditions. On the other hand, lower pH, in the regions of ≤ 4 would increase H^+ reduction reaction contribution to the limiting cathodic current density and increase corrosion rate. It has also been shown that a non-crystalline form or amorphous form of $FeCO_3$ is favoured in these conditions and may become the precursor for pitting corrosion in carbon steel materials.

For a simple brine solution like NaCl, minimum buffering effect will be expected and dissolved chloride ions will directly influence the ionic strength and conductivity of solution resistance of the corrosion system. And depending on the temperature of the corrosion system, the chloride ion concentration may become very aggressive to the material. This is just one means by which chloride can influence the corrosion degradation process of carbon steel material in CO_2 environment, often leading to aggravated material loss at higher concentration. Chloride ion or ionic strength has also been shown to have some influence on the solubility limit of $FeCO_3$. However it is not likely to be on the same scale as other parameters. Hence exploring chloride ion effect on corrosion and pitting corrosion of carbon steel in sweet environment proffer an opportunity to define its actual role in the degradation of carbon steel in these environments.

Chapter 4. Literature Review: Sour (H_2S) corrosion

4.1 Definition of concepts: Sour (H_2S) corrosion

The term "sour corrosion" is used to describe oilfield corrosion and damage that relates to the presence of significant amounts of H_2S gas dissolved in the brine phase. H_2S gas in its dry form is usually non-corrosive just like dry CO_2 gas. However, in most oilfield scenarios; H_2S gas is usually present naturally in mixtures with brines in oil and gas reservoirs and also in association with other acidic gases; CO_2, organic acids and other free radicals and ions from dissolved salts. This makes oilfield produced fluids acidic and corrosive to the carbon steel pipes used for its transportation [4, 10, 13, 115]. Reservoir souring by the activities of sulphate reducing bacteria (SRB) in produced water is also considered as one of the key steps that exacerbating the risks of H_2S corrosion and the occurrence of microbiologically induced corrosion (MIC) [28, 116]. This increases H_2S gas content in oil and gas production lines and most times in previously sweet oilfield conditions. The activities of SRB are significantly enhanced within microbial (biofilms) at the produced water-seawater/steel interface, a condition usually favoured by the chemistry and constituents (presence of volatile fatty acids and SRB's) at these interfaces [28, 116]. These biofilms frequently develop anaerobic regions that promote the formation of a variety of sites on the steel surface that are electrochemically and physically different from neighbouring sites. This situation in conjoint with the presence of dissolved H_2S has been strongly linked with incidences of localised/pitting corrosion of carbon steels and the resultant formation of iron sulphide films at active sites [19, 28]. This is one of the major corrosion related challenges of exploring aging oilfields.

4.2 Characterisation of sour corrosion conditions

The characterisation of sour service conditions for oil and gas production wells was driven by the need to effectively manage wet hydrocarbons as a result of the increasing number of oilfields with significant levels of H_2S gas and under challenging operating conditions. Characterisation of sour environments provides a tool for extrapolated technical and commercial evaluation of facilities integrity in oilfields containing H_2S gas, especially those that were not designed for sour services. Hence the following domains of oilfield sour service have been defined and can be applied with good judgement when establishing the probability of H_2S related corrosion damages of oilfield installations. National Association of Corrosion Engineer's (NACE) characterisation of oilfield sour service conditions with respect to corrosion challenges is presented in Figure 4-1.

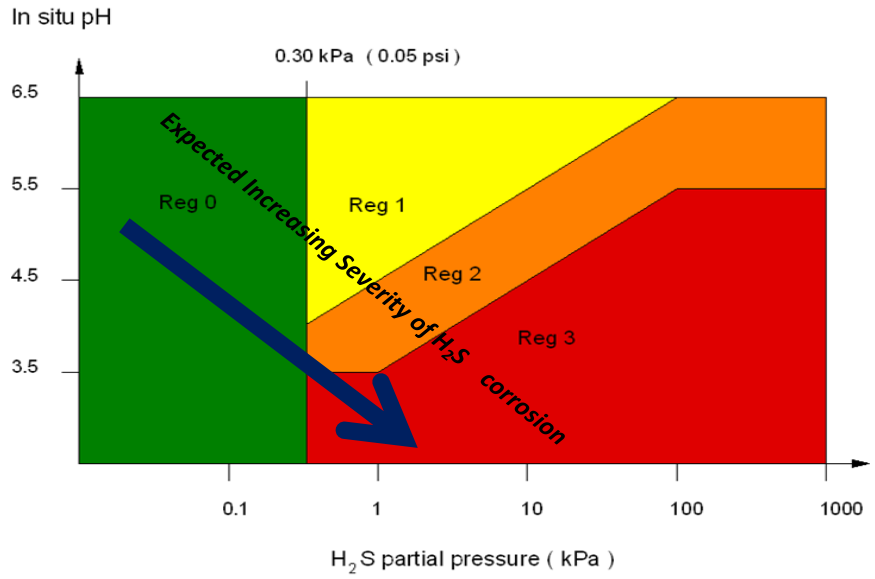

Figure 4-1 NACE MR0175/ISO 15156 "Domain of Service" for Sour Conditions for carbon steels, low alloy steels and cast iron. [15, 117]

Reg "0" or Domain "0": is characterised by trace amount of hydrogen sulphide gas, and the corrosion mechanism is usually CO_2 dominated.

Reg "1" or Domain "1": is characterised as "mild sour service" condition with H_2S amount relatively higher than the minimum threshold above which the oilfield condition is termed "sour" (0.30kPa or 0.05psia).

Reg "2" or Domain "2": is the intermediate sour service condition that is also influenced by the slightest change in H_2S partial pressure.

Reg "3" or Domain "3": this zone of sour service condition is defined as severe sour condition and is characterised by very high of H_2S content and low in-situ pH [15, 117].

Figure 4.1 clearly shows NACE MR0175/ISO 15156 defined standard of 0.3kPa ≈ 0.05psi as the lower boundary of H_2S partial pressure for sour corrosion systems. It also shows that any detectable increase in the amount of H_2S poses a precarious restriction of corrosion environment to very severe sour service condition (domain "3"), especially when in-situ pH is below pH of 3.5.

There is also a suggested general rule of thumb used in defining the dominating corrosion reaction in H_2S-CO_2 environment and also used as a tool in characterising the relative domains

of dominant corrosion product for CO_2 and H_2S containing systems. This rule of thumb is in terms of the ratios of the partial pressures of the two gases present in the system.

- For a gas pressure ratio of $\frac{p_{CO_2}}{p_{H_2S}} < 20$ **,** the corrosion regime is dominated by H_2S.
- While for gas pressure ratio within the boundary $\frac{p_{CO_2}}{p_{H_2S}} > 200$ [40] corrosion regime is dominated by CO_2 at temperatures above 60℃ and $\frac{p_{CO_2}}{p_{H_2S}} > 500$ at temperatures below 25℃ [37].

In the latter rule of thumb, the upper boundary condition is often limited by temperature and Fe^{2+} considerations during its application [37]. While on the other hand, within the lower limit of 200 is the likelihood for the formation of iron sulphide (mainly Mackinawite), especially at H_2S gas pressure > 0.01 psi from the fast and direct "solid state" reaction between F^{2+} and S^{-2} at the metal surface [39, 40, 73, 115, 118].

4.3 Mechanism of sour corrosion and formation of iron sulphide

It is almost generally acknowledged within the oil and gas corrosion research community that the chemistry of "sour" corrosion in oilfields is relatively complex, especially in relative terms to the mechanism of CO_2 corrosion. However, on a general note, it can be postulated that the hydrolysis and dissolution processes of H_2S gas can be described by the following reactions [119-121]:

Hydrolysis of H_2S gas in water:

$$H_2S_{(g)} \rightleftarrows H_2S_{(aq)} \qquad 4.1$$

H_2S gas is diprotic and dissociates in two reaction steps when dissolved in water;

H_2S dissociation reaction;

$$H_2S \rightarrow HS^- + H^+ \qquad 4.2$$

Bisulphide dissociation reaction;

$$HS^- \rightarrow H^+ + S^{2-} \qquad 4.3$$

4.3.1 Cathodic reaction

Theoretically, the expected magnitude of measured corrosion rate of carbon steel materials exposed to H_2S-containing oilfield environments is expected to be relatively comparable to measured corrosion rates in completely sweet corrosion environments. This is because, for

similar conditions (for example; temperature and pH), it is expected that the acid created by the dissolution of H_2S is about three times weaker than that of carbonic acids, but H_2S is also known to be about three times more soluble than CO_2 gas. Therefore, the effect of both CO_2 and H_2S gases on lowering the solution pH and potentially increasing corrosion is expected to be fundamentally the same [9, 120]. This makes an interesting case for a critical review of the cathodic reaction mechanisms as is influenced by the presence and dissolution of H_2S. A direct reduction reaction of H_2S was proposed by Bolmer [122] as the overall cathodic reaction in H_2S environments has been surmised;

$$2H_2S + 2e^- \rightarrow H_2 + HS^- \qquad 4.4$$

The reaction of Eq.4.4 was found to be limited by H_2S diffusion and the over-potential associated with H_2 evolution from water reduction [122]. Bolmer [122] also stated that in the regions below the limiting diffusion current, and higher cathodic over-potential, cathodic reaction current density is a function of bisulphide concentration and/or H_2S/HS^- ratio. Therefore, the evolution of H_2 results from the cathodic reduction of HS^- to S^{2-} as well as the reduction of H_2O [122, 123]. In a different study by Ogundele and White [123], it was proposed that the reduction of H_2S to produce H_2 may occur via the following reactions;

$$H_2S + e^- \xrightarrow{RDS} H + HS^- \qquad 4.5$$

$$H_2S + H + e^- \rightarrow H_2 + HS^- \qquad 4.6$$

In this case, is was assumed that H_2S gas is directly reduced at the steel surface to atomic hydrogen and bisulphide ion in a rate controlling step [123].

In addition to the reactions of Eq. 4.4-4.6, bisulphide reduction has also been thought to contribute to the total cathodic current according to the reaction [120, 121];

$$2HS^- + 2e^- \rightarrow H_2 + 2S^{2-} \qquad 4.7$$

Bisulphide is usually produced by the dissociation reaction of Eq.4.2. However, it is has been suggested that the local concentration of HS^- at the metal-corrosion media interface will increase with increasing pH due to H^+ reduction [121]. Hence, HS^- reduction reaction of Eq.4.7 becomes more significant as the HS^- : H_2S ratio at the corrosion interface increases with increasing pH. A schematic of the overall cathodic reaction at the metal- H_2S containing corrosion media interface is given in Figure 4-2

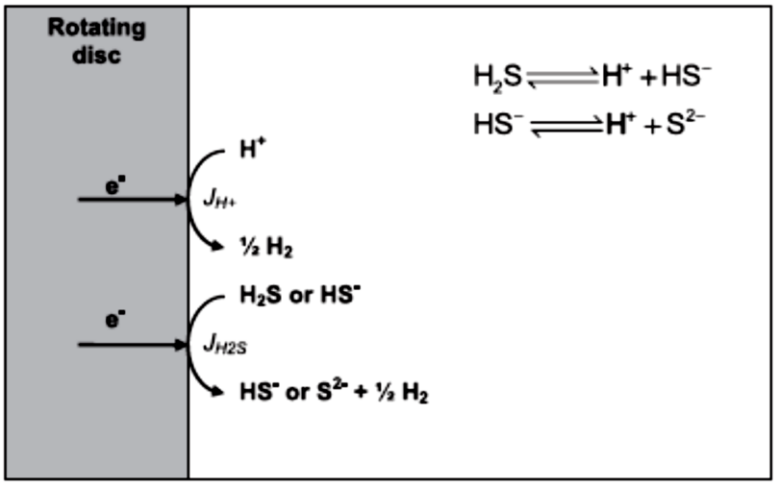

Figure 4-2 Schematic representation of the system describing cathodic reactions in acidic H_2S-containing corrosion media[121] .

4.3.2 Anodic dissolution of steel

Generally, the anodic dissolution co carbon steel is expected to follow the reaction;

$$Fe \rightarrow Fe^{2+} + 2e^- \qquad 4.8$$

However, other different reaction pathways have been proposed by other researchers. In some instances, it was proposed that Fe is first converted to a catalyst $(FeHS^-)_{ads}$ that is absorbed to the metal surface, which then transforms to hydrosulphide ion ($FeHS^+$). Hydrolysis of $FeHS^-$ was proposed to facilitate the formation of Fe^{2+} [123]. This model of Fe dissolution is given by the following reaction sequence;

$$Fe + H_2S + H_2O \rightarrow (FeHS^-)_{ads} + H_3O^+ \qquad 4.9$$

$$(FeHS^-)_{ads} \xrightarrow{RDS} FeHS^+ + 2e^- \qquad 4.10$$

$$FeHS^+ + H_3O^+ \rightarrow Fe^{2+} + H_2S + H_2O \qquad 4.11$$

An alternative Fe dissolution pathway was also discussed by several authors [32, 123, 124]. This model is given by the following reaction sequence;

$$Fe + HS^- \rightarrow (FeHS^-)_{ads} \qquad 4.12$$

$$(FeHS^-)_{ads} \xrightarrow{RDS} FeHS^+ + 2e^- \qquad 4.13$$

$$FeHS^+ \rightarrow Fe^{2+} + HS^- \qquad 4.14$$

This reaction mechanism of Eqns. 4.12-4.14 is almost similar to the previous in terms of conversion of Fe to an intermediate catalyst $(FeHS^-)_{ads}$ and the rate determining step of the anodic dissolution process. However, the active species in this case is the bisulphide (HS^-) ion rather than the H_2S component.

From the foregoing information, the overall reaction for the corrosion of carbon steel materials in H_2S containing brine and leading to the formation of iron sulphide films can be written as;

Anodic reaction;

$$Fe \rightarrow Fe^{2+} + 2e^- \quad 4.15$$

Cathodic reaction;

$$2H_2S + 2e^- \rightarrow HS^- + H_{2\,(g)} \uparrow \quad 4.16$$

$$2HS^- + 2e^- \rightarrow 2S^{2-} + H_{2\,(g)} \uparrow \quad 4.17$$

$$Fe_{(s)} + H_2S_{(aq)} \rightarrow FeS_{(s)} + H_{2\,(g)} \uparrow \quad 4.18$$

However, when the intrinsic complexities of H_2S/iron sulphide controlled corrosion are factored in (as would be discussed later in this chapter), the overall reaction of the chemical and electrochemical process leading to H_2S induced corrosion and the formation of iron sulphide films is often represented by the generic equation below and with arbitrary stoichiometric annotations. So that we can now give a generalised equation for corrosion of steel in sour environment as follows;

$$_xFe + {}_yH_2S_{(aq)} \rightarrow Fe_xS_y + {}_yH_2 \quad [39] \quad 4.19$$

4.3.3 The anomaly of H_2S corrosion and iron sulphide formation

The corrosion behaviour and subsequent formation of iron sulphide films so generally depicted by Eq. 4.15 - 4.19, is more complex than has been depicted by these equations. It has been suggested that H_2S corrosion is primarily dominated by two electrochemical processes: "solid state" or "direct" corrosion reaction and aqueous phase corrosion reactions [35, 39, 73, 115, 118, 120]. The former is a fast and direct heterogeneous chemical reaction between H_2S and/or HS^- and Fe at the steel surface leading to a fast process of formation of iron sulphide films; mainly *mackinawite* [32, 123, 124]. *Mackinawite* is a form of iron sulphide film commonly encountered in sour oilfield corrosion environments [118]. The latter scenario is such that H_2S acts as a corrosive species like every other dissolved acidic gas by influencing the cathodic process [115], and distorting the redox equilibrium of the electrical double layer (EDL) at the brine-metal interface.

It has been suggested that the kinetics and severity of H_2S (sour) induced pitting/localised corrosion are strongly controlled by the nature of corrosion product film (FeS) in terms of both its chemistry and morphology [34, 35, 125]. Hence, it becomes evident based on the aforementioned assumption, that the fast and direct reaction of between Fe and H_2S and/or HS^-,

process is likely to be a major factor in the reactions leading to the formation of iron sulphide films. This has been based on the hypothesis that most of the dissolved Fe^{2+} in the bulk solution are not being used up in the formation of iron sulphide films, which in turn controls the overall corrosion behaviour of steel in these conditions. Hence, there is no significant effect of solution supersaturation (with Fe^{2+} and HS^-) levels on the rate of *mackinawite* formation [115, 118, 126] in the early stages of sour corrosion reactions and unlike the case with CO_2 corrosion. The initial layer of *mackinawite* is usually very thin and has the potential to significantly influence the corrosion behaviour in these environments [124]. *Mackinawite* has also been reported to be susceptible to rupture and subsequently leading to localised corrosion/pitting, depending on the level of saturation with respect to Fe^{2+} and HS^- ions, as well as other environmental parameters [34, 39, 115, 125]. These are obviously in sharp contrast to the mechanism of CO_2 corrosion and iron carbonate film formation. The two electrochemical reaction routes in H_2S corrosion of carbon steel are illustrated in the Figure 4-3

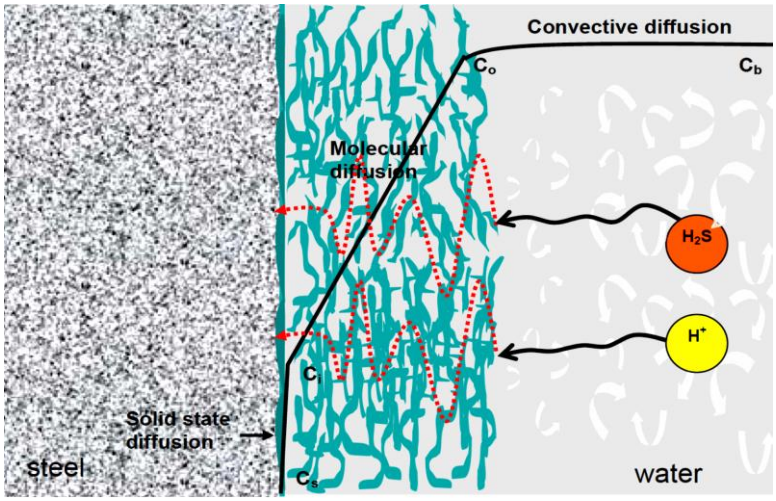

Figure 4-3 Schematic illustration of the two dominating electrochemical processes in H_2S corrosion [118]

4.4 Different types/nature of iron sulphide films

In addition to the ambiguous electrochemical processes associated with H_2S dominated corrosion systems, there is still some inherent level of complexity in the chemistry/morphology/structure of iron sulfide films formed in sour systems. Eq. 4.19 reflects such complexities and represents the tendency for formation of different thermodynamic state of iron sulfide films for which a slight change in environmental conditions can lead to different corrosion behavior of test steel [42]. In most corrosion scenarios, the type of corrosion product scale formed on the steel, defines the rate-limiting step of the corrosion degradation process [34,

127]. Sour oilfield corrosion environments are such that there is the possibility for the formation of different types of iron sulfide films, such as;

1. Amorphous ferrous sulfide (FeS),
2. Mackinawite ($Fe\,S_{1-X}$) and/or Stochiometric FeS
3. Cubic ferrous sulfide (FeS),
4. Smythite ($Fe_{3+X}S_4$),
5. Greigite (Fe_3S_4),
6. Pyrrhotite ($Fe_{1-X}S$),
7. Troilite (FeS), And
8. Pyrite (FeS_2) [37, 118, 128].

The different iron sulphide films all have distinct crystal structures, oxidation states, and stoichiometries of Fe and S. This may be due to the formation of different complexes, ions and ion pairs in solution depending upon the pH, the Fe^{2+} and H_2S concentrations [36] . Some of these complexes include: FeS (ion pair), $Fe(HS)^+$, $Fe(HS)_2$ or FeS• H_2S, $Fe(HS_2)^-$ or FeS•HS, FeS_2^{2-} or FeS•S^{2-} [127]. However, pyrite, pyrrhotite and mackinawite are the three main types of Fe_xS_y that are commonly encountered in sour oilfield corrosion environments [42, 127].

4.4.1 Mackinawite

Mackinawite is a thermodynamically semi-stable or metastable form of iron sulphide film that forms under the special conditions of low H_2S activity in the corrosion environment , which will be referred to herein as slightly sour. Under such conditions, iron sulphide is still soluble in the bulk solution; i.e., the concentrations of Fe^{2+} and HS^- are still below the saturation threshold in the bulk solution for the formation of iron sulphide from dissolved Fe^{2+} and HS^- ions. Hence, mackinawite formation is expected to be via "direct" or "solid state reaction". Mackinawite is formed in such conditions rather than other more thermodynamically stable forms because its formation kinetics is much faster than other forms of iron sulphide films [39, 115, 118, 127]. Mackinawite is often defined as the sulphur deficient iron sulphide film and often represented as $Fe\,S_{1-x}$ or $Fe_{1+x}S$ [129, 130], where $0 < x < 1$.

Another possible pathway for formation of mackinawite form of iron sulphide is via the formation of the metastable complex catalyst $(FeHS^+)_{ad}$ described in section 4.3. It has been reported that the species $(FeHS^+)_{ad}$ formed at the corrosion interface could be incorporated directly into an already growing layer of mackinawite film in less acidic media [32, 124, 131, 132] and via the reaction;

$$(FeHS^{+})_{ads} \rightarrow Fe\,S_{1-x} + xSH^{-} + (1-x)H^{+} \quad 4.20$$

Ma *et al* [124] also stated that the formation of one or more of other forms of iron sulphide films is likely to occur if reaction of Eq. 4.20 leads to local supersaturation at the electrode surface.

Experiments by Li *et al* [130] have shown that the Mackinawite form of iron sulphide film is very sensitive to oxygen (O_2) and changes to other forms of iron sulphide films, especially the sulphur rich forms of iron sulphide films. The likelihood for this transformation to occur also increases with increasing H_2S concentration at lower temperature [129, 130]. Mackinawite is also known to be the least electronically conductive form of the iron sulphide films [133].

4.4.2 Pyrrhotite

Pyrrhotite is a sulphur rich form of iron sulphide film that forms in most sour environments. It is often defined as ($Fe_{1-x}S$ or $Fe\,S_{1+x}$), where $0 < x < 1$ [129, 130] and is formed as a result of transition from mackinawite, depending on environmental parameters. Pyrrhotite is believed to be more thermodynamically more stable than mackinawite because the pyrrhotite formation kinetics are much slower than those of mackinawite [120]. In the presence of excess H_2S gas, the transition to pyrrhotite from mackinawite would occur at relatively lower temperature than at lower concentration of H_2S gas [71, 72]. This transition mechanism simply implies an increase in Fe:S ratio.

4.4.3 Pyrite

Pyrite is an ordered solid solution of FeS and elemental sulfur, and is found only when elemental sulfur is present in the system [120]. It is primarily represented as FeS_2 and is the most stable iron sulphide phase and requires the presence of dissolved low-valance sulphur species acting as electron acceptors for its formation. Reaction of oxidant with mackinawite often leads to gregite, which is more of an intermediate phase in the transition of macknawite to pyrite [130]. pyrite is also the most electronically conductive of the different iron sulphide films [133].

The transition from one form of iron sulphide film to the other has been shown in Figure 4-4 to be influenced by temperature and H_2S gas concentration, especially for the three main types of iron sulphide films described.

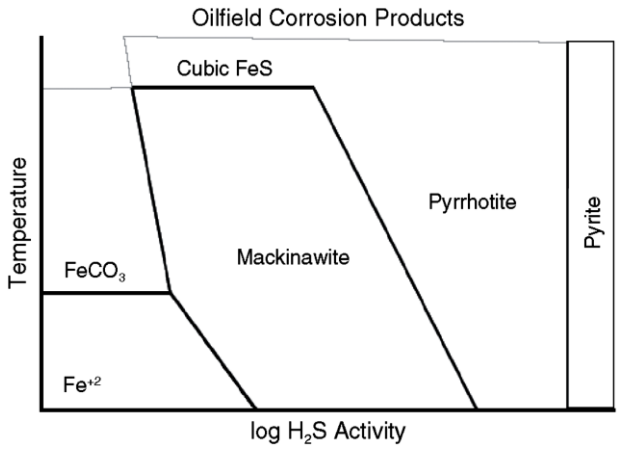

Figure 4-4 Corrosion product formation as a function of temperature and H_2S concentration [39, 120, 127]

In addition to the three different types of iron sulphide films discussed thus far, is the characteristic tendency for the formation of different iron sulphide films in a multi-layered frame as mentioned earlier in this section. The discrete multi-layered film structures can be explained by mass diffusion of corrosive and precipitating species across the electronically conductive iron sulphide corrosion film, and as such, thermodynamic stability of at least two types of iron sulphide films can be attained simultaneously as a result of the concentration and electrode potential gradients across the cross section layer of corrosion films [24, 34, 73, 129, 134, 135]. This concentration gradient ensures that sulphide concentration decreases towards the steel surface and less sulphur rich sulphides (pyrrhotite and pyrite) are formed and more of the sulphur deficient mackinawite is formed creating multiple layers of different form of iron sulphide films [124, 129]. This is shown in Figure 4-5 for test at a H_2S/CO_2 ratio of 0.4 and a temperature of 120ºC in a flow loop with a wall shear stress of about d 130 Pa [129].

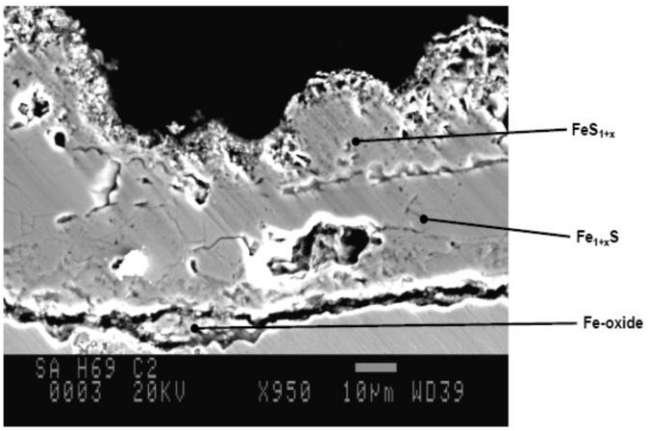

(a)

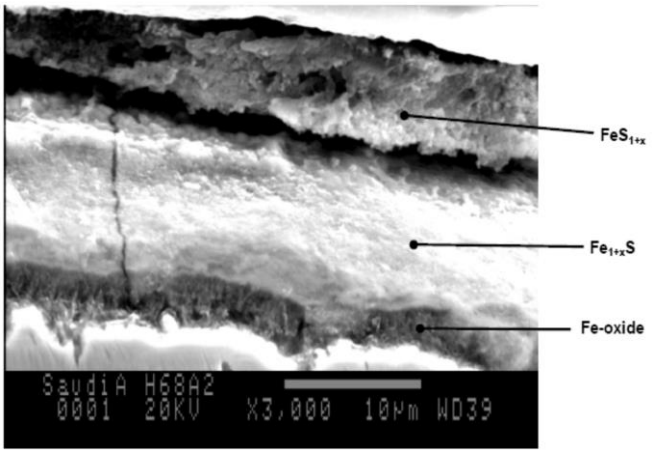

(b)

Figure 4-5 Multilayer orientation of different iron sulphide scales (a) 120 ^{0}C, exposure time of 166hrs and H_2S/CO_2 gas ratio of 0.4 and (b) 120 ^{0}C, exposure time of 138 hours and H_2S/CO_2 gas ratio of 0.4 [129].

4.5 Factors affecting thermodynamics and kinetics of sour corrosion of carbon steels and iron sulphide formation

In relative terms, it is a known fact that aqueous H_2S is about three times a weaker acid and hence expected to be less corrosive than aqueous CO_2 [9, 118]. However, solubility of H_2S has been suggested to be three times more soluble than CO_2 under the same conditions [9, 118]. Hence, it is fundamentally not expected to experience significant difference in metal damage rate between both systems of dissolved gases. Under such varying scenario, it would be expected that H_2S corrosion reaction will proceed faster in H_2S-CO_2 systems leading to the formation of iron sulphide films. The proposed "direct" or "solid state" reaction process is known to be very fast [124]. Such corrosion reaction between the steel surface and un-dissociated aqueous H_2S/HS^- tend to support the likelihood for mackinawite form of iron sulphide to form first. [39, 115, 118, 136]. This is also expected to influence the overall corrosion behaviour of steel in H_2S-CO_2 systems. However, the extent to which the sequence of formation of $FeCO_3$/FeS corrosion products in these systems may affect the nature of corrosion damage (most especially pitting and localised corrosion) has remained elusive to the research community. Direct or solid state reaction process significantly controls the kinetics of iron sulphide film formation much more than reaction between Fe^{2+} and HS^- in the bulk solution [34-37, 118, 125, 126]. Hence, as a way of understanding the key environmental factors that affects sour corrosion, it is also very useful to review and explore the effects of such environmental parameters on the thermodynamics and kinetics of iron sulphide film formation and H_2S

induced corrosion damage in general. The key environmental factors to be reviewed in this section include;

a) H_2S - CO_2 concentration/partial pressure and H_2S-CO_2 gas ratio
b) *In-situ* pH
c) Temperature
d) Solution chemistry and presence of chloride ions
e) Exposure time [31, 39, 41, 115, 118, 135, 137, 138]

4.5.1 H_2S and CO_2 concentration/partial pressure and H_2S-CO_2 gas ratio

Most currently soured and souring wells and oilfield pipeline systems usually have a corrosion history often initially dominated by CO_2 corrosion. This is because these wells have been previously characterised as sweet, hence most research has been focused on low levels or concentration of H_2S gas [39]. Several studies on the mechanism of corrosion in H_2S-containing environments have presented contrasting viewpoints on the effect of H_2S gas on the corrosion of carbon steel in mixed CO_2-H_2S containing environments. Videm and Kvarekvål [139] reported an increase of uniform corrosion rate of carbon steel in mixed CO_2-H_2S containing environments with small amounts of H_2S gas. On the other hand, Zheng *et al* [140] and Ma et. al [124] reported a decrease in general corrosion rate of carbon steel in mixed CO_2-H_2S and H_2S-containing environments, respectively with small amounts of H_2S gas. Zheng *et al* [140] attributed this effect to the inhibition of the reduction of H_2CO_3, but with no consideration to the formation of iron sulphide film, while Ma *et al* [124] suggested the influence of iron sulphide film in the absence of CO_2 gas but only after an initial increase in corrosion rate from a H_2S-free acidic environments. The conclusions on the inhibition effect presented by Zheng *et al* [140] was almost similar to the suggestion by Singer *et al* [120] on the prevention of the influence of other active species (H^+ and H_2CO_3) by the presence of H_2S gas in the corrosion system. Singer *et al* [120] suggested that the mackinawite forms quickly with small quantities of H_2S gas and creates a diffusion barrier for the influence of H^+ and H_2CO_3 for a 22 hours test duration. There were also observation of an increase in corrosion rate of carbon steel with an increase in H_2S concentration and/or partial pressure (usually at completely sour corrosion environment) in both mixed CO_2-H_2S and pure H_2S-containing environments [119, 120, 131, 140]. One of such results by Tang *et al* [131] is provided in Figure 4-6.

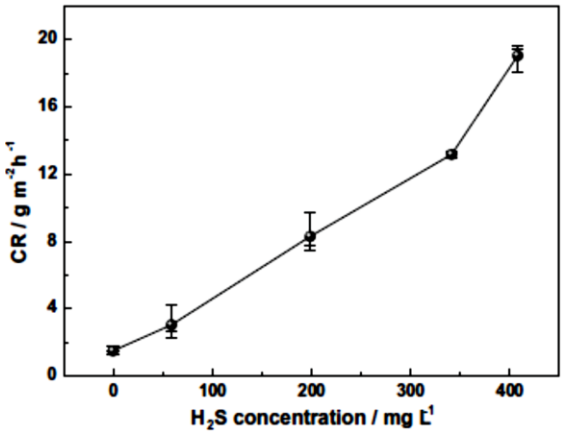

Figure 4-6 Plot of corrosion rate as a function of H_2S concentration in solution at 90ºC [131].

With respect to the formation of iron sulphide film during sour corrosion, low concentration and partial pressure of H_2S gas in H_2S-CO_2 gas mixture have been found to favour the formation of a mackinawite form of iron sulphide film [127]. This scenario is largely favoured by the "solid state" corrosion reaction by which the first layer of iron sulphide film (mackinawite) is formed on the steel surface [39, 73, 115, 118]. Experimental results by smith [127] suggested that iron sulphide scale formed within a range of H_2S partial pressure between 0.04 and 0.12 bar, assumes significant control of the corrosion reaction, such that corrosion rate decreases from approximately 5 mm/yr. in CO_2 dominated corrosion system to 1-2 mm/yr. in low H_2S containing H_2S-CO_2 corrosion systems [127]. Therefore, it can be implied that the mackinawite film formed at relatively low partial pressures of H_2S could offer some degree of protection against corrosion [115]. Sun *et al* [126], also reported an increase in corrosion rate with increase in H_2S gas compositions in the range of 0.1-10% and at temperatures 60℃ and 80℃ and that under these conditions, Mackinawite appears to be the dominating FeS film type formed on the surface of the metal. Thus, one can infer that the initially formed mackinawite film (usually very thin (<<1μm)) is, dense, non-stoichiometric and yet could also be protective [73, 118].

These findings have however, fallen short of providing useful scientific explanation to the incidence of corrosion layer breakdown (most likely mackinawite) coinciding with localised corrosion [138], as well as the suggestion of a shift in the mechanism of corrosion damage with progression from low to higher concentrations of H_2S. In such a scenario, the type of iron sulphide film formed seemed to exert a decisive influence [115, 129] on corrosion behaviour of substrate steel especially with respect to progression towards localised and pitting corrosion. This scenario has also been suggested by some researchers to be attributed to an imbalance

between corrosion rate (iron dissolution rate) and iron sulphide scale retention rate (FeS deposition rate) on the surface of the steel [118]. In most corrosion cases, the corrosion rate was always higher than the scale retention rate even if both the corrosion rate and scale retention rate are expected to increase with increase in H_2S gas concentration [118]. However, the scaling tendency under test conditions indicates that between 40% and 72% of the iron consumed by corrosion ended up as iron sulphide on the steel surface, with the balance lost to the solution [118], which may strongly suggest that there is no significant effect of solution supersaturation levels on the rate of mackinawite formation [115, 118, 126]. The comparison of corrosion rate behaviour and scale retention rate on surface of steel with increase in H_2S partial pressure is provided in Figure 4-7.

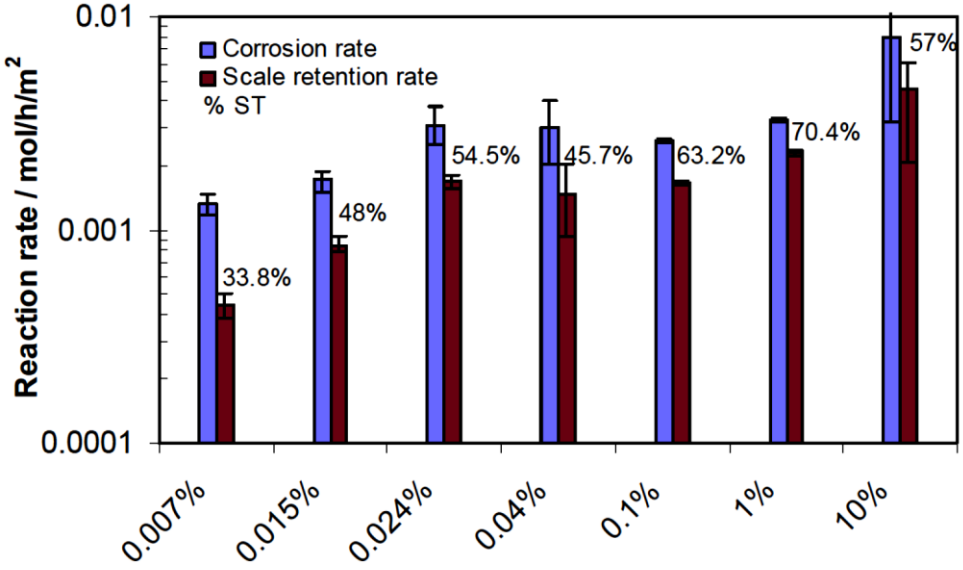

Figure 4-7 The comparison of corrosion rate (CR) and scale retention rate (SRR) in the same molar units as a function of H_2S gas concentration; ST=SRR/CR stands for scaling Tendency; total pressure p=1 bar, T=80℃, initial Fe^{2+} aqueous concentration: 0 ppm, pH 5.0-5.5, reaction time: 24 hr.[118]

Based on the abovementioned corrosion scenario, it has also been suggested that the aforementioned imbalance between iron dissolution rate and scale precipitation and retention rate is likely to induce some form of internal stress in the mackinawite film. It was explained that a combination of continuous precipitation of iron sulphide films from Fe^{2+} and HS^- in the bulk solution and across an electronically conductive iron sulphide film could be responsible for such internal stress build-up in the iron sulphide corrosion product layer. This internal stress build up was linked to epitaxial stresses and Pilling-Bedford ratio. Pilling-Bedford ratio has been defined in this case as the ratio of the molar volumes of the mackinawite film formed to that of the corroding iron. This is because mackinawite is considered to be of larger volume,

when compared to iron. These stresses lead to micro-cracking and eventually delamination and breakdown of the mackinawite film [73, 136, 141], which are the most likely precursors for localised corrosion and pitting.

On the significance and role of CO_2 partial pressure, there is still a vague understanding of the subject as CO_2 partial pressure effect on sour corrosion has not been fully established [115]. However, while there have not been clear evidence to suggest that CO_2 partial pressure have significant effect on H_2S corrosion [115], it has been reported that there is an inherent competition between iron carbonate from CO_2 and Mackinawite and other forms of FeS films from H_2S corrosion [126]. This is more significant because the formation of iron carbonate is very much dependent on the supersaturation levels of the bulk solution unlike in the case for the formation of iron sulphide. This might have significant influence on film morphology and the processes leading to film breakdown, pit initiation and propagation.

4.5.2 Solution pH

pH is a measure of solution acidity, and is one of the most important environmental factors that significantly influence corrosion reactions [9, 40, 115]. At constant temperature and CO_2/H_2S partial pressures, corrosion rates generally decreases with increasing pH of the aqueous phase due to the reduction in the number of the H^+ ion available for reduction at cathodic sites. Hence, the corrosiveness of the environment may be expected to increase by increasing the partial pressure of acidic gases (H_2S and CO_2) [9, 40] because of a resulting increase in H^+ reservoir. Experimental data has also demonstrated that the corrosion rate in H_2S-CO_2 systems tends to decrease linearly with increasing pH of solution containing trace amounts of H_2S. This is because the solution is generally under-saturated with respect to protective corrosion products; iron sulphide/iron carbonate at low pH especially at pH as low as below ~ 4-4.5 [115]. However, the formation of iron sulphide which can significantly control the overall corrosion behaviour of steel in sour environments is considered more dependent on the rate of "solid state" or "direct reduction" reaction of H_2S and Fe at the steel surface [39, 73, 115, 118] by which mackinawite (the first type of FeS film to be formed) is formed and could be less dependent on solution saturation. Hence, by the initial inference that the rate of H_2S (sour) induced pitting corrosion is strongly controlled by the nature of corrosion product film (FeS) in terms of both its chemistry/composition and morphology [34, 35, 125], it means that the effect of solution supersaturation levels and possibly, pH may be less significant on the rate of mackinawite formation and overall kinetics of sour corrosion; localised/pitting corrosion inclusive [115, 118, 126]. Potentiodynamic experiment conducted by Zheng *et al* [119, 140] at

10% H_2S gas concentration in both H_2S-CO_2 and H_2S-N_2 shows that the mechanism of corrosion reaction is fully controlled by the presence of H_2S gas and there was no significant difference in the trend and corrosion rate by increasing the pH from 4 to 5. The potentiodynamic sweeps from the experiments is provided in Figure 4-8.

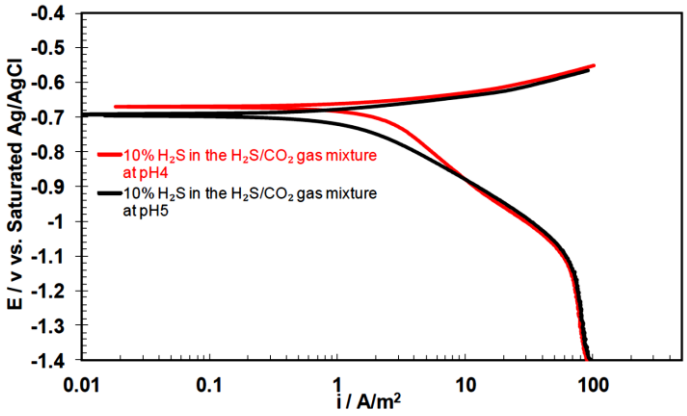

Figure 4-8 Effect of pH on potentiodynamic sweeps of mild steel corrosion in the solution purged with 10% H_2S in the H_2S/CO_2 gas mixture at total pressure of 0.1MPa, 30°C, 1wt% NaCl,1000rpm rotating speed, exposure time < 2 hours Zheng *et al* [140].

It could be seen that the limiting current was almost the same at pH of 4 and pH of 5, which is a different behaviour to the effect of changing the pH in a "CO_2 only" corrosion environment. Zheng *et al* [140], suggested that the main contribution to the cathodic limiting current at 10% H_2S concentration is from the aqueous H_2S species, whose concentration is independent of pH. It remains unclear how the concentration of H_2S specie could be independent on pH, since the reverse relationship would be expected.

It has also been shown from a thermodynamic perspective, that pH exerts some significant influence on the tendency for the formation of different types of iron sulphide films as well as on the stability of iron carbonate films at constant experimental conditions. pH influence on the thermodynamics of iron sulphide films has been linked to the stability of mackinawite film across an increasing range of H_2S partial pressure [37, 39]. Richard *et al* [37] was able to show from corrosion product stability diagrams for $FeS/FeCO_3$ in H_2S/CO_2 corrosion systems (see Figure 4-9) that when pH is reduced from pH of 6 to pH of 4, the area of the dominant domain for Fe^{2+} increases, indicating that the boundary between Fe^{2+} and FeS and that between Fe^{2+} and $FeCO_3$ is a strong function of pH, provided temperature and Fe^{2+} ion concentration are kept constant [37].

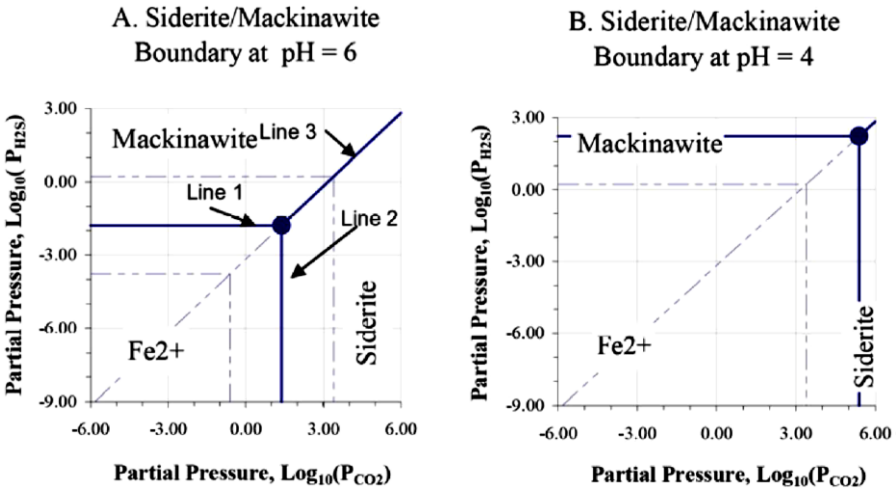

(a) (b)

Figure 4-9 Partial pressure of CO_2 vs. H_2S plot showing Mackinawite (FeS) / siderite ($FeCO_3$) for temperature = 25℃ and varied with pH. (a) Represents graph for pH =6 and (b) represents graph for pH = 4. Line 1 represents boundary between Fe^{2+} ion and mackinawite (FeS), Line 2 represents boundary between Fe^{2+} ion and siderite ($FeCO_3$), Line 3 represents boundary between mackinawite (FeS) and siderite ($FeCO_3$) [37].

In an almost similar frame, Smith *et al* [39] presented a modified form of H_2S corrosion product relationship provided in Figure 4-4 in Figure 4-10, as a function of pH to suggest that a neutral pH of 7 increases the stability of mackinawite to higher H_2S levels at low and moderate temperatures, while a more acidic pH such as 4 would potentially increase the tendency for the formation of pyrrhotite at low H_2S levels, thereby reducing the size of the mackinawite stability range. The tendency for film transformation from one thermodynamic state of iron sulphide film (mackinawite) to other forms (pyrrhotite, pyrite, etc.) as influenced by changing solution pH, may also be contributing to loss of integrity and final breakdown of iron sulphide corrosion product layers [39, 73, 138].

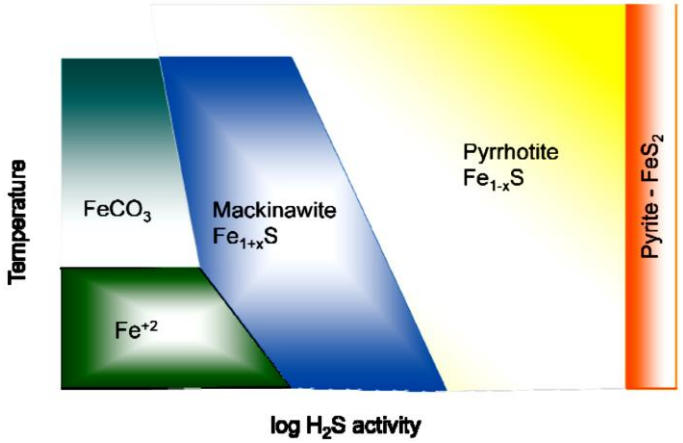

(a)

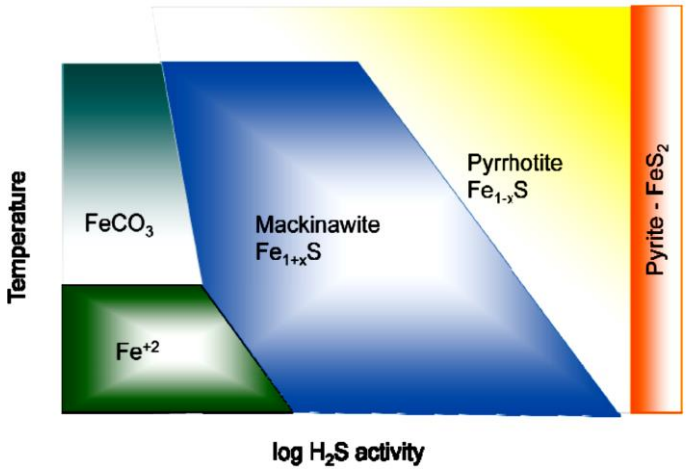

(b)

Figure 4-10 (a) Decrease in mackinawite stability range at lower H_2S levels at pH = 4, (b) increase in mackinawite stability range at lower H_2S levels by increased pH = 7 [39].

The above discussion has shown that while pH is generally a very important parameter in terms of the corrosion mechanisms in H_2S and CO_2 containing environments, it also appears to be very influential in restricting the thermodynamic state of iron sulphide films over a range of H_2S partial pressure, on the kinetics of H_2S corrosion (pitting corrosion). However, the kinetics of iron sulphide formation may be less dependent on the pH of the corrosion system. This is also justified by the facts that pH stabilisation method is not often as effective in inhibiting corrosion in sour systems as it is in sweet systems [115].

4.5.3 Temperature

Temperature has been reported by many researchers to have a strong influence on the corrosion behaviour of carbon steel in different corrosion systems (CO_2 and H_2S/CO_2 systems). It has been generally agreed that temperature influences the kinetics of film formation as well as the rate of corrosion processes at metal – brine interface of steel [9, 40] in any one of the following ways as suggested by Yap and Srinivasan, [40];

a) Speeding up the corrosion process with increasing temperature.
b) Decreasing solubility of dissolved gases, with increasing temperature which increases the pH of the environment.
c) Change in equilibrium constants with temperature change which causes pH change.
d) Brine phase behaviour change and increase in the aggressiveness of chloride ions in aqueous solutions with increasing temperature by thermal activation.

e) Formation of protective scale in aqueous corrosion environments at elevated temperatures (depending on solution chemistry and other environmental parameters).

While the last two points appear to be more critical to the study of pitting corrosion and iron sulphide film formation, the kinetics of iron sulphide formation is still less strongly dependent on super saturation with respect to $Fe^{2+}$and S^{2-} in the bulk solution at elevated temperatures [40]. This is because increasing temperature speeds up corrosion process, frees up some of the Fe^{2+} from the metal lattice into the bulk solution for reaction with HS^-. However, most of these ions are not normally used up in the formation of iron sulphide films [115, 118, 126]. Iron sulphide film formation is also occurring concurrently via the process of "direct reduction" or "solid state" reaction between the iron surface and aqueous H_2S [39, 115, 118, 136]. This process tend to significantly control the kinetics of iron sulphide film formation much more than reaction between Fe^{2+} and HS^- in the bulk solution, and thus, the overall pitting corrosion behaviour of carbon steel in sour environment [34-37, 118, 125, 126].

Experiments results by Sun and Nesic [118], suggested a weak dependency of corrosion rate and iron sulphide scale formation on temperature. Although the results showed an increase in corrosion rate with increase in temperature from 25-80℃ for a 1 hour test exposed to 1 vol. % and 10 vol. % H_2S gas concentration in mixture with nitrogen gas, the change in the rate of iron sulphide corrosion product with increasing temperature appears to be insignificant as shown by the data on scale retention rate in Figure 4-12. This trend was found to be consistent with the experimental results of Zheng *et al* [119] as shown in the polarisation curves of Figure 4-11 for three different temperatures for a duration of up to 2 hours. However, the scale retention rate (which measures the amount of dissolved Fe^{2+} used up in the formation of corrosion product) estimated by Sun and Nesic [118] appears to only increase with temperature from 60 to 80ºC and remained constant over the temperature range of 25 to 60ºC at 1 vol. % H_2S. With 10 vol. % H_2S the scale retention rate increased with increasing temperature. After 24 hours of testing, the scale retention rate increases significantly from 60-80℃ and remained constant from 25 to 60℃ at 1 vol. % of H_2S gas, while with 10 vol. % of H_2S gas, the corrosion rate increases slightly from 25 to 60ºC and then decreases over the range of 60 to 80ºC. The scale retention rate increased significantly from 25 to 60ºC and only slight increase over the temperature range 60 to 80ºC. These results are provided for test in 10 vol. % H_2S gas in Figure 4-12. Although Sun and Nesic [118] concluded from these results of the weak dependency of corrosion kinetics and iron sulphide formation on temperature, the results do suggest that corrosion kinetics and kinetics of iron sulphide formation still show some significant dependence on temperature. This

was most apparent after 24 hours where corrosion rate decreased with change in temperature from 60 to 80ºC for both 1 and 10 vol. % H_2S. This was also observed to be consistent with the increased scaling tendency variation with temperature.

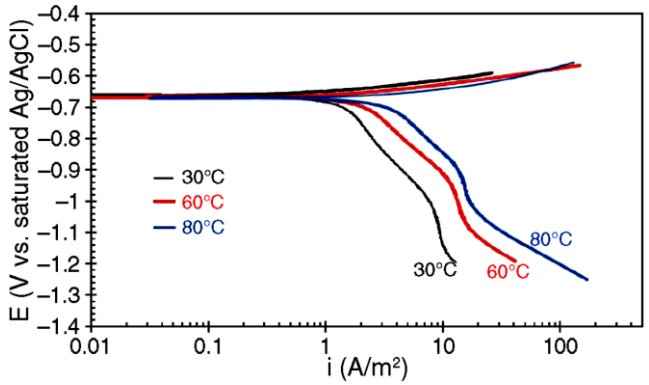

Figure 4-11 Polarization curves at pH 4 for temperatures 30°C, 60°C, and 80°C, $[H_2S]_{aq}$ = 8.3×10–4 mol/L, 1,000 rpm, total pressure 1 bar, 1 wt% NaCl [119].

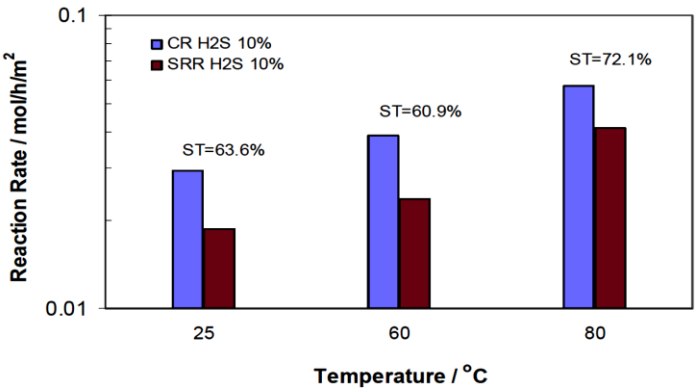

(a)

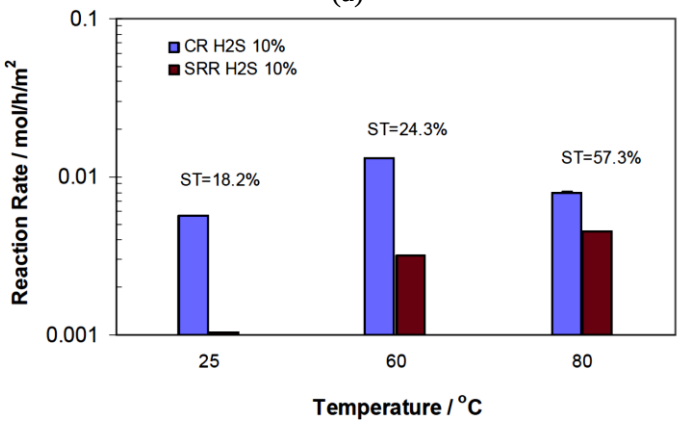

(b)

Figure 4-12 The corrosion rate (CR) and scale retention rate (SRR) vs. temperature, ST=SRR/CR stands for scaling tendency; conditions: total pressure p=1 bar, H_2S gas concentration: 10%, initial Fe^{2+} aqueous concentration: 0 ppm, pH 5.0-5.5, and reaction time of (a) after 1 hours and (b) after 24 hours [118]

The results shown in Figure 4-12 also show that scaling tendency (ST) was higher after just 1 hour of exposure when compared to tests after 24 hours of exposure. This may be suggesting the stronger influence of "direct" or "solid state" reactions on iron sulphide film formation than the effect of temperature to increase corrosion rate and enhance supersaturation of the bulk solution. This could also be the reason why corrosion rate is lower after 24 hours exposure at 80ºC, as a result of the formation of protective sulphide films.

Therefore, it can be inferred that pitting corrosion rate (as influenced by the kinetics of iron sulphide films formation) may be less influenced directly by temperature changes at relatively low concentration of H_2S, but at high H_2S concentrations, temperature changes can significantly affect the type, chemistry and protectiveness of scales and further affect the tendency and rate of pitting corrosion. This can also be easily correlated with the thermodynamic tendency for the stability of the different possible iron sulphide films as depicted by the graphs of H_2S corrosion products relationship in Figure 4-4 and Figure 4-10 [115], across a wide range of operating conditions. The strong link between different thermodynamic forms of sulphide film and temperature changes with variable H_2S gas pressure could as well be linked to the tendency of iron sulphide film breakdown, leading to initiation and propagation of pits, especially when changing conditions appears to favour the transition from a very thermodynamically unstable meakinawite to other forms of iron sulphide films [31, 33, 39, 73, 138].

4.5.4 Solution chemistry and presence of chloride ions

Solution composition is also an important environmental parameter that influences the corrosion rate in acid gas environments. The solution composition parameters that are strongly significant to sour corrosion include pH, Fe^{2+} concentration, chloride concentration, total ionic concentration and brine composition. However, because the effect of pH have been extensively discussed above, this section will focus primarily on parameters that may directly or indirectly influences the thermodynamics and kinetics of H_2S corrosion, iron sulphide formation, and pitting corrosion. These includes; Fe^{2+} concentration and chloride concentration.

4.5.4.1 Fe^{2+} concentration

Experimental results have shown that Fe^{2+} concentration has a negligible effect on the corrosion rate and iron sulphide film formation rate in H_2S environments [126]. Theoretically, the solubility of iron sulphide scale is relatively low and therefore it is very easy for iron sulphides to reach supersaturation even at room temperature [115]. This has been observed during experiments as black powder suspensions in the solution [115], because increasing Fe^{2+}

concentration accelerates the precipitation of iron sulphides in the bulk solution. However, precipitated iron sulphide in the bulk solution barely influences the rate of deposition of iron sulphide formation on the steel surface and as a result does not affect the pitting corrosion behaviour directly. This is possibly a near accurate assertion because the controlling step of sour corrosion and pitting behaviour of carbon steel and iron sulphide film formation is the process of mackinawite formation by direct reduction reaction and its subsequent breakdown, or non-protective nature respectively [34-37, 118, 125, 126]. Such that during pitting corrosion, the activity of Fe^{2+} at metal surface across a mackinawite-bulk solution boundary layer is determined by the dissolution rate or breakdown rate of mackinawite iron sulphide film and the charge and mass transfer rate of Fe^{2+} away from the surface and H_2S or HS^- to localised regions of the metal surface respectively [39, 73].

Thus, if pitting corrosion of carbon steel is a strong function of the heterogeneous solid state reaction of iron and sulphide ions directly at the steel surface, and the latter (reaction of iron and sulphide ions) is less dependent on the supersaturation of the bulk phase with Fe^{2+} and H_2S or HS^-, especially at low H_2S gas concentration, then it is unlikely that Fe^{2+} concentration will exert a very significant influence on the rate of precipitation of iron sulphide films on metal surface. Therefore similar relationship is to be expected between Fe^{2+} concentration and pitting corrosion behaviour of carbon steel in sour corrosion conditions.

4.5.4.2 Chloride concentration

In the science of localised corrosion/pitting corrosion of metallic components in oilfield environments, chloride ion content is considered a key exponent for localised acidification during pitting in stainless steel and other CRA's and breakdown of film within crevices and localised regions of discontinuities on metal surfaces in the case of carbon steels. This is because chloride ions are readily present in reservoir produced water and have been reported to show the tendency to impair the consistency of corrosion products (iron sulphide films inclusive). Although there have been few experimental data to back up these hypothesis with respect to iron sulphide films, it is expected that chloride ion can as well undermine the integrity of iron sulphide films across the surface of steel in sour environment and increase pitting tendency with increasing concentration [40, 115]. This can be evident from experimental results that show the doubling of weight loss due to corrosion from a near constant value when the chloride concentration is increased from between 0-3% to 20% in some cases [115]. The expected increase in corrosion rate with increasing chloride ion content is made worse with

increase in temperature as a result of incorporation and penetration of chloride ions present in the solution into surface corrosion films which can lead to destabilisation of the corrosion film and increased localised/pitting corrosion with minimal control over the cathodic reaction. This phenomenon can best be described as an increase in aggressiveness of chloride ions in aqueous solutions with increasing temperature by thermal activation [40, 41]. Experimental results by Fang et al [18] on the effect of chloride ion at 25ºC had suggested that increasing chloride ion concentration retards corrosion rate of steel in H_2S containing environments. Although Fang *et al* [18] also suggested that the presence of chlorides is an indication of an increase in solution conductivity and ionic strength, it still appears contradictory to the general consensus on the effect of chlorides.

4.5.5 Duration of steel exposure to sour conditions

In the context of H_2S corrosion and especially induced localised and pitting corrosion, time has become one of the most potent experimental parameters that is also strongly linked with the thermodynamics and kinetics of H_2S corrosion and iron sulphide film formation and hence, H_2S induced pitting corrosion behaviour of carbon steel [39, 115]. This is because time has been considered as one key variable upon which the complex formation of iron sulphide films may depend on as well as the sequence of in-situ metamorphoses of the different possible outcomes of iron sulphide films. It has also been suggested that the time dependent transition from one thermodynamic state of iron sulphide film (mackinawite) to other forms could be responsible for film rupture or breakdown depending on H_2S partial pressure, pH, temperature, presence of CO_2 gas [33, 39, 73, 138]. Thus, possibly influencing the final outcome of the protectiveness of sulphide films, as well as the tendency for initiation and propagation of pits [115].

According to experimental results by several authors [118, 129], by increasing the reaction time, the corrosion rate decreased significantly. In the first two weeks of testing by Kvarekval *et al* [129], corrosion rate decreased from a significantly high corrosion rate and then appeared to decrease further, but only very slightly to 0.75 mm/y afterwards [129]. Similarly, long duration tests conducted between 2 and 20 weeks also showed a continuous reduction in corrosion rate from 2 to 20 weeks [115]. It is also apparent that H_2S initially absorbed onto the steel surface reacts very fast with iron to form a very thin ($<<1$ μm) layer of iron sulphide [18, 73], which may be protective and often a non-stoichiometric form of iron sulfide film – mackinawite [73]. However, it is also very likely to lose some of its protectiveness [73, 118, 141]. Experiments by Fang *et al* [18] was able to show a steady increase in the thickness of iron sulphide films over a 12 days exposure period from a very thin layer after 24 hours to a thick and dense layer of iron

sulphide after 12 days at 25ºC. This findings appears to be consistent with results of Sun and Nesic [118], that shows that as exposure time increases, another outer porous layer of mackinwite is likely to be formed (1-10μm) which depending on H_2S concentration and temperature, may be transformed into the more protective pyrrhotite and pyrite. This scenario best explains the reduction in corrosion rate as reported by Kvarekval *et al* [129], in which total exposure time dependent sulphide film thickness was found to vary from $10-20\ \mu m$ for one (1) day exposure of test specimen to about $40-50\ \mu m$ for a 1-2 weeks exposure of test specimen [129]. The iron sulphide film on the 1-2 weeks exposed test specimen was found to constitute three different layers of corrosion product films.

This thus raises the question of the reliability of the conservative approach by the research community towards exploring the time dependence evaluation of the corrosion behaviour of carbon steel in H_2S environment. There are limited correlations between results from short-term laboratory experiments and long-term based experiences of H_2S induced corrosion and pitting that could have help to improve on the understanding of the mechanism of H_2S induced localised corrosion of carbon steel in typical oilfield environment.

4.6 H_2S induced localised /pitting corrosion of carbon steel

On a general note, the mechanism of H_2S induced localised and pitting corrosion of carbon steel can be attributed to the formation and breakdown of semi-protective Fe_xS_y film, in similar sequence to the classical pitting corrosion process that involves;

1. The formation of a passive film on the metal surface,
2. The initiation of pits at localised regions on the metal surface where film breakdown occurs, and
3. Pit propagation and eventually, perforation [33]

However, the envisaged complex order of in-situ Fe_xS_y metamorphoses and the different types of possible Fe_xS_y outcomes has prompted the suggestion that some kind of transition from one thermodynamic state of iron sulphide film could also be contributing to film breakdown or loss of integrity, especially the transition from the very metastable meakinawite to other forms of iron sulphide films. This transition process is also known to be dependent on factors like H_2S partial pressure, pH and temperature, presence of CO_2 and exposure time [39, 73, 138]. The iron sulphide transition process and interrelationship for carbon steel corrosion in H_2S containing environment is provided in Figure 4-13, highlighting the stage of mackinawite film rupture and possibly initiation of pitting.

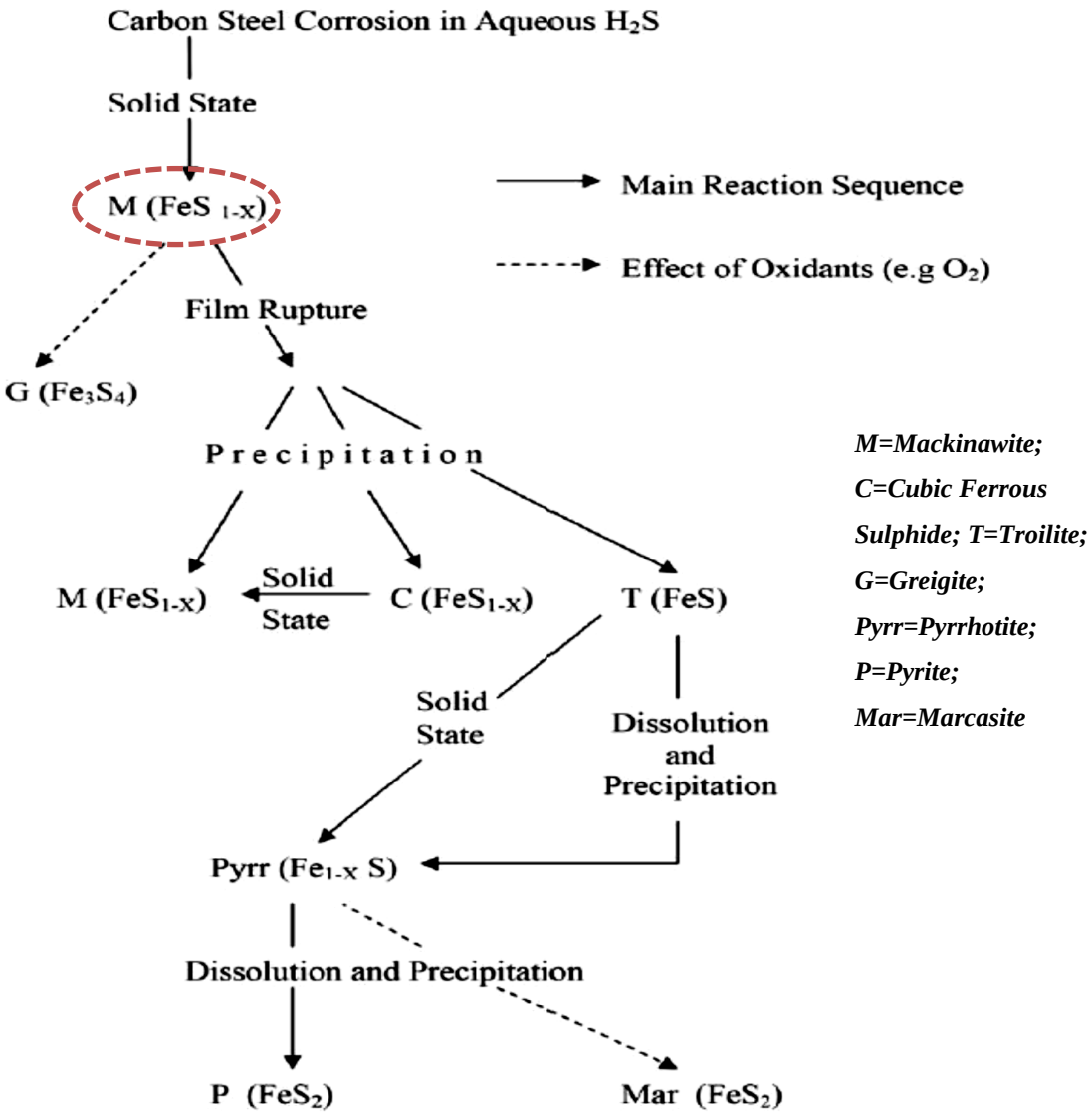

Figure 4-13 The iron sulphide corrosion scheme interrelationships for carbon steel in aqueous H_2S [37]

It has been postulated that the iron sulphide transition process could be a potential driving force of initiation and propagation of localised pits [33], especially beneath areas of extensive build-up of FeS films. Brown and Nesic [138] have shown this from experiments under a higher total pressure of 8bar containing 10mbar of H_2S gas that any ferrous ions released in the corrosion process are expected to be trapped within or underneath the initially formed layer of mackinawite, leaving minimum potential for precipitation onto the surface. This corrosion product layer was later shown to have failed in some regions, leading to severe localised corrosion up to 681 um in depth after 7 days and at 60ºC and is provided in Figure 4-14.

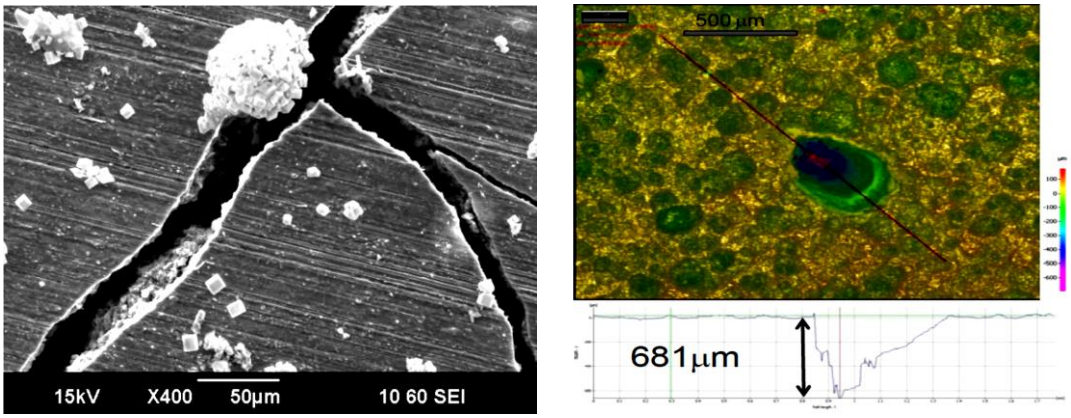

(a) **(b)**

Figure 4-14 SEM image of (a) on corrosion product layer and (b) IFM analysis of surface features after removal of corrosion product layer (60°C, pH 4.0,Ptotal = 8 bar, pH_2S = 10 mbar, 10wt% NaCl, SP, 7 days exposure) [138].

Pitting corrosion in H_2S environment could also be influenced by the galvanic effect between FeS film and substrate metal and also between competing corrosion product scales of CO_2 and H_2S corrosion [37, 126, 134, 135] . FeS Film rupture and breakdown has also been attributed to a recurring process of internal stress build-up in the films, and the eventual breakdown of such films when a critical stress level is reached. The stress build-up is an inherent system property caused by the volumetric ratio (Pilling-Bedworth ratio) between the metal and the corrosion product and has been reported to be a measure of the fraction of corroded iron that is captured in the corrosion layer and defined as the ratio of the volume of the metal corrosion product to the consumed metal volume; which is expected to increase with increasing temperature [73, 141].

4.7 Summary of literature review on H_2S controlled localised and pitting corrosion

The most important step of H_2S induced corrosion and pitting is associated with the fast corrosion process govern by a heterogeneous “direct” or “solid state” reaction mechanism, that leads to the formation of the first layer of iron sulphide film (mackinawite) and controls the overall corrosion and pitting corrosion processes. This step in the H_2S corrosion process may only become dominant in fully sour corrosion environment and make a good case for exploring a relatively moderate H_2S concentration regime that literature has shown to favour the boundaries within which H_2S corrosion will become dominant. This would help unravel the process of formation of the iron sulphide film; potentially mackinawite and improve the understanding of how it influences the corrosion and pitting corrosion behaviour of carbon steel. It is also expected that this will help unravel the potential transition to other thermodynamic

forms of iron sulphide films (where possible). Working within the confines of moderate H_2S concentration levels would also be useful in providing information of how FeS (Mackinawite) and possibly $FeCO_3$ could influence pitting corrosion; pitting corrosion initiation and pit growth in H_2S dominated corrosion systems and serve as a very useful baseline for future studies of H_2S/FeS influenced corrosion and development of a near accurate and successful inhibition strategy.

The discussion on the effect of H_2S concentration has shown that H_2S concentration levels has the tendency to either reduce or accelerate carbon steel corrosion rate in sour corrosion environments. However, as corrosive species under relatively moderate H_2S conditions, the formation of iron sulphide corrosion product layer/film may also exert decisive control on the overall corrosion processes of carbon steel in H_2S-ontaining environments. This usually includes the corrosion damage morphology; pitting and /or general corrosion. Observations on pitting corrosion among the research communities have not been robust enough to clearly explain how the corrosion damages (pitting and/or general corrosion) are correlated with the key process parameters such as gas phase composition as well as the formation of iron sulphide under such variable conditions. Such studies, which is a key aspect of this research work becomes very relevant since sour corrosion is independent of the saturation levels of dissolved H_2S/HS^- in bulk solution and will help in providing a clear understanding of the mechanisms of pitting corrosion in sour corrosion systems. It will also help to isolate the significance of $CO_2/FeCO_3$ in sour corrosion conditions that has remained elusive to the research community. It is important to also note that while sour corrosion may be relatively independent of supersaturation, the amount of H_2S/HS^- in the bulk solution could still be significantly important as an ionic source for creating a concentration and electrode potential gradient across initially-formed corrosion product layers and providing H_2S/HS^- ions for reduction across an electronically conductive FeS films.

It has been shown from the literature review that pH is very influential in restricting the thermodynamic state of iron sulphide films over a range of H_2S partial pressure, which in this case of this research work, it would be expected to be at an acidity levels that favours the stability of mackinawite film but not limited to it. However, it would be very interesting to explore and monitor the natural pH of the corrosion system in order to have a very clear perspective the overall H_2S corrosion process. This approach implies exploring unbuffered experimental conditions with the aim of understanding how the different gas phase

compositions to be explored will be influencing the *in-situ* pH as well as the overall corrosion processes and corrosion damages.

Temperature changes have been shown to affect iron dissolution rate and super-saturation of metal–brine interface with respect to Fe^{2+}, S^{2-} and CO_3^{2-} and also the increase in aggressiveness of chloride ions in aqueous solutions with increasing temperature by reason of thermal activation. However, because of the important step of iron sulphide formation, temperature may be having both direct and indirect influence on the overall corrosion and pitting corrosion behaviour of steel in sour environment. Lower temperatures from as low as 25ºC to 120ºC was found in the literature to favour formation of corrosion products that are often dominated by mackinawite form of iron sulphide film, such that a variable temperature range up to 80ºC may likely offer the necessary experimental conditions of temperatures that could ensure the formation of all the commonly formed iron sulphide films as encountered in oilfield environments. While there have been some research on the effect of temperature on sour corrosion, such studies have been limited in the areas of exploring the effect of temperature on the corrosion behaviour of carbon steel in H_2S-containing in synergy with the constituting gases in the gas phase. It is expected that the scope of such influence will include; corrosion kinetics (the independent and synergistic kinetics of CO_2 and H_2S corrosion mechanisms), corrosion damage morphology (pitting and/or general corrosion) and the morphology of corrosion products layers. In this study, conditions of temperature among other experimental variables will be chosen in other to explore these scopes of influence of temperature on the corrosion behaviour of carbon steel materials in sour service conditions, but with emphasis on the process of pitting corrosion initiation and pit growth.

Due to the fact that localised and pitting corrosion of carbon steel in sour service condition has been strongly linked to the heterogeneous reaction of iron and sulphide ions directly at the steel surface, it becomes unlikely that Fe^{2+} concentration in the bulk phase will exert a very significant influence on the thermodynamics and kinetics of iron sulphide formation and hence, the pitting corrosion behaviour of carbon steel in sour service conditions, especially at moderate H_2S gas concentration. It is also suggested that increased aggressiveness of chloride ions in aqueous solutions is expected with increasing temperature by reason of thermal activation. However, in the context of this aspect of this study, factors such as Fe^{2+} concentration and chloride ion content have not been explored as these (especially Fe^{2+} concentration) considered

secondary parameters since the Fe^{2+} concentration made available is usually a function of the rate of metal dissolution.

Generally, duration of experiment has also been identified as a key parameter because of the constraints of lack of adequate correlation between short-term laboratory results and long-term based field experiences on efforts to fully understand the mechanism of H_2S induced localised and pitting corrosion and the consequences on the reliability of previous findings. However, and also on a technical note, these constraints may also be linked to the time dependent complexities associated with the *in-situ* metamorphosis of iron sulphide films/iron carbonate films and the overall effect on the localised/pitting corrosion behaviour of steel in sour service conditions. Hence, the need to explore scientific techniques, which could minimise the effect of not having the luxury of time within the research community, becomes even more important. This is a very significant consideration for designing the experiment methodologies to be adopted in this study.

Chapter 5. Experimental Methods

5.1 Overview

This chapter is divided into four main sections; the first sections describes the materials used in this study, the generic sample preparation methods adopted and the electrochemistry techniques used in this work. The next section of this chapter describes the test set-up, procedures and experimental conditions explored for sweet corrosion studies. The third section describes the test set up for sour corrosion experiments, including the designs for bubble cell and test sample and sample holder, details of experiment conditions and procedures; including health and safety measures put in place and a comprehensive sour corrosion test protocol are also discussed. The fourth and final section describes the post-experiment surface analysis techniques used in this work.

5.2 Materials used for this study

The material used for the test sample in this research work was X-65 (UNS K03014) grade of carbon steel. The steel was in a normalised form and consequently possessed a ferrite-pearlite microstructure. The nominal composition of the X-65 steel is provided in Table 5-1.

Table 5-1 X-65 carbon steel elemental composition (wt. %)

C	Si	P	S	Mo	Ni	Nb	V	Mn	Fe
0.15	0.22	0.025	0.002	0.17	0.09	0.054	0.057	1.422	97.81

5.3 Sample preparation

Sample preparation for corrosion testing was designed to be the same for tests in CO_2 environments and H_2S-containing environments. However, the general sample preparation process involves cutting sample to desired dimension, mounting into resin, polishing and cleaning. The carbon steel sample was sectioned to a dimension of 10 mm x 10 mm x 5 mm to give an exposed surface area of 1.00 cm^2. Wires were subsequently soldered to the back of each test sample before embedding in a non-conducting resin. Prior to the start of each experiment, samples are wet-ground up to 1200 using silicon carbide (Buehler SiC) grit paper. The ground surfaces of the samples were degreased with acetone, rinsed with distilled water and dried with compressed air before immersion into the test solution.

5.4 Electrochemistry techniques used for this study

Three different electrochemistry techniques were implemented to record electrochemical responses in this study; linear polarisation, Tafel polarisation and electrochemical impedance spectroscopy (EIS).These electrochemical technique are already explained in sections 2.1.7 to 2.1.9 of this thesis. The three-electrode cell used in this work also comprised of an Ag/AgCl reference electrode and a platinum auxiliary electrode. Corrosion rate and solution resistance measurements were conducted using both DC and AC measurements with a potentiostat.

Linear polarisation resistance (LPR) measurements were performed by polarising the working electrode from 15 mV below the open circuit potential (OCP) to 15 mV more positive than OCP at a scan rate of 0.25 mV/s to obtain a polarisation resistance measurement (Rp).

Tafel polarisation measurements were performed on freshly polished samples in separate tests at each condition (after a stable OCP and corrosion rate was achieved) to determine anodic and cathodic Tafel constants and ultimately the Stern-Geary coefficient, which was subsequently used in conjunction with Faraday's law and the measured values of polarisation resistance (Rp) to estimate general corrosion rates. Tafel plots were obtained by performing anodic and cathodic sweeps ± 250 mV about the OCP at a scan rate of 0.25 mV/s and typically at the end of a 7 hour linear polarisation tests. Both anodic and cathodic sweeps were performed on separate samples to ensure reliable measurements.

AC impedance measurements were performed between every four LPR measurements and were used to measure for solution resistance in the system.

5.5 Set up for CO_2 corrosion experiment

The CO_2 corrosion set up was developed to study the processes of in-situ evolution of corrosion products layers, localised breakdown of corrosion products formed leading to potential pitting corrosion of carbon steel material over a 168 hours period of testing. The CO_2 corrosion set up consist of a twin electrochemical bubble cell (volume of 2 litres each) to house up to 10 test samples each as shown in Figure 5-2. The orientation and dimension of the test sample is shown in a sample-sample holder assembly in Table 5-2. Each of the bubble cells also houses a reference electrode usually connected to two of the test samples at the same time and also connected to a potentiostat.

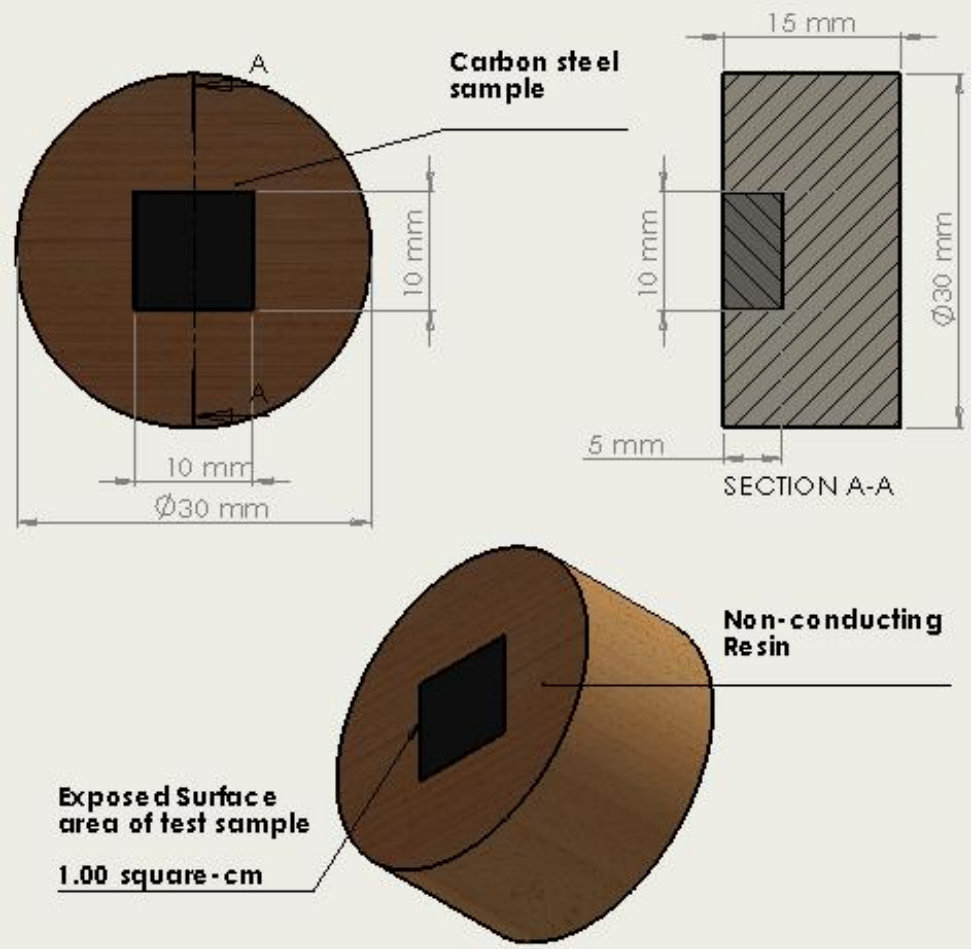

Figure 5-1 Test samples for CO_2 corrosion experiments

Some the special features of the experimental set up are;

1. The large volume of the bubble cell to house up to 10 test samples at an instant.
2. The ease of removal of test samples from the bubble cell at chosen experimental sampling intervals without disrupting the whole experiments.
3. The ability to run concurrent experiment at the same time as recording multiple electrochemical responses across the multiple bubble cells.
4. All other experimental parameters like pH and temperature can also be managed effectively across the multiple bubble cells.

Figure 5.2 shows a schematic of the overall set up for CO_2 corrosion testing.

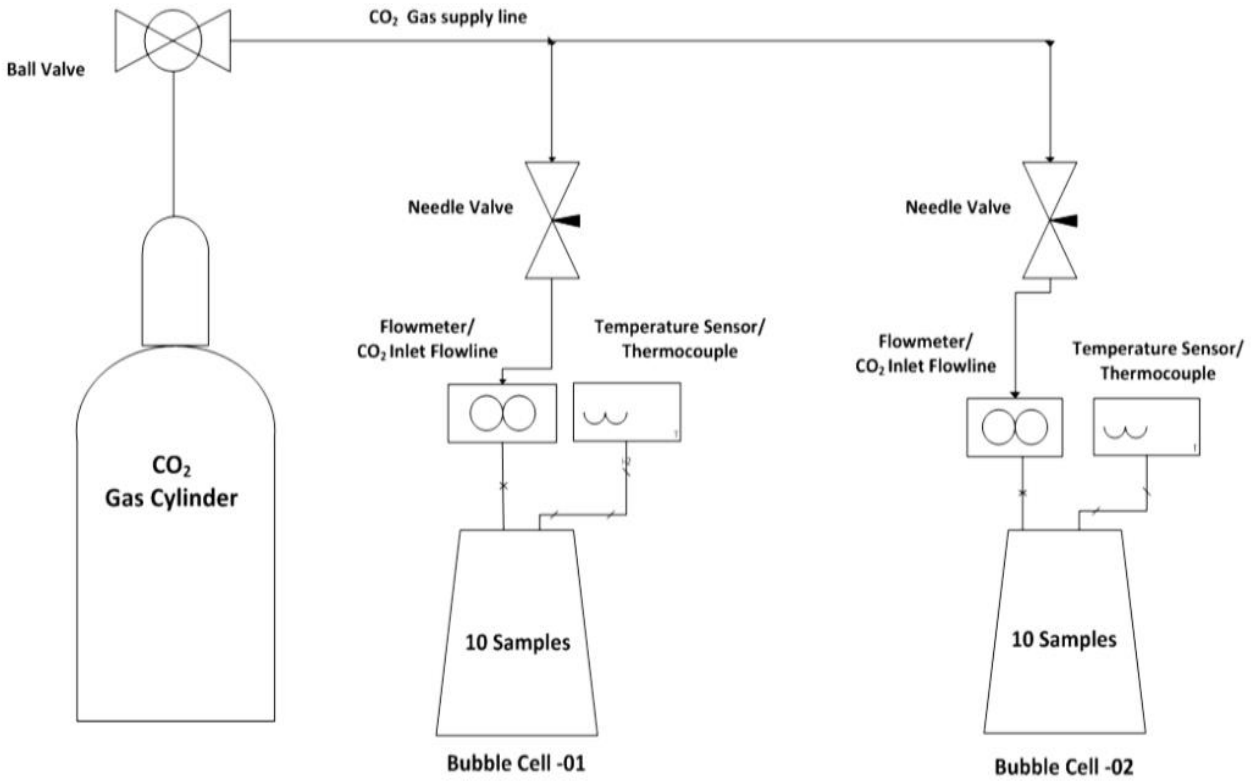

Figure 5-2 Schematic representation of CO_2 corrosion experiment set up

5.6 Experimental procedure for CO_2 corrosion experiments

The procedures stated 5.6.1 and 5.6.2 were followed in carrying out all experiments in corrosion systems saturated with 100 mol. % CO_2 gas. The procedures highlighted herein were designed to investigate the evolution of corrosion products and pitting corrosion with time for the duration of each test. The experiment procedure is divided into two sections. The first section describes the procedure for experiments in an unbuffered corrosion system while the second section describes experimental procedures for tests in buffered corrosion environments.

5.6.1 Procedure for unbuffered CO_2 corrosion experiments

Prior to the start of electrochemistry, the electrolyte is sparged with CO_2 gas for a minimum of 12 hours in order to de-aerate the solution down to 20ppb and saturate it with CO_2 gas. A completely CO_2 saturated solution of 10 wt.% NaCl at 25°C will be at a pH of 3.64. This data is also provided for all other concentrations of NaCl solutions in Crolet and Bonis [96] and were used for checking that solutions are fully saturated before commencement of test. The working electrodes (10 samples) are polished, degreased with acetone, rinsed with distilled water and

dried with compressed air before immersion into the test cell, along with the reference and counter electrode. Details of the step-by-step procedures are provided in Appendix C. In the course of the experiments, samples (two from each bubble cell) not connected to the potentiostat are removed at experimental sampling time intervals. The samples are washed, air dried, and carefully stored in a de-aerated chamber to avoid oxidation of corrosion products prior to surface analysis. Some samples are also cleaned with Clark's solution to remove all corrosion products prior to pitting corrosion analysis.

5.6.2 Procedure for buffered CO_2 corrosion experiments

In buffered CO_2 corrosion test systems, procedure (1)-(4) of Appendix C is repeated. The test solution is buffered to desired pH and controlled at this pH through the addition of sodium bicarbonate ($NaHCO_3$). A detail of the buffering action is presented in a later section of this Chapter. The pH probe is inserted into the electrolyte to record the pH of the electrolyte and ensure the recorded pH is stable at the desired solution pH. Once a stable solution pH is achieved, the test samples are immersed as stated in procedure (6) – (15) of Appendix C.

5.7 Test matrix for CO_2 corrosion experiments

This section presents a summary of the experimental condition explored for corrosion experiments in CO_2 saturated systems. The experimental conditions are divided into two sub-sections. The first section is focused on experiments conducted in an unbuffered CO_2 corrosion environment, while the second section describes experiments conducted in a buffered CO_2 corrosion environment. In the later, the pH of the corrosion environment is controlled through the addition of sodium bicarbonate ($NaHCO_3$).

5.7.1 Test matrix for unbuffered CO_2 corrosion experiments

This section of the experimental conditions was developed to investigate pit initiation and propagation with the aimed of unravelling useful information about localised/pitting corrosion of carbon steel materials in CO_2 saturated environments. The chosen experimental conditions were based on a parametric study that explores key factors such as temperature, and chloride ion content of the bulk solution that helps to answer questions on how these parameters could be independently or synergistically influencing the nature and chemistry of corrosion products, the corrosion damage morphology (uniform and localised/pitting corrosion) in CO_2 saturated systems. The experimental conditions explored are provided in Table 5-2.

Table 5-2 Summarised experimental matrix for tests in unbuffered CO_2 corrosion environment at a Total constant gas phase pressure of 1.103 bar.

Temperature (°C)	Approximate chloride ion concentration (wt. % of NaCl)/(ppm of Cl^-)
30	1 (6,000)
50	3.5 (21,000)
80	10 (60,000)

For post-experiment analysis, two samples are each removed from each of the twin bubble cells for surface and pitting corrosion analysis. The sample removal times used in this aspect of the study are 7, 36, 72, 120, and 168 hours and were adopted for all experiments conducted in CO_2 saturated environments. Details of experimental conditions to be explored as a result of different combination of the test conditions listed in Table 5-2 is presented in Table 5-3.

Table 5-3 Summary of experimental conditions for assessing the effect of temperature and chloride concentration using the Tafel polarisation tests

Temperature (°C) NaCl Concentration (Wt. %)	30°C	50°C	80°C
1 %	1 %, 30°C	1 %, 50°C	1 %, 80°C
3.5 %	3.5 %, 30°C	3.5 %, 50°C	3.5 %, 80°C
10 %	10 %, 30°C	10 %, 50°C	10 %, 80°C

5.8 Test matrix for buffered CO_2 corrosion experiments

All experiments under this aspect of study were conducted at a constant temperature, chloride ion concentration and CO_2 partial pressure, but variable pH. Three distinct pH levels were explored to promote the evolution of three distinctly different corrosion product layers and evaluate the role that these corrosion product and the respective conditions have on the localised and general corrosion rate of carbon steel. A summary of the test conditions explored under this section is provided in Table 5-4. The sample removal time used in this aspect of the work is the same as has already been described in section 5.7.1.

Table 5-4 Summarised experimental matrix for tests in buffered CO_2 corrosion environment

Temperature	50°C
Solution pH	Unbuffered (starting pH of ≈ 3.8), pH of 6.6 and 7.5
Chloride ion concentration	3.5 wt. % NaCl or (21,000 ppm of Cl^-)
CO_2 partial pressure	0.53 bar

5.9 Set up for H_2S-containing corrosion experiments

The sour corrosion test rig/set-up is located inside a fume chamber. The sour rig was designed with the aim of simulating sour corrosion conditions (H_2S Containing environment) as encountered in oilfields and also provide a near realistic scenario for studying the corrosion behaviour of different metallic materials in H_2S dominated corrosion conditions. The test set-up consists of two bubble test cells that usually contains about 1000 ml in volume of brines through which different mixture of H_2S-CO_2-N_2 gas are bubbled until saturation is attained, a vessel serving as air trap for excess gas from the test vessels, three scrubbing vessels; two consisting of aqueous Sodium hydroxide (NaOH) and connected in series and the other containing Potassium permanganate ($KMnO_4$). These vessels are all connected in series to each other to reduce the concentration of H_2S gas being extracted away in the Fume chamber to the lowest acceptable minimum. The bubble test also houses the test sample in a closed system that ensures that there is no leakage of H_2S gas. The test sample is connected electrically to a potentiostat for monitoring the electrochemical responses via a specifically designed sample holder. A system of tubes, flow meter, vent, pressure gauge and blow off valves (with maximum designated pressure rating of 1.013, 1.143 and 1.213 bar for the main gas inlet to the rig, to the test vessel and scrubbing vessels respectively) is designed to convey the gases into the test cell, as well as allow for extraction of excess gases through the scrubbing system.

5.9.1 Health and safety considerations

In the course of designing the sour corrosion test rig, health and safety of the personnel working directly and indirectly with the set-up and within its vicinity was given the highest priority. The consequences of which is the use of hydrogen sulphide gas detectors; one of which is placed inside the fume chamber, while another is placed inside the lab. The H_2S detectors in the fume chamber and in the laboratory are programmed for a maximum allowable H_2S concentration of l0ppm and 5ppm respectively, above the alarm inside and outside the lab goes off and the H_2S

gas supply is automatically shut down. Appropriate risk assessment and safety procedure would be followed before every sour experiment is to be conducted.

5.10 Set up for sour corrosion experiments

All sour corrosion experiment will be conducted in a closed glass cell and with a primary target of completely sealing the bubble cell from the surroundings in the course running experiments. The sour corrosion set up was developed to study the early and later stages of evolution of corrosion products layers, localised breakdown of corrosion products formed leading to potential pitting corrosion of carbon steel material. Investigations were carried out for sample over 7 and 168 hours test duration to represent the early and later stages of sour corrosion. The sour corrosion set up consists of a twin electrochemical bubble cell (each filled with test solution to 1 litre) to house up to 5 test samples each. The five (5) samples are all embedded in one resin assembly as shown in Figure 5-3.

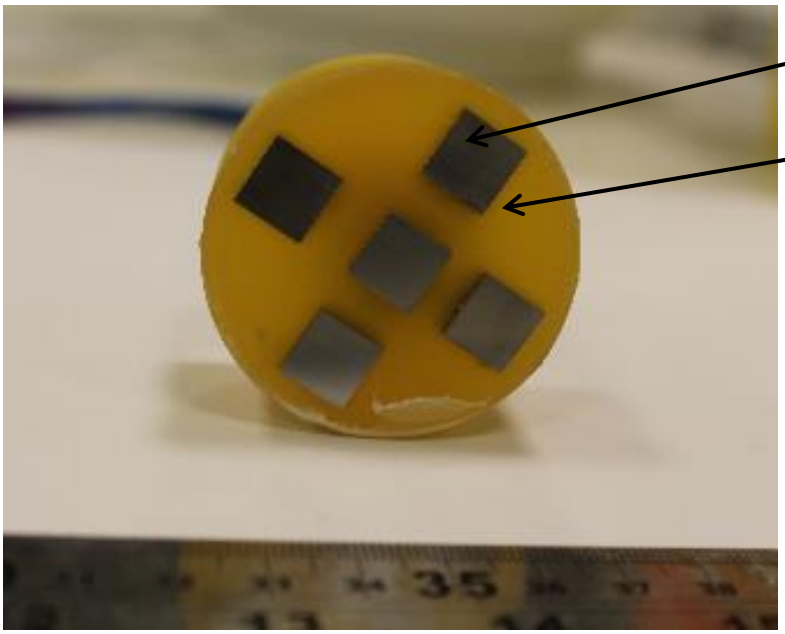

(a)

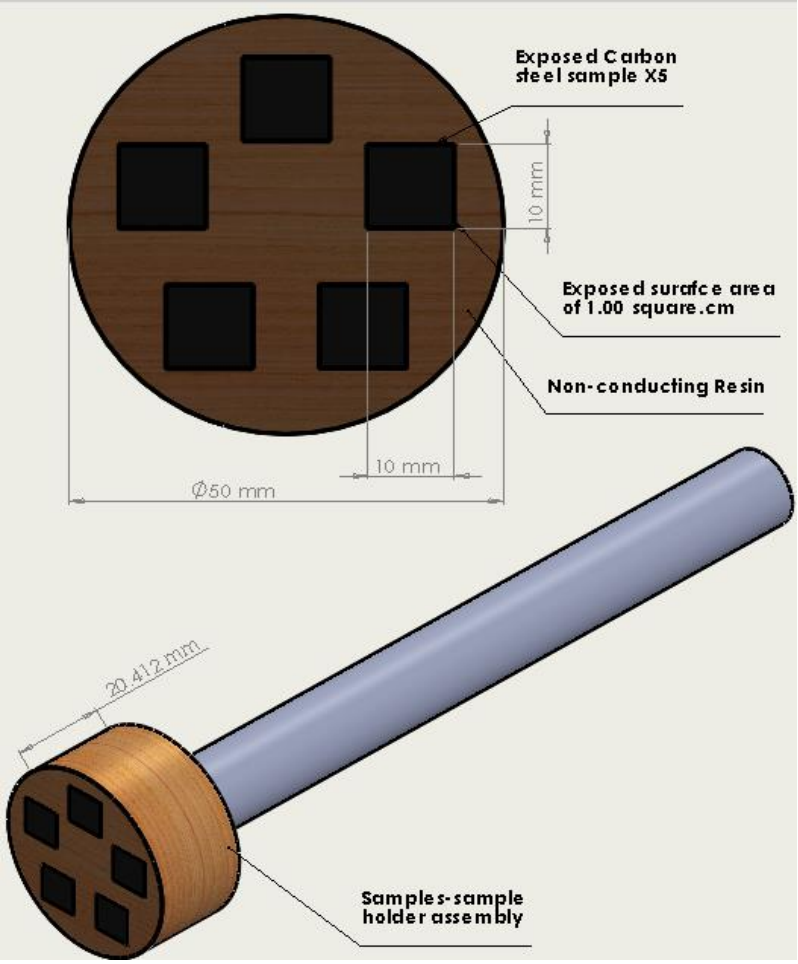

(b)

Figure 5-3 (a) Schematic of already prepared test samples and (b) schematic of test samples and sample-sample holder assembly used for sour corrosion experiments.

Five (5) samples were used in this case to maintain similar sample-to--volume of solution ratio with tests in CO_2 environment and allows of some comparative discussion of results across the different systems. Each of the bubble cells also houses a reference electrode usually connected to two of the test samples at the same time and also connected to a potentiostat. The bubble cell is shown in Figure 5-4, with some of the following special features;

1. The bubble cell to house up to 5 test samples at an instant.
2. Very good sealing mechanism in place to ensure that there is no escape of H_2S containing gas mixture from the bubble cell during experiments.
3. The ability to run concurrent experiment at the same time as recording multiple electrochemical responses across the multiple bubble cells.
4. All other experimental parameters like pH and temperature can also be monitored effectively across the multiple bubble cells.

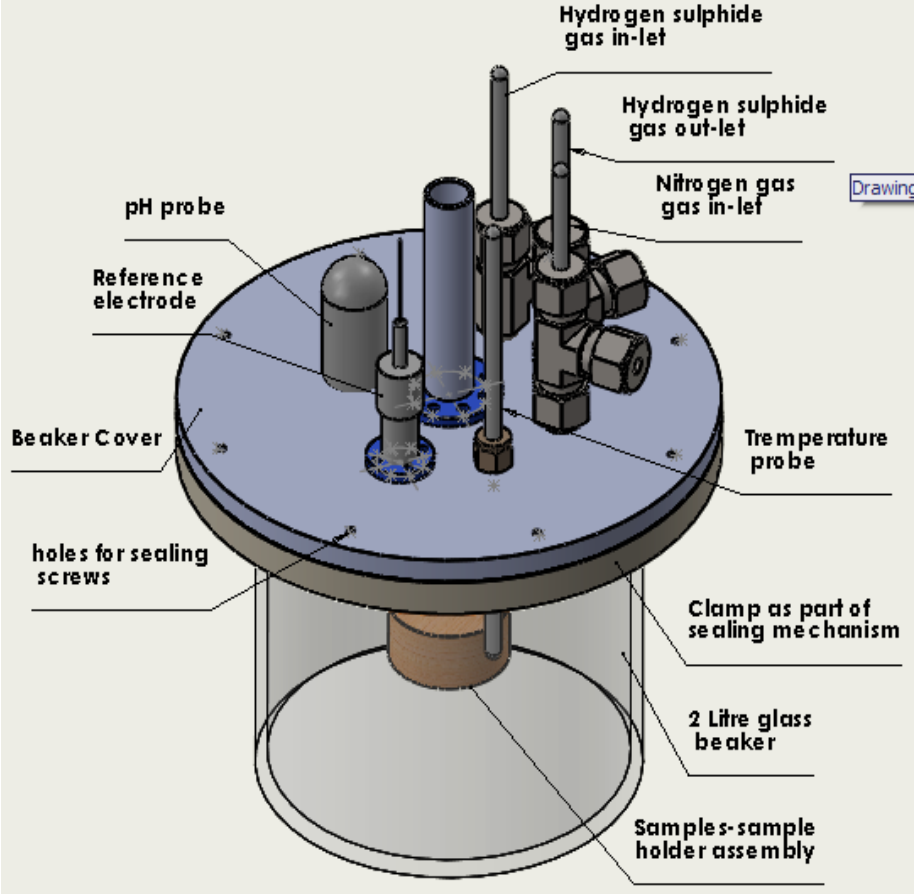

Figure 5-4 Bubble cell assembly used for sour corrosion experiments

5.11 Description of key components of the sour experiment set-up

All external fittings and tube that will likely be in contact with H_2S gas and for transporting the as respectively are made of stainless steel materials. Any other component/probe that may be inserted into the test cell and in contact with acidic aqueous H_2S is either made from highly resistant plastic material (natural acetal) or from Nickel based alloys (Hastelloy C276). Figure 5-5 presents a schematic drawing of the whole sour corrosion testing rig, showing all the different aspects and components. Figure 5-6 also shows a picture of a working sour corrosion rig as used in this research work.

Schematic Diagram of Sour Corrosion Test Rig

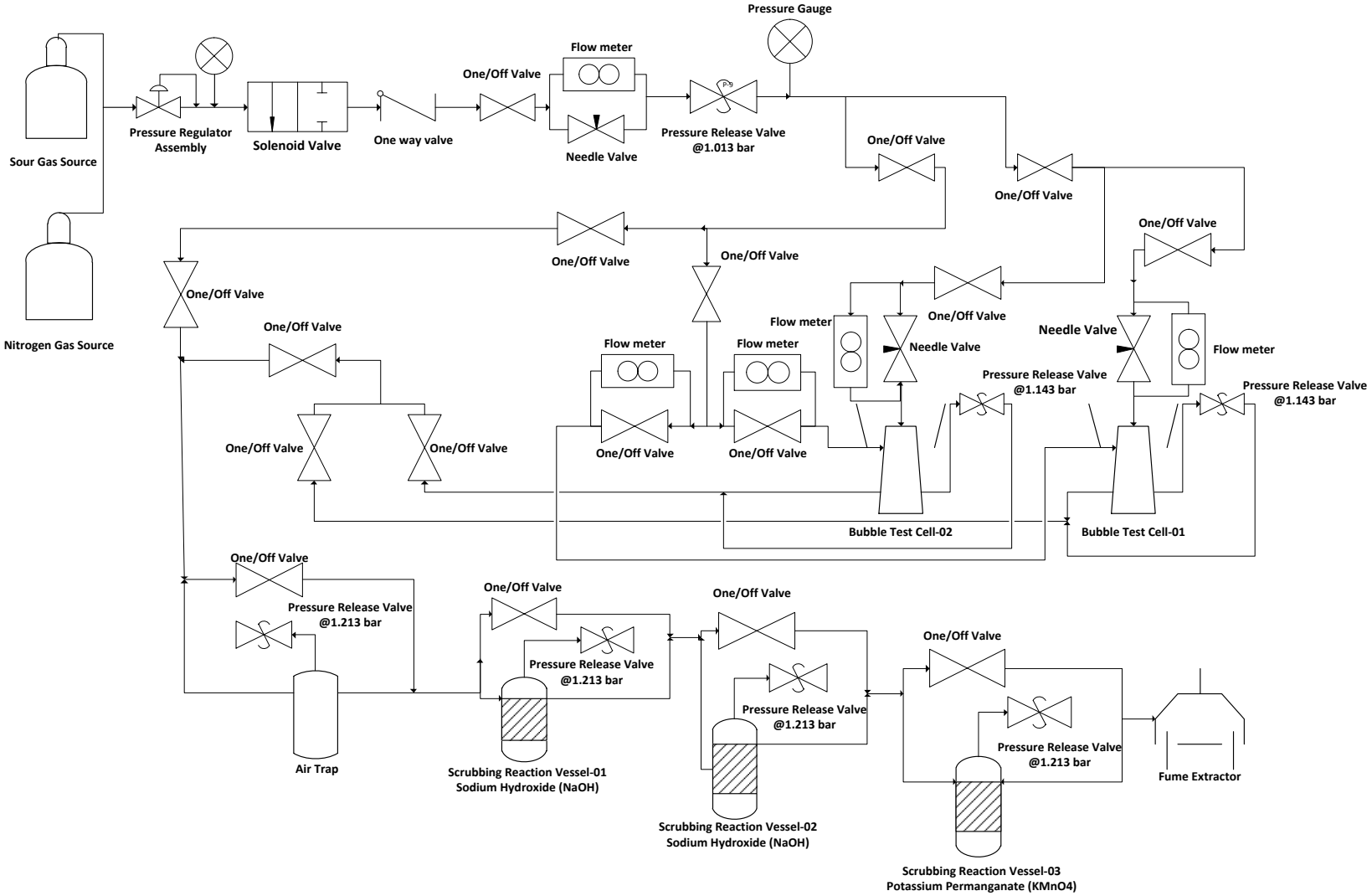

Figure 5-5 Schematic representation of the sour corrosion test rig

Figure 5-6 A picture of the sour corrosion test set up while in use.

5.12 Scrubber system

The scrubber system comprises of two vessels of Sodium hydroxide (usually 10wt. % NaOH) connected in series to each other and in series to a third vessel containing Potassium Permanganate (usually 10wt. % $KMnO_4$). These systems are employed to chemically reduce the health and safety risk of dealing with H_2S in the laboratory. NaOH chemically deactivates H_2S/CO_2 via a neutralisation reaction, while potassium permanganate oxidises the remaining H_2S in the system to acceptable levels before venting to the atmosphere via the fume chamber. The reaction below illustrates the scavenging mechanisms for H_2S.

Using Sodium Hydroxide (NaOH):

$$H_2S_{(aq)} + NaOH_{(aq)} \rightarrow NaSH_{(aq)} + H_2O \quad 5.1$$

$$NaSH_{(aq)} + NaOH_{(aq)} \rightarrow Na_2S_{(aq)} + H_2O \quad 5.2$$

$$CO_{2\,(aq)} + NaOH_{(aq)} \rightarrow Na_2CO_{3\,(aq)} + H_2O \quad 5.3$$

The boundary between the option of reaction of Eq. 5.1 and 5.2 is dependent on the strength of caustic soda. A higher pH favours reaction of Eq. 5.2.

Using Potassium Permanganate ($KMnO_4$)

$$3H_2S_{(aq)} + 8KMnO_{4\,(aq)} \rightarrow 2H_2O + 3\,K_2SO4_{(aq)} + 2KOH_{(aq)} + 8MnO_{2\,(aq)} \quad 5.4$$

Figure 5-6 shows the complete experimental set-up for the sour (H_2S) corrosion test rig.

5.13 H_2S test protocols and experimental procedures

A comprehensive detail of the logistics for operation of the sour corrosion test rig and for conducting experiments in H_2S-containing environment is provided in Appendix C of this thesis. This also includes the health and safety considerations. A detailed step-by-step procedure for carrying out H_2S based corrosion test; short and long-term tests, procedure following completion of tests and the cleaning and maintenance procedure for the scrubber system is also provided in Appendix C of this thesis.

5.14 Test matrix for sour corrosion experiments

This section of the experimental conditions was developed to investigate early and later stages pitting corrosion of carbon steel materials in H_2S-containg corrosion environments. Three distinct gas atmospheres were explored; pure CO_2 saturated corrosion systems, H_2S-CO_2 containing systems and H_2S-N_2 containing systems at variable temperatures. The experimental conditions explored in this aspect of the work are provided in Table 5-5.

Table 5-5 Summarised experimental matrix for tests in unbuffered H_2S corrosion environment

	Mole % of combining gases		
Temperature (°C)	**100 mol. % CO_2**	**10 mol.% H_2S - 90 mol.% CO_2**	**10 mol.% H_2S - 90 mol.% N_2**
30	30°C, 100 mol. % CO_2	30°C, 10 mol.% H_2S - 90 mol.% CO_2	30°C, 10 mol.% H_2S - 90 mol.% N_2
50	50°C, 100 mol. % CO_2	50°C, 10 mol.% H_2S - 90 mol.% CO_2	50°C, 10 mol.% H_2S - 90 mol.% N_2
80	80°C, 100 mol. % CO_2	80°C, 10 mol.% H_2S - 90 mol.% CO_2	80°C, 10 mol.% H_2S - 90 mol.% N_2

The total gas phase pressure of CO_2, H_2S:CO_2 and H_2S:N_2 test systems are constant at 1.013 bar $\equiv$ 100KPa. The solution chemistry is also constant at 3.5 wt. % NaCl (21,000 ppm of Cl^-) The partial pressures of the gas phase constituents at different temperature were determined by combining Raoult's law, daltons law and vapour pressure data provided for pure water (H_2O) as a function of temperature (T) in handbooks of thermodynamic properties for substances [142]. Raoult's law helps to define the relative lowering of the vapour pressure of a solution containing a non-volatile solute from that of a pure solvent., in which case, the vapour pressure

of the solution (p) will be equal to the vapour pressure of the pure solvent (p_i), over the solution [143, 144]. A breakdown of the partial pressure of the different gas systems are provided in Table 5-6. All tests were conducted at atmospheric pressure.

Table 5-6 Approximate partial pressures of CO_2 and H_2S gas in a 3.5 wt, % NaCl solution at various temperatures

Temperature (°C)	Partial pressure of combining gases (bar)				
	100 mole% CO_2	10 mole% H_2S - 90 mole% CO_2		10 mole% H_2S - 90 mole% N_2	
	p-CO_2	p-H_2S	p-CO_2	p-H_2S	p-N_2
30	0.971	0.0971	0.874	0.097	0.874
50	0.893	0.089	0.804	0.089	0.804
80	0.553	0.055	0.498	0.055	0.498

Summarised solubility analysis provided in Table 5-7 to Table 5-9 carried out for all experimental conditions to estimate the concentration of active constituent of feed gas in both liquid and gas phases. Solubility analysis was also based on the assumptions;

1) That the total pressure of gas phase above the brine at any given time of the test is constant at 1.013 bar, and
2) Partial pressures of H_2S (P_{H_2S}) and CO_2 (P_{CO_2}) were assumed as equal to the fugacity of H_2S gas in the solution [145, 146].

Assumptions (1) and (2) were combined with Henry's law and extrapolated Henry's solubility data from literature to obtain the solubility values provided in Table 5-7 and Table 5-9. Figure 5-7(a) and (b) presents the solubility data for H_2S and CO_2 in different concentrations of NaCl solutions and at different temperatures. A detail of this process is provided in Appendix A of this thesis. Solubility data plotted in Figure 5-7(b) were extrapolated data from curve fitting on experimental results of experiment conducted by Zheng *et al* [147]. The data presented here in Figure 5.7(b) represented an average of two repeated tests at chosen temperatures. These data were confirmed to be accurate by comparing with the solubility data at various temperatures in the literature [148, 149].

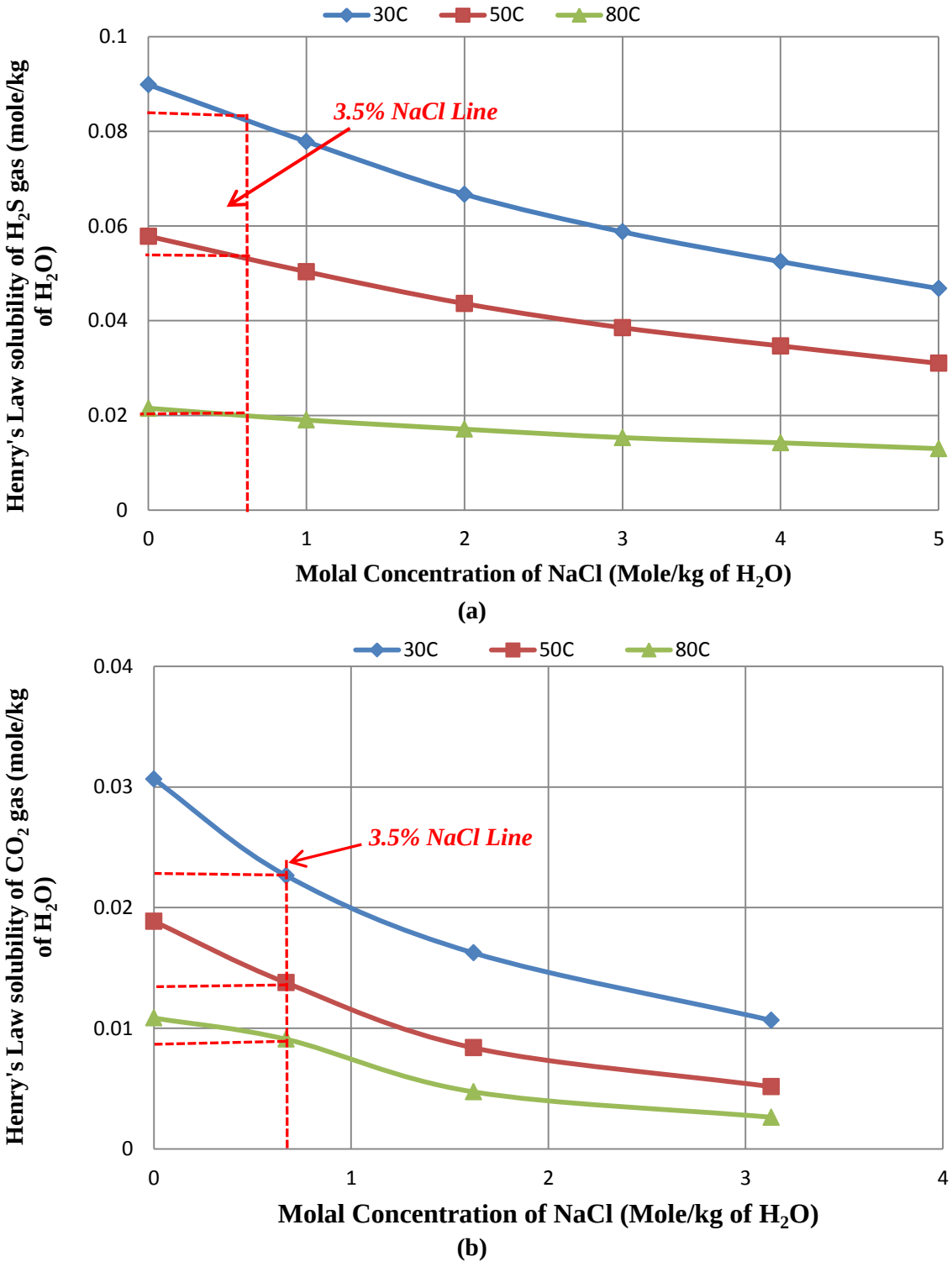

Figure 5-7 Generated plot of solubility of (a) H_2S gas as a function of Molality of NaCl from experiments by Barrett *et al* [145] and (b) of CO_2 vs Molality of NaCl from Experimental data found in literatures[147].

Table 5-7 Approximate concentration of gas phase of 10 mole% H_2S - 90 mole% CO_2 gas composition in the gas phase of a 3.5 wt. % NaCl solution at various temperatures

Temperature (°C)	Concentration of H_2S in gas phase (ppm)	Concentration of CO_2 in gas phase (ppm)	Solubility of H_2S Gas (Mole/L)	Solubility of CO_2 Gas (Mole/L)
30	$8.753\times \times 10^4$	$7.878\times \times 10^5$	0.008	0.020
50	$7.548\times \times 10^4$	$6.793\times \times 10^5$	0.005	0.012
80	$4.277\times \times 10^4$	$3.850\times \times 10^5$	0.002	0.008

Note; the gas mixture of 90% N_2-10% H_2S will have the same partial pressure and concentration for H_2S in the gas and brine phase as the gas mixture of 90% CO_2-10% H_2S provided in Table 5-7.

Table 5-8 Approximate concentration of 100 mole% CO_2 gas composition in the gas phase of a 3.5 wt. % NaCl solution at various temperatures

Temperature (°C)	Concentration of CO_2 in gas phase (ppm)	CO_2 Gas Solubility (mol/L)
30	$8.753\times \times 10^5$	0.022
50	$7.548\times \times 10^5$	0.014
80	4.277×10^5	0.009

Table 5-9 Approximate concentration H_2S and CO_2 gas dissolved in both 10 mol. % H_2S - 90 mole% CO_2 and 100 mol. % CO_2 gas composition in the liquid phase of a 3.5 wt. % NaCl solution at various temperatures

Temperature (°C)	Concentration of $[H_2S]/[HS^-]$ in liquid phase (ppm) (based on H_2S-CO_2 and H_2S-N_2 gas mixtures)	Concentration of CO_2 in liquid phase (ppm) (based on H_2S-CO_2 gas mixtures)	Concentration of CO_2 in liquid phase (ppm) (based on pure CO_2 gas system)
30	270	879	977
50	174	535	594
80	66	345	383

5.15 Characterization of solution Chemistry and saturation Ratio for unbuffered CO_2 corosion test environment

The solubility analysis is based on series of equilibrium reactions assumed to be occurring in the CO_2- NaCl Brine fluid system as listed in literatures [96, 150, 151]. The saturation ratio of the reaction;

$$Fe + CO_3^{2-} \leftrightarrow FeCO_3 \downarrow \quad 5.5$$

The saturation ratio for $SR = (\frac{[Fe^{2+}]\ [CO_3^{2-}]}{K_{sp}})$ 5.6

Where $[Fe^{2+}]$ and $[CO_3^{2-}]$ are the non-equilibrium concentrations of Fe^{2+} and CO_3^{2-} [moles/L] in the bulk solution. K_{sp} [moles^2/L^2] is the solubility product constant at specific temperature and ionic strength and is given by the unified equation by Sun *et al* [84] as follows;

$$\log K_{sp} = -59.3498 - 0.041377T_K - \frac{2.1963}{T_K} + 24.5724 \log T_K + 2.518I^{0.5} - 0.657I \quad 5.7$$

T_K= Temperature in Kelvin and I =Ionic Strength

$$I = {}^1/_2 \sum_i C_i Z_i^2 = {}^1/_2 (C_1 Z_1^2 + C_2 Z_2^2 + \cdots) \quad 5.8$$

Based on these equations, K_{sp} was estimated as follows for $FeCO_3$ at different temperatures

Table 5-10 Calculated solubility constant for $FeCO_3$ at different temperatures in 10wt. % NaCl solution

Temperature(°C)	Temperature(K)	Ionic Strength	K_{SP} [moles^2/L^2] For 10% NaCl Solution
80	353.15	1.711	6.47E-10
50	323.15	1.711	1.27E-09
30	303.15	1.711	1.78E-09

The $[CO_3^{2-}]$ in the bulk solution at every point in time is estimated on the assumption that the charge balance of weak acid like H_2CO_3 is provided mainly by the dissociation of H_2CO_3 to $[H^+]$ and $[HCO_3^-]$, and the dissociation of $[HCO_3^-]$ to $[H^+]$ and $[CO_3^{2-}]$ [152]. The relevant dissociation reactions for estimating $[CO_3^{2-}]$ are listed the literature [150, 151]. The solubility of carbon dioxide in water at low CO_2 partial pressures is estimated using Henry's Law and provided in Table 5-8. Week carbonic acid forms according to reaction in Eq.5.9:

$$CO_{2(g)} + H_2O_{(l)} \leftrightarrow H_2CO_{3(aq)}, \quad K_{hy} = \frac{C_{H_2CO_3}}{C_{CO_2}} , \quad K_{hy} = 2.58\times10^{-3} \qquad 5.9(a)$$

The value of the equilibrium constant K_{hy} does not change significantly within the temperature range of 20-100°C, is 0.00258 according to Eldik and Palmer's work [153].

Analysis to estimated $[HCO_3^-]$, $[CO_3^{2-}]$ from carbonic acid dissociation in water and Water dissociation (in molar^2) is carried out using for K_{ca}, K_{bi} and K_{wa} from the work of Duan and Li [154] as provided in Eq.5.10-5.15.

$$H_2CO_3 \leftrightarrow H^+ + H_2CO_3^- \qquad K_{ca} = \frac{C_{HCO_3^-}C_{H^+}}{C_{H_2CO_3}} \qquad 5.10$$

$$\begin{aligned} InK_{ca} &= 233.5159304 - 11974.38348\cdot T^{-1} - 36.50633536InT + \\ &(-45.08004597\cdot T^{-1} + 2131.318848\cdot T^{-2} + 6.714256299\cdot T^{-1}InT)(P-P_s) + \\ &(0.008393915212\cdot T^{-1} - 0.4015441404\cdot T^{-2} - 0.00124018735\cdot T^{-1})(P-P_s)^2 \end{aligned} \qquad 5.11$$

Where P is total pressure, P_s is saturation pressure of water and T is temperature in Kelvin. The constant K_{ca} (in molar) can be used reliably from 0 to 100°C and pressure ranges from 1 to 3000 bar.

The Bicarbonate anion dissociation, in molar) is based on this reaction;

$$HCO_3^- \leftrightarrow H^+ + CO_3^{2} \qquad K_{bi} = \frac{C_{CO_3^{2-}}C_{H^+}}{C_{HCO_3^-}} \qquad 5.12$$

The dissociation constant K_{bi} is estimated as follows;

$$InK_{bi} = -151.1815202 - 0.088695577 \cdot T - 1362.259146 \cdot T^{-1} + 27.79798156InT - (29.51448102 \cdot T^{-1} + 1389.015354 \cdot T^{-2} + 4.41962584 \cdot T^{-1}InT)(P - P_s) + (0.003219993525 \cdot T^{-1} - 0.1644471261 \cdot T^{-2} - 0.0004736672395 \cdot T^{-1}InT)(P - P_s)^2 \quad 5.13$$

Water dissociation is based on reaction in Eq. 5.14;

$$2H_2O \leftrightarrow H_3O+ + OH- \qquad K_{wa} = C_{H^+}C_{OH^-} \quad 5.14$$

The dissociation constant K_{wa} is estimated as follows;

$$LogK_{wa} = -4.098 - 3245.2 \cdot T^{-1} + 2.2362 \cdot 10^5 \cdot T^{-2} - 3.984 \cdot 10^7 \cdot T^{-3} + (13.957 - 1262.3 \cdot T^{-1} + 8.5641 \cdot 10^5 \cdot T^{-2}) \log \rho_{H_2O} \quad 5.15$$

Where ρ_{H2O} is the density of water in g/cm^3 and T is temperature in K.

Based on the total alkalinity equation [152, 155] in Eq. 5.16, it is assumed that the total [H^+] in the solution is dominated by [H^+] provided by the reactions in Eq.5.10-5.15. [H^+] produced by these reactions is as already captioned in the pH measurements.

$$H_2O = H^+ + OH^-$$
$$CO_2 + H_2O = H_2CO_3$$
$$H_2CO_3 = HCO_3^- + H^+ \quad (5.16)$$
$$HCO_3^- = CO_3^{2-} + H^+$$

Total Alkalinity; $C_{H^+} = C_{OH^-} + C_{HCO3^-} + 2C_{CO3^{2-}}$ [152, 155]

The Fe^{2+} concentration used for estimating solution saturation ratio (SR) in the bulk (according to Eq. 5.6) is calculated from Faraday's law on the assumption that the total Fe^{2+} lost due to corrosion goes into the bulk solution according to corrosion attack on carbon steel described in equation (6)[2],

$$Fe \rightarrow Fe^{2+} + 2e^- \quad 5.17$$

Therefore, total number of charge in terms of N (number of moles of electrons) and n (number of electrons per reactions) is given as;

$$Q = \int_0^t Idt = F.N.n \quad 5.18$$

Where I = Current (A), F = Faraday Constant (96,485C/mole of electrons)

Number of moles of electrons for Fe^{2+} is given as;

$$N_{Fe^{2+}} = \frac{\int_0^t Idt}{Fn} = 5.182 \times 10^{-6} \int_0^t Idt \text{ [Molar]} \quad 5.19$$

It is important to note that the Saturation ratio in the bulk is is not a true representation of the saturation ratio in at the corrosion double Layer. Detials of estimated Saturation ratio is provided and described in Chapter 6 of this thesis.

5.16 Post-experiment analysis

Various surface analyses were implemented in this study to investigate and identify the chemistry and morphology of corrosion product layers and pitting corrosion. Corrosion product layers were investigated and identified using a combination of different techniques that includes;

1) Scanning electron microscopy (SEM) and Energy dispersive X-ray analysis (EDX)
2) X-ray diffraction (XRD) spectroscopy
3) Raman spectroscopy
4) Focused ion beam (FIB)
5) Transmission electron microscopy (TEM) with energy dispersive X-ray analysis (EDX)

Pit depth measurements (that includes maximum an average pit depths) were carried out through the implementation of surface interferometry to study discrete pit geometry; namely, the size and depth. These post-experiment analysis techniques are briefly described in the following subsections.

5.16.1 Scanning Electron Microscope/Energy Dispersive X-ray analysis (SEM/EDX)

Scanning electron microscopy (SEM) is a tool used for characterising heterogeneously framed surfaces of both organic and inorganic materials on a micro scale. The SEM has the capacity of obtaining three-dimensional images of surfaces and is mainly used as a (but not limited to) topography imaging tool, ranging from 10X to 10s of thousands in magnification [156, 157]. The SEM used in this study is the Zeiss EVO MA15 and works by irradiating the primary surface of interest (corrosion product covered surfaces) for analysis with finely focused electron beam which interacts with the surface to produce an array of secondary electrons, backscattered electrons, characteristics X-rays and other photons. These signals provide characteristic features of the surface, reflecting on surface topography, crystallography, composition, e.t.c.

Secondary electrons (SE) are usually of lower energy (≤ 10 eV) than the backscattered electrons (BE). Secondary electrons are generated from the near surface of specimen (with strong sensitivity to surface topography) under investigation (≈50Å) while the backscattered electrons are generated much deeper (≈ 5μm) in the specimen and proportional to the atomic number of the host specimen. Generally, the SEM image relies on surface processes, hence it is able to image bulk samples up to many centimetres in size and (depending on instrument design and settings) has a great depth of field, and so can produce images that are good representations of the three-dimensional shape of the sample [156, 157].

Energy-Dispersive X-ray spectroscopy (EDX) is a micro-analytical technique often combined with the SEM to aid elemental analysis or chemical characterisation of a sample. It relies on investigating the interaction of focused source beam of electron/of X-ray excitation and the substrate sample. The characterisation capabilities are due in large part to the fundamental principle that each element has a unique atomic structure allowing unique set of peaks on its X-ray spectrum. The SEM-EDS are not often considered the best surface analytical technique the accuracy of the generated spectrum is easily affected by many elements with overlapping peak as well as the by the nature of the sample. However, this technique has been explored in this research work to obtain useful semi-quantitative information with regard to surface characterisation of corroded steel. Figure 5-8 shows the SEM-EDX technique in use.

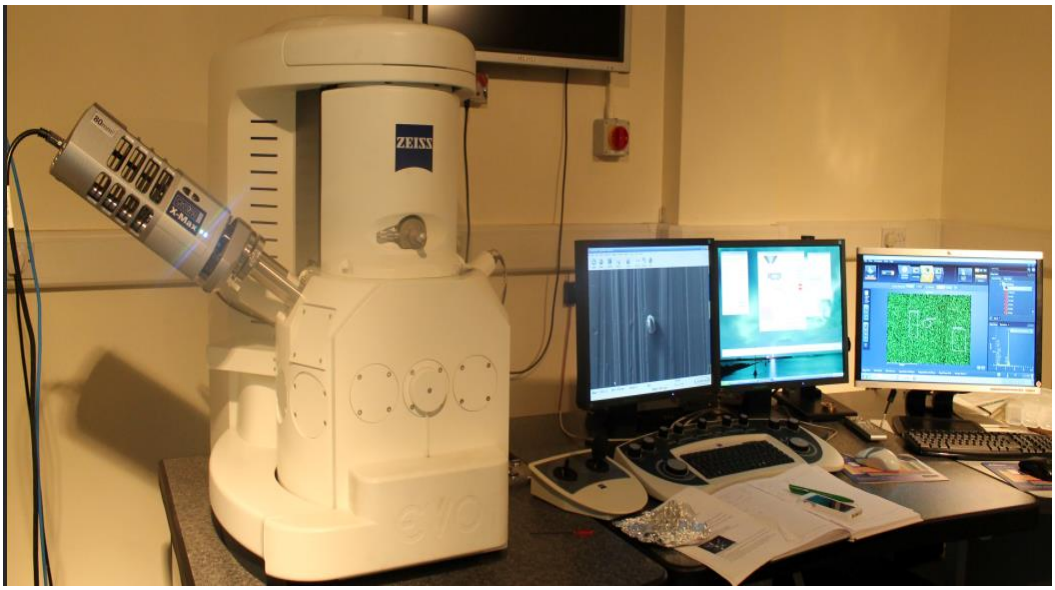

Figure 5-8 Scanning electron microscopy and energy dispersive X-ray analysis in use

5.16.2 X-Ray Diffraction (XRD) spectroscopy

The X-ray Diffraction (XRD) technique is a unique method used for identifying the chemistry of a compound. XRD technique is mostly suited for identifying crystalline compounds and in some cases amorphous compounds too. The PHILIPS X'PERT 1 X-ray diffractometer was used in this study and works on the principle of constructive interference of monochromatic X-rays and a target sample. The interaction of the incident X-rays with the sample produces constructive interference (and a diffracted X-ray) when conditions satisfy Bragg's Law ($n\lambda=2d \sin \theta$). This law relates the wavelength of electromagnetic radiation to the diffraction angle and the lattice spacing in a crystalline sample. The characteristic x-ray diffraction pattern generated in a typical XRD analysis provides a unique "fingerprint" of the crystals present in the sample. Figure 5-9 presents a picture of the PHILIPS X'PERT 1 X-ray diffractometer used in this work.

Figure 5-9 PHILIPS X'PERT 1 X-ray diffractometer used for XRD analysis

5.16.3 Focused Ion Beam (FIB)

The focused Ion Beam (FIB) system used in this study is the FEI NOVA200 Dualbeam SEM/FIB. This technique uses Ga^+ ion beams to sputter the sample to enable precise machining of samples. The FIB instrument is somewhat similar to a scanning electron microscope (SEM), except that an ion beam rather than an electron beam is rastered over the sample. Secondary electrons are generated by the interaction of the ion beam with the sample surface and can be used to obtain high-spatial-resolution images. The ion beam allows etching of the sample at well localised sites, so that cross-sectional images of the structure can be obtained or that

modifications in the structures can be made [158]. The FIB was used in this work for micro-machining to investigate the cross section of corrosion product layers.

5.16.4 Transmission Electron Microscopy (TEM)

The Transmission Electron Microscopy (TEM) is a surface analytical technique that employs energetic electrons to provide morphologic, compositional and crystallographic information on samples. Beam of electrons is transmitted through an ultra-thin specimen, interacting with the specimen as it passes through to create an image that is magnified and focused onto an imaging device. TEM used in this work are the FEI Tecnai TF20 FEGTEM and Philips CM200 FEGTEM and were used to examine fine details of corrosion product layers across a cross section. TEM offers the most powerful magnification, potentially over one million times or more, while providing information on element and compound structure with very detailed images of very high-quality [157]. Imaging capabilities at a significantly higher resolution than SEM were obtained for this study to examine fine details of corrosion product layers.

5.16.5 White light interferometry

White light interferometry refers to techniques that employ the interference between wave fronts of light beams exiting the same source. In the case of this study, the white light interferometry technique was used. It is an important investigative technique in the fields of spectroscopy and surface profiling and in the science of measurement of small surface irregularities, especially with respect to evaluating corrosion damages on a corroded surface. The interferometer simply acts as an optical device that divides a beam of white light exiting a single source (like a laser) into two beams and then recombines or superimposes them in order to extract information about the original state of the source waves and to create an interference pattern.

The NPFLEX 3D interferometer was used in this work in a non-contacting process, that is based on the use of white light interference, open-access sample loading, and an intuitive analysis software to characterise surface texture, roughness, depths, peaks, and numerous other characteristics at angstrom-level accuracy. A picture of the 3D NPFLEX interferometer in use is shown in Figure 5-10.

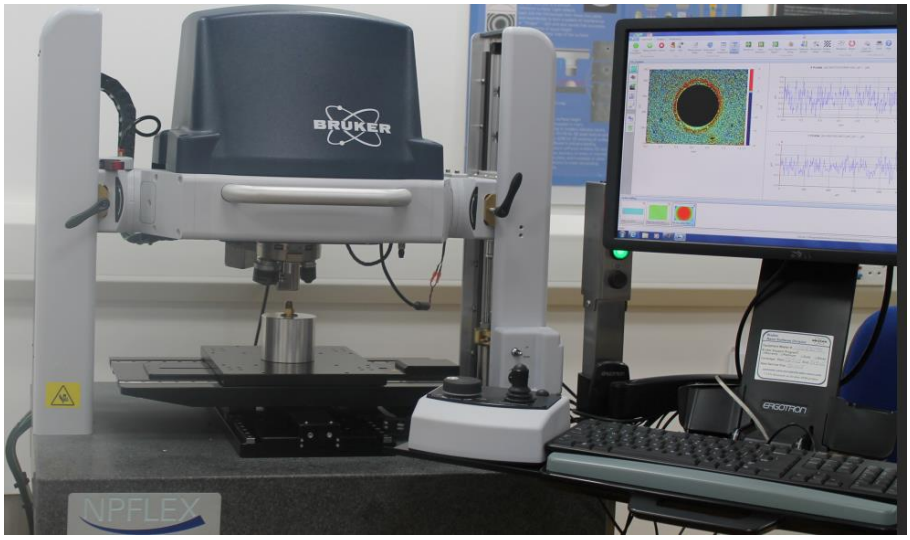

Figure 5-10 The NPFLEX 3D interferometer

The NPFLEX 3D interferometer offers the most comprehensive tool for surface characterisation for pitting corrosion damages (maximum and average pit depths, pit diameter, volume, area, etc) based on the following capabilities;

- The NPFLEX 3D interferometer performs extremely precise and accurate non-contact 3D surface measurement of extra-large samples
- Software can extend measurements capabilities to large areas by automatically stitching overlapping scans
- Yields accuracy in the nanometre range for rough and stepped surfaces.

In the context of the scope and objectives of this research work, the NPLFEX interferometer is used to characterise the damage morphology of corroded steel surfaces by quantification and qualitative evaluation of geometry of pits in terms of the following important outcomes that are relevant to this work;

1) Roughness valley (Rv); Rv is the lowest valley distance from the mean line.

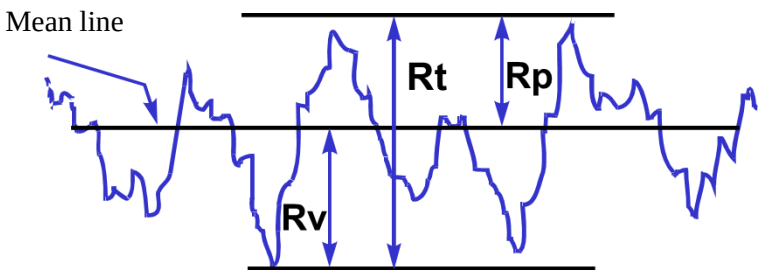

Figure 5-11 Schematic representation of discrete surface parameters as measured by the NPFLEX 3D Interferometer.

2) The volume of pits; this parameter determines the volume of space or void on a pitted surface occurring in-between a surface and a plane parallel to the reference plane of the surface which intersects the maximum (Rp) of the surface. i.e., the volume of a liquid required to completely "submerge" the surface.

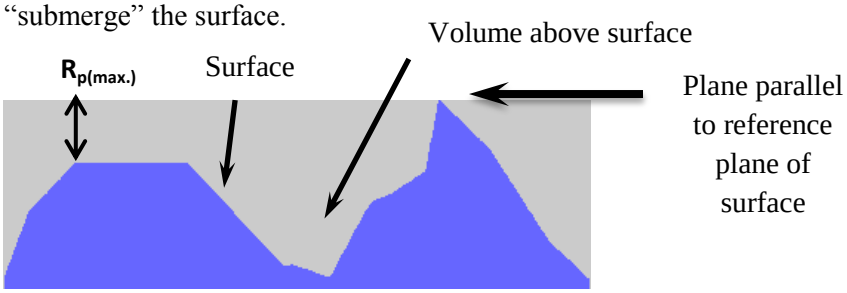

Figure 5-12 Schematic representation of volume of craters/pits as identified and measured by the NPFLEX Interferometer.

3) Other outcomes of relevance for pit characterisation that are obtainable from the NPFLEX interferometer are the discrete area and diameter of pits. The pit diameter used in this study is the diameter of a circle drawn to circumscribe the edges of a pit. This is obtained via careful and systematic application of the vision 64 software.

5.16.6 Systematic technique for surface profiling of a corroded X-65 steel sample

The concept of "maximum pit depth" and average of the 10 deepest pits have been established in section 2.4 of this thesis as the most important parameters for evaluation of pitting corrosion damages in corrosion systems. These parameters have been shown to be more appropriate for estimation of the pit and total metal penetration rate. It has also been shown in Figure 5-1 and Figure 5-3(a) that the dimension of the exposed surface area of the test steel sample is 10mm x 10mm. Based on this dimension, the following procedures were developed and followed in the course of profiling the entire surface a corroded carbon steel sample with the primary objectives of identifying the number of pits on the surface, identifying the deepest pits and evaluation of the discrete parameters of deepest pits.

Base on this procedure, the entire surface area of corroded sample is analysed by stitching 9 different 3mm by 3mm area as shown in the Figure 5-13 and Figure 5-14. A 0.5 mm by 0.5 mm area is excluded along the edges of the sample. The surface profile for each of the 9 stitched 3 mm by 3 mm surface area is collated as a true representation of the entire surface area of a 10 mm by 10 mm carbon steel sample. A comprehensive summary of the discrete parameters of interest for the pits of important interest with respect to pitting corrosion study is created for each experimental condition according to the procedures stated in the ASTM standard G46 for evaluation of pitting corrosion [70].

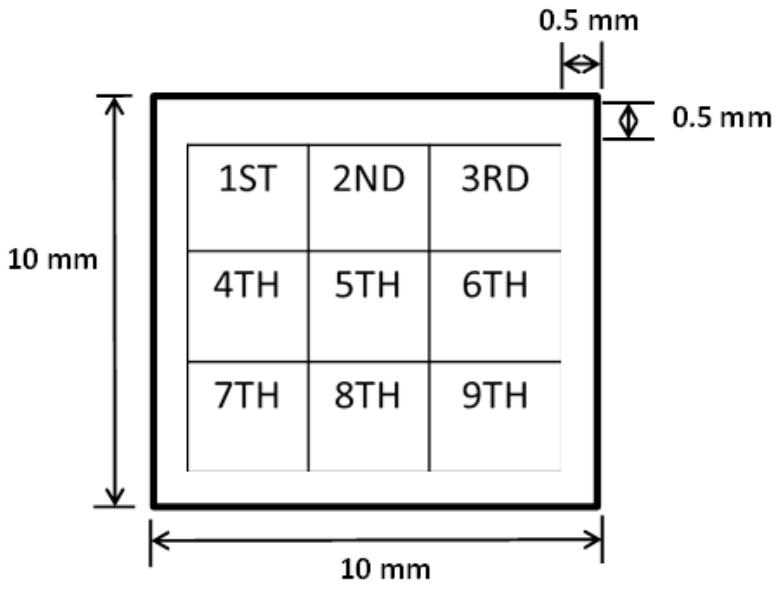

Figure 5-13 Stitching technique using the NPFLEX 3D interferometer.

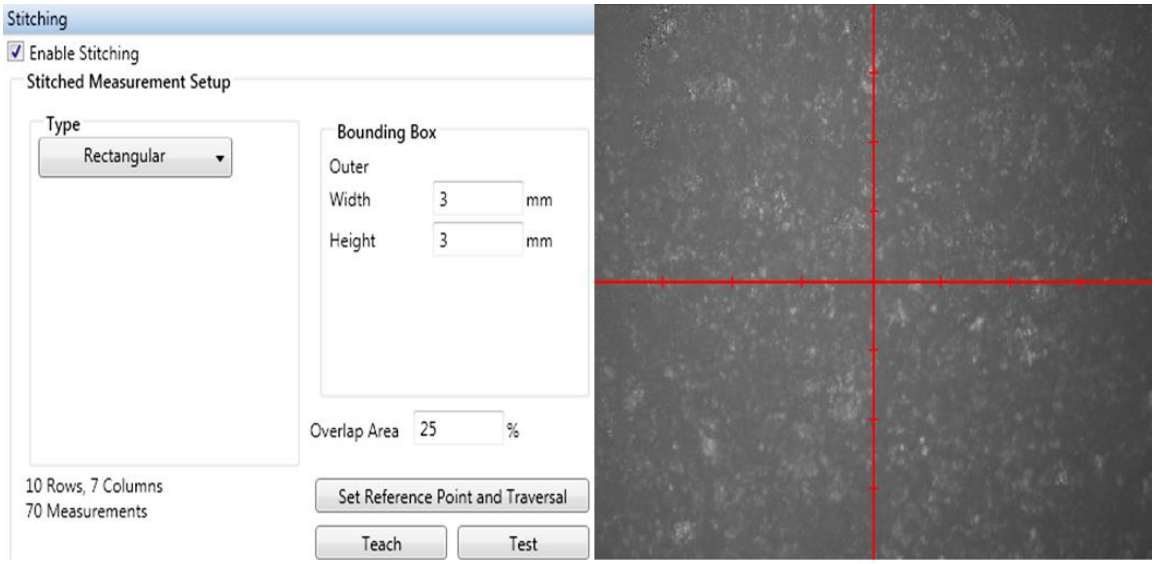

Figure 5-14 NPFLEX 3D interferometer user interface showing the stitching process during pitting corrosion damage investigation.

5.16.7 Characterising pitting corrosion damage and surface interferometry

This section briefly describes how the surface interferometry technique was used for characterizing the morphology of damaged surfaces in this study. Characterisation of pitting corrosion in terms of depth measurements were conducted in alignment with ASTM G46-94 [70]. Pit cavities were identified based on carefully chosen thresholds which allow distinct pit depths, diameters and areas to be accurately quantified. ASTM G46-94 stipulates that an average of the 10 deepest pits and the maximum pit depth relative to corroded surface (based on

pit depth measurement after removal of corrosion products) should be used for pit damage characterisation for the sample area.

It is also very important to also note that there is no generally accepted consensus on the minimum dimensions a pit can take in terms of depth and diameter, especially in non-passivating alloys like carbon steels. However, there are various suggestions of the different possible shapes, orientations and sizes of pits in ASTM G46-94 [70]. Nonetheless, attempts have been made in this work (to be shown later in this thesis) to provide visual evidence of pits/cavities in terms of both 2D pit depth profiles and 3D images of largest and/or deepest pits identified on a corroded sample by the implementation of the multiple region analysis technique. The multiple region analysis technique is described in the next paragraphs.

The stitching technique described in section 5.16.6 was combined with an advance data analysis technique known as the multiple region analysis. This data analysis technique was applied in the following ways with some dummy examples to clearly illustrate the procedure:

1) Firstly, pitted/corroded surfaces of carbon steel (10mm X 10mm in dimension) with pits characterise are scanned by the non-contacting NPFLEX 3D interferometer using the stitching approach (see section 5.16.6).

2) These pits were identified using the multiple region analysis user interfaces and discrete geometry of the pits was generated. This is shown in Figure 5-15 and is based on carefully chosen thresholds. The thresholds used in this study vary for different studies and is dependent on the overall surface roughness of the corroded samples. For example it varies from 0.5µm to 10µm for the least corroded surface to the heavily corroded surface respectively.

3) The generated pitting data are collated for all stitched surfaces (9 stitched regions), and ranked according to the procedures listed in the ASTM standard G46 for evaluation of pitting corrosion [70]. Important criteria such as the R_{sk}, diameter, and pixels are used to screen real data from data due to software generated errors.

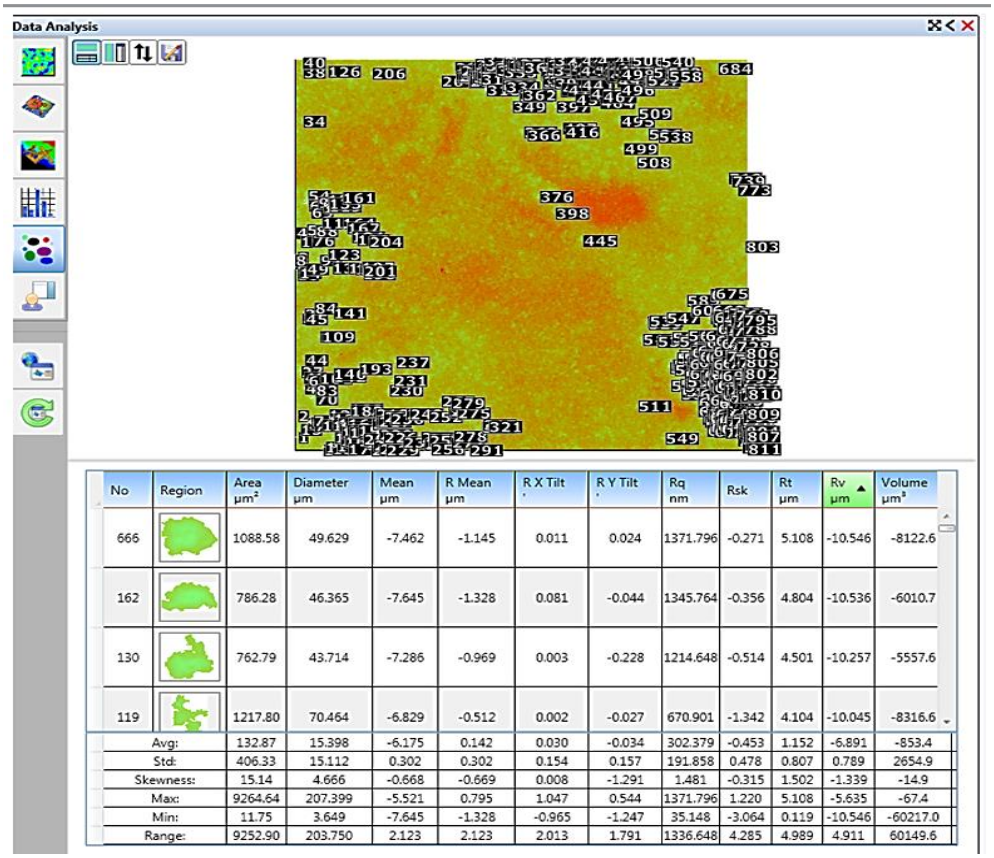

No	Region	Area µm²	Diameter µm	Mean µm	R Mean µm	R X Tilt °	R Y Tilt °	Rq nm	Rsk	Rt µm	Rv µm	Volume µm³
666		1088.58	49.629	-7.462	-1.145	0.011	0.024	1371.796	-0.271	5.108	-10.546	-8122.6
162		786.28	46.365	-7.645	-1.328	0.081	-0.044	1345.764	-0.356	4.804	-10.536	-6010.7
130		762.79	43.714	-7.286	-0.969	0.003	-0.228	1214.648	-0.514	4.501	-10.257	-5557.6
119		1217.80	70.464	-6.829	-0.512	0.002	-0.027	670.901	-1.342	4.104	-10.045	-8316.6
Avg:		132.87	15.398	-6.175	0.142	0.030	-0.034	302.379	-0.453	1.152	-6.891	-853.4
Std:		406.33	15.112	0.302	0.302	0.154	0.157	191.858	0.478	0.807	0.789	2654.9
Skewness:		15.14	4.666	-0.668	-0.669	0.008	-1.291	1.481	-0.315	1.502	-1.339	-14.9
Max:		9264.64	207.399	-5.521	0.795	1.047	0.544	1371.796	1.220	5.108	-5.635	-67.4
Min:		11.75	3.649	-7.645	-1.328	-0.965	-1.247	35.148	-3.064	0.119	-10.546	-60217.0
Range:		9252.90	203.750	2.123	2.123	2.013	1.791	1336.648	4.285	4.989	4.911	60149.6

Figure 5-15 The multiple region analysis user interface to illustrate how discrete pitting corrosion parameters were generated.

Note that in this study, the possibility of scanning the entire surface of exposed steel surface was prioritised over and above the number of surfaces scanned. This is influenced by the importance of this approach on locating the deepest pit on an entire corroded surface. However, data for repeated surface profilometry analysis were carried out across the different aspect of this study and for selected experimental conditions to emphasis the repeatability and reliability of this technique in evaluating pitting corrosion damage of carbon steel materials. The results of these analyses are presented and discussed in the next few chapters of this thesis.

Chapter 6. Investigation of uniform and pitting corrosion in CO_2 saturated corrosion environments; Effect of Temperature

6.1 Introduction

Carbon dioxide (CO_2) corrosion and CO_2-related pitting and localised corrosion failures have been well documented within the oil and gas industry. Pitting corrosion of carbon steel can be complex and in the main unpredictable in nature with significant challenges that are usually associated with inhibiting pit propagation once it has initiated. It has been envisaged that factors such as temperature, *in-situ* pH, exposure time of metallic components to corrosive media and solution chemistry (e.g. chloride ion concentration) that can influence the CO_2 corrosion process along with associated film formation characteristics and morphology could also influence the tendency for pits to initiate and propagate on carbon steel materials [58, 59, 110, 159].

There has been lack of clarity in terms of the actual mechanism of pitting corrosion in carbon steel materials, especially in comparison to understanding of pitting corrosion of passive alloys such as stainless steel materials. In the latter, the mechanisms of corrosion, passivation and pitting corrosion are relatively well understood and generally revolve around the localised breakdown of the passive film leading to propagation of pitting attack [33, 38]. The presence of sulphide inclusions is known to be the precursor for pit initiation in passive materials such as stainless steels [112-114]. Sulphide inclusions become soluble because they tend to become more active than passive oxide-covered layers [112].

However, what remains a point of debate is a clear understanding of pitting corrosion in cases of non-passivating materials such as carbon steel in CO_2 saturated environments [9, 38, 65, 68]. While it is also likely that sulphide inclusions could also be a precursor for pit initiation among other electrochemical processes, it is still essential to understand the initiation and propagation of pits in these environments in order to determine when pitting corrosion will become a threat and how to mitigate it effectively, especially over extended periods. This is significant in the case of carbon steels where it is expected that significant general corrosion precedes corrosion product formation and initiation of localised corrosion/pitting [88, 159].

The results presented in Chapter 6, Chapter 7 and Chapter 8 focuses on investigating the effect of temperature and water chemistry as critical environmental factors on the corrosion and pitting corrosion behaviour of carbon steel materials in CO_2-saturated brine. Temperature and water chemistry are usually influential parameters affecting CO_2 corrosion of oilfield pipeline steels. This approach of a parametric study is considered very important since the mechanism of

CO_2 corrosion is known to be dependent on many interrelated physicochemical factors whose interactions with steel in CO_2 environment is considered very important [105]. In addition to temperature, some of the physicochemical factors include dissolved chloride ion concentration [40, 83, 106] and solution pH.

The results of all electrochemical corrosion reactions presented in this Chapter for investigating the effect of temperature were obtained in an un-buffered environment with a view of elucidating how critical environmental variable such as temperature may be influencing the mechanism of pitting corrosion in oilfield environments. The work presented in this Chapter intends to contribute towards a more comprehensive understanding of the influence of temperature and associated corrosion product morphologies on overall corrosion behaviour of carbon steel materials but with emphasis on pitting corrosion. The findings will help to improve on the existing understanding of the pitting corrosion behaviour of carbon steels in CO_2-saturated environment.

6.2 Measurement and validation of electrochemical responses

6.2.1 Tafel Polarisation measurements

Tafel polarisation experiments were performed at atmospheric pressure for all nine conditions provided in Table 5-3 and as described in section 5.4 of this thesis. Figure 6-1 presents the Tafel polarisation curves for carbon steel sample exposed to the conditions provided in Table 5-3.

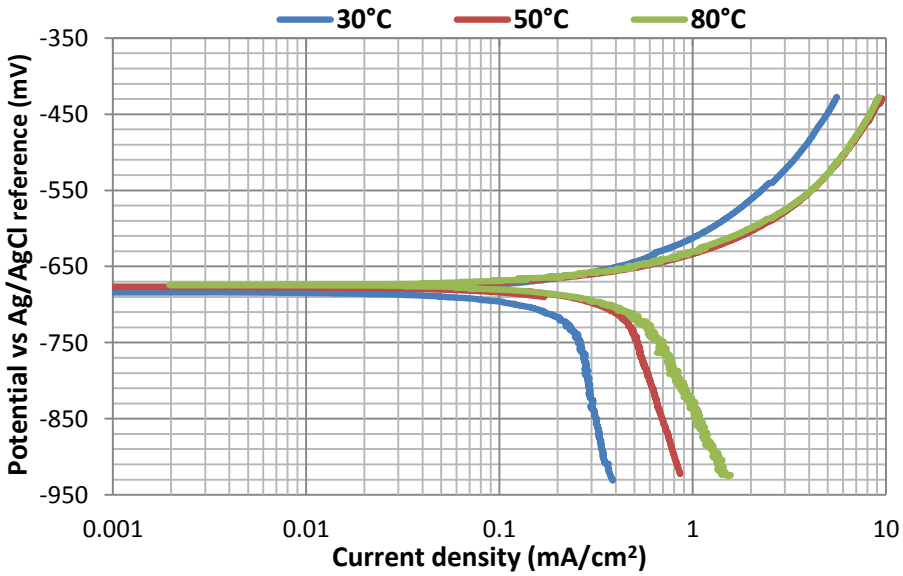

(a)

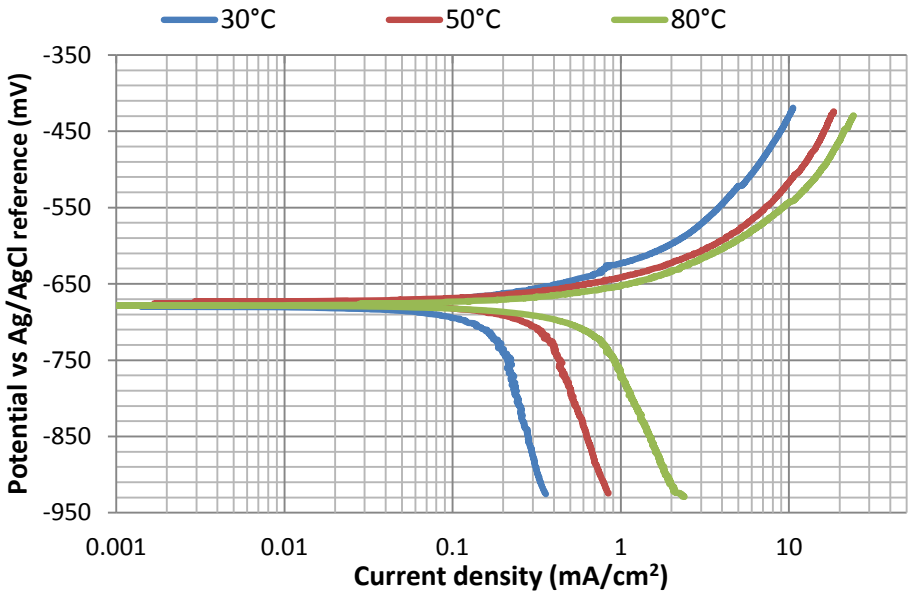

(b)

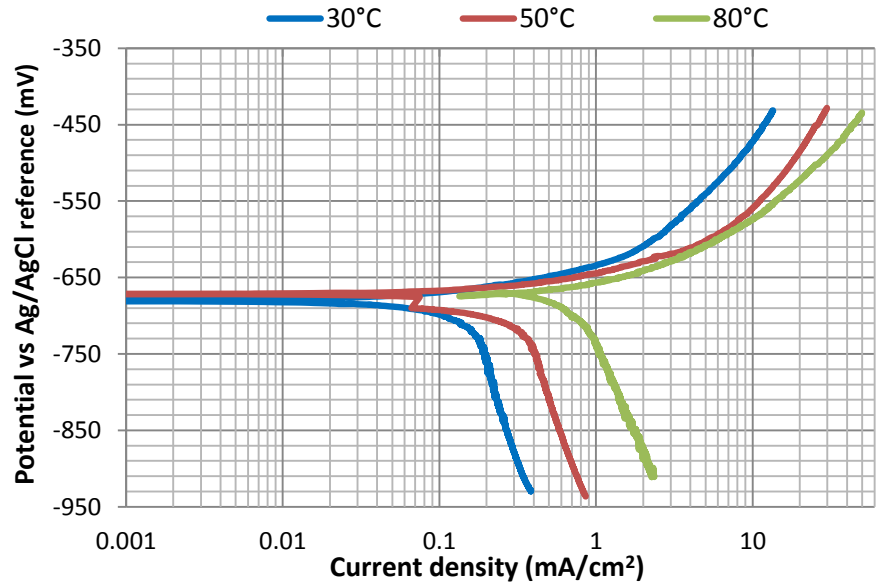

(c)

Figure 6-1 Tafel polarisation curves for X65 carbon steel exposed at to (a) 1 wt. % NaCl solutions under CO_2 gas atmosphere (b) 3.5 wt. % NaCl solutions under CO_2 gas atmosphere and (c) 10 wt. % NaCl solutions under CO_2 gas atmosphere at 30, 50 and 80°C after 7 hours.

Each of the polarisation tests provided in Figure 6-1 were repeated at least two times to ensure reliability of data collation for accurate estimation of uniform corrosion rate. Repeated Tafel polarisation test results for solution of 3.5 wt. % NaCl for 30, 50 and 80°C are presented in appendix D. Figure 6-2 is used to provide some details on how the Tafel extrapolation was carried out as well as for the estimation of Tafel constants (β_a and β_c).

The Tafel polarisation curves presented in Figure 6-1 are under activation control at lower cathodic potential range. However, in the course of Tafel extrapolation and Tafel constant estimation process presented in Figure 6-2, the appropriate guidelines provided in the ASTM standard, G102-89[160] and corrosion tests and standards by Baboian [47] was used. According to the guidelines in the ASTM standard, G102-89 [160], The Tafel constants β_a and β_c can be estimated from the deviation from linearity of polarisation curves in the 20-50mV region around the corrosion potential (E_{corr}) in cases where the activation control and diffusion control effects are significant and/or of equal magnitude in a mixed control system. This guideline has been applied in such cases in this work and the corresponding Stern-Geary coefficient is provided for some of the conditions in Table 6-1.

It is important to note that while the Tafel polarisation tests were performed after 7 hours of immersion of test samples into the electrolyte, it is expected that the polarisation curves and hence the estimated Tafel slopes changes with changes in the electrochemical processes at the sample-corrosion media interface with longer exposure time. Such changes may involve evolution of corrosion products with time. However, by performing the polarisation measurements after 7 hours ensures that the Tafel slopes were estimated while the corroding surface is in an active state without masking the possibility of understanding the various electrochemical reactions that contributes to the cathodic and anodic reactions during the corrosion of test samples.

It is also understood that the Tafel slopes may also change with time during corrosion process over a 168 hours period. However, the Tafel slopes estimated after 7 hours has been adopted for the entire duration of the experiment to simplify the analysis with the limits of an accurate corrosion rate measurement. Tafel polarisation measurements obtained from separate cathodic and anodic polarisation measurements as in the case of this work, also poses some difficulty in the curves converging at a perfect E_{corr}. However, attempts have been made in this study to ensure that the best possible convergence is achieved.

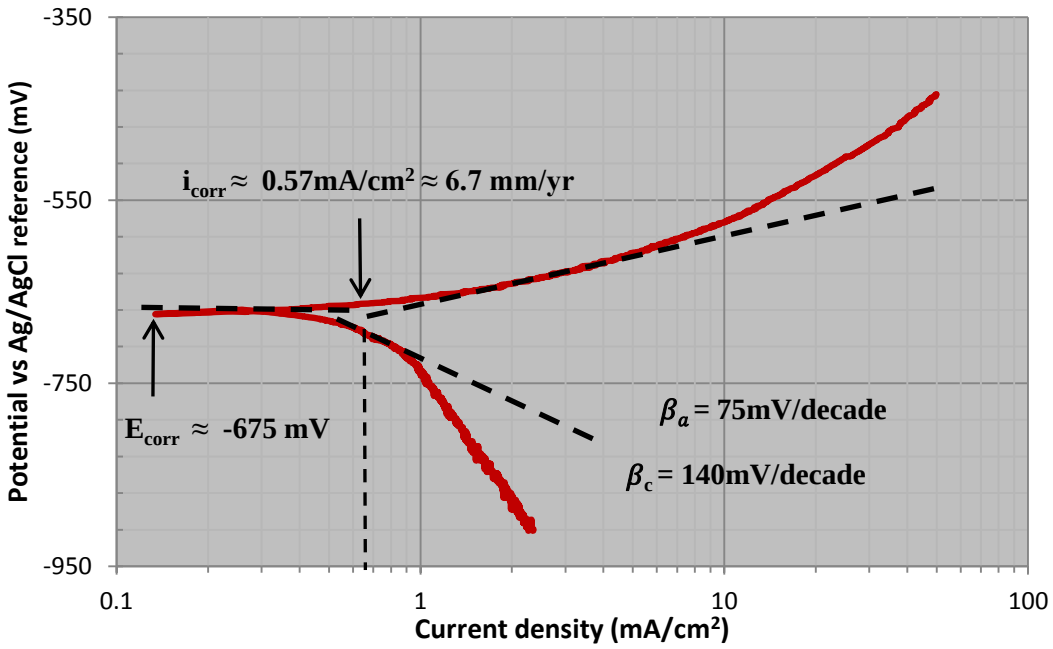

Figure 6-2 Tafel Extrapolation and estimation of Tafel constants for test solution system of 10 wt. % NaCl at 80°C under a CO_2 gas atmosphere.

DC Linear Polarization Resistance (LPR) measurements were conducted over the duration of each experiment, using an ACM Gill 8 potentiostat. The working electrode was polarized ± 15 mV about the open circuit potential (OCP) at a scan rate of 0.25 mV/s. Tafel constants used for the corrosion rate calculation were estimated from the Tafel polarisation tests with graphs shown in Figure 6-1.

Estimated values of Tafel constants were used to determine the Stern-Geary coefficient (B) using the following equations;

$$B = \frac{1}{2.303}\left[\frac{1}{\beta_a} + \frac{1}{\beta_c}\right]^{-1} \quad 6.1$$

Where β_a and β_c are Tafel constants for anodic and cathodic reactions respectively.

The corrosion current density (i_{corr}) could then be determined by combining the Stern-Geary coefficient (B) with the linear polarisation (R_p) values according to the following equation;

$$i_{corr} = \frac{1}{2.303 R_p}\left[\frac{1}{\beta_a} + \frac{1}{\beta_c}\right]^{-1} = \frac{B}{R_p} \quad 6.2$$

Finally, corrosion rates were estimated using the corrosion current density i_{corr} and the following equation;

$$CR\left(^{mm}/_{yr}\right) = \frac{3.27 \times 10^3 i_{corr} A_w}{n\rho} \quad 6.3$$

Where Aw is the molecular weight of the corroding substrate, n is the number of transferred electrons and ρ is the density of corroding substrate.

The Stern Geary coefficients for some of the experimental conditions provided Table 5-3 are provided in Table 6-1.

Table 6-1 Summary of Stern-Geary coefficient for conditions provided in Table 5-3

Test conditions	Stern-Geary Coefficient (B) (mV/decade)
10 NaCl %, 30°C	15.07
10 NaCl %, 50°C	17.77
10 NaCl %, 80°C	21.21

Tafel polarisation plots were confirmed by comparing the corrosion rate from Tafel extrapolation with the estimated corrosion rate using obtained Tafel constants and are provided in Table 6-2 some of the test conditions. Estimation of corrosion rate from Tafel polarisation curves was performed using the same guidelines adopted for estimation of Tafel slopes (β_a and β_c) to ensure consistency.

Table 6-2 Comparison between current densities (mA/cm^2) and corrosion rate (mm/yr) obtained from Tafel extrapolation and from the use of the estimated Stern-Geary constants.

Test conditions	Corrosion current density from Tafel extrapolation (mA/cm^2)	Corrosion rate from Tafel extrapolation (mm/yr)	Corrosion current density using Tafel constants (mA/cm^2)	Calculated corrosion rate using Tafel constants (mm/yr)
1 %, 30°C	0.09	1.05	0.09	1.01
10 %, 30°C	0.09	1.05	0.13	1.01
3.5 %, 50°C	0.18	2.10	0.22	2.58
10 %, 50°C	0.22	2.56	0.29	3.44
3.5 %, 80°C	0.41	4.77	0.45	5.23
10 %, 80°C	0.58	6.7	0.60	7.00

6.3 Validation of electrochemical responses

The Tafel polarisation slopes as a function of temperature are provided in Figure 6-3.

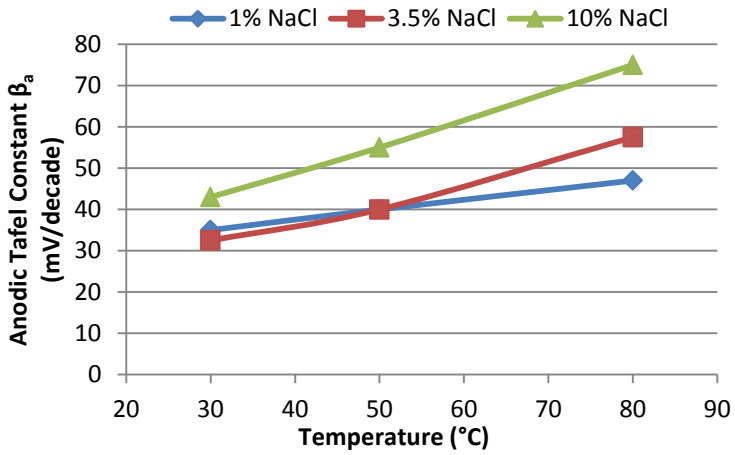

Figure 6-3 Estimated Tafel slopes for (a) anodic reaction with temperature for some experimental conditions explored in this study.

The Tafel polarisation slopes plotted in Figure 6-3 have been shown to vary linearly with temperature just as implied by the expressions for Tafel slopes of anodic and cathodic line respectively [47, 103] as;

$$\beta_a = \frac{2.303RT}{\alpha_a F} \qquad 6.4$$

Where T = temperature in Kelvin (K)

R = Universal gas constant (m^3 Pa K^{-1} mol^{-1})

F = Faraday's constant at 96500 (Coulomb/mole of electrons).

And α, represents an ion transfer coefficient for a multi-step reaction process.

Tafel slopes estimated for test conditions at 30℃ for 10% NaCl solution saturated with CO_2 gas in this work (from Figure 6-3), gave a value 43mV/decade for (β_a). This value was verified using Eq. 6.4, and gave an anodic Tafel slope of 40.1mV/decade which was also found to be consistent with the calculated value by Nesic *et al* [103] at 25 ℃ (40mV/decade) using Eq. 6.4, an ion transfer coefficient of $\alpha_a = 1.5$ at pH = 4.0 as provided by Bockris *et al* [81]. Calculations carried out by Bockris *et al* [81] using Eq. 6.4 also gave β_a of 42. However, application of ion transfer coefficient of $\alpha_a = 1.5$ by Bockris *et al* [81] and Eq. 6.4, shows significant difference at 50 and 80℃. This has been attributed to the variation of ion transfer coefficient with temperature. The ion transfer coefficient has also been reported by Bronner *et al* [161] to change with current density such that higher currents resulted in lower α values. This implies that the ion transfer coefficient would be significantly lower at higher temperature.

This thus validates the relationship between ion transfer coefficient α and temperature as depicted by Eqns. 6.4. Hence, the higher values of β_a at higher temperature as shown in Figure. 6.4. This statement is consistent with the trend shown in Figure 6-3 and reflects the linearity of Eqns. 6.4. With reference to ion transfer behaviour with temperature, the solvation energy, ΔG°_{sol} of an ion (especially Fe^{2+}) within the vicinity of the EDL is considered to be composed of an electrostatic contribution, and as such, the standard Gibbs transfer energy, ΔG°_{tr}, of an ion at the aqueous (w)/metal interface is attributable to the difference between ΔG°_{sol} of the iron ion in the aqueous phase and that in metal lattice [162]. This could also be applicable to the dissolved ionic species in the brine phase:

$$\Delta G^{\circ}_{tr} = \Delta G^{\circ}_{tr\,(electrolyte)} - \Delta G^{\circ}_{tr\,(metal)} \qquad 6.5$$

Since the dielectric constants (ε) of solvents, the thermal motion of solvent molecules and the number of hydrogen bonds among water molecules vary with temperature [162], Therefore $\Delta G^{\circ}_{tr\,(electrolyte)}$ and $\Delta G^{\circ}_{tr\,(metal)}$ and therefore ΔG°_{tr} may be affected by temperature. Hence the observed increase of ΔG°_{tr}, with rising temperature just as the entropy change of the ion transfer process becomes more negative [163]. This is the concept of electrochemical activation process in corrosion reaction with increasing temperature, which has been clearly reflected in the Tafel plots provided in Figure 6-3.

6.4 Corrosion rate measurements at different temperatures

This section presents the measured corrosion rate for all experimental conditions presented in Table 5-3 over a 168 hour test period. The DC linear polarisation resistance technique was used to monitor the electrochemical responses of carbon steel; corrosion rate and corrosion potential during the duration of the tests as the corrosion product layer formation process occurs in CO_2 corrosion environment. Figure 6-4 and Figure 6-5 shows the corrosion rate and corrosion potential for all experimental conditions presented in Table 5-3. Error bars on the data points plotted in Figure 6-4 and Figure 6-5 are based on the averages of the corrosion rate and E_{corr} from up to four measurements from a minimum of three separate and repeatable experiments over the 168 hours.

Figure 6-4 shows that for all brine systems, the corrosion rate increased with increasing temperature. This trend as observed for all brine systems in Figure 6-4 is also consistent with observations by several authors in the literature [77, 98]. The peak corrosion rate recorded in a 1 wt. % NaCl solution for all 30, 50 and 80°C; 1.2 mm/yr, 2.37 mm/yr and 3.2 mm/yr

respectively compares very well with the corrosion rate measurement reported by Nesic *et al* [103]; 1 mm/yr at 20°C, 2.5 mm/yr 50°C and 3 mm/yr at 80°C. These corrosion rates have also been confirmed by the potentiodynamic sweeps shown in Figure 6-1, which shows a shift in cathodic current density towards higher values. This observation in the potentiodynamic sweeps is also consistent with observations by Nesic *et al* [103] and Ogundele and White [80]. The increase in total cathodic current with increase in temperature is associated with the increase in the rate of cathodic reduction of H_2CO_3 and of H^+ [103].

Temperature is known to accelerate most of the chemical and electrochemical processes occurring in the present corrosion environment [119]. The most pronounced effect is the increase in the mass transfer-controlled limiting current with an increase in the diffusion coefficient (D) for H^+ and a decrease in viscosity at higher temperatures. The potentiodynamic curves also show that the anodic reaction is not significantly influenced by increasing temperature when compared to temperature influence on the cathodic reaction. A similar observation has been reported by Nesic *et al* [103] and is true for all brine systems. The only difference is just the magnitude of the variation of corrosion rate with temperature for the three different brine systems used in this work. This aspect of the results will be presented in subsequent sections of this chapter. The free corrosion potential variation with temperature is not as significant as the corrosion rate. However, Figure 6-5 shows a consistent trend for the free corrosion potential as a function of temperature for the three brine systems in this work.

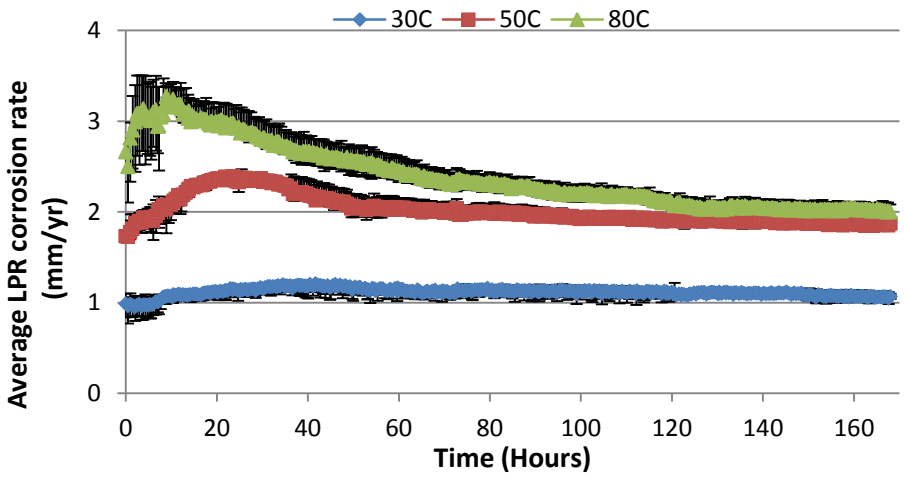

(a)

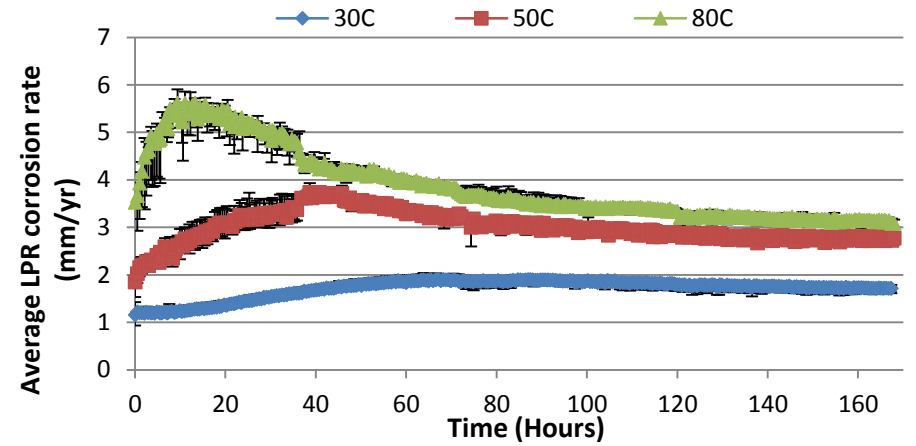

(b)

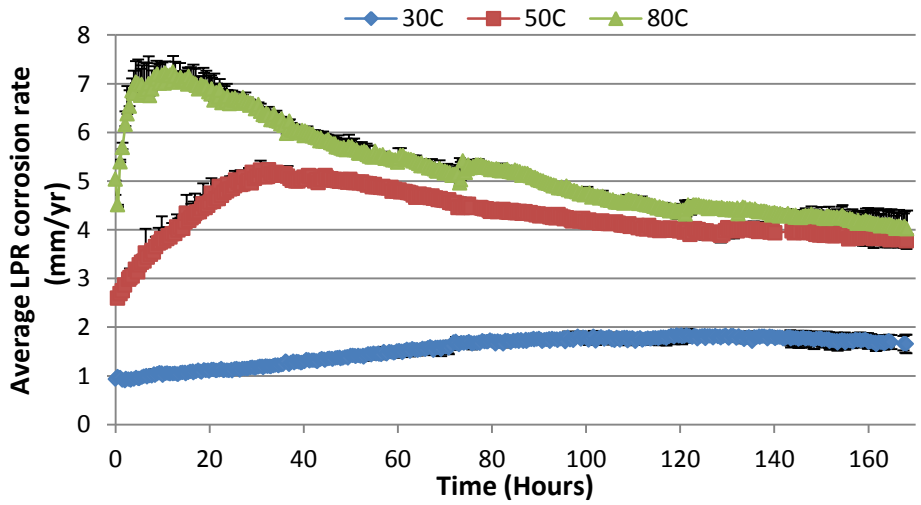

(c)

Figure 6-4 Average corrosion rate from linear polarisation resistance measurement for X65 carbon steel exposed at to (a) 1 wt. % NaCl solutions (b) 3.5 wt. % NaCl solutions and (c) 10 wt. % NaCl solutions under CO_2 gas atmosphere at 30, 50 and 80°C, over a test duration of 168 hours (Static condition).

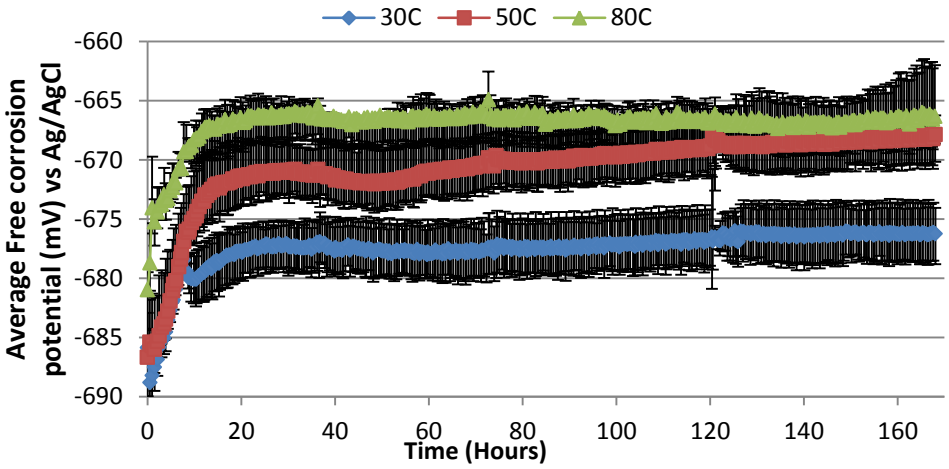

(a)

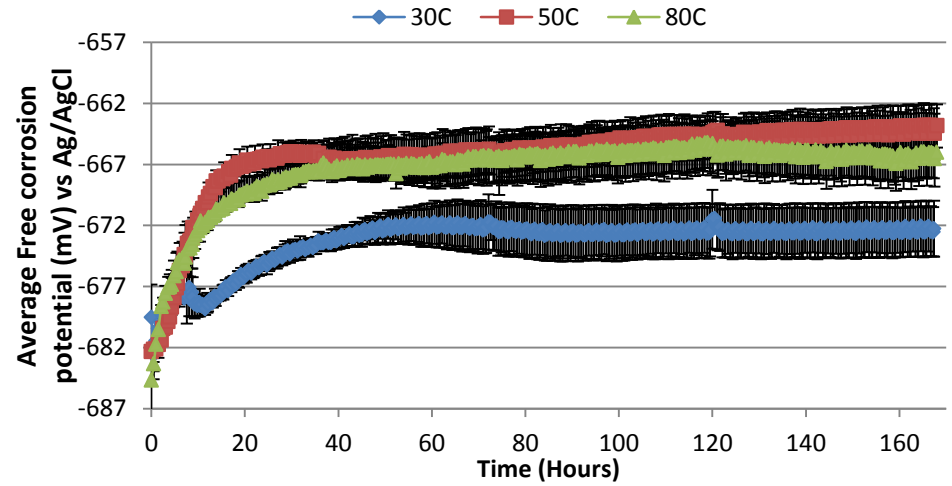

(b)

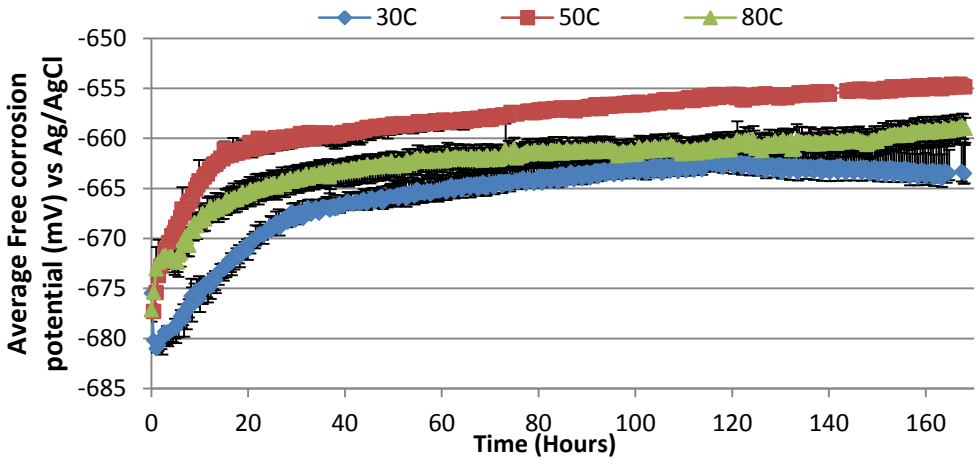

(c)

Figure 6-5 Average free corrosion potential for X65 carbon steel exposed at to (a) 1 wt. % NaCl solutions (b) 3.5 wt. % NaCl solutions and (c) 10 wt. % NaCl solutions under CO_2 gas atmosphere at 30, 50 and 80°C, over a test duration of 168 hours. Each error bars represent the average of data points from at least three repeatable corrosion potential measurements (Static condition).

6.5 Correlation between electrochemical responses and formation of corrosion products as a function of temperature

This section discusses the relationship between the electrochemical activities at the metal-brine interface and the different stages and processes of corrosion product formation, including networks of iron carbide (Fe_3C) often revealed after the preferential dissolution of the ferrite phase. In this section the discussion would be focused on a single brine system (10 wt. % NaCl solutions) only but with a strong emphasis on the effect of temperature on the corrosion behaviour of carbon steel materials in CO_2 saturated environments.

Figure 6-6(a) and (b) presents the total concentration of Fe^{2+} and saturation ratio (SR) as a function of time for 30, 50 and 80C respectively. A detail analysis on how the values plotted in Figure 6-6(a) and (b) were obtained has already been explained in section 5.15. The analysis presented and explained in section 5.15 was based on the assumption that the measured corrosion rate response represents the total amount of Fe^{2+} lost into the bulk phase of the corrosion environment. The data presented in Figure 6-6(a) and (b) will be explored in the course of elucidating the process of corrosion product formation of X65 carbon steel in an unbuffered CO_2 saturated environments.

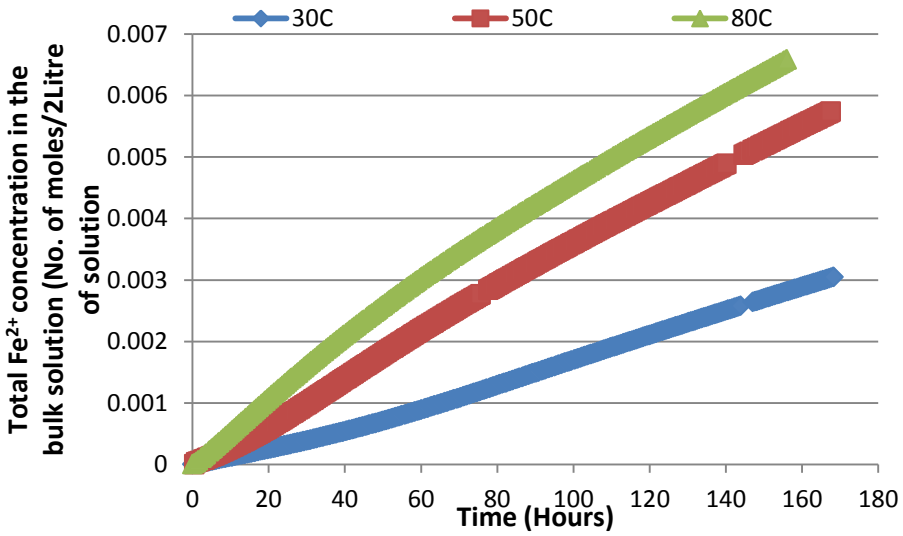

(a)

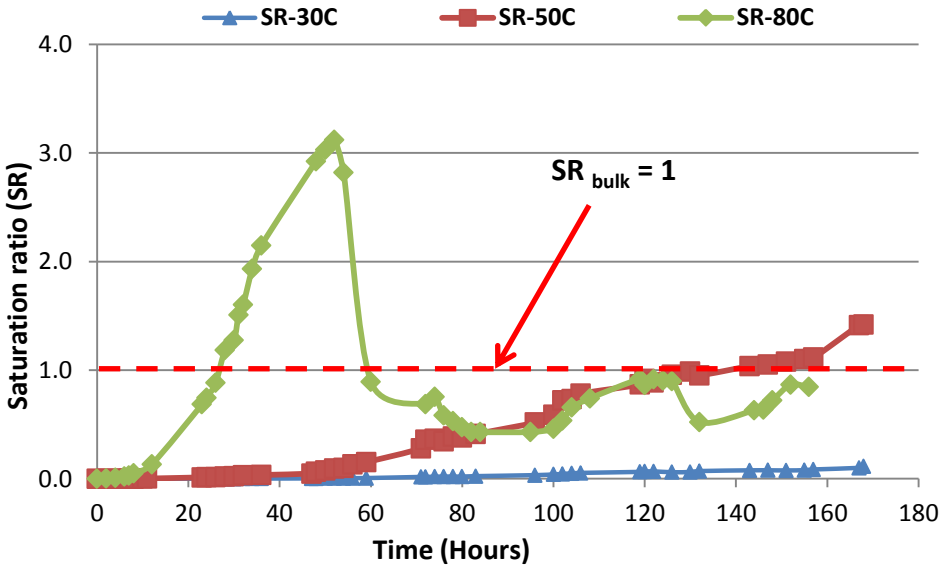

(b)

Figure 6-6 Graphs of (a) Total bulk concentration of Fe^{2+} and (b) the saturation ratio (SR) during corrosion of X65 carbon steel in 10wt. % NaCl solution saturated with CO_2 for a duration of 168 hours.

6.5.1 Corrosion behaviour and formation of corrosion product at 30°C

Figure 6-7 shows the electrochemical behavior (E_{corr} and LPR corrosion rate) of X-65 steel over 168 hours of exposure to the 10 wt. % NaCl solutions at 30°C. The different stages of observed corrosion products on the metal surface over the exposure time of 168 hours are also provided in Figure 6.8 in the form of SEM images, as well as being annotated within Figure 6.7 itself. Referring to Figure 6-7, between 0 and 7 hours of corrosion testing, a steady increase in general corrosion rate and ennoblement of E_{corr} are apparent. The marked increase in E_{corr} is in alignment with the revealing of an Fe_3C layer, as shown in Figure 6-8(a) and has been observed by several other authors when ferrite preferentially dissolves from the steel surface [9, 88, 164]. There is also the suggestion in literature that the revealing of this undissolved layer may lead to the accentuated corrosion rate at anodic regions [9, 88, 165]. Such an observation has been suggested to create a galvanic effect between local anodic and cathodic sites of the same steel surface, ultimately leading non-uniform precipitation of corrosion products and thus acting as a precursor for pitting/localised corrosion attack [9, 88, 164, 165]. After 36 hours of exposure the onset of A non-crystalline form of $FeCO_3$ corrosion product (often referred to as "amorphous" several authors [93, 95]) is shown to establish itself on the steel surface and potentially within the voids of the Fe_3C layer. The seemingly amorphous corrosion product layer (believed to be $FeCO_3$) was observed to develop into a continuous layer with very small traces of nano-scale crystals of $FeCO_3$ existing on top of this layer (highlighted in Region 'A' within Figure 6-8(b)).

The formation of amorphous $FeCO_3$ is made favourable by the low pH of the system (shown in Figure 6-7) and has been previously observed and characterised in the literature within similar environments [93, 166]. The period of formation of the amorphous layer also coincides with a transitory stabilization of E_{corr} with a steady increase in general corrosion rate (Figure 6-7). Referring by the SEM images in Figure 6-8(a) and (b), it is clear that the surface layer is still dominated by Fe_3C during this period, suggesting that the deposition of this corrosion product layer had not been occurring for a particularly long period of time.

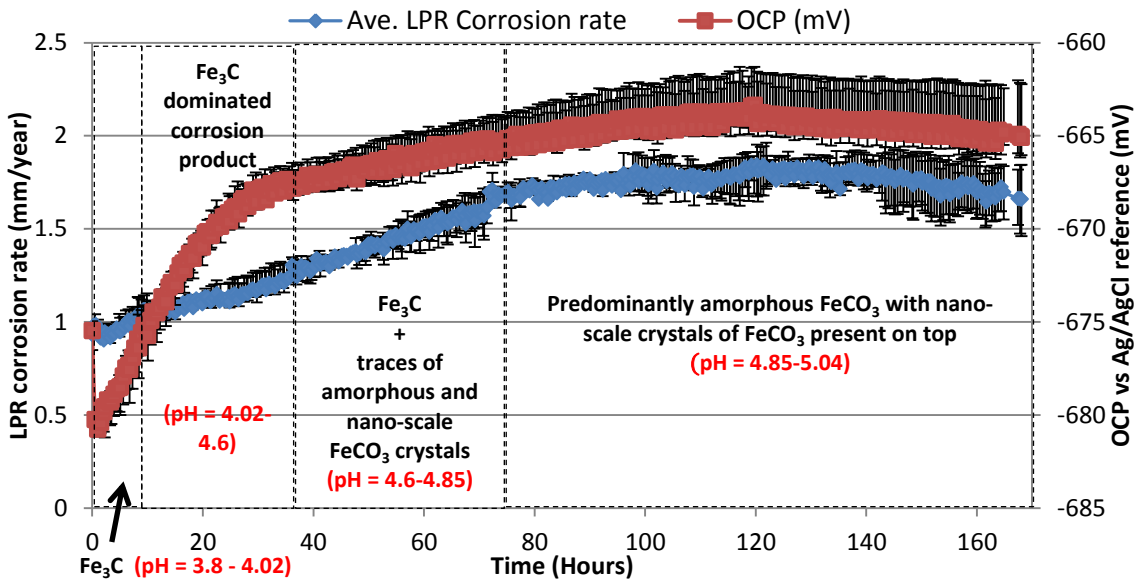

Figure 6-7 A plot of LPR corrosion rate and open circuit potential of X-65 steel over a duration of 168 hours in a 10 wt.% NaCl solution saturated with CO_2 at 30°C.

Between 36 and 72 hours of immersion there was an apparent increase in the quantity and coverage of the amorphous $FeCO_3$ layer. The morphology of the corrosion product layer shown in Figure 6-8(c) indicated the slight presence of nano-scale crystals growing together on top of the amorphous layer. This period of immersion is marked by continued increase in general corrosion rate and a slight increase in E_{corr} of the steel. The increase observed could be related to galvanic effects between Fe_3C and the steel surface, as suggested by Crolet *et al* [88], but cannot be proven. What is evident though is that the presence of the different corrosion product morphologies observed at this stage (Fe_3C and amorphous/nano-crystalline $FeCO_3$) is having little or no effect on reducing the general corrosion rate of the underlying steel. From 72 hours onwards, a marginal increase in general corrosion rate is observed, followed by a subsequent reduction after almost 150 hours. The corrosion product layer formed on the steel sample at this time is dominated by amorphous $FeCO_3$, as well as traces of more nano-scale crystals whose composition is confirmed as $FeCO_3$ by the distinct peak at 32° on the XRD patterns (as well as other diffraction angles) provided in Figure 6-9 which can be compared to the reference patterns of Fe, Fe_3C and $FeCO_3$ shown in Figure 6-10.

The results suggest that the precipitation of amorphous and/or nano-polycrystalline $FeCO_3$ could have the ability to keep the general corrosion rate of the steel surface at this temperature. However, it could also be suggested that the pH change in the solution from 4.85 to 5.00 may also have helped suppressed general corrosion rate through reduction of the cathodic reaction. At this temperature, this fact cannot be discounted [167]. Regardless of this effect, the change is

only slight and it can be confirmed that no substantial level of protection is offered by the corrosion product especially since saturation ratio in the bulk (**SR_{bulk}) ≪1 (**see Figure 6-6**).**

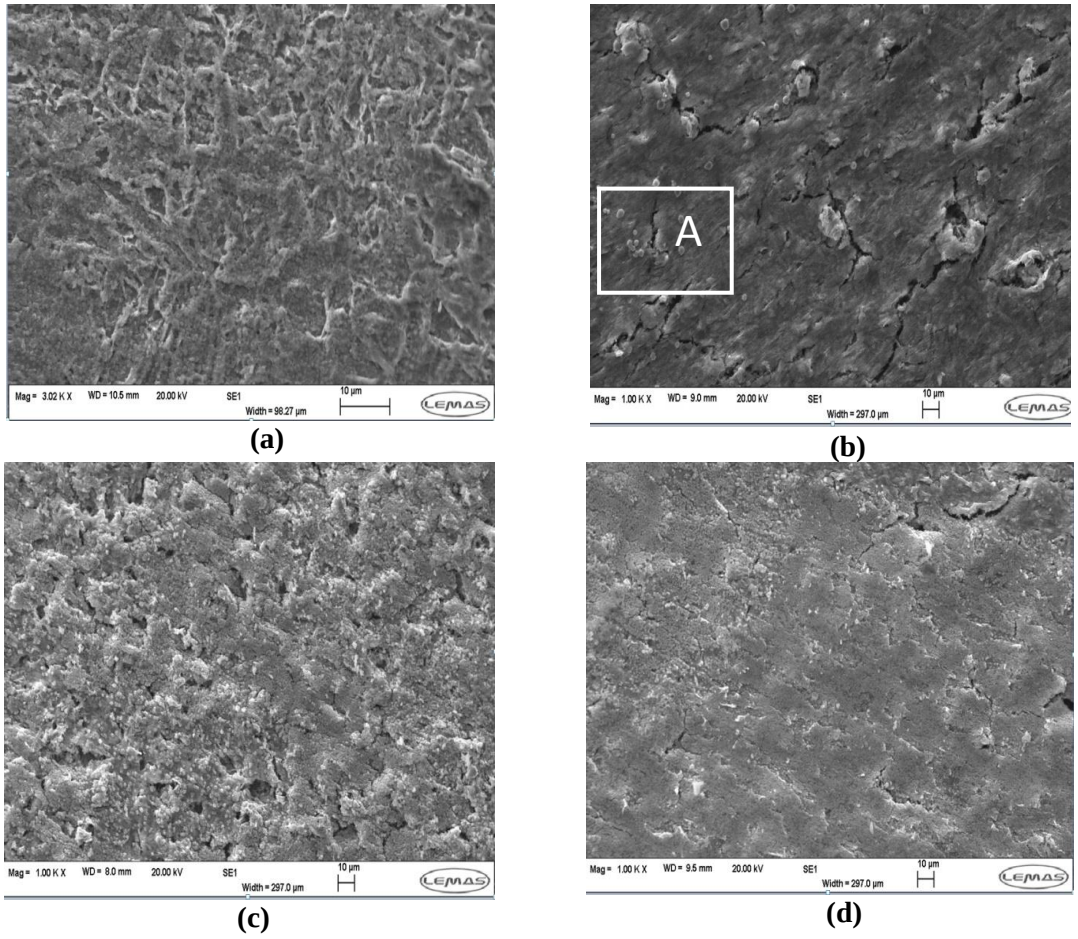

Figure 6-8 SEM images of corrosion product on X-65 samples exposed to 10 wt.% NaCl solution saturated with CO_2 at 30°C (a) 7 hours, (b) 36 hours, (c) 72 hours and (d) 168 hours.

It is worth noting that the XRD pattern of the sample exposed to the electrolyte for 168 hours provided in Figure 6-9 confirms the presence of crystalline $FeCO_3$ (a corrosion product known to offer protection to the steel surface through either blocking active sites on the steel surface or acting as a diffusion barrier to electrochemically active species involved in the cathodic reaction) [9]. However, the extent and mode of precipitation was not adequate enough or suitable to significantly influence the general corrosion behaviour of the underlying steel substrate.

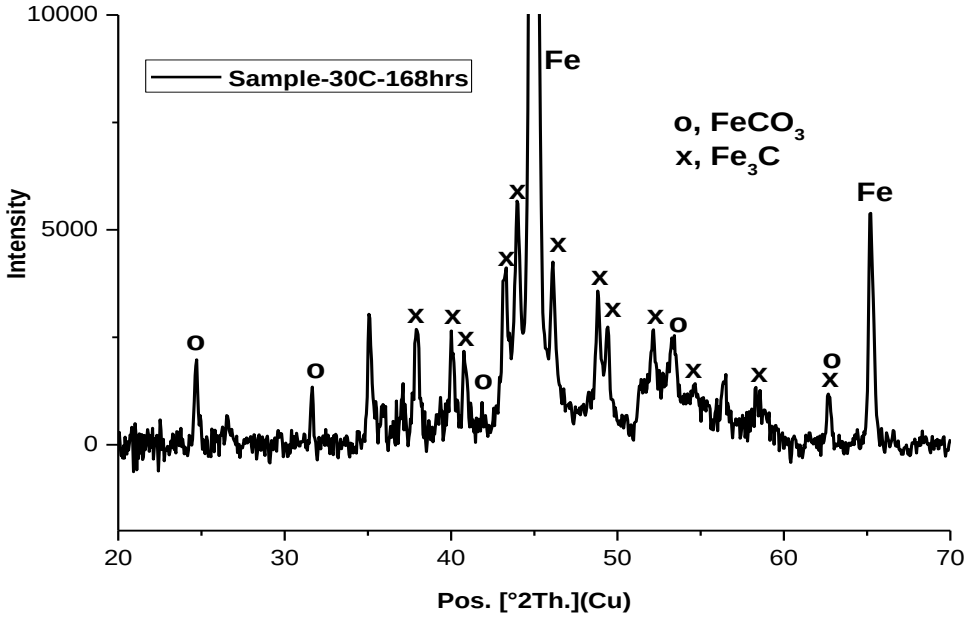

Figure 6-9 XRD pattern for corrosion product on X-65 steel after exposure to a 10 wt.% NaCl solution for 168 hours at 30°C (SEM image of Figure 6.7(d)) *(Note that the intensity scale is arbitrary)*.

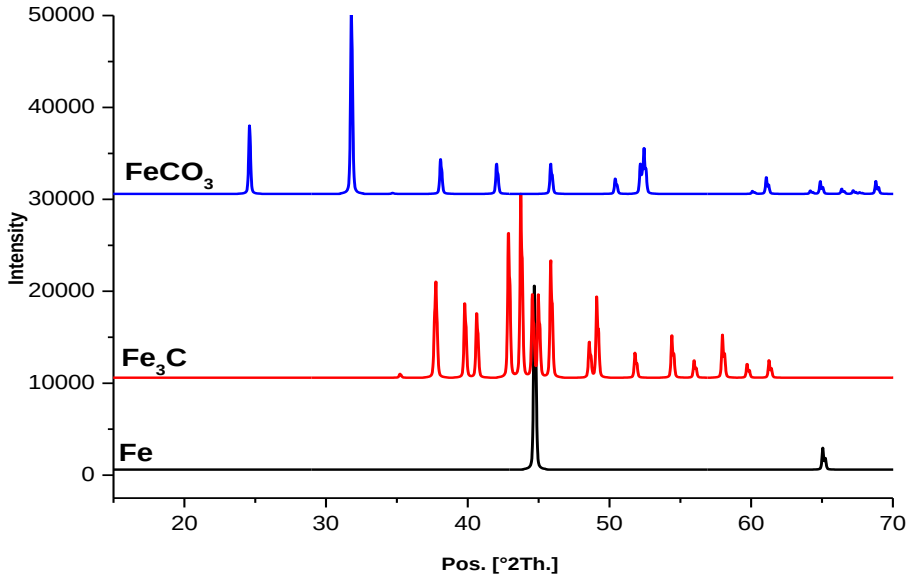

Figure 6-10 Reference XRD patterns for Fe, Fe_3C and $FeCO_3$ [168-170].

6.5.2 Corrosion behaviour and formation of corrosion product at 50°C

The variation in general corrosion rate and E_{corr} over the course of the 168 hour experiment at 50°C is provided in Figure 6-11. The surface layer consists of a network of Fe_3C between 0 to 7

hours at 50°C which was produced by the fast rate of preferential ferrite dissolution. The formation of such a film is supported by a rapid increase in both E_{corr} and general corrosion rate, as depicted in Figure 6-11. The rise in E_{corr} observed with corrosion rate is likely to be attributed to an increase in the cathodic reaction as a result of more Fe_3C sites progressively revealing themselves [9, 58, 88, 103]. The rate of increase in corrosion rate and potential is much faster than that observed at 30°C, suggesting a quicker rate of revealing of the Fe_3C network. Between 7 and 36 hours, the general corrosion rate continues to increase rapidly and peaks after 30 hours. This coincides with the E_{corr} starting to stabilise.

The point at which general corrosion rate starts reducing (≈ 40 hours) coincides with evidence of the deposition of traces of localised agglomerations of $FeCO_3$ crystals (SEM images shown in Figure 6-12(a) to (d)), which become more evident with time. As stated previously, similar observations of nano-scale $FeCO_3$ crystals were recorded at 30°C but did not appear as quickly as at 50°C, reflecting the effect of increasing temperature on the rate of formation of $FeCO_3$ corrosion products. In reference to Figure 6-6(a) and (b), while the total assumed Fe_{2+} lost increases with time, $\mathbf{SR_{bulk}}$ exceeded 1 only after ≈ 125 hours, while the corrosion rate started reducing after ≈ 40 hours. This is an indication that $\mathbf{SR_{bulk} \ll SR_{interface}}$.

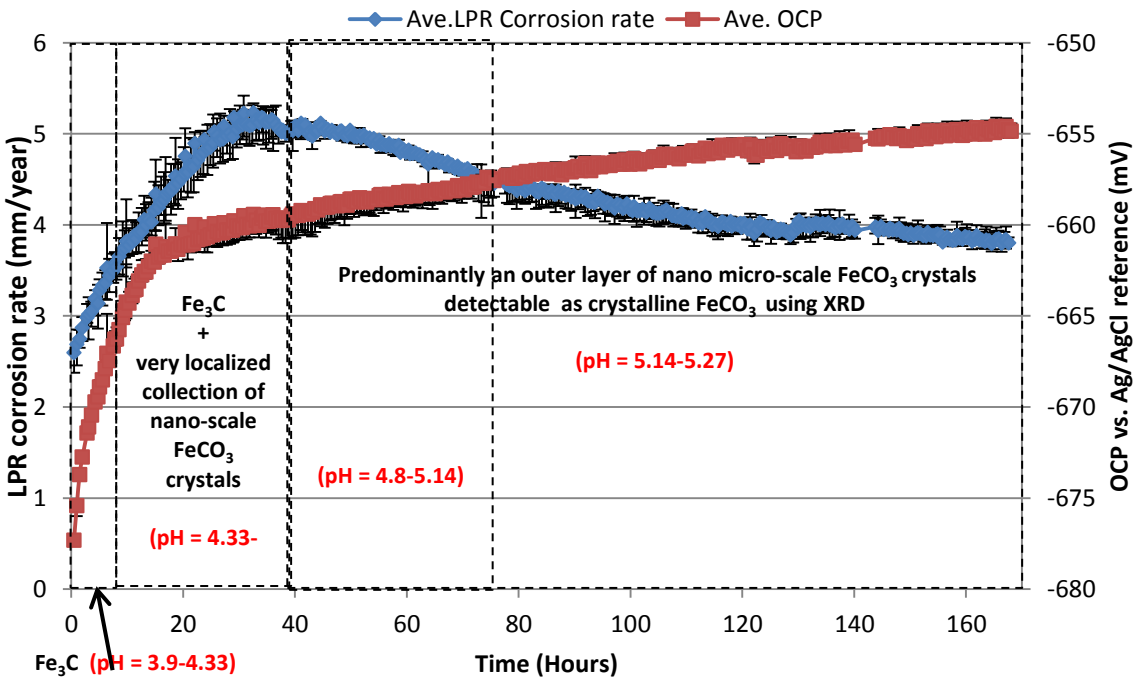

Figure 6-11 A plot of LPR corrosion rate and open circuit potential of X-65 steel over a duration of 168 hours in a 10 wt.% NaCl solution saturated with CO_2 at 50°C.

Between 36 and 72 hours, the $FeCO_3$ crystal size becomes larger, occupying a greater proportion of the steel surface (Figure 6-12(b)). The crystal initiation and growth process

coincides with a gradual reduction of corrosion rate and increase in OCP. This behaviour was also observed up to the end of the test and could be influenced by a higher pH than at 30°C, leading to a higher nucleation and growth rate of $FeCO_3$ crystals. The reduction in general corrosion rate in Figure 6-11 from 30 hours onwards could be partially attributed to the increase in pH observed over this period (4.8 to just over 5.14 after 168 hours). However, a reduction in general corrosion rate with a steady increase in OCP suggests suppression of anodic reaction relative to cathodic process, which could potentially be linked to the blocking of active sites (although only slight) on the surface by the precipitation of $FeCO_3$. As stated previously, an increase in surface pH typically leads to a drop in OCP towards more cathodic potential by reducing the rate of the overall cathodic reaction [103].The XRD pattern of the X-65 sample surface after 168 hours (shown in Figure 6-13) indicates strong peaks for $FeCO_3$, confirming the substantial presence of crystals deposited on the surface of the steel relative to those observed at 30^{o}C. Figure 6-12(d) shows the developed crystals on the steel surface clearly, which possess an average diameter of approximately 1 µm.

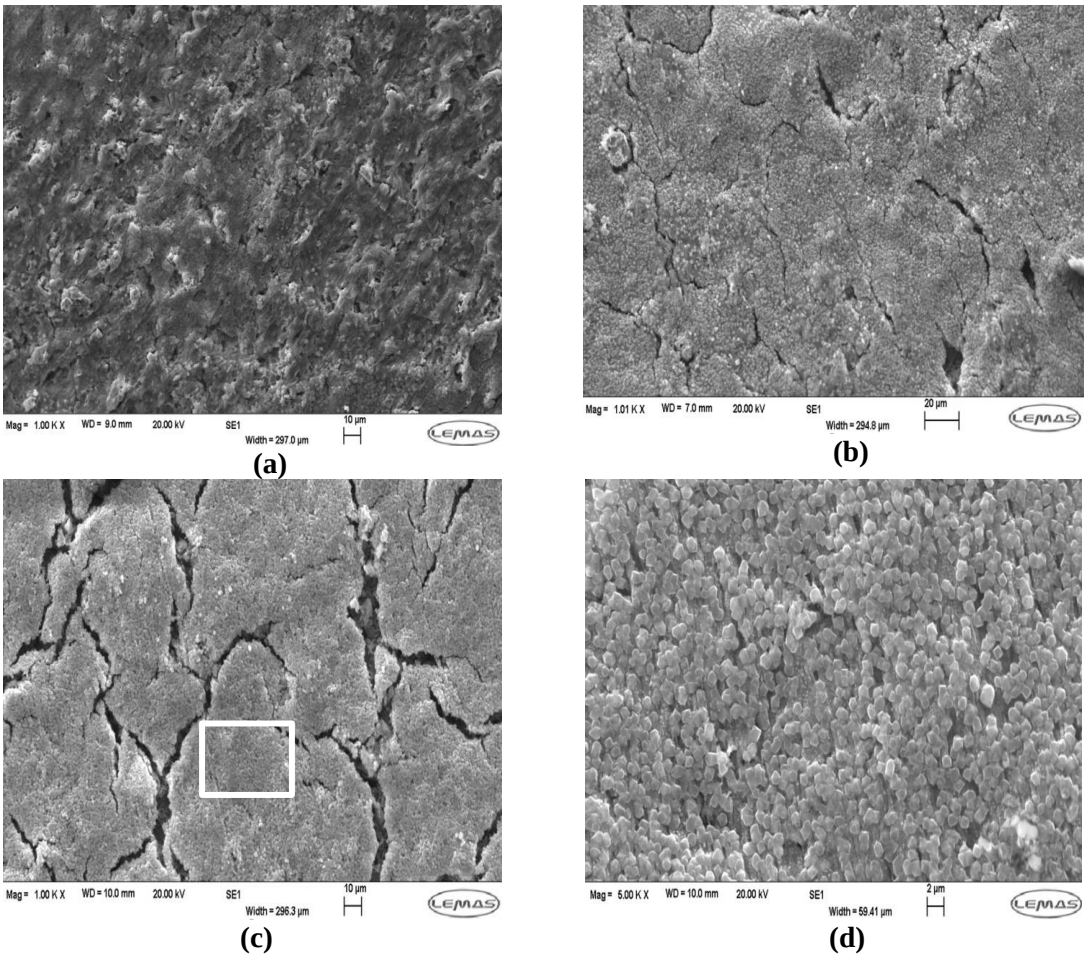

Figure 6-12 SEM images of corrosion product on X-65 samples exposed to 10 wt.% NaCl solution saturated with CO_2 at 50°C (a) 36 hours, (b) 72 hours, (c) 168 hours and (d) magnified image of region identified in (c).

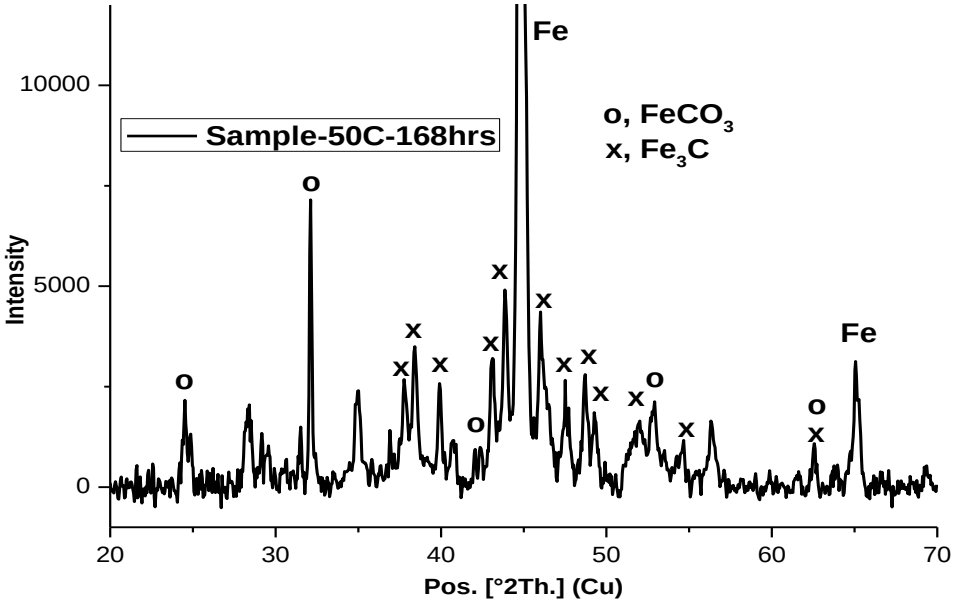

Figure 6-13 XRD pattern for corrosion product on X-65 steel after exposure to a 10 wt.% NaCl solution for 168 hours at 50°C (SEM image in Figure 6.11(d)) *(Note that the intensity scale is arbitrary).*

6.5.3 Corrosion behaviour and formation of corrosion product at 80°C

The general corrosion rate, OCP and corrosion product formation observed throughout the test at 80°C is presented in Figure 6-14. The corrosion behaviour is characterised by a very rapid increase in general corrosion rate and OCP between 0 and 7 hours. General corrosion rate peaks at about 11 hours while the corresponding effect of this is the evidence of a layer which consisted of an agglomeration of nano-scale $FeCO_3$ crystals which were visible after only 7 hours of immersion and similar to those recorded at 50°C beyond 36 hours (Figure 6-12(d)). The film became distinctly more visible after 36 hours and is shown within Figure 6-15(a) as a layer exhibiting a smudge-like texture.

Based on the ratio of uniform corrosion rate at start of each test to when it peaks at each respective temperature, the revealing of Fe_3C at 50°C appears to be having the greatest effect on corrosion rate i.e. the ratio of peak corrosion rate to initial corrosion rate for each temperature was largest at 50°C. However, in terms of the actual magnitude of uniform corrosion rate, an increase of approximately 2.5 mm/year from the initial corrosion rate is observed at both 50°C and 80°C, while there is only an increase of 1 mm/year at 30°C, indicating that the revealing of

the Fe_3C network had a greater effect on increasing corrosion rates at higher temperatures in these particular experiments.

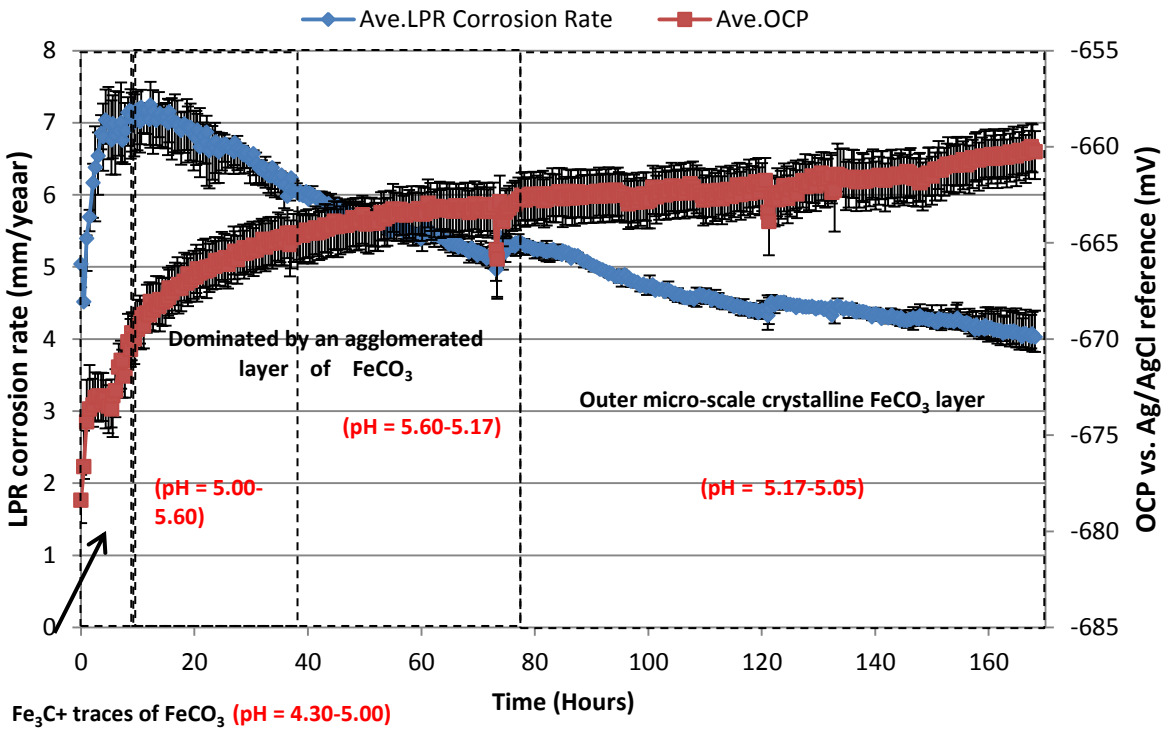

Figure 6-14 A plot of LPR corrosion rate and open circuit potential of X-65 steel over a duration of 168 hours in a 10 wt.% NaCl solution saturated with CO_2 at 80°C.

Between 7 and 36 hours at 80°C, uniform corrosion rate starts to reduce, whilst OCP increases (Figure 6-14) in conjunction with the formation of a top layer of amorphous $FeCO_3$ above the Fe_3C network based on SEM images (Figure 6-15(a)). The observed decrease in corrosion rate at this time could potentially be linked to increasing pH from 5.0 to 5.6. However, continuous increase in potential suggests that some of the active corrosion sites are being blocked as a result of $FeCO_3$ formation. Continuous reduction in corrosion rate was also observed between 36 and 72 hours, even while the potential appears to be relatively stable. This also coincides with evidence of further formation of crystalline $FeCO_3$, which is verified from the XRD pattern provided in Figure 6-16(a).

From 72 hours onwards, E_{corr} stabilises in conjunction with a marginal but steady decline in general corrosion rate. Evidence of the presence of crystalline $FeCO_3$ became stronger after 168 hours on the XRD pattern (Figure 6-16(a)) and the SEM images (Figure 6-15(d)) despite the low measured pH of 5.05. Theoretically, a decrease in pH in the bulk solution from 5.6 to 5.05 from 36 to 168 hours would have implied an increase in corrosion rate [9]. pH vs time data is

shown later in this thesis in Figure 7-13. However, corrosion rate tends to decrease over this period, most likely because of the formation of $FeCO_3$ [93] .

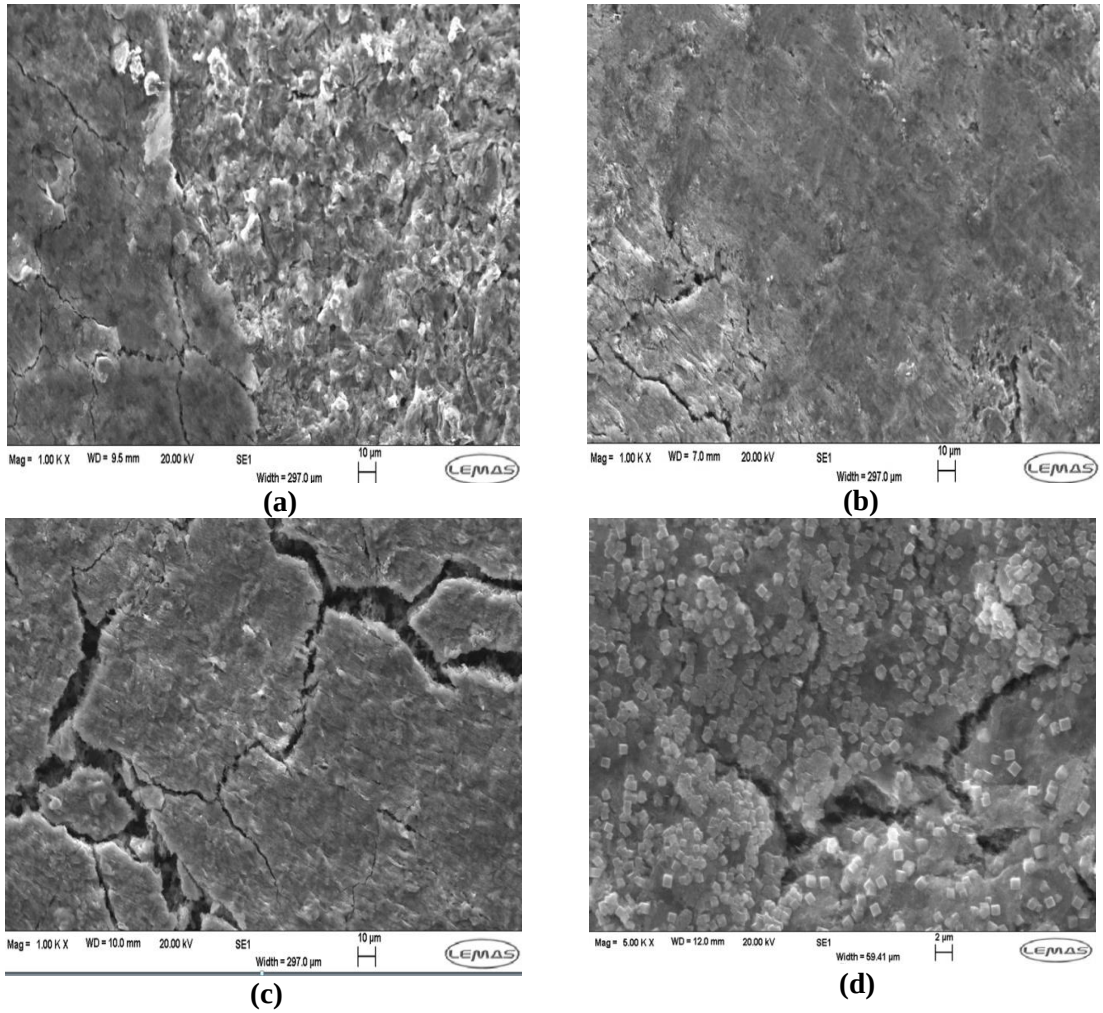

Figure 6-15 SEM images of corrosion product above X-65 samples exposed to 10 wt. % NaCl solution saturated with CO_2 at 80°C (a) 36 hours, (b) 72 hours, (c) 168 hours (d) $FeCO_3$ crystals on a different region of sample shown in (c).

Raman analysis of the samples was conducted using the Renishaw Invia spectrometer. Spectra from the samples were obtained in backscattering configuration with the 488 nm wavelength laser, at 0.5 mW laser power, 1s exposure time and 50 accumulation. Peak analysis was conducted using the Renishaw WiRE program for peak position. The Raman pattern for the sample shown in Figure 6-15(d) is provided in Figure 6-16(b) for the crystalline and amorphous regions on the steel surface. Both spectra exhibit a strong peak at 1086cm-1 and a second diagnostic peak for siderite is at 300 cm^{-1}, indicative of $FeCO_3$ to further confirm the presence of $FeCO_3$ corrosion product [171, 172]. Raman spectra provided in Figure 6-16(b) are for two different regions of sample shown in Figure 6.15(c) and (d). This is also supported by the fact that the measured corrosion rate starts reducing after ≈ 15 hours, which is an indication that

supersaturation in bulk solution is higher than unity. According to Figure 6-6(b), SR_{bulk} =1 after ≈ 25 hours, while the corrosion rate starts reducing after ≈ 15 hours. This is also an indication of the difference between saturation ratio (SR) at corrosion interface and the bulk.

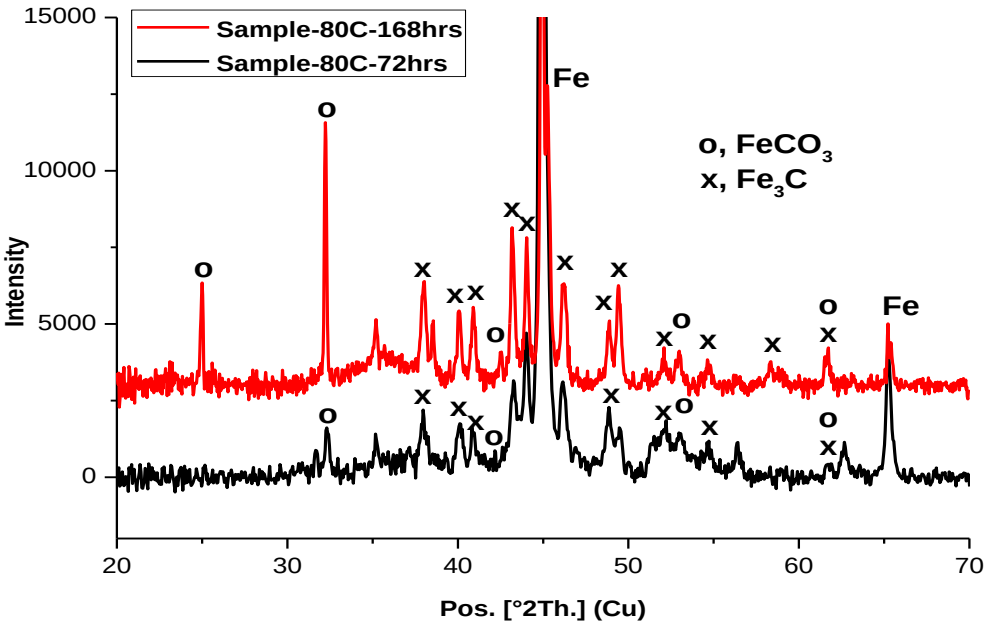

(a)

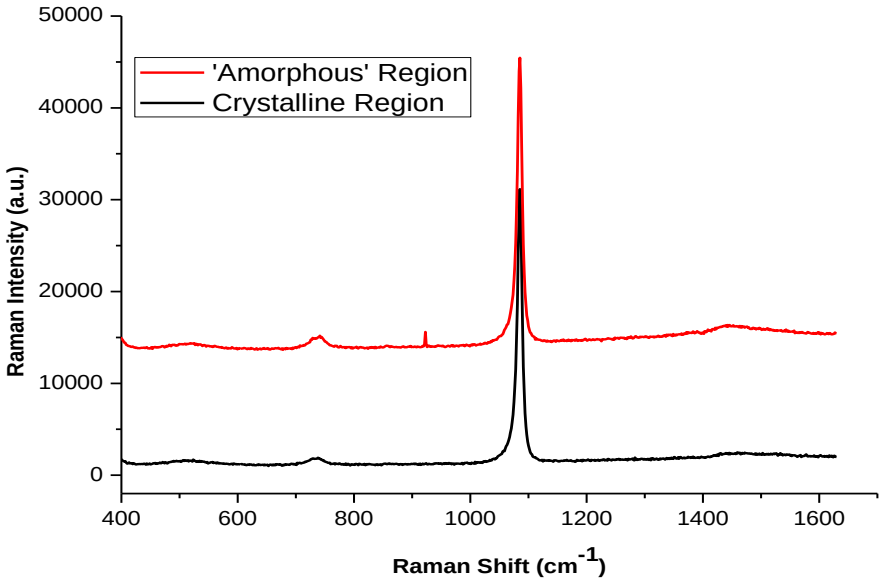

(b)

Figure 6-16 (a) XRD patterns for corrosion product on X-65 steel after exposure to a 10 wt. % NaCl solution for 72 and 168 hours at 80°C (SEM images in Figures 6.14(b) and 6.14(d)) and (b) Raman spectra for corrosion product on X65 steel after 168 hours at 80°C on crystalline layer and amorphous inner layer only where no crystalline deposits were located (SEM image in Figure 6.14(d)) *(Note that the intensity scale is arbitrary)*.

6.6 Correlation between corrosion product evolution and pitting corrosion behaviour of carbon steel as a function of temperature

This section presents the relationship between the different stages and process of corrosion product formation, including networks of iron carbide (Fe_3C) and the pitting corrosion behaviour of carbon steel in CO_2 saturated environments. In this section the discussion would be focused on one (1) brine system (10 wt. % NaCl solutions) only but with a strong emphasis on the effect of temperature on the pitting corrosion behaviour of carbon steel materials in CO_2 saturated environments. A pit in the case of carbon steel and from this study is considered relative to surrounded surface area around a localised cavity that is evidently deeper than the surrounding surface area.

6.6.1 Pitting corrosion behaviour of carbon steel at 30°C

Over the course of the experiment performed at 30°C, relatively continuous pit growth was observed, from maximum depths of ≈ 4 µm after 7 hours, up to ≈ 26 µm after 168 hours, as shown in Figure 6-17. However, between 36 and 72 hours, pit growth rate was only marginal. The reduction in pit growth rate shown in Figure 6-17 may be attributed to the accelerated level of general corrosion which occurs in this region (referring back to Figure 6-7 between 36 and 72 hours). It is important to note that the pit depths presented in Figure 6-17 are depths relative to the corroded surface. Consequently, if general corrosion rate increases and pit growth remains constant, the relative growth of pits will appear to be slowing down.

Over the initial stages of exposure, the pits formed on the steel surface are very shallow (< 15 µm) and thus could significantly be masked by the general corrosion rate contribution to total thickness loss. Unlike passive materials, a substantial level of general corrosion exists throughout the test in conjunction with the growth of the pit on the surface. Such a contrasting mode of corrosion damage could be underplaying the fact that pits are actually still continuously growing despite the small increase in pit depth measured. This aspect is described in detail later on in this chapter. Finally, for the tests at 30°C, pit growth is continued between 72 and 168 hours, indicating that the presence of amorphous $FeCO_3$ on top of the Fe_3C network has little or no effect in terms of inhibiting pit propagation. Instead there is a possibility that the Fe_3C layer may even promote pitting corrosion on other localised anodic regions through a galvanic effect. Figure 6-18 presents a 3D and 2D image and profile of the deepest pit on the entire exposed steel surface at 30°C after 168 hours.

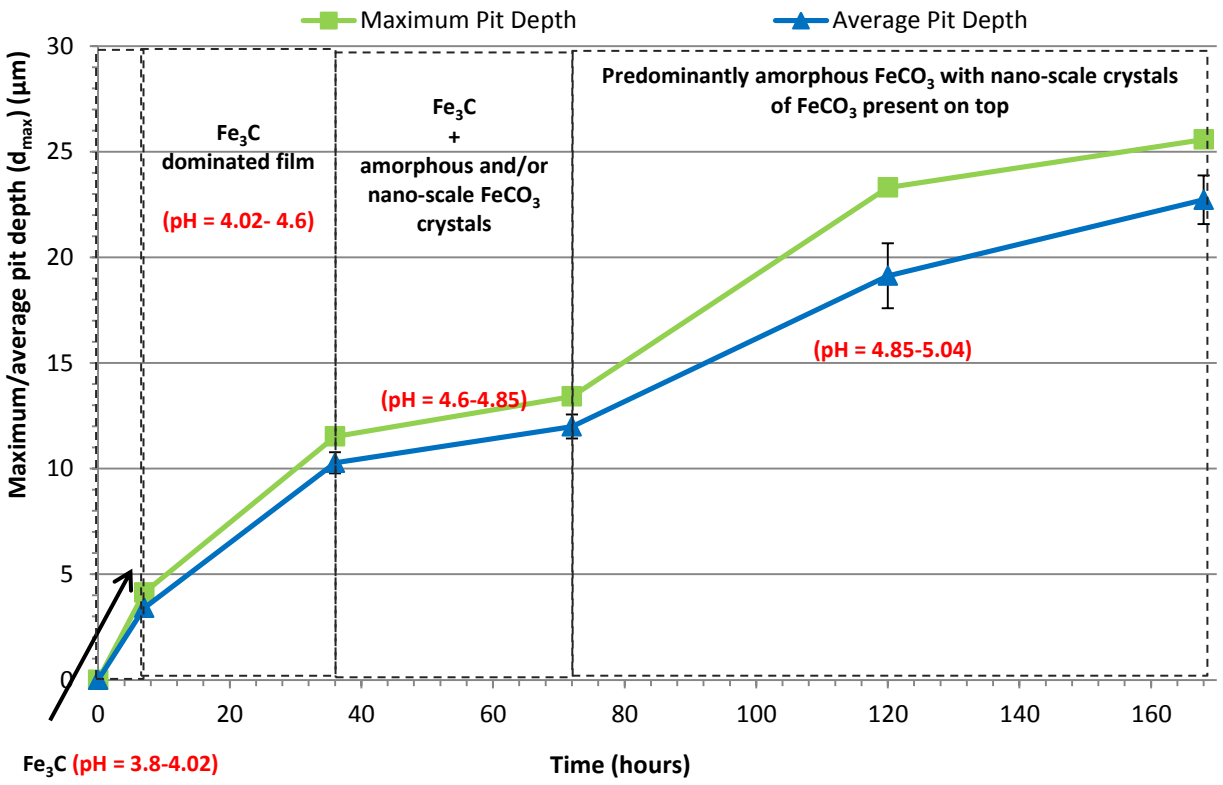

Figure 6-17 Plot depicting the variation of relative pit depth (maximum and average) with time at 30°C, over a duration of 168 hours in a 10 wt.% NaCl solution saturated with CO_2. Error bars represent the standard deviation based on the 10 deepest pits.

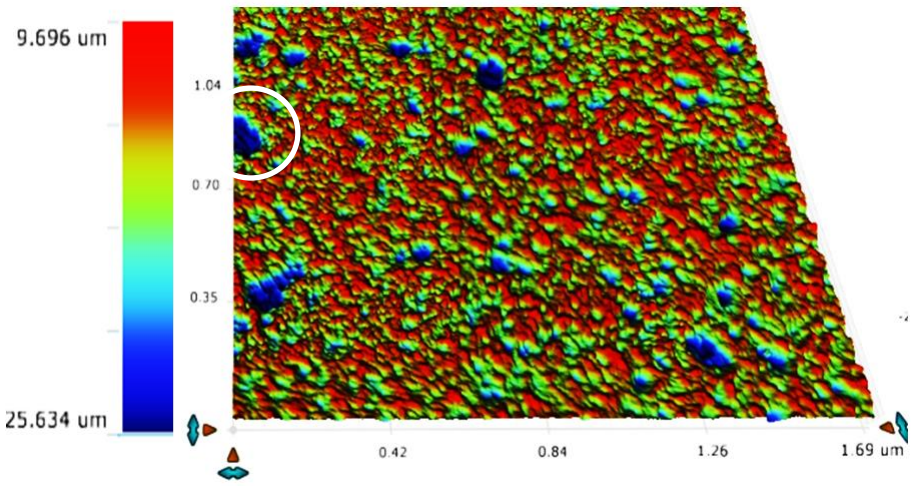

(a)

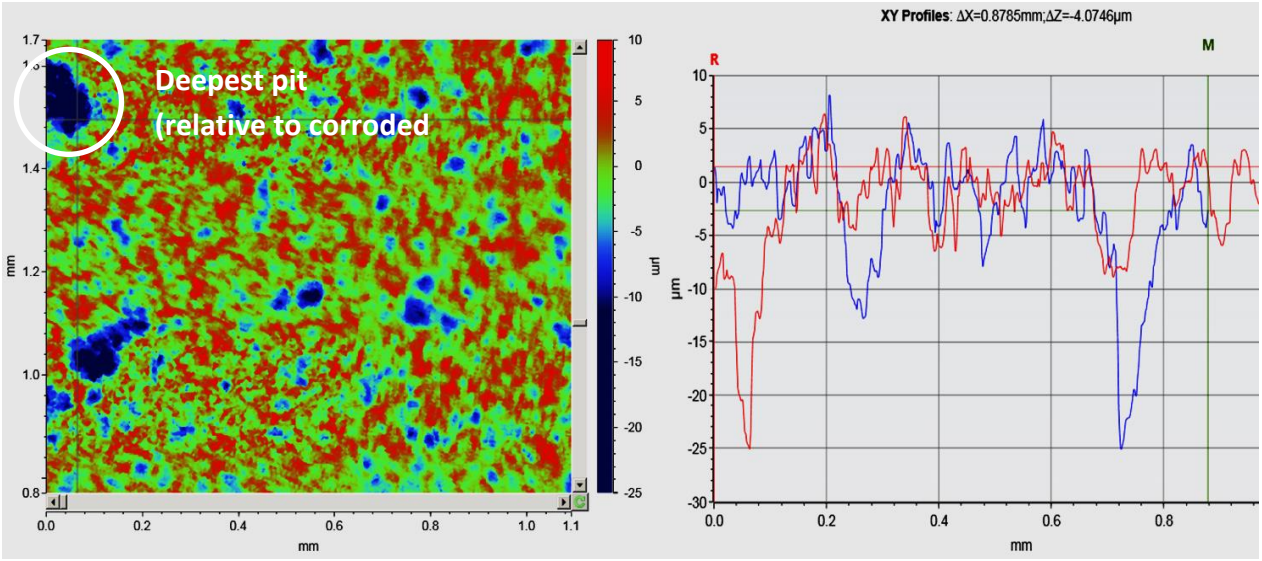

(b)

Figure 6-18: Examples of 3D and 2D profiles of measurable maximum pits on the surface of X-65 carbon steel; (a) 3D and (b) 2D at 30°C after 168 hours exposed to a 10 wt. % NaCl solution saturated with CO_2.

6.6.2 Pitting corrosion behaviour of carbon steel at 50°C

Referring to Figure 6-19, once pits initiate, as recorded after 7 hours, there is an observed steady and almost linear growth rate of pits from ≈ 8 µm after 7 hours up to ≈ 53 µm after 168 hours. 3D and 2D images of deepest pit on an entire sample surface after 168 hours in this condition is provided in Figure 6-20. Most importantly, despite the evidence of the formation of a crystalline $FeCO_3$ outer layer, the role of this particular corrosion product morphology and/or corrosion environment on reducing general corrosion rate appears not to have the same influence on the ability of pits to propagate. The fact that pit growth continues unhindered may be due to the non-uniformity of the coverage of $FeCO_3$ crystals on steel surface and hence, the semi-protective nature of the corrosion product layer at this temperature. Furthermore, any potential galvanic effects between Fe_3C regions and exposed areas of localised pores and the associated corrosion kinetics would be enhanced by the higher temperature, leading to the more substantial pit growth process at 50°C compared to 30°C. Such behaviour is consistent with the trend reported by papavinasam *et al* [38]. In the model developed by papavinasam *et al* [38] (based on experimental data) to predict internal pitting corrosion rates of oil and gas pipelines, it was reported that pitting corrosion rates increased from 10 mpy at ≤ 25°C to 80 mpy at ≥ 50°C based on the readily available operational parameters from the field. In this work, a time scale for this observation was not provided.

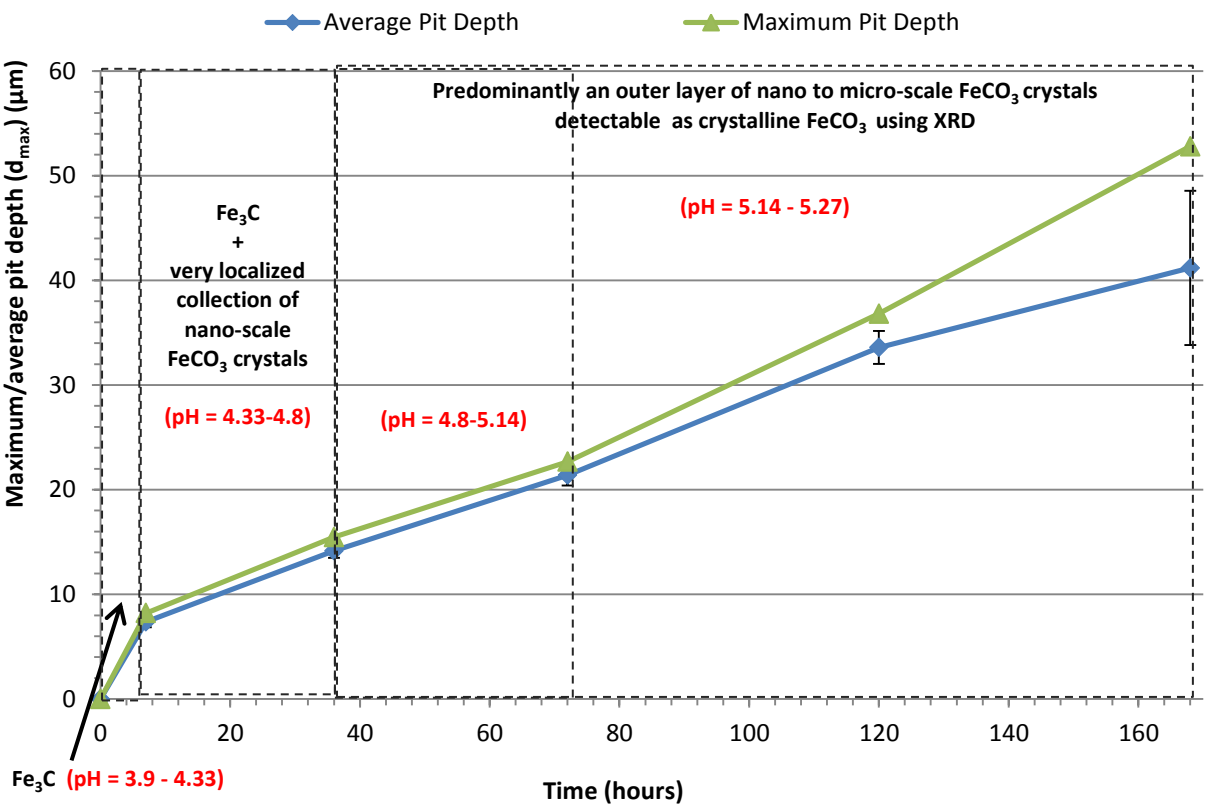

Figure 6-19: Plot depicting the variation of relative pit depth (maximum and average) with time at 50°C, over a duration of 168 hours in a 10 wt.% NaCl solution saturated with CO_2. Error bars represent the standard deviation based on the 10 deepest pits.

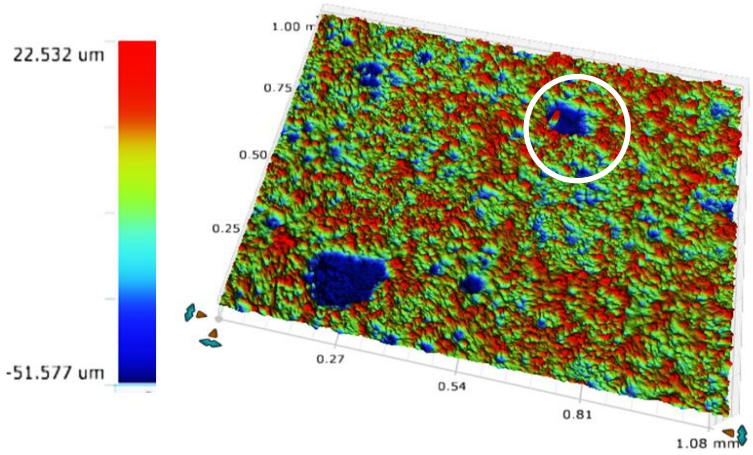

(a)

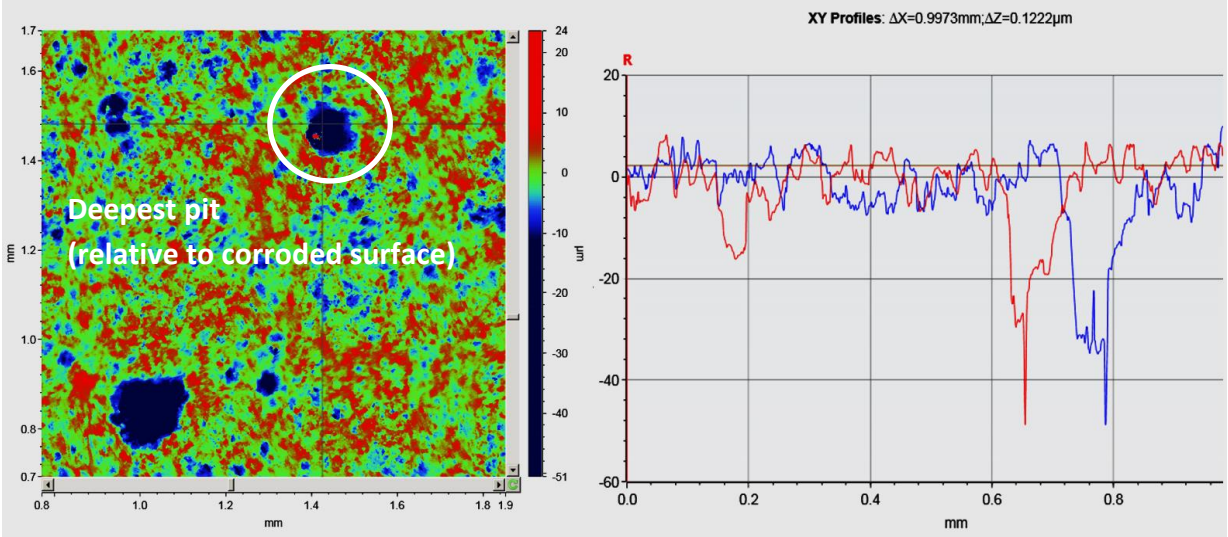

(b)

Figure 6-20 : Examples of 3D and 2D profiles of measurable maximum pits on the surface of X-65 carbon steel; (a) 3D and (b) 2D at 50°C after 168 hours exposed to a 10 wt. % NaCl solution saturated with CO_2.

6.6.3 Pitting corrosion behaviour of carbon steel at 80°C

Stable growth of pits was observed between 0 and 36 hours once pits initiated (shown in Figure 6-21). Over this stage, the nature of the corrosion product layer comprises of Fe_3C and very small crystals of $FeCO_3$. At some point between 36 and 72 hours where SR_{bulk} is expected to be greater than unity, precipitation of $FeCO_3$ becomes thermodynamically feasible. After the 72 hour mark a distinct reduction in pit growth rate is observed. Referring back to Figure 6.14, the rate of general corrosion rate also decreases between 36 and 72 hours, making it less likely for the pit growth rate to be underestimated, while at the same time suggesting a possible healing effect of initially active pits. The healing effect of initially active pits has also been observed by Han *et al* [164] at 80°C.Crystalline $FeCO_3$ is also detected on the XRD pattern as a weak signal in Figure 6-16(a) at 72 hours, which indicates that the presence of $FeCO_3$ crystals may be playing a major role in the reduction of both the growth of pits and general corrosion rate.

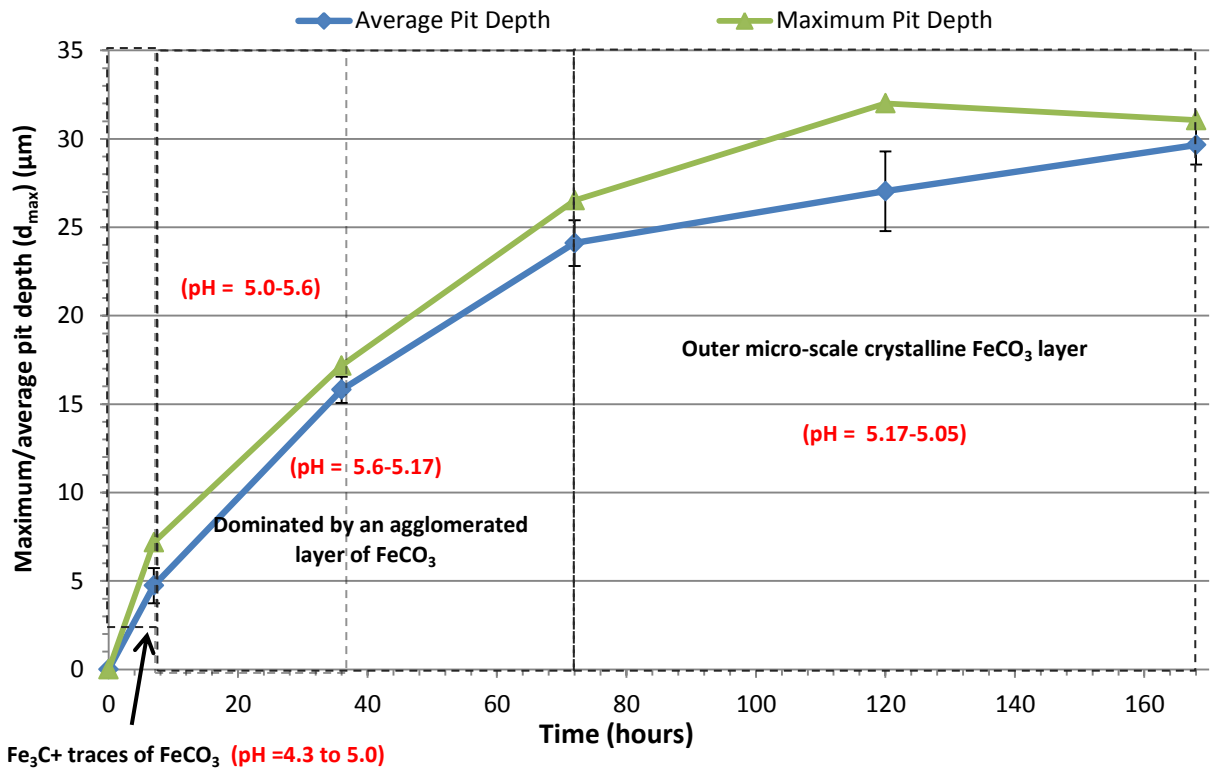

Figure 6-21: Plot depicting the variation of relative pit depth (maximum and average) with time at 80°C, over a duration of 168 hours in a 10 wt.% NaCl solution saturated with CO_2. Error bars represent the standard deviation based on the 10 deepest pits.

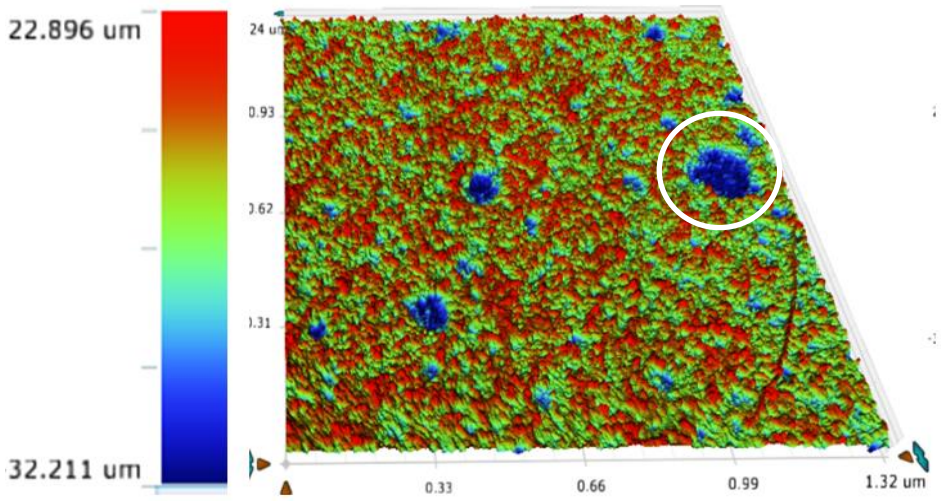

(a)

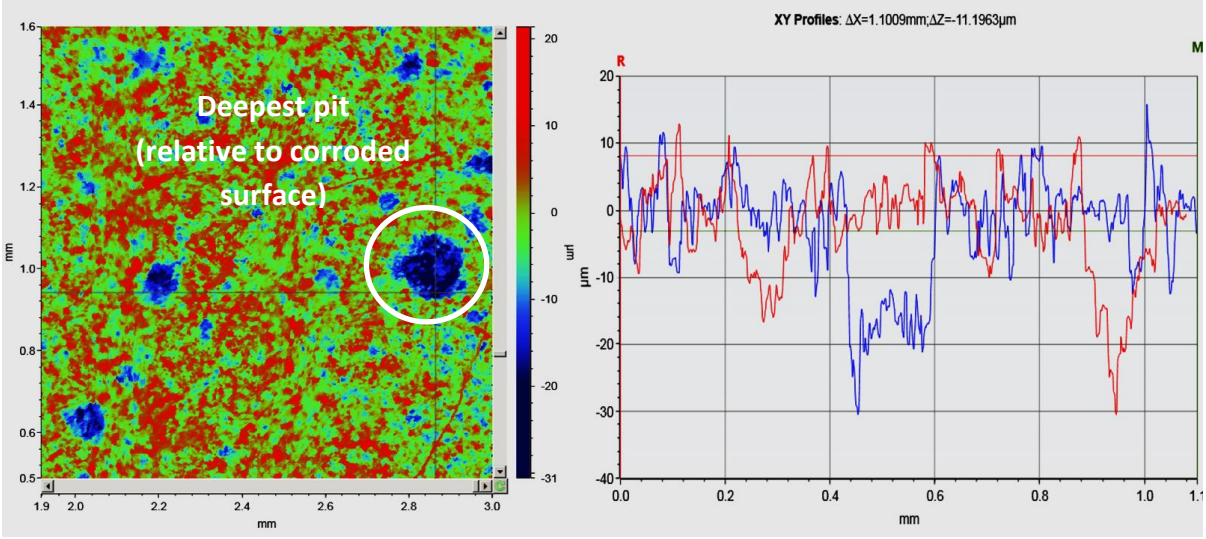

(b)

Figure 6-22 Examples of 3D and 2D profiles of measurable maximum pits on the surface of X-65 carbon steel; (a) 3D and (b) 2D at 80°C after 168 hours exposed to a 10 wt. % NaCl solution saturated with CO_2.

The experiment conditions have been shown to be very repeatable for electrochemical measurements presented in Figure 6-1 to Figure 6-5. The results from pit depth analysis were from a single sample with error bars on the average pit depth data shown in Figure 6-17, Figure 6-19 and Figure 6-21 representing a standard deviation based on the 10 deepest pits. However, to illustrate the repeatabilty and reliability of the results from pit depth analysis, maximum and average pit depth for tests conducted after 72 hours from separate tests are presented for the 30, 50 and 80°C in Figure 6-23.

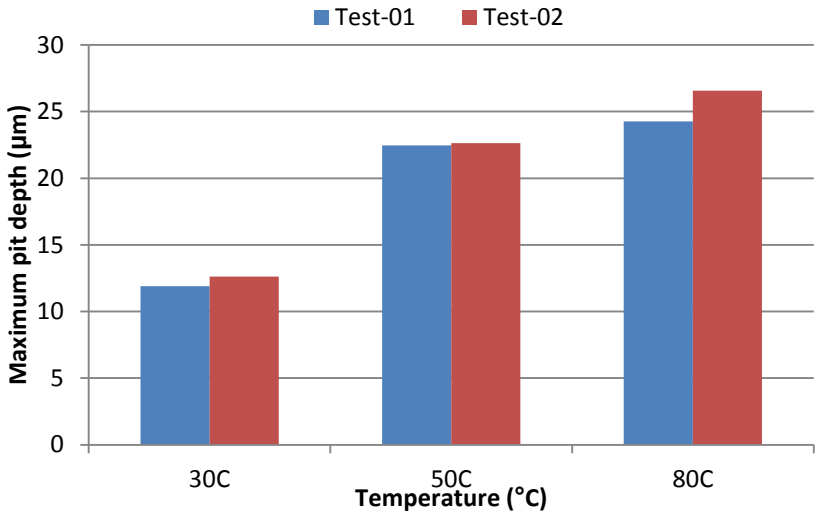

(a)

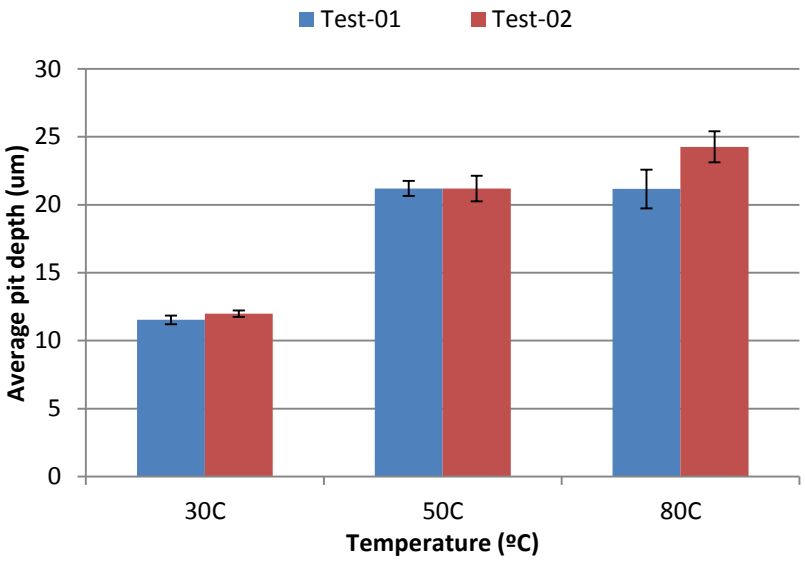

(b)

Figure 6-23 Repeatable pit depth analysis on samples exposed to a 10 wt.% NaCl under a CO_2 atmosphere after 72 hours in separate tests at 30, 50 and 80°C. Error bars are based on the standard deviation of the 10 deepest pits relative to corroded surface used for calculating the average pit depth.

6.6.4 Pitting corrosion and metal penetration

It is evident that the pitting corrosion behaviour of active steels such as X-65 is significantly different from that of passive materials. Unlike carbon steels, stainless steel materials were developed to provide very good corrosion resistance, 10-20 times better than in carbon steel materials through the formation of passive oxide layers [106]. However, the breakdown of these passive layers is usually the precursor for pit initiation and propagation in stainless steels, but most importantly with minimal uniform corrosion of surrounding surfaces [106, 173]. From the results shown thus far in this chapter, there is still evidence of substantial uniform corrosion of carbon steel materials, even while pitting corrosion is also occurring. This has led to the evolution of pit with relatively larger diameters. Pit growth can usually be easily characterised in passive metals such as stainless steel due to relatively minimal uniform corrosion occurring at surrounding surfaces. On the other hand, significant general corrosion is likely to occur on the surrounding surfaces of an active metal such as carbon steel. This unique scenario results in increased complexity when studying the pit initiation and propagation behaviour of carbon steels. Therefore, it could be argued that by purely considering the change in pit depth relative to the surrounding corroded surfaces (provided in Figure 6-24(a)) the actual growth rate of pits is underestimated and effectively masked by high levels of corrosion to the surrounding surface. This discrepancy is shown by comparing Figure 6-24(a) with Figure 6-24(b). Such behaviour is

generally not an issue with respect to passive materials, which generally exhibit low uniform corrosion rates.

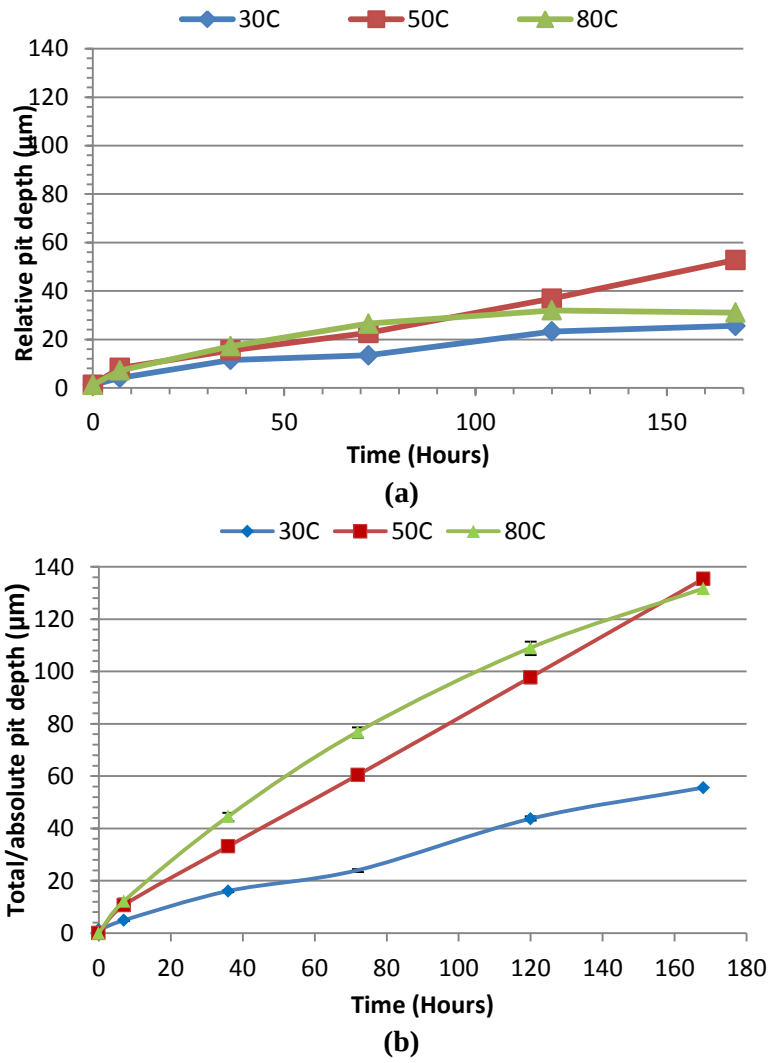

Figure 6-24 (a) Pit depth relative to the surrounding corroded surfaces and (b) total pit depth relative to an un-corroded surface vs time for X-65 carbon steel immersed in CO_2 saturated 10 wt.% NaCl solutions at different temperatures over 168 hours of exposure.

One method of assessing the extent of pitting corrosion with such system and with respect to pitting corrosion of carbon steel is to perform a pitting factor analysis. Pitting factor (P_f), is used to reflect the relative contribution of degradation between uniform and pitting corrosion (see details in the previous chapter) and has been defined in ASTM G46-94 [70] as:

$$P_f = \left(\frac{P_d}{P_u}\right) = \left(\frac{P_u + d_{max}}{P_u}\right) \qquad 6.6$$

Where P_d is the 'absolute' pit depth (the sum of the 'relative' pit depth to the corroded surface (d_{max}), plus the average metal penetration from general corrosion rate measurements (termed P_u), i.e. $P_d = P_u + d_{max}$).

Values are usually referred to in µm and d_{max} is determined through profilometry measurements of the steel surface after cleaning, whilst values of P_u is quantified by converting the average LPR corrosion rate into a general thickness loss based on the exposure time of the sample to the test solution. A pitting factor of 1 represents uniform corrosion. The greater the pitting factor, the greater the depth of penetration relative to the surrounding surface area.

Figure 6-25 gives a clear indication that the corrosion damage mechanism observed in these conditions is actually pitting (with pitting factor > 1) even while there is still substantial uniform corrosion taking place in all experiments. Interestingly, towards the end of all three tests, the pitting factors tend towards values between 1.3-1.9. This indicates that over the duration of the tests, the contribution of general corrosion to thickness loss increases as a result of continuous general corrosion along with pitting. All three experiments also show the same trend in terms of a reduction in pitting factor as exposure time increases, before the values stabilise.

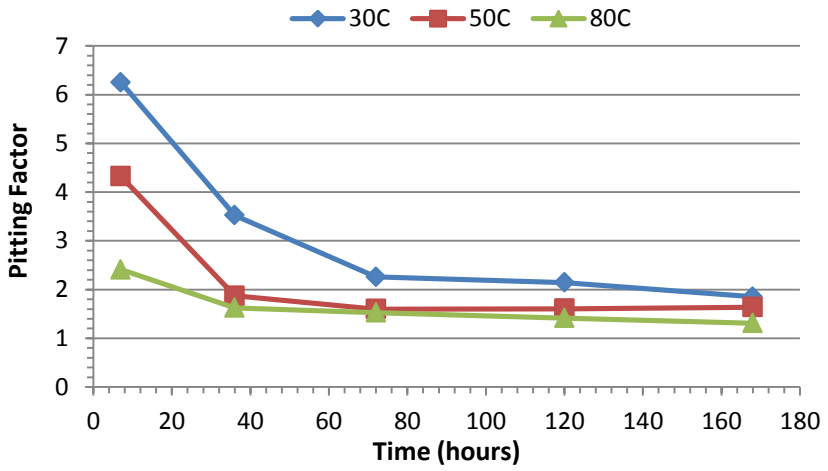

Figure 6-25 Variation of pitting factor with time for all three test conditions.

6.6.5 Pit healing mechanism on carbon steel at 80°C

To investigate the potential pit healing mechanism or pit retardation mechanism shown in Figure 6-21 by the slowing down of pit growth, a cross-section of the corrosion product of test after 168 hours (Figure 6-15(d)) was removed from the sample surface using a focused ion beam-SEM. This cross-section was subsequently taken to a transmission electron microscope (TEM) for detailed analysis. Figure 6-26(a) and (b) show that the corrosion product layer

formed in the un-buffered corrosion system at 80°C is very porous, with a $FeCO_3$ layer on top and a Fe_3C network between the top layer and the carbon steel substrate. What is most interesting is that traces of $FeCO_3$ were identified within the porous Fe_3C network, and also at the surface of the substrate. It is therefore suggested that a possible self-healing mechanism exists whereby the precipitation of $FeCO_3$ is occurring at the steel surface and within the surface pits, resulting in pit propagation being significantly hindered.

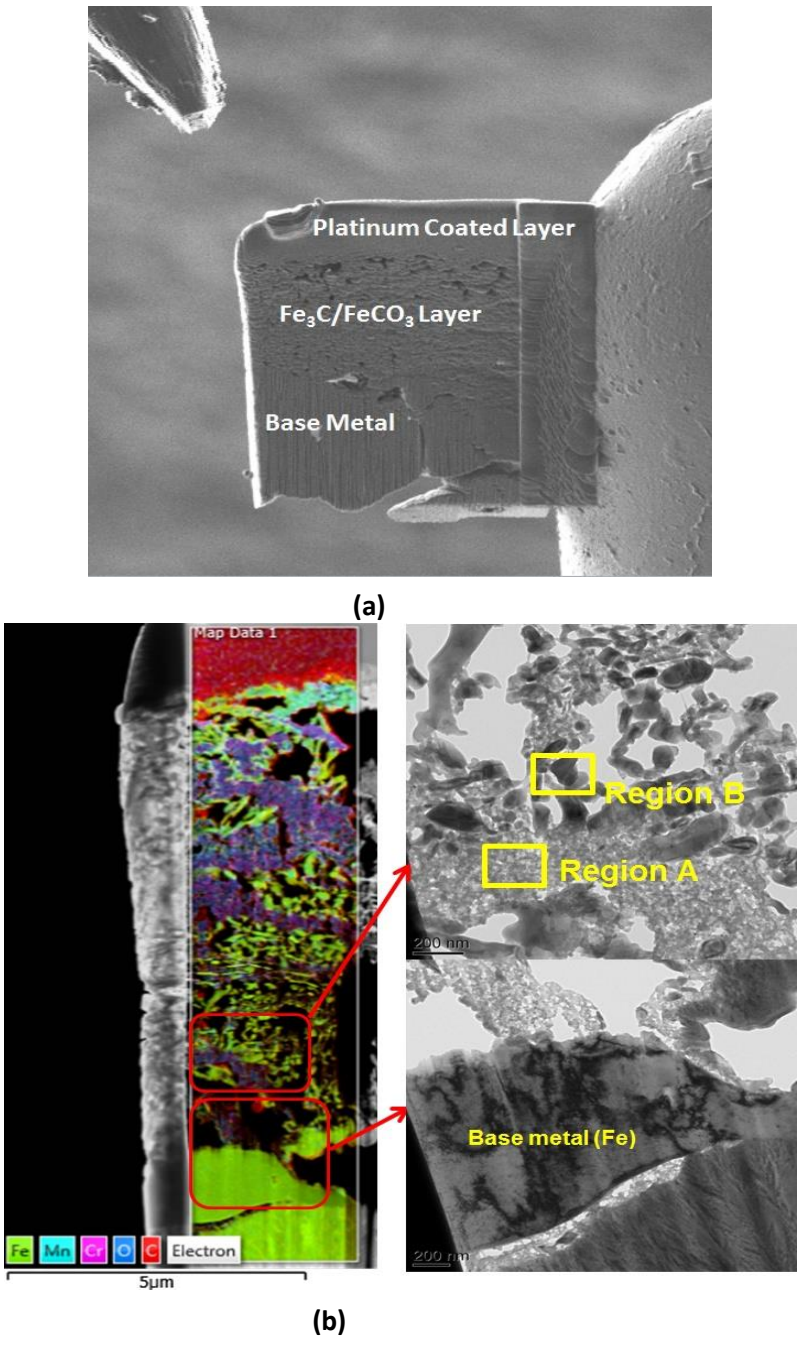

Figure 6-26 (a) TEM image of a cross-section of corrosion product on X65 steel exposed to a CO_2 saturated 10 wt. % NaCl at 80°C and after 168 hours. (b) Selected area for EDX mapping and electron diffraction pattern from the TEM.

The presence of $FeCO_3$ was confirmed from a combination elemental analysis using EDX analysis over Regions A and B in Figure 6-26(b) and the electron diffraction pattern from TEM analysis. The elemental ratios of Fe, C, and O in the corrosion product layer under investigation (Rgions A and B of Figure 6-26(b)) are provided in Table 6-3. The elemental ratios strongly suggest the presence of $FeCO_3$ within the Fe_3C network. This is also supported by the selected area electron diffraction pattern from TEM analysis in Figure 6-27.

Further analysis of the corrosion deposits observed underneath porous corrosion product layer and on top of the base metal (Figure 6-26 (a) and (b)) using selected area electron diffraction (provided in Figure 6-27) produced a continuous ring pattern, confirming that corrosion product is nano-polycrystalline in nature with the prescribed indices; (116), (110), and (104) corresponding with $FeCO_3$ [169] based on estimated interplanar spacing (d-spacing) of the rings as shown in Figure 6-27. This confirms that $FeCO_3$ is precipitating underneath the initially formed Fe_3C layer and may well be responsible for the observed reduction in pit growth recorded. According to Guo *et al* [93], such a nano-polycrystalline structure of $FeCO_3$ would be expected given the low pH of the system. It is perhaps also worth noting that a typical pH in oilfield environments tends to exist in the range of 4-6 [102].

Table 6-3 Elemental analysis from EDX spectra of regions shown in Figure 6.26

Element	Region A Normalised ratio by at.% relative to carbon	Region B Normalised ratio by at.% relative to carbon
Fe	1.28	2.99
C	1.00	1.00
O	3.70	0.32
Remarks	Elemental ratio indicative of $FeCO_3$	Elemental ratio indicative of Fe_3C

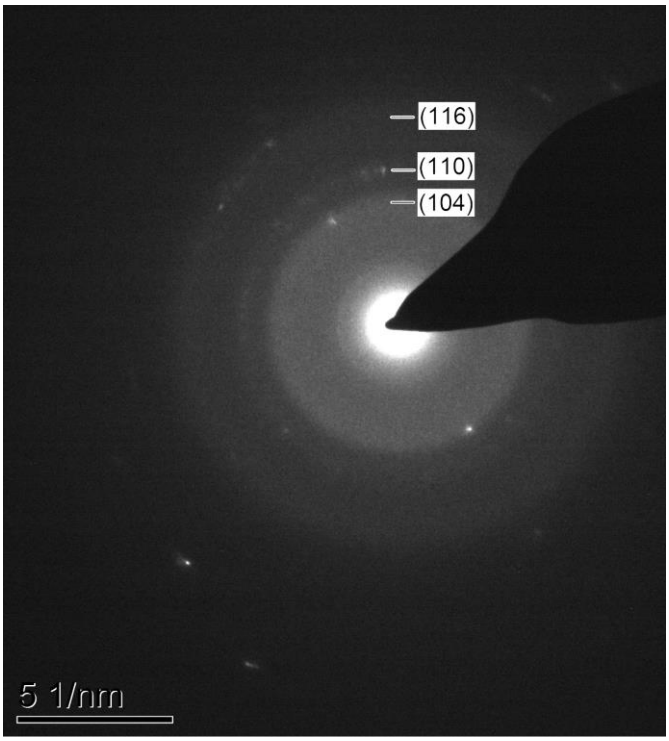

Figure 6-27 Electron diffraction pattern from TEM analysis of $FeCO_3$ corrosion product underneath initially developed Fe_3C layer on X-65 steel exposed to a CO_2-saturated 10 wt. % NaCl at 80°C for 168 hours.

This observation is an indication of a pit self-healing mechanism. Observation of self-healing of pits in this study has also been attributed to the electro-migration of precipitable anions (HCO_3^- /CO_3^{2-}) across a porous corrosion product formed in environments where uniform corrosion precedes corrosion product formation and nucleation of pits [88]. The suggested self-healing mechanism at 80°C appears to be similar with results published by Han *et al* [164]. In the work by Han *et al* [164], an artificial pit was used to investigate the galvanic effect during localised corrosion at 80°C, at an initial $FeCO_3$ supersaturation between 3 and 9. The galvanic current density, which starts very high, was observed to rapidly reduce to zero and initially active pits became covered with $FeCO_3$ corrosion products. Han *et al* [164] concluded from these observation that initial propagation of localised corrosion is stifled due to protective $FeCO_3$ layer formation on the anode. The artificial pit was observed to heal and the corrosion rates on both cathode and anode equalized and remained low (< 0.1 mm/y).

6.6.6 Summary on the effect of temperature on pitting and uniform corrosion behaviour of carbon steel in CO_2-saturated brines

The results presented and discussed thus far have shown that in an unbuffered CO_2 saturated corrosion environment, the formation of an amorphous and/non-crystalline form of $FeCO_3$

dominates the corrosion product formation process. This has been shown to be true for all temperatures investigated in this work. The amorphous form of $FeCO_3$ formed under these conditions was non-protective and hence became the precursor for pitting corrosion. Pitting corrosion rate relative to corroded surface and the continuous corrosion of surrounding surfaces was observed to be significantly influenced by temperature. Thus, pitting corrosion (relative to corroded surface) is observed to be higher in magnitude at an intermediate temperature (50°C), while the total metal penetration was higher at a higher temperature (80°C).

Chapter 7. Investigation of uniform and pitting corrosion in CO_2 saturated corrosion environments; Effect of chloride concentration

This section of this chapter discusses the relationship between the electrochemical activities at the metal-brine interface as influenced by chloride ion concentration. In this section the discussion is focused on three different brine systems (1, 3.5, and 10 wt. % NaCl solutions) at three different temperatures (30, 50, and 80°C). However, the results presented in this section are aimed at emphasising the effect of chloride ion concentration and the synergy with temperature on the corrosion behaviour of carbon steel materials in CO_2 saturated environments.

With stainless steels, chloride ion concentration in the solution considered is a decisive parameter to define the pitting resistance of stainless steel [106]. Chloride ions were found to be more aggressive than other halides because of their smaller atomic diameter, and as such can fundamentally be considered as an aggressive agent of corrosion capable of destabilising corrosion product layers, leading to initiation of localised corrosion of carbon steel in CO_2 containing environment [40, 105, 107].

The results of all electrochemical corrosion reactions presented in this Chapter for investigating the effect of chloride ion concentration at different temperature were obtained in an un-buffered environment with a view of elucidating the synergy of how critical environmental variable such as temperature and chloride ion concentration may be influencing the mechanism of pitting corrosion in oilfield environments.

7.1.1 Tafel polarisation measurements

Tafel polarisation results presented in this section are to show the electrochemical behaviour of carbon steel in three different brines of varying chloride concentration, and presented for 30, 50 and 80°C in Figure 7-1 after 7 hours. These results are the same as those presented in section 6.2 but only presented differently to clearly isolate the effect of chloride ion concentration. Referring to Figure 7-1(a)-(c), there is a shift in the anodic polarisation line towards higher anodic current density at higher anodic potential with increase in chloride ion concentration from 1 wt. % to 10 wt. % NaCl. This shift in an anodic current density towards higher values is observed to be consistently the same for all temperatures, with the most effect observed at higher temperatures (50 and 80ºC).

Similar observations have also been reported by Eliyan *et al* [105], especially within the concentration thresholds within which it was observed that the anodic current increases with

increasing chloride ion concentration. At 80°C, there is a significant difference in the magnitude of anodic current density. The corrosion current extrapolated from potentiodynamic curves increases from ≈ 250µA/cm^2 in 1 wt. % NaCl solution to ≈ 410µA/cm^2 in 3.5 wt. % NaCl solution at 80°C. This is also consistent with the results from experiments at 90°C by Eiyan, *et al* [105], where the corrosion current increase from ≈ 160µA/cm^2 in 0 wt. % NaCl solution to ≈ 400µA/cm^2 in 3.5 wt.% NaCl solution at 90°C. This trend correlates with the concept of thermal activation of chloride ions as suggested by Yap and Srinivasan [40]. Thermal activation of chloride ions poses the potential effect of increasing the aggressiveness of the corrosion media and hence, enhanced anodic dissolution rate of substrate metals [38, 40, 108]. The cathodic polarisation curves were of very similar trend; depicting a mass transferred controlled reduction reaction of H^+ /H_2CO_3 at more higher cathodic potential. At 80°C, increasing chloride ion concentration from 1 wt. % to 10 wt. % NaCl, appears to cause a shift to higher total cathodic current and hence corrosion current. The aggressiveness of the corrosion media containing variable concentration of chloride ion in the form of NaCl is presented for 30 and 80°C in Figure 7-2 (a) and (b) in terms of solution resistance (R_s). Solution resistance in this case is a measure of the conductivity of the corrosion media to support the charge transfer process during corrosion reaction.

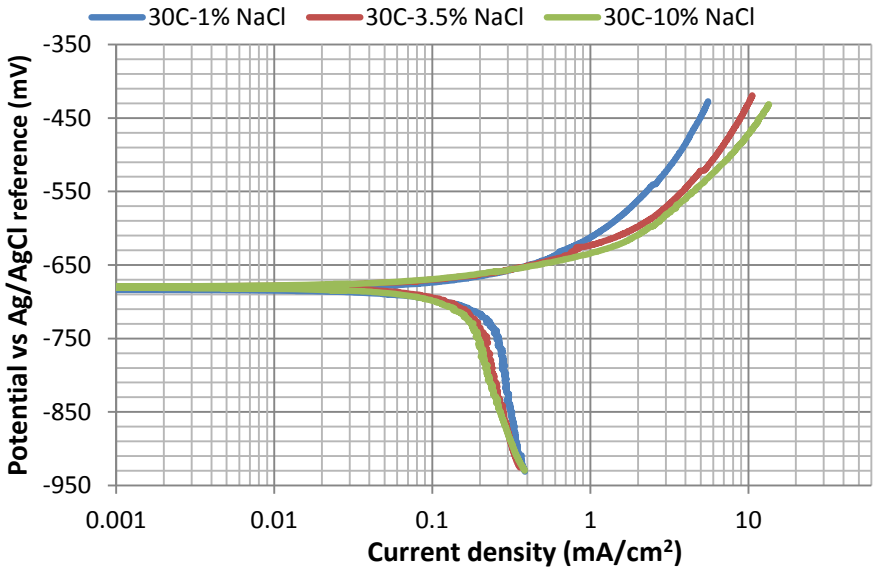

(a)

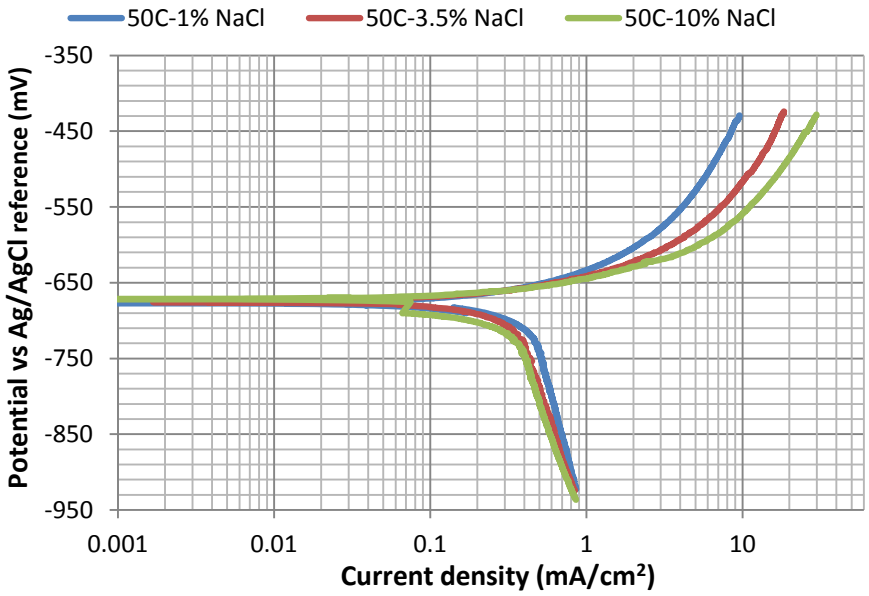

(b)

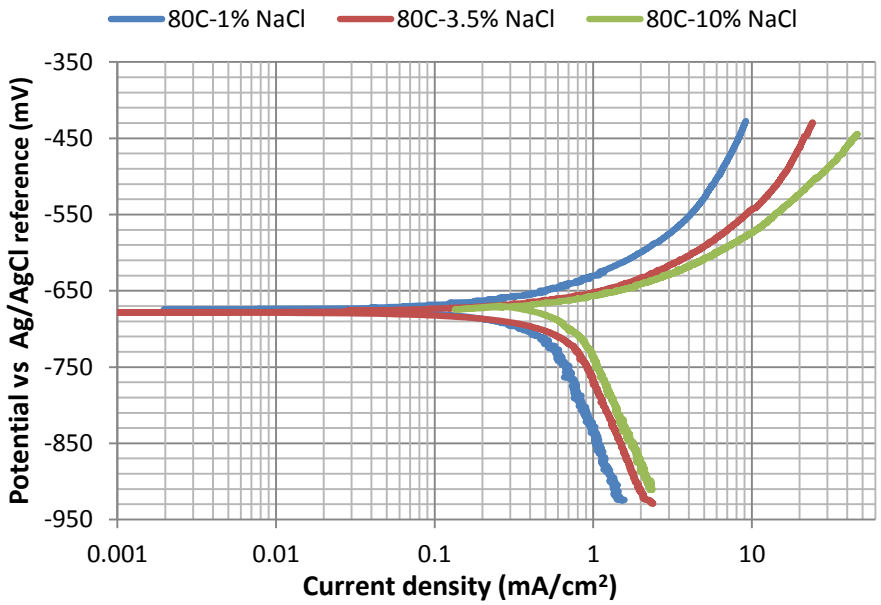

(c)

Figure 7-1: Tafel polarisation curves for X65 carbon steel exposed at to 1, 3.5, and 10 wt. % NaCl solutions under CO_2 gas atmosphere at (a) 30, (b) 50 and (c) 80°C after 7 hours.

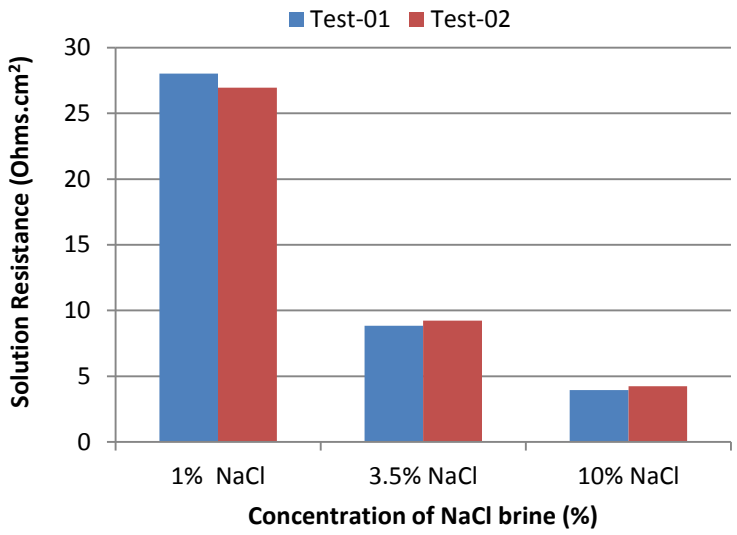

(a)

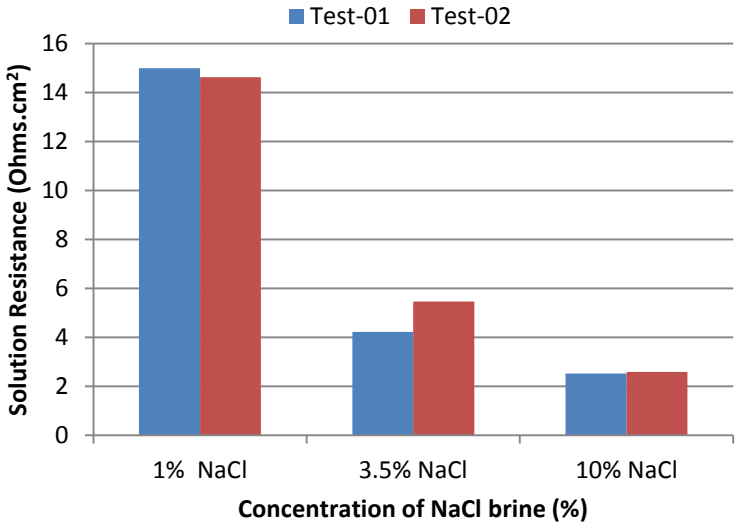

(b)

Figure 7-2: Estimated solution resistance of test solution from electrochemical impedance spectroscopy (EIS) measurements as a function of chloride ion concentration at (a) 30°C and (b) 80°C.

It should be noted that the solution resistance could also be influenced by the path length of the electrical circuit for the corrosion system. However, Figure 7-2 provides a different perspective for qualitative appreciation for the effect of chloride ion on the corrosion media. Jiang *et al* [109] and Fang *et al* [18] had stated similar variation in the solution resistance with chloride ion concentration for experiments at an initial pH of 6 and 80°C and initial pH of 5 and 25°C respectively. However, the solution resistance in both instances were only correlated to the ionic strength and conductivity of the corrosion media without emphasising the impact on the corrosion rate of substrate metal or aggressiveness of the corrosion media.

7.2 Corrosion rate measurements and corrosion product formation as a function of chloride ion concentration

From Figure 7-1 and Figure 7-2, it is expected that the corrosion rate will increase with increasing chloride ion concentration and increasing temperature except at 30°C, where the potentiodynamic curves suggests an almost equal corrosion rate after 7 hours. This section of this thesis discusses the electrochemical behaviour of carbon steel in the three different brine solutions used in this work at 30, 50 and 80°C. The electrochemical behaviour will be discussed in terms of corrosion rate from linear polarisation measurements, while also correlating corrosion measurements, chloride ion concentration with corrosion product layer formation. The corrosion potential has already been described in Chapter 6 and shows that the corrosion potential is not influenced by the concentration of chloride ion over the duration of the experiments (see Figure 6-5).

7.2.1 Effect of chloride ion concentration on corrosion behaviour of carbon steel and formation of corrosion product at 30°C

Figure 7-3 shows the LPR corrosion rate of X-65 steel over 168 hours of exposure to 1, 3.5, and 10 wt. % NaCl solutions at 30°C. Different stages of observed corrosion products on the metal surface over the exposure time of 168 hours are also provided in Figure 7.5 in the form of SEM images.

Referring to Figure 7-3, the first 72 hours depict very interesting and contrasting results in terms of corrosion rate. Although the sampling time for post-experiment analysis started from 7 hours, the first 24 hours is showing an almost equal corrosion rate of 1.13mm/yr for tests conducted in both 1 and 10 wt. % NaCl solutions at 30°C. On the other hand, result of the test conducted in 3.5 wt. % NaCl solution was observed to be higher at ≈1.5mm/yr. Within the first 24 hours, the higher measured corrosion rate for test conducted in 3.5 wt. % NaCl solution than for tests conducted in both 1 and 10 wt. % NaCl solutions contradict the observation on solution resistance at 30°C (see Figure 7-2(a)). These results also appear to be consistent with the observation from potentiodyanmic tests shown in Figure Figure 7-1(a). Similar trend in corrosion rate measurements after 24 hours tests has also been reported by Fang *et al* [125] at 20°C. According to Fang *et al* [125], an increase in the chloride ion concentration from 3 wt.% NaCl to 10 wt.% NaCl, resulted in a decrease in the corrosion rate from linear polarisation tests by 50%, which is similar to the trend observed in this work. In another instance, Eliyan *et al* [105] also reported a steady increase in corrosion rate by increasing chloride ion concentration in terms of NaCl from 0 to 15g/L at 20°C, after which the corrosion rate decreases steadily to

35g/L and remained constant up to a concentration of 80g/L NaCl. Observations by Eliyan *et al* [105] is indicative of a threshold after which the corrosion rate is decelerated or remains constant with chloride ion concentration. Figure 7-4 presents the results of Eliyan *et al* [105].

From the results of Eliyan *et al* [105] and Fang *et al* [125], it is clear that at 30°C, increasing chloride ion concentration may be having retardation effect on ccorrosion rate. While the mechanism of the retardation effect remains unclear, it may be limited by the exposure time. This is because the results of Fang *et al* [125] was based on a 24 hours exposure while the exposure time for the experiment by Eliyan *et al* [105] remained unclear. From the results shown in Figure 7-3, it is clear that the initial observation is consistent with the results of Eliyan *et al* [105] and Fang *et al* [125] at 20°C. However, over the 168 hours duration, the corrosion rate for tests in 3.5 and 10 wt. % NaCl solution increases gradually with time to an equal corrosion rate value of ≈1.7 mm/yr while the corrosion rate remained relatively constant at ≈ 1.1mm/yr for test in 1 wt. % NaCl at 30°C.

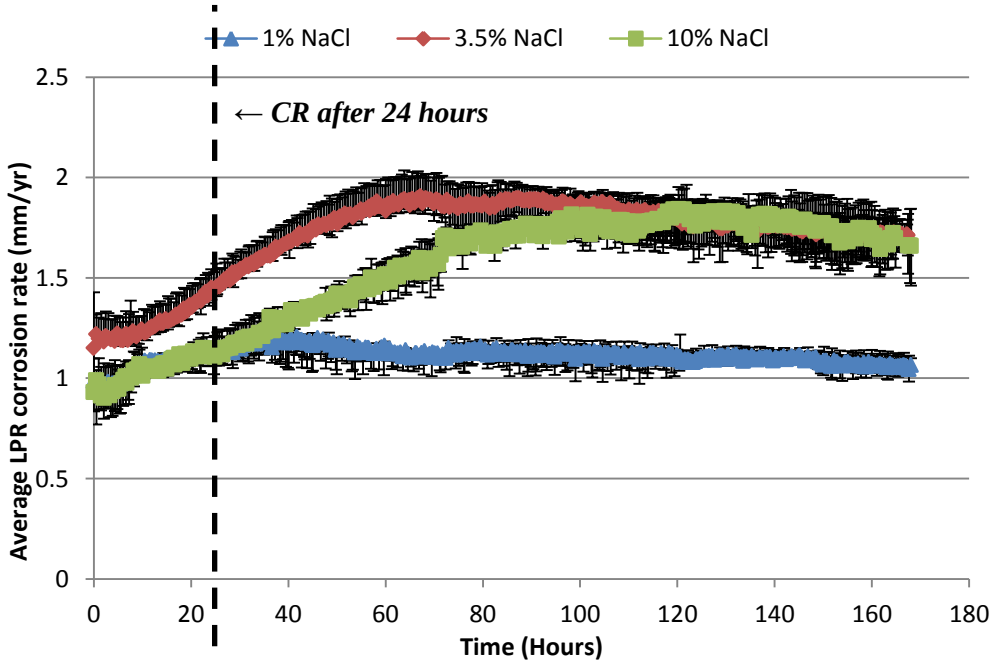

Figure 7-3 A plot of LPR corrosion rate for X65 carbon steel exposed at to 1, 3.5 and 10 wt. % NaCl solution saturated with CO_2 at 30°C.

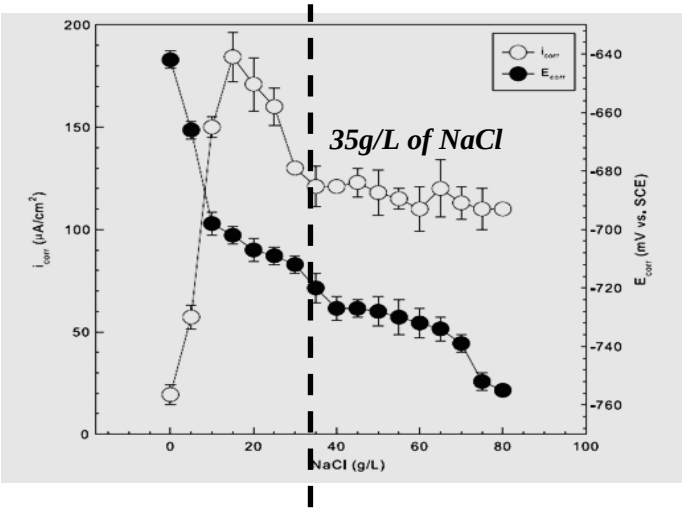

Figure 7-4 Corrosion current and potential as a function of chloride ion concentration at 20°C [105].

With respect to the formation of iron carbonate corrosion product layer, the effect of chloride ion concentration and/or ionic strength on the formation of iron carbonate observed in this work was found to be consistent across the three different chloride ion concentration regimes. A detail of the evolution process of corrosion product for X-65 carbon steel exposed to a 10 wt. % NaCl solution saturated with CO_2 gas over 168 hours and at different temperature has been discussed in section 6.5.1 of Chapter 6. The first of the parameters that confirms this trend is the measured bulk pH of the test solution. For the three different chloride ion concentrations used in this study, there was only a slight variability in the pH of the bulk solution as a result the changing chloride ion concentration as shown in Figure 7-5. Although, there is also a slightly lower pH for test in 10 wt. % NaCl solution, a similar observation has been suggested to be an added effect of chloride ion on corrosion of stainless steel [106, 174].

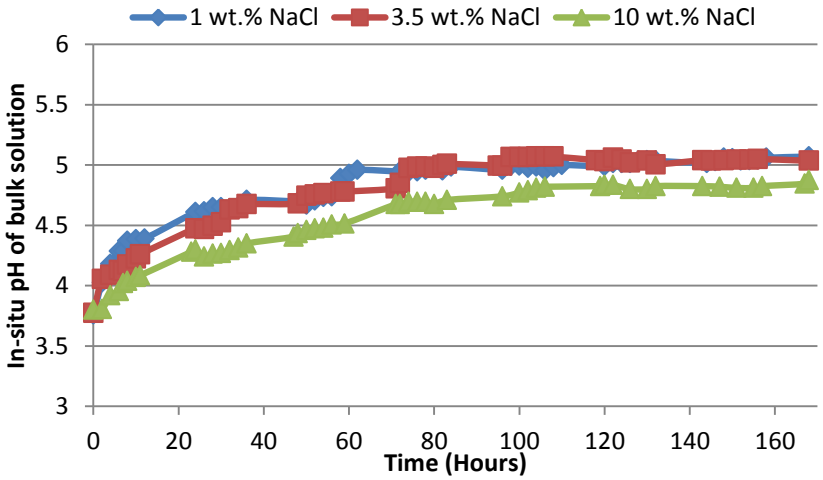

Figure 7-5 Measured *in-situ* pH of corrosion media containing different chloride ion concentration and saturated with CO_2 gas at 30°C.

This seems to have a contrasting influence on the corrosion product formation process as has been reported by several authors [40, 84, 107], which has emphasised the role of chloride ion in the destabilisation of iron carbonate corrosion products once it is formed, on increasing the solubility product that raises the saturation limit required for the formation of $FeCO_3$ corrosion products. In the findings of Gao *et al* [107], $FeCO_3$ corrosion product were initially formed at a high initial pH of 6.6 and Fe^{2+} concentration of 100ppm in a 0.1-1 wt.% NaCl solution before subjecting the corrosion media to higher chloride ion concentration. While this may have shown that higher chloride ion concentration could be destabilising the corrosion products, it does not really answer the question of the effect of chloride ion concentration on the corrosion behaviour and corrosion product formation in systems where the corrosion product formation process is slowly preceded by electrochemical dissolution of Fe^{2+}, leading to supersaturation of the bulk solution without the aid of buffering the bulk pH.

In the light of the evidence provided by the SEM images in Figure 7-6 and the XRD patterns for the different test systems after 168 hours presented in Figure 7-7, the corrosion process at the start of the tests for the three different chloride ion concentration regimes (within the first 7 hours as shown in Figure 7-6 (a), (b) and (c)) shows the revealing of iron carbide. This is usually as a result of the preferential dissolution of ferrite from the steel surface and no corrosion product precipitation occurring within the system [9, 88, 164]. The effect of this on the tendency for initiation of pitting corrosion process has also been highlighted in section 6.6 of this thesis. After 168 hours, the SEM image show only slight changes in an otherwise consistent corrosion morphology with increasing chloride ion concentration.

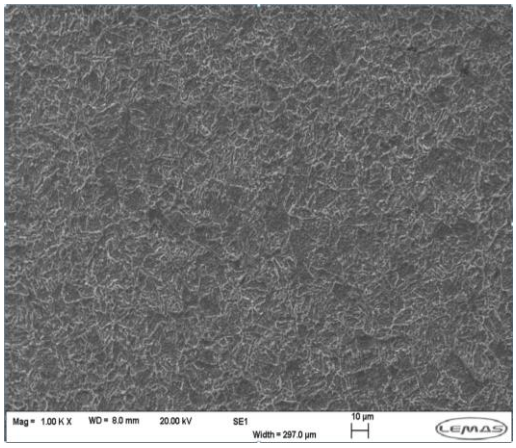

(a)

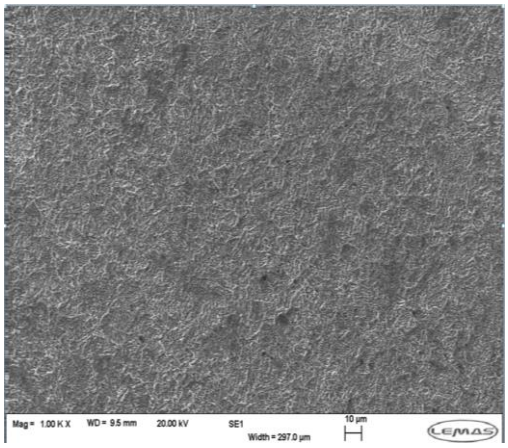

(b)

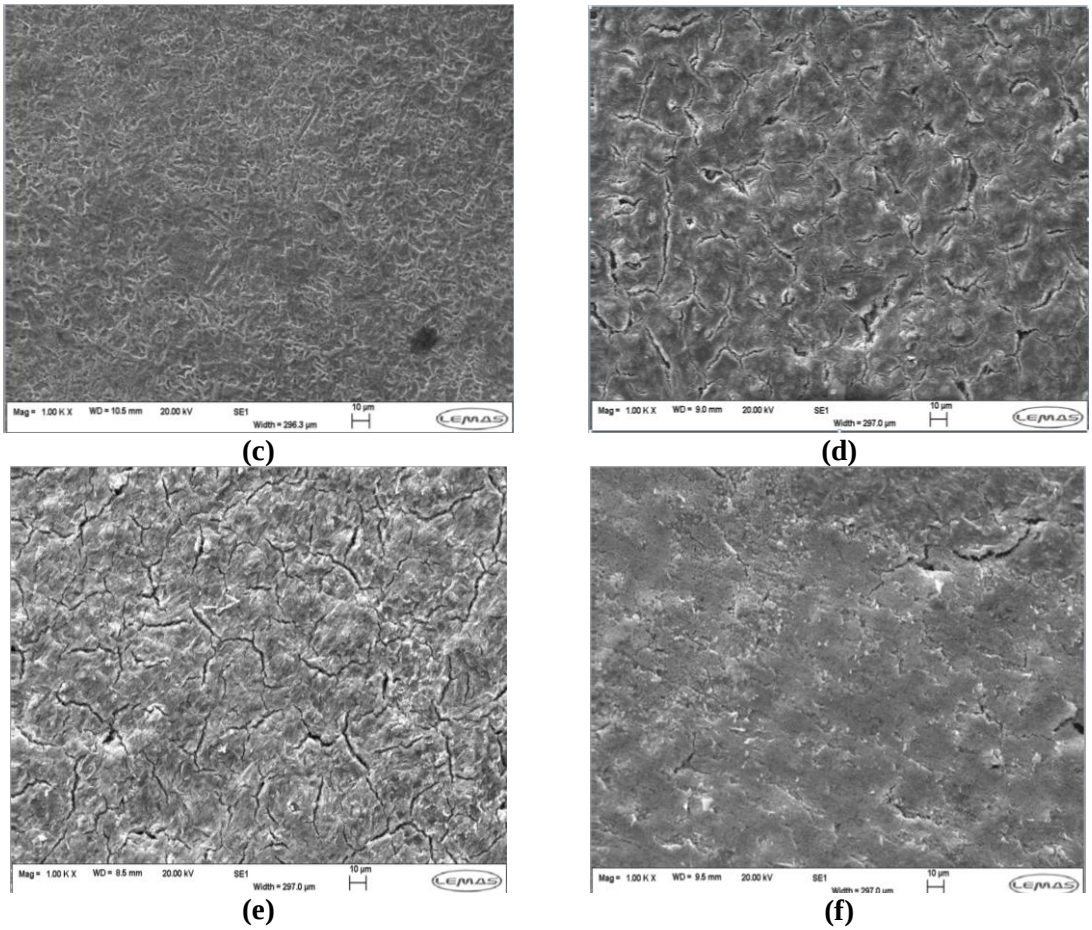

Figure 7-6 Corrosion product layer on X-65 carbon steel sample exposed at 30°C to a solution of (a) 1 wt. % NaCl solution after 7 Hours, (b) 3.5 wt.% NaCl solution after 7 Hours(c) 10 wt.% NaCl solution after 7 Hours (d) 1 wt.% NaCl solution after 168 Hours, (e) 3.5 wt.% NaCl solution after 168 Hours, and (f) 10 wt.% NaCl solution after 168 Hours.

There is also evidence of nano-scale crystalline form of $FeCO_3$ for tests in 10 wt.% (but not as obvious for the regions considered for SEM imaging for tests in 1 and 3.5 wt.%) as shown in Figure 7-6 (d), (e) and (f) and the XRD pattern of Figure 7-7 (a), (b) and (c). This shows that in an un-buffered corrosion system, the effect of chloride ion concentration is more correlated on the electrolytic strength of the solution and the aggressiveness of the dissolved ions and anions than on its effect on the nature, properties of the corrosion products. There is also the potential influence of retardation of the thermodynamic tendency for iron carbonate precipitation as implied by the work of Sun *et al* [84]. However, this has not been observed in this work.

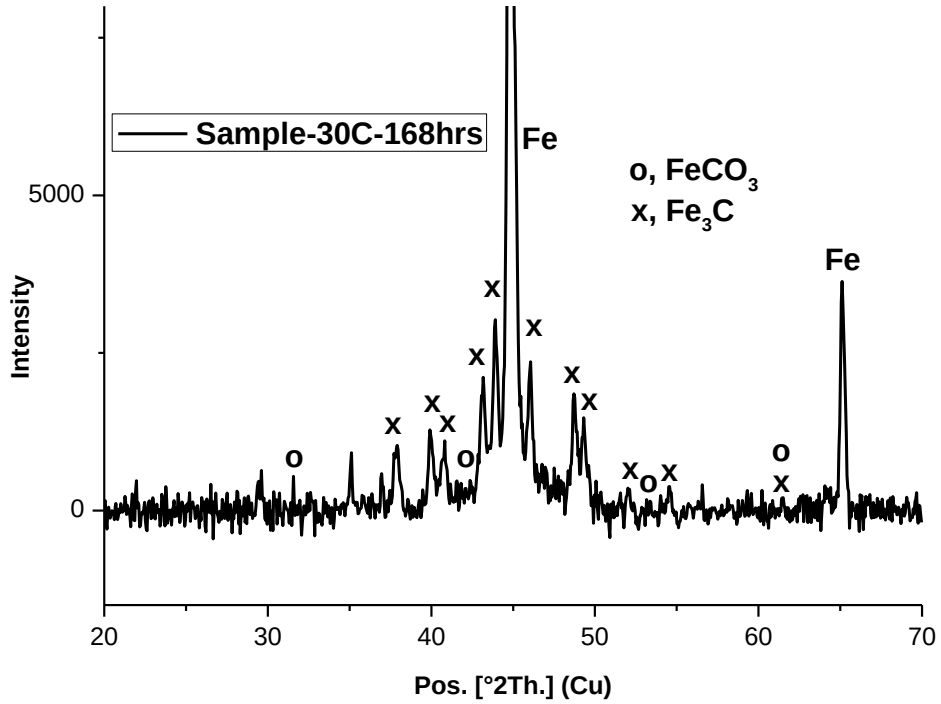
Sample-30C-168hrs
Fe
o, FeCO3
x, Fe3C
Fe
Intensity
5000
0
20
30
40
50
60
70
Pos. [°2Th.] (Cu)

(a)

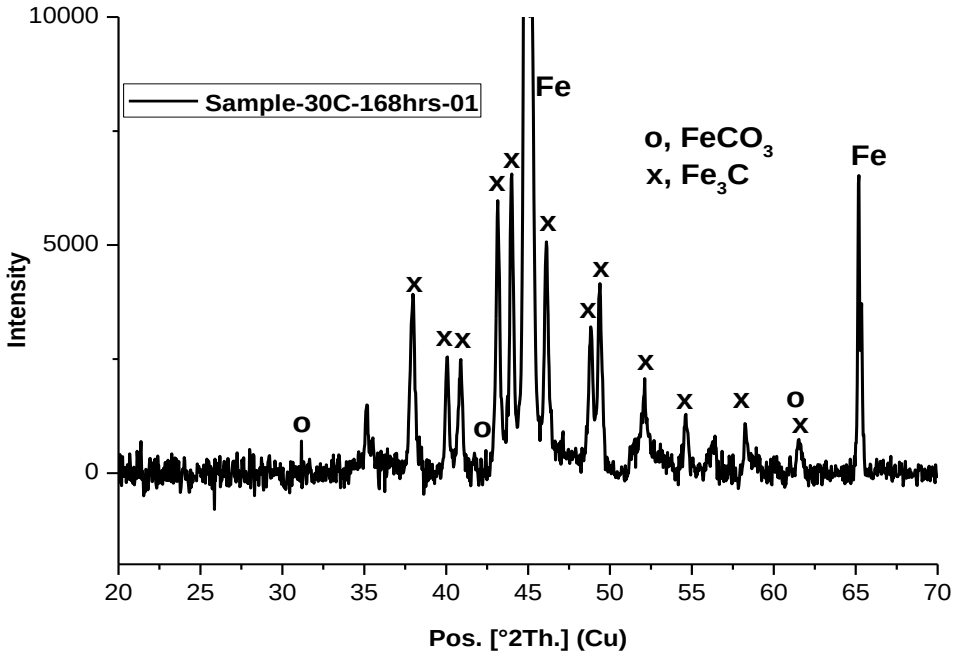
Sample-30C-168hrs-01
Fe
o, FeCO3
x, Fe3C
Fe
Intensity
10000
5000
0
20
25
30
35
40
45
50
55
60
65
70
Pos. [°2Th.] (Cu)

(b)

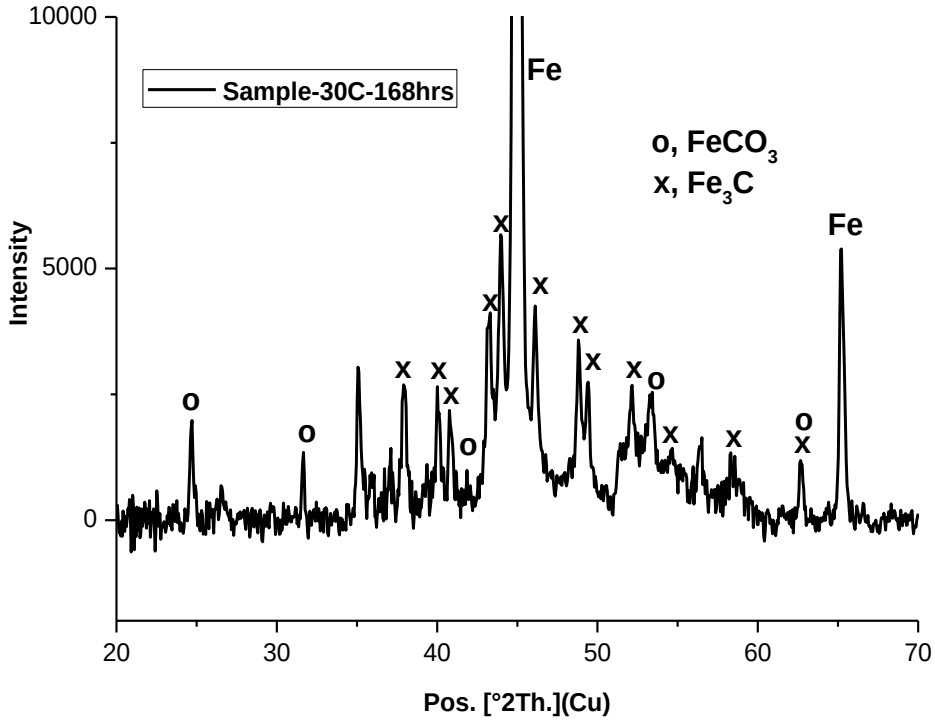

(c)

Figure 7-7 XRD pattern for corrosion product on X-65 steel after exposure to (a) 1wt. % (b) 3.5 wt. % and (c) 10 wt. % NaCl solution for 168 hours at 30°C *(Note that the intensity scale is arbitrary)*.

7.2.2 Effect of chloride ion concentration on corrosion behaviour of carbon steel and formation of corrosion product at 50°C

By increasing the temperature of the test environment from 30 to 50ºC, Figure 7-8 shows a significant increase in the general corrosion rate with increasing chloride ion concentration. This observation is very different from the variation in corrosion rate with chloride ion at 30ºC (see Figure 7-3) and also consistent from the start to the end of the tests and is in agreement with the observed shift in the anodic polarisation line to higher current at higher anodic potential. This observation is also consistent with observations by various authors [98, 108] at higher temperatures that emphasises the increase in aggressiveness of the corrosion media with increasing chloride ion content at higher temperatures [40]. The pH of the bulk solutions did not change significantly over the 168 hours test period as shown in Figure 7-9, which also show similar trend as with the case of tests at 30ºC. There is also a slightly lower solution pH with 10 wt. % NaCl in the test solution as it is with the tests at 30ºC. The corrosion rate measured for

the tests conducted at 50ºC also seems to clearly reflect the variation in the solution resistance with increasing chloride ion concentration as shown in Figure 7-2.

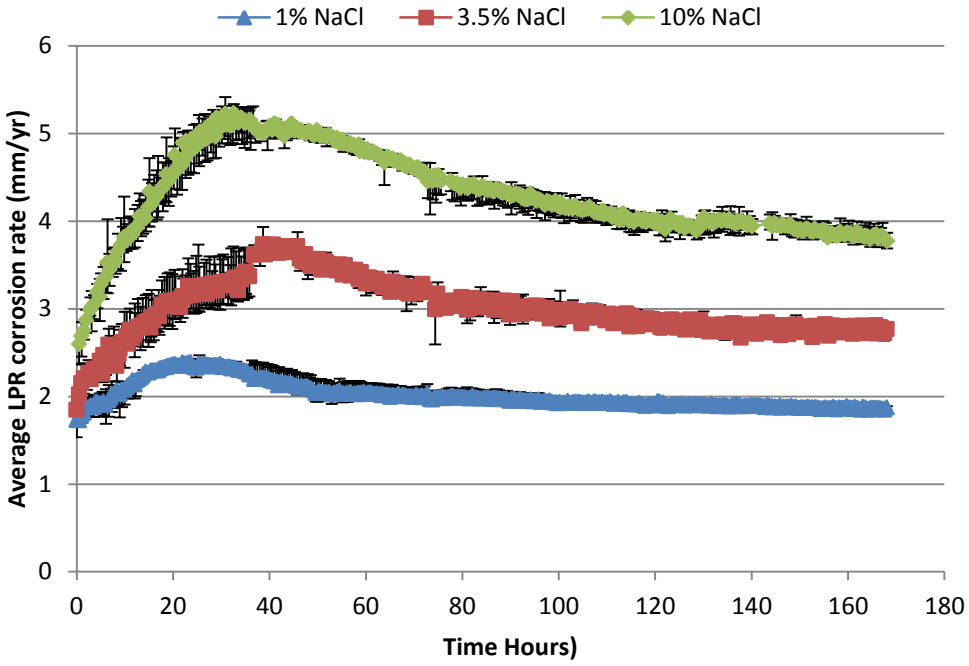

Figure 7-8 A plot of LPR corrosion rate for X65 carbon steel exposed at to 1, 3.5, and 10 wt. % NaCl solution saturated with CO_2 at 50°C.

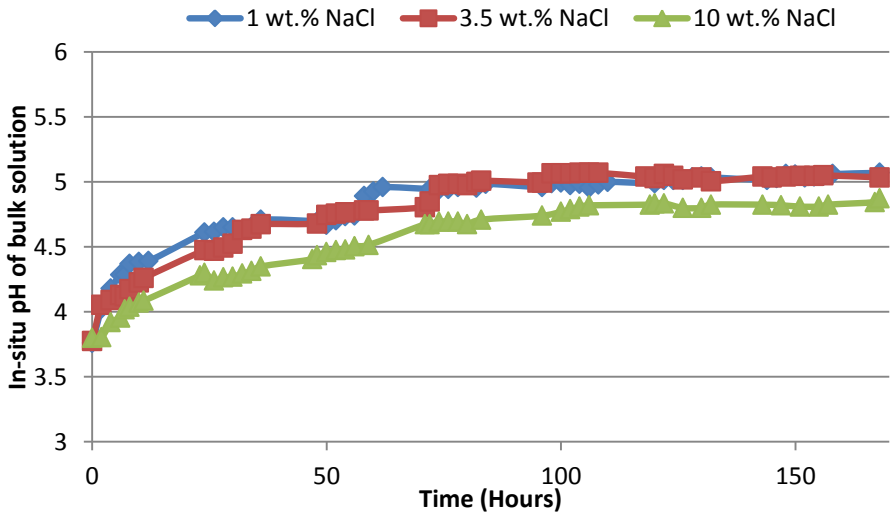

Figure 7-9 Measured *in-situ* pH of corrosion media containing different chloride ion concentration and saturated with CO_2 gas at 50ºC.

With respect to the iron carbonate formation process at 50ºC, the SEM images provided in Figure 7-10 show that the effect of chloride ion on corrosion product formation process is similar to the observations at 30ºC. The revealing of iron carbide clearly dominates the surface products after 7 hours for the three different chloride regimes under investigation. After 168

hours the XRD pattern provided in Figure 7-11 shows evidence of nano-scale/polycrystalline iron carbonate corrosion product being deposited on the steel surface for all chloride ion concentration. Although the SEM images (Figure 7-10 (d) and (e)) does not show any visual evidence as much as it is in Figure 7-11 (f), the XRD pattern does suggest the presence of deposited nano-scale crystals of iron carbonate (maybe localised) as described for test at 50ºC in 10 wt.% NaCl solution discussed in section 6.5 of Chapter 6. The signal on the XRD patterns of Figure 7-11 (a) and (b) for tests in 1 and 3.5 % NaCl solutions were also not as strong as the signal for test in a 10 wt. % NaCl solution. This shows that in systems where corrosion rate is expected to precede solution supersaturation and corrosion product deposition, the initial rate of corrosion or rate of dissolution of ferrous ions becomes very important to the corrosion product deposition process, especially in terms of determining the nature and properties of the corrosion product layer [88]. From the evidence provided thus far, this is a potential route by which chloride ion concentration may be influencing the process of $FeCO_3$ formation.

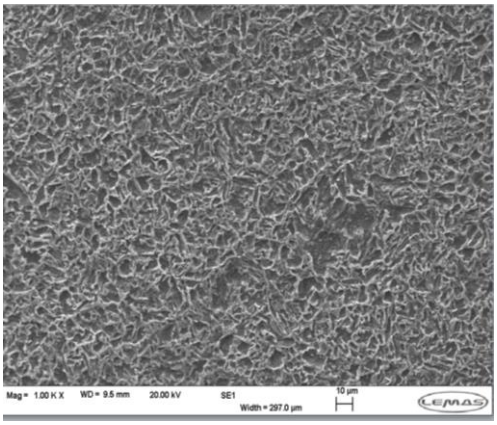

(a)

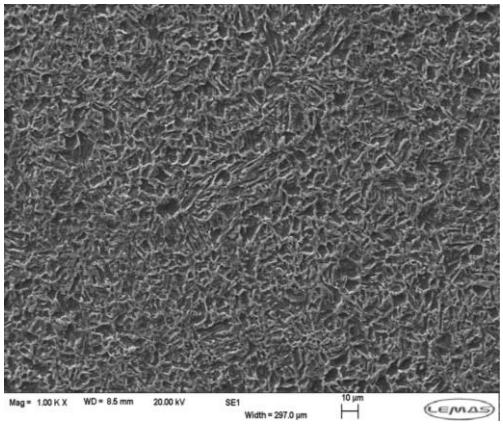

(b)

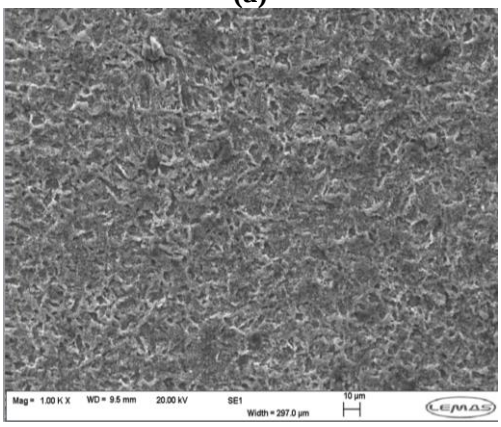

(c)

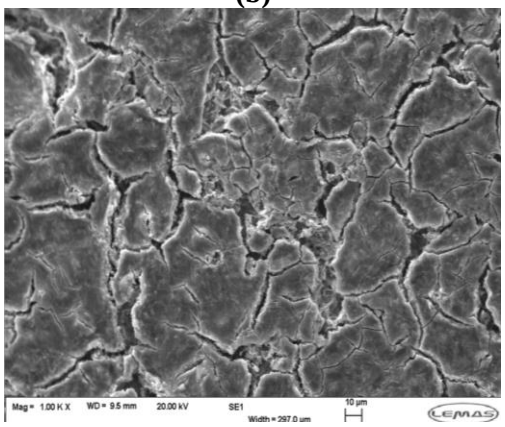

(d)

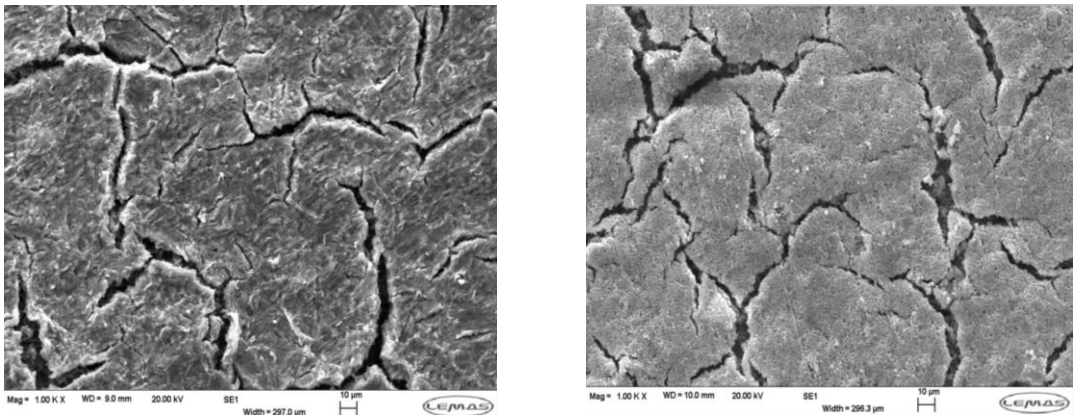

(e) (f)

Figure 7-10 Corrosion product layer on X-65 carbon steel sample exposed at 50ºC to a solution of (a) 1 wt. % NaCl solution after 7 Hours, (b) 3.5 wt. % NaCl solution after 7 Hours (c) 10 wt. % NaCl solution after 7 Hours (d) 1 wt. % NaCl solution after 168 Hours, (e) 3.5 wt. % NaCl solution after 168 Hours, and (f) 10 wt. % NaCl solution after 168 Hours.

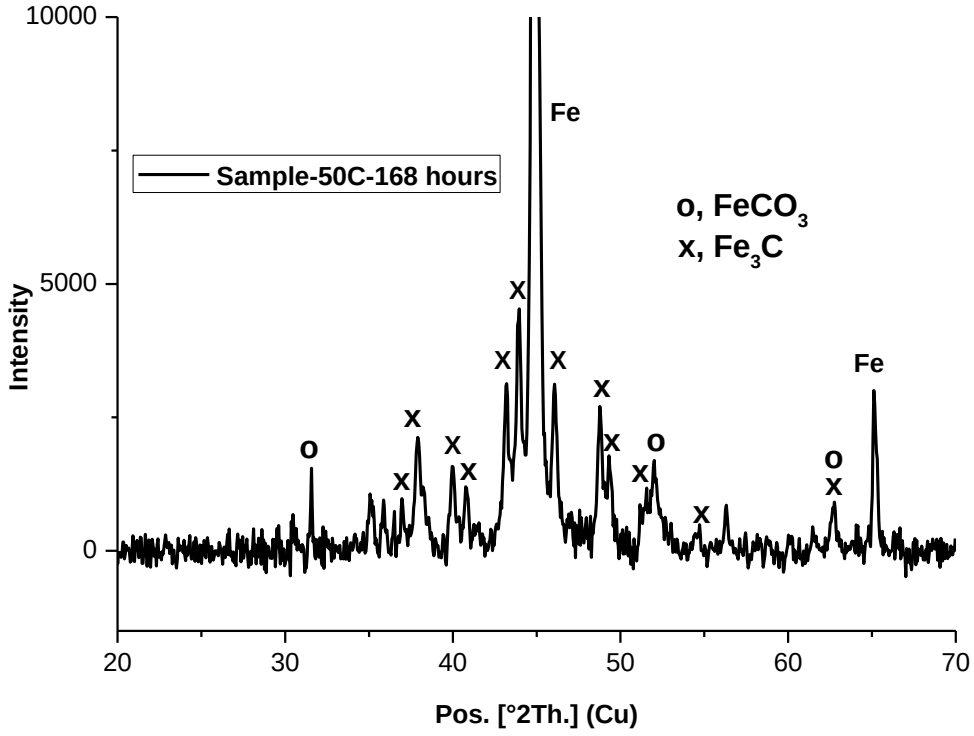

(a)

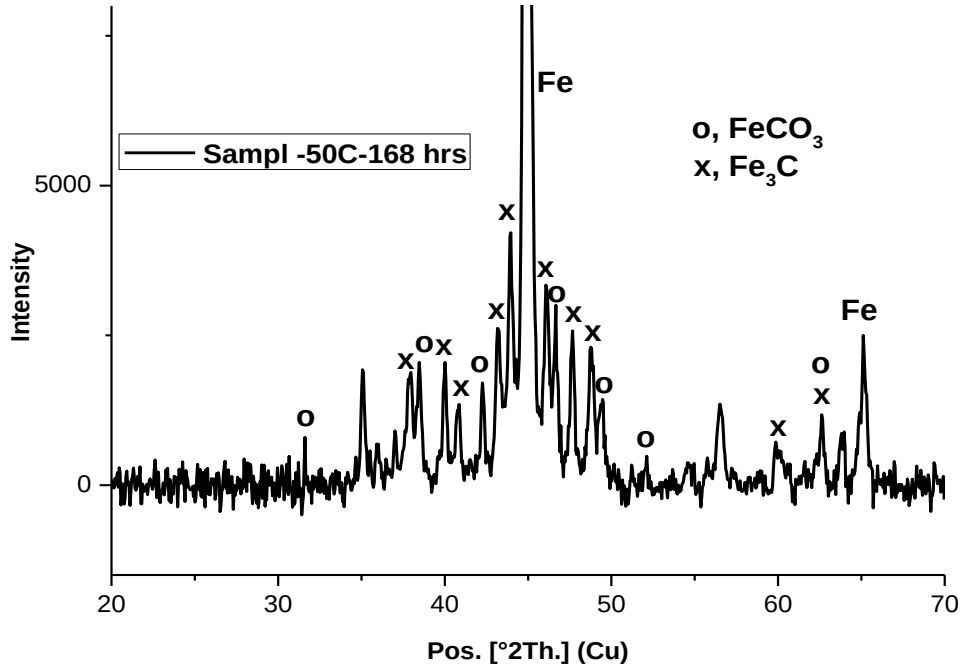

(b)

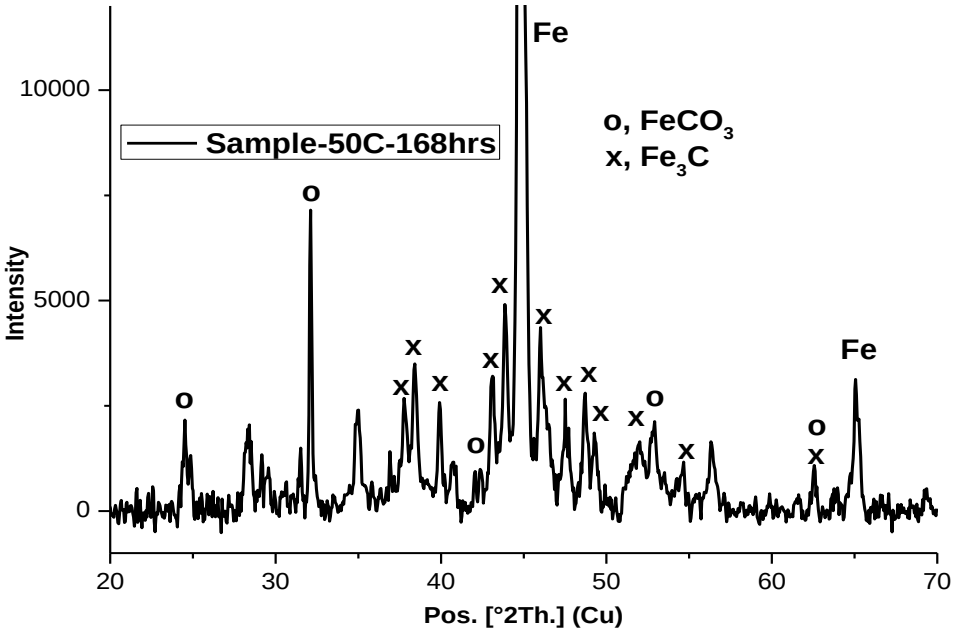

(c)

Figure 7-11 XRD pattern for corrosion product on X-65 steel after exposure to (a) 1wt. % (b) 3.5 wt. % and (c) 10 wt. % NaCl solution for 168 hours at 50°C *(Note that the intensity scale is arbitrary)*.

7.2.3 Effect of chloride ion concentration on corrosion behaviour of carbon steel and formation of corrosion product at 80°C

Figure 7-12 presents the corrosion rate of carbon steel in different chloride ion-containing solutions at 80ºC. The corrosion rate does show similar trends at for chloride ion concentration under investigation. The only variation is in terms of the magnitude of the corrosion rate. Corrosion rate peaked within the first 11 hours (at ≈ 3.25mm/yr, 5.5mm/yr and 7.25 mm/yr) and gradually decreases afterwards towards a steady corrosion rate of ≈ 2.00 mm/yr, 3.15 mm/yr and 4.0 mm/yr for tests in 1, 3.5 and 10 wt. % NaCl solution respectively. The variation in the corrosion rate values in Figure 7-12 is consistent with the observations reported for tests at 50ºC in section 7.2.2. This also correlates well with the variation in the solution resistance with chloride ion concentration. The relatively faster rate of reduction of corrosion rate with time has been discussed in section 6.5 of this thesis for tests in 10 wt. % NaCl solution. However, while the corrosion rate dropped by ≈ 37.5% and ≈ 42.7 % for tests conducted in 1 and 3.5 wt. % NaCl solutions respectively, the corrosion rate dropped by 45% for tests conducted in a 10 wt. % NaCl solution. The observed reduction in corrosion rate has also been linked with the evolution of corrosion products (examples of which are shown in Figure 7-14).

This observation thus confirms that in systems where iron dissolution rate precedes solution supersaturation and corrosion product layer formation, increasing chloride ion concentration may actually be increasing the rate of formation of iron carbonate corrosion products. This is clearly shown in the morphology of the corrosion products after 168 hours in 10 wt % NaCl (see SEM images in Figure 7-14 (f) and (g)), where there is visible evidence of crystalline $FeCO_3$. For tests in 1 and 3.5 wt. % NaCl (see SEM images in Figure 7-14 (d) and (f)), there are no visible evidence of crystalline $FeCO_3$ even though the XRD pattern (Figure 7-15 (a) and (b)) does shows peaks for $FeCO_3$. The signal for peaks of $FeCO_3$ in Figure 7-15 (a) and (b) is weaker than then the signal for $FeCO_3$ in Figure 7-15 (c) for tests in 10 wt. % NaCl. Although not necessarily very protective, the rate may be influenced by the balancing effect of role of chloride ion concentration on the aggressiveness of the corrosive media and iron dissolution rate, leading to potential supersaturation and the effect of chloride on the solubility product (Ksp) of iron carbonate formation as illustrated in a unified equation for estimating K_{sp} for $FeCO_3$ by Sun *et al* [84].

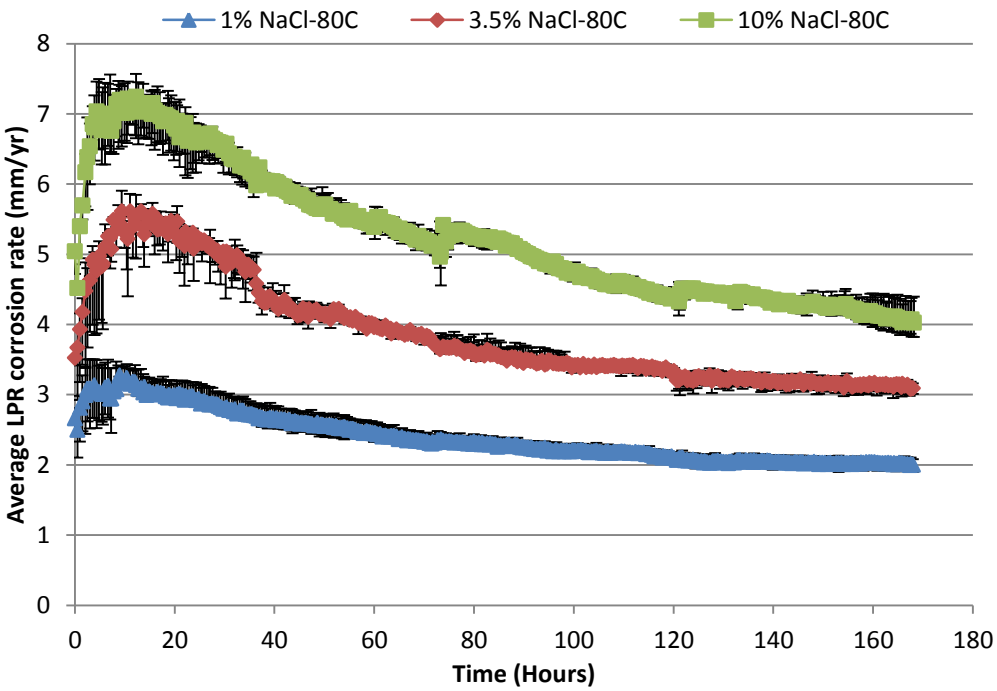

Figure 7-12 A plot of LPR corrosion rate for X65 carbon steel exposed at to 1, 3.5, and 10 wt. % NaCl solution saturated with CO_2 at 80°C.

The measured in-situ pH data (Figure 7-13) shows that the final pH is almost similar for the chloride ion concentrations under investigation. However, an initial increase in pH within the first ≈ 50 hours does suggest a unique trend in terms of the corrosion behaviour of carbon steel in these environments (most especially for test in a 10 wt. % NaCl solution). This initial increase in *in-situ* pH has also been reported by Guo *et al* [93] to indicate that the rate of dissolution of ferrous ions from the metal lattice is greater than the rate of precipitation of iron carbonate corrosion products. This process induces a buffering effect on the bulk solution. This also confirms the trend in the saturation ratio data with time provided in Figure 6-6 (b). This means that in an unbuffered corrosion environment, the formation of $FeCO_3$ leads to the lower saturation ratio and hence hinders the growth of nucleated nano-scale crystals of $FeCO_3$ as shown in Figure 7-14 (f) and (g).

This also correlates with the initial corrosion rate and solution resistance of test solutions (especially for solutions containing 10 wt. % NaCl with respect to tests in solution containing 1 and 3.5 wt. % NaCl). After 50 hours, the in-situ pH of solution of 10 wt. % NaCl appear to drop to almost similar value as the in-situ pH in the test solutions containing 1 and 3.5 wt. % NaCl. This drop in pH has also been attributed to the scenario where the rate of precipitation of iron carbonate becomes greater than the rate of dissolution of ferrous ions [93].

According to observations by Guo *et al* [93], the in-situ pH will also remain constant when the rate of metal dissolution equals the rate of iron carbonate precipitation which correlates very well with the corrosion rate data (Figure 7-12). XRD patterns provided in Figure 7-15 for tests at a temperature of 80ºC, also shows that the strength of the signal at the relevant position (≈ 25º, 32º, and 38º) for identification of iron carbonate increases with increasing concentration of the chloride ion concentration from 1 wt. % to 10 wt. % of NaCl. This further supports the initial observation on the role of chloride ion on the process of iron carbonate formation.

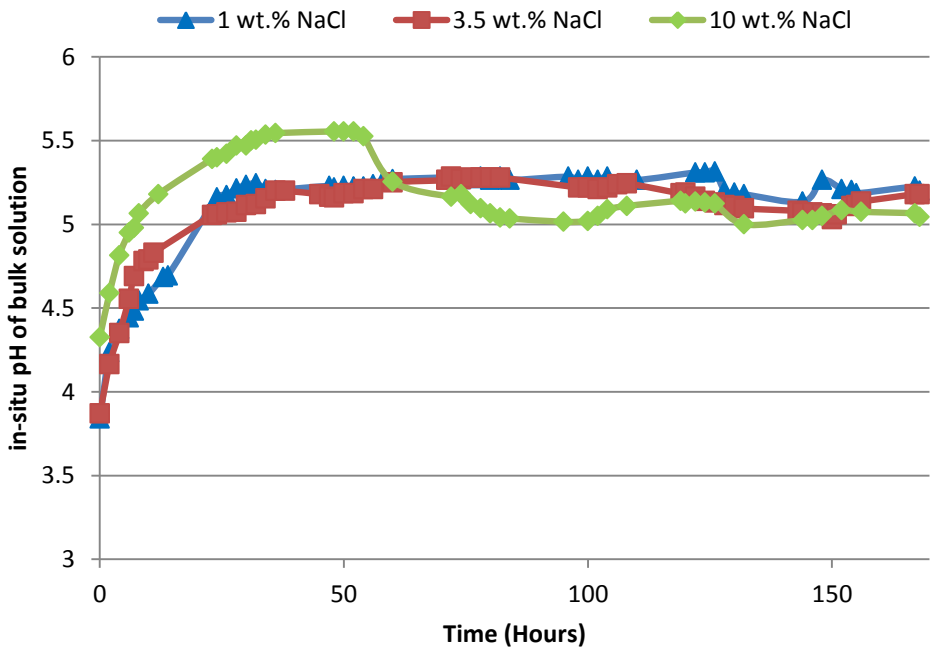

Figure 7-13 Measured *in-situ* pH of corrosion media containing different chloride ion concentration and saturated with CO_2 gas at 80ºC.

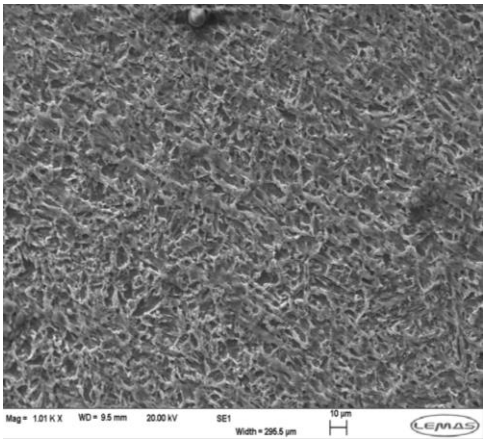

(a)

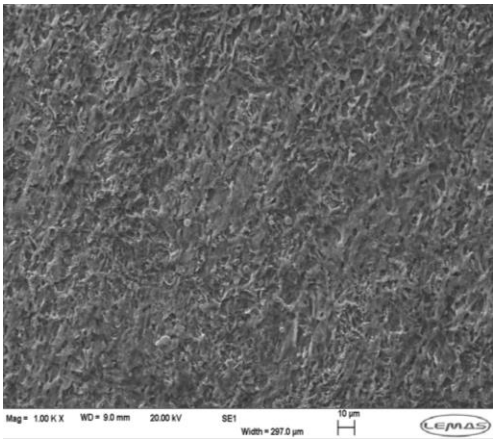

(b)

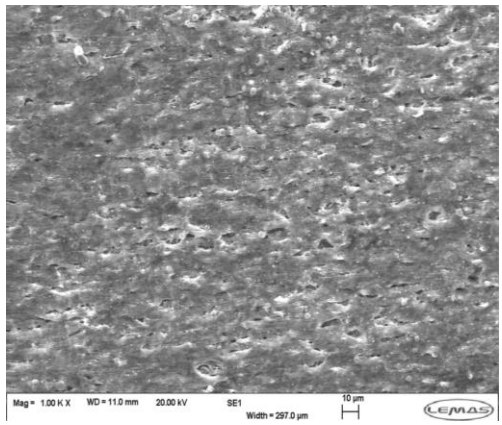

(c)

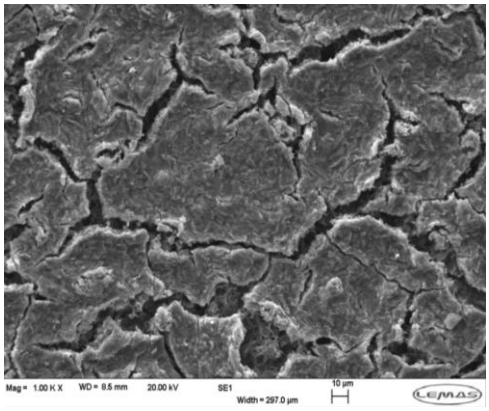

(d)

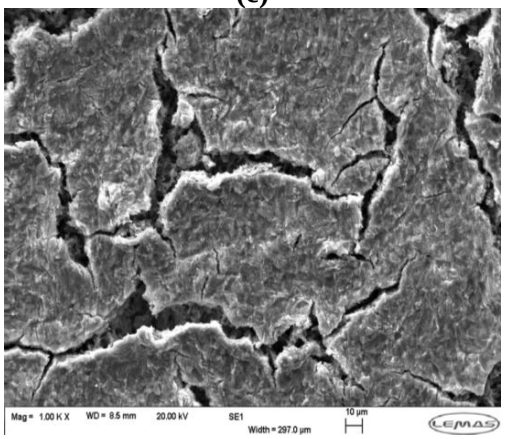

(e)

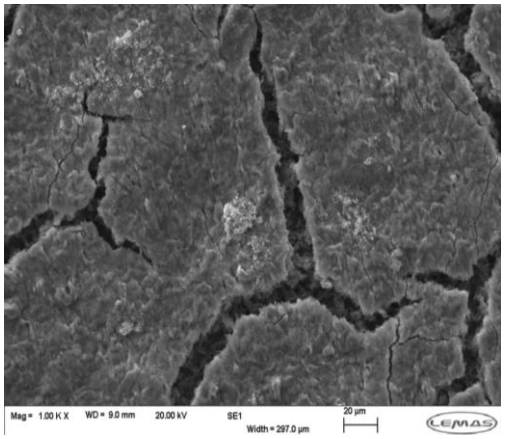

(f)

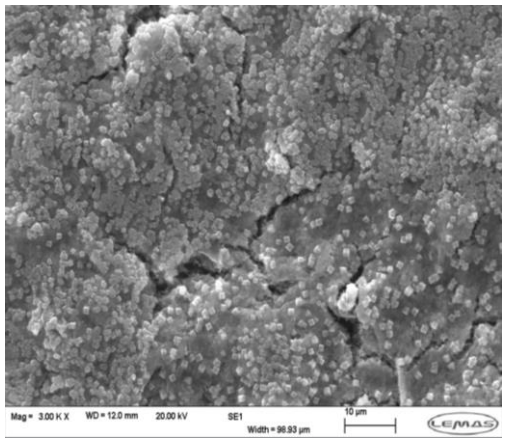

(g)

Figure 7-14 Corrosion product layer on X-65 carbon steel sample exposed at 80ºC to a solution of (a) 1 wt.% NaCl solution after 7 Hours, (b)) 3.5 wt.% NaCl solution after 7 Hours(c) 10 wt.% NaCl solution after 7 Hours (d) 1 wt.% NaCl solution after 168 Hours, (e) 3.5 wt.% NaCl solution after 168 Hours, (f) 10 wt.% NaCl solution after 168 Hours and (g) $FeCO_3$ crystals on a different region of sample shown in (f).

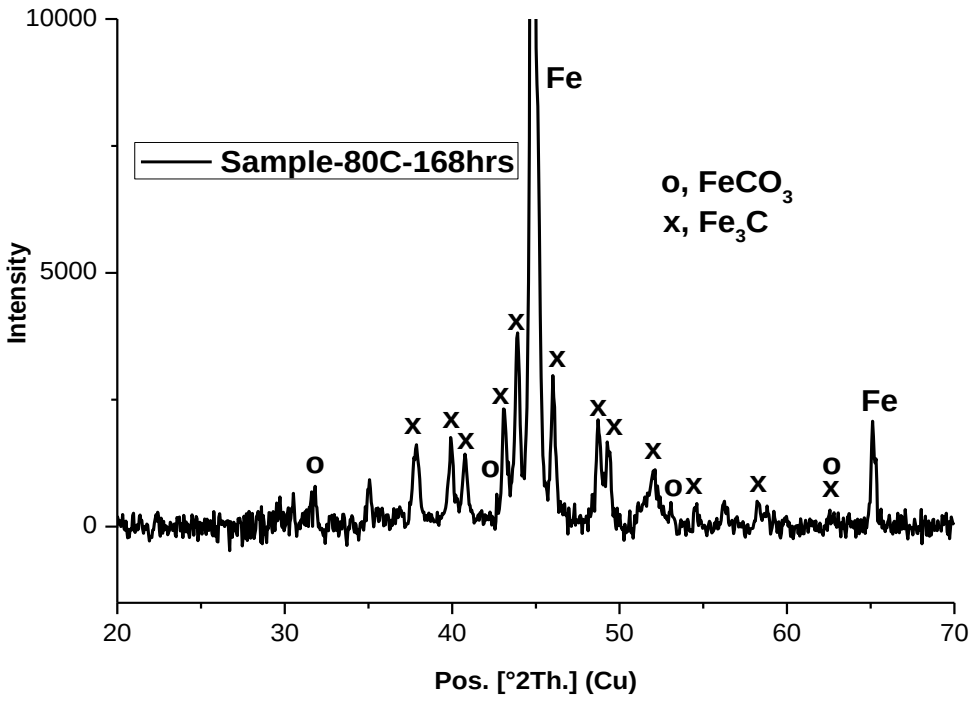
10000
5000
0
Intensity
Sample-80C-168hrs
o, FeCO3
x, Fe3C
Fe
Fe
20
30
40
50
60
70
Pos. [°2Th.] (Cu)

(a)

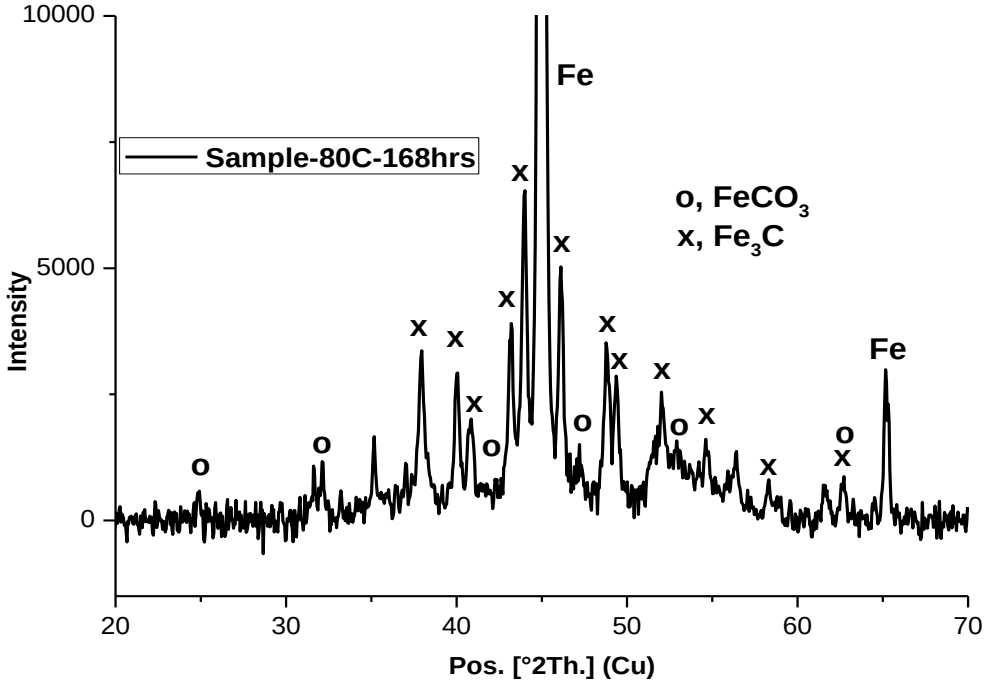
10000
5000
0
Intensity
Sample-80C-168hrs
o, FeCO3
x, Fe3C
Fe
Fe
20
30
40
50
60
70
Pos. [°2Th.] (Cu)

(b)

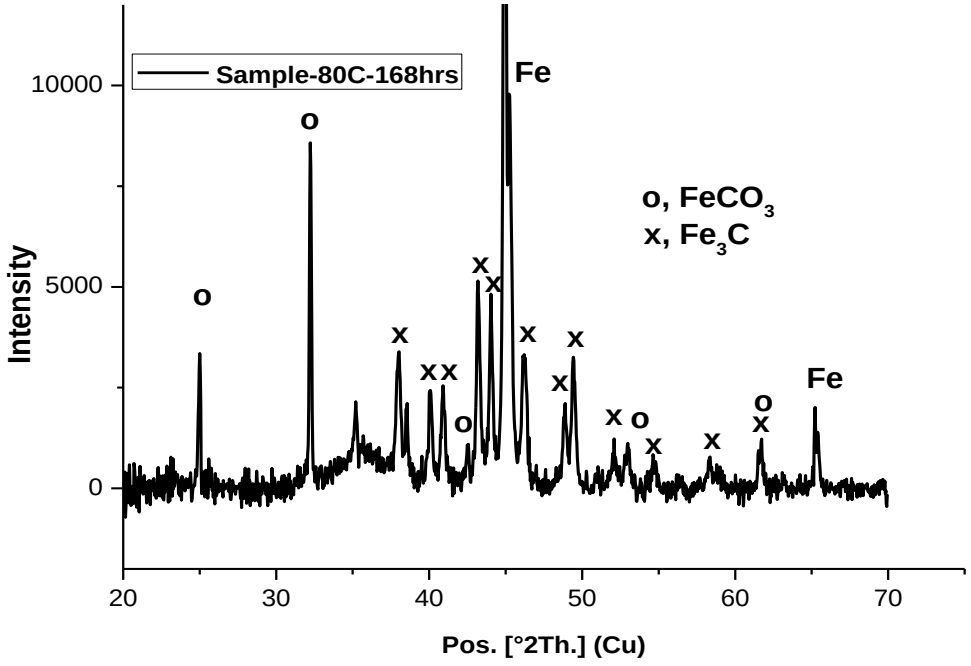

(c)

Figure 7-15 XRD pattern for corrosion product on X-65 steel after exposure to (a) 1wt. % (b) 3.5 wt. % and (c) 10 wt. % NaCl solution for 168 hours at 80°C *(Note that the intensity scale is arbitrary)*.

7.3 Pitting corrosion behaviour of carbon steel and metal penetration as a function of chloride ion concentration

This section of this Chapter presents and discusses the results to establish a relationship between pitting corrosion damage of carbon steel and chloride ion concentration. It is important to note that a relationship between corrosion product evolution and corrosion rate over 168 hours duration has been established for all temperature in section 6.5 of this thesis. It is expected that the correlation between corrosion product evolution and pitting corrosion for all chloride ion concentration under investigation will have almost similar trend as the case discussed in section 6.5 for tests in 10 wt. % NaCl. This is because from section 7.2, it has been shown that the effect of chloride ion concentration does not significantly influence the nature of corrosion products formed. On the other hand, chloride ions tend to influence the corrosivity and agrressivenes of the corrosion environment and hence, directly influencing metal penetration. In this section of the thesis, the emphasis will be on the effect of chloride ion concentration on pitting corrosion as well as metal penetration rate. The synergy between chloride ion and temperature will also be established in this section.

7.3.1 Pitting corrosion behaviour of carbon steel and metal penetration at 30°C

Over the course of the experiment performed at 30°C, relatively steady pit growth was observed for all chloride ion concentration except for test in 1 wt.% NaCl solution. Referring to Figure 7-16 (a) and (b), pits were quickly observed for tests in 1 wt.% NaCl solution (≈ 7 µm) when compared to tests in 3.5 wt.% NaCl solution (where no pits were recorded) and 10 wt.% NaCl solution (≈4 µm). This is also consistent with the concept of total metal penetration as described in section 6.6.4 of this thesis, in which case, instances where the general or uniform corrosion rate is large, the maximum and average pit depth relative to corrorded surface is usually masked and/or undersetimated. This distinctive observation that has been associated with corrosion of active metals like carbon steel materials [159]. With reference to Figure 7-3 of this Chapter, it is evident that within the first 36 hours, tests in 3.5 wt.% NaCl solution measured the largest uniform corrosion rate, while tests in 1 and 10 wt.% NaCl solution measured the least uniform corrosion rate. This correlates inversly with the observed pit depth recorded relative to corroded surface across the three NaCl solutions under investigation. This is also consistent with the threshold effect on the general corrosion rate across this range of chloride concentration at 20°C reported by Eliyan *et al* [105] and Fang *et al* [125]. With test in 3.5 wt. % NaCl solution, there was no measurable pit after 7 hours which is in contrast to tests in 1 and 10 wt.% NaCl solutions. This also corroborates the double effect of initial ferrite dissolution on both initiation of local anodes and masking of the pitted surfaces.

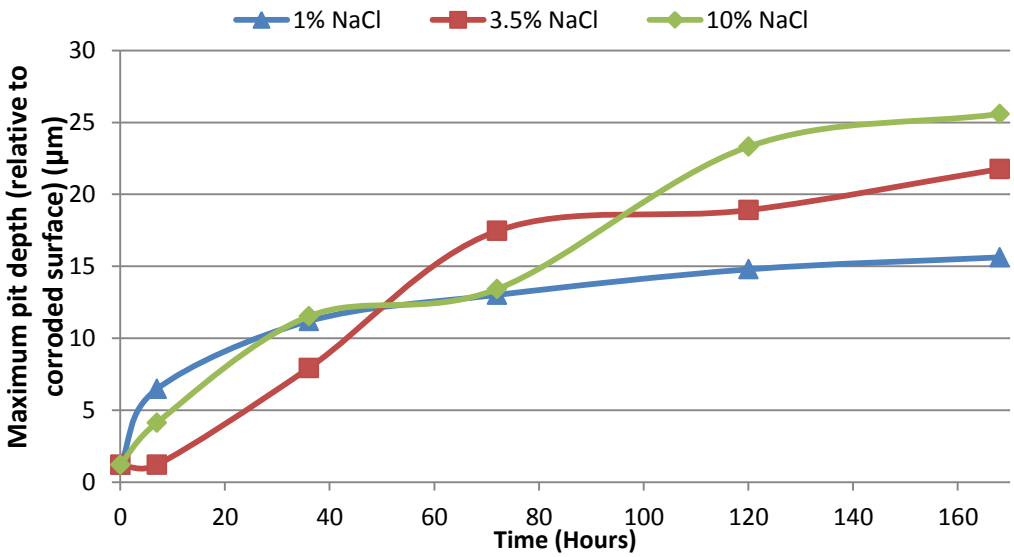

(a)

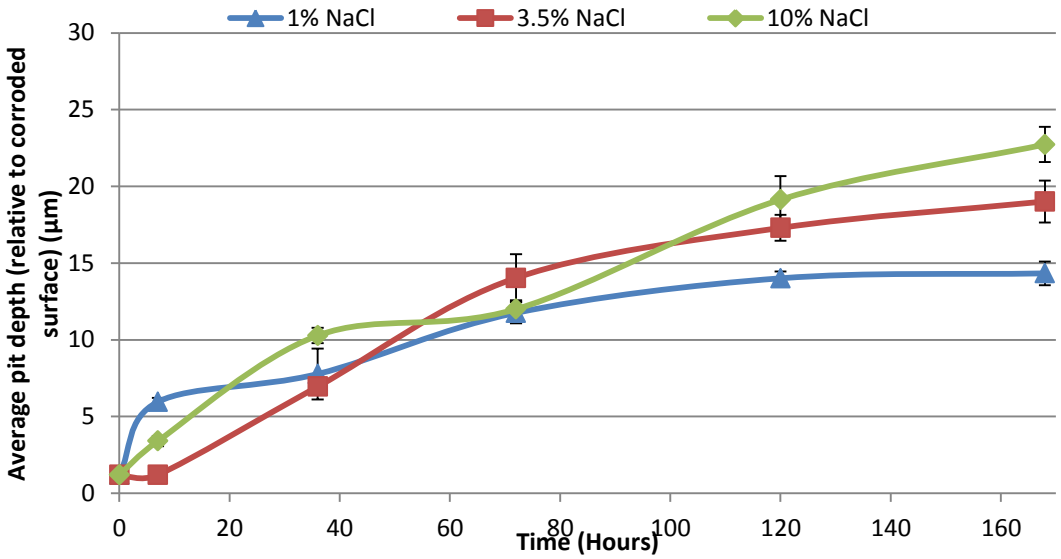

(b)

Figure 7-16 (a) Maximum pit depth (relative to corroded surface) and (b) average pit depth on X-65 carbon steel exposed to different NaCl-containing solution over 168 hours duration for at 30ºC.

Once, the pits are initiated after 36 hours, and the corrosion rates stabilises (after 72 hours), the pit depths for tests in 1 wt. % NaCl remained almost constant (with only a marginal increase) for the remaining duration of the test at ≈ 15 µm, pit depths for test in 3.5 wt.% NaCl increases only slighlty from ≈ 17 µm to ≈ 22 µm, while the pit depths in 10 wt. % NaCl solution increased the most between 72 and 168 hours from ≈ 13 µm to ≈ 26 µm. This observation also correlates with the fact that with 10 wt. % NaCl, cummulative thickness loss due to unform corrosion is still lower than for tests in 3.5 wt. % NaCl solution. The lower pit propagation rate for tests in 1 wt. % NaCl is likely related to the lower corrosion kinetics and rate of supersaturation of solution for the formation of an 'amorphous' and non-protective form of $FeCO_3$ to sustain pit growth process. This is shown in Figure 7-17 for metal penetration at all sampling time over 168 hours. Figure 7-17 shows a relatively constant thickness loss from uniform corrosion for tests in 1 wt. % NaCl solution. The concept of metal penetration presented in Figure 7-17 have clearly illustrated that the influenced by the chloride ion concentration on pitting corrosion of carbon steel in an un-buffered corrosion environment, is correlated on its influence on the aggressiveness of the corrosion media, its restriction of the uniform corosion rate and corrosion product eveolution.

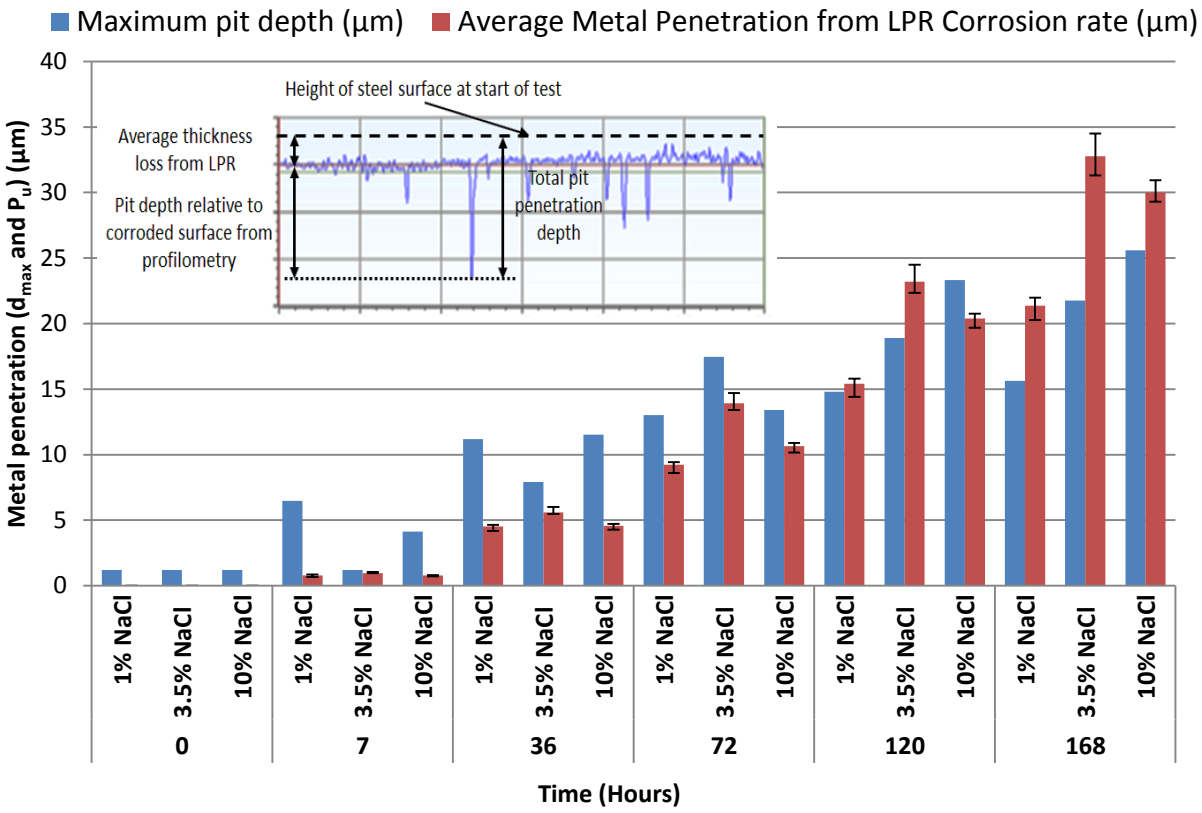

Figure 7-17 Variation of total material thickness loss and pit depth relative to corroding surface with time for 1, 3.5, and 10 wt. % NaCl-containing solutions at 30°C.

7.3.2 Pitting corrosion behaviour of carbon steel and metal penetration at 50°C

For all experiments conducted at 50ºC, the corrosion rate over the course of 168 hours have been presented in Figure 7-8 and discussed in section 6.5.2 for all chloride ion concentration. With reference to pitting corrosion, Figure 7-18 (a) and (b) presents the maximum pit depth and the average of the ten (10) deepest pits on almost an entire exposed steel surface. Figure 7-18 show that the pit depth measured over 168 hours test duration depicts similar trend for all chloride ion concentration. It also show a continuous linear pit growth process as initially describe in section 6.6.2 of this thesis. The only noticeable difference in the pit depth profiles for tests in the three chloride ion concentration could be observed within the first 120 hours. Between 7 and 120 hours, the highest pit depth (≈ 30 µm) was recorded for test in 1 wt. % NaCl after 72 hours, with test in 10 wt. % NaCl recording the least pit depth (≈ 23 µm). This trend also correlates inversely with the initial corrosion rate within this period as shown in Figure 7-8. This observation further emphasis the point that general corrosion in carbon steel is always masking and/or underestimating the extent of pitting in these tests.

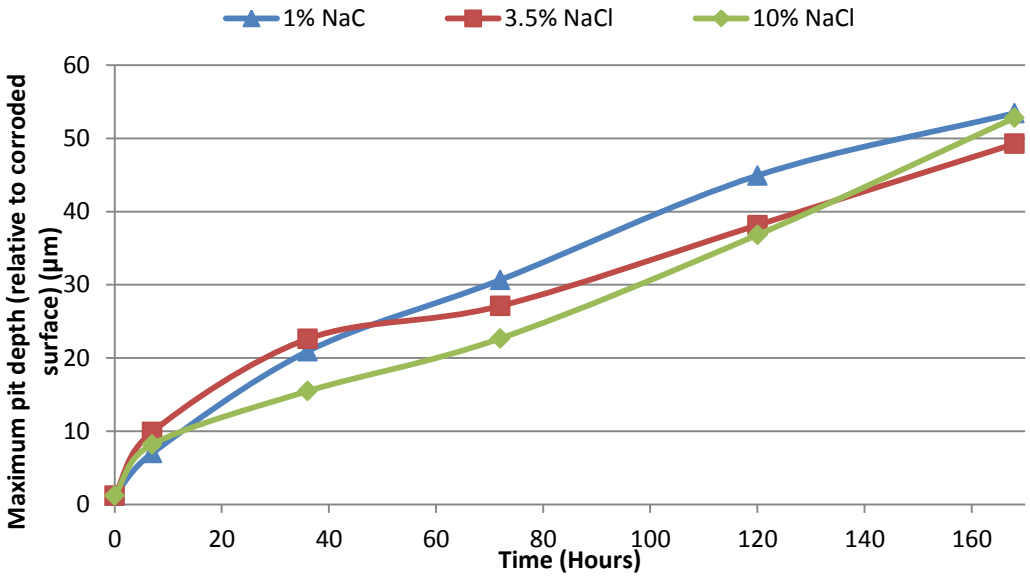

(a)

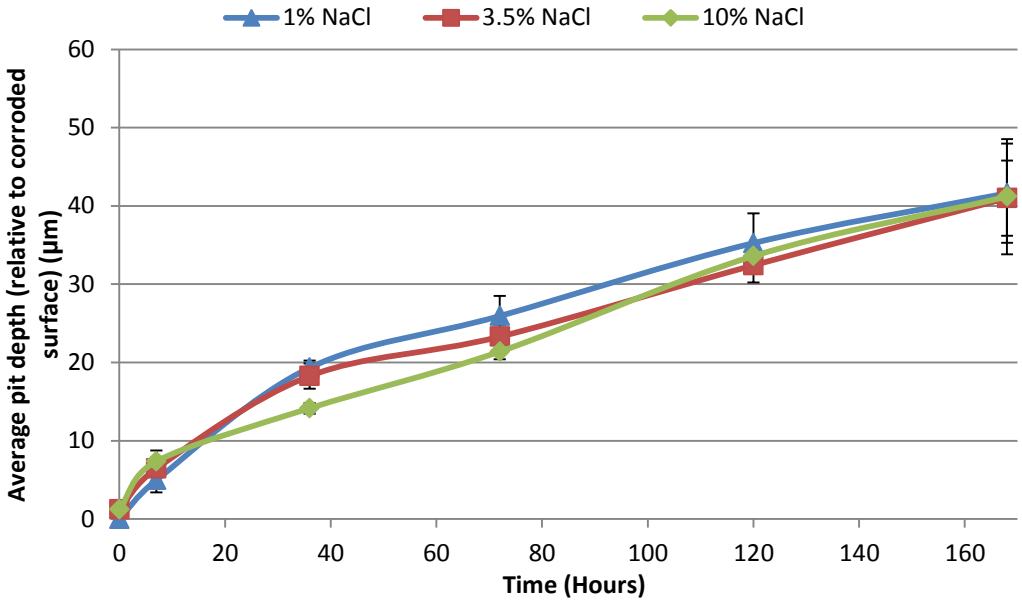

(b)

Figure 7-18 (a) Maximum pit depth (relative to corroded surface) and (b) average pit depth on X-65 carbon steel exposed to different NaCl-containing solution over 168 hours duration for at 50ºC.

It is also important to note that the magnitude of pit depths recorded for all chloride ion concentration under investigation were higher for 50ºC than for tests at 30ºC. This is related to the rate of formation and the nature of the $FeCO_3$ corrosion product formed on steel surface at 50ºC. $FeCO_3$ corrosion product formed at 50ºC are also known to be non-protective [9, 87]; a very important proponent for localised/pitting corrosion to occur. Between 7 and 120 hours, the rate of pit depth increases with chloride from 1 to 3.5 wt. % NaCl, possibly due to the increase

in the rate of ferrite dissolution and supersaturation. However, with 10 wt. % NaCl the effect of higher rate of ferrite dissolution is also masking the extent of pit penetration, leading to a lower pit depth than for test in 3.5 wt. % NaCl solution.A further breakdown of the overall contribution of uniform/general corrosion and pitting corrosion to total metal penetration is presented in Figure 7-19.

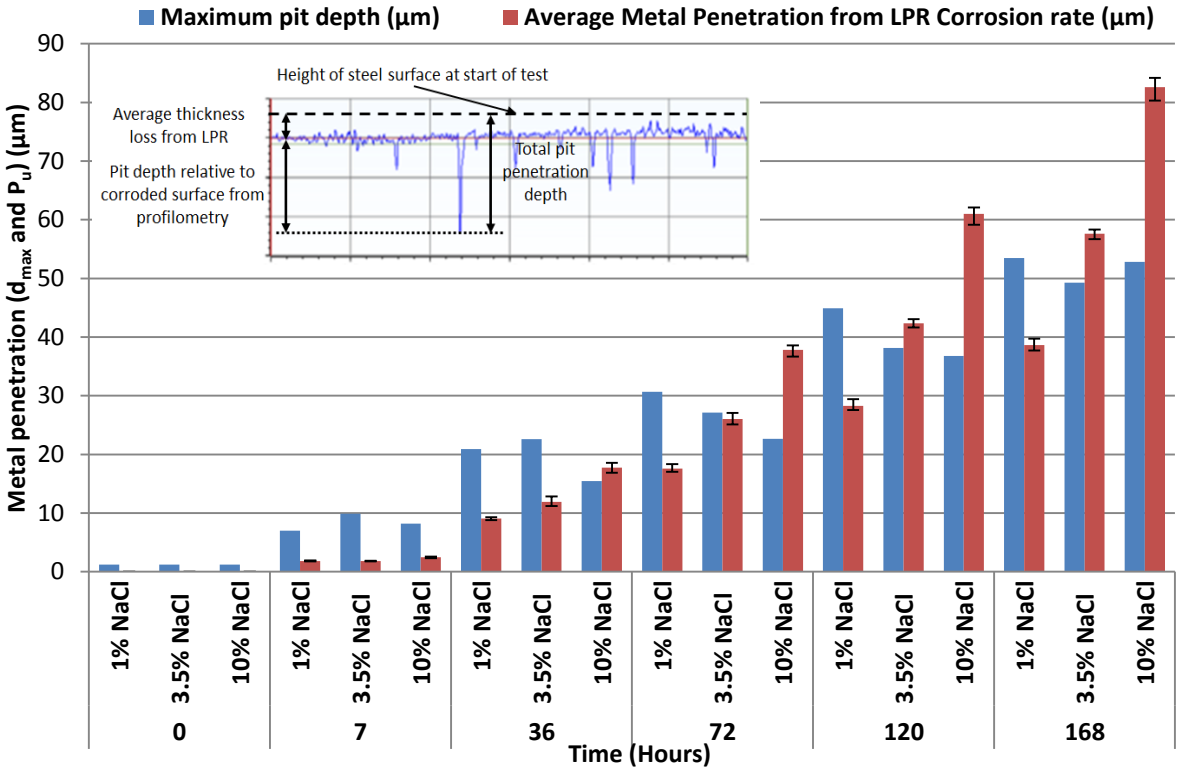

Figure 7-19 Variation of total material thickness loss and pit depth relative to corroding surface with time for 1, 3.5, and 10 wt. % NaCl-containing solutions at 50°C.

7.3.3 Pitting corrosion behaviour of carbon steel and metal penetration at 80°C

The effects of chloride ion concentration on the corrosion behaviour of carbon steel material have been clearly highlighted in section 7.2.3 of this Chapter. The potentiodynamic plots provided in Figure 7-1(c) and the variation in solution resistance with chloride ion concentration provided in Figure 7-2 showed consistent correlation with the corrosion rate measured across the three chloride ion concentration under investigation (provided in Figure 7-12). The measured corrosion rate provided in Figure 7-12 has already shown that at high temperatures, the effect of chloride ion on the aggressiveness of the corrosion media becomes more prominent. Such observations have also been shown to have inverse correlation with the maximum and average pit depth (measured relative to corroded surface) in Section 7.3.1 and 7.3.2. However, there also appears to be a distinctive correlation across the three different

temperature regimes explored in this work. Figure 7-20 presents the maximum and average pit depth (measured relative to corroded surface) for 1, 3.5 and 10 wt. % NaCl at 80°C. Within the first 36 hours, the maximum pit depth shows an inverse correlation with measured corrosion rate during this period in the test. Within this time, the corrosion rate peaked at ≈ 3.25mm/yr, 5.5mm/yr and 7.25 mm/yr for tests in 1, 3.5 and 10 wt. % NaCl solution respectively, while the maximum pit depths after 36 hours were ≈ 24 µm, 20µm and 17µm for tests in 1, 3.5 and 10 wt. % NaCl solution respectively.

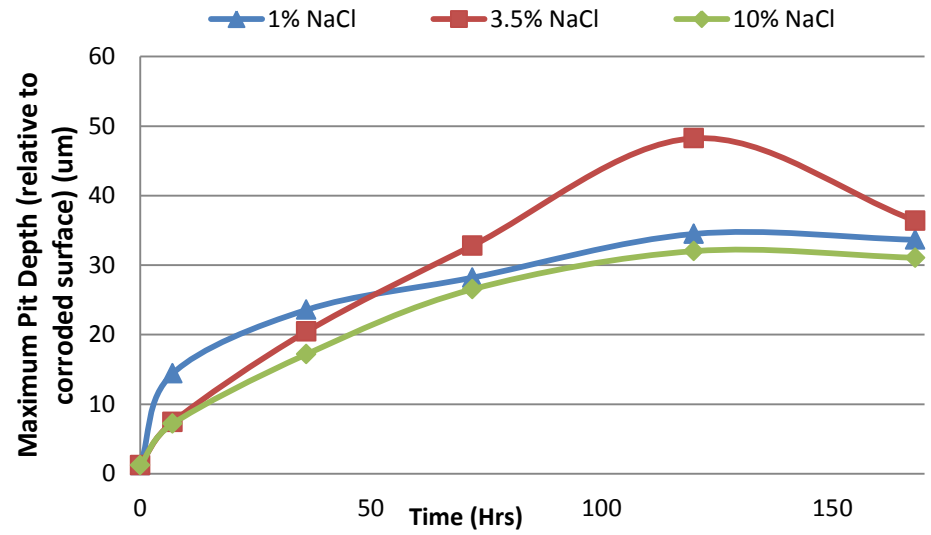

(a)

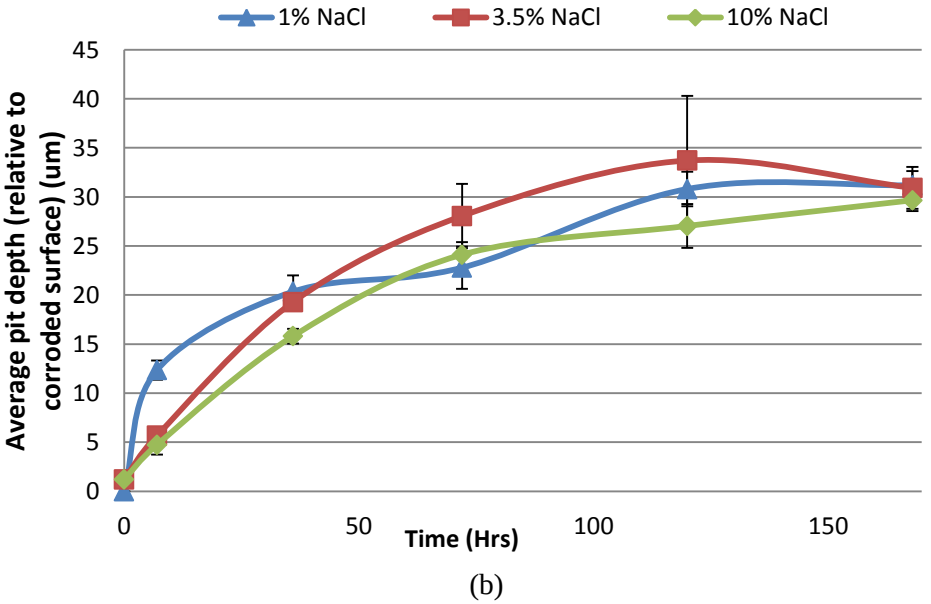

(b)

Figure 7-20 (a) Maximum pit depth (relative to corroded surface) and (b) average pit depth on X-65 carbon steel exposed to different NaCl-containing solution over 168 hours duration for at 80°C.

From 72 hours onwards, the pit growth rate on steel sample from test solution containing 3.5 wt. % NaCl was higher than on steel sample from test solutions containing 1 and 10 wt. % NaCl. In the case of test in 1 wt. % NaCl solution, the rate of iron dissolution that usually precedes corrosion product formation is expected to be lower than test in 3.5 % NaCl solution. The XRD pattern and discussion on corrosion product in section 7.2.3 has shown that the initial rate of corrosion is a very important proponent in terms of corrosion product formation. Hence, the less aggressive the corrosion environment is, the less likely it is for the attainment of solution supersaturation and consequently formation of $FeCO_3$ corrosion product that is able to sustain pit propagation. In systems where this scenario plays out (i.e, un-buffered corrosion media), the corrosion product that is usually formed is usually non-protective and often leading to pitting [88]. It has also been reported by Papavinasam *et al* [38], that if corrosion product does not form, then the uniform corrosion dominates the corrosion damage mechanism. By implication, this means that in systems where the corrosion product is non-protective, the level of pitting may also be related to the rate of formation of non-protective corrosion product layers. This scenario may be responsible for the variation in pit depth profile after 72 hours between tests in 1 wt. % NaCl and tests in 3.5 wt. % NaCl, especially as the corrosion rate becomes constant for both conditions after this time.

Referring to the test in 10 wt. % NaCl after 72 hours, the pit depth is also lower than for test in 3.5 wt. % NaCl. This is attributed to the higher corrosion rate over the 168 hours period that tends to mask or underestimate the actual metal penetration or thickness loss. The observations highlighted thus far are clearly illustrated in Figure 7-21 to show how the corrosion rate and pitting rate correlates with total material loss for the chloride ion concentrations under investigation. It also important to note that between 120 and 168 hours, there is a consistent trend of reduction in pit depth for all chloride concentrations (See Figure 7-20), which has been attributed to a potential self-healing effect of initially active pits in section 6.6.5 of Chapter 6. The process of self-healing of pits as explained in section 6.6.5 is also correlated to the rate of supersaturation of the bulk solution and the transport of precipitable ions across the porous $FeCO_3$ to deposit at the base of the pits. The rate of supersaturation is also dependent on the rate of ferrous ions availability; a process that is expected to be promoted by higher chloride ion (10 wt. % of NaCl) and temperature. At lower chloride ion concentration, the effect of self-healing mechanism on pit retardation occurs slower than for test in 10 wt. % NaCl solution (See Figure 7-20).

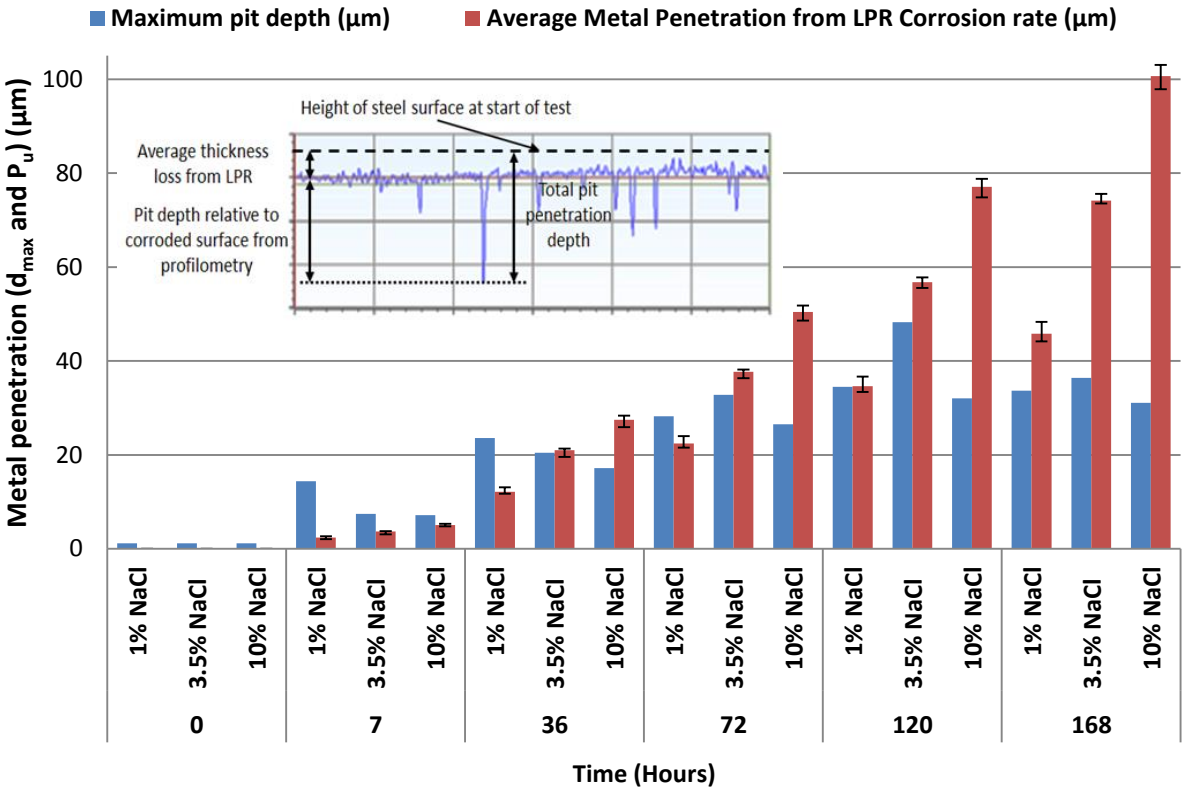

Figure 7-21 Variation of total material thickness loss and pit depth relative to corroding surface with time for 1, 3.5, and 10 wt. % NaCl-containing solutions at 80°C.

7.3.4 Summary on the effect of chloride ion concentration on pitting and uniform corrosion behaviour of carbon steel in CO_2-saturated brines

The effect of chloride ion concentration on the pitting corrosion behaviour of carbon steel materials within 168 hours, has been shown in this study to be correlated on how it influences the aggressiveness of the corrosion environment prior to $FeCO_3$ formation, as well as on the kinetics of $FeCO_3$ formation than on how it influences the properties of $FeCO_3$ corrosion product formed. The corrosion environment was more aggressive with 10 wt. % NaCl at 80°C. The extent of metal penetration (pitting and uniform corrosion) is influenced by the synergy of temperature and chloride ion concentration.

Chapter 8. Investigation of uniform and pitting corrosion in CO_2 saturated corrosion environments; Effect of *in-situ* bulk pH

This section focuses on correlating pitting and localised corrosion of carbon steel with an important process parameter; bulk solution pH which also used to characterise water chemistry. The complex process of pitting corrosion is correlated on with the influenced solution pH. The results presented and discussed in this section explore the potential relationship between pit initiation and propagation in CO_2-saturated environments and bulk solution pH of solutions and the presence of corrosion products. The corrosion product characteristics and the pitting behaviour of X65 carbon steel in CO_2-saturated brine over a wide range of environment acidity/alkalinity; un-buffered corrosion media, corrosion media at pH 6.6 and 7.5 at 50°C in 3.5 wt.% NaCl solution are discussed but with emphasis on pitting corrosion in these conditions.

A change in bulk solution pH is known to change the rate of cathodic reduction of H^+ and thus, significantly influence the rate of anodic dissolution of iron [100]. This has been the underlying principle of mitigating corrosion rate of wet gas carrying gas pipelines using pH-stabilisation [100, 101] where corrosion rate has been significantly reduced to 0.1 mm/yr. However, by cconsidering the fact that pH plays such a critical role in influencing both the kinetics of corrosion reactions [100, 103] as well as the morphology and composition of corrosion products [100, 102], it has also been envisioned that the initiation and propagation of pitting corrosion may also be affected by solution pH. Pitting corrosion such circumstances could be occurring even when the general corrosion rate of 0.1 mm/yr is attained. Based on the literature review on CO_2 corrosion (chapter 3 of this thesis), three starting solution pH regimes of 3.8 (un-buffered), 6.6 and 7.5 were evaluated in an effort to create three distinctly different corrosion films on the steel surface which would all theoretically offer varying levels of protection to the substrate. Solution pH values of 6.6 and 7.5 at the start of the tests were achieved by adding sodium hydrogen trioxo-carbonate (III) ($NaHCO_3$) into the test solution as provided in Table 8-1.

Table 8-1 $NaHCO_3$ required for different levels of pH for in a 3.5 wt. % solution at 50°C

pH	Amount of $NaHCO_3$ used as buffer (g) per 2L solution
3.8 (un-buffered)	Nil
6.6	≈10
7.5	≈250

8.1.1 Tafel Polarisation and corrosion rate measurements

Tafel polarisation results presented in this section are to show the electrochemical behaviour of carbon steel in the three solution pH regime under investigation and also for estimation of Tafel constants for accurate estimation of corrosion rates. Figure 8-1 shows the Tafel plots obtained by performing separate anodic and cathodic sweeps as already described in section 5.4 of this thesis after a few hours of immersion in the test solution. For test solutions at pH of 6.6 and 7.5, the potentiodynamic sweeps were carried out once stable corrosion potential is established and active currents is still measurable. This was to elucidate the influence of pH on the electrochemical processes.

The Tafel polarisation curves in Figure 8-1 correspond to solutions of starting pH of 3.8, 6.6 and 7.5. Table 8-2 indicates the measured Tafel constants and the resulting Stern-Geary coefficient which was used with the polarization resistance (R_p) to determine corrosion rate as a function of time, after taking into account solution resistance (solution resistance was very low and ranged between 4-7 Ohm.cm^2). Figure 8-1 indicates signs of passivation occurring on the steel surface exposed to the solution of pH 7.5 higher anodic potentials.

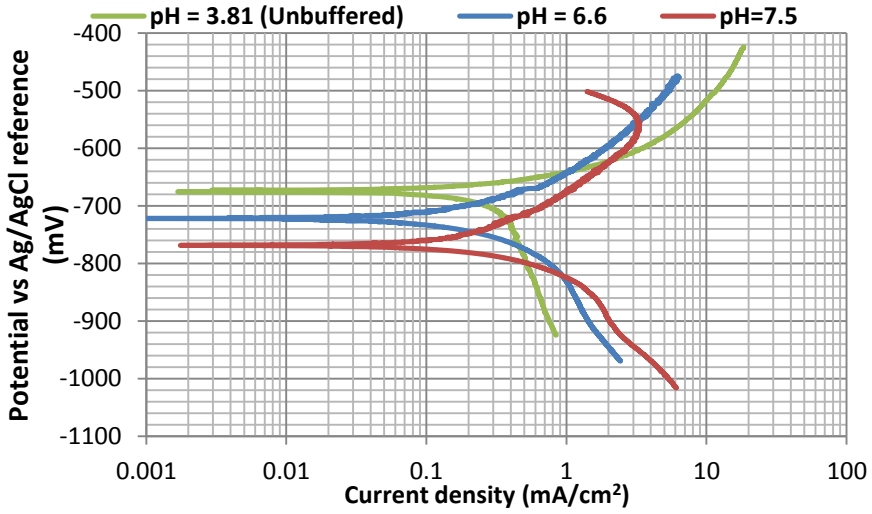

Figure 8-1 Tafel plots for X65 carbon steel in 3.5 wt.% NaCl solution at 50°C and pH values of 3.8, 6.6 and 7.5.

Figure 8-1 also shows very good consistency with results by several authors [103, 140] to suggest that by increasing the pH, the contribution from the cathodic reduction of H^+ is significantly reduced such that the cathodic reaction line flattens out at lower cathodic potentials and H_2O reduction becomes dominant at higher pH. The extrapolated corrosion current from Figure 8-1 is almost within the same ranges (with only marginal variation) for the three solution

pH because the time it took for electrochemical responses to stabilise in these environments were different (7 hours at pH 3.8 and 6.6, and 2.5 hours at pH 7.5) and this correlates with the initial corrosion rates at these times as shown in Figure 8-2.

Table 8-2 Tafel constants at different *in-situ* pH for X65 in a 3.5 wt. % solution at 50°C

pH	β_a (mV/decade)	β_c (mV/decade)	B (Stern-Geary Coefficient) (mV/decade)
3.8	40	168	14.0
6.6	80	95	18.9
7.5	95	100	21.1

Referring to Figure 8-2(a), at pH 3.8 the corrosion rate increases with time to a peak value of ≈ 3.8 mm/yr, before reducing slowly and stabilising at ≈ 2.8 mm/year. At pH 6.6, the corrosion rate reduces continuously over the test duration, reaching a final corrosion rate of ≈ 0.09 mm/year. At pH 7.5, the initial corrosion rate is in excess of ≈ 3.5 mm/year but reduces rapidly to values of approximately ≈ 0.02 mm/year. The point where the lowest corrosion rate is reached coincides with the onset of a pseudo-passivation effect of the steel surface for test at pH 7.5, which is indicated by the increase in potential of the steel surface from -770 to in excess of ≈ -250 mV. The pseudo-passivation effect occurred after 1-2 days as expected from the results by Han *et al* [91] given the similarity between these conditions and those conducted by Han *et al* [91] .

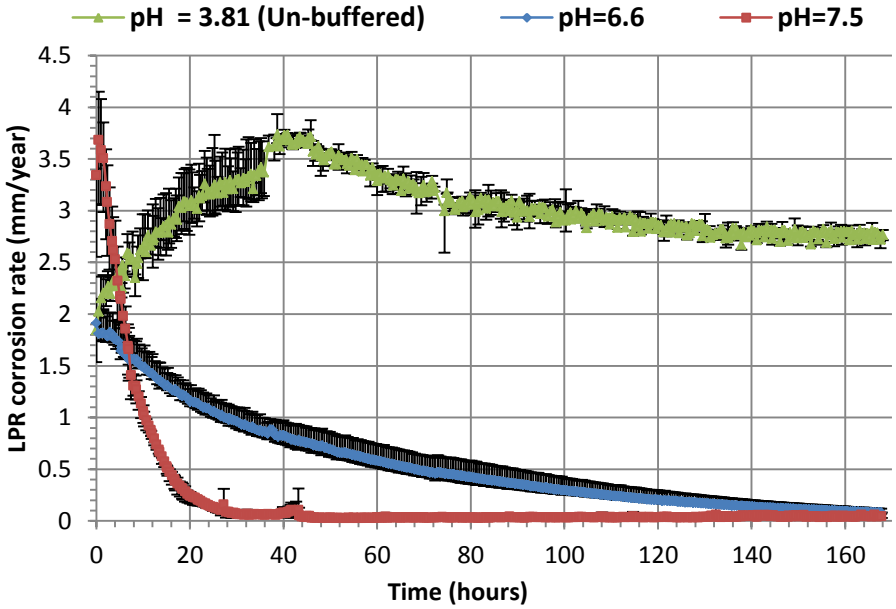

(a)

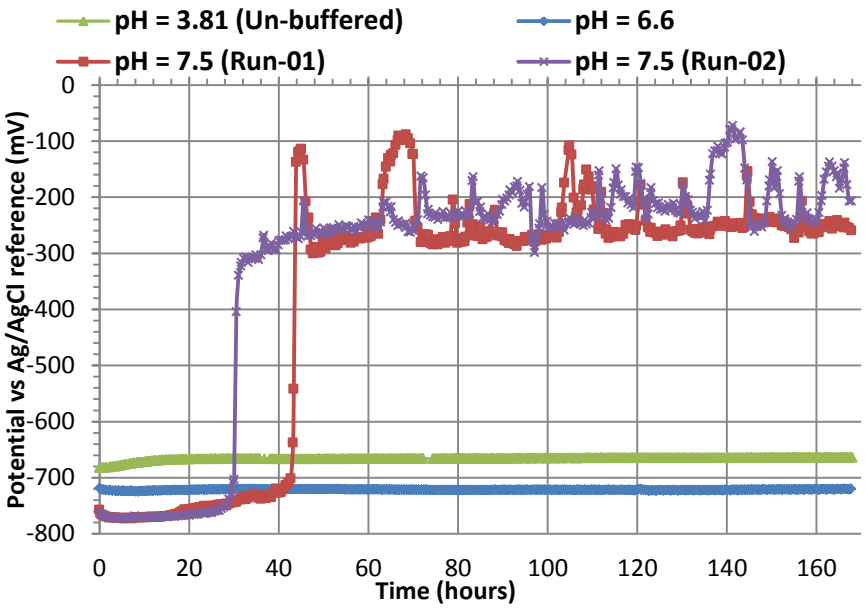

(b)

Figure 8-2 (a) LPR corrosion rate and (b) E_{corr} over 168 hours for X65 carbon steel in a 3.5 wt.% NaCl solution at 50°C and solution pH values of 3.8, 6.6 and 7.5. All graphs represent averages of four repeatable experiment except the OCP reading for pH 7.5, where repeats are shown individually for clarity due to the passivation process.

8.2 Correlating corrosion behaviour with surface morphology of corrosion products

This section of this thesis presents and discusses the correlation between the corrosion product morphology formed in corrosion environment at starting pH values of 3.8, 6.6, and 7.5 and the measured corrosion rates in these test environments.

8.2.1 Corrosion rate and evolution of corrosion products at pH of 3.8

SEM images of the X65 surface when exposed to the solution at pH 3.8 (unbuffered) at the start of the experiment are provided in Figure 8-3. The evolution of corrosion product in this condition is expected to be similar to the evolution of corrosion product in 10 wt. % NaCl as already discussed in sections 6.5 and 7.2. Since details of the evolution of corrosion products in 3.5 wt.% NaCl at 50°C was not described in section 7.2 (Just SEM images for 7 and 168 hours), the SEM images presented in Figure 8-3 is aimed at providing more details in this condition.

Referring to Figure 8-2 (a), over the first 7 hours, the corrosion rate increases in conjunction with the corrosion potential. Figure 8-3(a) indicates the presence of Fe_3C on the steel surface after 7 hours whose evolution is believed to be predominantly responsible for the change in corrosion rate and corrosion potential by promoting the cathodic reaction on the steel surface

[86, 88, 165]. After 36 hours, corrosion rates reach a maximum and begin to reduce in conjunction with the formation of a 'smudge-like textured' corrosion product on the steel surface after 168 hours (shown in Figure 8-3(b) to (d)). A similar description on the development of this surface corrosion product has already been presented in sections 6.5.2 of this thesis and was found to consist of nano-crystalline or an amorphous-like form of $FeCO_3$.

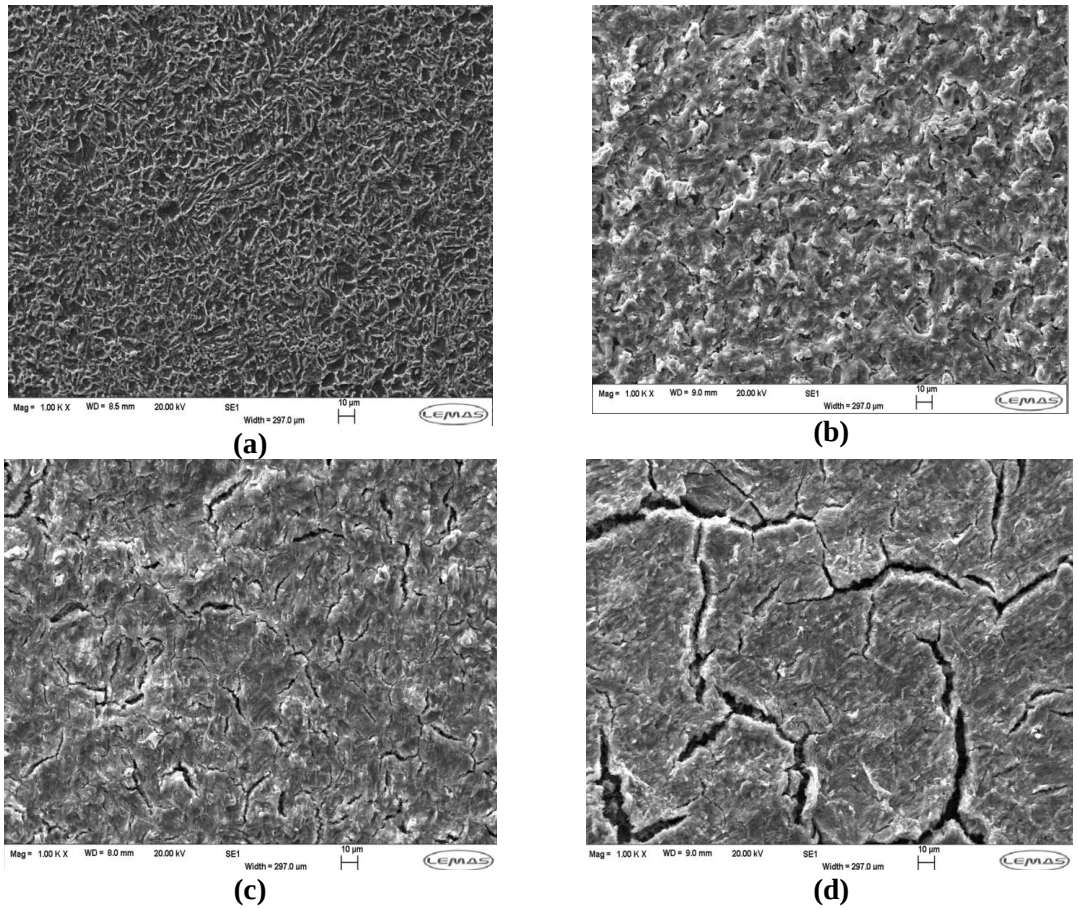

Figure 8-3 SEM images of surface films present on X65 carbon steel after exposure to 3.5 wt. % NaCl solution at 50°C and pH of 3.8 for a period of (a) 7 hours, (b) 36 hours, (c) 72 hours and (d) 168 hours.

The amorphous layer was shown to build up over time along with some localised crystals of $FeCO_3$ after 168 hours. It appears that the amorphous film is capable of offering slight protection to the steel surface. The XRD pattern provided in Figure 8-4 also confirms the presence some localised crystals of $FeCO_3$ after 168 hours.

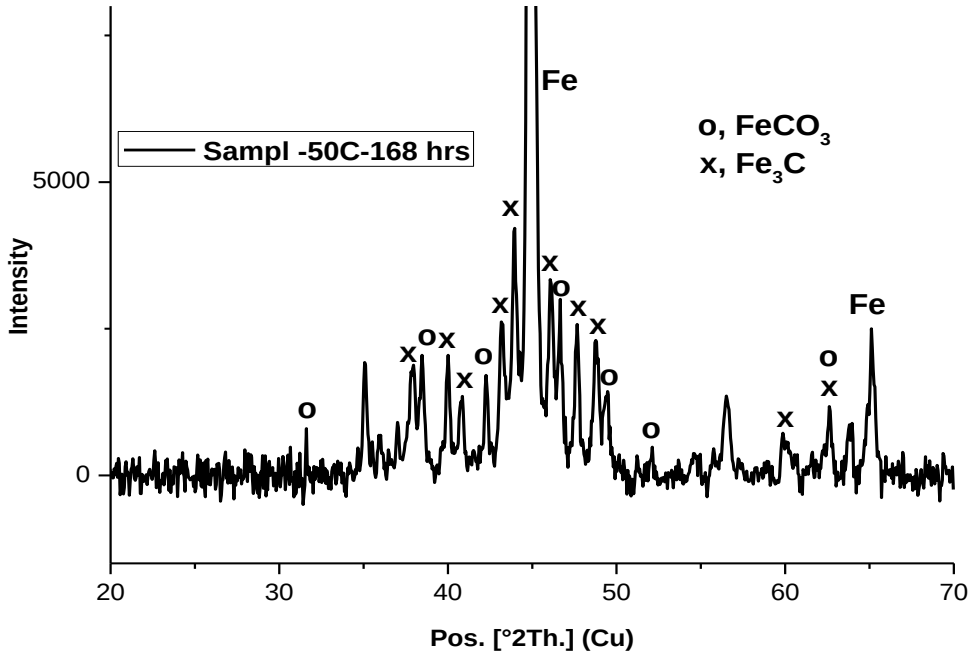

Figure 8-4 XRD pattern for corrosion product on X-65 steel after exposure to an un-buffered 3.5 wt. % NaCl solution at a starting pH of 3.8 for 168 hours at 50°C *(Note that the intensity scale is arbitrary)*.

8.2.2 Corrosion rate and evolution of corrosion products at pH 6.6

SEM images of the X65 steel surface after exposure to the pH 6.6 solution after 7, 36, 72 and 168 are provided in Figure 8-5. A higher solution pH has resulted in the faster rate of formation of $FeCO_3$ crystals which have already nucleated on the steel surface after 7 hours (Figure 8-5 (b)). A higher bulk pH significantly decreases the solubility of $FeCO_3$, resulting in its precipitation. In these particular conditions, Dugstad [78] determined that the solubility of ferrous ions required is only a fraction of a ppm, as opposed to an expected ferrous ion concentration of over 100 ppm in the bulk solution at pH 3.8. Consequently, $FeCO_3$ precipitation is far more favourable at the higher pH and has resulted in the formation of a crystalline corrosion product layer in this condition.

After 36 hours, the nucleated crystals have grown on the steel surface from 1-2 µm to over 10 µm in width (Figure 8-5 (b)). In conjunction with this behaviour, the corrosion rate also declines over this period as a result of the $FeCO_3$ crystals blocking active sites on the steel surface. From 36 hours onwards, there is continued nucleation and growth of the $FeCO_3$ crystals which results in a substantial layer being formed. From this point, the $FeCO_3$ corrosion products has the

ability to also act as a diffusion barrier to electrochemically active species involved in the charge-transfer reaction on the steel surface.

By considering Figure 8-5(c) and (d), it is evident that areas still exist on the steel surface where the electrolyte has a direct pathway to the steel surface (see Figure 8-5(d) in particular). However, extensive SEM analysis indicated that the number and size of these localised regions did reduce significantly, even between 72 and 168 hours as crystals continued to grow. The XRD pattern is provided for steel sample after 72 and 168 hours in Figure 8-6 to confirm the iron carbonate corrosion layer.

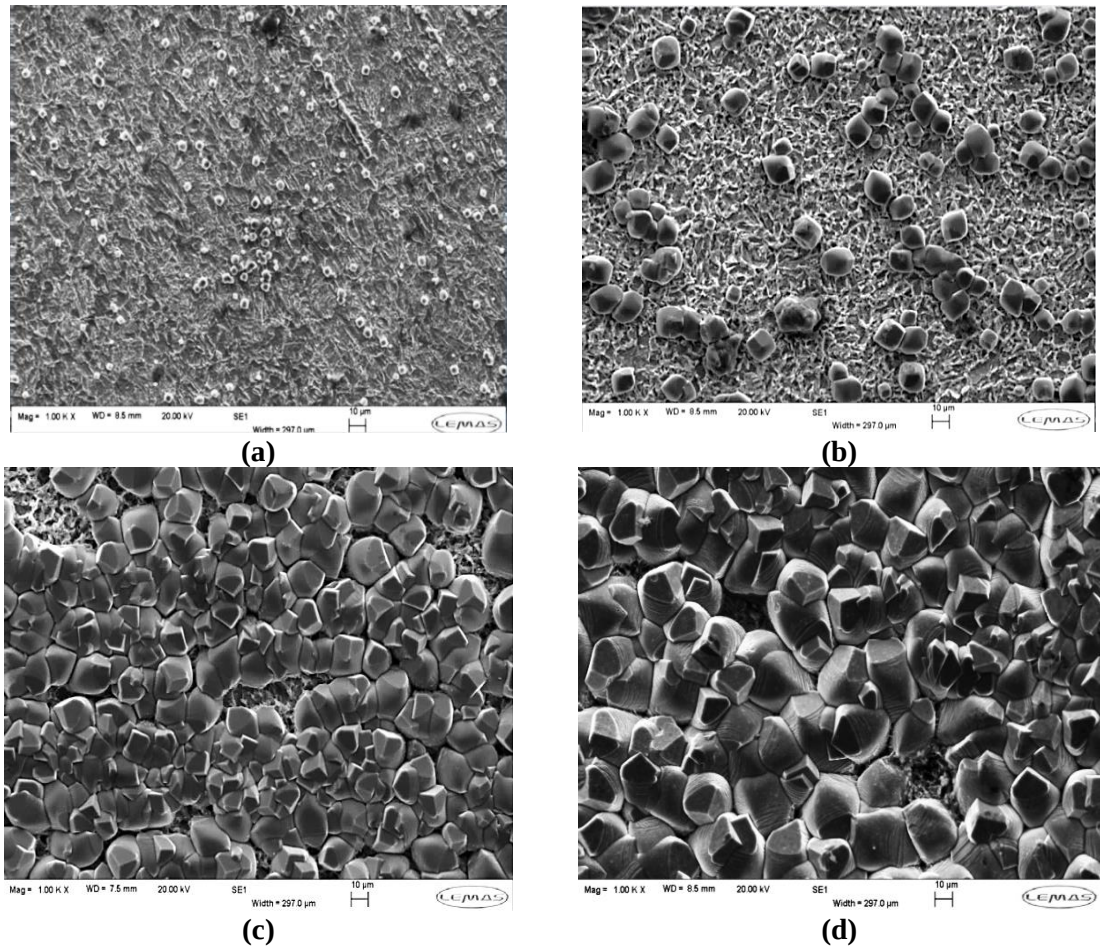

Figure 8-5 SEM images of surface films present on X65 carbon steel after exposure to 3.5 wt.% NaCl solution at 50°C and pH of 6.6 for a period of (a) 7 hours, (b) 36 hours, (c) 72 hours (d) 168 hours.

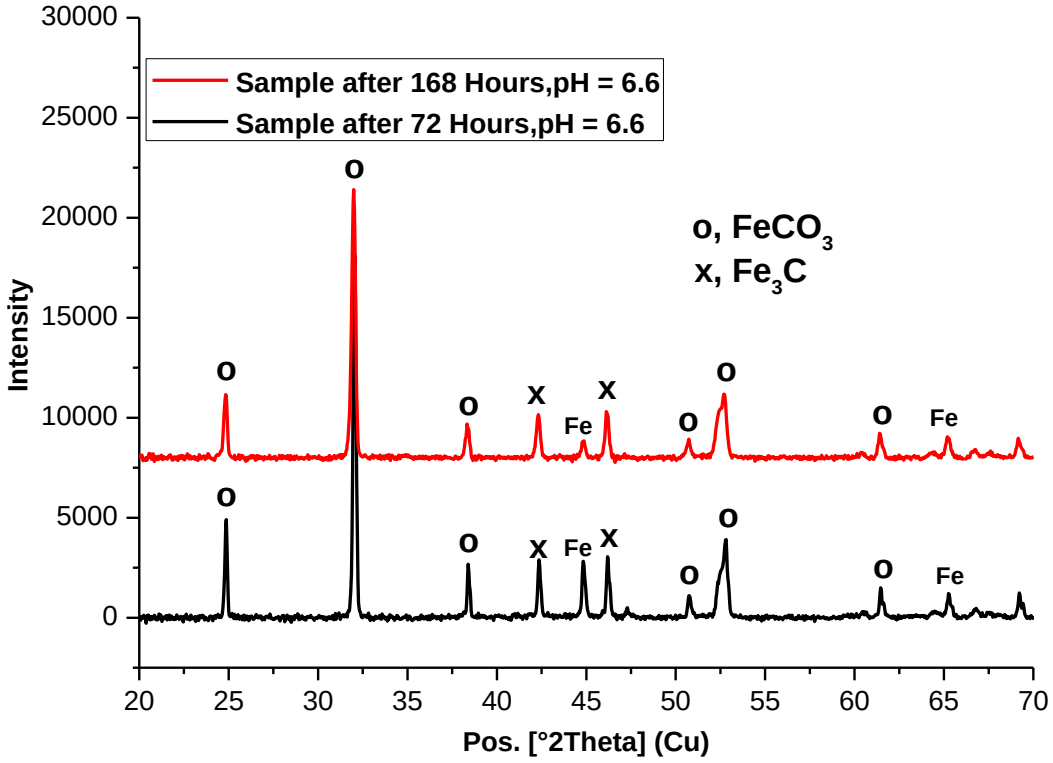

Figure 8-6 XRD pattern for corrosion product on X-65 steel after exposure to 3.5 wt. % NaCl solution at a starting pH of 6.6 for 168 hours at 50°C *(Note that the intensity scale is arbitrary)*.

8.2.3 Corrosion rate and evolution of corrosion products at pH of 7.5

SEM images of the X65 steel surface exposed to the pH 7.5 solution for 7, 36, 72 and 168 hours are provided in Figure 8-7. With a higher system pH of 7.5, an even more substantial levels of $FeCO_3$ precipitation occurred earlier in the experiment than at an *in-situ* pH of 6.6. This was attributed to a further reduction in the solubility of $FeCO_3$ in the bulk solution as a result of the increase in pH. Pseudo-passivation on this particular sample occurred after 40 hours (see Figure 8-2(b)). No significant change in the top view morphology of the film was observed between 36 and 72 hours, other than the film becoming more extensive. It has been suggested that the pseudo-passivation effect occurs underneath the film [92] . Regrettably, the nature of this pseudo-passive film could not be identified using XRD in this instance. However, it is clear that 'pseudo-passivation' had occurred based on the significant change in corrosion potential towards a positive potential. As mentioned previously, it has been suggested by Han *et al* [92] that the pseudo-passive film comprises of Fe_3O_4. However, this was not confirmed in this work.

In this condition, a significant proportion of the surface was covered in $FeCO_3$ crystals after 7 hours (Figure 8-7(a)). The corrosion products were of a very different structure to those observed at pH 6.6. The crystals formed at pH 7.5 consist of a platelet/prism structure with sharper, more defined edges and corners as opposed to the rounded-edged cubic crystals observed at pH 6.6. After 36 hours, the entire surface was almost entirely covered by $FeCO_3$ crystals. Very little changes were observed from the top view SEM images from 36 hours onwards. The only noticeable change was an increase in crystal size.

Figure 8-8 shows the XRD pattern for the corrosion product layer for carbon steel in 3.5 wt. % NaCl solutions at 50˚C after 72 and 168 hours at pH 7.5. The XRD pattern of Figure 8-8 confirms the formation of an extensive layer of crystalline $FeCO_3$ crystals at pH 7.5.

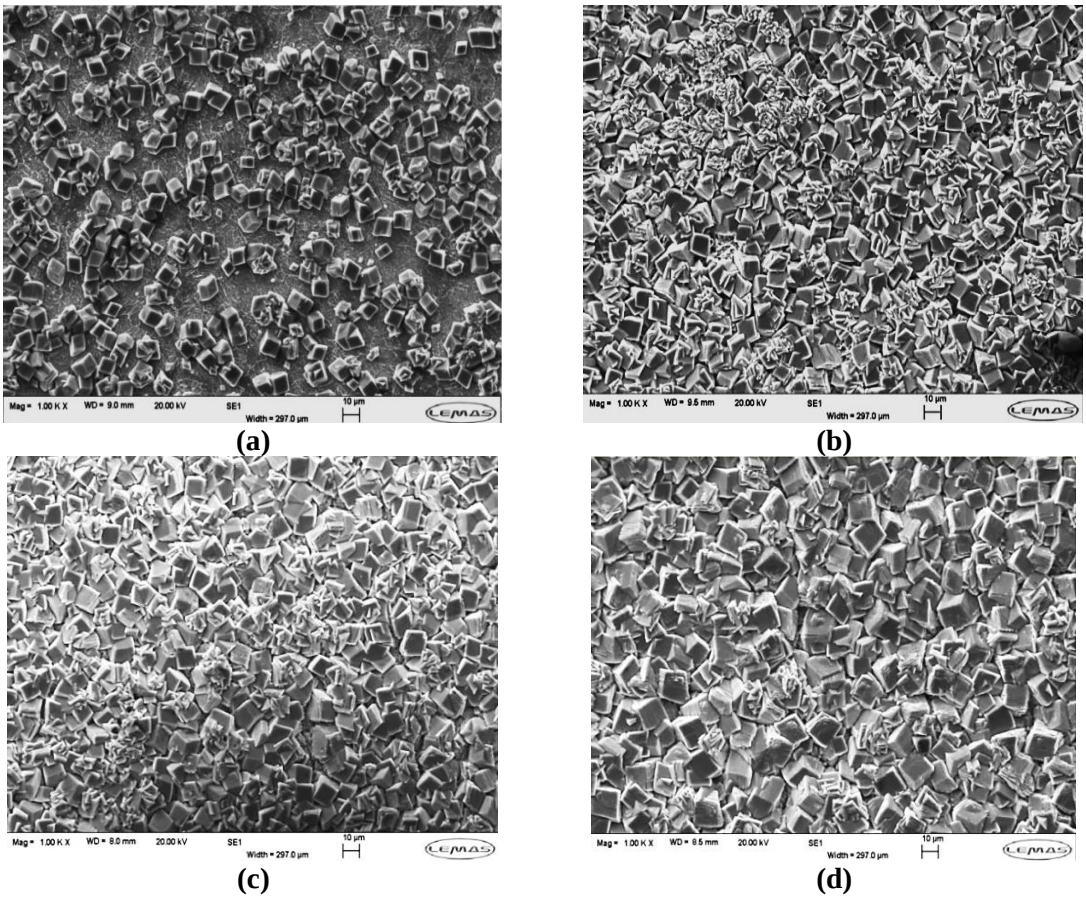

Figure 8-7 SEM images of surface films present on X65 carbon steel after exposure to 3.5 wt.% NaCl solution at 50°C and pH of 7.5 for a period of (a) 7 hours, (b) 36 hours,(c) 72 hours and (d) 168 hours.

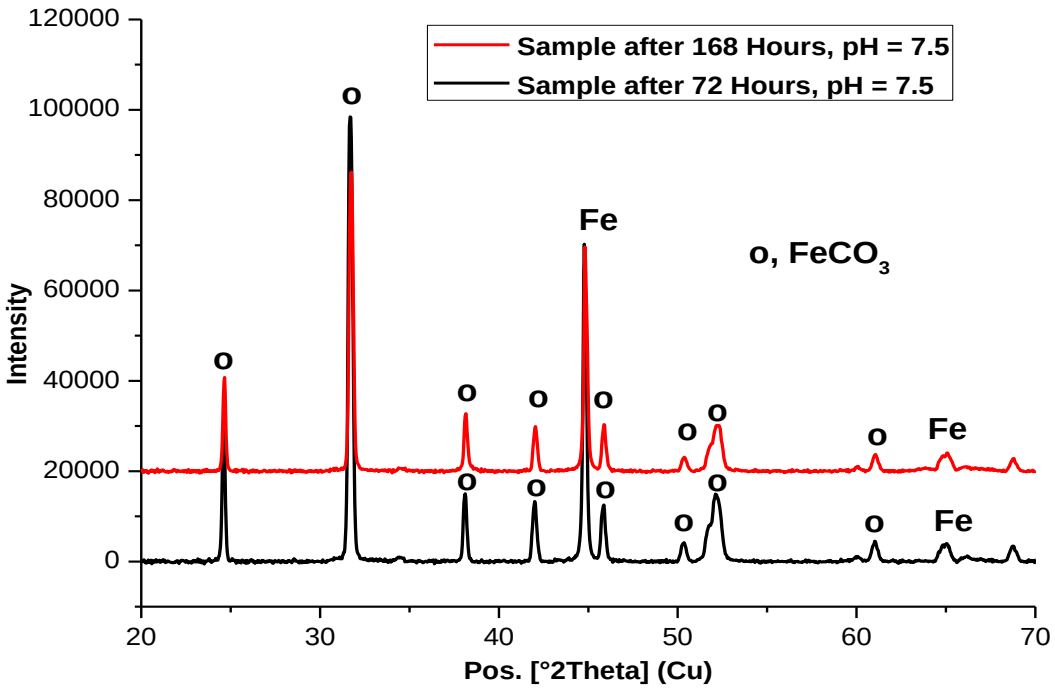

Figure 8-8 XRD pattern for corrosion product on X-65 steel after exposure to 3.5 wt. % NaCl solution at a starting pH of 7.5 for 168 hours at 50°C *(Note that the intensity scale is arbitrary)*.

8.3 Correlating pitting behaviour with surface morphology, corrosion rate and open circuit potential

The main focus of this section of this research work is to assess and establish the link between the pitting behaviour, the surface morphology of corrosion products and electrochemical response of the carbon steel sample. Figure 8-9 shows the maximum and average pit depths measured on the sample surface in relation to the linear polarisation corrosion rate and open circuit potential measurements for each test performed at a starting pH 3.8, 6.6 and 7.5.

Referring to the tests at pH 3.8 (Figure 8-9(a) and (b)); pit growth is continuous and linear throughout the entire experiment. The formation of the amorphous-like $FeCO_3$ appears to have little influence on reducing pit growth, which is logical given that the film has had little impact on reducing the general corrosion rate on the steel surface. Pits reached a depth of 50 µm by the end of the experiment. Experiments performed at pH 6.6 (Figure 8-9 (c) and (d)) show a marked difference in comparison to those at pH 3.8. Pit growth over the first 72 hours is very slow, where only a depth of 13 µm is reached (half that at pH 3.8 after the same exposure time). Interestingly, between 72 and 120 hours, there is a significant increase in pit depth.

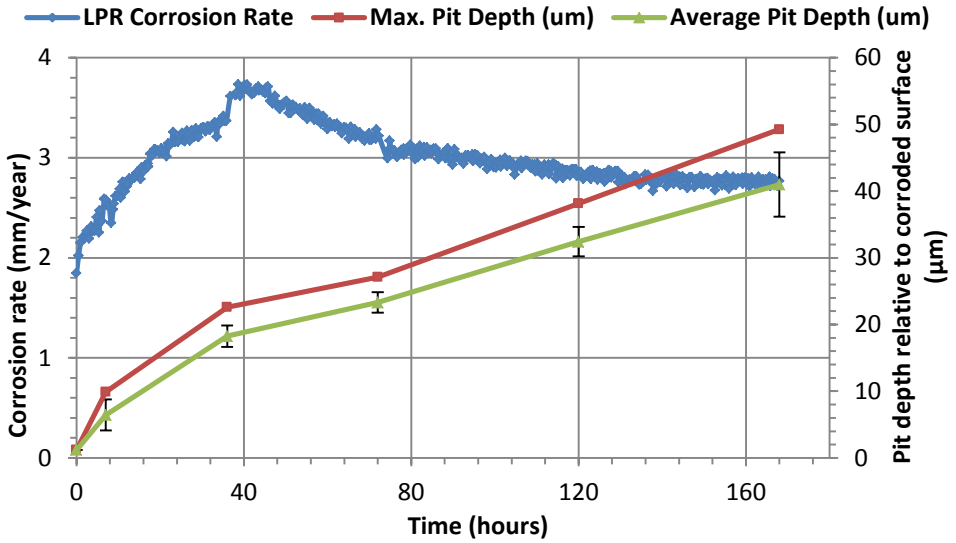
LPR Corrosion Rate
Max. Pit Depth (um)
Average Pit Depth (um)
Corrosion rate (mm/year)
Pit depth relative to corroded surface (µm)
Time (hours)
0
1
2
3
4
0
10
20
30
40
50
60
0
40
80
120
160

(a)

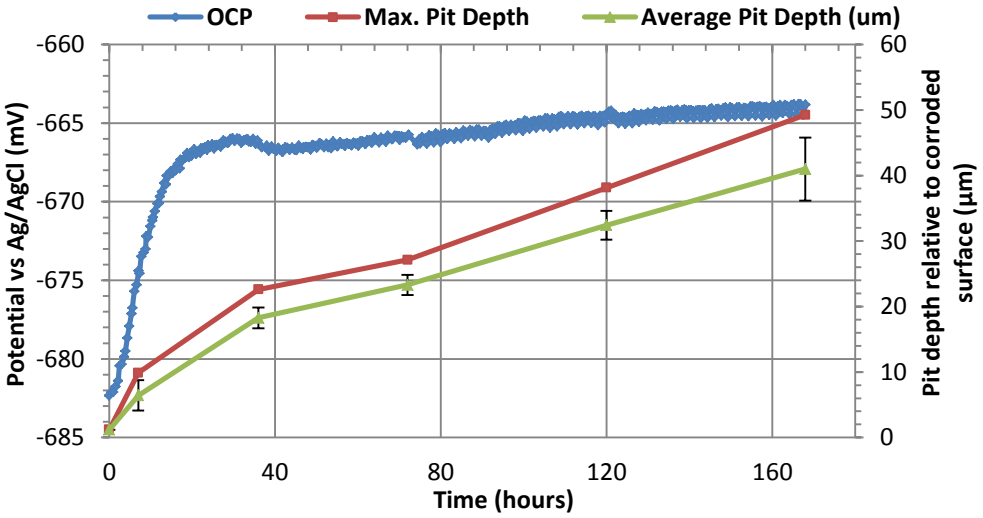
OCP
Max. Pit Depth
Average Pit Depth (um)
Potential vs Ag/AgCl (mV)
Pit depth relative to corroded surface (µm)
Time (hours)
-660
-665
-670
-675
-680
-685
0
10
20
30
40
50
60
0
40
80
120
160

(b)

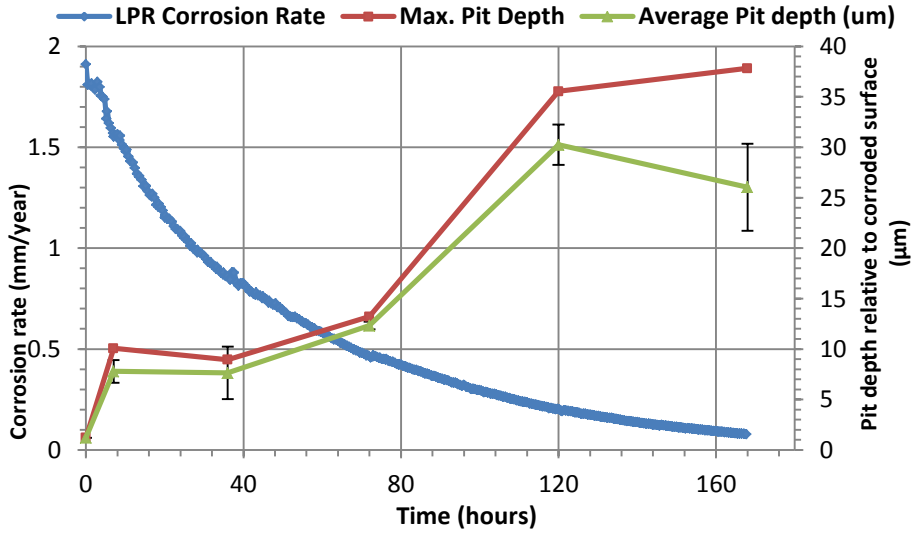
LPR Corrosion Rate
Max. Pit Depth
Average Pit depth (um)
Corrosion rate (mm/year)
Pit depth relative to corroded surface (µm)
Time (hours)
0
0.5
1
1.5
2
0
5
10
15
20
25
30
35
40
0
40
80
120
160

(c)

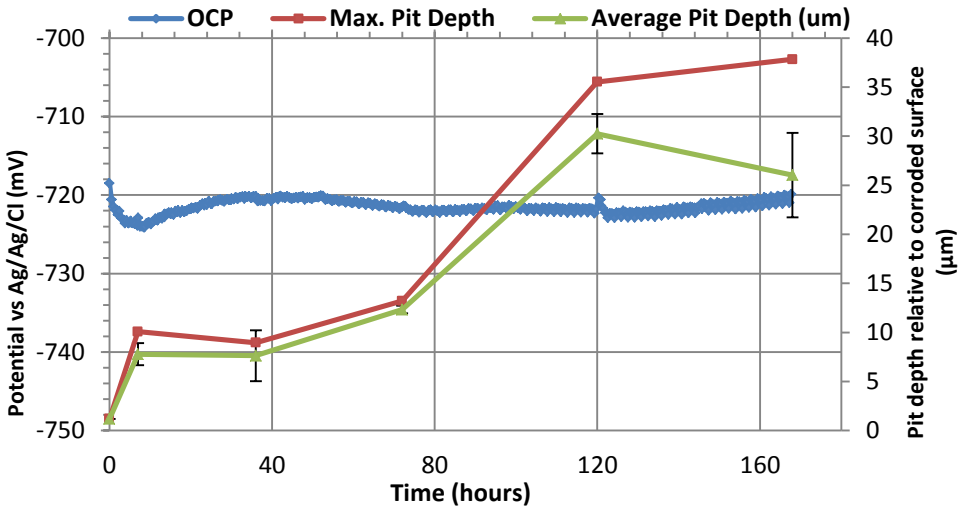

(d)

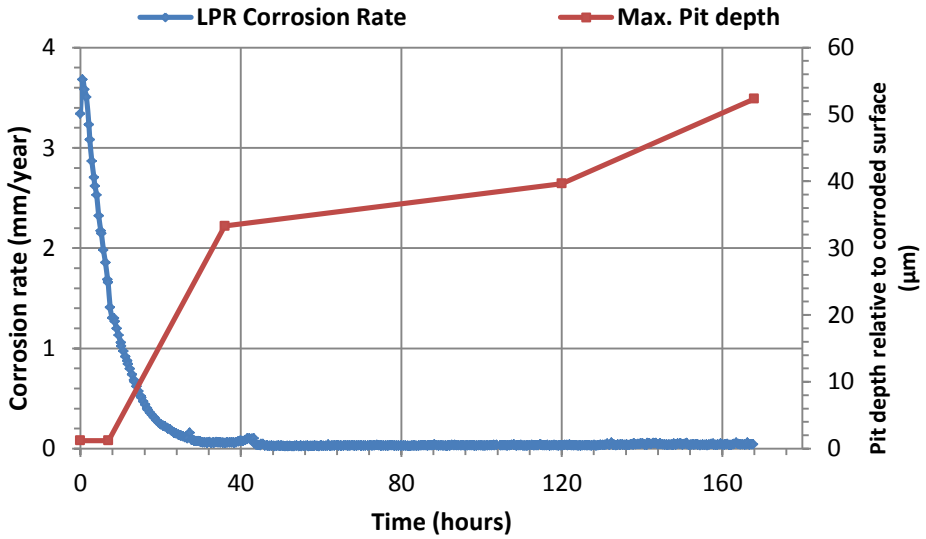

(e)

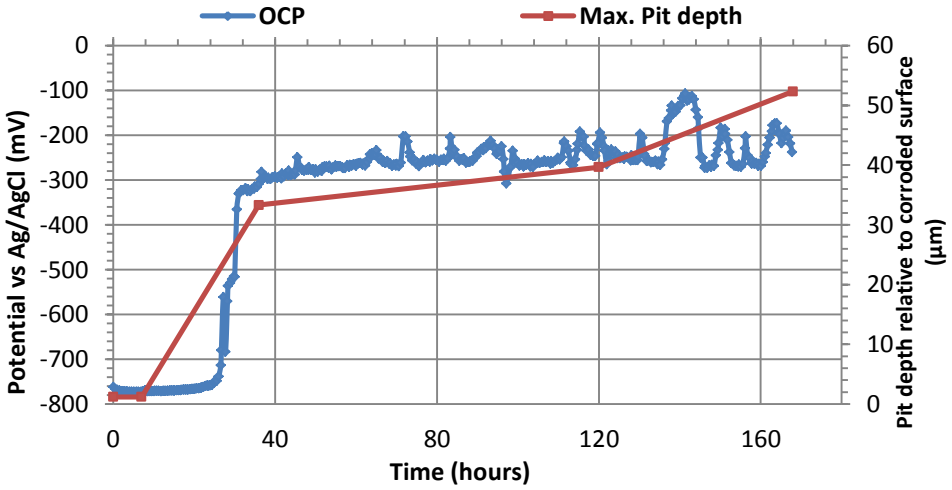

(f)

Figure 8-9 Pit growth in conjunction with LPR corrosion rate and OCP measurements for (a)/ (b) pH 3.8, (c)/ (d) pH 6.6 and (e)/ (f) pH 7.5.

The observed pit growth occurs in conjunction with the high degree of surface coverage of the $FeCO_3$ film, as shown in the SEM images in Figure 8-5. It is very likely that the small cavities in the $FeCO_3$ films have resulted in the increase in regions of localised attack and the accelerated growth in pit depth. Once these voids become filled through further precipitation, the pit growth is decelerated as shown in the pit depth values at 168 hours. The formation of the extensive $FeCO_3$ film appears to have reduced the pit propagation.

At pH 7.5, only maximum pit depths are presented in Figure 8-9(e) and (f) due to the limited number of pits identified on the entire steel surface. After 7 hours, no pits were identified on the entire steel surface. However, after the pseudo-passivation process, pits in excess of 30 μm were clearly recorded. By considering the maximum pit depths, it appears that pit growth continues under the passive regime, but at a much slower rate than that recorded at pH 3.8. In order to verify the repeatability of this observation, another sample from a separate test was analysed for pits and gave exactly similar trend with a maximum pit depth of ≈ 52 and 42 μm from test 1 and 2 respectively. Visual evidence of this is provided in Figure 8-12(c) and (d). The results suggest that the pseudo-passivation process results in the initiation and propagation of pits on the steel surface, but once E_{corr} stabilises, the rate of pit growth is reduced. Further research is required to explore the relationship between E_{corr} and pit growth when pseudo-passivation of steel occurs.

8.3.1 Concept of total metal penetration and pitting factor

The concept of total metal penetration rate as an effective tool for characterising the actual threat posed to carbon steel pipework subject to pitting corrosion has already been described and explored in section 6.6.4 of this thesis. This is a very imortant tool because the potential failure of a pipeline will depend not only upon the rate at which pits propagate relative to the corroding surface, but also on the uniform corrosion rate of the surrounding area.Figure 8-10 introduces the concept of total pit penetration depth or total metal penetration depth, which is essentially the contribution of the average thickness loss determined from linear polarisation corrosion measurements in addition to the pit depth relative to the corroding surface from profilometry measurements.

Referring to Figure 8-10, the change in total penetration depth (i.e. uniform thickness plus pit depth relative to the corroded surface) as a function of time can be observed for each solution pH. The results indicate that due to the substantial general corrosion rate of the sample exposed to the pH 3.8 solution, the total metal penetration depth far exceeds that of the samples exposed to the higher pH solutions, where the uniform thickness loss is negligible in comaprison to the

pit depth. It could be considered that the high general corrosion rate observed at pH 3.8 has the ability to essentially mask pit growth. Metal penetration and/or pitting corrosion may be occuring at a faster rate than usually identified from purely the profilometry depth measurements relative to the corroding surface.

For tests performed at pH 6.6 and 7.5, the growth of the pit is not significantly masked by the general corrosion rate. The results shown in Figure 8-10 also suggest that increasing solution pH does not necessarily reduce the risk of pitting of carbon steel pipelines.

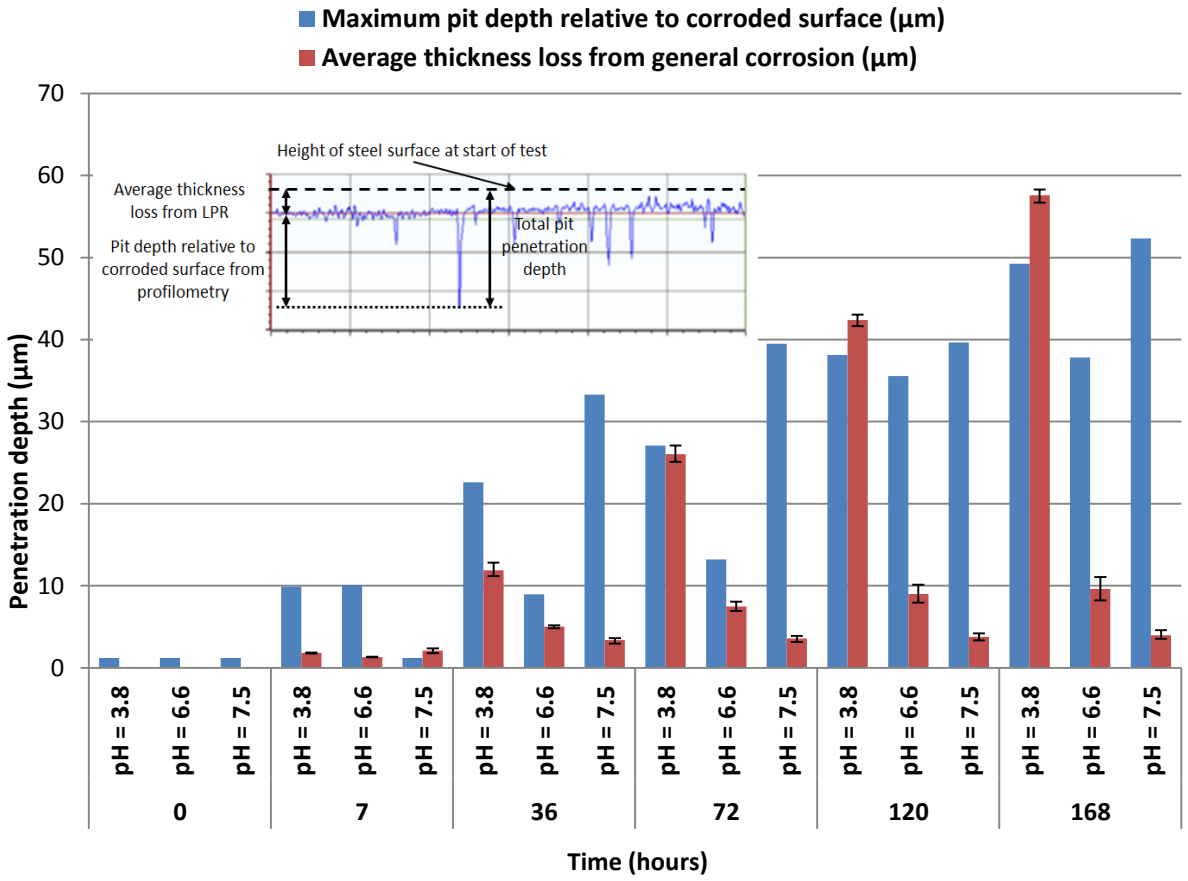

Figure 8-10 Total pit penetration on steel surface for each system pH as a fuunction of time indicating the contribution of general thickness loss (from LPR) and pit depth relative to corroded surface (determined from surface profilometry).

8.3.2 Pitting factor, pit count and pit morphology

The concept of pitting factor(P_f) has been introduced as a tool for characterisation of the nature of corrosion damage and has been defined in section 6.6.4. The pitting factor was used to reflect the relative contribution of the corrosion damage mechanism (between uniform and pitting corrosion) at each experimental sampling time.

The pitting factor analysis presented in Figure 8-11 are a clear indication that the corrosion damage mechanism observed at pH 3.8 conditions is actually pitting even while there is still substantial uniform corrosion taking place. At pH 6.6, the pitting factor was higher after 76 hours once significant protection was achieved from precipitated $FeCO_3$ films. This suggests that pitting corrosion dominated the corrosion damage mechanism in this situation once the film became significantly protective. The pitting factor at pH of 7.5 was higher after just 7 hours.

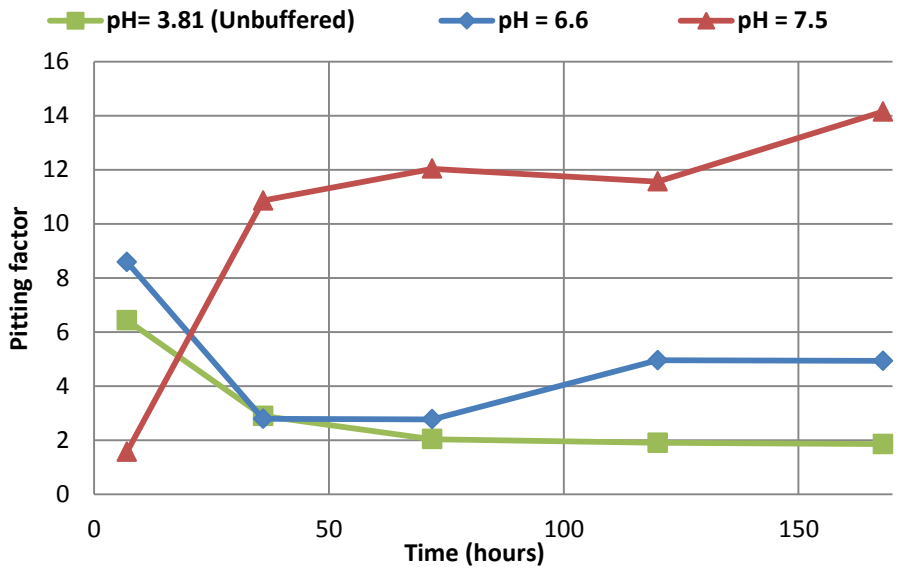

Figure 8-11 Variation of pitting factor for steel surface exposed to each system pH as a function of time.

Figure 8-12 (a), (b), (c) and (d) also provides combined 2D and 3D images as examples of pit morphologies for the tests conducted in solution at pH values of 3.8, 6.6 , 7.5 from test-1 and 7.5 from test-2 after 168 hours espectively. Although no quantative pit count was conducted, the number of pits on the surface were observed to significantly reduce with an increase in solution pH.

At pH 7.5, only 4-6 pits above a depth of 10 µm were observed on the entire steel surface after 168 hours. The difficulty in locating pits under these conditions highlights the importance of ensuring that the entire steel surface is scanned in order to accurately determine the true susceptibility of the surface to pitting corrosion, particularly at high pH when the steel enters a pseudo-passive regime.

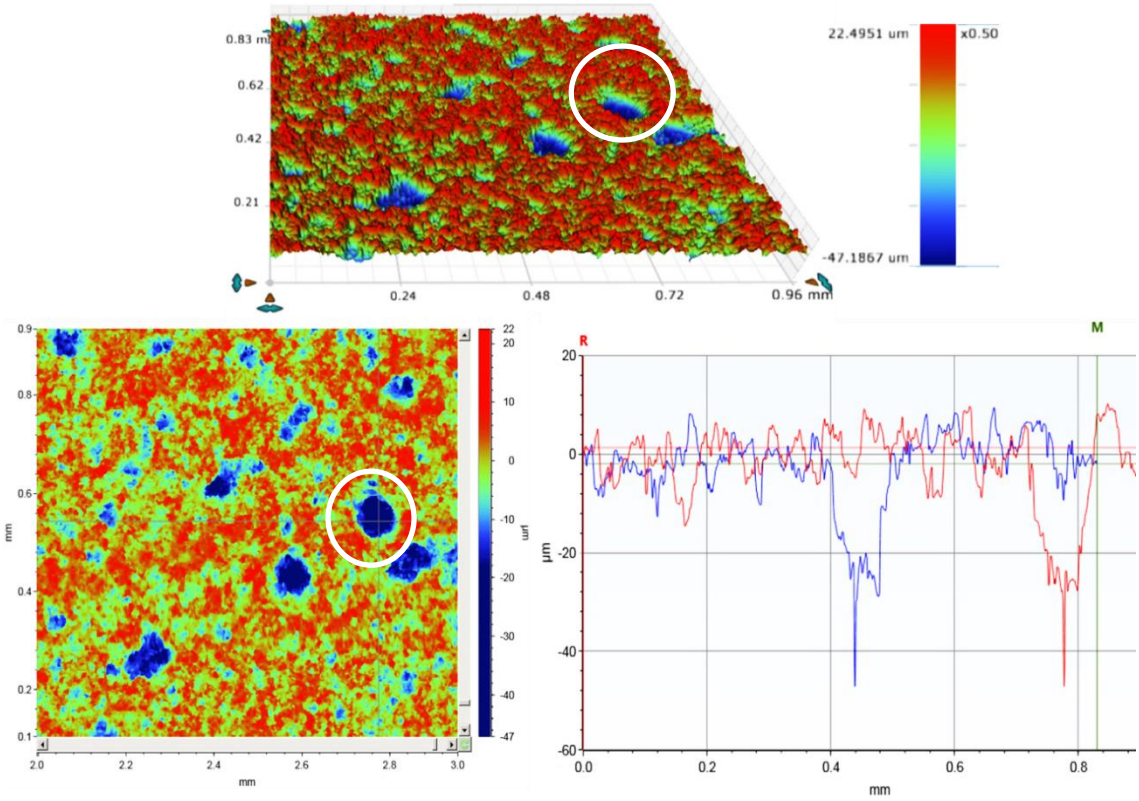
22.4951 um
x0.50
-47.1867 um
0.83 mm
0.62
0.42
0.21
0.24
0.48
0.72
0.96 mm
R
M
20
0
-20
-40
-60
µm
0.0
0.2
0.4
0.6
0.8
mm
0.9
0.8
0.6
0.4
0.2
0.1
2.0
2.2
2.4
2.6
2.8
3.0
22
20
10
0
-10
-20
-30
-40
-47
µm

(a)

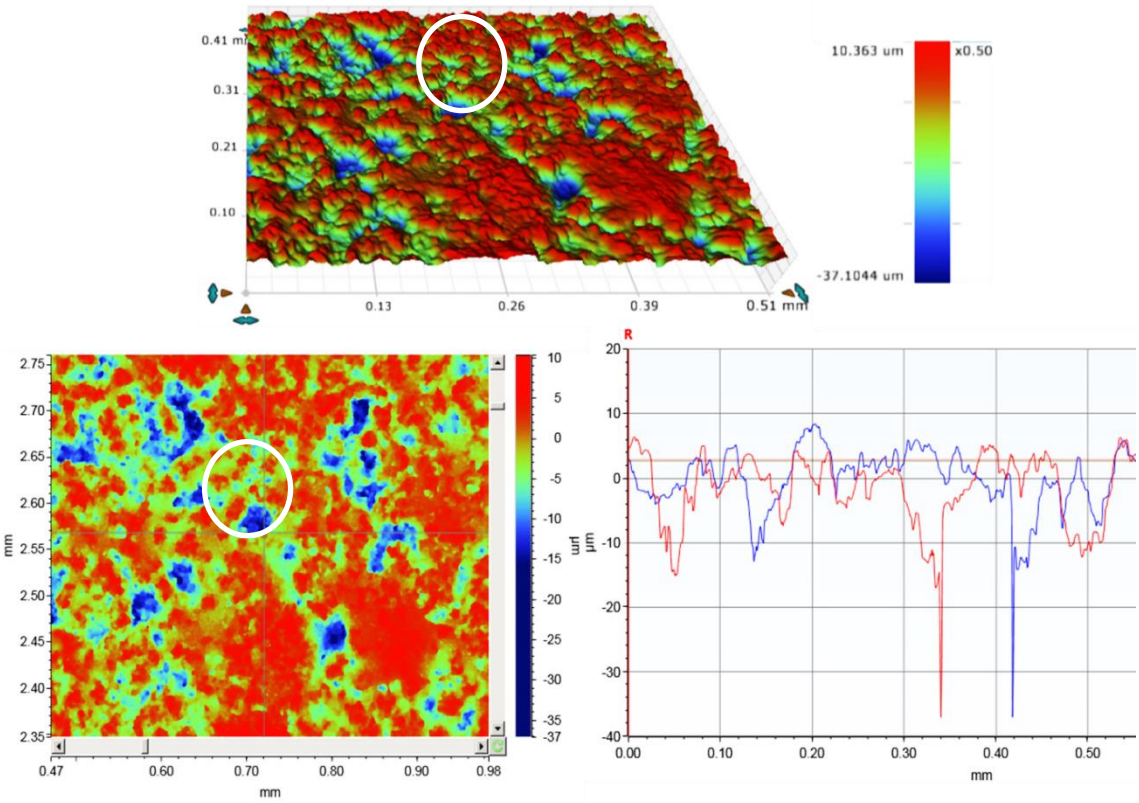
10.363 um
x0.50
-37.1044 um
0.41 mm
0.31
0.21
0.10
0.13
0.26
0.39
0.51 mm
R
20
10
0
-10
-20
-30
-40
µm
0.00
0.10
0.20
0.30
0.40
0.50
mm
2.75
2.70
2.65
2.60
2.55
2.50
2.45
2.40
2.35
0.47
0.60
0.70
0.80
0.90
0.98
10
5
0
-5
-10
-15
-20
-25
-30
-35
-37
µm

(b)

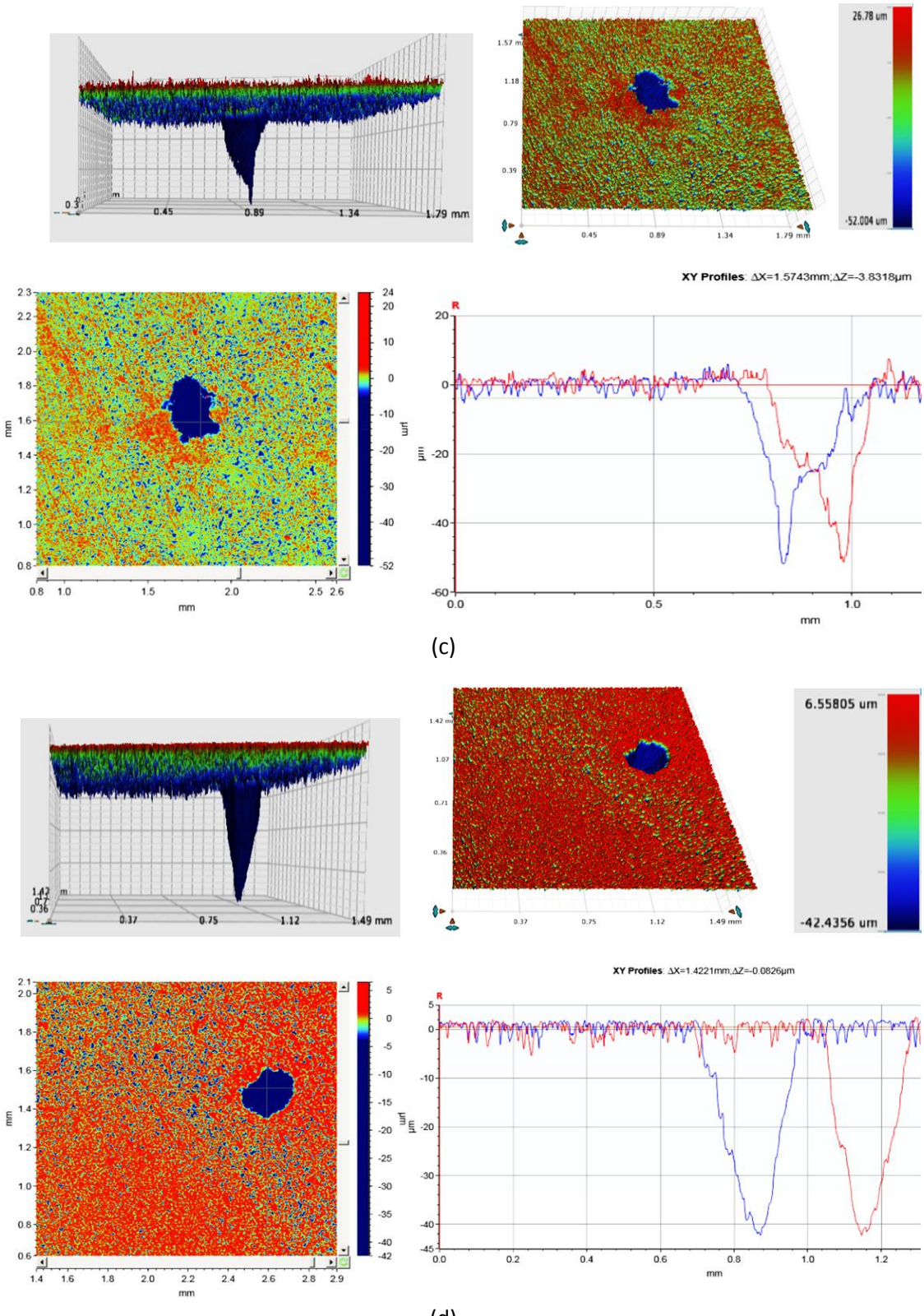

Figure 8-12 2D and 3D profilometry images to indicate the morphology and quantity of pits observed on the steel surface after 168 hours exposure to CO_2-saturated brine at a pH of (a) 3.8, (b) 6.6 (c) 7.5 from test-1 and (d) 7.5 from test-2.

8.3.3 Summary on the influence of pH of bulk solution on pitting and uniform corrosion behaviour of carbon steel in CO_2-saturated brines

The results presented and discussed in this section of the thesis has shown that for solutions at different bulk pH; starting pH value of 3.8 (unbuffered), pH value of 6.6 and pH value of 7.5, three different combinations of corrosion products were produced on the surface of X65 carbon steel in 3.5 wt.% NaCl at 50°C. A non-protective and porous network of Fe_3C layer was revealed with traces of an amorphous-like product (believed to be $FeCO_3$), a protective iron carbonate film was produced, and pseudo-passive film composed of a very protective $FeCO_3$. For all three pH values explored, pitting corrosion was observed but to varying degree and profile, even while there were significant reduction in the uniform corrosion rate at higher pH values.

Chapter 9. Investigation of the early stages of general and pitting corrosion in sour corrosion environments; Effect of CO_2 and H_2S and temperature

9.1 Introduction

This chapter presents and discusses results of experiments conducted to investigate the corrosion behaviour of X65 carbon steel materials in H_2S-containing environments. In this aspect of this study, experimental conditions were developed to explore and understand the potential effect of temperature and the combining gases (CO_2 and H_2S) on the corrosion processes; corrosion kinetics, corrosion product layer formation, and the overall corrosion damage (general and/or pitting corrosion). The potential synergy between temperature and the combining gases will also be described in this Chapter. Although the emphasis of results presented and discussed in this Chapter will be on corrosion conditions characterised as being sour, all description of results and discussions will be presented in relation to results of experiments conducted in CO_2 corrosion environments. This chapter is divided into two main sections. The first section describes and discusses experimental results focused on investigating the early stages of sour corrosion (over 7 hours); investigation to include pitting corrosion initiation, while the second section focuses on the experimental results from long-term exposure (over 168 hours).

The short-term experimental route was explored to investigate how the fast process of iron sulphide corrosion product formation may be influencing the corrosion behaviour and corrosion damage morphology of carbon steel materials in these environments. It is believed from the literature that iron sulphide corrosion products (mainly mackinawite) form very quickly via solid state reduction reaction. Hence, there is a need to understand how this initially formed iron sulphide corrosion product could possibly be influencing the corrosion initiation kinetics and early growth of FeS corrosion products at the corrosion interface at the earliest possible times. On the other hand, the long-term experimental route was explored to investigate the potential competitive influence of CO_2 corrosion and $FeCO_3$ precipitation (where possible) kinetics in sour corrosion environments as well as the impact of such scenarios on the corrosion damage morphology; general and pitting corrosion over an extended period of exposure. The long-term experimental approach ensures significant time for test solution under H_2S-CO_2 gas atmosphere to be supersaturated with Fe^{2+} and CO_3^{2-} for $FeCO_3$ precipitation.

9.2 Early stages of corrosion behaviour of carbon steel in sour corrosion environments; effect of temperature, CO_2 and H_2S gas

The results presented and discussed in this section are based on 7 hour tests. The experimental matrix for this aspect of the study is based on the three different temperatures and gas phase compositions as provided in Table 5-5 and Table 5-6. Nine (9) different test conditions were created based on Table 5-5. A summary of the partial pressures of the active gas components is already provided in table Table 5-6 (section 5.9). In the context of the experimental conditions listed in Table 5-5, and the envisaged significance of exploring these test conditions without buffering the corrosion environment, the *in-situ* pH of the bulk solution is monitored over the duration of the experiments. However, the results presented and discussed in this section are based on short-term tests; hence an average of the *in-situ* pH of the experimental conditions (Table 5-5) for the first seven hours is provided in Table 9-1. The *in-situ* pH measurement is considered to be an important secondary parameter that needs to be taken into consideration in order to fully understand the possible corrosion reactions and their impact.

Table 9-1 Average measured in-situ pH of solutions under different gas phases for 7 hours

Temperature (°C)	In-situ pH of test solutions		
	100% CO_2	**10mol.% H_2S - 90mol.% CO_2**	**10mol.% H_2S - 90mol.% N_2**
30	4.0 ± 0.2	4.3 ± 0.0	4.7 ±0.0
50	4.1 ± 0.2	4.1 ± 0.1	4.6 ± 0.1
80	4.3 ± 0.3	4.4 ± 0.1	4.8 ±0.1

9.2.1 Tafel Polarisation measurements

The potentiodynamic sweeps for all six experimental conditions under investigation (See Table 5-5), are presented in Figure 9-1, to show the electrochemical behaviour of carbon steel in the three different gas phase composition under investigation at 30, 50 and 80°C.

Referring to Figure 9-1(a)-(b), the three Tafel polarisation curves suggest that in tests under a gas atmosphere of 10 mol.% H_2S - 90 mol.% CO_2, the presence of 10 mol. % H_2S gas, influences the anodic (especially at 30°C) and cathodic reactions at all temperatures. The

influence on the cathodic reaction is more significant than on the anodic reaction (even at 30°C). In sweet environment, the cathodic process is mixed activation – mass transferred controlled, while the cathodic reaction process becomes dominated by direct reduction of H_2S/HS^- in sour environment. This change in the cathodic reaction has been attributed to the suppression of the collective influence of H^+ and H_2CO_3 reduction reaction. The observations from the potentiodynamic curves of Figure 9-1 compares well with the literature [140, 175, 176], especially at 30°C and for 10 mol. % H_2S - 90 mol. % CO_2 gas systems in comparison with 100 mol. % CO_2 corrosion systems. Although the concentration and pH of the H_2S component differs, the trend in variation of corrosion potential and shape of cathodic polarisation lines were similar. At higher temperatures (50°C), the potentiodyanmic curve compares well with the results of Woollam *et al* [176] at 60°C. In terms of the potential effect of a gas phase with H_2S gas as the only active acid gas (10 mol.% H_2S - 90 mol.% N_2), the results shown in Figure 9-1 (a) at 30°C was also very consistent with the published potentiodyanmic curves of Zheng *et al* [119].

The observed change in the potentiodynamic curves as the gas phase composition changes from 100 mol. % CO_2 to 10 mol.% H_2S - 90 mol.% CO_2 and to 10 mol.% H_2S - 90 mol.% N_2, is also clearly having the effect of reduced corrosion rate in the same order. These observations have also been reported at 30°C in an acidic media relative to corrosion rate in 100 mol.% CO_2 gas systems [140, 176]. In some of the literature [140, 176, 177], this observed effect of a lower corrosion rate in H_2S-containing corrosion environment is attributed to the formation of a thin layer of an adsorbed sulphur onto the steel surface (Fe-S_{ad}).

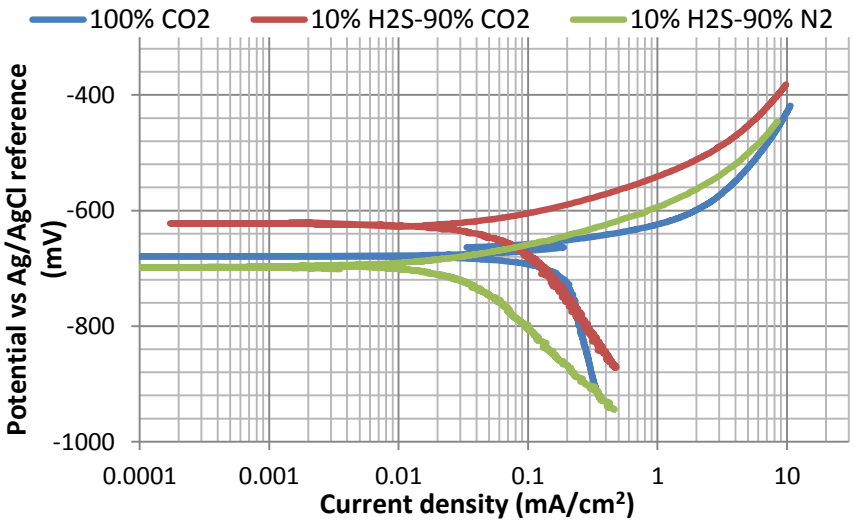

(a)

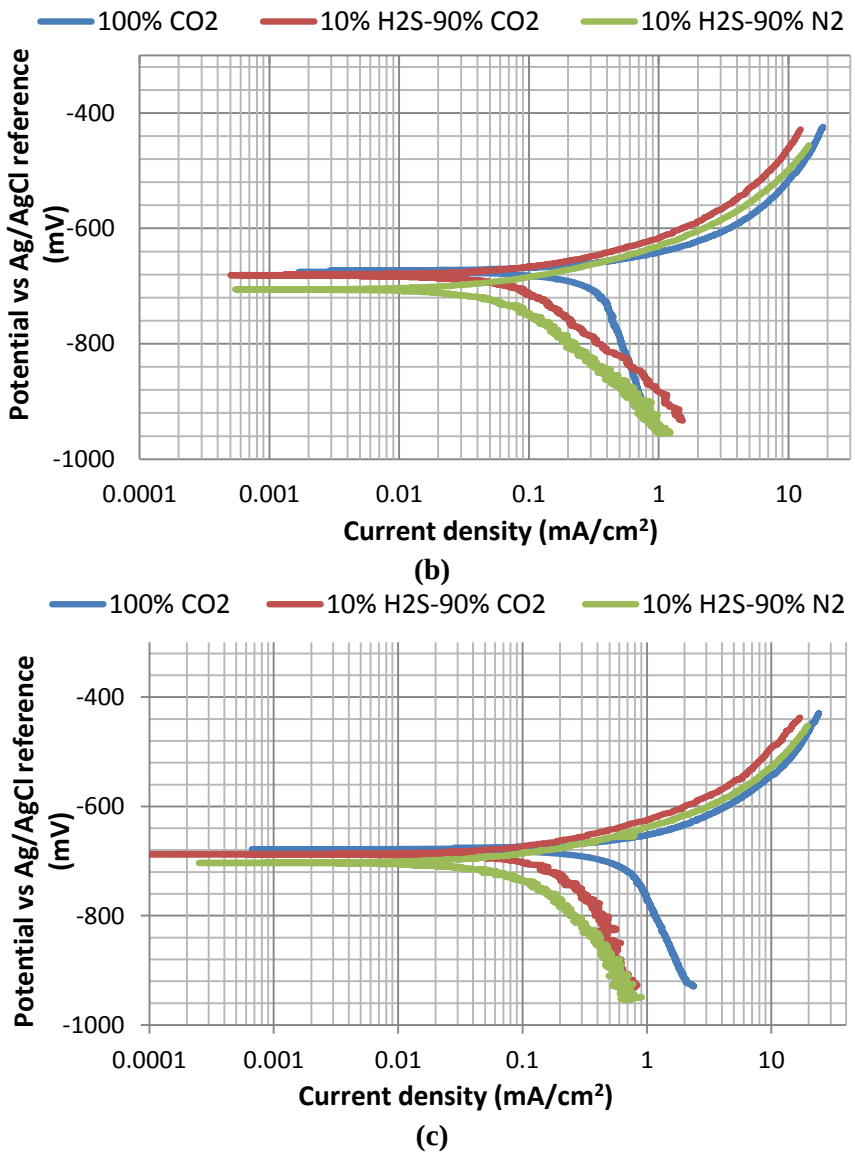

Figure 9-1 Tafel polarization plots for X65 carbon steel in 3.5 wt.% NaCl solution under 100 mol.% CO_2, 10 mol.% H_2S- 90 mol.%CO_2 and 10 mol.% H_2S-90 mol.% N_2 gas atmospheres after 7 hours at (a) 30°C (b) 50°C and (c) 80°C.

It was proposed by Zheng *et al* [140] that this thin layer can have the potential effect of influencing the corrosion boundary layer by displacing the corrosion interface of reducible species (OH^- and H_2O), leading to retardation of hydrogen-evolution. A similar suggestion was also put forward by Kittel *et al* [121] by proposing that change in the cathodic reaction line and hence, the reduced corrosion rate in H_2S-containing corrosion environments relative to 100 mol.% CO_2 gas systems as shown in Figure 9-1(a)-(c) may be attributed to the suppression of the collective influence of H^+ and H_2CO_3 reduction reaction. H^+ and H_2CO_3 reduction reactions usually dominate the cathodic current in a sweet corrosion environment even with the addition of 0.65% of H_2S [140]. There is also the additional effect of a direct or heterogeneous cathodic

reduction reaction of HS^- [119, 121, 124], which is expected, especially at higher concentration of H_2S gas in the gas phase, as is the case in this work. Ma *et al* [124] and Choi *et al* [175] had observed that the heterogeneous cathodic reduction reaction of H_2S/HS^- occurs quickly leading to the formation of an iron sulphide (usually mackinawite) corrosion product, which has the potential to also influence corrosion kinetics as is being observed in Figure 9-1.

It is important to note here that the shift from mass-transfer influenced cathodic reaction process in sweet corrosion environment to activation-controlled in H_2S-containing environment becomes more apparent with decreasing temperature. This behaviour suggests that there is still a significant contribution of H_2CO_3/H^+ reduction reactions to the total cathodic current with a shift from completely sweet corrosion scenario to sour corrosion scenario. The contribution of H_2CO_3/H^+ reduction reactions to total cathodic current appears to increase with temperature for systems containing 10 mol. % H_2S – 90 mol. % CO_2.

According the *in-situ* pH measurement provided in Table 9-1, the *in-situ* pH of un-buffered test solutions under the three gas phase composition under investigation almost the same between 100 mol. % CO_2 and 10 mol.% H_2S - 90 mol.% CO_2 gas systems but increased slightly for 10 mol.% H_2S - 90 mol.% N_2, gas system at all temperatures. Based on these pH measurements, it would be expected that the pH and hence H^+ reduction reaction may become significant to varying degrees for the different experimental conditions. While Zheng *et al* [140] had reported that the main contribution to the cathodic current at 10% H_2S concentration is from the direct reduction of aqueous H_2S species, it can also be argued from results shown in Figure 9-1, that the corrosion reaction of steel with H_2S in H_2S-containing environments dominates the reaction mechanism at lower temperature and becomes less dominant as the temperature increases and that the H^+ reduction mechanism which is strongly influenced by solution pH (and H^+ concentration) is not as influential.

In addition to the above-described observations from the potentiodynamic curves, the Tafel polarisation curve is also used in this work to estimate the Tafel constants and then, estimate the Stern-Geary coefficient. Tafel constants and Stern-Geary coefficient are provided in Table 9-2 for all test conditions and was used with the polarization resistance (R_p) and Faraday's law to determine corrosion rate as a function of time. The anodic Tafel slopes (β_a) in purely sour corrosion environment only decreases marginally in a similar trend as the estimated anodic Tafel constant by Ogundele and White [123]. The repeatability of the Tafel polarization curves was also confirmed by comparing corrosion rate from Tafel extrapolation with estimated corrosion rate from linear polarization measurements after 7 hours. This is provided in Table

9-3. The extrapolated corrosion rate from the potentiodynamic sweeps was found to be very consistent with the corrosion rates presented in Figure 9-2, Figure 9-6 and Figure 9-10 from separate tests.

Table 9-2 Tafel constants at different temperatures and gas mixtures

Temperature (°C)	Mole % of combining gases								
	100mol.% CO_2			10mol.% H_2S - 90mol.% CO_2			10mol.% H_2S - 90mol.% N_2		
	β_a	β_c	B	β_a	β_c	B	β_a	β_c	B
30	33	200	12	35	140	12	55	170	18
50	40	168	14	45	140	15	58	140	18
80	58	135	18	58	160	18	47	135	15

Table 9-3 Comparison between corrosion rates (mm/yr) obtained from Tafel extrapolation and from the use of the estimated Stern-Geary constants.

Temperature (°C)	Corrosion rate (mm/yr) after 7 hours					
	100mol.% CO_2		10mol.% H_2S - 90mol.% CO_2		10mol.% H_2S - 90mol.% N_2	
	CR-LPR	CR-Tafel	CR-LPR	CR-Tafel	CR-LPR	CR-Tafel
30	1.05	1.19	0.41	0.39	0.26	0.29
50	2.10	2.58	1.02	0.95	0.56	0.55
80	4.77	5.23	1.44	1.25	0.59	0.63

9.3 Correlation between electrochemical responses and formation of corrosion products as a function of process parameters

This section presents and discusses experimental results for short-term (7 hours) test that investigates the relationship between the electrochemical activities; corrosion kinetics and corrosion product formation at the metal-brine interface for the three different gas phase composition under investigation and at all temperatures. Discussions will be focused on understanding from a mechanistic perspective, the effect of temperature, the absence and/or presence of H_2S and CO_2 gas on the corrosion behaviour of carbon steel materials.

9.3.1 Corrosion behaviour and corrosion product formation of at 30°C

The corrosion rate measurements at 30ºC for test solutions under gas atmospheres composed of 100 mol. % CO_2 gas, 10 mol. % H_2S – 90 mol. % CO_2 gas mixture and 10 mol. % H_2S – 90 mol. % N_2 gas mixtures for 7 hours are presented in Figure 9-2. The corrosion rate is constant for the three different gas systems. However, with 100 mol. % CO_2 in the gas phase, the corrosion rate three times higher than the corrosion rate for test under a gas atmosphere composed of 10 mol. % H_2S – 90 mol. % CO_2 gas and almost four times higher than the corrosion rate at a gas phase composition of 10 mol. % H_2S – 90 mol. % N_2. Similar observation was recorded by Woollam *et al* [176] and Choi *et al* [175] at 30°C and 25°C, respectively. According to Woollam *et al* [176], there was a 70% reduction in corrosion rate from 100 mol. % CO_2 to a gas phase composed of 1 mol.% H_2S and 90 mol.% CO_2. There was no significant difference between corrosion rate of carbon steel with a gas phase of 10 mol. % H_2S – 90 mol. % CO_2 gas mixture and 10 mol. % H_2S – 90 mol. % N_2 within the first 7 hours of tests. This correlates well with the Tafel polarization plot of Figure 9-1(a) as well as observations by other authors [124, 175].

The observed lower corrosion rate with the presence of H_2S gas in the gas has been associated with H_2S/HS- dominating the cathodic current at 30ºC and similar ranges of temperatures [119, 124, 140, 175, 176]. Since the pH for 10 mol. % H_2S – 90 mol. % CO_2 is always slightly lower than for 10 mol. % H_2S – 90 mol. % N_2 Table 9-1, it can therefore be inferred that H_2S/HS^- reduction reaction may be dominating the cathodic reaction mechanisms in H_2S-containing systems. However, most authors still have differing opinions on the mechanisms by which H_2S/HS^- reduction reaction may be dominating the cathodic reaction in H_2S-containing systems. Zheng *et al* [140] reported a slight drop in corrosion rate from ~1.8mm/yr in 100% CO_2 system to ~1.2 mm/yr in 10 mol. % H_2S – 90 mol. % CO_2 at 30ºC, pH of 5,1000rpm rotating speed and after 2 hours and linked this behaviour (even at lower concentration of H_2S gas) to the formation of a very thin layer of FeS on to the steel surface (possibly via chemisorption). It is assumed that this thin layer of FeS_{ad} corrosion product may be creating a restriction to the reduction of reducible anions, thereby retarding the process of hydrogen evolution.

Similar phenomenon was also proposed by Woollam *et al* [176] (in this case as a monolayer of Sulphur on to the steel surface) to be potentially responsible for a 70% reduction in corrosion rate in H_2S containing corrosion environments. This proposed explanation was based on thermodynamic analysis carried out by Marcus *et al* [177]. On the other hand, results by Ma *et al* [124] confirmed that with increase in exposure time, the formation of an iron sulphide corrosion product layer could reduce the corrosion rates in a similar way as presented in Figure

9-2. This was also the case with the results of Choi *et al* [175]. In both cases, the iron sulphide corrosion product layer was responsible for the reduced corrosion rate, with an indication that it forms very quickly. It is also important to note that before the start of electrochemical measurements, the pH was allowed to stabilize for up to 30 minutes. Hence, early reaction kinetics may have been missed.

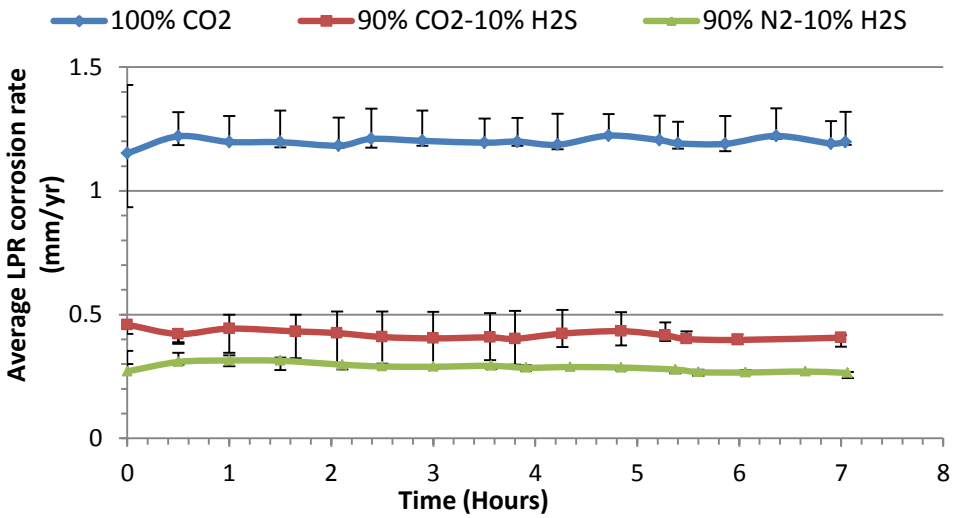

Figure 9-2 Corrosion rate of X65 carbon steel in 3.5 wt.% NaCl solution under three different gas atmospheres at 30°C, over 7 hours.

Referring to Figure 9-3(a)-(b), the SEM images show that corrosion of carbon steel materials in 100 mol. % CO_2 environments is characterised by the preferential dissolution of ferrite from the steel surface and that no corrosion product precipitation is expected on the steel surface [9, 88, 164]. This is shown to be the case in this work as shown in Figure 9-3(a), in which a network of cementite is seen to be revealed. For corrosion tests in solutions under 10 mol. % H_2S – 90 mol. % CO_2 atmosphere, the corrosion rate is seen in Figure 9-3(b) to be a very thin layer of iron sulphide corrosion product with visual evidence of polishing marks and with a non-uniform coverage. Although the XRD pattern presented in Figure 9-4 showed a strong signal for an iron sulphide corrosion product, it does suggest the formation of iron sulphide corrosion product (mackinawite). Mackinawite has been identified as stoichiometric iron sulphide in line with recent findings and analysis of mackinawite as against being initially reported as an iron excess, non-stoichiometric compound, $Fe_{1+x}S$ [128]. This is also supported by the EDX pattern labelled spectrum 10 (Figure 9-5(a)). In the case of test in solution under 10 mol. % H_2S – 90 mol. % N_2 atmosphere, SEM image of Figure 9-3(c) clearly shows a visual evidence of an iron sulphide corrosion product layer with a non-uniform coverage. However, in this case, The XRD pattern presented in Figure 9-4 for test in solution under 10 mol. % H_2S – 90 mol. % N_2 atmosphere

also show a weak signal for iron sulphide corrosion product (mackinawite). This also suggests what can be referred to as a non-crystalline form of iron sulphide [37, 118]. The SEM image Figure 9-3(c) is backed by the EDX 19 peaks for sulphur (S) and iron (Fe) in Figure 9-5(b). It is therefore, evident that reduction in corrosion rate observed for test in H_2S-containing corrosion environments relative to test in 100 mol.% CO_2 is influenced by the formation of iron sulphide (mackinawite) corrosion product layer as observed by other authors [115, 124]. This form of iron sulphide is known to be the most "kinetically-favoured" phase of iron sulphide and therefore expected to form quickly via direct-reduction reaction [115]. Although it is apparent that the film morphology in both gaseous systems are physically different, it is still not clear if the presence of, or absence of CO_2 gas in the gaseous phase is the cause of this difference, especially as presence of, or absence of CO_2 gas appears to have a slight influence on the solution pH of the test solutions in H_2S-containing environments (see Table 9-1).

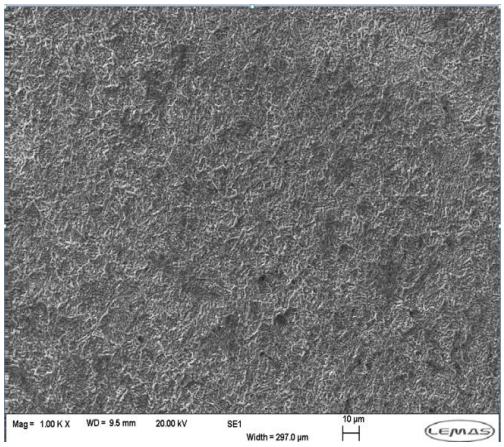

(a)

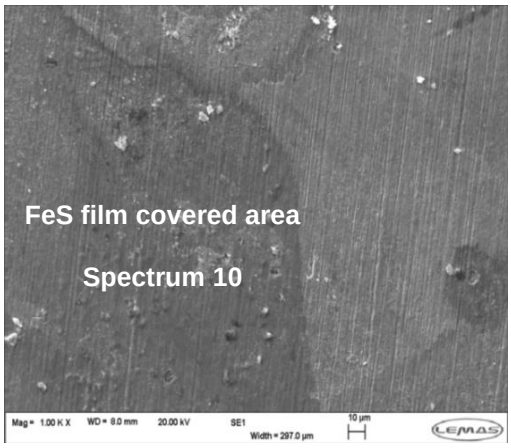

(b)

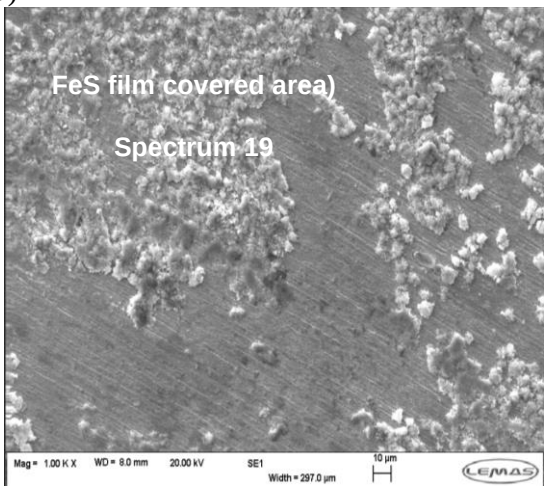

(c)

Figure 9-3 SEM images of corrosion product layer on X65 carbon steel in 3.5 wt. % NaCl solution under gas atmospheres composed of (a) 100 mol. % CO_2, (b) 10 mol. % H_2S- 90 mol. %CO_2 and (c) 10 mol. % H_2S-90 mol. % N_2 at 30°C and after 7 hours.

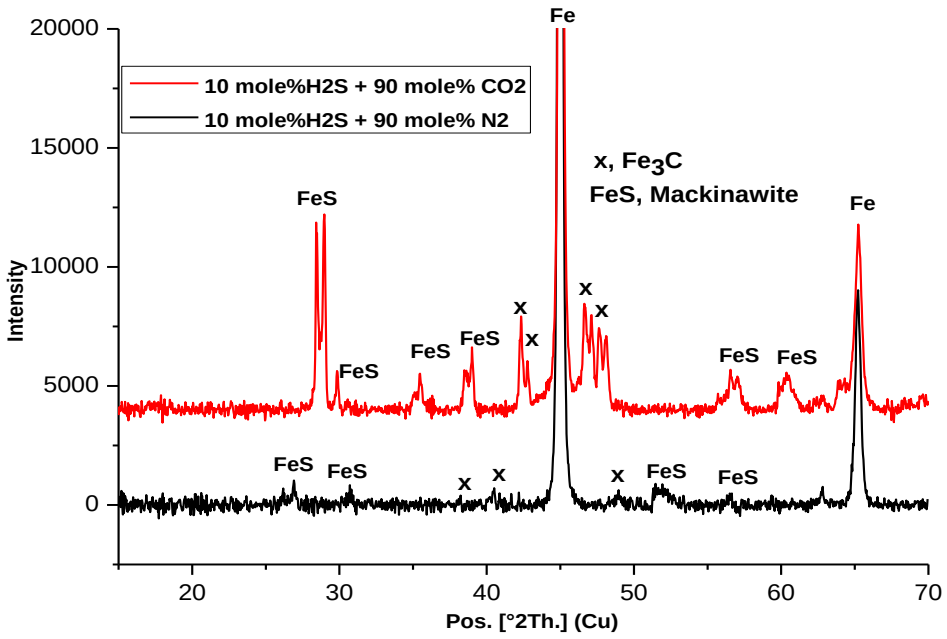

Figure 9-4 XRD pattern for corrosion product layer on X65 carbon steel in 3.5 wt.% NaCl solution under a gas atmosphere composed of 10 mol. % H_2S- 90 mol. %CO_2 and 10 mol. % H_2S-90 mol. % N_2 at 30°C. Images are for test duration of 7 hours *(Note that the intensity scale is arbitrary)*. XRD peaks referenced to database in literature [168, 170, 178, 179].

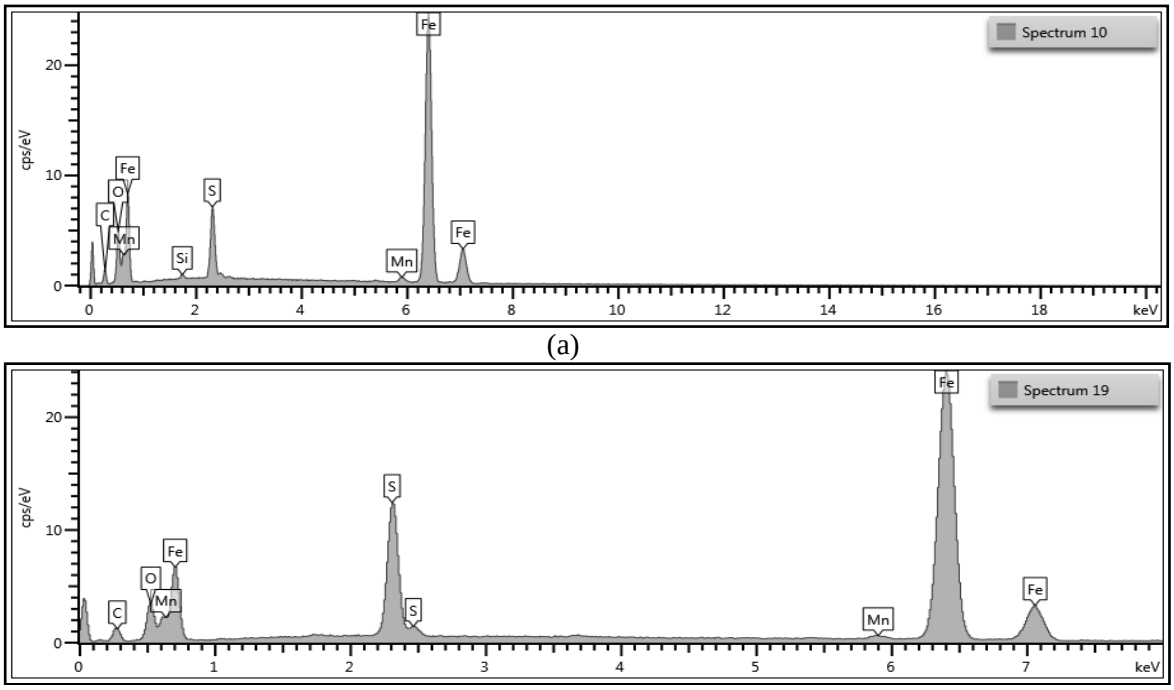

(a)

(b)

Figure 9-5 EDX pattern for corrosion product layer on X65 carbon steel in 3.5 wt.% NaCl solution under a gas atmosphere composed of (a)10 mol. % H_2S- 90 mol. %CO_2 and (b) 10 mol. % H_2S-90 mol. % N_2 at 30°C. Images are for test duration of 7 hours.

9.3.2 Corrosion behaviour and corrosion product formation at 50°C

The corrosion rate measurements at 30ºC for test solutions under gas atmospheres composed of 100 mol. % CO_2 gas, 10 mol. % H_2S – 90 mol. % CO_2 gas mixture and 10 mol. % H_2S – 90 mol. % N_2 gas mixtures for 7 hours are presented in Figure 9-6. The corrosion rate of carbon steel in the test solution is shown to depict a distinctive difference in magnitude for the three different gas systems under investigation in this work. The results show that highest corrosion rate values were recorded with a gas phase composed of only CO_2. This is almost three times higher than a gas system composed of 10 mol. % H_2S – 90 mol. % CO_2 and 10 mol. % H_2S – 90 mol. % N_2 at the start of the experiment. The trend in the corrosion rates presented in Figure 9-6 is different from the results obtained for tests conducted at 30ºC in terms of the disparity in the magnitude of corrosion rate among the three gas systems, which also increases with time. This suggests an increase in the kinetics of corrosion with increase in temperature and time. This is most evident in CO_2-containing corrosion scenarios, while for tests under 10 mol. % H_2S – 90 mol. % N_2 gas atmosphere, the corrosion rate was almost constant for 7 hours. The trends observed in CO_2-containing corrosion scenarios was also observed to be consistent with the potentiodynamic sweeps presented in Figure 9-1(b) at 50°C and the results of Woollam *et al* [176] at 60°C.

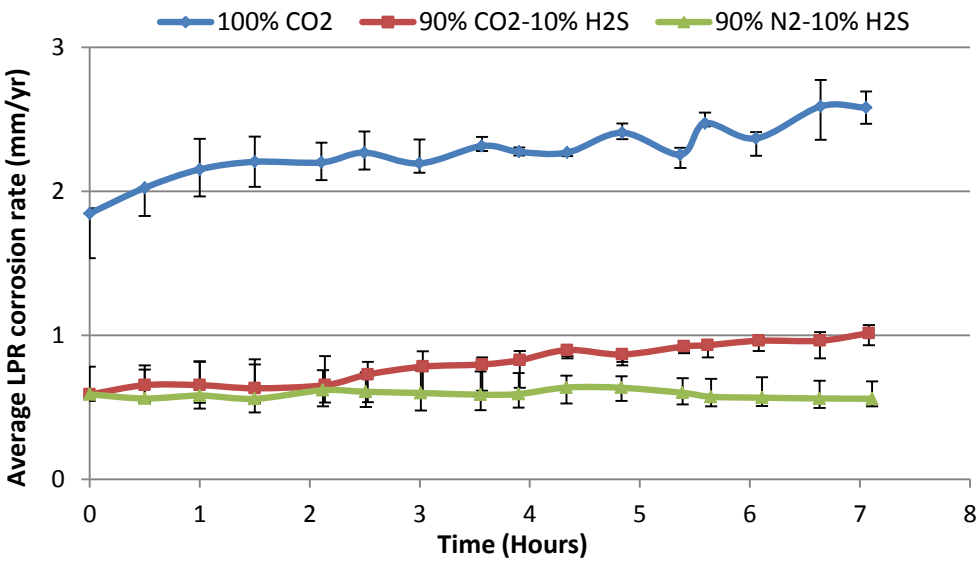

Figure 9-6 Corrosion rate of X65 carbon steel in 3.5 wt.% NaCl solution under three different gas atmospheres at 50ºC, over 7 hours.

The observed trend in the potentiodynamic sweep presented in Figure 9-1(b) and the measured corrosion rates presented in Figure 9-6 seem to be indicating that the combined cathodic reduction reaction of H^+ and H_2CO_3 becomes more influential at 50°C than at 30°C. This can be related to the Arrhenius-type dependence of CO_2 corrosion on temperature as reported by other

authors [77, 103]. The potential impact of this is the increase in material degradation in tests under 10 mol. % H_2S – 90 mol. % CO_2 gas atmosphere at higher temperatures. This is very significant given the fact that the lower corrosion rates in H_2S-containing corrosion environments is most likely due to the formation of iron sulphide corrosion products.

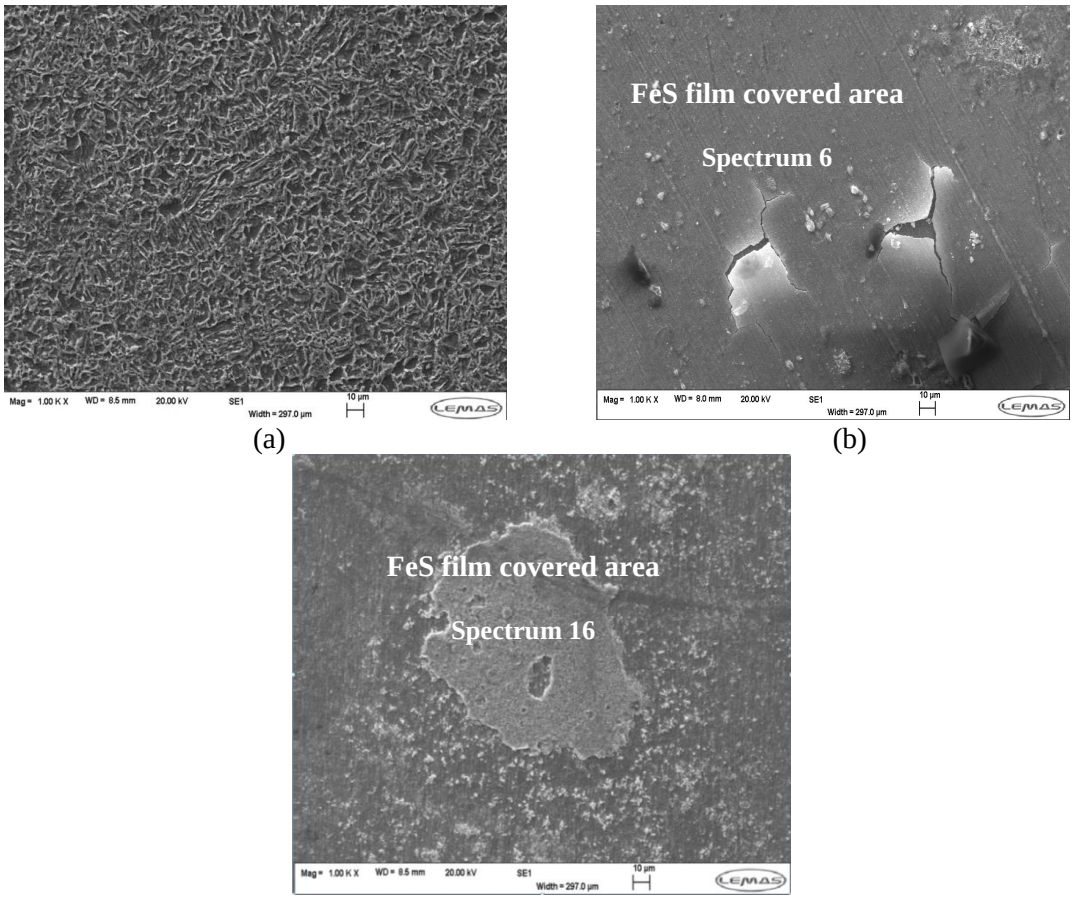

(a) (b)

(c)

Figure 9-7 SEM images of corrosion product layer on X65 carbon steel in 3.5 wt. % NaCl solution under gas atmospheres composed of (a) 100 mol. % CO_2, (b) 10 mol. % H_2S- 90 mol. %CO_2 and (c) 10 mol. % H_2S-90 mol. % N_2 at 50°C and after 7 hours.

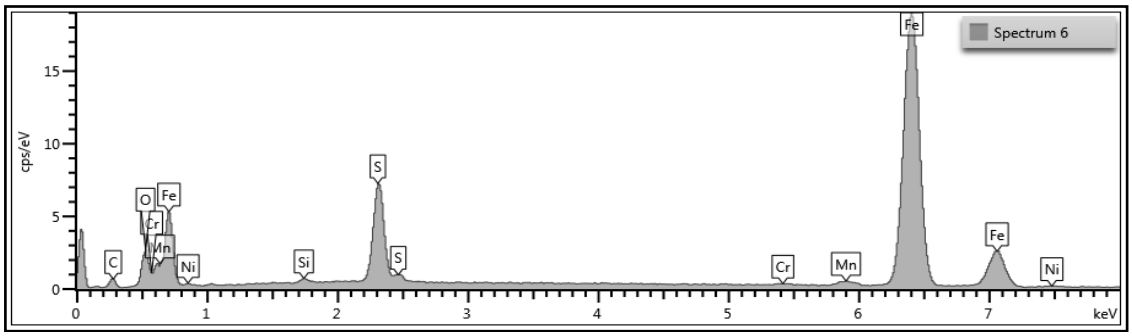

(a)

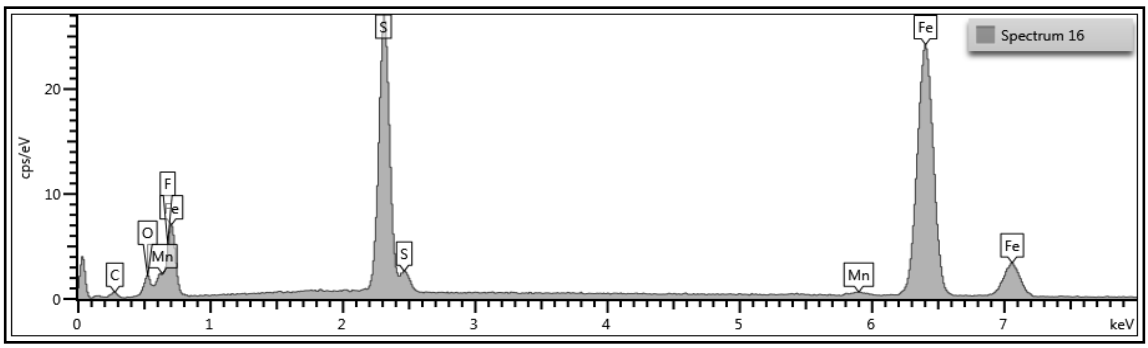

(b)

Figure 9-8 EDX pattern for corrosion product layer on X65 carbon steel in 3.5 wt.% NaCl solution under a gas atmosphere composed of (a)10 mol. % H_2S- 90 mol. %CO_2 and (b) 10 mol. % H_2S-90 mol. % N_2 at 50°C. Images are for test duration of 7 hours.

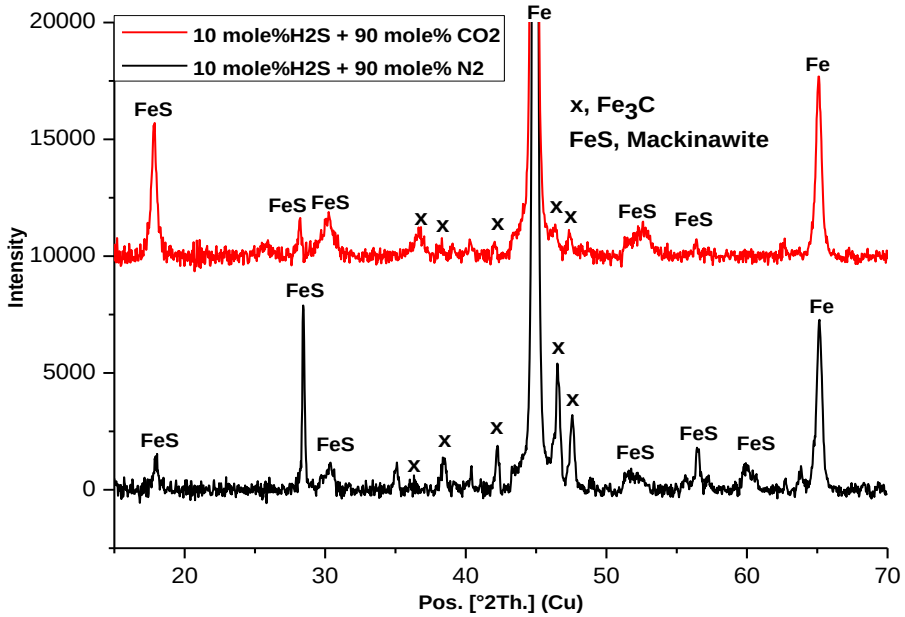

Figure 9-9 XRD pattern for corrosion product on X65 carbon steel in 3.5 wt.% NaCl solution under a gas atmosphere composed of 10 mol. % H_2S- 90 mol. %CO_2 and 10 mol. % H_2S-90 mol. % N_2 at 50°C. Images are for test duration of 7 hours *(Note that the intensity scale is arbitrary)*. XRD peaks referenced to database in literature [168, 170, 178, 179].

The rate of formation of iron sulphide films in these test conditions also appears to be very fast when compared to the rate of formation of iron carbonate corrosion product layer for tests in un-buffered CO_2-saturated environments. This has been strongly linked to what has been described as the direct reduction reaction mechanism of H_2S that governs the kinetics of iron sulphide formation [119, 121, 140]. The morphology of the iron sulphide films are also quite different for 10 mol. % H_2S – 90 mol. % CO_2 gas and 10 mol. % H_2S – 90 mol. % N_2 gas combination. For iron sulphide corrosion product formed in 10 mol. % H_2S – 90 mol. % CO_2 gas systems appears

to be relatively thin but the nature of the cracks suggests some unit of microns thickness of the corrosion product layers. There is also evidence of the polishing marks printed on the corrosion product layer. Similar observations have also been reported by Brown and Nesic [138]. However, in the case of the results by Brown and Nesic [138], the test was conducted at 60°C, pH of 4.0, P_{total} of 8 bar, pH_2S of 10 mbar, 10wt% NaCl after a 7 days exposure. For iron sulphide corrosion product formed in 10 mol. % H_2S – 90 mol. % N_2 gas systems, the coverage is localised but relatively more compact.

9.3.3 Corrosion behaviour and corrosion product formation at 80°C

The corrosion rate of carbon steel in brine saturated with the three different gas combinations under investigation at 80ºC is presented in Figure 9-10. The observed difference in corrosion rate over 7 hours duration between the three different gas phases; 100 mol. % CO_2 gas, 10 mol. % H_2S – 90 mol. % CO_2 gas mixture and 10 mol. % H_2S – 90 mol. % N_2 gas mixtures correlates well with the behaviour observed at 50ºC for these three gas systems. By referring to Figure 9-10 for corrosion rates at 80ºC, the magnitude of general corrosion rate over 7 hours increases with the presence of CO_2 gas in the gas phase and decreases with H_2S gas in the gas phase. The latter effect is likely due to the formation of iron sulphide corrosion product layer. In the case of completely CO_2-saturated corrosion environments, the evolution of empty cementite has been shown (in Chapter 6 of this thesis) to occur in the initial stages of corrosion and is quickly replaced by the formation of an amorphous and/or nano-scale polycrystalline form of $FeCO_3$ corrosion products. This form of $FeCO_3$ do not offer any form of protection at this stage of the corrosion process. The higher magnitude of corrosion rate in test under 10 mol. % H_2S – 90 mol. % CO_2 gas mixture gas mixture at 80°C than at 50 and 30°C is an indication that the contribution of H^+ and H_2CO_3 reduction reactions to total cathodic current in 10 mol. % H_2S – 90 mol. % CO_2 containing atmosphere appears to be more significant at higher temperatures than at lower temperatures.

This also correlates well with the observation from potentiodynamic sweeps shown in Figure 9-1(c). Such observation at 80ºC implies the potential for increased contribution from uniform corrosion to total material penetration as a result of the presence of CO_2 in the H_2S-containing corrosion environment. There is also marginally enhanced contribution from cumulative uniform corrosion to total metal penetration at 80ºC for 10 mol. % H_2S – 90 mol. % N_2 gas systems than at 50 and 30ºC. However, the uniform corrosion contribution was relatively higher for 10 mol. % H_2S – 90 mol. % CO_2 gas system due to the presence of CO_2 gas in the gas phase. It is believed that the significant increase in corrosion rate as a function of gas phase

composition at 80ºC when compared to 30 and 50ºC could be linked to the combined effect of H^+ and H_2CO_3 reduction reactions to the corrosion process. This also clearly depicts the Arrhenius-type dependence of H^+/H_2CO_3 corrosion reactions on temperature [77, 103], even with the presence of H_2S gas. From the results described thus far for experiments conducted at 80°C, it is quite evident that the CO_2 corrosion reaction becomes dominant at higher temperature. However, what remains elusive thus far is the extent to which the temperature changes could be influencing the kinetics of iron sulphide formation. A slight indication of such effect can be seen on the SEM images provided Figure 9-11(a)–(c), the corresponding EDX pattern in Figure 9-12 and XRD pattern for test in H_2S-containing environments (Figure 9-13). The empty cementite network of Figure 9-11(a) for the test containing only CO_2 gas corresponds to what has been initially reported in Chapter 6 and 7 of this report to consist of only traces of a non-crystalline forms of iron carbonate corrosion products (or amorphous $FeCO_3$) at 80ºC.

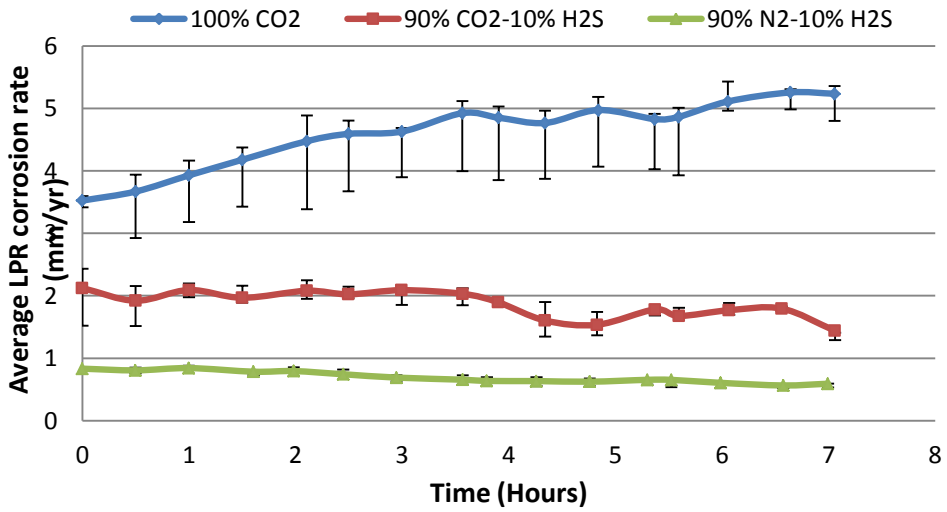

Figure 9-10 Corrosion rate of X65 carbon steel in 3.5 wt. % NaCl solution under three different gas atmospheres at 80ºC, over 7 hours.

In tests conducted under 10 mol. % H_2S – 90 mol. % CO_2 gas atmosphere, the iron sulphide corrosion product layer appears to be a continuous layer but with non-uniform coverage surrounded by heavily corroded localised regions (showing areas of empty cementite). This is provided in Figure 9-11(b). In 10 mol. % H_2S – 90 mol. % N_2 gas atmosphere, the corrosion product morphology is quite different from the former and shows evidence of less corrosion of surrounding regions without the iron sulphide corrosion product layer, but with significant coverage as shown in Figure 9-11(c). Iron sulphide corrosion products formed at 80°C are also confirmed by the EDX pattern showing these corrosion product layers to be rich in sulphur (S) and iron (Fe) in Figure 9-12. With gas atmosphere of 10 mol.% H_2S – 90 mol.% N_2, the

corrosion rate also appears to be decreasing very slowly with time over the 7 hour duration of the test at 80ºC (Figure 9-10) when compared to tests at 30 and 50ºC. This could be the influence of the higher temperature at 80ºC in a way that promotes the rate of precipitation of iron sulphide. However, it remains unclear if the higher temperature is influencing the kinetics of iron sulphide formation by both direct reduction reaction and aqueous corrosion reaction. The latter involves the loss of Fe^{2+} into the bulk as suggested by several authors [35, 73, 115], especially in the 10mol. % H_2S - 90mol. % N_2 gas atmosphere.

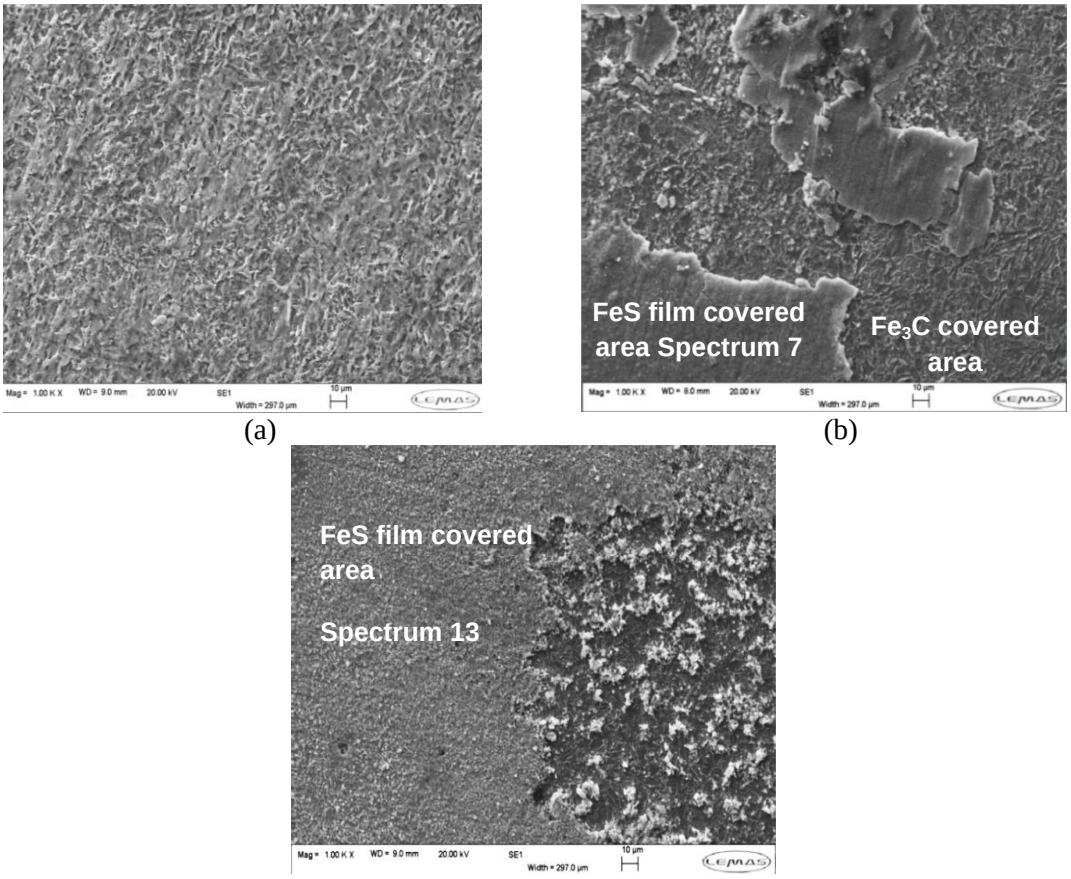

(a) (b)

(c)

Figure 9-11 SEM images of corrosion product layer on X65 carbon steel in 3.5 wt. % NaCl solution under gas atmospheres composed of (a) 100 mol. % CO_2, (b) 10 mol. % H_2S- 90 mol. %CO_2 and (c) 10 mol. % H_2S-90 mol. % N_2 at 80°C and after 7 hours.

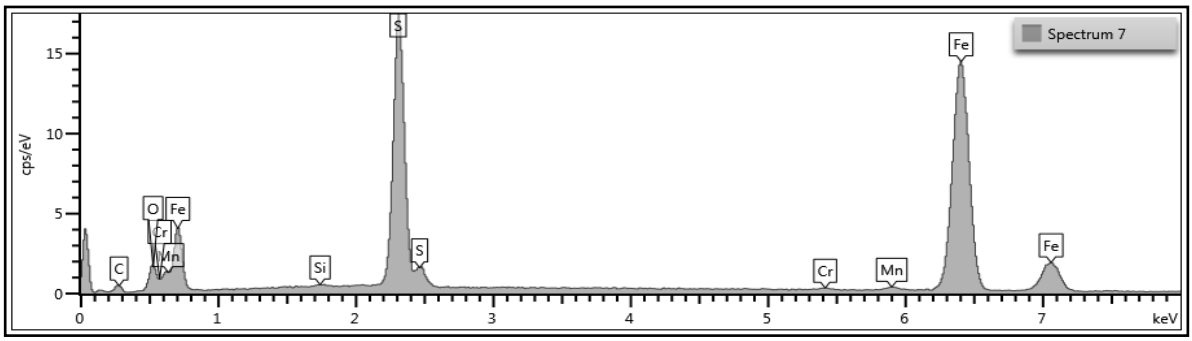

(a)

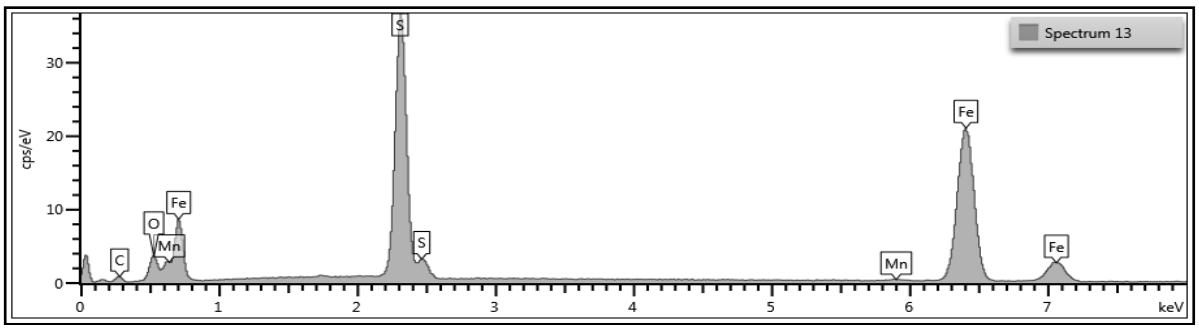

(b)

Figure 9-12 EDX pattern for corrosion product layer on X65 carbon steel in 3.5 wt.% NaCl solution under a gas atmosphere composed of (a)10 mol. % H_2S- 90 mol. %CO_2 and (b) 10 mol. % H_2S-90 mol. % N_2 at 50°C. Images are for test duration of 7 hours.

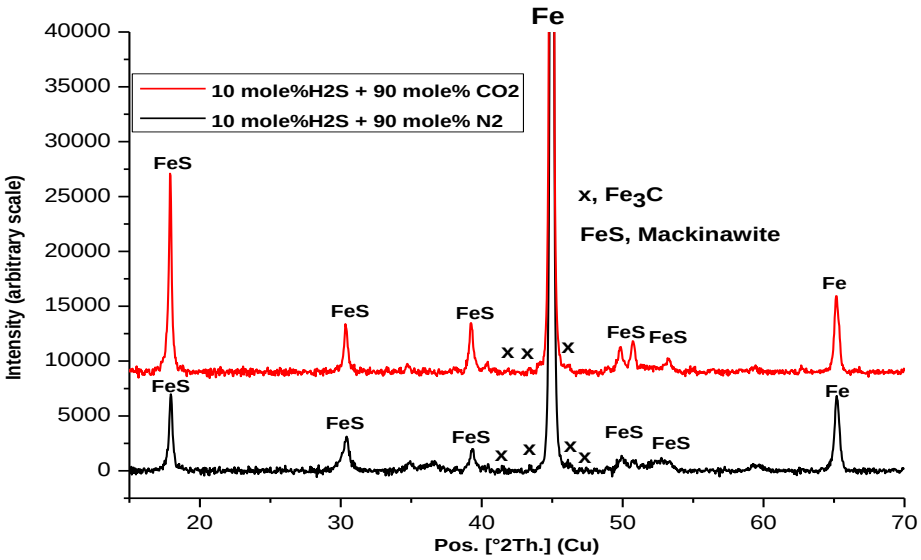

Figure 9-13 XRD pattern for corrosion product on X65 carbon steel in 3.5 wt.% NaCl solution under a gas atmosphere composed of 10 mol. % H_2S- 90 mol. %CO_2 and 10 mol. % H_2S-90 mol. % N_2 at 80°C. Images are for test duration of 7 hours *(Note that the intensity scale is arbitrary).* XRD peaks referenced to database in literature [168, 170, 178, 179].

9.4 Supplementary results on the corrosion behaviour of carbon steel and corrosion product formation at 80°C

This section discusses results of supplementary experiments carried out as part of the study to investigate the sour corrosion behaviour of carbon steel. It is important to recall that as part of the methodology for tests in H_2S-containing environments (described in section Chapter 5 of this thesis), H_2S-containing gas mixture is bubbled into the nitrogen saturated solution for up to 30 minutes prior to the start of electrochemical measurements. This was to allow the *in-situ* pH and corrosion potential to stabilise prior to the commencement of electrochemical measurements. However, it is also probable that the iron sulphide film formation process will be

very fast and may have been formed quickly enough to give a lower corrosion rate from the start. Thus, it is also probable that within the first 30 minutes window before electrochemical responses are measured, some of the electrochemical responses that will help understand the characteristic behaviour of the corrosion interface at the immediate start of the experiments may have been missed. Based on this assumptions, two different supplementary experiments (provided in Table 9-4) were carried out at 80°C to help answer the questions of how quick the FeS formation process is, and to what extent the initially formed iron sulphide corrosion product layer can influence the corrosion behaviour.

Table 9-4 A summary of the supplementary experiments to the corrosion behaviour of carbon steel and corrosion product formation at 80°C

Test parameters	Supplementary experiment-01	Supplementary experiment-02
Temperature	80°C	80°C
Test duration	4.5 hours	14 hours
Gas systems	100 mol.% CO_2 for 2.5 hours Before adding; 10 mol. % H_2S – 90 mol. % CO_2 gas for 2 hours	10 mol. % H_2S – 90 mol. % CO_2 gas for 7 hours. Before tests in; 100 mol.% CO_2 for 7 hours

One aspect of the supplementary tests entails monitoring corrosion rate and potential in 100 mol. % CO_2 for 2.5 hours after which a 10 mol. % H_2S – 90 mol. % CO_2 gas mixture is introduced into the test solution for another 2.0 hours at 80°C. The second aspect of the supplementary experiments entails monitoring the corrosion rate and potential in tests under 10 mol. % H_2S – 90 mol. % CO_2 gas atmosphere and then exposed the test sample to a solution completely saturated 100 mol. % CO_2 for another 7 hours. Although electrochemical response was monitored for a total of 14 hours, the total duration of the experiment in this case prior to removal of test sample for post-experiment analysis was 21 hours.

9.4.1 Supplementary experiment-01

The results of measured electrochemical responses; corrosion potential and corrosion rate for supplementary experiment-01 are presented in Figure 9-14(a) and (b) respectively. Referring to Figure 9-14(a) and (b), the corrosion potential when the test solution is completely saturated with 100 mol. % CO_2 is rightly in in arrange of potential consistent with test in CO_2 saturated corrosion systems [175]. However, as soon as the 10 mol. % H_2S – 90 mol. % CO_2 gas mixture

is introduced into the test media after 2.5 hours, the corrosion potential suddenly shifts to a more negative potential (from -672 mV to -695mV) within 30 minutes. This observation is also consistent with published results by Choi *et al* [175] for similar tests at pH of 4 and 25ºC.

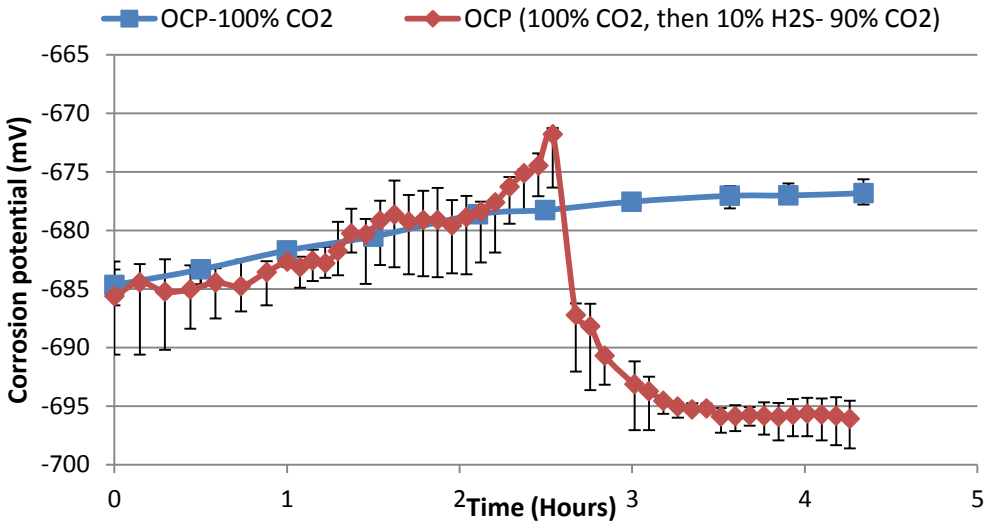

(a)

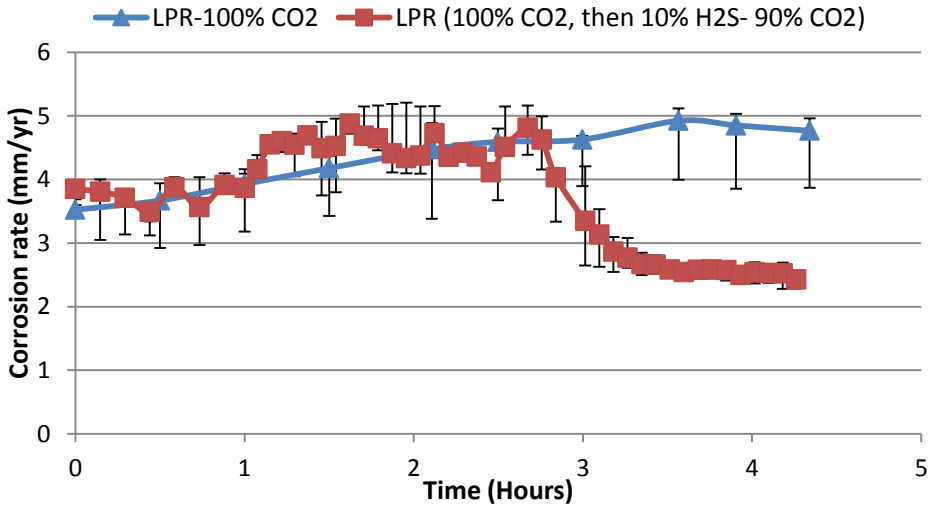

(b)

Figure 9-14 a) Corrosion potential and (b) average corrosion rate of X-65 carbon steel initially exposed to a 3.5 wt. % NaCl solution under 100 mol. % CO_2 for 2.5 hours and then 10 mol. % H_2S-90 mol. % CO_2 for another 2 hours in comparison to test under a gas atmosphere of 100 mol. % CO_2 for 4.5 hours.

As shown in Figure 9-14 (b), the corrosion rate was also observed to increase slightly within the first minutes and then gradually decrease within 30 minutes from ≈ 5mm/yr down to ≈ 2.5 mm/yr which compares well with the corrosion rate at the start of the test conducted under a 10 mol. % H_2S – 90 mol. % CO_2 gas atmosphere (Figure 9-10). Similar observation have also been reported by Ma *et al* [124] for tests conducted in an acidic media. In the results of Ma *et al*

[124], the corrosion rate (based on impedance measurement) also increased within the first 5 minutes with the introduction of H_2S-gas into the corrosion environment and then decreases after 2 hours due to the formation of iron sulphide corrosion product layer potentially mackinawite).

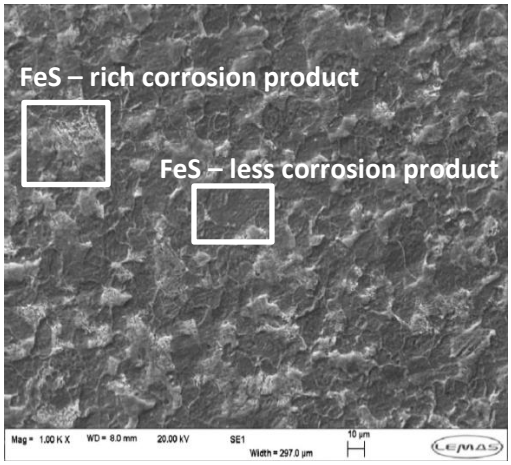

(a)

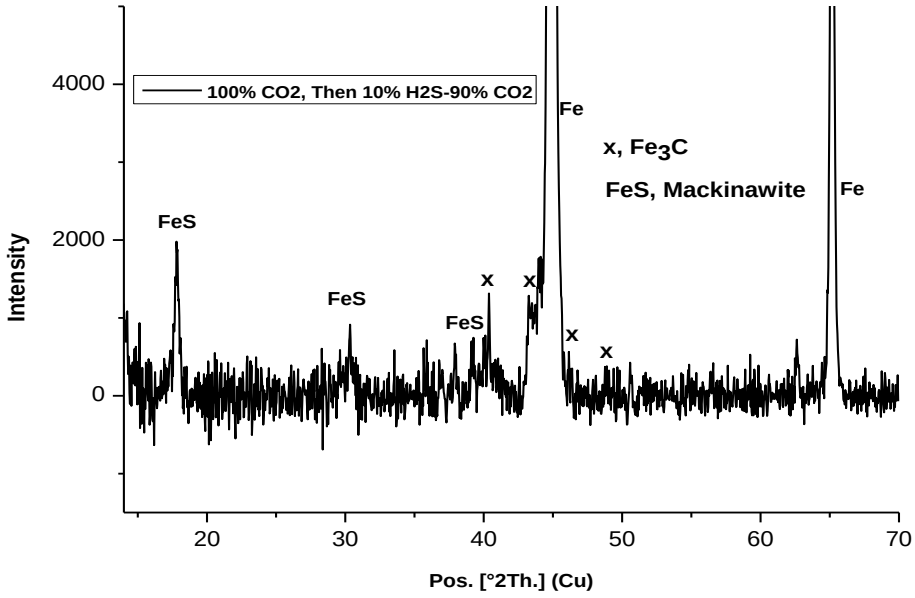

(b)

Figure 9-15 (a) SEM image and (b) XRD pattern for X-65 carbon steel initially exposed to a 3.5 wt. % NaCl solution under 100 mol. % CO_2 gas atmosphere for 2.5 hours and then under 10 mol. % H_2S- 90 mol. % CO_2 gas atmosphere for another 2 hours *(Note that the intensity scale is arbitrary)*. XRD peaks referenced to database in literature [168, 170, 178, 179].

The SEM image and XRD pattern provided in Figure 9-15(a) and (b) respectively also confirm the presence of iron sulphide corrosion products on the steel surface after 2 hours. This clearly shows that the formation of iron sulphide occurs quickly and it can significantly influence the

corrosion behaviour of steel in these conditions. This viewpoint is supported by the observations of Ma *et al* [124] and Choi et al [175].

9.4.2 Supplementary experiment-02

The results of the supplementary experiment presented in this section are aimed at evaluating the stability and level of protection to be expected from the initially formed iron sulphide corrosion products at 80°C. The electrochemical responses from this aspect of the work are presented in Figure 9-16 and Figure 9-17(a) and (b). Referring to Figure 9-16, the corrosion potential (OCP) is more negative in the H_2S-containing corrosion system than in the CO_2-saturated corrosion system. Once the corrosion environment is changed to a completely CO_2-saturated system, the corrosion potential shifts to a more positive potential. Although the corrosion potential increases slightly before stabilising after 5 hours within the H_2S-containing corrosion domain, this trend is consistent with observations by Choi *et al* [175] at 25°C and pH of 3 and other authors[124, 176, 180] from poteniodynamic measurements. The corrosion rate in Figure 9-16 is shown to remain relatively constant after changing corrosion environment to a completely CO_2-saturated system. This coincides interestingly with the ennobled corrosion potential once the corrosion environments is changed to suggest that the iron sulphide corrosion product layer shown in Figure 9-11 could be keeping the corrosion rate constant. This is significant because as shown in the Figure 9-17(b), the corrosion rate in the CO_2-saturated corrosion system is expected to be in the range of 5.6 mm/yr as against the 1.5-2 mm/yr range for H_2S-containing systems as shown in Figure 9-16 and Figure 9-17(b).

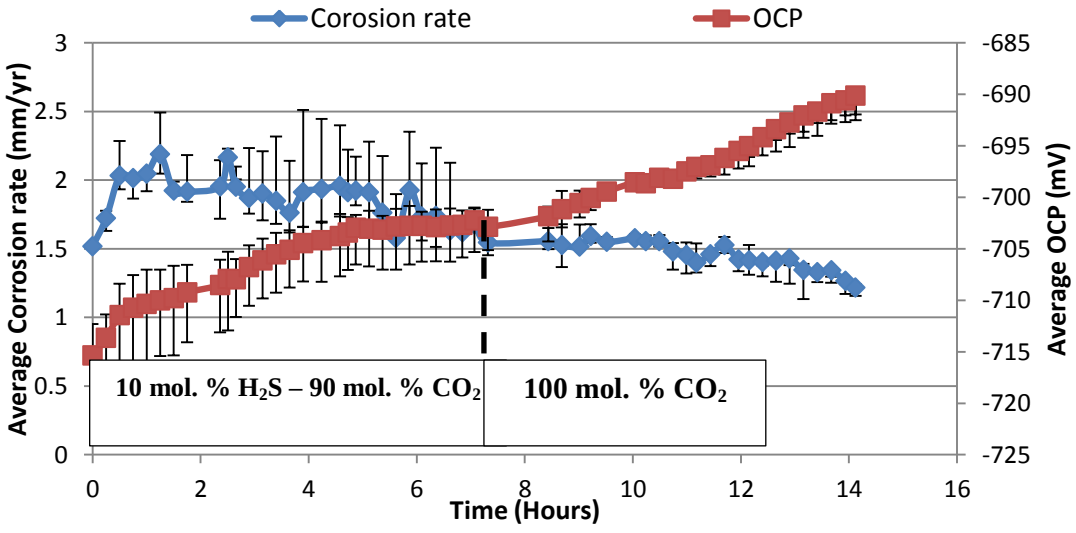

Figure 9-16 Corrosion potential and average corrosion rate on a single plot for X-65 carbon steel initially exposed to a 3.5 wt. % NaCl solution under 10 mol. % H_2S- 90 mol. % CO_2 gas atmosphere for 7 hours and then 100 mol. % CO_2 gas atmosphere for another 7 hours.

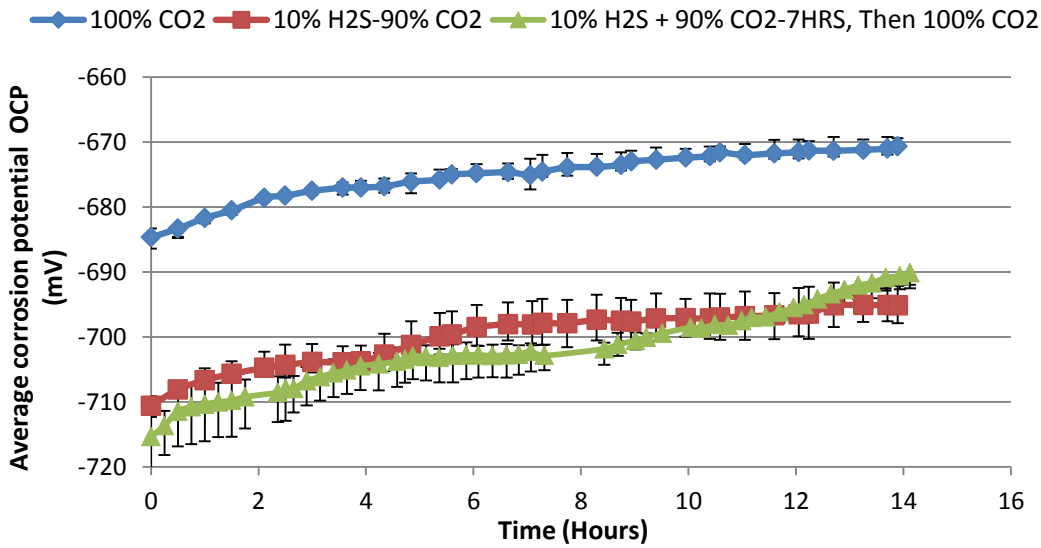

(a)

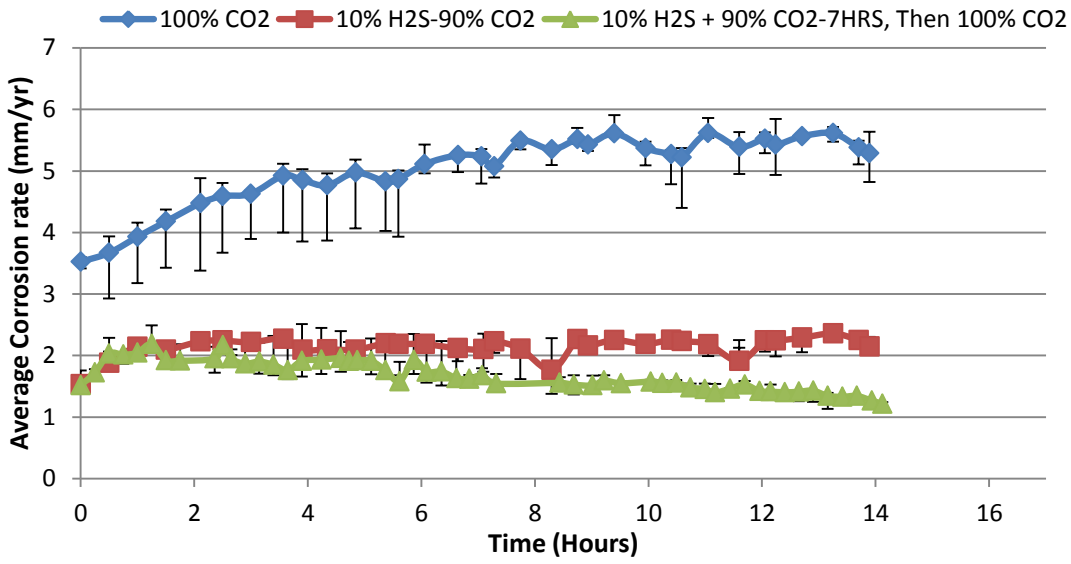

(b)

Figure 9-17 Graphs comparing a) Corrosion potential and (b) average corrosion rate of X-65 carbon steel initially exposed to a 3.5 wt. % NaCl solution under 10 mol. % H_2S- 90 mol. % CO_2 gas atmosphere for 7 hours and then 100 mol. % CO_2 gas atmosphere for another 7 hours with those of tests in 100 mol. % CO_2 corrosion systems and corrosion environment under 10 mol. % H_2S- 90 mol. % CO_2 atmosphere.

The SEM image and XRD pattern provided in Figure 9-18 (a) and (b) is for a 14 hour experiment in 100 mol. % CO_2 corrosion domains after an initial 7 hour experiment in a H_2S-containing corrosion domain. The SEM image shown in Figure 9-18 (a) shows a surface covered at numerous sites with iron sulphide corrosion product along with exposed networks of empty cementite. The distribution of the iron sulphide corrosion product was established based on EDX analysis. According to the published work of Choi *et al* [175] at 25°C and pH of 4, it is

also very likely that the initially formed iron sulphide corrosion product layer may be dissolving over a 14 hour period in a more aggressive CO_2 corrosion domain and at higher over-potential. This iron sulphide corrosion product is also confirmed by the XRD pattern shown in Figure 9-18 (b).

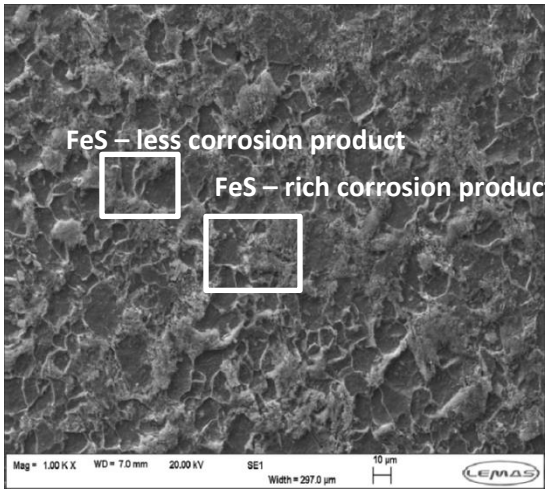

(a)

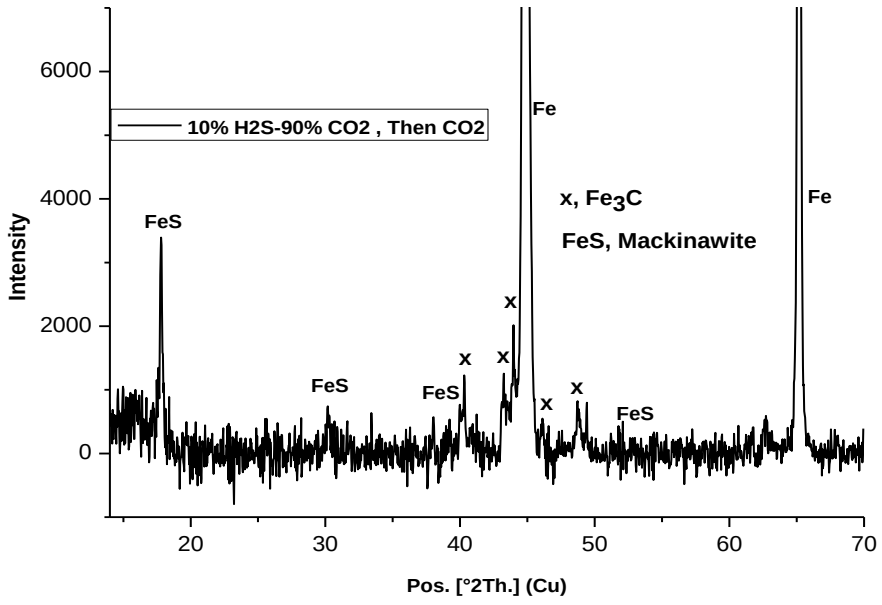

(b)

Figure 9-18 (a) SEM image and (b) XRD pattern for X-65 carbon steel initially exposed to a 3.5 wt. % NaCl solution under 10 mol. % H_2S- 90 mol. % CO_2 gas atmospheres for 7 hours and then 100 mol. % CO_2 gas atmosphere for another 14 hours. *(Note that the intensity scale is arbitrary)*. XRD peaks referenced to database in literature [168, 170, 178, 179].

9.5 Pitting corrosion initiation of carbon steel in sour corrosion environments; effects of temperature, CO_2 and H_2S gas

The main focus of this aspect of this research is to investigate the pitting corrosion initiation and propagation process of carbon steel material in H_2S-containing corrosion environments with respect to sweet corrosion environments. Figure 9-19(a) and (b) presents the maximum pit and average pit depth recorded on test samples exposed to the different conditions under investigation respectively (relative to the corroded surface after removal of corrosion products). The average pit depth represents an average of the 10 deepest pits as stipulated by ASTM G46-94 [70].

Referring to Figure 9-19, at the end of the 7 hours, there were no pits on the test sample at 30ºC in a test atmosphere composed of 100mol. % CO_2. In this same gas atmosphere, the maximum pit depth on the surface also increases to a maximum at 50ºC and then decreases slightly at 80ºC. Similar behaviour with temperature change has previously been reported presented and discussed in Chapter 6 of this thesis from separate tests. The initial increase in pit depth from 30 to 50ºC was attributed to the effect of temperature on the kinetic of corrosion and corrosion product formation. The rate of initial corrosion, evolution of empty cementite and formation of non-protective form of $FeCO_3$ corrosion product has been linked to pitting/localised corrosion [9, 88], which is also a function of temperature. However, the slight decrease in pit depth from 50 to 80ºC is strongly linked to the extensive uniform corrosion of the surrounding surface in this condition as already described in Chapter 6 of this thesis. Examples of the maximum pit depth identified in H_2S-CO_2-containing gas atmospheres are provided in Figure 9-20(a)-(c) as visual evidence of measurable pits.

In the 10mol. % H_2S - 90mol. % CO_2 and 10mol. % H_2S - 90mol. % N_2 gas atmospheres, the results in Figure 9-19 also show that the pit depth increases from a gas atmosphere of 100 mol. % CO_2, to 10mol. % H_2S - 90mol. % CO_2, and 10mol. % H_2S - 90mol. % N_2 in that order, while at the same time the general corrosion rate increases in the reverse direction. This was observed to be similar for all temperatures. However, the trend of change in pit depth with changing temperature was the same for all gas combinations under investigation. This suggests that CO_2 corrosion component of the overall corrosion process manifests mainly in the form of uniform corrosion in an un-buffered test system more than on pitting corrosion, especially in the initial stages of corrosion in H_2S-containing corrosion environments.

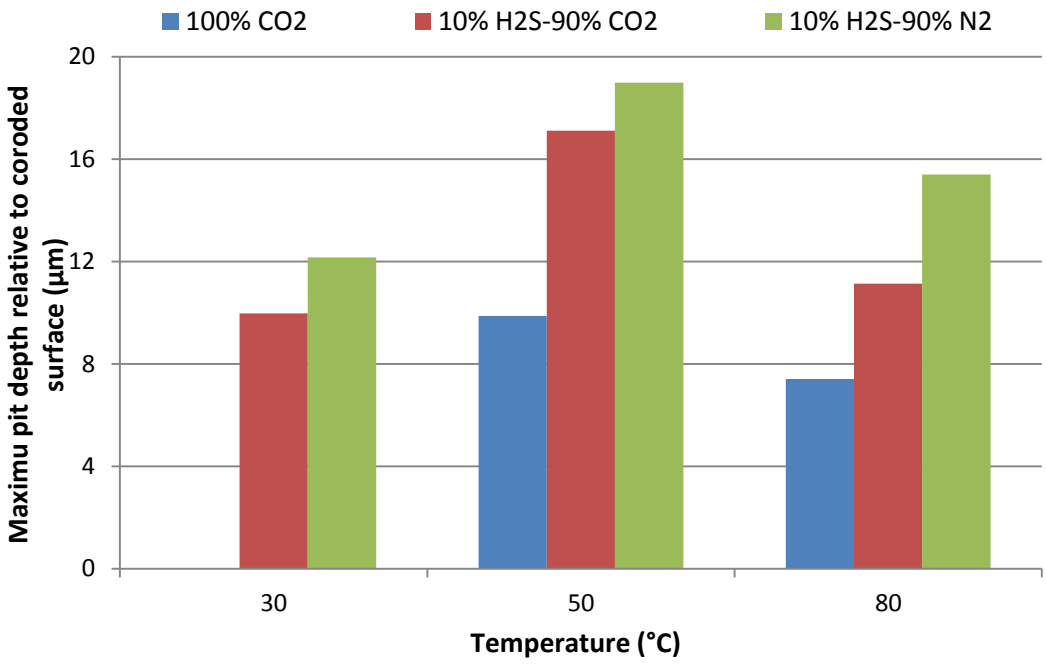

(a)

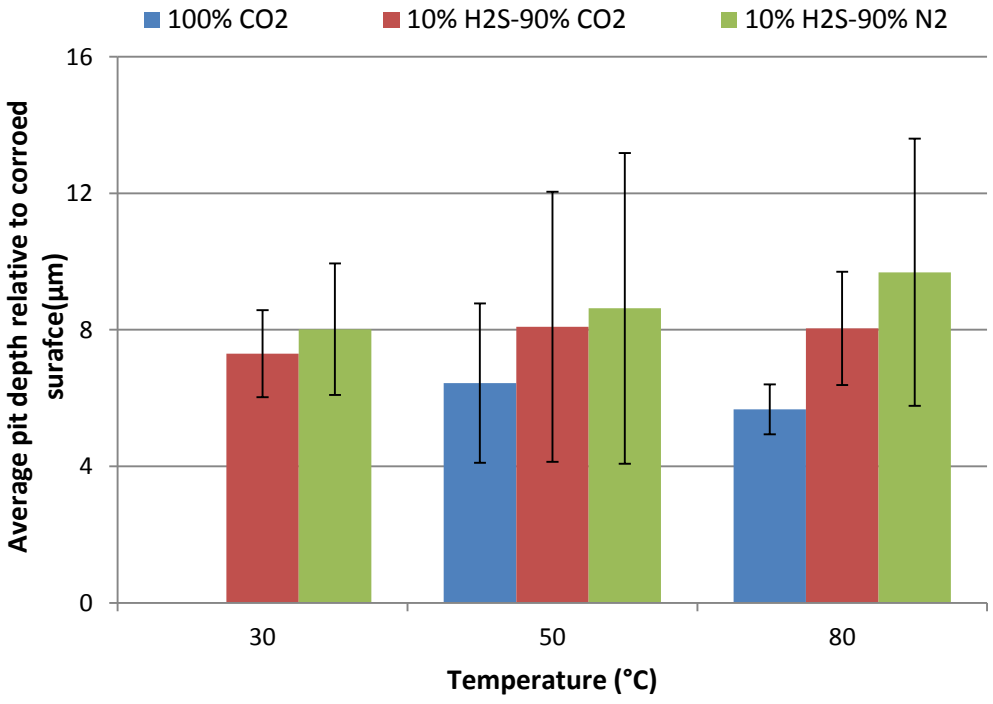

(b)

Figure 9-19 (a)Maximum pit depth (relative to corroded surface) and (b) Average pit depth (relative to corroded surface) on carbon steel surface exposed to corrosion system under 100mol. % CO_2, 10mol. % H_2S - 90mol. % CO_2 and 10mol. % H_2S - 90mol. % N_2 gas atmosphere for 7 hours as a function of temperature.

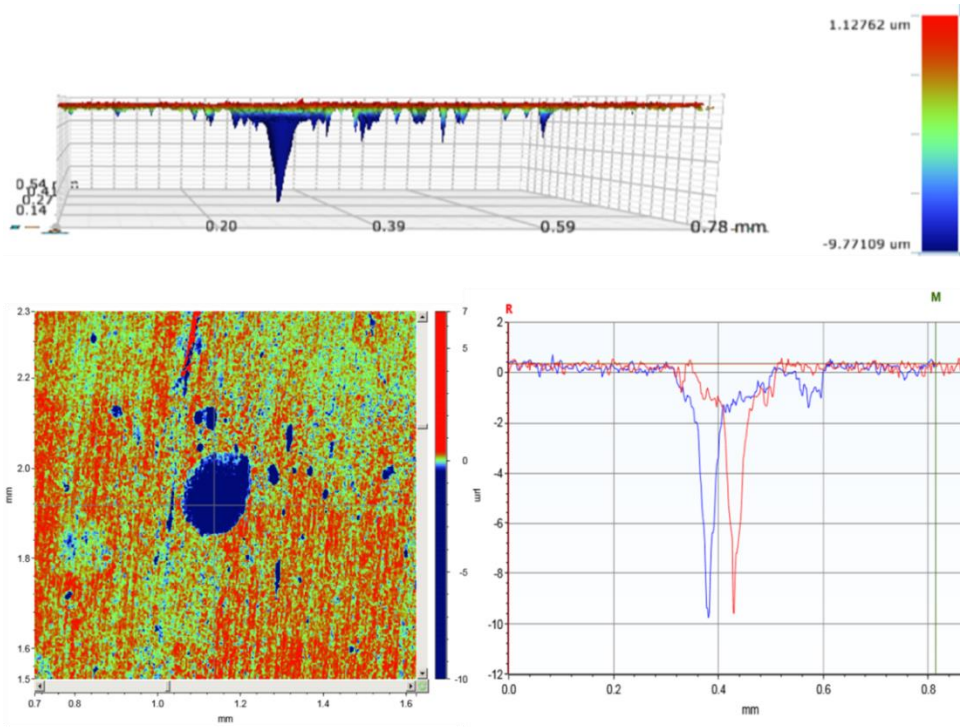
1.12762 um
-9.77109 um
0.20
0.39
0.59
0.78 mm
R
M
mm
um
mm

(a)

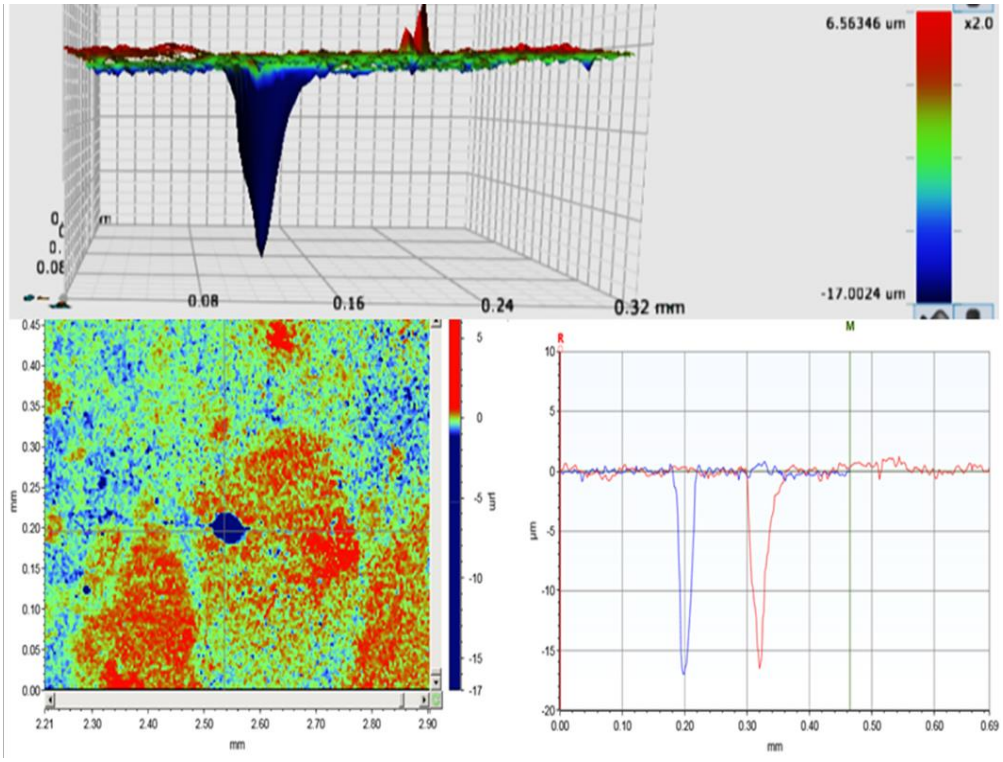
6.56346 um
x2.0
-17.0024 um
0.08
0.16
0.24
0.32 mm
R
M
mm
um
mm

(b)

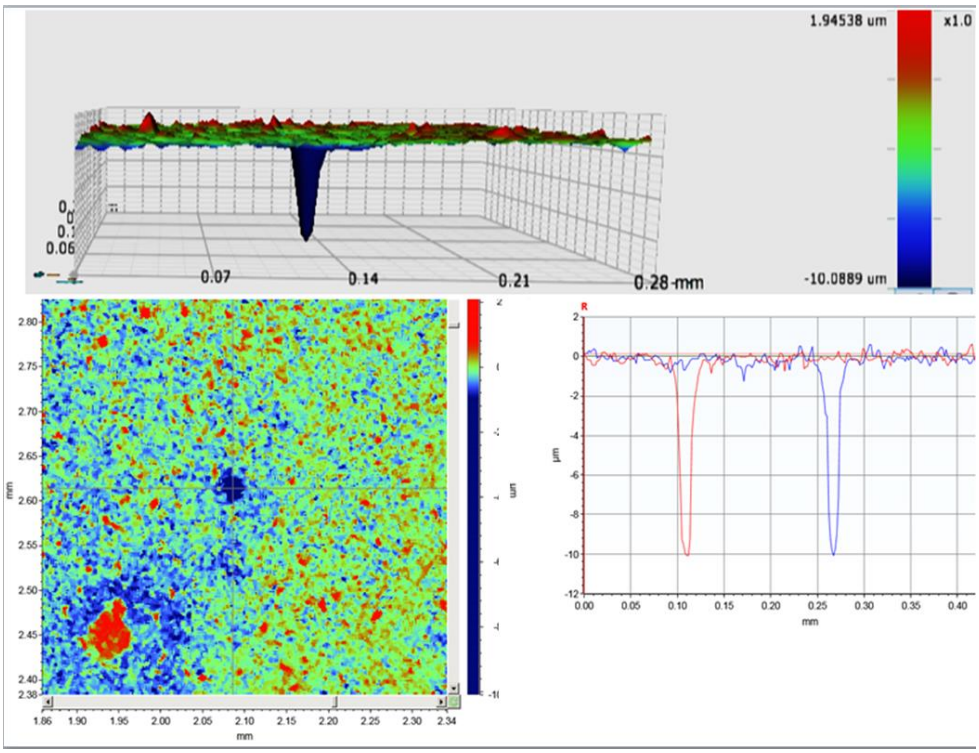

(c)

Figure 9-20 2D and 3D images of Deepest pit (relative to corroded surface) on carbon steel surface exposed to corrosion system under 10mole% H_2S - 90mole% CO_2 after 7 hours at (a) 30°C, (b) 50°C, and (c) 80°C.

It is also important to recognize that the significant pitting or propensity for pit to initiate in 10mol. % H_2S - 90mol. % CO_2 and 10mol. % H_2S - 90mol. % N_2 gas atmosphere is observed to be strongly related to the formation of iron sulphide corrosion product layer with non-uniform coverage. These films have been confirmed to be mainly mackinawite using the XRD pattern shown in Figure 9-4, Figure 9-9, Figure 9-13 and literature data [178, 179, 181]. Pitting corrosion as observed in this work and in H_2S-containing gas atmosphere has also been reported by other authors [138]. However, it has clearly been shown in this aspect of the work that the presence of H_2S gas and formation of an iron sulphide (mackinawite) corrosion product are the main agents for pitting corrosion initiation and that the presence of CO_2 in a CO_2-containing sour corrosion environment may be increasing total material loss due to the CO_2 corrosion contribution to uniform corrosion damage than to pitting corrosion damage. In an almost similar way, the contribution of CO_2 corrosion to material loss via uniform corrosion have also been shown in these results as being supressed by low levels of H_2S gas and even at much lower levels than used in this work [140, 176].

9.5.1 Pitting corrosion and metal penetration

The concept of total metal penetration has been introduced in Chapter 6 and 7 of this report as a useful tool for characterising the corrosion damage morphology of carbon steel in envrionement where the steel is predesposed to both pitting and uniform corrosion as the case in this study. This concept is very useful since the actual threat posed to carbon steel pipework subject to the prospect of pitting corrosion will always depend on both pit penetration rate relative to the corroding surface as well as on the uniform corrosion rate of the surrounding area. Refering to Figure 9-21, the change in total depth of metal penetration (i.e. uniform thickness plus pit depth relative to the corroded surface) as a function of temperature can be observed for each of the three gas systems used in this work. The results indicate that due to the substantial general corrosion rate of the sample exposed to solution in 100mol.% CO_2 gas atmosphere, the total thickness loss or total depth of metal penetration far exceeds that of the samples exposed to the solution under 10mol. % H_2S - 90mol. % CO_2 gas and 10mol. % H_2S - 90mol. % N_2 gas atmophere, where the uniform thickness loss is negligible in comparison to the pit depth relative to corroded surface. The uniform corrosion contribution to total metal penetration also increases with temperature and CO_2 content in the gas phase.

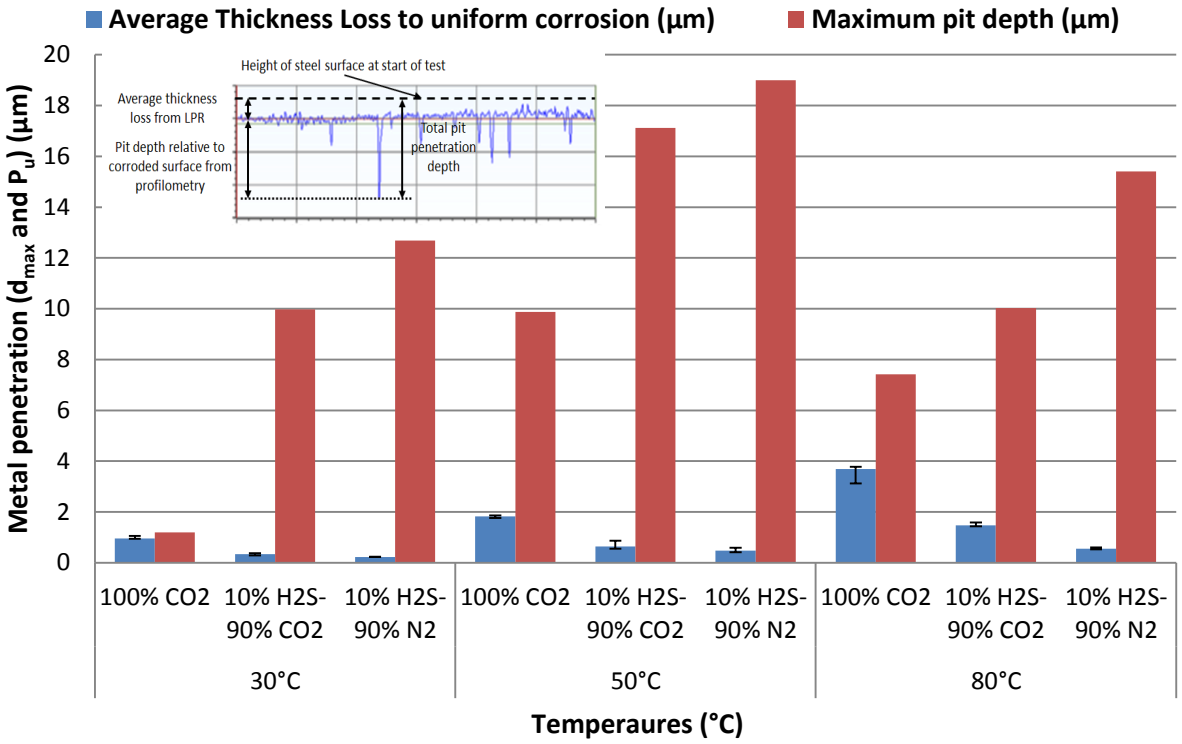

Figure 9-21 Total pit penetration on carbon steel surface exposed to corrosion system for 7 hours under 100mol. % CO_2, 10mol.% H_2S - 90mol. % CO_2 and 10mol.% H_2S - 90mol. % N_2 gas atmosphere as a fuunction of temperature indicating the contribution of general thickness loss (from LPR) and pit depth relative to corroded surface (determined from surface profilometry).

It could also be argued that the high general corrosion rate observed at 80ºC and in 100mol. % CO_2 gas atmopshere has the ability to essentially mask pit growth. However, the uniform corrosion contribution reduces significantly with the presence of H_2S gas, but still higher than at 50ºC. This suggests that at 80ºC, there is significant protection from iron sulphide that must be influencing both pitting and uniform corrosion. The mechanism by which this may be occurring remains unclear, but could be related to the contribution of iron sulphide formation from the aqueous corrosion reaction mechanism as suggested by other authors [35, 73, 115].

It could be imagined that the higher rate of metal dissolution at the start of the experiment at 80ºC could be favouring the kinetics of iron sulphide formation in the corrosion interface. Based on the results presented in Figure 9-21, pitting corrosion is occuring at a faster rate than that identified from purely the profilometry depth measurements relative to the corroding surface. However, for tests performed under 10mol.% H_2S - 90mol.% CO_2 gas and 10mol.% H_2S - 90mol.% N_2 gas atmophere, pitting corrosion initiation is not significantly masked by the general corrosion rate. The results shown in Figure 9-21 also suggest that the presence of H_2S gas in the gas atmopshere is reducing the general corrosion rate, but not necessarily reducing the risk of pitting of carbon steel pipelines.

9.5.2 Pitting Factor

The concept of pitting factor (P_f) has already been introduced and described in 6.6.4 of this thesis as a tool for characterisation of the nature of corrosion damage mechanisms (uniform and pitting corrosion). The pitting factor analysis presented in Figure 9-22 are a clear indication that the corrosion damage mechanism observed in the test solution of 100mol.% CO_2 gas atmosphere is actually pitting even while there is still substantial uniform corrosion taking place. Under a gas atmosphere of 10mole% H_2S - 90mole% CO_2 gas and 10mol.% H_2S - 90mol.% N_2, the pitting factor was higher and decreases with temperature because of the effect of corrosion rate on uniform corrosion of the surrounding surface. This suggests that pitting corrosion initiation occurs and dominates the corrosion damage mechanism in the sour corrosion environment once FeS is formed. The pitting factor of carbon steel under a purely CO_2 corrosion atmosphere confirms that there was very significant general corrosion.

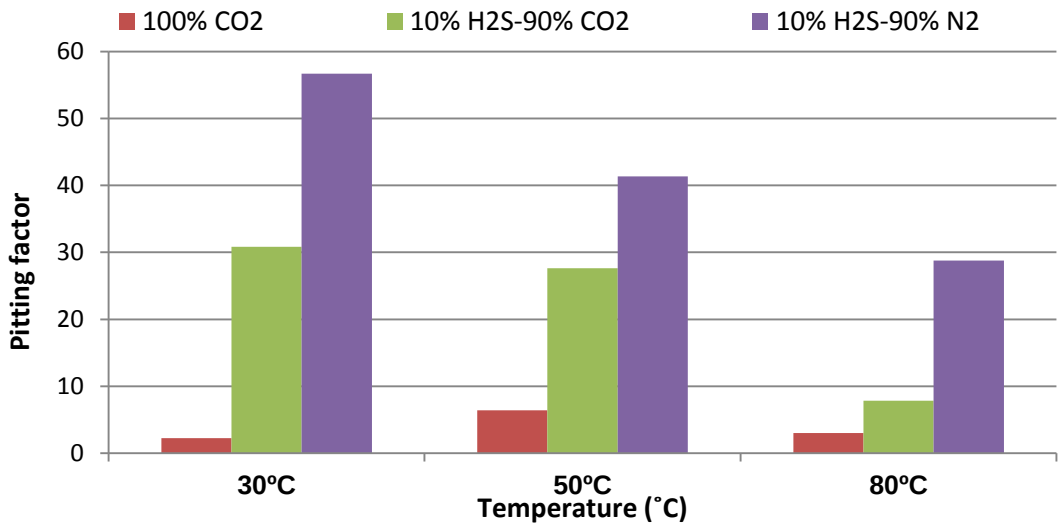

Figure 9-22 Variation of pitting factor for steel surface exposed to corrosinon system under 100mol. % CO_2, 10mol. % H_2S - 90mol. % CO_2 and 10mol. % H_2S - 90mol. % N_2 gas atmosphere as a function of temperature after 7 hours.

9.5.3 Summary on uniform and pitting corrosion behaviour of carbon steel in sour corrosion environment

The results presented and discussed in this chapter have shown that in the early stages of corrosion of carbon steel materials in H_2S-containing corrosion environments, the presence of CO_2 in the gas phase will enhance the electrochemical activities at the corrosion interface, leading to the competitive manifestations of both uniform corrosion and pitting corrosion initiation. The uniform corrosion contribution is more associated with CO_2 corrosion kinetics than with H_2S corrosion kinetics. Pitting corrosion component of material degradation is more related to the H_2S corrosion and iron sulphide formation kinetics. This influence of the presence of and /or absence of CO_2 gas in the gas phase is most prominent at higher temperatures, especially at 80°C.

Chapter 10. Investigation of the Long-term corrosion behaviour of carbon in sour corrosion environments; Effect of CO_2 and H_2S and temperature

The results presented and discussed in this section are based on 168 hour tests conducted based on the chosen experiment conditions provided in Table 5-5 and experimental procedure described in section 5.8.2 of this thesis. This part of the study was explored to investigate and potentially understand the possible changes (as a function of time) in the electrochemical properties of a corrosion interface characterised by the envisioned complexities that could be associated with corrosion of carbon steel pipe works in H_2S-containing corrosion environments. This approach is extended to all gas systems and temperatures under investigation. The results of this part of the study are described in the sections below.

10.1.1 Corrosion behaviour and formation of corrosion product at 30°C

The corrosion potential and corrosion rate measurements at 30ºC for test solutions under gas atmospheres composed of 100 mol. % CO_2 gas, 10 mol. % H_2S – 90 mol. % CO_2 gas mixture and 10 mol. % H_2S – 90 mol. % N_2 gas mixtures over a 168 hours period is presented in Figure 10-1(a) and (b) respectively. Referring to Figure 10-1(a), the corrosion potential at the start of the test in solutions under 100 mol. % CO_2 gas, 10 mol. % H_2S – 90 mol. % CO_2 gas atmospheres were the same at ≈ -680 mV. However, over the course of the experiment, the corrosion potential increased more in magnitude in the direction of a more positive potential in test solution under 100 mol. % CO_2 gas atmosphere than in test solution under 10 mol. % H_2S – 90 mol. % CO_2 gas atmosphere. Although the trend is very similar, the magnitude of the increase in potential differs slightly as shown in Figure 10-1(a). The gradual increase in corrosion potential over time and subsequent stabilisation after nearly 48 hours in 100 mol. % CO_2 gas saturated corrosion systems is likely connected to the evolution of iron networks of empty cementite as a result of preferential dissolution of ferrite from the metal lattice; an electrochemical process that normally precedes supersaturation of the bulk solution and corrosion interface [9, 88, 164], and the formation of a corrosion product layer composed of empty cementite network and an amorphous or non-crystalline form of $FeCO_3$ corrosion product. These viewpoints have already been discussed in Chapters 6 and 7. The amorphous or non-crystalline form of $FeCO_3$ has been shown in the literature to be typical at similar pH [93, 95].

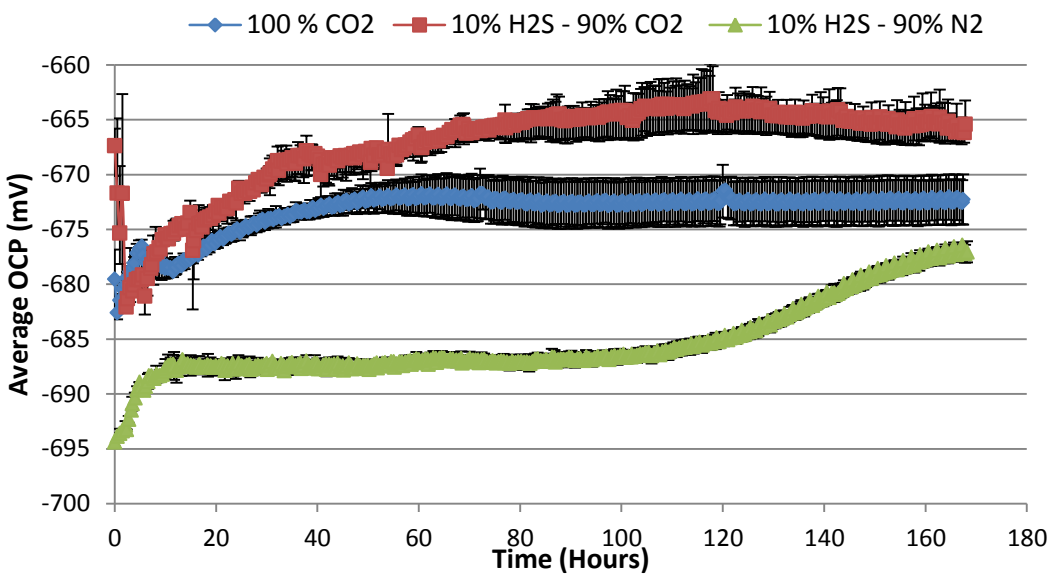

(a)

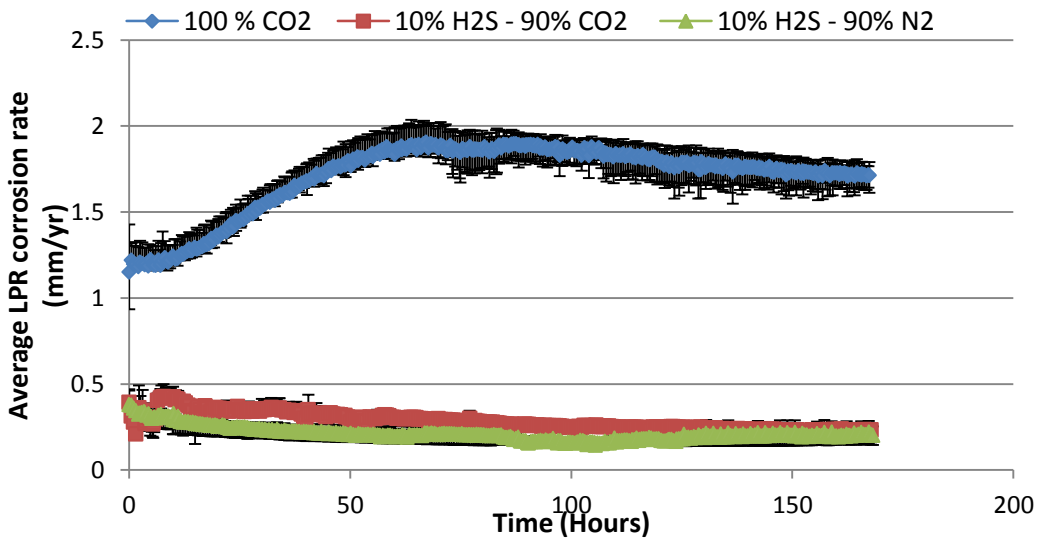

(b)

Figure 10-1 Graphs of (a) corrosion potential and (b) corrosion rate of X65 carbon steel in 3.5 wt.% NaCl solution under three different gas atmospheres at 30°C, over 168 hours.

In corrosion systems under 10 mol. % H_2S – 90 mol. % CO_2 gas atmosphere, the magnitude of corrosion potential became more negative as would be expected due to the presence of H_2S gas [124, 180]. Similar observations have also been reported by Ma *et al* [124] for tests at a pH of 3 in 0.5mol.dm^{-3} H_2SO_4/$NaSO_4$ solution at 22°C. In these conditions, the corrosion potential changes from -615 mV in H_2S-free acid solution to -653 mV in 0.02 mmol.dm^{-3} H_2S-containing acid solution after 5 minutes. However, the magnitude of the corrosion potential for test under 10 mol. % H_2S – 90 mol. % CO_2 gas atmosphere at 30°C in this study is still in the same range as magnitude of the corrosion potential in 100 mol. % CO_2 gas systems. This may also be

related to the overbearing influence of CO_2 corrosion kinetics on the overall kinetics of the corrosion environment and potentially due to the fact that the kinetics of iron sulphide corrosion product formation is also limited by the relatively low temperature. The corrosion potential variation for test in solutions under 10 mol. % H_2S – 90 mol. % N_2 gas atmosphere changes differently with time. Firstly, is the fact that the magnitude of corrosion potential at the start of the experiment is more negative than the corrosion potential in CO_2-saturated corrosion environment. Secondly, the initial increase in corrosion potential usually associated with ferrite dissolution and evolution of empty cementite [88, 165].

After about 90 hours of stable potential, the corrosion potential increases slightly towards a more positive potential. The sudden increase in corrosion potential is most likely linked to the presence of an iron sulphide corrosion product layer with more surface coverage. This has become more apparent because of the absence of CO_2 gas in the gas phase. This viewpoint has also been confirmed by the results of Ma *et al* [124]. In Ma *et al* [124], once the H_2S gas is introduced at the start of the experiment in an acidic media, the corrosion potential drops quickly from an initial value of -632 mV to -690 mV in 5 minutes. However, after 2 hours of exposure, the corrosion potential increased back to -620 mV and was attributed to the potential formation of iron sulphide corrosion products. It is important to mention that the results of Ma *et al* [124] were based on potentiodyanmic sweeps.

With reference to the corrosion rate measurements presented in Figure 10-1(b), the corrosion rate is observed to be increasing within the period of the test that is characterised by the evolution of empty cementite network leading to increased corrosion rate at the anodic regions of the steel surface. This observation has already been described in Chapter 6 of this thesis and is very consistent with the literature [9, 88, 165]. However, once, the amorphous or non-crystalline and nano-scale polycrystalline form of $FeCO_3$ corrosion product is fully established on the surface of the steel as shown by the SEM image in Figure 10-3(a) after 168 hours, the corrosion rate became almost constant at ≈ 1.7 mm/yr. Identification of corrosion product layer is confirmed by the XRD pattern shown in Figure 10-4(a). The corrosion rate in H_2S-containing corrosion environments; 10 mol. % H_2S – 90 mol. % CO_2 and 10 mol. % H_2S – 90 mol. % N_2 is almost the same and constant throughout the duration of the experiment at about one-third of the corrosion rate in 100 mol. % CO_2 saturated corrosion environment. Woollam *et al* [176], also reported a 70% reduction in corrosion rate after 48 hours from 100 mol. % CO_2 saturated corrosion environment to a 1% H_2S-99% CO_2 containing corrosion environment.

According to Woollam *et al* [176], the formation of an adsorbed mono-layer of Fe-S_{ads} could be responsible for this decrease in corrosion rate in H_2S-CO_2 containing corrosion environment, a standpoint that has also been adopted by Zheng *et al* [140] to explain similar reduction in corrosion rate after 2 hours in the presence of H_2S gas. In the context of the results presented and discussed in section 8.3 for 7 hours tests, this may also be true at this temperature, even while the SEM images a significant but non-uniform coverage of steel surface by iron sulphide corrosion products (confirmed by XRD pattern).

From the SEM images of Figure 10-3(b) and (c) and Figure 10-4(b) and (c), it is evident that over the course of the 168 hour experiments the lower corrosion rate observed in test solutions under 10 mol. % H_2S – 90 mol. % CO_2 and 10 mol. % H_2S – 90 mol. % N_2 gas atmosphere is most likely due to the formation of iron sulphide corrosion product layer as shown in Figure 10-3(b) and (c) and confirmed by the XRD patterns provided in Figure 10-4(b) and (c) and given that Ma *et al* [124] had reported a similar effect just after 2 hours. Although these corrosion product layers are very thin, their respective impact cannot be ignored along with the effect of low temperature on the kinetics of corrosion reactions in both CO_2 and H_2S containing corrosion environments.

It is also important to note that theoretically, a lower pH would imply that the rate of H^+ reduction would be increased leading to increased corrosion rate as reported by Nesic *et al* [103]. However, in the context of the *in-situ* pH data provided in Figure 10-2, It is evident that the lowest pH recorded for test solutions under 10 mol. % H_2S – 90 mol. % CO_2 gas atmosphere does not necessarily translate into higher corrosion rate potentially due to the over-riding influence of iron sulphide corrosion product layer. The pH in solutions under 10 mol. % H_2S – 90 mol. % N_2 gas atmosphere is also slightly higher than in the case of 100 mol. % CO_2, potentially due to the higher solubility of the H_2S gas and lower acidity of the solution containing only H_2S as the only active gas when compared to the case with 100 mol.% CO_2 gas.

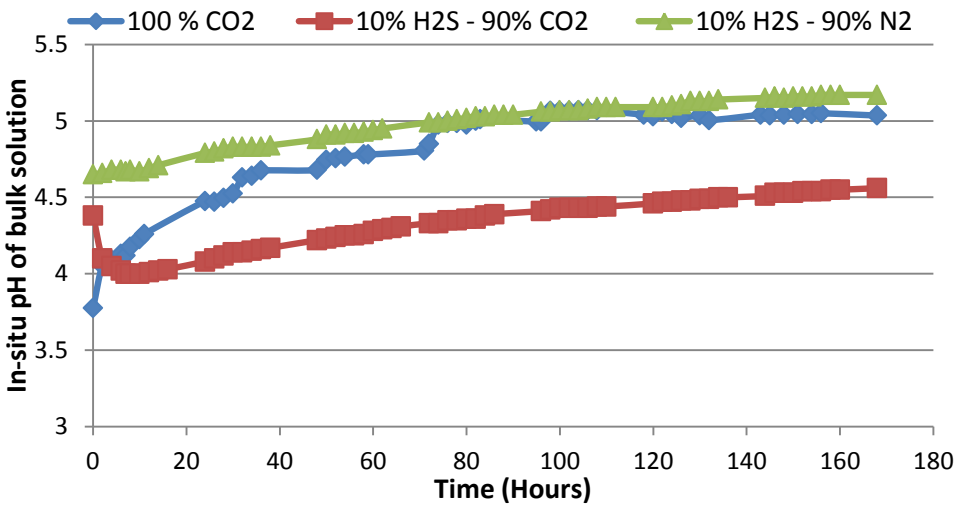

Figure 10-2 Measured *in-situ* pH of corrosion media under three different gas atmospheres at 30°C, over 168 hours.

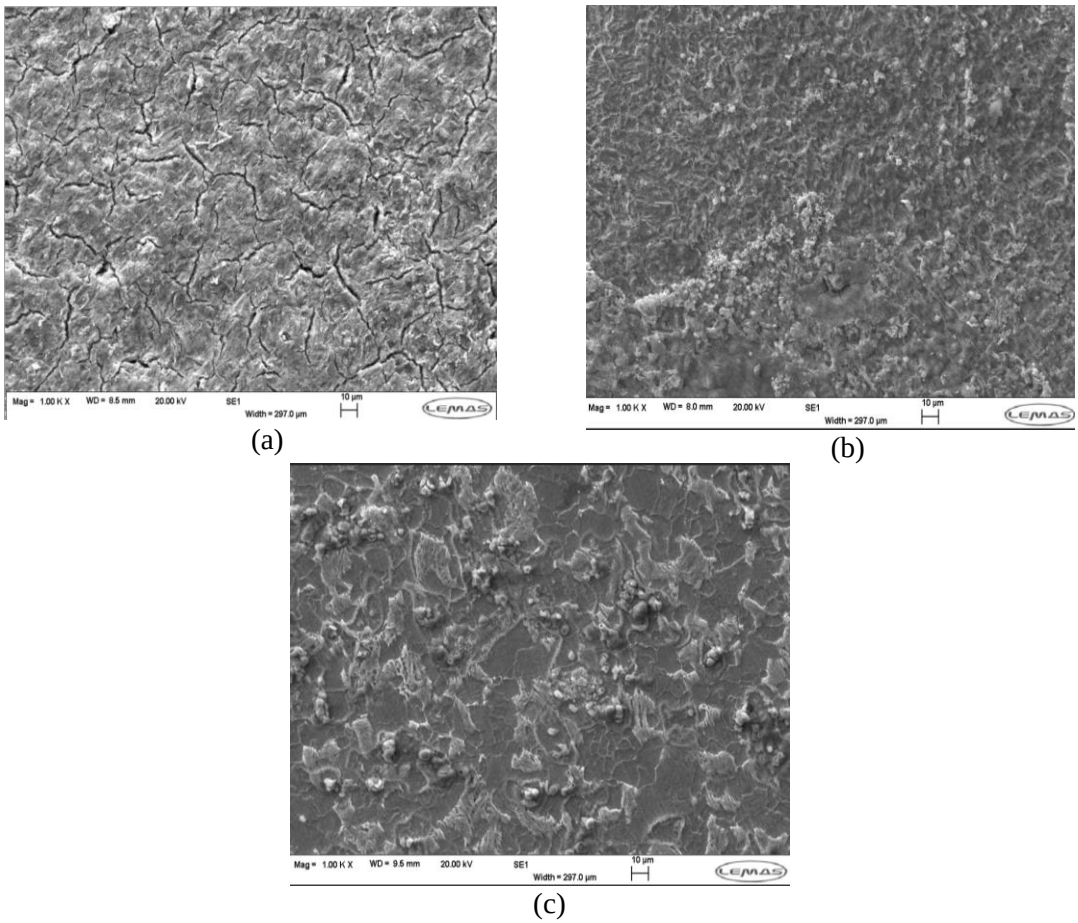

(a) (b) (c)

Figure 10-3 SEM images of corrosion product layer on X65 carbon steel in 3.5 wt. % NaCl solution under gas atmospheres composed of (a) 100 mol. % CO_2, (b) 10 mol. % H_2S- 90 mol. %CO_2 and (c) 10 mol. % H_2S-90 mol. % N_2 at 30°C and after 168 hours.

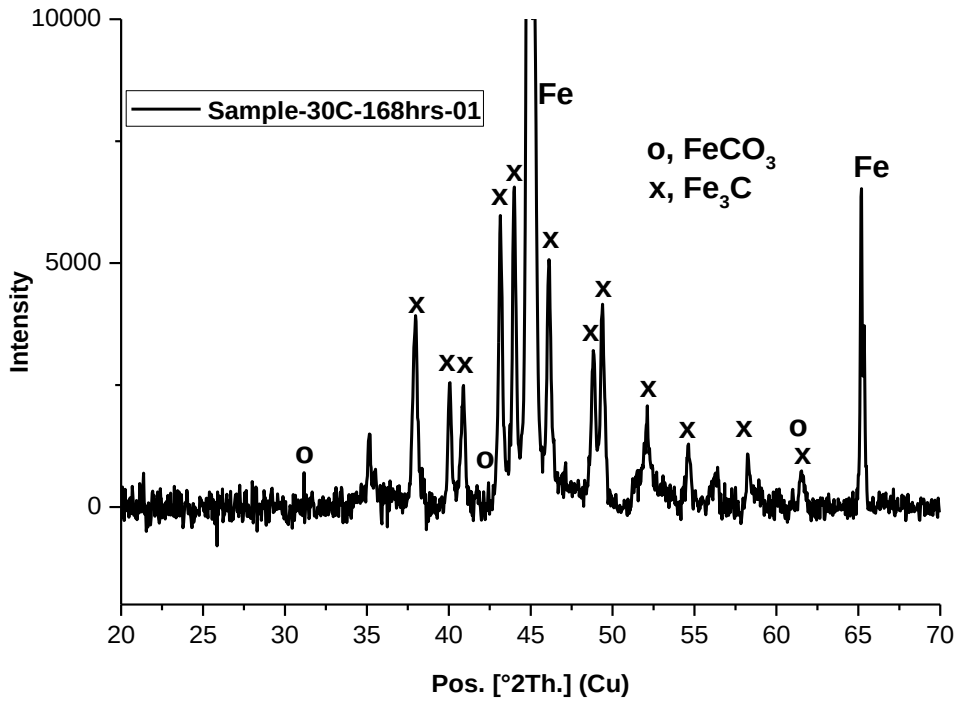
Sample-30C-168hrs-01
Fe
o, FeCO3
x, Fe3C
Fe
Intensity
Pos. [°2Th.] (Cu)

(a)

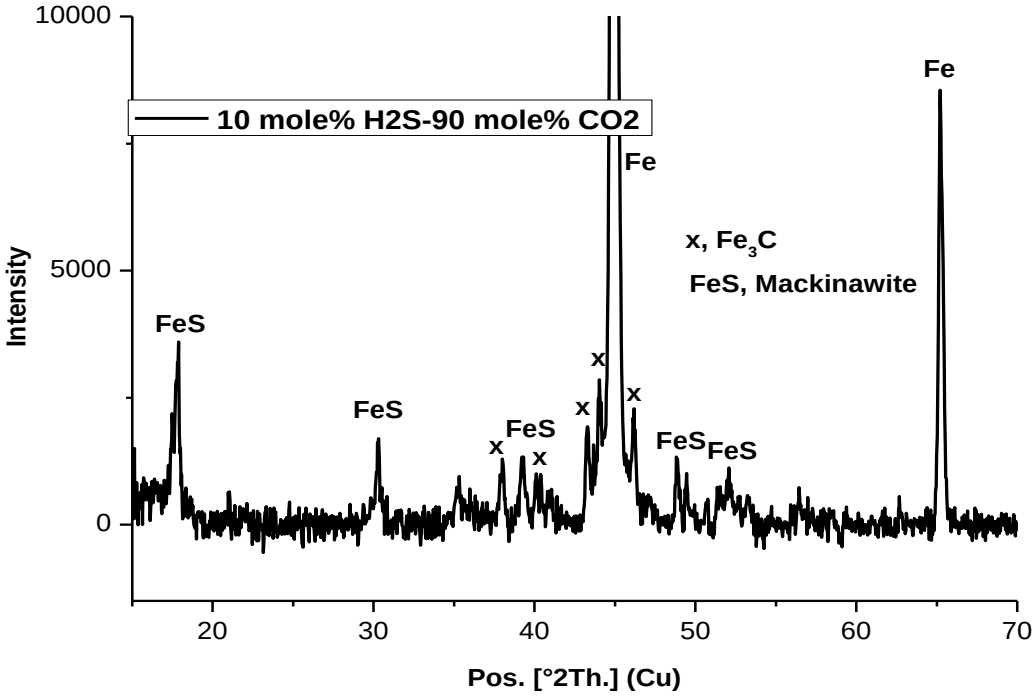
10 mole% H2S-90 mole% CO2
Fe
x, Fe3C
FeS, Mackinawite
FeS
Intensity
Pos. [°2Th.] (Cu)

(b)

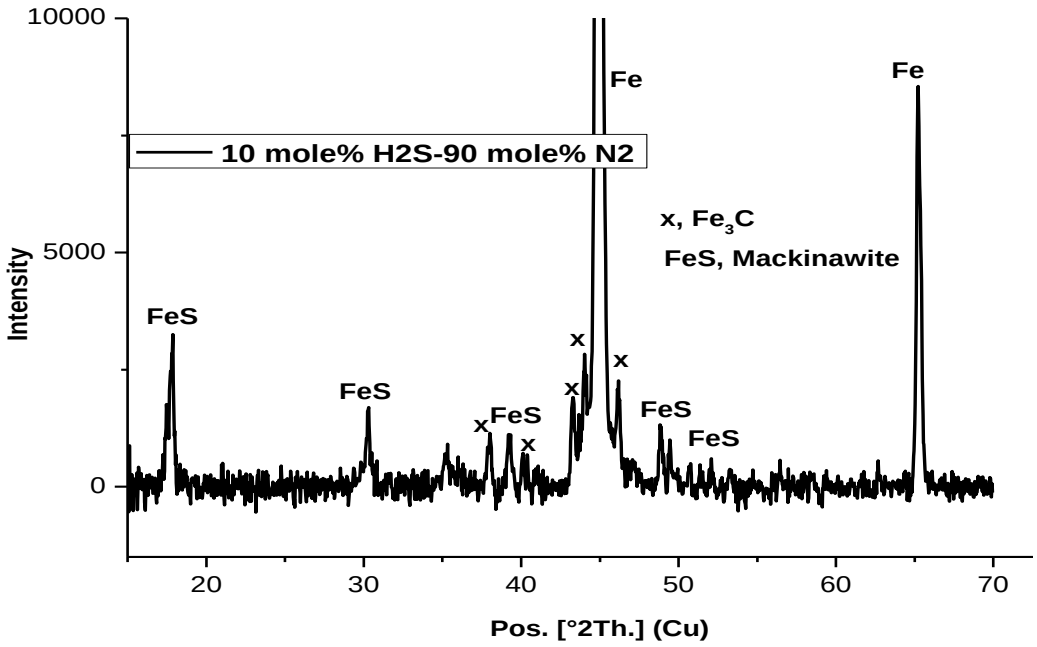

(c)

Figure 10-4 XRD pattern of corrosion product layer on X65 carbon steel in 3.5 wt. % NaCl solution under gas atmospheres composed of (a) 100 mol. % CO_2, (b) 10 mol. % H_2S- 90 mol. %CO_2 and (c) 10 mol. % H_2S-90 mol. % N_2 at 30°C and after 168 hours. *(Note that* the *intensity scale is arbitrary)*. XRD peaks reference to database in literatures [168-170, 178, 179].

10.1.2 Corrosion behaviour and formation of corrosion product at 50°C

Figure 10-5(a) and (b) presents the corrosion rate and potential measurements respectively for test at 50ºC for solutions under gas atmospheres composed of 100 mol. % CO_2 gas, 10 mol. % H_2S – 90 mol. % CO_2 gas mixture and 10 mol. % H_2S – 90 mol. % N_2 gas mixtures over a 168 hours period. At the start of the experiment, the corrosion potential for test in the three gas systems under investigation were distinctly different in magnitude at ≈ -682 mV, -696 mV and -711 mV for corrosion environment under 100 mol. % CO_2 gas, 10 mol. % H_2S – 90 mol. % CO_2 gas mixture and 10 mol. % H_2S – 90 mol. % N_2 gas atmosphere respectively. The corrosion potentials of -696 mV and -711 mV for corrosion in 10 mol. % H_2S – 90 mol. % CO_2 and 10 mol. % H_2S – 90 mol. % N_2 gas systems at 50°C from this study, compares well with corrosion potentials of ≈ -735 mV at 40°C in a gas system composed of 1 % H_2S and 99% CO_2 in the published results by Woollam *et al* [176] and ≈ -680 mV at 60°C and pH of 4 in H_2S-N_2 gas system composed of $[H_2S]_{aq}$ of 8.3 x10^{-4} mol/L in the published results by Zheng *et al* [119]. Although the results from the literature were at slightly lower or higher temperature than 50°C, it helps to validates the trends in the magnitude of the corrosion potential observed in this study and also as suggested by Morris *et al* [180].

In the course of the experiment, the corrosion potential variation with time for tests under 100 mol. % CO_2 gas atmospheres is very similar to the case at 30°C. As previously described in this thesis, the initial increase in corrosion potential in this condition is usually an indication of the initial dissolution of ferrite from metal lattice, leading to the evolution of cementite [9, 88, 164]. Following supersaturation in the bulk solution and corrosion interface, the process is followed by the formation of a non-crystalline/amorphous form of $FeCO_3$ as shown in the SEM image of Figure 10-7(a). The formation of a non-crystalline/amorphous form of $FeCO_3$ is usually alongside some nano-scale polycrystalline form of $FeCO_3$ (not visible from the SEM image) as confirmed by the XRD pattern provided Figure 10-8(a). Once this form of $FeCO_3$ is fully established on the steel surface, the corrosion potential is seen to be stable and constant at ≈ -664 mV throughout remaining period of the experiment.

In tests under 10 mol. % H_2S – 90 mol. % CO_2 gas atmosphere, the corrosion potential is initially increases almost in the same way as tests under 100 mol. % CO_2 gas atmosphere to suggests that there is still the process of initial ferrite dissolution and cementite evolution in this condition and potentially contributing to metal dissolution even when the formation of an FeS layer is expected to occur quickly. The corrosion potential is stable after this initial increase towards a more positive potential at ≈ -678 mV from an initial corrosion potential of ≈ -696 mV. This corrosion potential was stable and constant up to 110 hours after which there is sudden drop in potential towards a more negative potential at ≈ -682 mV. This observation is likely connected to the thinning effect or dissolution of initially formed iron sulphide as reported by Choi *et al* [175] at pH of 4 and 30°C in a 100 ppm H_2S-containing corrosion system as a result of changing the environment from H_2S-containing to completely CO_2 saturated. Choi et at [175] had suggested that initially formed FeS corrosion product may have been damaged at higher anodic potential leading to this observation in corrosion potential. Brown and Nesic [138] also confirm the observation in this work by stating that the initially formed FeS corrosion product layer (mackinawite) usually undergoes a cyclic process of growth, damage (cracking, and delamination) and potentially dissolution to develop an FeS corrosion product layer.

As shown by the SEM image of Figure 10-7(b) and (c), the iron sulphide corrosion product layer appears to be very porous with large spaces in between and different from the iron sulphide corrosion product observed after 7 hours in Figure 9-7(b) for the same test condition. This has also been confirmed by the XRD pattern of Figure 10-8(b) to be an iron sulphide layer composed dominated by mackinawite but with evidences to show the presence of pyrrhotite with needle-like and/or hexagonal plate morphology [128] as shown in Figure 10-7(c). The

corrosion potential for test under 10 mol. % H_2S – 90 mol. % N_2 gas atmosphere is observed to be relatively very stable after the initial increase in corrosion potential from ≈ -711 mV to -700 mV. Although the corrosion potential does not change significantly over time after this initial increase, the SEM image in Figure 10-7(d) showed a very porous and loosely formed iron sulphide corrosion product layer that has been characterised by the XRD pattern shown in Figure 10-8(c) to be dominated by mackinawite but also with evidences to show the presence of pyrrhotite. The morphology of the corrosion product layer is also different to the morphology of corrosion products after 7 hours in the same test condition. This also shows that over time, the initially formed iron sulphide corrosion product must have undergone some form of cyclic transformation.

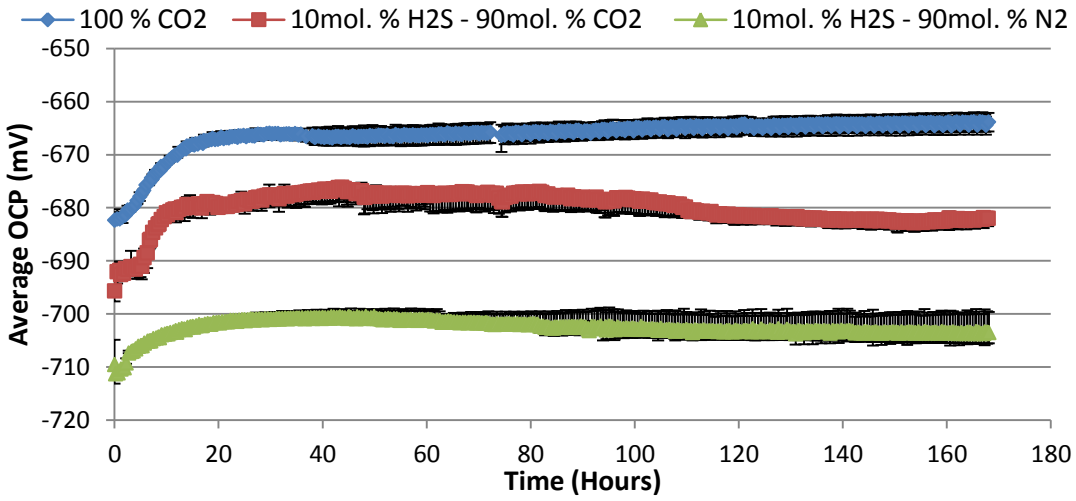

(a)

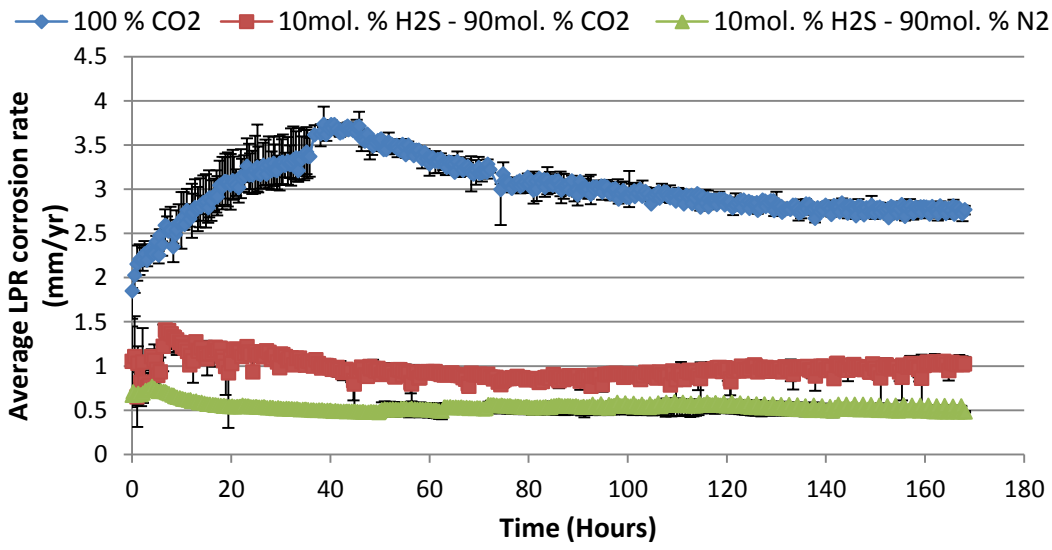

(b)

Figure 10-5 Graphs of (a) corrosion potential and (b) corrosion rate of X65 carbon steel in 3.5 wt.% NaCl solution under three different gas atmospheres at 50°C, over 168 hours.

In terms of the corrosion rate over a 168 hour period, there is an observed initial increase in corrosion rate in Figure 10-5(b) for test under 100 mol. % CO_2 gas atmosphere, which has already been related to the evolution of empty cementite according to other authors [9, 88, 165]. This also coincides with the observed initial increase in corrosion potential within this same period of the test (0 - 42 hours). However, once an amorphous or non-crystalline form of $FeCO_3$ corrosion product is established unto the steel surface, the corrosion rate is shown to gradually reduce to a constant value of ≈ 2.7 mm/yr from ≈ 3.7 mm/yr. In comparison to the corrosion rate for test in 10 mol. % H_2S – 90 mol. % CO_2 gas systems, the corrosion rate in test under 10 mol. % H_2S – 90 mol. % CO_2 gas atmosphere is lower than test under 100 mol. % CO_2 gas atmosphere. Corrosion rate increases slightly within the first 7 hours to ≈ 1.4 mm/yr before dropping down to ≈ 0.7 mm/yr after almost 100 hours. The corrosion potential is also relatively stable and more positive than at the start of the experiment to suggest that the slight decrease in corrosion rate up to 100 hours is due to the formation of FeS corrosion product.

The corrosion rate also increases slightly after the 100 hour mark (Figure 10-5(b)), coinciding with a drop in corrosion potential at about the same time during the test (Figure 10-5(a)). This confirms the initial assertion that this may be related to the thinning effect or dissolution of initially formed iron sulphide layer. Smith [128] stated that once the mackinawite film has formed on the surface of the steel, a reverse reaction may occur where the mackinawite begins to dissolve into the solution to order to maintain equilibrium conditions with the solution. The rate of re-dissolution of initially formed mackinawite as observed in this study also depends on other environmental parameters like temperature [128]. This process could also influence the nature of corrosion damage in this system. In the test under 10 mol. % H_2S – 90 mol. % N_2 gas atmosphere, the corrosion rate is relatively constant for the duration of the experiment showing less changes in the electrochemical activity at the corrosion interface at 50°C. This is also consistent with changes in the corrosion potential. The transformation in the morphology of the iron sulphide corrosion product over time still continued unhindered. The difference in the corrosion behaviour with reference to the potential dissolution of initially formed iron sulphide between H_2S-CO_2 and H_2S-N_2 corrosion systems may be related to the presence and/or absence of CO_2 in H_2S-containing gas systems. This is an interesting perspective since the results have suggested that the corrosion media becomes more aggressive with the presence of CO_2 gas.

In-situ pH of the solutions under the three gas atmospheres under investigation presented in Figure 10-6. H_2S-CO_2 gas system recorded the lowest pH compared to CO_2-saturated systems. However the corrosion rate is found to be lower for tests in the H_2S-CO_2 corrosion system than

in the CO_2-saturated system. Lower corrosion rate in H_2S-CO_2 containing system than in the CO_2-saturated system is due to the influence of the iron sulphide corrosion product over the buffering effect from H^+ and H_2CO_3 reduction at the corrosion interface during corrosion. The buffering effect in CO_2-saturated environment is due to higher iron dissolution than $FeCO_3$ precipitation from the bulk solution [93] leading to increasing pH with time.

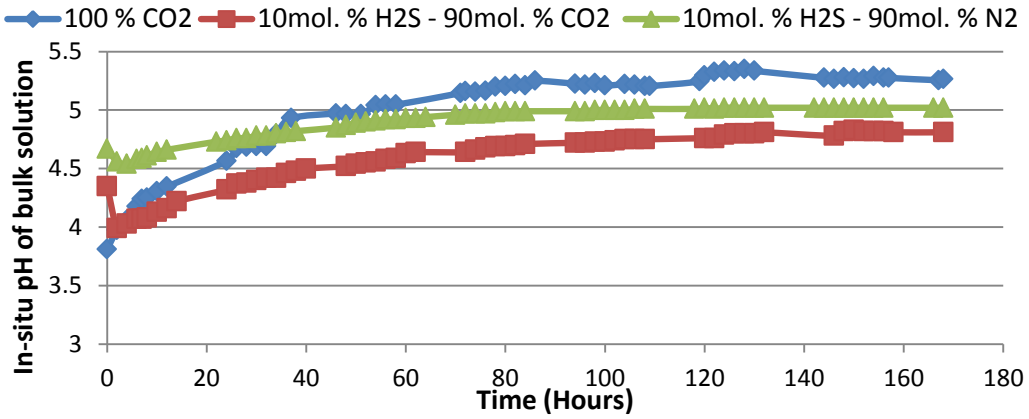

Figure 10-6 Measured *in-situ* pH of corrosion media under three different gas atmospheres at 50°C, over 168 hours

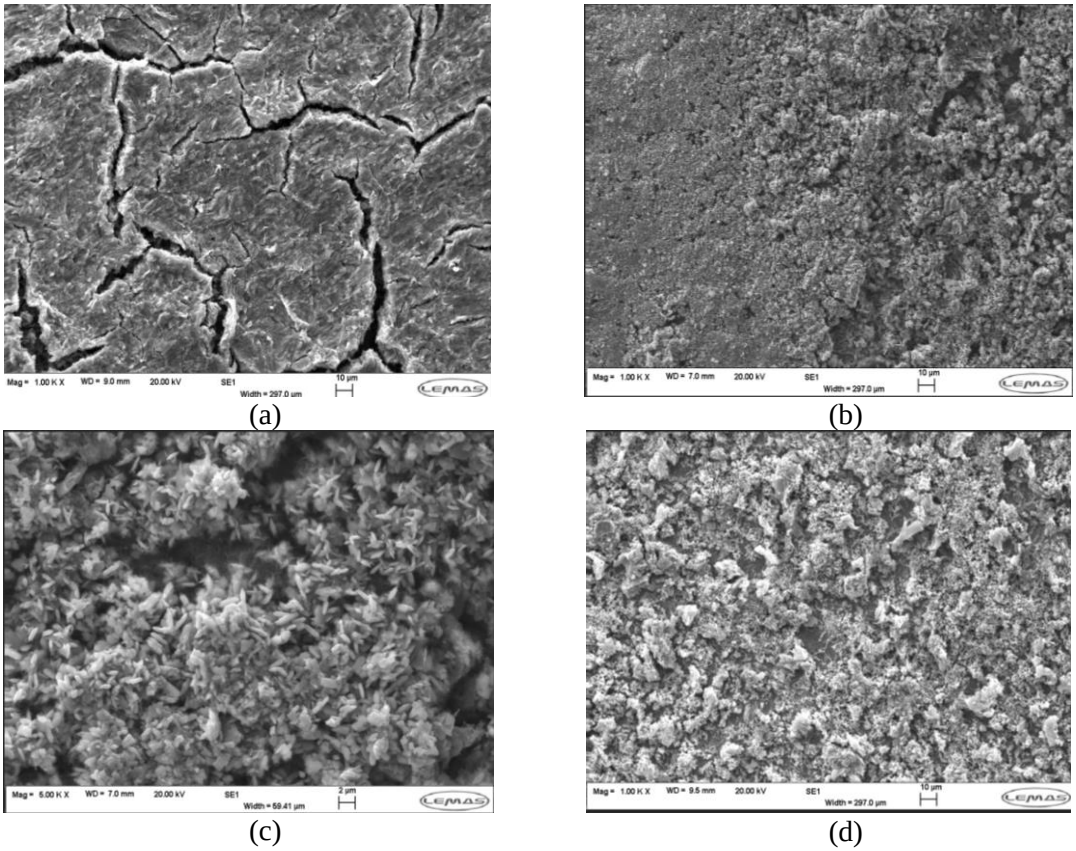

Figure 10-7 SEM images of corrosion product layer on X65 carbon steel in 3.5 wt. % NaCl solution under gas atmospheres composed of (a) 100 mol. % CO_2, (b) 10 mol. % H_2S- 90 mol. %CO_2, (c) 10 mol. % H_2S- 90 mol. %CO_2 at X5000 magnification and (d) 10 mol. % H_2S-90 mol. % N_2 at 50°C and after 168 hours.

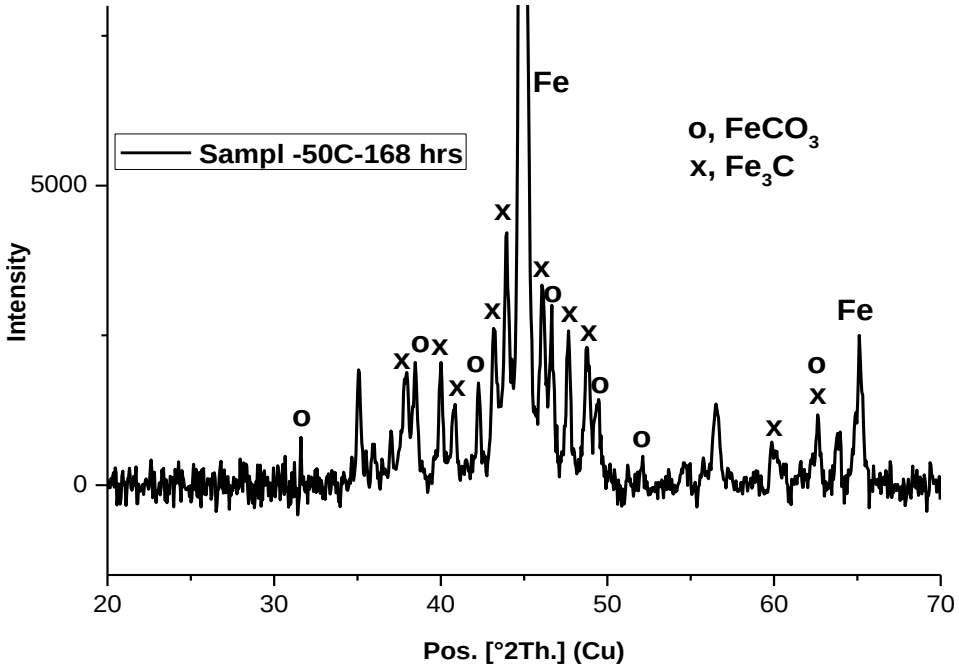
Sampl -50C-168 hrs
o, FeCO3
x, Fe3C
Fe
Intensity
Pos. [°2Th.] (Cu)

(a)

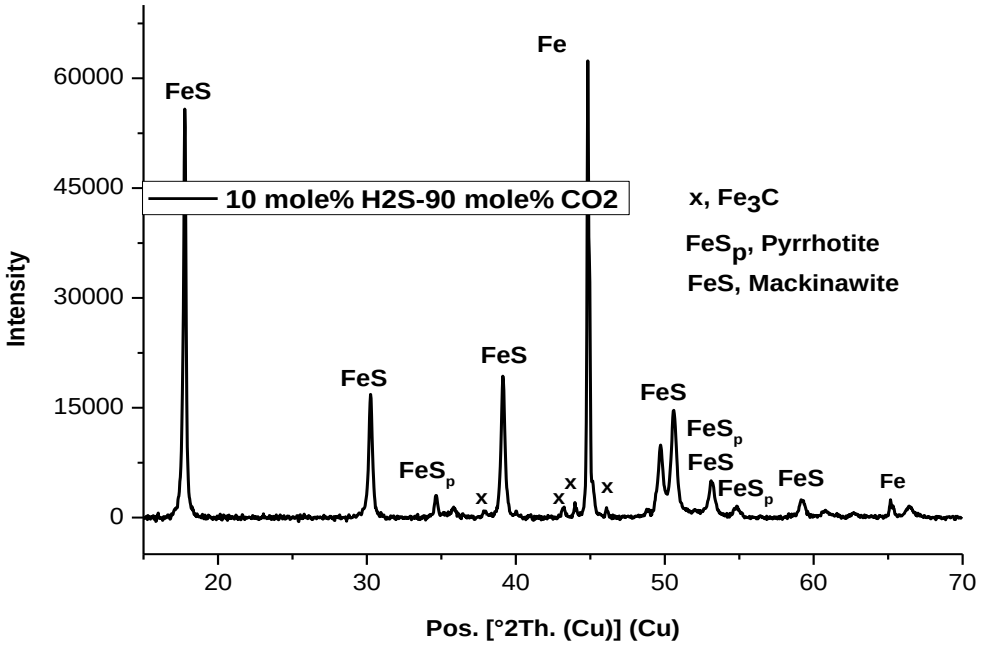
10 mole% H2S-90 mole% CO2
x, Fe3C
FeSp, Pyrrhotite
FeS, Mackinawite
FeS
Fe
FeSp
Intensity
Pos. [°2Th. (Cu)] (Cu)

(b)

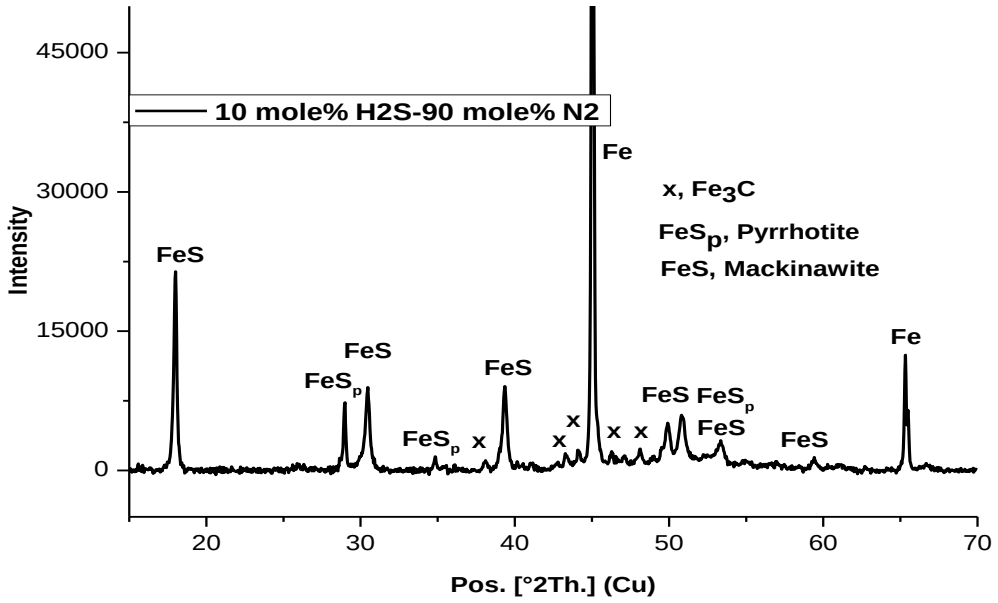

(c)

Figure 10-8 XRD pattern of corrosion product layer on X65 carbon steel in 3.5 wt. % NaCl solution under gas atmospheres composed of (a) 100 mol. % CO_2, (b) 10 mol. % H_2S- 90 mol. %CO_2 and (c) 10 mol. % H_2S-90 mol. % N_2 at 50°C and after 168 hours. *(Note that the intensity scale is arbitrary).* XRD peaks reference to database in literatures [168-170, 178, 179, 182].

10.1.3 Corrosion behaviour and formation of corrosion product at 80°C

The corrosion potential and corrosion rate over a 168 hour experiment for the three gas systems under investigation in this aspect of the work are presented in Figure 10-9 (a) and (b) respectively. Referring to Figure 10-9(a) for corrosion potential measurement, it is evident that for the three different gas atmospheres; 100 mol. % CO_2 gas, 10 mol. % H_2S – 90 mol. % CO_2 gas mixture and 10 mol. % H_2S – 90 mol. % N_2 gas, there is an initial increase in corrosion potential from ≈ -684 mV, -710 mV and -730 mV to ≈ -674 mV, -695 mV and ≈ -720 mV for test under 100 mol. % CO_2 gas, 10 mol. % H_2S – 90 mol. % CO_2 gas mixture and 10 mol. % H_2S – 90 mol. % N_2 gas atmospheres respectively. This initial increase in corrosion potential across the three different gas atmospheres within the first 7 hours is due to the ferrite dissolution process that precedes evolution of cementite. This is observed to be occurring faster at 80°C than at 50°C for all gas systems, potentially due to the influence of temperature on the corrosion kinetics in 100 mol. % CO_2 gas, 10 mol. % H_2S – 90 mol. % CO_2 gas mixture and 10 mol. % H_2S – 90 mol. % N_2 gas systems [77, 103, 119]. The trend in the magnitude of corrosion potential among these gas systems is also supported by the published results of Morris *et al* [180] and other authors [175, 176] in terms of the effect of H_2S gas on the corrosion potential

relative to H_2S-free corrosion environment. After the initial increase in corrosion potential, all three corrosion environments showed very different behaviour over the 168 hours tests. In 100 mol. % CO_2 gas systems, the corrosion potential became stable and constant at ≈ -667 mV until the end of this test. This is attributed to the formation of a mixture of an amorphous/non-crystalline form of $FeCO_3$ and localised formation of nano-scale crystals of $FeCO_3$ as shown in the Figure 10-11(a) and confirmed by the XRD pattern provided in Figure 10-12(a). Although the nano-scale $FeCO_3$ crystals are hardly visible on the SEM image, it has been shown to be the case in Chapters 6 of this Thesis.

With test under 10 mol. % H_2S – 90 mol. % CO_2 and 10 mol. % H_2S – 90 mol. % N_2 gas atmospheres, there is an observed and significant increase in the corrosion potential in the direction of positive potential by ≈ 70 mV and ≈ 100 mV respectively from the corrosion potential at the start of the test. As shown in the SEM images in Figure 10-11(b)-(d), the observed increase in corrosion potential in 10 mol. % H_2S – 90 mol. % CO_2 and 10 mol. % H_2S – 90 mol. % N_2 gas systems is due to the formation of iron sulphide corrosion product layer. However, it is important to note that in the 10 mol. % H_2S – 90 mol. % CO_2 gas system, the corrosion potential is increasing rather gradually from 20th hour to the 168th hour of the test when compared to 10 mol. % H_2S – 90 mol. % N_2 gas system, where it took up to the 88th hour to observe an increase in corrosion potential.

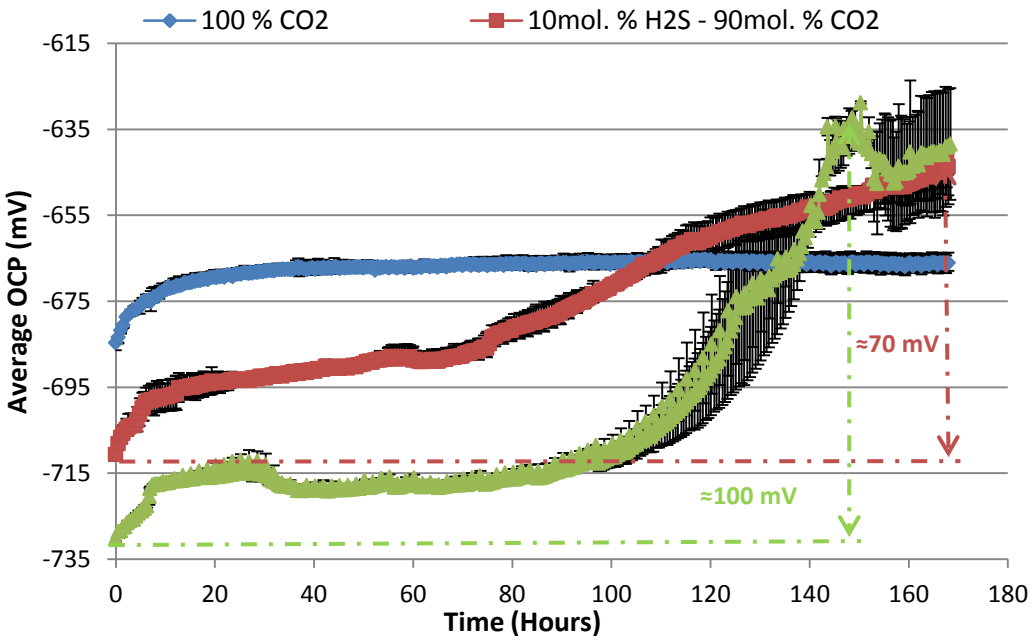

(a)

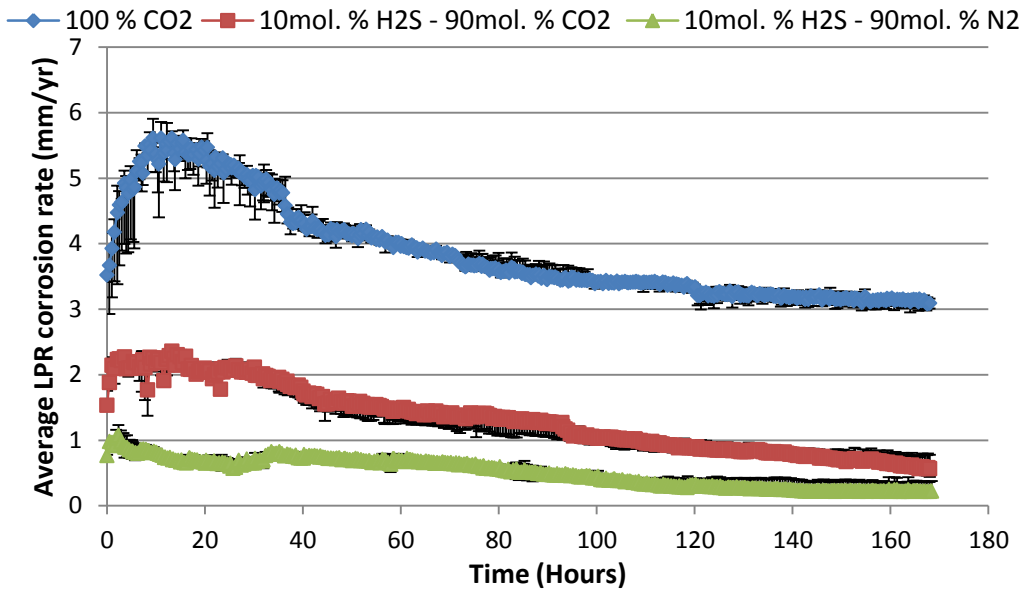

(b)

Figure 10-9 Graphs of (a) corrosion potential and (b) corrosion rate of X65 carbon steel in 3.5 wt.% NaCl solution under three different gas atmospheres at 80°C, over 168 hours.

On one hand, the gradual increase in corrosion potential in the 10 mol. % H_2S – 90 mol. % CO_2 gas system may be related to the presence of CO_2 in the gas phase, such that the surface is continuously electrochemically active over the duration of the test even with the formation of iron sulphide corrosion product layer. This process is also increasing the rate of availability of ferrous ions into the bulk solution to promote the precipitation of FeS from the bulk solution and encourage the build-up of FeS on the steel surface (especially at high temperature). It is therefore likely that the gradual increase in corrosion potential in the 10 mol. % H_2S – 90 mol. % CO_2 gas system after 20 hours is due to faster rate of build-up of FeS on to the steel surface than in the 10 mol. % H_2S – 90 mol. % N_2 gas system. On the other hand, the increase in corrosion potential in 10 mol. % H_2S – 90 mol. % N_2 gas system is also due to the formation of FeS. However, there is minimum effect of ferrite dissolution and as such the rate of build-up of FeS is mainly influenced by FeS formation kinetics via direct reduction reaction and minimum aqueous precipitation. Aqueous precipitation is enhanced in the 10 mol. % H_2S – 90 mol. % CO_2 gas system as a result of more ferrite dissolution.

As shown in Figure 10-11(b) and (c), these corrosion products are shown to be very porous on the top end of the corrosion product layer with a mixture of different morphologies. On the other hand, the absence of CO_2 in the gas is also seen to have allowed a more stable potential over large periods in 10 mol. % H_2S – 90 mol. % CO_2 and 10 mol. % H_2S – 90 mol. % N_2 gas system, potentially as a result of less non-uniform coverage of the iron sulphide corrosion

product, as well as lesser electrochemical activities at the corrosion interface. The SEM image in Figure 10-11(d) also shows that the FeS corrosion product in this condition could be more closely packed at the top end of the corrosion product layer than in the case of test in 10 mol. % H_2S – 90 mol. % CO_2 and 10 mol. % H_2S – 90 mol. % N_2 gas system at 80°C. XRD pattern shown in Figure 10-12(b) and (c) also confirms the presence of mackinawite and pyhrrotite in the iron sulphide corrosion product layer. Although obvious peaks was expected for $FeCO_3$ formed the 10 mol. % H_2S – 90 mol. % CO_2 gas system, this was however not the case as signals from any trace amount of $FeCO_3$ that could be formed in this condition and at this temperature may be masked by the dominant iron sulphide corrosion products.

Referring to the corrosion rate data presented in Figure 10-9(b), the magnitude by which the corrosion rate is reduced with the formation $FeCO_3$ corrosion product layer from ≈ 5.6 mm/yr to 3.2 mm/yr after 18 hours in 100 mol.% CO_2 corrosion environment is observed to be higher than in test in 10 mol. % H_2S – 90 mol. % CO_2 (from a peak corrosion rate of ≈ 2.4 mm/yr to ≈ 0.57 mm/yr) and 10 mol. % H_2S – 90 mol. % N_2 gas atmospheres (from a peak corrosion rate of ≈ 1.03 mm/yr to ≈ 0.24 mm/yr) due to the formation of FeS corrosion product layers. However, the final corrosion rate observed in test under H_2S-containing gas atmospheres gave a more beneficial corrosion rate. This helps to confirm earlier assertions in this section that there is an increased electrochemical activity in the corrosion interface with the presence of CO_2 gas in H_2S-containing corrosion systems.

This behaviour is also shown to be most evident at 80°C than at 30 and 50°C, thus suggesting a synergy with temperature change. This is reflected in the higher corrosion rate for test under 10 mol. % H_2S – 90 mol. % CO_2 gas atmosphere than under 10 mol. % H_2S – 90 mol. % N_2 gas atmosphere over the duration of the experiment. The results presented from this aspect of this study also compares well with the literature [126] or similar experimental condition. In Sun *et al* [126], the corrosion rate in test under 10 mol. % H_2S – 90 mol. % CO_2 and 10 mol. % H_2S – 90 mol. % N_2 gas atmospheres were ≈ 2.5 mm/yr after 1 hour (at pH 6.5-6.6 and 80°C) and ≈ 0.6 mm/yr after 24 hours at 80°C respectively. This compares very well to corrosion rates of ≈ 2.3 mm/yr after 1 hour in test under 10 mol. % H_2S – 90 mol. % CO_2 gas atmosphere and ≈ 0.65 mm/yr after 24 hours in test under 10 mol. % H_2S – 90 mol. % N_2 gas atmosphere in this study.

The variation in pH shown in Figure 10-10 also does confirm the initial assertion that pH of the bulk solution does not significantly influence the corrosion behaviour of Carbon steels in H_2S-containing corrosion environments.

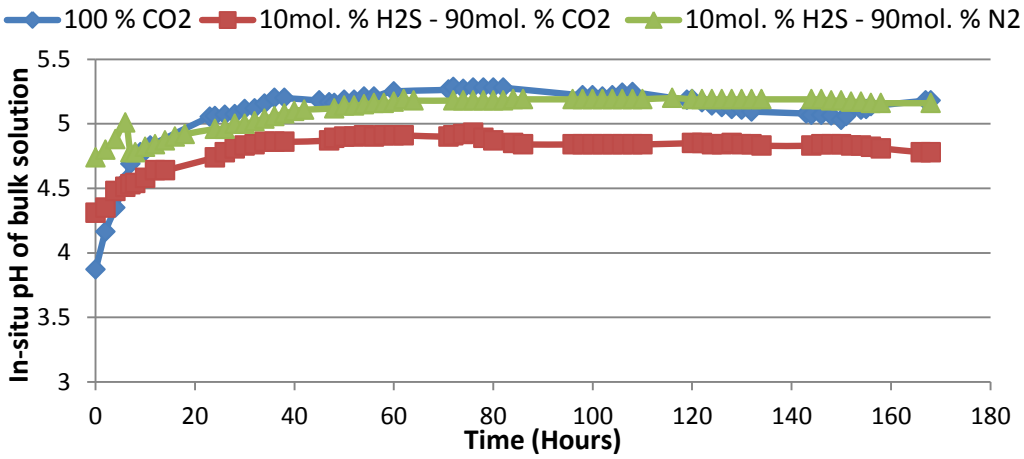

Figure 10-10 Measured *in-situ* pH of corrosion media under three different gas atmospheres at 80°C, over 168 hours

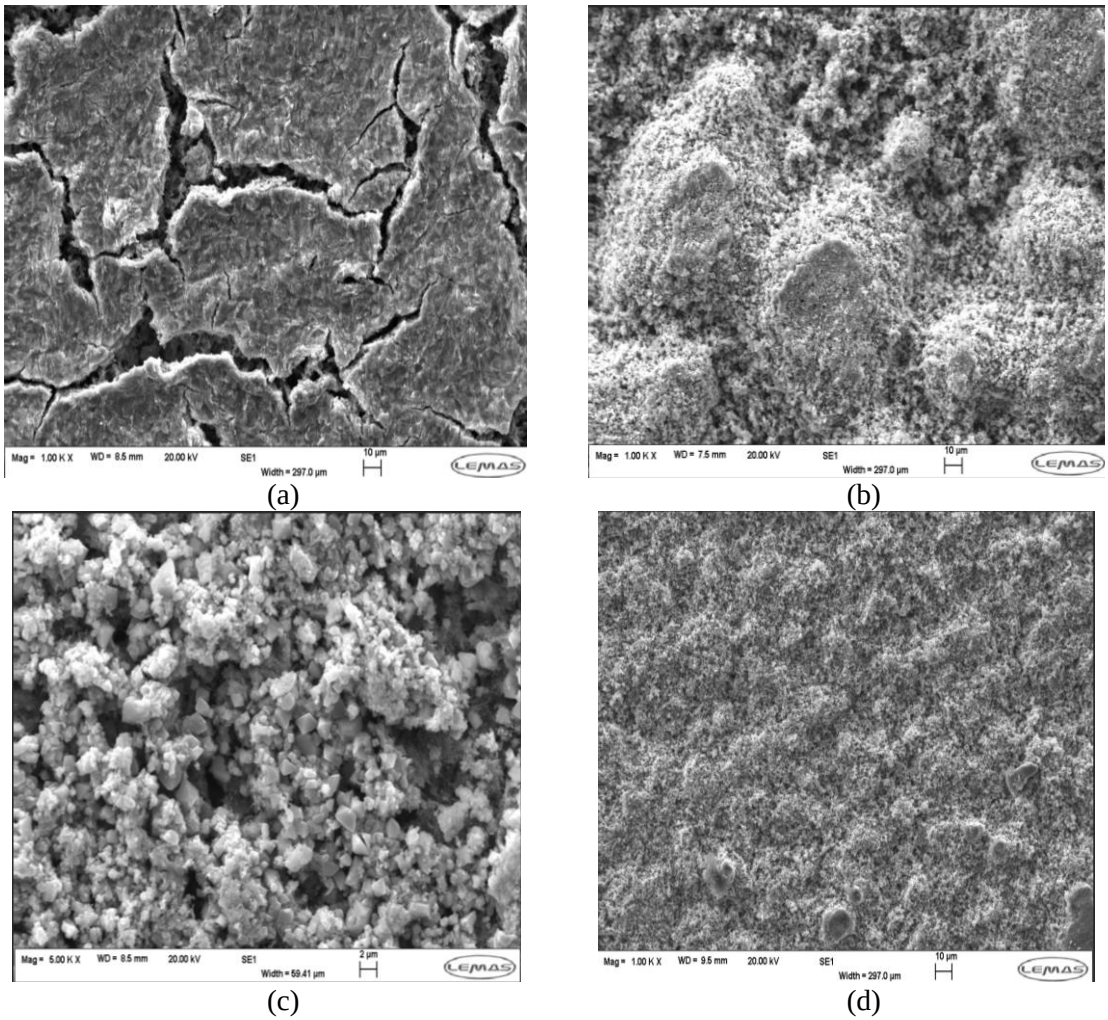

Figure 10-11 SEM images of corrosion product layer on X65 carbon steel in 3.5 wt. % NaCl solution under gas atmospheres composed of (a) 100 mol. % CO_2, (b) 10 mol. % H_2S- 90 mol. %CO_2, (c) 10 mol. % H_2S- 90 mol. %CO_2 at X5000 magnification and (d) 10 mol. % H_2S-90 mol. % N_2 at 80°C and after 168 hours.

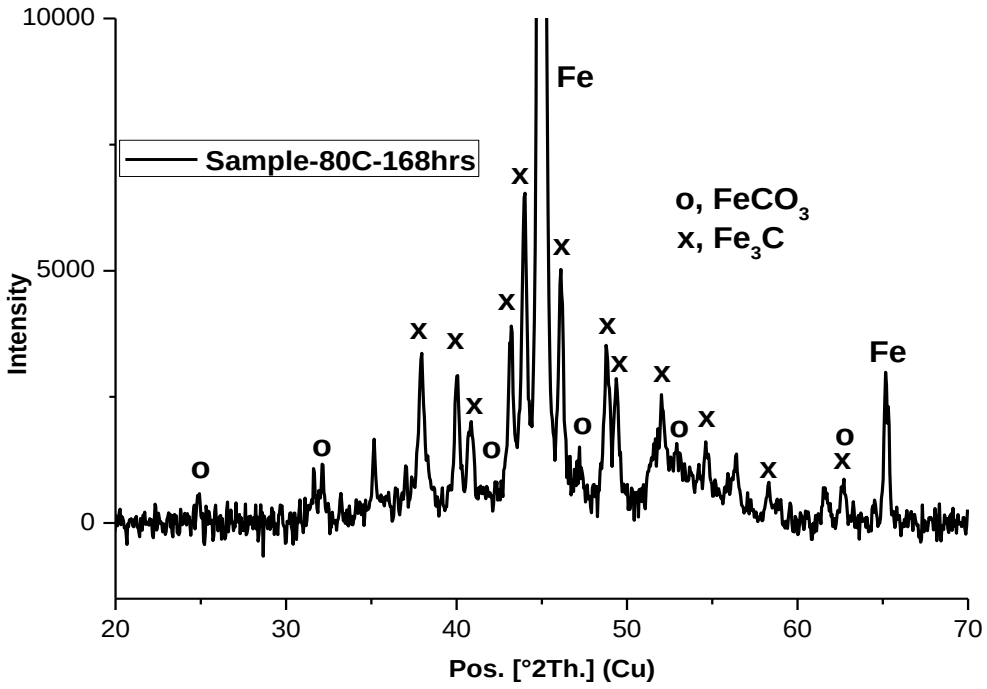
Sample-80C-168hrs
o, FeCO3
x, Fe3C
Fe
Intensity
Pos. [°2Th.] (Cu)

(a)

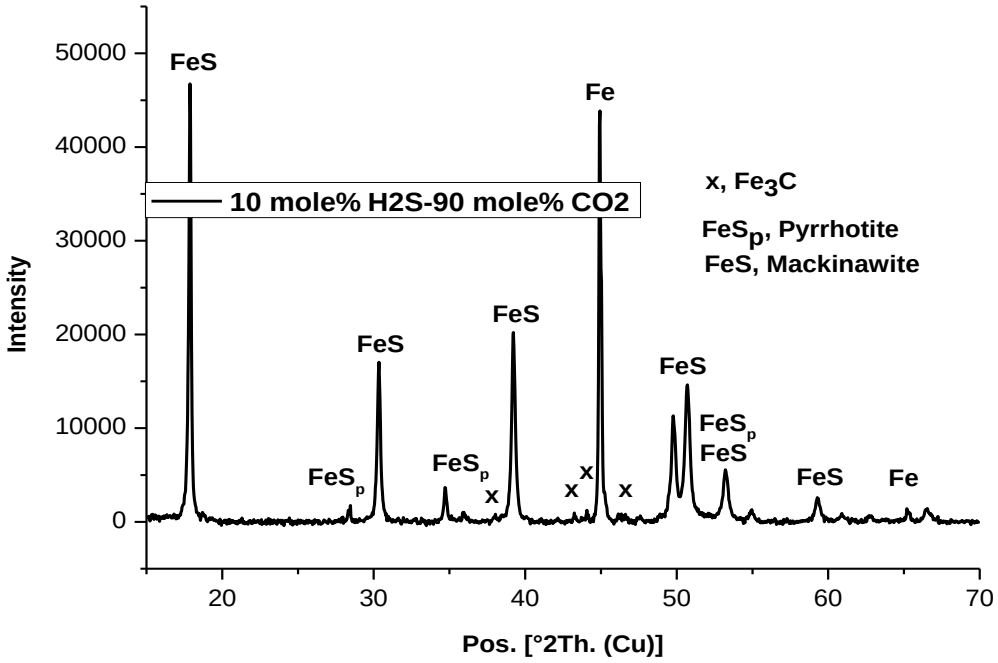
10 mole% H2S-90 mole% CO2
x, Fe3C
FeSp, Pyrrhotite
FeS, Mackinawite
FeS
Fe
FeSp
Intensity
Pos. [°2Th. (Cu)]

(b)

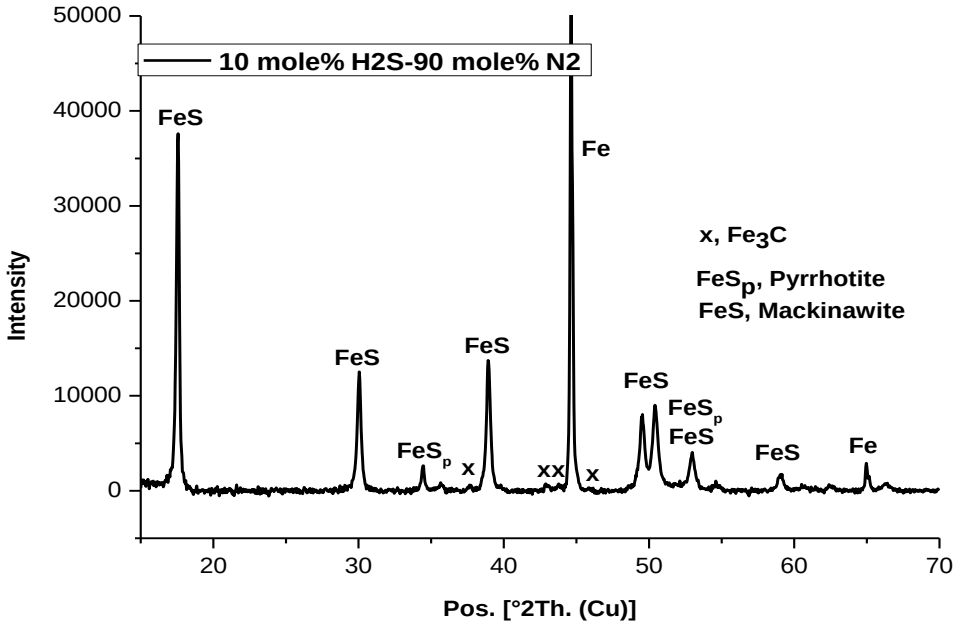

(c)

Figure 10-12 XRD pattern of corrosion product layer on X65 carbon steel in 3.5 wt. % NaCl solution under gas atmospheres composed of (a) 100 mol. % CO_2, (b) 10 mol. % H_2S- 90 mol. %CO_2 and (c) 10 mol. % H_2S-90 mol. % N_2 at 80°C and after 168 hours. ***(Note that the intensity scale is arbitrary).*** **XRD peaks reference to database in literatures [168-170, 178, 179, 182].**

10.1.4 Transmission electron microscope analysis of corrosion products formed in H_2S-containing corrosion environments

This section of the thesis presents and discusses the results from post-experiment surface analysis on samples from experiment in H_2S-containing; tests under 10 mol. % H_2S – 90 mol. % CO_2 and 10 mol. % H_2S – 90 mol. % N_2 gas atmospheres at 80°C after 168 hours, using a combination of Focused Ion Beam (FIB), Transmission Electron Microscopy (TEM), Scanning Electron Microscopy (SEM) and Energy Dispersive X-ray (EDX) analysis. The main purpose of the part of this study is to investigate the potential for competitive formation of and distribution of FeS and/or $FeCO_3$ corrosion on the corrosion interface. This has been carried out in this work by exploring conditions of H_2S-containing corrosion systems; test under 10 mol. % H_2S – 90 mol. % CO_2 gas atmosphere and over a test duration of 168 hours where it is thermodynamically possible for both the formation of both $FeCO_3$ and/or FeS corrosion products to occur. This study was also carried out in test under 10 mol. % H_2S – 90 mol. % N_2 gas atmosphere as a reference for investigating the effect of CO_2 corrosion and/or $FeCO_3$ corrosion product formation. Figure 10-13 (a) and (b) presents the top view and cross-sectional view respectively of corrosion product layer for test under 10 mol. % H_2S – 90 mol. % CO_2 gas atmosphere, while Figure 10-17 (a) and (b) presents the top view and cross-sectional view respectively of

corrosion product layer for test under 10 mol. % H_2S – 90 mol. % N_2 gas atmosphere. The cross-section views of the corrosion product layers were obtained using the SEM attached to the FIB. The latter is used for micro-machining of the corrosion product layers.

One of the initial observations from the cross-sectional views from the tests in the two conditions under investigation is the difference in the thickness of the corrosion product layers. The corrosion product formed in tests under 10 mol. % H_2S – 90 mol. % CO_2 gas atmosphere is seen to be thicker (at an average of ≈ 8 μm) than for test under 10 mol. % H_2S – 90 mol. % N_2 gas atmosphere (at an average of ≈ 6 μm). The difference in the thickness of the corrosion product layers for both conditions may be attributed to the influence of the presence of CO_2 gas in an H_2S-containing corrosion environment. The presence of the CO_2 corrosion kinetics to the corrosion process increases the rate of dissolution of Fe^{2+} into the bulk solution as shown in the higher corrosion rate in test under 10 mol. % H_2S – 90 mol. % CO_2 gas atmosphere relative to test under 10 mol. % H_2S – 90 mol. % N_2 gas atmosphere (Figure 10-9(b)). The presence of Fe^{2+} in the bulk solution also creates the conditions for the formation of both $FeCO_3$ and FeS corrosion products from the bulk solution.

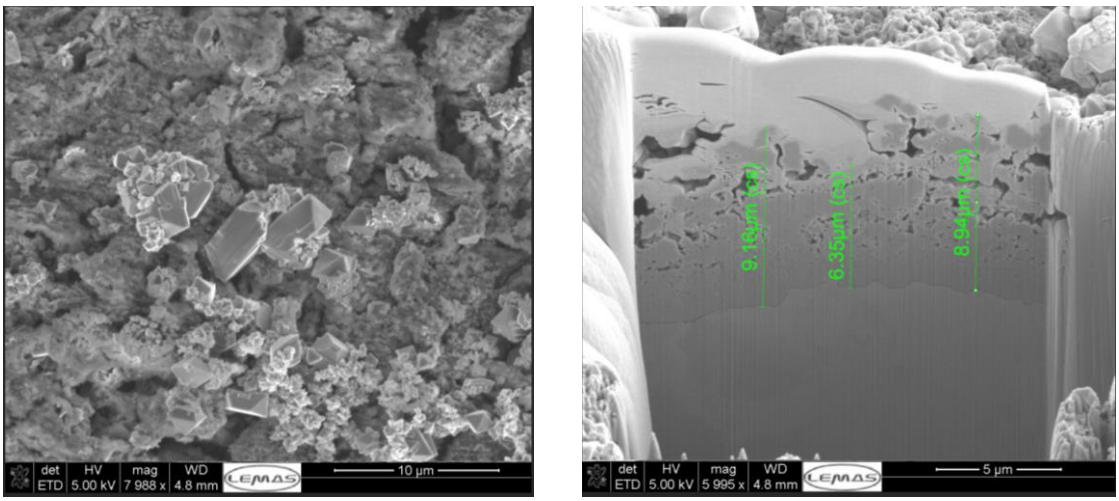

(a) (b)

Figure 10-13 SEM images corrosion product layer on X65 carbon steel in 3.5 wt. % NaCl solution under gas atmospheres composed of 10 mol. % H_2S- 90 mol. %CO_2 at 80°C and after 168 hours (a) Top view before and (b) cross-sectional view after micro-machining using the FIB.

Referring to Figure 10-13(a) and Figure 10-17(a), the morphology of the top view also shows the formation of an amorphous corrosion product layer (possibly a mixture of FeS and $FeCO_3$) underneath the crystals for corrosion product formed under 10 mol. % H_2S – 90 mol. % CO_2 gas atmosphere while it is completely crystalline in nature for corrosion product formed in 10 mol. % H_2S – 90 mol. % N_2 gas atmosphere. The top end of the corrosion product layer for test under 10 mol. % H_2S – 90 mol. % CO_2 gas atmosphere have been identified as an amorphous form of

$FeCO_3$ in this work (see Figure 10-15(b)) and are shown in Figure 10-14(a), (b) and (c). When compared with the TEM image of the cross-section of corrosion product formed under 10 mol. % H_2S – 90 mol. % N_2 gas atmosphere Figure 10-18 (a) and (b), it is evident that in both H_2S-containing corrosion systems, FeS forms very close to the steel surface as a thick and continuous layer (for the area under focus) according to the electron diffraction patterns provided in Figure 10-15(b) and Figure 10-19 (a) and (b). However, in the test under 10 mol. % H_2S – 90 mol. % CO_2 gas atmosphere and as shown in Figure 10-14(a), (b) and (c), there is a porous top-end of the corrosion product layer consisting of an amorphous/non-crystalline form of $FeCO_3$ corrosion product.

This form of $FeCO_3$ was confirmed from indexing the continuous ring patterns (which indicates that that corrosion product is nano-polycrystalline in nature) on the selected area electron diffraction patterns provided in Figure 10-15(b). From the interplanar spacing (d-spacing) of the rings shown in Figure 10-15(b), the prescribed indices correspond with $FeCO_3$ [169]. Similar analysis with exactly similar outcomes have already been presented and discussed in section 6.44 of this thesis. This form of corrosion product has been shown to be common in such ranges of pH [93, 95]. This indicates that at some point in the experiment, the bulk solution must have been supersaturated with respect to $FeCO_3$. On the other hand, the top end of the corrosion product layer formed in test under 10 mol. % H_2S – 90 mol. % N_2 gas atmosphere, consists of a crystalline form of iron sulphide corrosion product, which is identified in this study as mackinawite (see Figure 10-19(a)); the same as the inner iron sulphide layer (see Figure 10-19(b)).

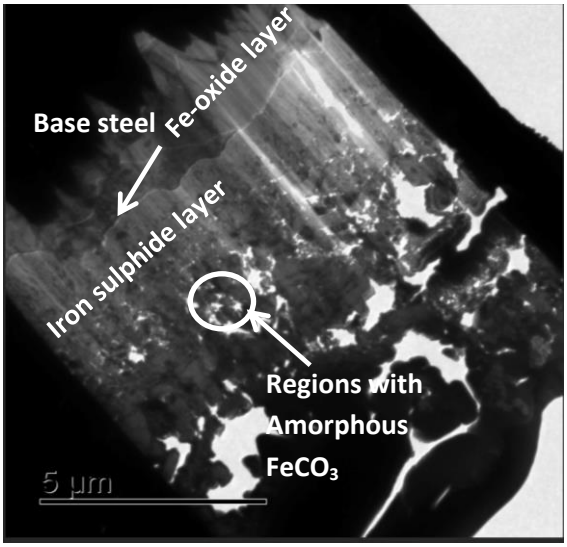

(a)

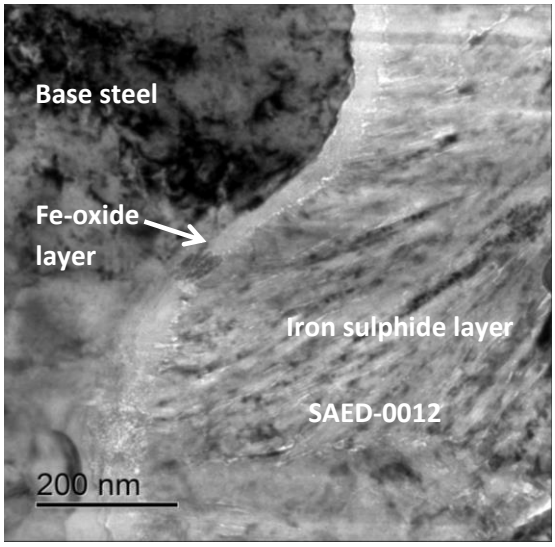

(b)

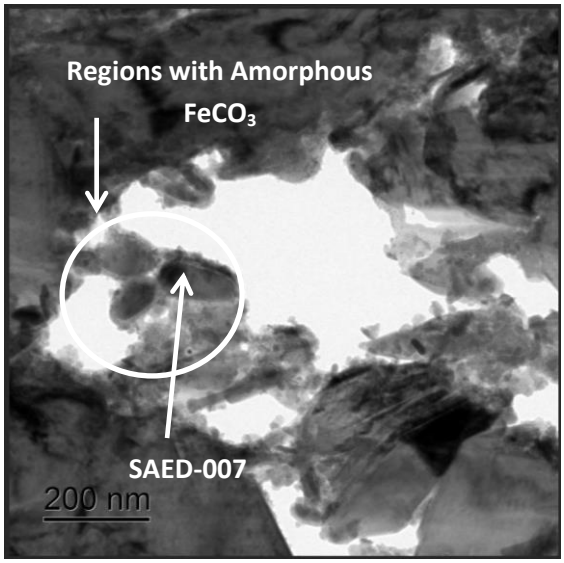

(c)

Figure 10-14 Images from TEM analysis to show the three different corrosion products on X65 carbon steel in 3.5 wt. % NaCl solution under gas atmospheres composed of 10 mol. % H_2S- 90 mol. %CO_2 at 80°C and after 168 hours (a) showing the cross-sectional distribution of corrosion the different corrosion products, (b) showing the Fe-oxide and iron sulphide corrosion product layers and (c) showing the local regions consisting of amorphous form of $FeCO_3$ corrosion products.

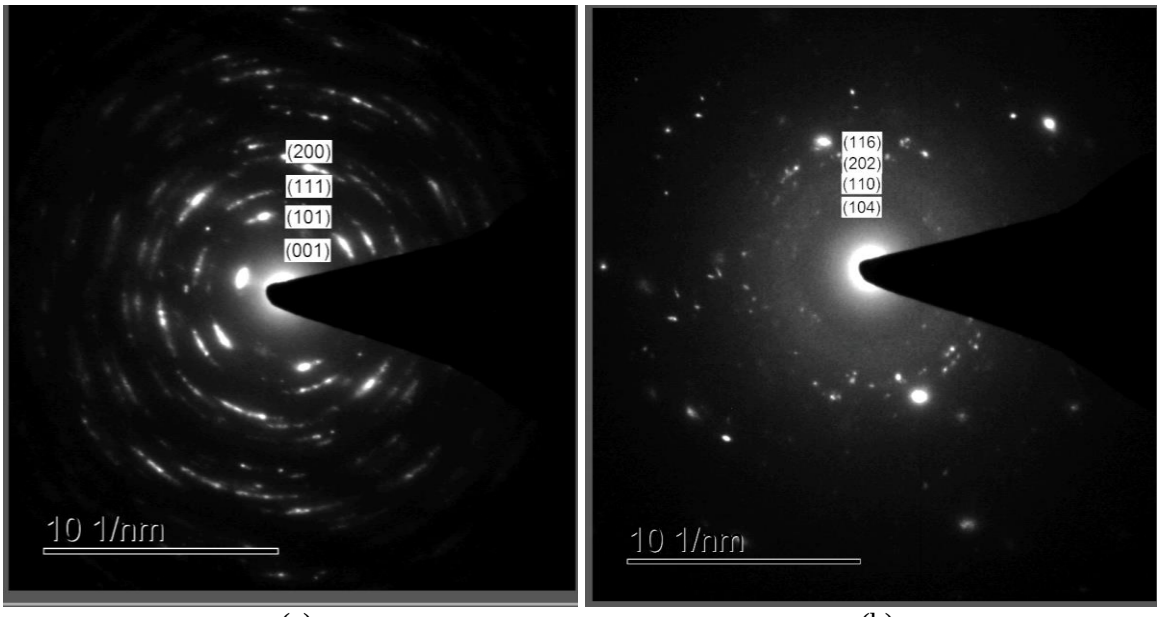

(a) (b)

Figure 10-15 Electron diffraction pattern for selected area labelled (a) SAED-0012 (for iron sulphide) and (b) SAED-007 (for $FeCO_3$) for corrosion products on X65 carbon steel in 3.5 wt. % NaCl solution under gas atmospheres composed of 10 mol. % H_2S- 90 mol. %CO_2 at 80°C and after 168 hours shown in Figure 10-14(b) and (c) respectively.

In addition to the corrosion product ($FeCO_3$ and/or FeS) identified in both test conditions under review, there is also a very thin Fe-oxide rich layer formed in-between the FeS corrosion product layer and the steel surface as shown in Figure 10-14 (a)-(c), Figure 10-18 (a) and (b)

and the EDX map presented in Figure 10-16 as a very thin oxygen rich layer. Similar observation have been reported by Kvarekval *et al* [129] for tests under a H_2S/CO_2 gas ratio of 0.4 at a CO_2 partial pressure of 6.9, at pH of 4.09, temperature of 120°C and after 166 hours. In this work, the Fe-oxide rich layer could not be conclusively identified. Kvarekval *et al* [129] proposed that as the sulphide concentration decreases towards the steel surface due to the formation of iron sulphide, the competitive formation of iron sulphide and iron oxide (probably magnetite,Fe_3O_4) takes place close to the steel surface where the sulphide concentration is low.

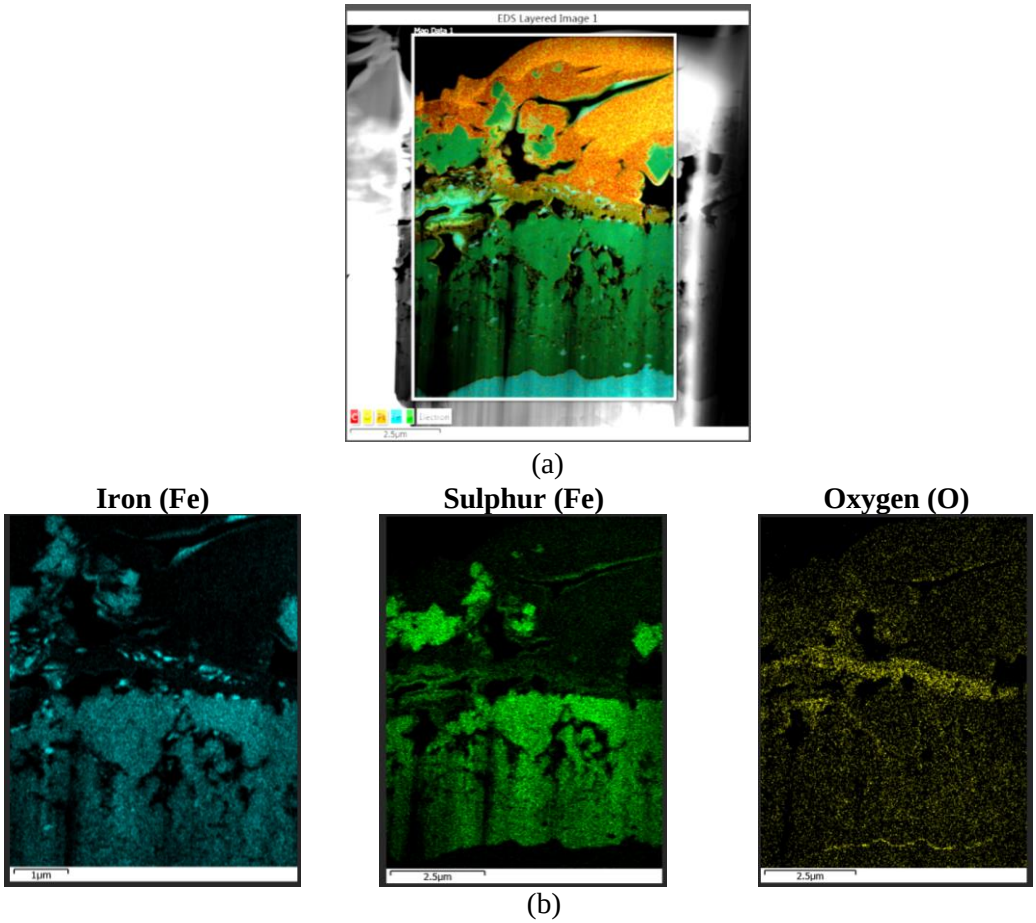

Figure 10-16 EDX map for the cross-section of corrosion product layer on X65 carbon steel in 3.5 wt. % NaCl solution under gas atmospheres composed of 10 mol. % H_2S- 90 mol. %CO_2 at 80°C and after 168 hours. (a) EDX layered image showing the distribution of constituting elements and (b) independent distribution of key individual elements.

The explanation by Kvarekval *et al* [129] and the observations in this study are also consistent with the viewpoint of Marcus *et al* [177]. According to Kvarekval *et al* [129], at temperatures above 110°C, magnetite may form through direct reaction between steel and water according to Eq. 10.1. However, Marcus *et al* [177] confirms from thermodynamic analysis that there could be competitive adsorption of oxygen and sulphur unto the steel surface as Fe-S_{ad} and Fe-O_{ad} and that sulphur adsorption is limited by oxygen at high temperatures. Although the temperature of

the corrosion environments in this work is 80°C, the formation of a thin inner Fe-oxide may as well be connected to the abovementioned phenomenon.

$$3Fe + 4H_2O \rightarrow Fe_3O_4 + 4H_2 \qquad 10.1$$

With the findings on the different corrosion products observed in this study, the most significant component of this aspect of this work is to understand and establish how these different corrosion products (as linked to the different corrosion environments and kinetics) may be influencing the overall corrosion damage of the exposed steel surface. This will be the focus of the results and discussion presented in the next section.

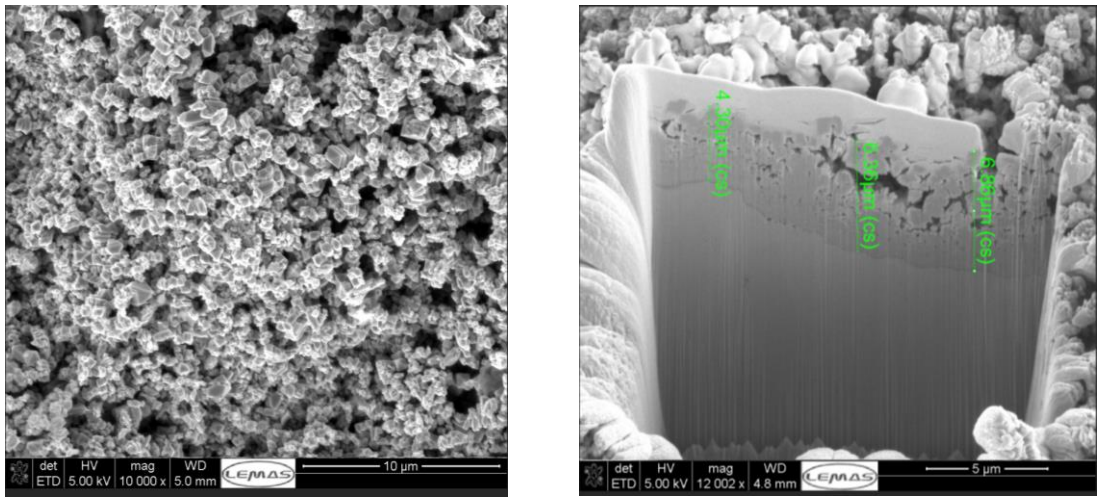

(a) (b)

Figure 10-17 SEM images corrosion product layer on X65 carbon steel in 3.5 wt. % NaCl solution under gas atmospheres composed of 10 mol. % H_2S- 90 mol. %N_2 at 80°C and after 168 hours (a) Top view before and (b) cross-sectional view after micro-machining using the FIB.

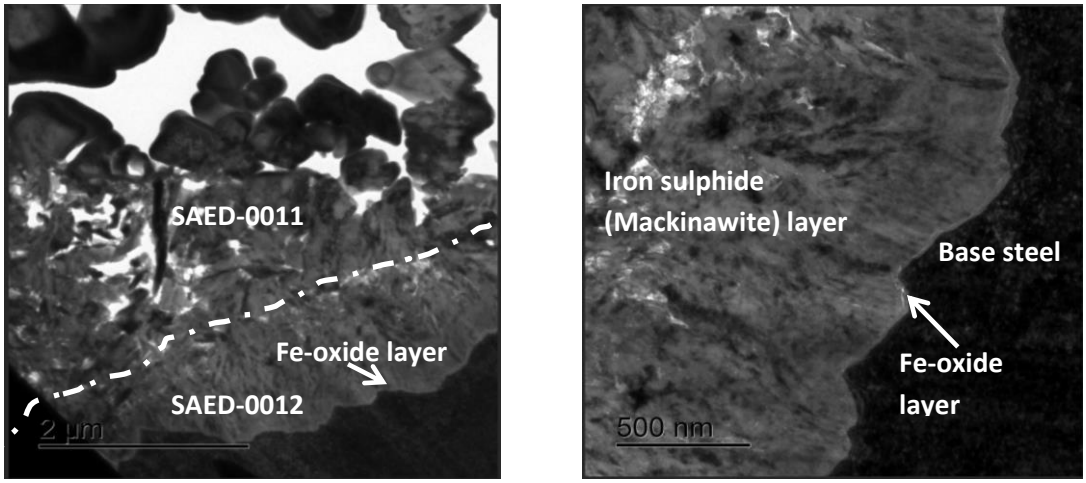

(a) (b)

Figure 10-18 Images from TEM analysis to show the different corrosion products on X65 carbon steel in 3.5 wt. % NaCl solution under gas atmospheres composed of 10 mol. % H_2S- 90 mol. %N_2 at 80°C and after 168 hours (a) showing the cross-sectional distribution of corrosion the different corrosion products and (b) showing the Fe-oxide and iron sulphide corrosion product layers.

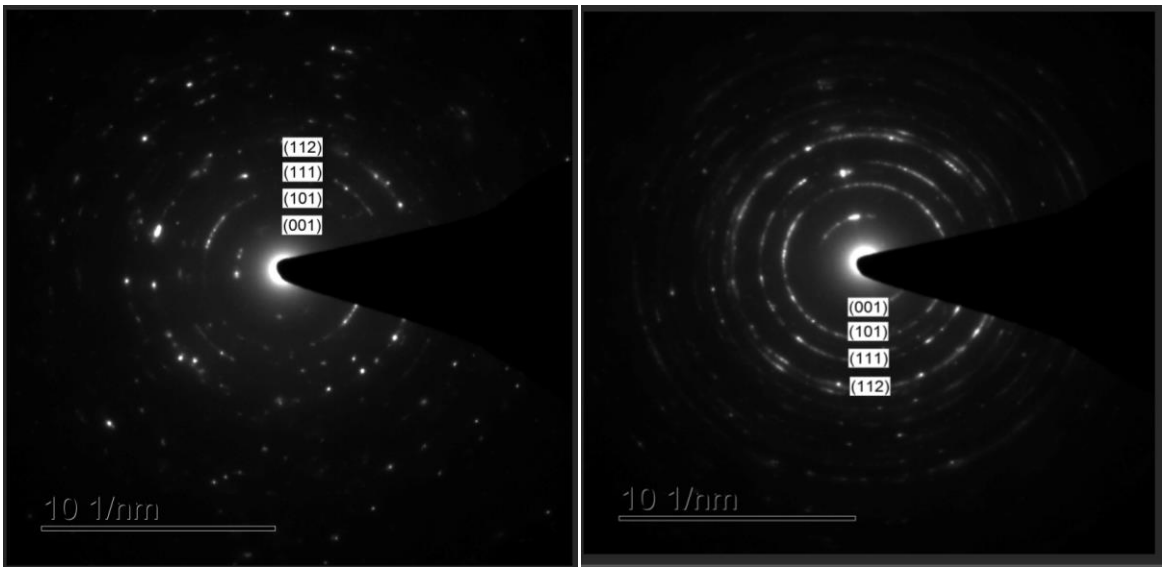

(a) (b)

Figure 10-19 Electron diffraction pattern for selected area labelled SAED-0011 and SAED-0012 for corrosion products on X65 carbon steel in 3.5 wt. % NaCl solution under gas atmospheres composed of 10 mol. % H_2S- 90 mol. %N_2 at 80°C and after 168 hours shown in Figure 10-18.

10.2 Long-term pitting corrosion of X-65 steel in sour corrosion environments; effect of temperature, CO_2 and H_2S gas

Investigation of the pitting corrosion behaviour of carbon steel is a very important aspect of this study. Results of this study over a 168 hour period is presented and discussed in this section and is focused on the potential corrosion damage resulting from pit propagation and/or localised corrosion processes of carbon steel material in H_2S-containing corrosion environments with respect to sweet corrosion environments. The maximum pit and average pit depth the tests samples relative to the corroded surface after removal of corrosion products are presented in Figure 10-20(a) and (b).

10.2.1 Pitting corrosion behaviour under 100 mol. % CO_2 gas atmosphere

Referring to Figure 10-20(a) and (b), the variation of maximum and average pit depth with temperature in test under 100 mol. % CO_2 gas atmosphere after 168 hours is similar to recorded pit depth after 7 hours. The only difference is in terms of the magnitude of pit depth recorded. The depth of pit increases from ≈ 22 µm at 30°C to ≈ 49 µm at 50°C and then measured ≈ 36 µm at 80°C. The reason for this behaviour has already been described in Chapter 6 and section 8.4 of this thesis. The initial increase from 30 to 50°C is attributed to the dependence of the kinetics of initial corrosion and formation of an amorphous or non-crystalline (non-protective) form of $FeCO_3$ on temperature. The formation of these forms of $FeCO_3$ has been shown in this work (Chapter 6 and 7) to be acting as a precursor for pitting and localised corrosion [9, 88, 95].

On the other hand, the lower pit depth measured at 80°C is linked to the higher contribution of uniform corrosion rate to the rate of metal loss, such that the pit depth relative to corroded surface is significantly masked. There is also observation of a self-healing mechanism for initially formed pits at 80°C as already reported in Chapter 6 of this thesis as well as being supported by the literature [164]. Visual evidence of pit depth in 100 mol. % CO_2 at 50°C is provided in Figure 8-12(a).

10.2.2 Pitting corrosion under 10mol. % H_2S - 90mol. % CO_2 gas atmosphere

For tests conducted in H_2S-containing systems, lower corrosion rate were recorded at all temperatures when compared to tests under 100 mol. % CO_2 gas atmosphere (see Figure 10-1(b), Figure 10-5(b) and Figure 10-9(b) for 30 , 50 , and 80°C respectively). This suggests that there is relatively minimum masking on pit depth relative to corroded surface by the uniform corrosion rate of surrounding surface in H_2S-containing corrosion systems. This observation is attributed to the effect of the formation of FeS corrosion product layer onto the steel surface. This process has been shown in 9.3 and 9.5 to significantly reduce the uniform corrosion contribution to metal loss within 7 hours, while at the same time acting as the main agents of pitting corrosion initiation (see section 9.5). However, over a 168 hours period, Figure 10-20(a) and (b) show the maximum pit depth relative to corroded surface for test under 10mol. % H_2S - 90mol. % CO_2 gas atmosphere as ≈ 32 µm at 30°C, ≈ 24 µm at 50°C and ≈ 147 µm at 80°C.

The irregular trend in the pit depth with temperature and the different gas phase composition may be connected to the complexities in the FeS formation process over 168 hours. As already discussed in section 10.1.1, there was only a marginal change in the FeS corrosion product layer at 30°C for test under 10mol. % H_2S - 90mol. % CO_2 gas atmosphere. This may be linked to the lower kinetic of iron dissolution, charge transfer and the FeS formation process, such that there is minimum change in corrosion product morphology with time. The consequence of this is limiting the corrosion product formation process to the initially formed FeS (mackinawite) capable of sustaining a marginal pit growth at this temperature. In the case of test at 50°C, the corrosion potential and corrosion rate data (Figure 10-5(a) and (b)) presented and discussed in section 10.1.2 indicates the dominance of dissolution and/or transformation of initially formed FeS corrosion product layer on the corrosion process, leading to the formation of a different form and/or morphology of FeS corrosion product from that formed after 7 hours. The consequence of this is a significant increase in uniform corrosion rate and formation of FeS corrosion product layer with localised regions that are still very porous (see Figure 10-7(b)).

The impact of this is a lower pit depth than at 30°C. It is important to emphasis here that the presence of CO_2 in the gas phase may be responsible for such behaviour at 50°C as already discussed in sections 10.1.2 and 10.1.3.

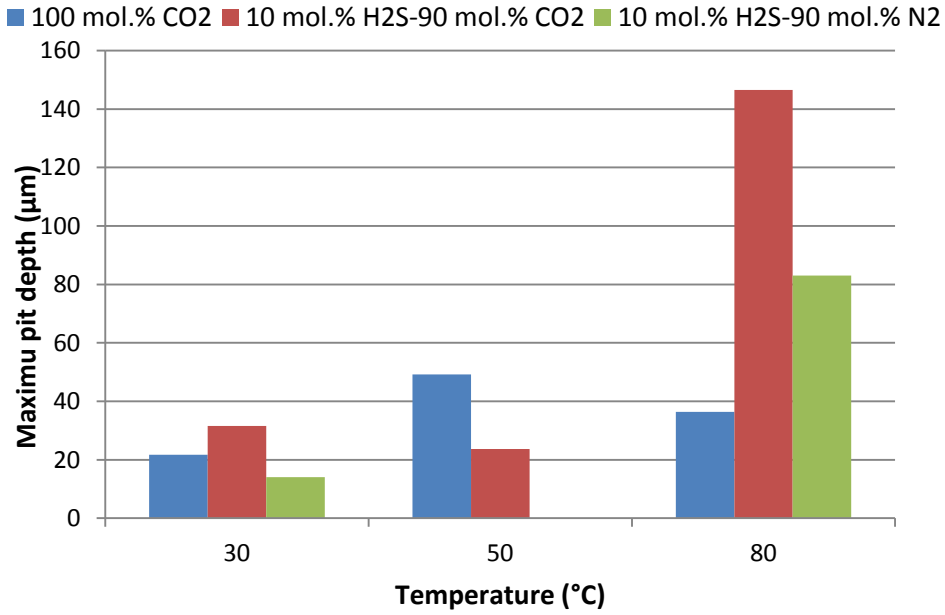

(a)

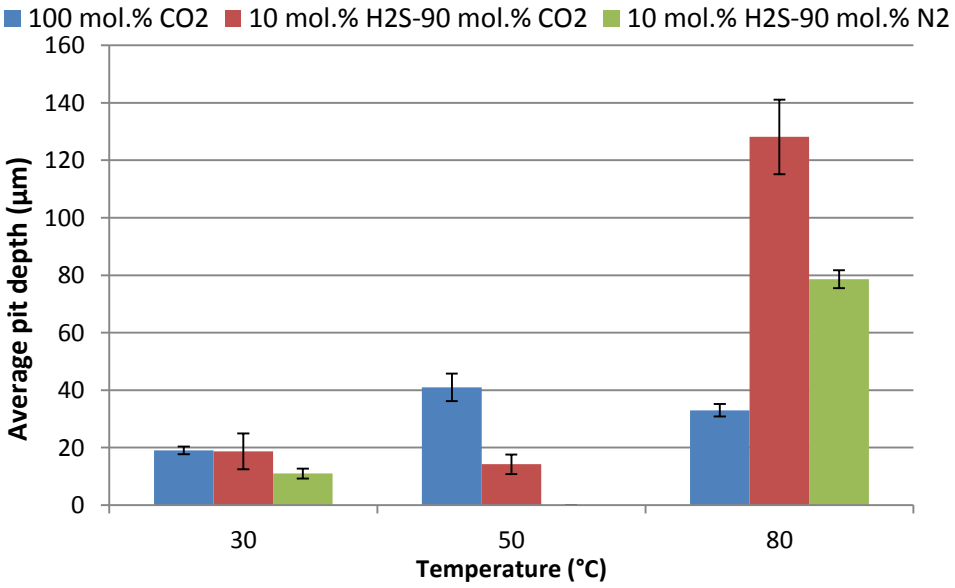

(b)

Figure 10-20 (a)Maximum pit depth (relative to corroded surface) and (b) Average pit depth (relative to corroded surface) on carbon steel surface exposed to corrosion system under 100mol. % CO_2, 10mol. % H_2S - 90mol. % CO_2 and 10mol. % H_2S - 90mol. % N_2 gas atmosphere for 168 hours as a function of temperature.

At a much higher temperature of 80°C, the nature of corrosion damage on the surface after removal of corrosion product is a combination of heavy localised corrosion and pitting corrosion. Visual evidence of this is presented in Figure 10-22(c). Figure 10-22(a) and (b) also shows visual evidences of pit from test under in 10mol. % H_2S - 90mol. % CO_2 gas atmosphere at 30 and 50°C respectively. At 80°C, the maximum depth of metal penetration from localised/pitting corrosion is ≈ 147 µm, which is 7 times greater than at 50°C and 5 times greater than at 30°C. Similar range of metal penetration (149 µm relative to corroded surface) from localised attack has also been reported by Brown and Nesic [138] for test conducted in a H_2S-CO_2 gas system at 60°C, pH 4.0, P_{total} of 8 bar, P_{H2S} of 10 mbar in 10wt% NaCl solution for 21 days. One of the main reasons for this behaviour is likely due to the nature of FeS formed in the presence of CO_2/$FeCO_3$ at higher temperatures. As already pointed out in section 10.1.3, the presence of CO_2 gas increases the rate of dissolution of Fe^{2+} into the bulk solution, such that the formation of iron sulphide corrosion product layer is also formed from bulk precipitation as well as via solid state reduction reaction [35, 39, 73, 115, 118].

There is also the potential for cycles of transformation and/or dissolution of initially formed iron sulphide corrosion product layers as suggested by Brown and Nesic [138]. The process of dissolution and/or transformation of initially formed mackinawite (FeS) on the steel surface have already been proposed by other authors [128, 138, 175]. The process of dissolution and/or transformation of initially formed mackinawite are believed to be dependent on environmental parameters such as temperature, pH and HS^-/H_2S concentration. It is known to occur faster with increase in temperature [128]. All of these could be influencing the formation of FeS corrosion product with distinct morphology across its cross section and a porous top-end as shown in Figure 10-11 (b) and (c) but with localised regions of very compact corrosion products.

It has also been shown in Figure 9-11(b) that with the presence of CO_2, the increased aggressiveness of the environment due to the influence of CO_2 corrosion is likely to lead to a non-uniform formation of FeS corrosion product layer. Such influence of non-uniformity is also likely to continue throughout the experiment as shown in Figure 10-11 (b). The non-uniform coverage of the FeS corrosion product layer (Figure 10-11 (b)) could also be partly attributed to the consequences of CO_2 corrosion in the form of competitive precipitation of $FeCO_3$ once supersaturation with respect to $FeCO_3$ in the bulk is attained. This has also been discussed in section 10.1.4 with evidences provided in Figure 10-14(c) and Figure 10-15 (b). The formation of a thick layer of FeS corrosion product in in H_2S-CO_2 corrosion system at 80°C, has the capacity to induce significant potential difference (70 mV) as shown in Figure 10-9(a) and

enough to induce a galvanic effect that sustains the propagation of pits. The FeS corrosion product formed is non-uniform across the surface, hence the manifestation of heavy localised/pitting corrosion as shown in Figure 10-22(c).

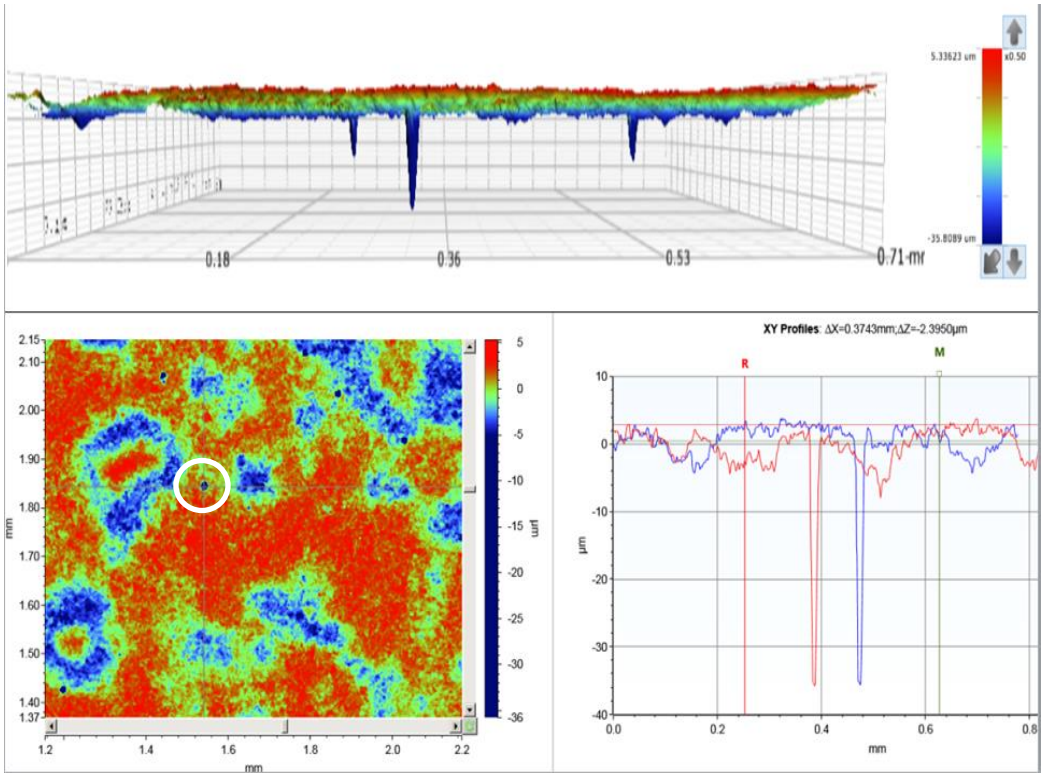

(a)

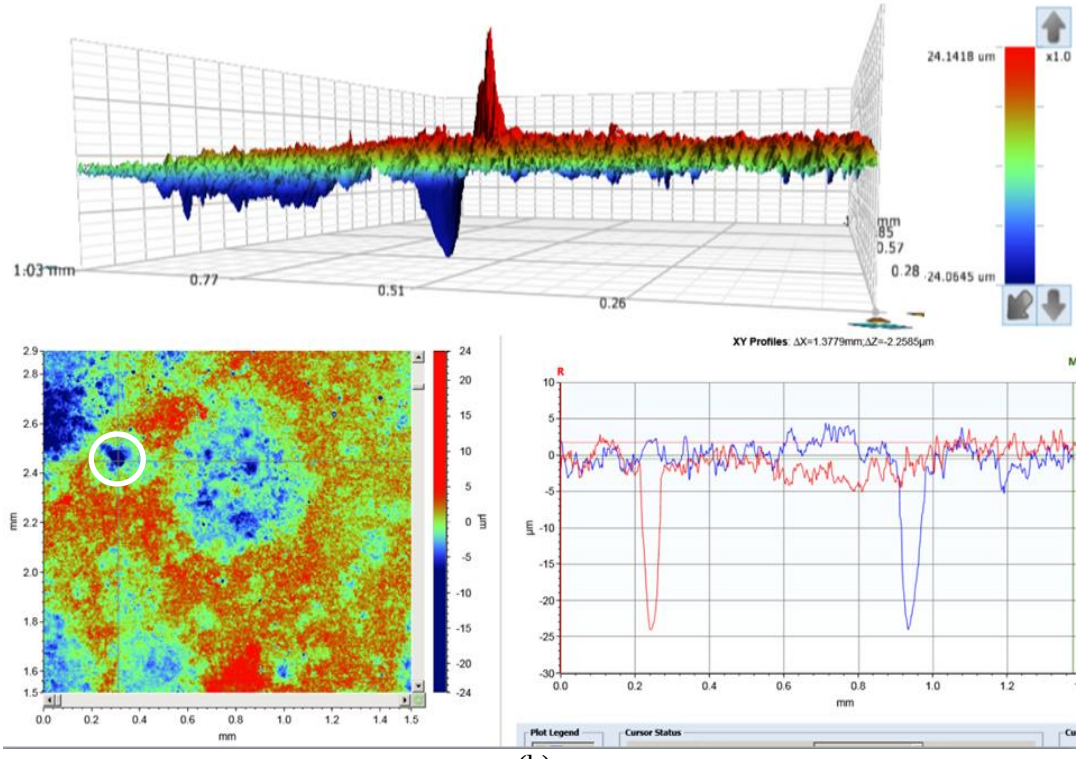

(b)

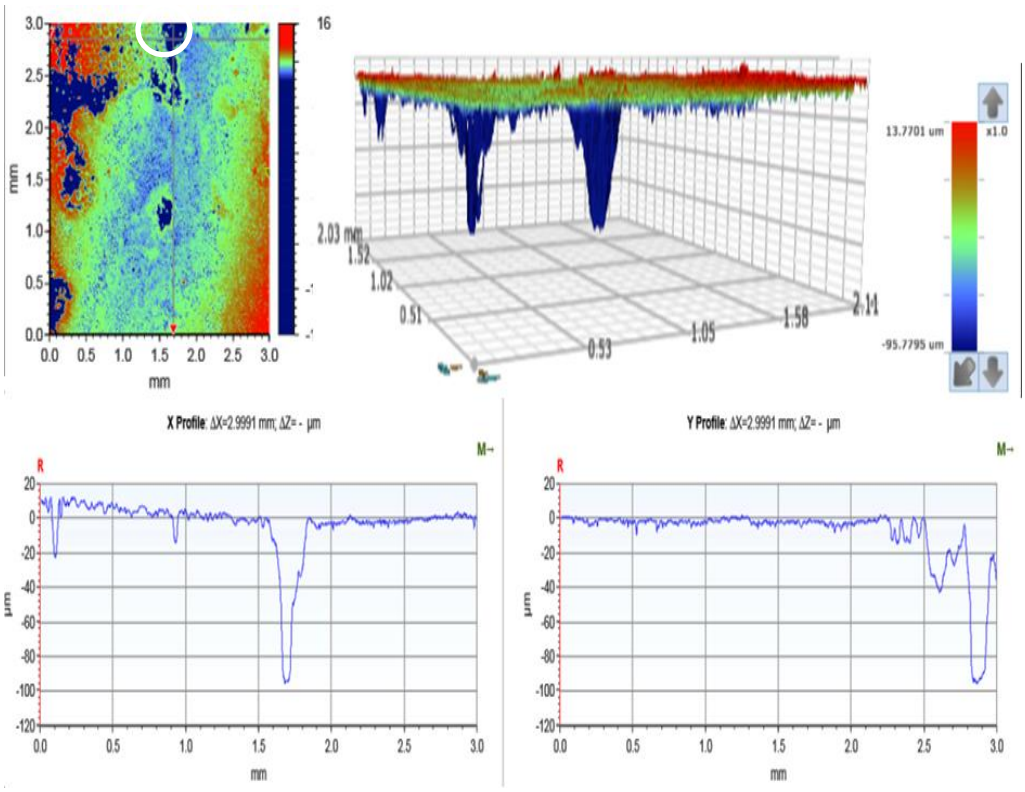

(c)

Figure 10-21 2D and 3D images of deepest pit (relative to corroded surface) on carbon steel surface exposed to corrosion system under 10mole% H_2S - 90mole% CO_2 after 168 hours at (a) 30°C, (b) 50°C, (c) 80°C, after 168 hours.

10.2.3 Pitting corrosion behaviour under 10mol. % H_2S - 90mol. % N_2 gas atmosphere

In test conditions under 10mol. % H_2S - 90mol. % N_2 gas atmospheres, the depth metal penetration due to pitting and/or localised corrosion after 168 hours is relatively less than in test conditions under 10mol. % H_2S - 90mol. % CO_2 gas atmosphere at all temperatures. At 30°C, the depth is ≈ 13 µm after 7 hours and ≈ 14 µm after 168 hours. This suggests a constant pit depth to indicate no change in the electrochemical activities at the steel surface over the 168 hours duration. This observation correlates with the constant corrosion rate at ≈ 0.2 mm/yr and slight increase in corrosion potential in the direction of positive potential. This is likely related to the role of corrosion kinetics on the potential pit growth. Corrosion kinetics is at a minimum at the corrosion interface at 30°C in corrosion environment without the more aggressive component of CO_2. This may have played a key role in limiting the iron sulphide corrosion product layer to only a very thin layer as shown in Figure 10-3(c), while the pit depth over time remained constant. At 50°C, there is hardly any pit on the surface as shown in Figure 10-22(a),

with evidence of extensive uniform corrosion across the entire steel surface. This also correlates well with the morphology of iron sulphide corrosion product layer provided in Figure 10-7(d), which shows a very lose corrosion products with minimum thickness. The uniform corrosion rate was also shown to be constant at ≈ 0.5-0.6 mm/yr after 7 hours for the remaining duration of the test. The low electrochemical activities for test under 10 mol. % H_2S – 90 mol. % N_2 gas atmospheres (without CO_2 gas) at 50°C also suggest that the rate of iron sulphide precipitation from the bulk is low and the only potential reason for the formation of iron sulphide of this nature at 50°C is possibly due to the higher temperature and increased kinetics of iron sulphide formation than at 30°C. Hence, it is likely that initially formed iron sulphide may have been dissolved prior to the formation of the porous layer of iron sulphide, therefore leading to the manifestation of only uniform corrosion as the only corrosion damage mechanism after 168 hours.

At 80°C and in test under 10mol. % H_2S - 90mol. % N_2 gas atmospheres, the depth of metal penetration from pitting corrosion after 168 hours is 83 µm. which is almost twice as small as the depth of metal penetration in test under 10mol. % H_2S - 90mol. % CO_2 gas atmospheres. The corrosion product for test under 10mol. % H_2S - 90mol. % N_2 gas atmospheres is shown to be composed of mainly iron sulphide corrosion products. Although the morphology of the corrosion product provided in Figure 10-11(d) also depicts that of a non-uniform coverage, it is still relatively far more compact than corrosion product layer formed under 10mol. % H_2S - 90mol. % CO_2 gas atmospheres (Figure 10-11(c)). This is likely due to the absence of CO_2 as discussed in section 10.1.3, as well as the relatively higher temperature than at 30 and 50°C. The implication of this observation on corrosion damage is the manifestation of pitting corrosion in the form of very narrow but deep pits (with smaller pit diameter) in most cases as shown in Figure 10-22(b).

It is also important to note that from the TEM analysis in section 10.1.4, the presence of a very thin Fe-oxide layer between the steel surface and FeS layer for tests under H_2S-containing gas atmospheres at 80°C has been established. However, it is still unclear if this could be influencing the localised corrosion damage observed in these conditions.

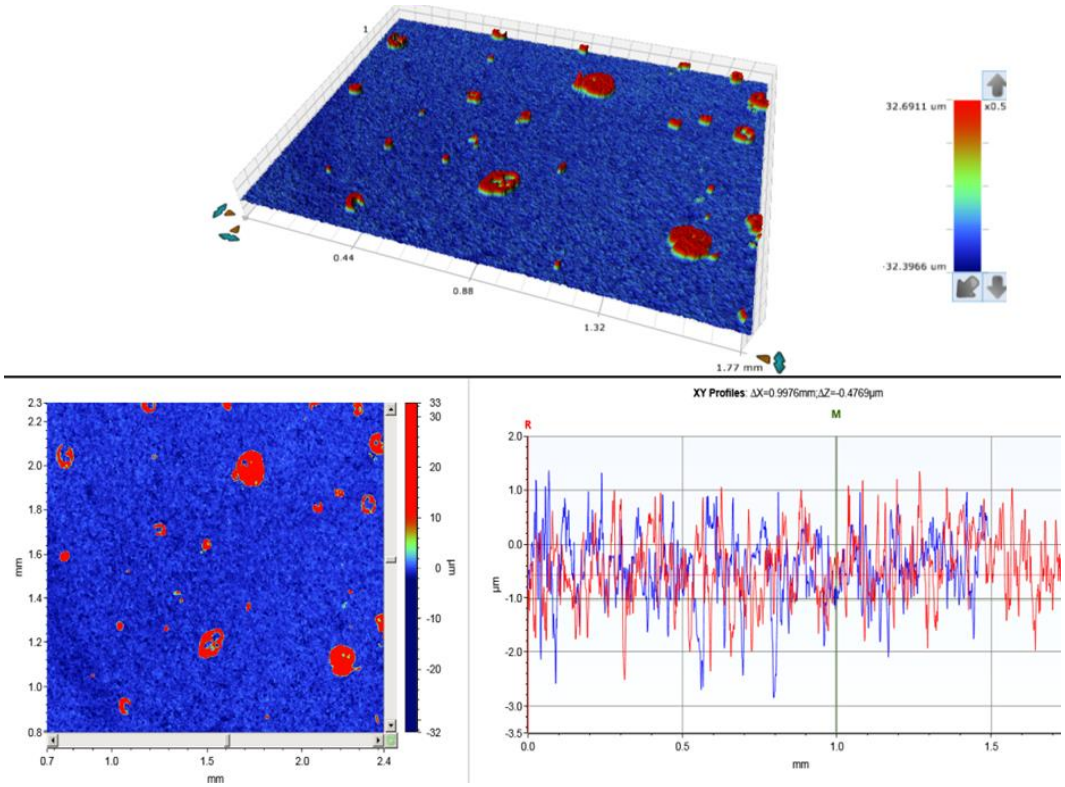

(a)

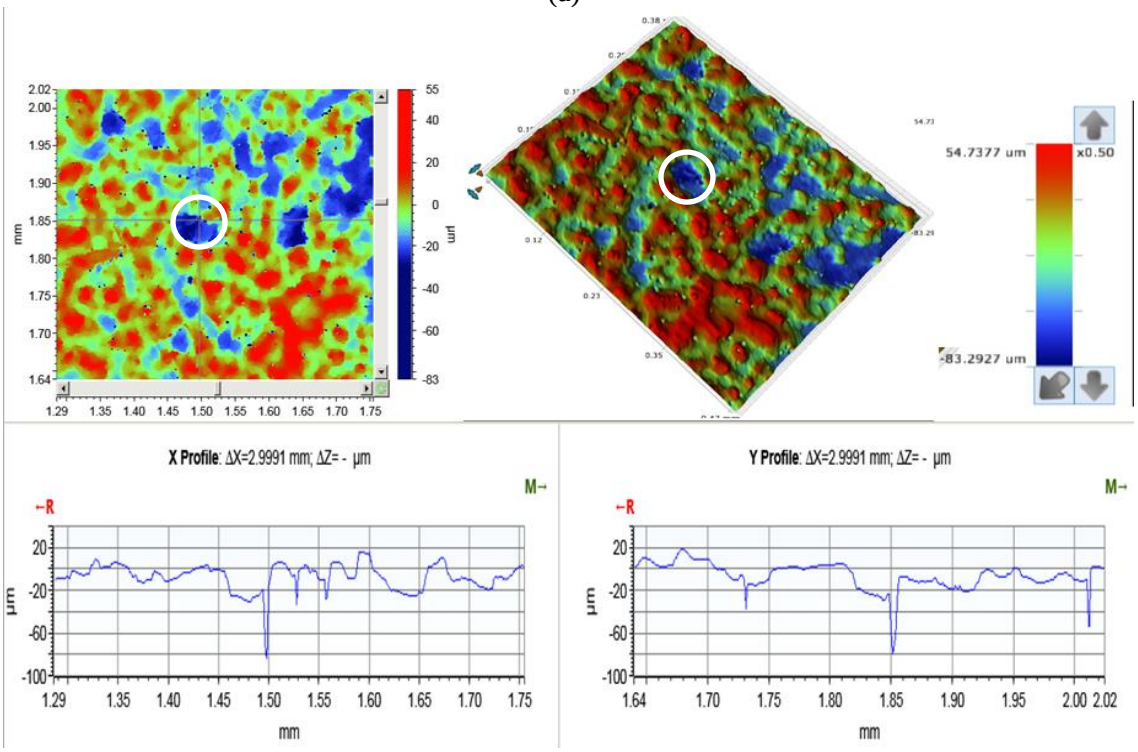

(b)

Figure 10-22 2D and 3D images of deepest pit (relative to corroded surface) on carbon steel surface exposed to corrosion system under 10mole% H_2S - 90mole% CO_2 after 168 hours at (a) 30ºC, (b) 50ºC, (c) 80ºC, and exposed to corrosion system under 10mole% H_2S - 90mole% N_2 after 168 hours at (d) 50°C (e) 80ºC.

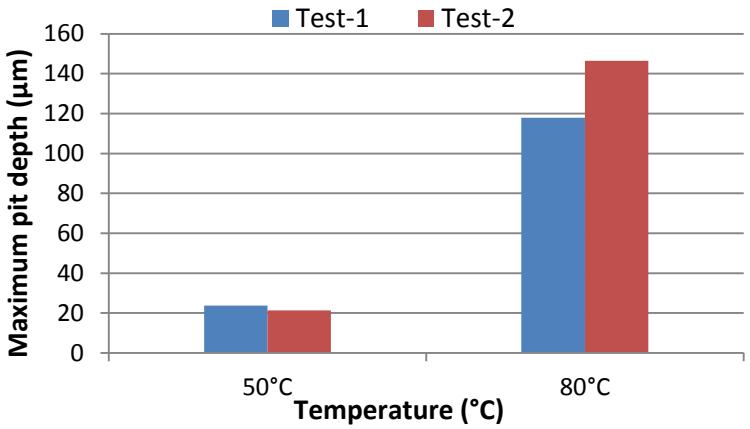

Figure 10-23 Repeatable pit depth analysis on samples exposed to a 3.5 wt.% NaCl solution under a 10mol. % H_2S - 90mol. % CO_2 gas atmosphere after168 hours in separate tests at 50 and 80°C.

The concept of total metal penetration and pitting factor has already been introduced in Chapter 6 of this thesis as a means of evaluating the contributing mechanisms to, as well as characterising corrosion damage across the different experimental conditions under investigation. The breakdown of the contributing mechanism to corrosion damage in tests under 100mol.% CO_2, 10mol. % H_2S - 90mol. % CO_2 gas and 10mol. % H_2S - 90mol. % N_2 gas atmopheres is presnted in Figure 10-24, while the pitting factor for these conditions is presented in Figure 10-25 as a function of temperature.

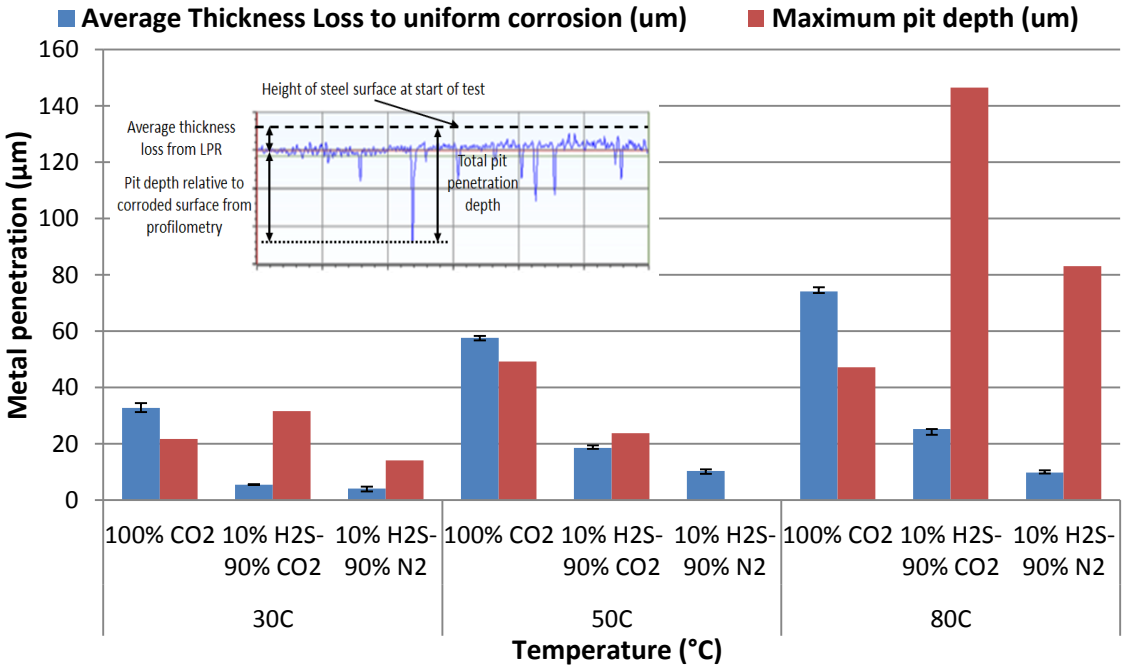

Figure 10-24 Total pit penetration on carbon steel surface exposed to corrosion system for 168 hours under 100mol. % CO_2, 10mol.% H_2S - 90mol. % CO_2 and 10mol.% H_2S - 90mol. % N_2 gas atmosphere as a fuunction of temperature indicating the contribution of general thickness loss (from LPR) and pit depth relative to corroded surface (determined from surface profilometry).

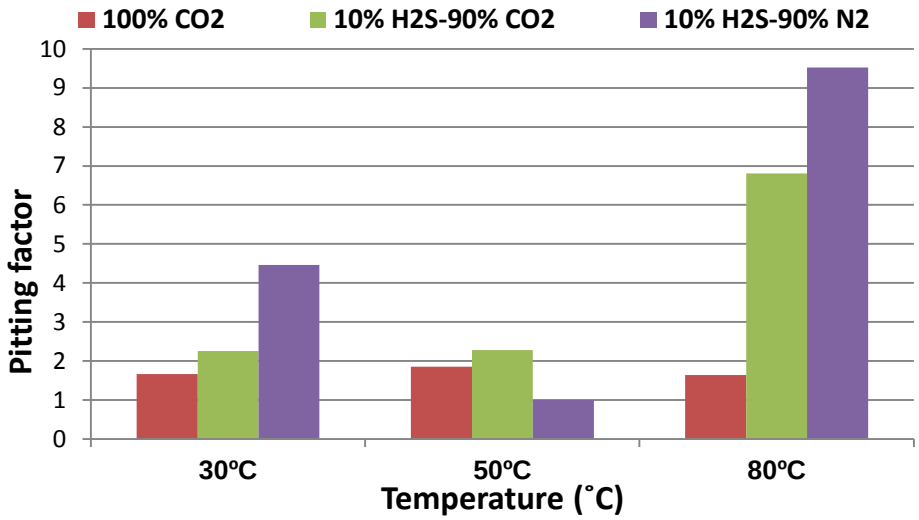

Figure 10-25 Variation of pitting factor for steel surface exposed to corrosinon system under 100mol. % CO_2, 10mol. % H_2S - 90mol. % CO_2 and 10mol. % H_2S - 90mol. % N_2 gas atmosphere as a function of temperature after 168 hours.

Referring to Figure 10-24, pitting and/or localised corrosion dominates the corrosion damage in H_2S-containing corrosion environment, especially at 80°C, while uniform corrosion is significantly reduced. However, uniform corrosion contribution increased with temperature for all gas composition and became more dominant with the presence of CO_2 gas in the gas phase. This effect is shown in Figure 10-24 to increase with increasing temperature to emphasis a synergy between CO_2 and temperature in CO_2-containing sour corrosion environments. At 50°C the contribution of uniform and pitting corrosion to corrosion damage is almost equal in CO_2-containing sour corrosion environments. This is also significantly different for test at 30°C in the same gas phase composition. At 30°C, pitting corrosion is more dominant. The reasons for these observations have already been discussed in section Chapter 10. By referring to Figure 10-25, the pitting factor for test under 10 mol. % H_2S – 90 mol. % N_2 gas atmopheres at 50°C is calculated and given as 1.0, which implies (by definition of pitting factor) a corrosion damage mechanism that is completely due to uniform corrosion. The lower pitting factor of test conditions after 168 hours relative to pitting factor after 7 hours (Figure 9-22) is due to increase in material loss due to continuous corrosion over 168 hours.

10.2.4 Summary on uniform and pitting corrosion behaviour of carbon steel in sour corrosion environment

The results presented and discussed in this chapter have shown that in the later stages of corrosion of carbon steel materials in H_2S-containing corrosion environments, the presence of CO_2 in the gas phase will enhance the electrochemical activities at the corrosion interface,

leading to the competitive manifestations of both ferrite dissolution and pitting corrosion propagation. The uniform corrosion contribution is more associated with CO_2 corrosion kinetics and leading to precipitation of FeS from the bulk solution. Pitting corrosion propagation is supported by the build-up of FeS during sour corrosion. The influence of the presence of and /or absence of CO_2 gas in the gas phase is most prominent at higher temperatures to encourage competitive precipitation of $FeCO_3$ and Fe_xS_y after significant exposure time (168 hours) H_2S-CO_2 containing corrosion environment, especially at 80°C. During extended experimental period, iron sulphide corrosion products do undergo some form of transformation which influences the corrosion morphology; uniform and pitting and/or localised corrosion. These observations are also a function of temperature.

Chapter 11. Discussion

11.1 Introduction

In the results chapters 6, 7, 8, 9 and 10, the findings from the experimental study of the corrosion behaviour of carbon steel materials in CO_2-saturated and H_2S-containing corrosion environments have been presented. The emphasis of discussion in this chapter is on the effect of the environmental parameters under investigation; temperature, chloride ion concentration, *in-situ* pH, CO_2 and H_2S gas on reaction kinetics, corrosion product formation and pitting corrosion.

This chapter is divided into two main sections, namely

- General corrosion behaviour and
- Pitting corrosion behaviour

In each of these sections, discussions will be based on the results presented in Chapters 6 and 7 of this thesis. Emphasis will be on how the results from this thesis add to the large body of work on sweet and sour corrosion and specially advance the understanding of pitting corrosion.

11.2 Corrosion behaviour and corrosion product formation

In order to fully appreciate the process of corrosion of carbon steel in H_2S and/or CO_2 containing environments, it is important to take into account the microstructure of typical X65 pipeline steel prior to corrosion. A typical X65 pipeline steel constitutes small deformed ferrite grains and large pearlitic areas [24, 183]. The pearlite phase in carbon steel microstructure is consist of ferrite and cementite (Fe_3C) with 88 wt.% of the ferrite phase [183]. It has been observed by several authors and from the results presented in Chapter 6 and 7, that ferrite preferentially dissolves from the steel surface during corrosion reaction of steel in CO_2 saturated and /or H_2S-containing environments [9, 24, 88, 164], such that an uncorroded cementite (Fe_3C) phase is left behind as a result of anodic dissolution of ferrite [9]. This process is a fundamental proponent of the overall corrosion behaviour; general and pitting corrosion, of carbon steel materials exposed to these environments.

11.2.1 CO_2 corrosion and iron carbonate formation

From the results of this study presented and described in Chapter 6, it has been established that the initial stages in the kinetics of corrosion of carbon steel in an unbuffered CO_2-saturated environment is correlated on the preferential dissolution of ferrite from the steel microstructure,

leaving behind a framework of empty cementite [9, 24, 88, 164]. This process is in agreement with the published results by Crolet *et al* [88], and emphasising role of empty cementite layers on the corrosion kinetics and corrosion product formation. In this study, the effect of environmental parameters; temperature, chloride ion concentration and bulk solution pH on the initial ferrite dissolution process and $FeCO_3$ formation process has been explored. The ferrite dissolution process is correlated to the anodic reaction through which Fe^{2+} ions are released into the bulk solution while at the same time the uncorroded cementite (Fe_3C) is left behind and becomes preferential sites for cathodic reduction reactions of H_2CO_3/HCO_3^- to take place [9, 88]. This scenario is depicted in Figure 11-1.

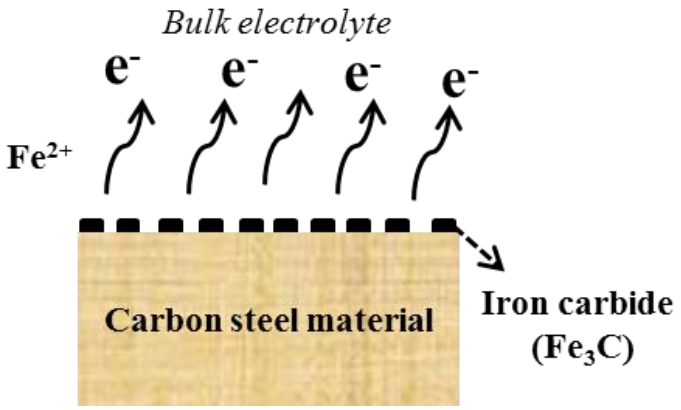

Figure 11-1 A schematic representation of the initial ferrite dissolution during the corrosion of carbon steel materials in an unbuffered CO_2 saturated environments.

In a typical unbuffered corrosion environment, the pH ranges between ≈ 4 and 5. In such a scenario, the rate of ferrite dissolution process is expected to contribute to the supersaturation of the bulk solution with Fe^{2+} and CO_3^{2-} as shown in Figure 6-6. The process of solution supersaturation has been shown in this study to be significantly influenced by temperature and chloride ion concentration (especially prior to $FeCO_3$ formation). It is therefore expected that the rate of ferrite dissolution and rate of supersaturation of the solution increases with temperature [77, 103]. This is because increasing temperature is known to accelerate most of the chemical, electrochemical and transport processes occurring in the system; such as H^+ reduction, H_2CO_3/HCO_3^- reduction, manifesting in increased cathodic and anodic reactions [103, 119]. The role of chloride ion concentration in CO_2 corrosion has been subject of contrasting viewpoints in recent years [18, 38, 108, 109]. There have been reports that a decrease in corrosion rate occurs with increase chloride ion concentration [18] (even with reported decrease in solution resistance with increase in chloride ion concentration) as well as

the suggestion of a potential threshold of chloride ion concentration after which rate of ferrite dissolution is retarded [105].

However, in the course of this study, a correlation between chloride ion concentration and the general corrosion rate is observed and correlated to the aggressiveness of the corrosion environment. This was also found to be consistent with solution resistance measurements provided in Figure 7-2 of this thesis and the reports of several authors [40, 105, 107]. The solution resistance is observed in this study to decrease with increasing chloride ion concentration. This also correlated with an increase in corrosion rate with increase in chloride ion concentration. This trend is expected to increase the rate of initial ferrite dissolution and the rate of supersaturation of the bulk solution and corrosion interface. Results described in section 7.2 help to establish the synergies that also exist between temperature and chloride ion concentration in terms of the general corrosion rate and rate of supersaturation corrosion environment. Higher temperatures and chloride ion concentrations were more aggressive than lower temperatures and chloride ion concentrations. This is supported by the concept of increased aggressiveness of dissolved chloride ions at elevated temperature reported by Yap and Srinivasan [40].

Iron carbonate corrosion products formed in corrosion environments where supersaturation is preceded by extensive ferrite dissolution, has often been described as being non-protective [9, 88]. The results presented in Chapter 6 of this thesis have established a relationship between the initial ferrite dissolution process in a corrosion scenario in which ferrite dissolution precedes solution supersauration and the formation of 'an amorphous' form of $FeCO_3$ corrosion product layer. This type of $FeCO_3$ corrosion product has been shown to be non-protective as suggested by Crolet *et al* [88]. The evolution of $FeCO_3$ corrosion product over a period of 168 hours adopted in this study has helped to establish a fundamental proponent in the formation of a non-protective form of $FeCO_3$. This proponent is the non-uniform distribution of Fe_3C from initial ferrite dissolution. Since the Fe_3C covered regions are believed to have a lower over-potential for cathodic reactions than the regions undergoing ferrite dissolution [9, 88], this will lead to a non-uniform distribution of corrosion product ($FeCO_3$) across the surface of the corroding metal once supersaturation is achieved at the corrosion interface and hence formation of a non-protective corrosion product layer. This scenario is expected in typical oilfield conditions where the bulk solution and corrosion interface is not initially saturated with Fe^{2+} and CO_3^{2-} for the formation of protective form of $FeCO_3$ corrosion products.

The rate of formation of non-protective and hence an 'amorphous' and/or non-crystalline (or nanoscale-polycrystalline) form of $FeCO_3$ corrosion products increases with the kinetics of corrosion, rate of ferrite dissolution and supersaturation. These processes are also influenced by increasing temperature and chloride ion concentration and most importantly exposure time. In comparison to the unified model developed by Sun *et al* [84] to show the dependecy of solubility limits of $FeCO_3$ on ionic strength and temperautre, it is expected that the solubility limits of $FeCO_3$ to reduce with increasing temperature and hence increase the rate of formation of $FeCO_3$ as observed in this study. However, it is important to note that the concept of solubility limits in the process of formation of $FeCO_3$ only offers a thermodynamic perspective (which seems to have a threshold effect with respect of to the effect of changing chloride ion concentration according to Sun *et al* [84]). The corosion scenario established from this study in which the rate of formation of $FeCO_3$ and the magnitude of protection (although not very protective) increases with chloride ion concentration is correlated more to the rate of ferrite dissolution and supersaturation as the solution becomes more aggressive and less on the effect of chloride ion on the morphology or stability of $FeCO_3$ as often suggested in the literature [107].

With respect to the effect of chloride ion concentration on the corrosion process in unbuffered CO_2-saturated corosion environments from this study, the rate of $FeCO_3$ corrosion product formation is more influential than the thermodynamic tendency for the formation of $FeCO_3$ corrosion product. The synergistic effect of chloride ion concentration and temperature on corrosion product formation as observed in this study is also correlated to the rate of superaturation of the bulk solution towards the formation of $FeCO_3$ corrosion products. The synergistic effect of chloride ion concentration and temperature on corrosion product formation has been estalished and shown by the increase in the crystallinity of the $FeCO_3$ at higher temperaure and chloride ion concentration from the SEM images and XRD patterns presented in section 7.2. A schematic repesentation of the corrosion processes and corrosion product formation as influenced by temperature and chloride ion concentration is provided in Figure 11-2.

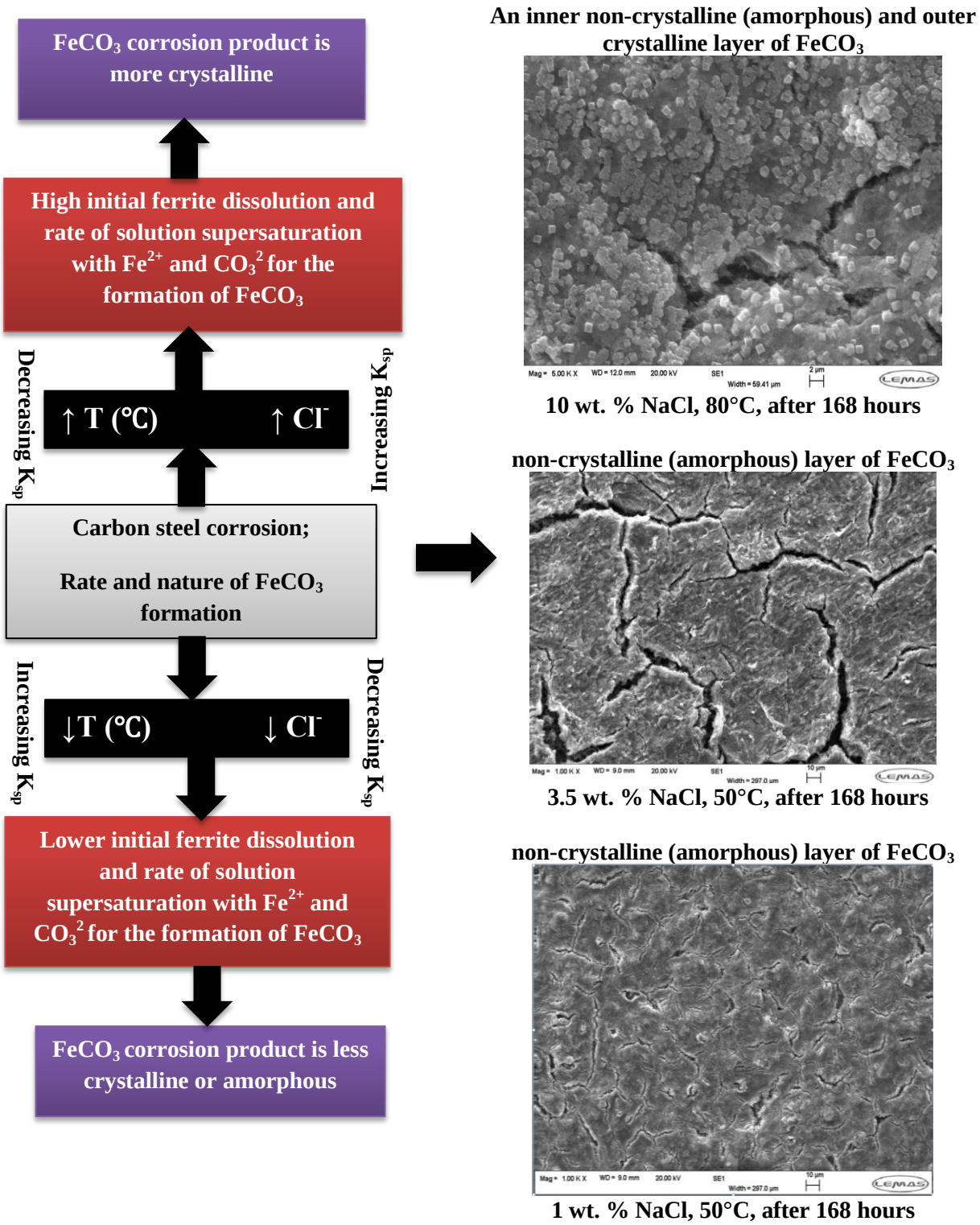

Figure 11-2 Schematic summary of the effect of temperature and chloride ion concentration on the corrosion behaviour of carbon steel materials in CO_2-saturated environments and formation of $FeCO_3$ corrosion products.

The propensity to form different forms of $FeCO_3$ corrosion products (protective or non-protective) has also been often correlated to the solution pH [9, 78]. This is usually on the basis that increasing the pH is expected to reduce the amount of H^+ in the bulk soultion available for the cathodic reaction process [103, 140]. With increasing solution pH, the cathodic reaction is significantly changed and dominated by water reduction and hence reduces the corrosion rate as well as lowering concentration of Fe^{2+} in the bulk for $FeCO_3$ precipitation. The formation of protective $FeCO_3$ still occurs at lower amount of H^+ and Fe^{2+} in the bulk soultion at higher pH because the solubility limit (K_{sp}) of $FeCO_3$ is decreased at higher solution pH. This is in contrast to the retardation of the rate of $FeCO_3$ formation when Fe^{2+} is reduced as is the case in unbuffered corrosion systems. This is because the solubility limit of $FeCO_3$ is significantly reduced at higher pH, such that only a fraction of a ppm of Fe^{2+} is needed to achieve supersaturation at higher pH [78].

In addition to the protectiveness of $FeCO_3$ corrosion products, this study has been able to show that the morphoplogy and crystallinity of $FeCO_3$ corrosion products is also linked to the pH of the corrosion system. According to Guo *et al* [93], lower pH values increase the critical supersaturation needed for the formation of $FeCO_3$, such that the rate of nucleation is higher than the rate of particle growth. This leads to the formation of an 'amorphous' $FeCO_3$ shown in Figure 8-3. The implication is that at pH value of 3.8 (unbuffered) and at 50°C, significant ferrite dissolution is needed at lower pH in order to exceed the critical supersaturation. On the other hand at higher pH values (pH values of 6.6 and 7.5 and at 50°C in this study), critical supersaturation is lower and hence minimum ferrite dissolution is required for the formation of a crystalline form of $FeCO_3$ corrosion products. A summarised representation of the overall corrosion behaviour of carbon steel as influenced by bulk solution pH is provided in Figure 11-3.

There are two other distinct observations at the extremes of the pH ranges explored in this study. Nano-scale crystals of $FeCO_3$ were observed as a top-layer at higher temperatures and higher chloride ion concentration in unbuffered CO_2-saturated corrosion environments. In some instances, localised distribution of nano-scale crystals of $FeCO_3$ were observed, while in other instances, nano-scale crystals of $FeCO_3$ could only be confirmed from XRD patterns. This helps to corroborate initial assertions on the effect of temperatures and chloride ion concentration on the formation of a non-protective $FeCO_3$ corrosion product layer. At much higher pH values; 7.5, the observed pseudo-passivation effect reflects the level of protection on the corroded surface. It is likely that the pseudo-passivating effect is due to the significant coverage of the

steel surface from an extensive formation of $FeCO_3$ corrosion product leading to a surface ennoblement (by ≈ 400mV). Although Han *et al* [91] had suggested that pseudo-passivation as observed in this study is attributed to an underlying layer of magnetite (Fe_3O_4), this could not be proven in this study from extensive post-experiment surface analysis.

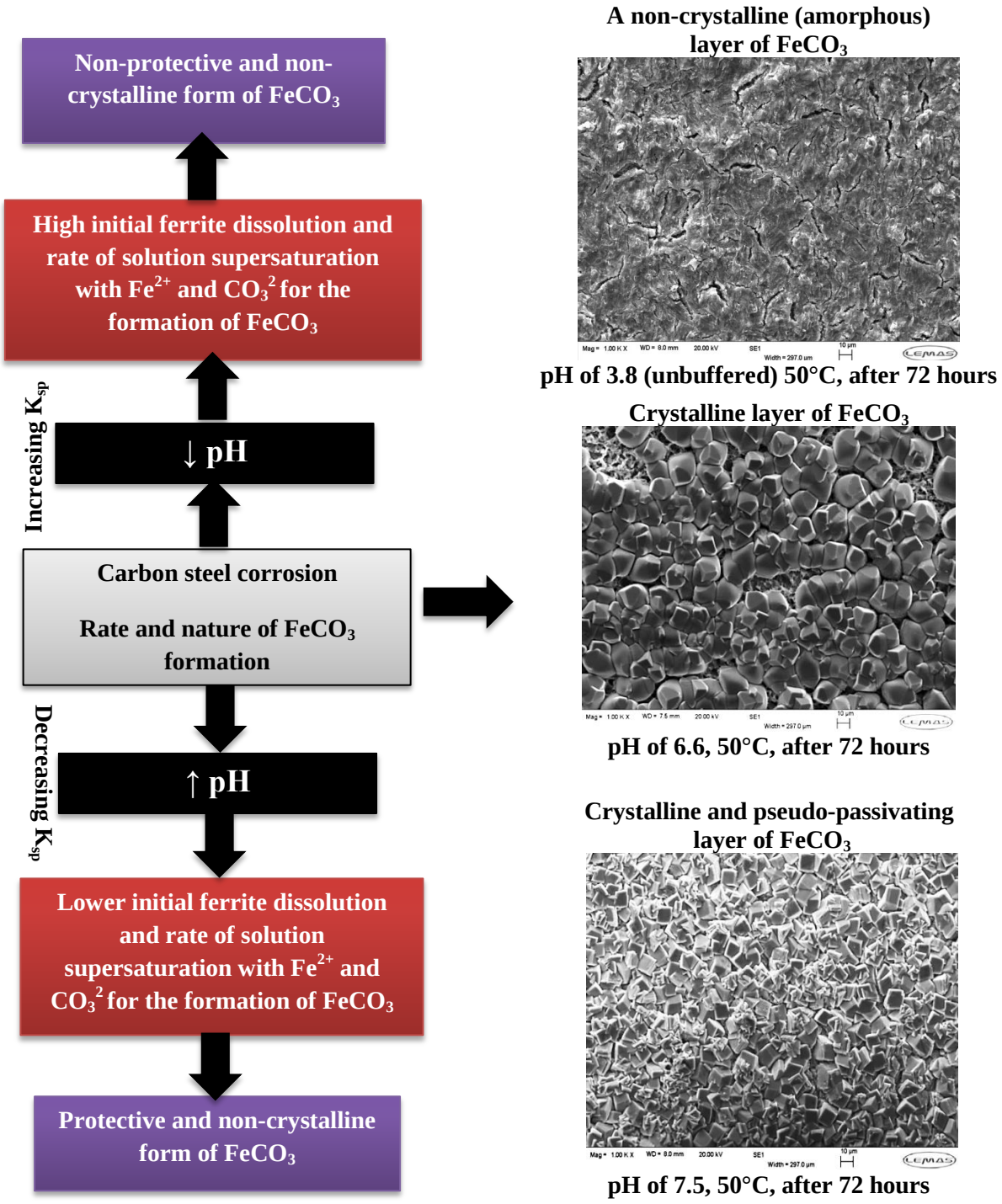

Figure 11-3 Schematic summary of the effect of bulk solution pH on the corrosion behaviour of carbon steel materials in CO_2-saturated environments and formation of $FeCO_3$ corrosion products.

11.2.2 Sour corrosion kinetics and corrosion product formation

This section discusses the corrosion of carbon steel materials exposed to H_2S-containing corrosion environments as influenced by a wide range of environmental parameters; temperature, the presence of and/or absence of H_2S and/or CO_2 gas. The results on sour corrosion presented and described in Chapter 7 of this thesis are discussed in detail and are referenced to some of the results already presented and discussed on CO_2 corrosion. In the course of this study, short and long-term duration of experiments were explored. While short term experiments may not necessarily offer information that would help in predicting the lifespan of pipeline materials, they however offer a useful insight into changing electrochemical process that may likely influence the long-term general and pitting corrosion behaviour of carbon steel materials exposed to these environments. On the other hand, tests based on long-term exposure; over 168 hours has helped to provide a more robust perspective of corrosion behaviour of carbon steel materials in sour corrosion environments. Long-term predictions of the pitting corrosion behaviour of pipeline steels in sour corrosion environments beyond 168 hours may also be limited by the time-dependency of pit propagation.

The kinetics of sour corrosion has been shown to be significantly different from that of CO_2 corrosion kinetics. One such point of distinction is correlated on the electrochemical pathways for metal dissolution in sour corrosion environments, especially when the gas phase composition contains significant amounts of CO_2 gas. In such corrosion scenarios, sour corrosion kinetics are described as two electrochemical processes: "solid state" or "direct" corrosion reactions and aqueous phase corrosion reactions [35, 39, 73, 115, 118]. The direct reduction reaction mechanism for H_2S/HS^- reduction has been shown by the potentiodyanmic curves in Figure 9-1 to dominate the cathodic reaction process. These electrochemical pathways have also been shown in this study to be influenced by the presence of and/or absence of CO_2 and/or H_2S gas and temperature.

Direct reduction reaction of steel in H_2S-containing corrosion environments leads to the formation of a very thin initial layer of FeS corrosion products identified as mackinawite (stoichiometric FeS) in this study [32, 124, 128, 184] in the early stages of corrosion. Results presented and discussed in section 9.4 have been able to put into clear perspectives the rate at which FeS (mackinawite) is likely to form in sour corrosion environments. The aqueous phase corrosion reaction process in the H_2S-containing corrosion environment is correlated to the initial preferential ferrite dissolution process that have been shown to dominate the early stage corrosion reactions in a CO_2-containing corrosion environment, leading to the evolution of the

empty cementite network [9, 24, 88, 164]. Corrosion rate data provided in section 9.2, 9.3 and 9.4 have shown that the rate of ferrite dissolution is higher in CO_2-containing sour corrosion systems than in H_2S-N_2-containing corrosion environment. The results presented in sections 9.2, 9.3 and 9.4 have also shown that the formation of FeS from solid-state reduction reaction and aqueous corrosion process significantly influences the corrosion kinetics (especially the cathodic reaction).

Referring to the potentiodynamic curves in Figure 9-1, the influence of direct reduction kinetics on overall corrosion kinetics decreases with increasing temperature (especially in the H_2S-CO_2-containing systems). On the other hand, the influence of the cathodic reduction reaction of H^+ and/or H_2CO_3 increases with increasing temperature as shown in Figure 9-1(a) – (c) to reflect the synergistic effect of CO_2 and temperature on the corrosion kinetics of carbon steel in sour corrosion environments. In the absence of H_2S gas in the gas phase, H^+ and/or H_2CO_3 reduction reaction is usually the main cathodic reaction. In this case, there is usually a higher rate of ferrite dissolution before the formation of corrosion product. Hence, in these conditions the rate of corrosion is expected to be higher. In H_2S-containing corrosion systems, the formation of FeS at the steel surface from direct reduction will quickly block some of the anodic sites and hence reduce corrosion rate as observed in this study after 7 hours. However, as the temperature increases, the influence of direct reduction kinetics on overall corrosion kinetics decreases, while the influence of the cathodic reduction reaction of H^+ and/or H_2CO_3 increases, leading to a higher rate of ferrite dissolution and hence higher corrosion rates. In a purely H_2S-containing corrosion system (in the absence of CO_2 gas in the gas phase), H^+ reduction is also still influential at higher temperature in an Arrhenius-type dependence of electrochemical and mass transfer processes on temperature as described by several authors [77, 103].

The consequence of such complex electrochemical processes in the early stages of sour corrosion is therefore linked to the rate of ferrite dissolution and the rate of formation of FeS. As mentioned earlier, the effect of solid-state reduction reaction kinetics in the early stages of corrosion process is the formation of an FeS corrosion product; mainly mackinawite as a stoichiometric FeS [128, 184]. Within the first 7 hours of exposure, mackinawite forms very quickly in H_2S-containing corrosion systems influencing the corrosion process by reducing the uniform corrosion rate as well as the corrosion potential (becoming more negative) when compared to the corrosion rate in CO_2 only-saturated system and consistent with observations by Morris *et al* [180]. The extent of reduction of corrosion rate as a result of the formation of FeS reduces with increasing amount of CO_2 in the gas phase and corroborated by the effect of

increasing temperature to illustrate the synergy of CO_2 gas presence and temperature on the rate of FeS formation and ferrite dissolution. The morphology of FeS corrosion product is also different as a result of such synergy. In such situations, there is an envisioned competition between initial ferrite dissolution and FeS formation, especially as the kinetics of FeS is increased with temperature in the same way as the increase in ferrite dissolution with increasing temperature. The implication of the variation in the rate of FeS precipitation and ferrite dissolution with temperature becomes increasingly more important over a long-term period as both processes are correlated to the direct and aqueous reduction reaction pathways for FeS formation. A summary of the corrosion kinetics and FeS formation in the early stages of sour corrosion of carbon steel is provided in Figure 11-4.

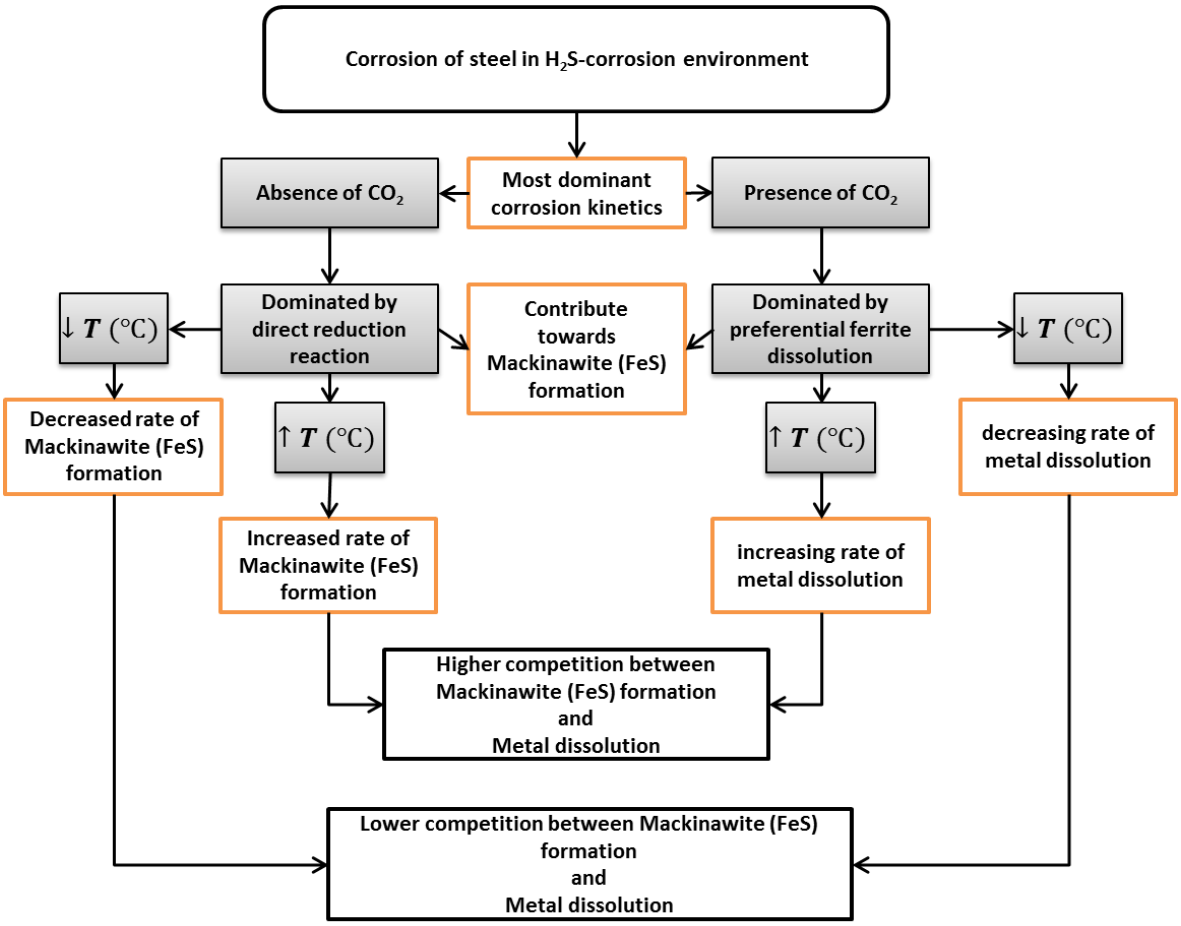

Figure 11-4 Schematic summary of the effect of temperature, CO_2 and H_2S on the sour corrosion kinetics and macknawite (FeS) formation in the early of sour corrosion kinetics.

The inherent complexities associated with sour corrosion kinetics and FeS formation becomes exacerbated with the prospect of an in-situ metamorphoses of initially formed FeS films [127] into other possible forms of FeS corrosion products. This process is also expected to be time-dependent. The electrochemical kinetics of sour corrosion monitored over 168 hours in this

study, as well as the FeS formation and/or transformation process is also dependent on environmental parameters. Beyond 7 hours, the time-dependent change in corrosion potential and corrosion rate data observed in this study has provided a unique means of understanding the *in-situ* changes in electrochemical process taking place in H_2S-containing corrosion systems. Generally, E_{corr} increases with the initial process of ferrite dissolution. This process is expected to increase with increase in temperature (even in the presence of FeS corrosion products) and correlated to the evolution of Fe_3C layer as already discussed in section 11.2.1 of this thesis.

Beyond the stages of initial ferrite dissolution, changes in temperature are a fundamental factor that influences the kinetics of sour corrosion and FeS formation and/or transformation. With extended exposure time, the FeS corrosion product layer becomes thicker as shown in Figure 10-13 and Figure 10-17, as well as becoming more protective. This is most apparent at higher temperature, especially with CO_2 gas in the gas phase. Based on the electrochemical responses (Figure 10-5 and Figure 10-9) at 50 and 80°C respectively, the CO_2 corrosion component in H_2S-CO_2-containing corrosion system, contributes to the corrosion process in terms of ferrite dissolution and availability of ferrous ions in the bulk solution, such that FeS could be precipitated from the bulk phase along with $FeCO_3$ corrosion product once supersaturation is attained at the corrosion interface. The implication of these processes is potentially a higher rate of FeS formation in H_2S-CO_2-containing corrosion system than in H_2S-N_2-containing corrosion system, correlating to the rate of ennoblement of the corroding surface (shift towards positive potentials). This has also led to higher cumulative thickness loss due to uniform corrosion (see Figure 10-9(b)). This observation is also linked to the synergistic contribution of CO_2 gas and higher temperature to the supersaturation of bulk solution with ferrous ions for the formation of FeS and/or FeS-$FeCO_3$ from the bulk solution unto the steel surface. This is corroborated by the corrosion potential and corrosion rate data which reflects the level of coverage and protectiveness of the corrosion product layers. At higher temperature (80°C), the corrosion potential showed evidence of ennoblement in both H_2S-CO_2 and H_2S-N_2-containing corrosion systems by ≈ 70 and 100 mV respectively, while the corrosion rate drops gradually from ≈ 2.4 mm/yr to 0.5 mm/yr and from ≈ 1mm/yr to 0.2 mm/yr respectively.

At lower temperature, the dissolution and/or transformation of initially formed mackinawite became the most dominant process over a significant period during the tests. This does not necessarily imply the non-existence of such transformation process at higher temperature. It only shows that the rate at which such dissolution and/or transformation process may be occurring as a function of temperature. While dissolution of and/or transformation of initially

formed makinawite could be tracked from the corrosion potential and corrosion rate data at lower temperatures, the process is likely to occur rapidly at higher temperature. This is supported by evidence of pyrrhotite as part of the corrosion products in sour environments at both 50 and 80° and not at 30°C. This also highlights the effect of temperature on the kinetics of FeS formation and transformation. These observations are in agreement with the process of dissolution and/or transformation of initially formed mackinawite (FeS) already proposed by several other authors [128, 138, 175]. Dissolution of initially formed mackinawite is believe to be dependent on environmental parameters such as temperature, pH and HS^-/H_2S concentration [128]. According to Tewari *et al* [185], the dissolution of initially formed mackinawite is controlled by the electrochemical interaction between a conductive mackinawite and H^+ and by the transport of the complexed intermediates $(FeHS^+)_{ad}$ from the interface to the bulk solution according to either of the following reactions [132, 185];

$$(FeHS^+)_{ad} + H_3O^+ \rightarrow Fe^{2+} + H_2S + H_2O \quad 11.1$$

or

$$(FeHS^+)_{ad} + H^+ \rightarrow Fe^{2+} + HS^- \quad 11.2$$

The reactions of Eq.11.1 and 11.2 lead to the dissolution of $(FeHS^+)_{ad}$ in acidic media [132].

As evidently shown in this study, the impact of dissolution and/or transformation of initially formed mackinawite becomes dominant, as well as occurring faster with increase in temperature [185]. This is also supported by the fact that most of the chemical, electrochemical, and mass transport processes that influence the reactions depicted in Eq. 11.1 and 11.2 are accelerated by increasing temperature. A thin layer of mackinawite remained the main corrosion product in sour corrosion environment at 30°C, with no significant changes in the electrochemical responses over 168 hours. The sour corrosion kinetics is slow and the FeS formation process becomes less complex with no evidence of dissolution and/or transformation of initially formed makinawite at very low temperatures.

The physical features of the FeS corrosion product layer formed in H_2S-CO_2-containing corrosion system at 80°C is non-uniform, possibly reflecting the uneven distribution of areas undergoing continuous ferrite dissolution process that dominates the corrosion mechanism in the presence of CO_2 gas, as well as the potential competition from $FeCO_3$ formation. Results from extensive FIB/TEM analysis in section 10.1.4 were able to show that a combination of an inner layer of Fe-O_{ad}, a middle layer of FeS and an outer porous layer of amorphous $FeCO_3$ constitute the corrosion product layer formed in H_2S-CO_2-containing corrosion system at 80°C,

while an inner layer of Fe-O_{ad} and an outer FeS layer constitute the corrosion product layer in H_2S-N_2-containing corrosion system at this temperature. The distribution of the different corrosion products on the steel surface helps to confirm the phenomenon of competitive precipitation of $FeCO_3$ and FeS in H_2S-CO_2-containing corrosion system and illustrated in Figure 11-5.

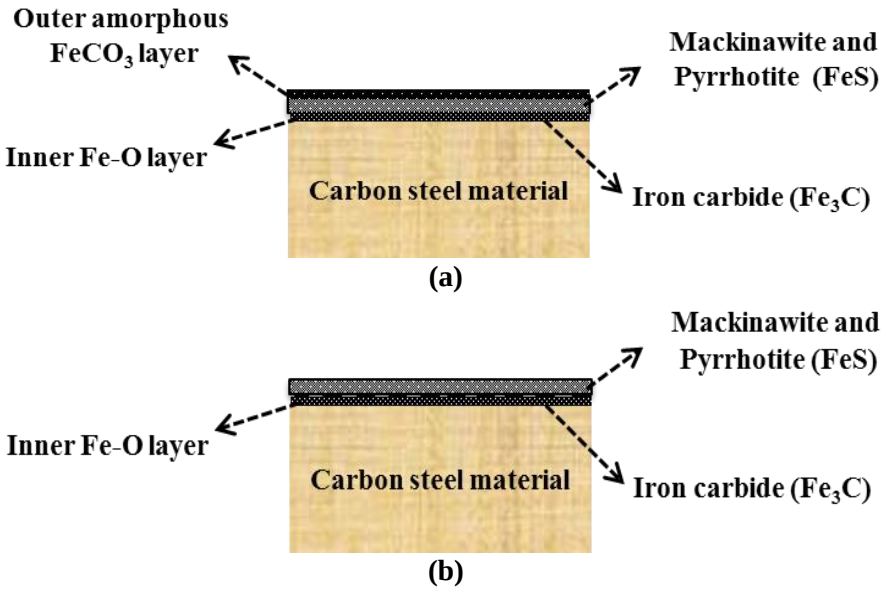

Figure 11-5 Schematic illustration of the corrosion product formation process in (a) H_2S-CO_2-containing corrosion system H_2S-CO_2-containing corrosion system and (b) H_2S-N_2-containing corrosion system after 168 hours at 80°C.

The 'amorphous' $FeCO_3$ is formed from bulk precipitation once supersaturation is attained from ferrous ions made available through the ferrite dissolution component of the corrosion process. It forms as an outer layer due to the faster rate of formation of FeS from solid-state or direct reduction reaction. Hence, the kinetics of $FeCO_3$ is slower than that of FeS in H_2S-CO_2-containing corrosion environments. An amorphous form of $FeCO_3$ is formed in this case due to the low pH of the corrosion environment [93]. The presence of an Fe-oxide layer as an inner corrosion product layer is not alien to the research community [129, 177] and is believed that it (Fe-O_{ad}) forms as a stable inner layer due to competitive adsorption of oxygen and sulphur unto the steel surface as either of Fe-S_{ad} and/or Fe-O_{ad} at higher temperatures [177]. The Fe-oxide or Fe-O_{ad} could not be identified in this study using some advanced surface analysis techniques as it is a very thin layer; on a nanoscale. It is likely that the presence of this oxide layer is related to the sour corrosion process when compared to the analysis of the corrosion products formed in pure CO_2 corrosion environment at the same temperature (see Chapter 6). The Fe-oxide layer could also be influencing the ennoblement process observed at this temperature. While it has also been reported by Han *et al* [92] that similar Fe-oxide layer could induce a potential change

of such magnitude as observed in this study for H_2S-containing corrosion systems, it was however not absolutely established from this study and will be a subject of future studies. A summary of the kinetics of sour corrosion and corrosion product formation as observed in this study in the later stages of sour corrosion is provided in Figure 11-6.

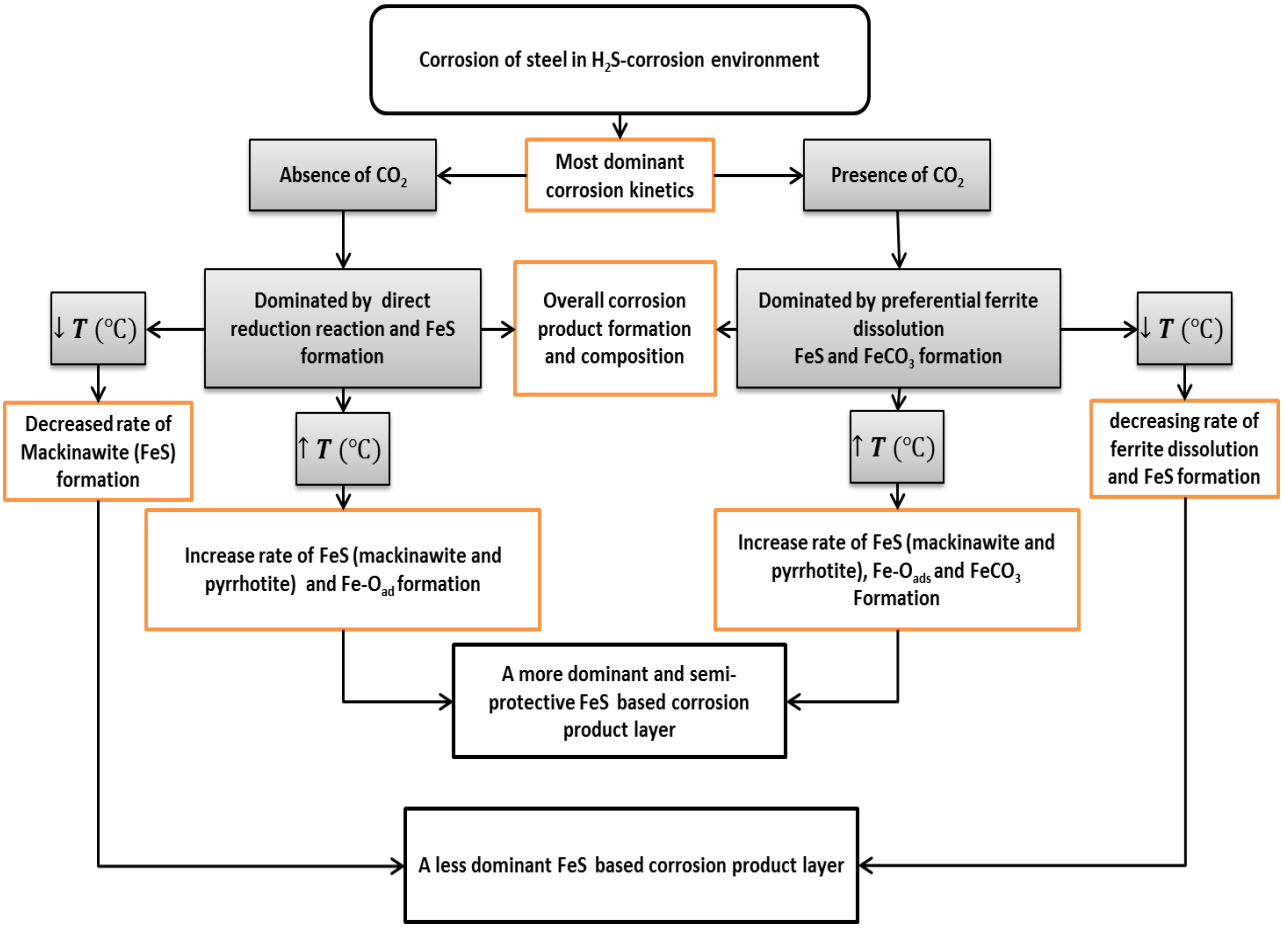

Figure 11-6 Schematic summary of the effect of temperature, CO_2 and H_2S on the sour corrosion kinetics and macknawite (FeS) formation in the later stages of sour corrosion kinetics.

11.3 Pitting corrosion of carbon steel in CO_2 and H_2S corrosion environments

The process of pitting corrosion of active materials like carbon steels have been shown from the results in this study (presented in Chapter 6 and 7 of this thesis) to be significantly different from pitting corrosion in passive materials like stainless steels. Pitting corrosion initiation is known to occur in passive materials as a result of localised breakdown of passive oxide layers with minimum uniform corrosion of surrounding surface (which is more cathodic due to the formation of a very protective oxide layer) [33, 38, 67-69]. In this study, significant uniform corrosion have been observed during pitting corrosion process of carbon steel as described in

sections (6.5 and 6.6), (7.2 and 7.3) and (8.2 and 8.3) of this thesis. In order to accurately characterise the pitting corrosion behaviour of carbon steels in CO_2 and H_2S-containing corrosion systems, the contribution from the different metal degradation mechanisms; uniform and/or pitting corrosion to total material penetration is estimated and taken into account. Hence, pitting corrosion have been characterised in this study based on the depth of pits (maximum pit depth and average pit depth) in "μm" relative to corroded surface rather than using the rate term; pitting rate in "mm/yr, especially since substantial uniform corrosion have also been shown to precede and continues to occur with pitting corrosion [88, 159]. The use of pit depth in "μm" instead of pitting rate in "mm/yr" also emphasises the difficulty in forecasting the rate of pit propagation by extrapolating on short term experimental data.

11.3.1 Pitting corrosion of carbon steel in CO_2 corrosion environments

This section discusses the overall pitting corrosion behaviour of carbon steel in CO_2-saturated environments and is divided into two sections; pit initiation and pit propagation.

11.3.1.1 Pit initiation

Fundamentally, the presence of sulphide inclusions has been considered one of the key precursors for initiation of pitting corrosion in both passive (stainless steels) and active materials like carbon steel albeit via different mechanism [112-114]. During corrosion of carbon steel materials, sulphide inclusions are more cathodic than the surrounding carbon steel matrix which preferentially dissolves [112, 114]. The role of preferential ferrite dissolution in the initiation of pitting corrosion of carbon steel in CO_2 saturated corrosion environment as postulated by Crolet *et al* [88] complements the proposed role of sulphide inclusions on initiation of micropits on carbon steel by other authors [112-114]. The use of an advanced pitting corrosion characterisation technique in this study has been able to show that the initiation of micropits is related to the initial ferrite dissolution process and evolution of Fe_3C and/or the uneven formation of a non-protective and non-crystalline (or 'amorphous') form of $FeCO_3$ layers, especially at higher temperature. This observation is also consistent with the reports by several other authors linking the process of localised corrosion initiation with initial ferrite dissolution and iron carbide evolution [9, 24, 88, 164, 165].

These initiated micropits are correlated to the higher rate of initial ferrite dissolution and formation of different forms of $FeCO_3$, such that parameters such as temperature, chloride ion concentration and bulk solution pH, that have been shown in this study to influence the early kinetics of the CO_2 corrosion process are also influencing the overall pitting corrosion behavior;

pit initiation and propagation. Micropits formed in carbon steel in the initial stages of corrosion as is the case observed in this study are usually expected to stop growing after some time [112]. However, evidence of pitting corrosion initiation (pit depths relative to corroded surface) was recorded after 7 and 36 hours (shown in Figure 6-17, Figure 6-19 and Figure 6-21) and after substantial initial ferrite dissolution to confirm the initiation of micropits during the early stages of corrosion. SEM images provided and described in sections 6.5 and 7.2 also show that within this period of pit initiation, the corrosion product formed on the steel surface is dominated by a mixture of Fe_3C and/or 'amorphous' $FeCO_3$ depending on the temperature. However, in cases where 'amorphous' $FeCO_3$ was formed, it offers only little protection against continuous uniform corrosion. On the other hand this combination of corrosion products also promotes the initiation of pits and/or micropits due to the non-uniform coverage and the manifestation of numerous cathodic and anodic sites across the entire corroding surface. This scenario is rarely the case for passive alloys where there is usually protection of surrounding surfaces by a passive oxide layer during the pit initiation stage to create a cathode-to-anode area ratio large enough to support the autocatalytic process that sustains pit propagation in the long-term. A schematic illustration of the process of pit initiation in carbon steels is shown in Figure 11-7.

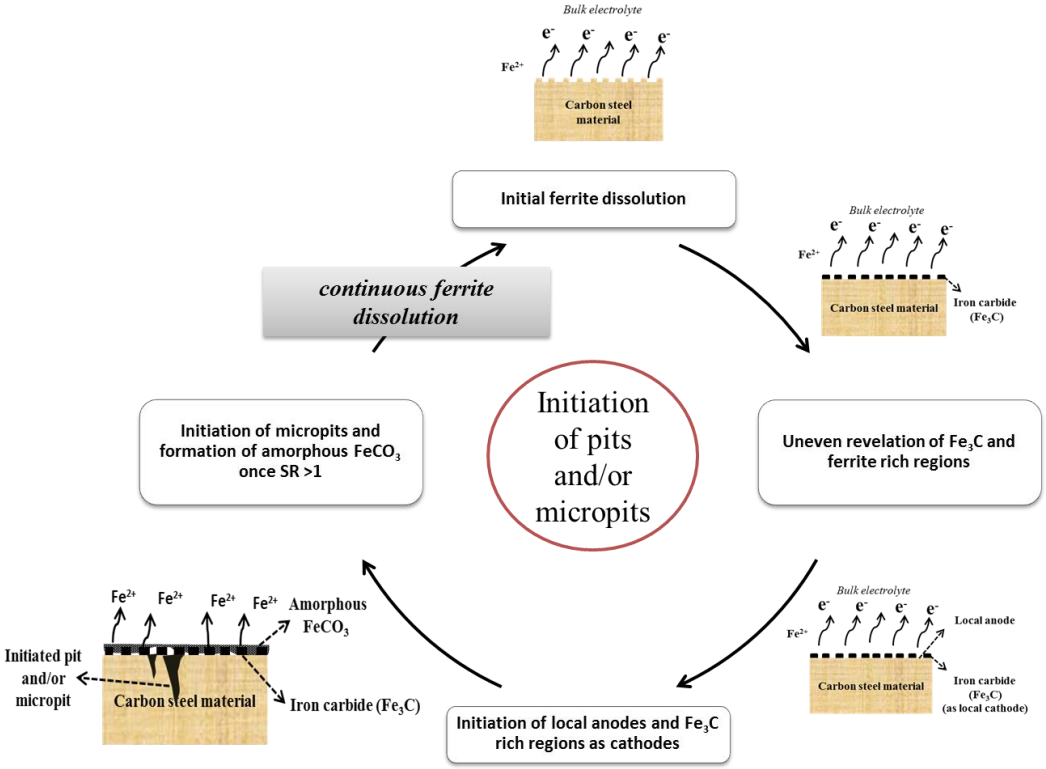

Figure 11-7 Schematic representation of the likely stages of pit initiation of carbon steel in an unbuffered CO_2 saturated environments.

In reference to pit initiation, the effect of chloride ion concentration is correlated to the effect of chloride ion on the aggressiveness of the corrosion environment. However, the results presented and described in sections 7.2 and 7.3 also show evidence of a synergistic effect of temperature and chloride ion concentration on the pitting corrosion initiation process as there is on the general corrosion and corrosion product formation process. Increasing both temperature and chloride ion concentration have been discussed in section 11.2.1 to increase initial ferrite dissolution and the rate of formation of 'amorphous' $FeCO_3$ in the early stages of the corrosion process. This means that by increasing temperature and chloride ion concentration, pits and/or micropits will be initiated faster. As already discussed in section 11.2.1, changes in any environmental parameters that tend to increase the rate of ferrite dissolution and solution supersaturation in CO_2 corrosion systems, also results in higher contribution of uniform corrosion to overall metal loss. This effect tends to recede the corroded surface, resulting in the reduction of pit depth. This scenario is usually dominant in the early stages of corrosion process but also with a cumulative effect over long period of exposure. The results shown in Figure 11-8 summarises the relationship between thickness loss due to uniform corrosion and pit depth relative to corroded surface after 36 hours.

Referring to Figure 11-8, the depth of initiated micropits or pits generally increases with increasing temperature for each chloride ion concentration levels. This is likely due to the rate of initial ferrite dissolution and formation of an 'amorphous' form of $FeCO_3$. These processes are known to increase with increasing temperature. However, the rate of initial ferrite dissolution also leads to significant metal loss due to uniform corrosion. This effect is also shown in Figure 11-8 to increase with increase in temperature and is likely the reason why the difference in the magnitude between pit depth at 50 and 80°C are smaller than the difference in magnitude of pit depth between 30 and 50°C. This trend is due to the masking effect from higher and continuous ferrite dissolution process that is usually associated with increasing temperature. In comparison to pit initiation in stainless steels, pitting potential and hence the likelihood for pit initiation to occurs is higher at higher temperature [106]. However, unlike in the case of pit initiation in carbon steels, there is no masking effect of the true extent of metal penetration by pitting in stainless steels.

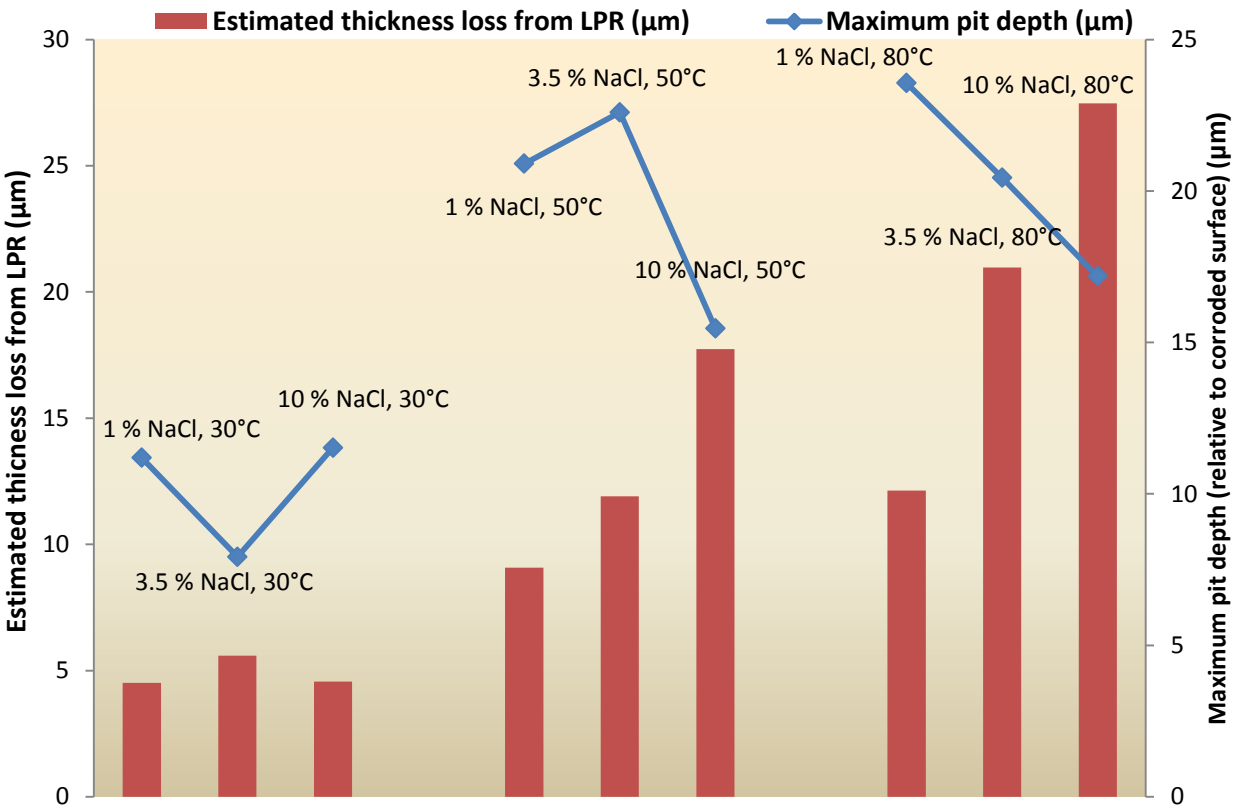

Figure 11-8 Schematic summary of relationship between estimated thickness loss due to uniform corrosion and depth of deepest initiated pit (relative to corroded surface) as a function of environmental parameters in CO_2-saturated corrosion systems after 36 hours.

At lower temperatures (at 30°C), there is a threshold effect on the effect of chloride ion concentration on the corrosion process within the first 72 hours (see Figure 7-3). Within the first 36 hours, the contribution to metal loss from uniform corrosion is equal for test in 1 and 10 wt.% NaCl, suggesting a threshold of 3.5 wt. % NaCl after which uniform corrosion rate is lower (only within the first 72 hours in this study). The reason for the threshold effect still remains unclear from this study. However, this behaviour is usually observed at low temperatures ≤ 30°C [125]. The variation in pit initiation with chloride ion concentration at 30°C varies inversely with the thickness loss from uniform corrosion as shown in Figure 11-8. The threshold effect of chloride ion concentration on uniform corrosion also correlates to the depth of initiated pits. The consequences of this trend is that after 36 hours, the depth of initiated pit on test sample exposed to 3.5 wt. % NaCl is lower than for test in 1 and 10 wt.% NaCl due to the masking effect form higher uniform corrosion. This is similar to the temperature effect on the depth of initiated pits.

At higher temperature, the threshold effect on pit initiation resulting from increasing chloride ion concentration disappears, which correlates to the uniform corrosion rate shown in Figure

7-8. However, at 50°C, the depth of initiated pits increased from 1 to 3.5 wt. % NaCl due to the role of increasing chloride concentration on the rate of initial ferrite dissolution and solution supersaturation (formation of amorphous $FeCO_3$) on the initiation of pits. Increasing the chloride ion further to 10 wt.% NaCl lead to the reduction of the depth of initiated pits. The later observation is due to the masking effect on pitted surface as the general corrosion contribution at this chloride ion concentration levels is higher (in synergy with increasing temperature). Once the temperature is increase further to 80°C, the chloride ions becomes even more aggressive leading to the rate of supersaturation for the formation of an 'amorphous' form of $FeCO_3$ as already mentioned in section 11.2.1. The effect of the aggressiveness of increasing chloride ion concentration on initiation of pits becomes completely inversely proportional to the increasing thickness loss from uniform corrosion as shown in Figure 11-8. This temperature range is probably so high that the masking effect from uniform corrosion subdues the effect of increasing chloride ion concentration (from 1 to 3.5 wt. % NaCl) on the depth of initiated pits as observed at 50°C.

The process of pit initiation in carbon steel is also observed in this study to vary with changes in the pH of the corrosion system. At higher pH values of 6.6 and 7.5, the corrosion environment is expected to change significantly as already discussed in section 11.2.1. However, once the environment changes so does the mechanism for $FeCO_3$ formation. The rates of initial ferrite dissolution (corrosion rate) were generally high at the start of the experiment for tests at pH values of 3.8 (unbuffered), 6.6 and 7.5. This implies that at some point in the corrosion process, the revealing of empty cementite is likely to occur (see SEM images in section 8.2). This is perhaps the reason why the pit depth (relative to corroded surface) after 7 hours at pH values of 3.8 and 6.6 are almost the same (see Figure 11-9(a). There was no pit depth on the surface of carbon steel sample exposed to a corrosion system at pH of 7.5 after 7 hours, possibly due to the masking effect of higher initial uniform corrosion rate as shown in Figure 8-2(a). The reason for the higher initial corrosion rate at this pH value is still not clear, but there is evidence in the literature [91] that suggests the idea of a certain pH threshold above which the corrosion rate of carbon steel may become high again. Fundamentally, the mechanism of pit initiation in carbon steel is therefore expected to be the same as depicted in Figure 11-7. However, for tests at pH values of 6.6 and 7.5, the corrosion rates reduce steadily and rapidly after 7 hours as a result of increasing coverage from the formation of protective $FeCO_3$ respectively and in contrast to the formation of a non-protective and 'amorphous' form of $FeCO_3$ in an unbuffered system at 50°C (pH value starting at 3.8).

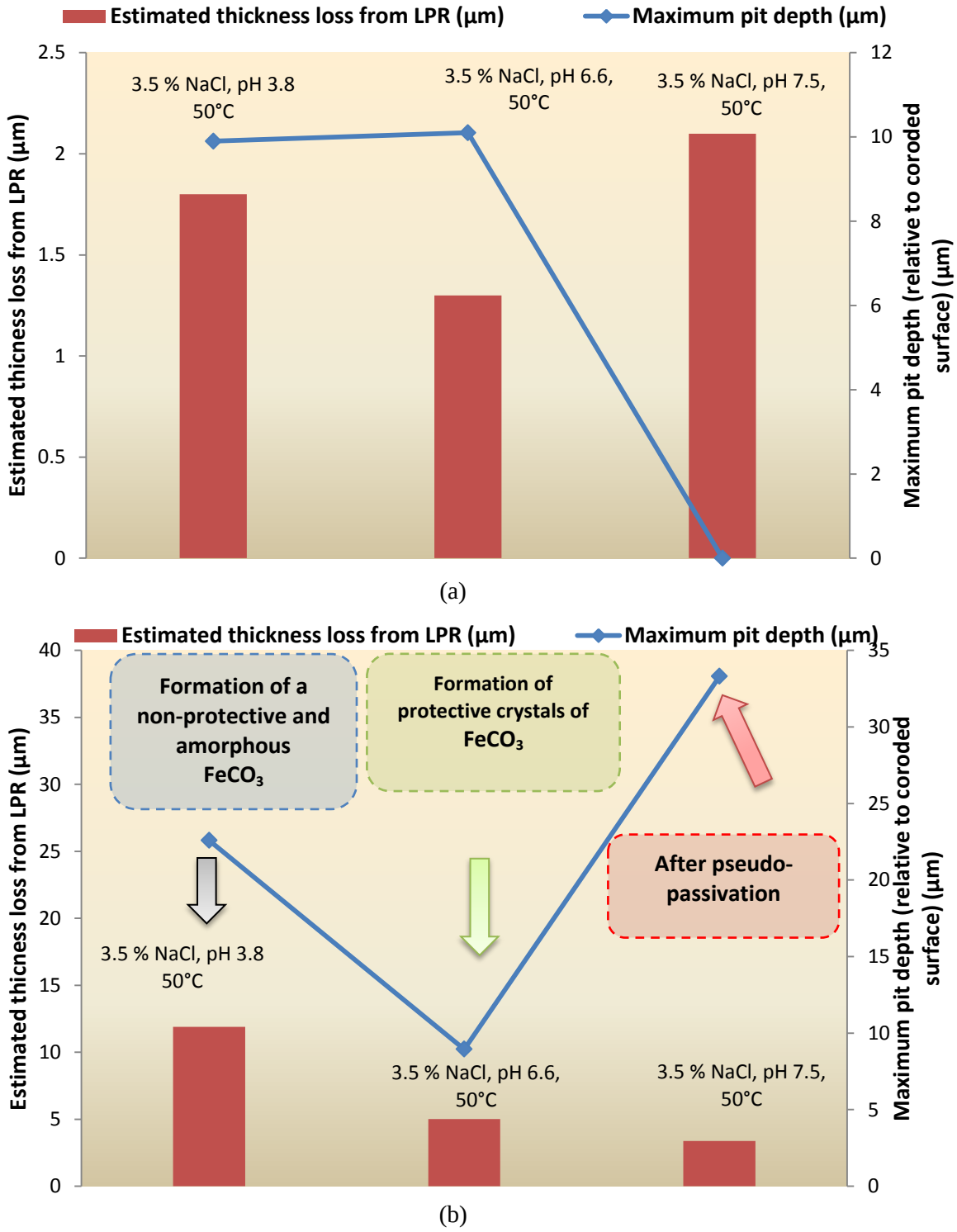

Figure 11-9 Schematic summary of relationship between estimated thickness loss due to uniform corrosion and depth of deepest initiated pit (relative to corroded surface) as a function of bulk solution pH in CO_2-saturated corrosion systems after (a) 7 hours and (b) 36 hours.

After 36 hours; during which pit initiation is considered to still be occurring in these corrosion systems, the level of protection offered to the corroding steel surface from the $FeCO_3$ formed at

pH of 7.5 is so high that it induces a pseudo-passivation effect. Pit initiation (≈ 30 μm) occurred rapidly after pseudo-passivation effect is established. It is possible that the initiation of pits at this pH level is linked to some discontinuity that continues to exist on the corrosion product as it is being formed (see Figure 8-7 (a)) or the localised breakdown of the initially formed pseudo-passivating corrosion product layer as soon as it is formed. Pit initiation in this case is likely due to well-defined local anodic and surrounding cathodic sites with a very large potential difference and in almost similar frame to the process of pit initiation in stainless steel. The only difference is that at pH 7.5, the pseudo-passivation effect is due to a $FeCO_3$ corrosion product layer rather than a passive oxide layer in stainless steels.

In the case of test at pH 6.6, the depth of initiated pit remained constant after 36 hours as shown in Figure 11-9(b). This is likely since the corrosion process is still dominated by initial ferrite dissolution but with much dispersed crystals of $FeCO_3$ corrosion products formed. Initial ferrite dissolution process is slow at this pH level due to the high pH. The corrosion product formed at pH 6.6 at this stage of the corrosion process is still not capable of changing the pitting initiation process. At a much lower pH level of 3.8, the formation of an amorphous $FeCO_3$ will help to drive the pit initiation process along with continuous ferrite dissolution. Figure 11-9, also depicts an inverse relationship between uniform corrosion and depth of initiated pits for tests at pH values of 3.8 (unbuffered) and 7.5 and less so for test at pH of 6.6. The latter is possibly due to the intermediate and slow corrosion kinetics associated with this pH value, as well as the kinetics of crystalline $FeCO_3$ formation.

11.3.1.2 Pit propagation

The pitting corrosion behaviour of carbon steel is tracked over 168 hours along with the evolution of corrosion product across a wide range of environmental parameters; temperatures, chloride ion concentration and bulk solution pH. Pits were observed to propagate albeit with different growth profiles depending on the conditions of the corrosion systems. This is against the notion that initiated micropits are often not expected to propagate. This may be expected, possibly due to the open-mouth nature of the pits as shown in Figure 6-18, Figure 6-20 and Figure 6-22. However, by tracking the evolution of corrosion products, it became clear that the propagation of pits is sustained by the non-protective nature and the uneven distribution of a predominantly non-crystalline and/or ‘amorphous’ form of $FeCO_3$ in unbuffered corrosion environments.

The nature and distribution of the pits observed in unbuffered corrosion environment from this study has also help to establish the fact that with the formation of a corrosion product layer dominated by an 'amorphous' form of $FeCO_3$, it is likely that there are usually multiple cathodic and anodic sites on a corroding surface during pitting corrosion. The cathodic sites are usually the corrosion product covered areas ($FeCO_3$ and/or Fe_3C) and usually adjacent to the localised anodes (pits). This observation is also likely due to the active nature of carbon steel in corrosion environments. Thus, the anode-to-cathode area ratio is larger for carbon steel than in stainless steels leading to the manifestation of shallow pits. This could be considered one of the fundamental differences between pit propagation in carbon steel and stainless steels as deduced from this study. In the case of pitting corrosion in stainless steels, localised anodic cavities in contact with localised electrolytic cells are surrounded by a large passive oxide-covered cathodic area acting as the cathode, such that the potential difference between these sites accounts for significant current flow with rapid corrosion of local anodes [65], leading to manifestation of deep pits.

Pit propagation beyond 36 hours was observed to increase quickly with increasing temperature at all chloride ion concentrations (already discussed in section 7.3). This is correlated to the rate of formation of non-protective (or amorphous) form of $FeCO_3$ capable of sustaining local galvanic cells and also consistent with the proposed mechanism of localised corrosion linked to the localisation of $FeCO_3$ by Crolet *et al* [88], especially in systems where initial ferrite dissolution, revealing of cementite and hence uniform corrosion precedes $FeCO_3$ formation in an unbuffered system. Therefore any changes in environmental parameters that are capable of promoting the rate of supersaturation increase of the interface solution for the formation of an amorphous or non-protective form of $FeCO_3$ is also likely to promote the pit propagation process as depicted in Figure 11-10. It is important to note that is in sharp contrast to the mechanism by which pit propagation is sustained in passive alloys like stainless steel. In stainless steels pit propagation is sustained via a self-sustaining or autocatalytic localised electrochemical process once a large potential difference is established between passive oxide covered cathodes and localised anodes (initiated pits). The autocatalytic process of pit propagation is often driven by aggressive anions such as chloride ions [65] acting to reduce the local pH to prevent the re-passivation of pits [68, 69] and leading to stable pit propagation. Therefore, unlike in carbon steels, the formation of a passive-oxide layer in stainless steels eliminates the process of ferrite dissolution such that the role of environmental parameters is correlated to the electrochemical processes within the local environment undergoing pit propagation.

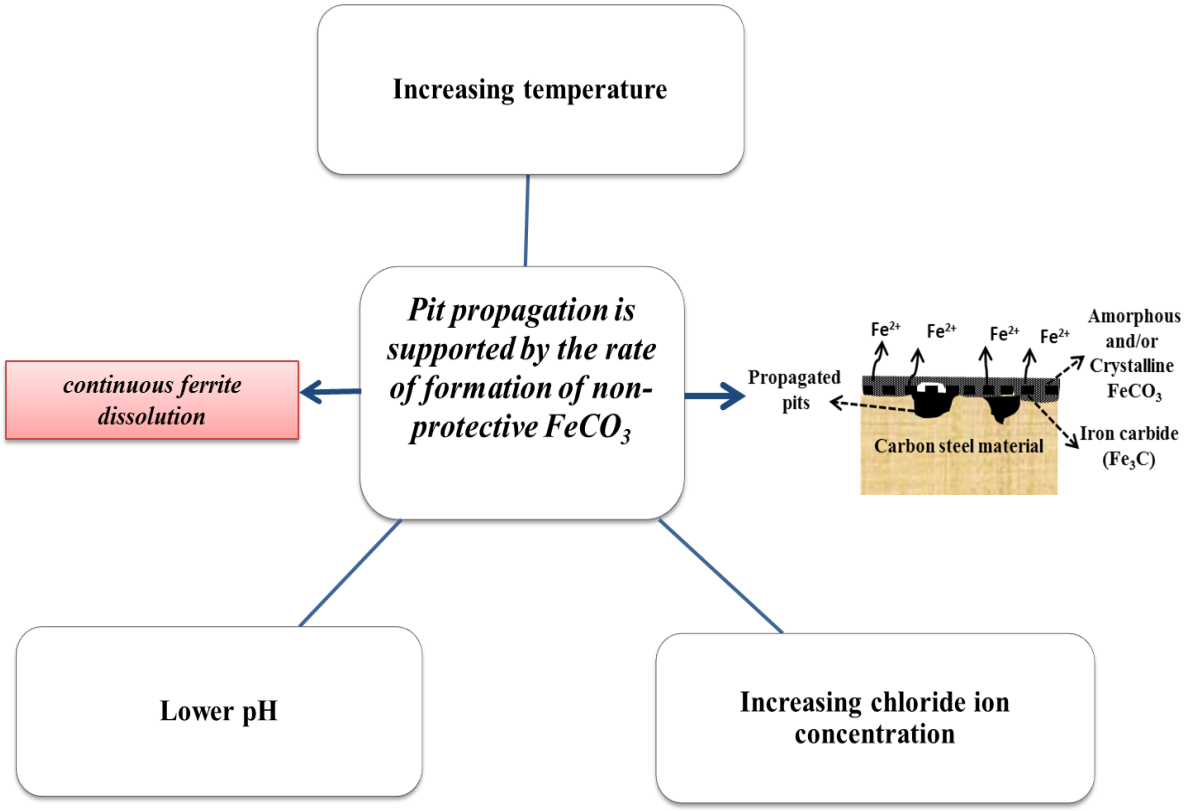

Figure 11-10 Schematic representation of the likely changes in environmental parameters that promotes pit propagation of carbon steel in an unbuffered CO_2 saturated environments.

Referring to Figure 11-10, it is therefore expected (and as shown in Chapter 6) that increasing temperature, increasing chloride ion concentration and decreasing pH promotes the process of pit propagation through the formation of a corrosion product layer dominated by an 'amorphous' $FeCO_3$. As shown in Figure 11-11, the pit depth after 168 hours increases with increase in temperature from 30 to 50°C for all chloride ion concentration. This is consistent with increase uniform corrosion rate and hence rate of formation of non-protective (amorphous $FeCO_3$). The lower rate of initial corrosion and formation of the non-protective $FeCO_3$ implies that pit propagates slower at 30°C than at 50°C. The trend; both in terms of the evolution of corrosion products and a linear pit depth profile was observed to be the same at all chloride ion concentration at 30 and 50°C. Once the temperature is increased to 80°C, the pit depth is masked significantly by the higher uniform corrosion at this temperature such that it records a lower pit depth after 168 hours than at 50°C.

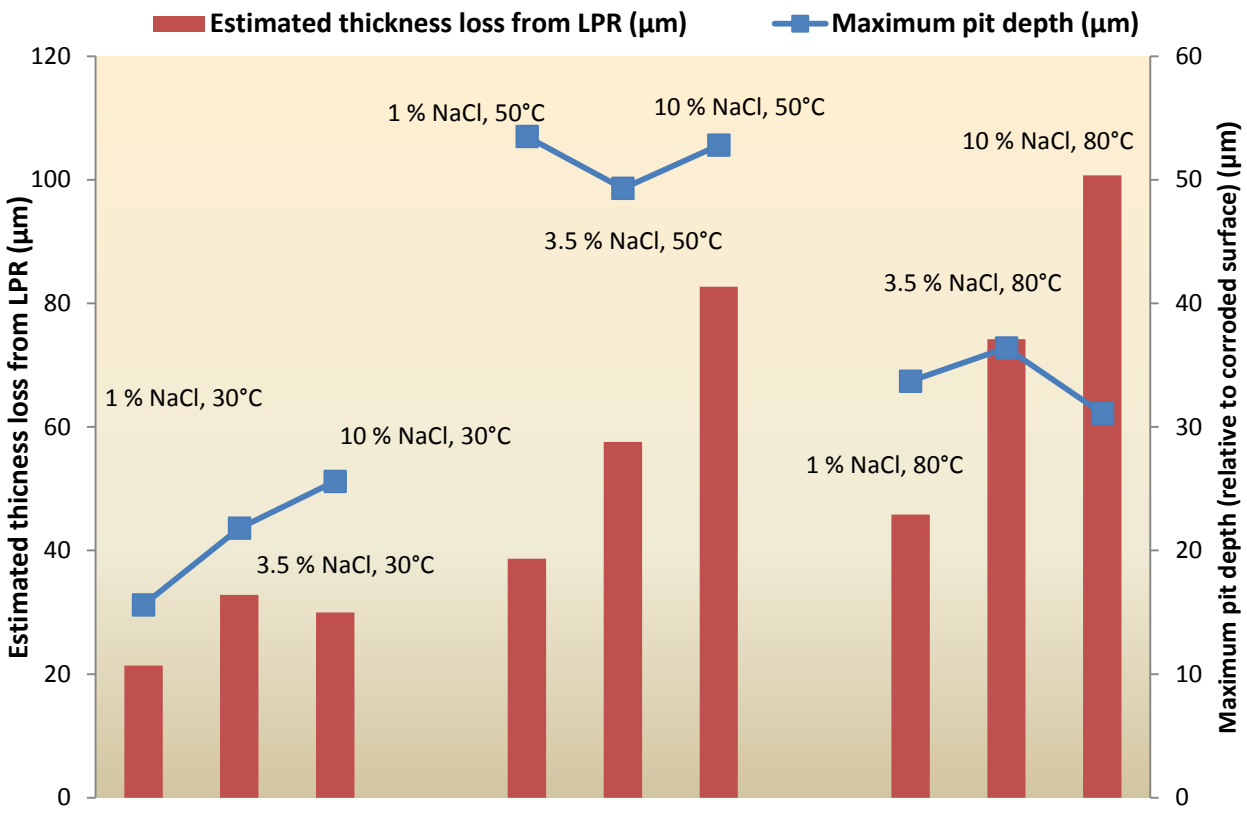

Figure 11-11 Schematic summary of relationship between estimated thickness loss due to uniform corrosion and depth of deepest initiated pit (relative to corroded surface) as a function of environmental parameters in unbuffered CO_2-saturated corrosion systems after 168 hours.

Referring to Figure 11-12, the aspect ratio; defined as the ratio of the diameter of the deepest pit on an entire surface (Dia.max.) and the depth of deepest pit (dmax) in Eq. 11.3 reflects highlights the role of uniform corrosion in the pitting corrosion process discussed in the paragraph above.

$$\text{Aspect ratio} = \frac{Dia_{max.}}{d_{max}} \qquad 11.3$$

The aspect ratio is higher with increasing temperature, suggesting higher uniform corrosion and broad diameter micro-pits. Once corrosion product is established onto the steel surface and pit growth is sustained, the aspect ratio reduces. It reduces quickly at 80°C because the higher temperature promotes the formation of $FeCO_3$ corrosion product quicker than at lower temperatures to support pit growth. Pit growth is. On the one hand, the constant aspect ratio at 30 and 50°C is a confirmation of linear pit growth profile presented in Figure 11-12(a) and (b). This also indicates that as the pit is growing, the pit diameter is also increasing due to the continuous uniform corrosion taking place. On the other hand, the aspect ratio for 80°C shown in Figure 11-12(c) reaches a minimum after 72 hours before increasing up to 168 hours to

confirm the masking effect from uniform corrosion, as well as the indication of continuous electrochemical activities within a pit in carbon steel components. After 168 hours, the cumulative effect of continuous ferrite dissolution also becomes dominant especially with the process leading to the formation of corrosion products. This process is masks the true extent of pit penetration as well as the promoting the precipitation of corrosion products within active pits to reduce the pit depth relative to corroded surface. It is important to note that the masking effect at 80°C is only a component of the contributing phenomena leading to a lower pit depth relative to corroded surface.

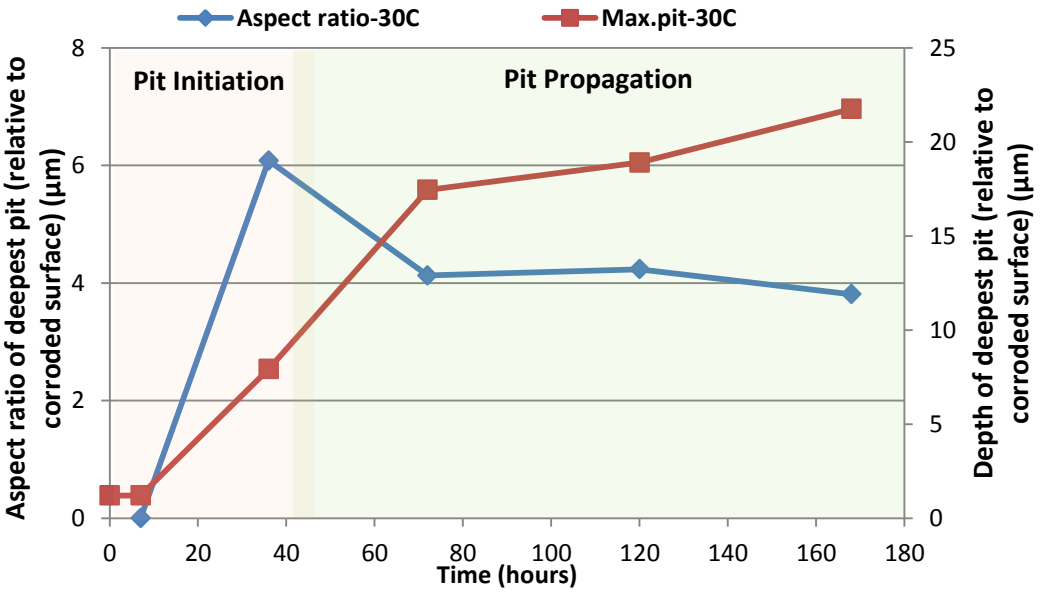

(a)

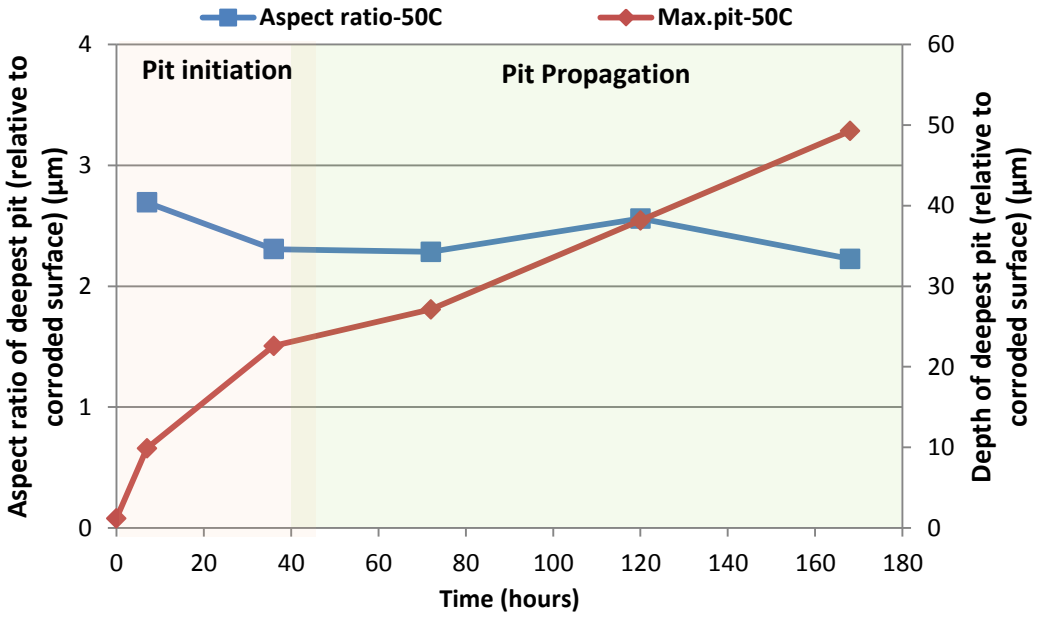

(b)

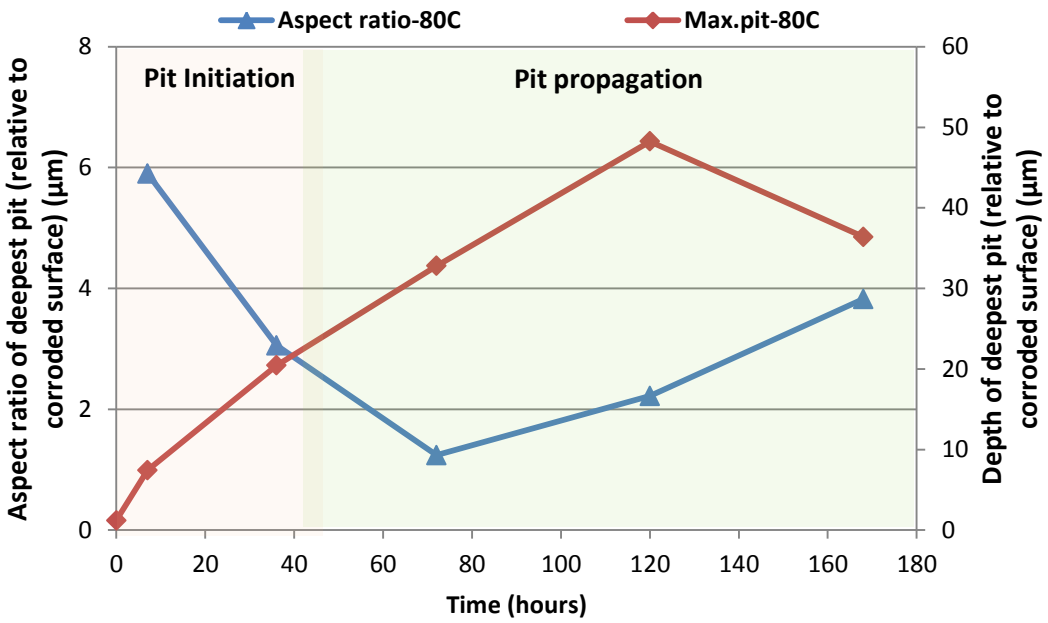

(c)

Figure 11-12 Aspect ratio of deepest pit (relative to corroded surface) of X65 carbon steel exposed to an unbuffered 3.5 wt.% NaCl solution saturated with CO_2 gas at (a) 30 °C (b) 50°C and (c) 80°C for a duration of 168 hours.

Pit self-healing mechanism is a second contributing phenomenon to the lower pit depth after 168 hours at 80°C than at 50°C as shown in Figure 11-11 and Figure 11-12. The pit self-healing mechanism at higher temperature along with the cumulative effect of continuous uniform corrosion rate are the two combining phenomena that are responsible for lower pit depth but not lower metal penetration. The porous and non-protective nature of corrosion products formed in these conditions could be a very important factor in the manifestation of the pit-self-healing process, especially as it allows for electro-migration of precipitable and/reducible anions such HCO_3^- and/or CO_3^{2-} as suggested by Crolet *et al* [88]. The implication of this process is the possibility of either of continuous ferrite dissolution to which the walls of the pits are less likely to be shielded from or the build-up of corrosion products within initially active pits. Both of these electrochemical processes remains valid and has been shown to be occurring simultaneously albeit to varying degrees to induce the retardion of pit propagation at 80°C.

The ***pit self-healing processes*** mentioned above have been summarised in Figure 11-13. Analysis to prove the self-healing mechanism have been described in sections 6.6.5 based on extensive FIB/TEM-EDX analysis to confirm the presence of non-crystalline form of $FeCO_3$ within confine spaces in a porous corrosion product layer at the steel end of the corrosion

product boundary layer. This confirms the concept of electro-migration of active ions into localised pits and also asks an important questions as to the actual distribution of both anodic and cathodic sites across the depth profile of active pits that has enabled continuous electrochemical activities that could lead to either more localised ferrite dissolution and/or the formation of corrosion products in such confine spaces. If it were to be a passive material like stainless steel, the localised environment is expected to be at a lower pH than the bulk solution at all times and pit propagation will continue unhindered. Providing answers to this question will certainly require more research effort.

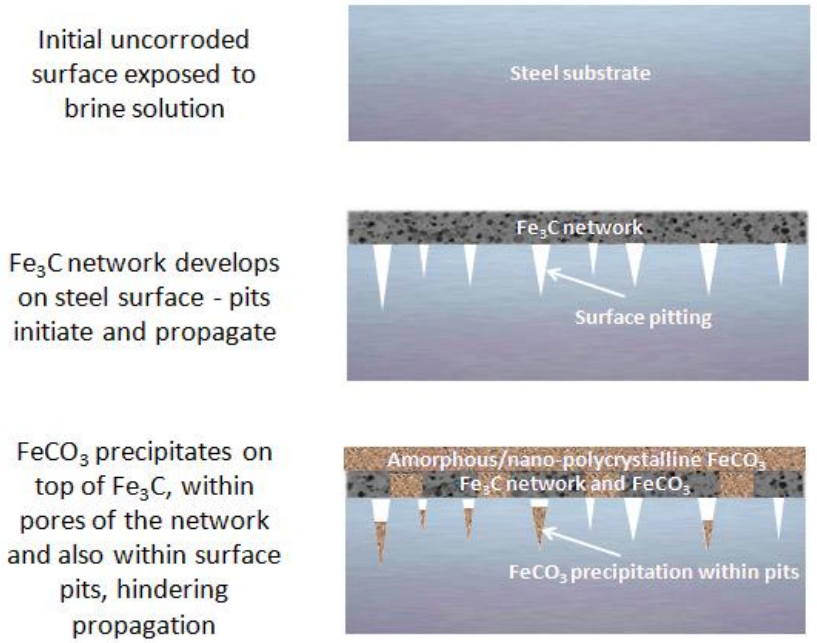

Figure 11-13 Schematic of the self-healing mechanism of pits proposed for experiments conducted at 80°C in a 10wt.% NaCl solutaion saturated with CO_2 gas.

Just as previously established in section 11.2.1 and as depicted in Figure 11-10, the effect of chloride ion concentration on the pitting corrosion of carbon steel is correlated to the aggressivity of the corrosion environment and how it supports the supersaturation of the bulk solution for the formation of $FeCO_3$ and supports pit growth. There was also no evidence in this study to suggest that an increase in chloride ion concentration could hinder the formation of a protective $FeCO_3$, promote acidification and the initiation of pitting corrosion as often suggested in the literature [107] based on corrosion scenarios where protective $FeCO_3$ is formed at the start of experiments before increasing the chloride ion concentration. This is also in contrast to the effect of chloride ions on pit propagation in passive alloys; in which case chloride ions supports and drive the self-sustaining process of pit propagation [106]. The trend in the pit depth profile observed in this study as influenced by chloride ion concentration is such that at

all temperatures (any constant temperature), the variation of chloride ion concentration with pit depth is different. This is fundamentally due to the change in the most dominant electrochemical process with changing temperature as well as the synergistic effect of chloride ions and temperature.

The pit depth after 168 hours increases with increase in chloride ion concentration at 30°C due to the increase in the aggressiveness of the corrosion environment with increasing chloride ion. Increasing chloride ion has a secondary effect of promoting the rate of ferrous ion availability and supersaturation of bulk solution for the formation of an 'amorphous' form of $FeCO_3$. As depicted in Figure 11-10 supported by Figure 11-11, this trend is capable of supporting pit propagation process. Similar trend is also expected at 50°C with change in chloride ion concentration between 1, 3.5 and 10wt.% NaCl. However the pit depth across the three chloride ion concentration is almost constant. This is because with increase in chloride ion concentration, the solution becomes increasingly aggressive such that uniform corrosion becomes more dominant as a material loss mechanism as shown in Figure 11-11. This is clear evidence of the synergistic effect of chloride ion concentration and temperature.

At 80°C, a similar trend (of almost equal pit depth with change in chloride ion concentration) to test at 50°C is observed between test in 1 and 3.5 wt.% NaCl solution. However, for test in 10 wt. % NaCl solution, the pit depth is lower than for test solution in 1 and 3.5 wt.% NaCl solutions. The masking effect of uniform corrosion on the pitting corrosion process is expected to be more dominant at this temperature range, especially as the uniform corrosion contribution to thickness loss is higher for 10 wt.% NaCl than for 1 and 3.5 wt.% NaCl solutions. It has been shown that in Figure 7-20 that the pit self-healing process also occurs faster (after 72 hours) for test in 10 wt. % NaCl solution than in 1 and 3.5 wt.% NaCl solutions (occurring after 120 hours). This also emphasises the synergy between chloride ion concentration and temperature. A higher temperature and chloride ion levels will promote supersaturation and formation $FeCO_3$ corrosion products (as shown in Figure 11-2), as well as supersaturating initially active pits with Fe^{2+} and CO_3^{2-} for the formation of $FeCO_3$ and induction of the pit self-healing process.

The abovementioned effect of the synergy of increasing temperature and increasing chloride ion concentrating on pit propagation of carbon steel in CO_2-satuared environment is also in sharp contrast the effect of this synergy on the pit propagation process in stainless steels in terms of the driving force behind pit propagation and the significance of the uniform corrosion contribution. In stainless steels, the autocatalytic and self-sustaining process of localised acidification and pit propagation is driven by chloride ions according to the reactions;

$$Fe^{2+}_{(aq)} + 2Cl^{-}_{(aq)} \rightarrow Fe(Cl)_{2(aq)} \quad 2.24$$

$$Fe(Cl)_{2\,(aq)} + 2H_2O_{(aq)} \rightarrow Fe(OH)_{2(aq)} + 2HCl_{(aq)} \quad 2.25$$

According to Anselmo *et al* [106], increasing temperature also reduces the pitting potential and increases the risk of pitting. This implies that a synergy of increasing temperature and chloride ion concentration would promote pit propagation with minimum uniform corrosion contribution. Pit propagation in this case will be more devastating as the local environment is more aggressive and supported by a large cathodic area. Therefore the pitting factor for stainless steels (P_{f-SS}) is proposed to be $\gg$ than the pitting factor for carbon steels(P_{f-CS}). The pitting factor comparison is based on the estimated pitting for carbon steels from this study and the general understanding that the uniform corrosion contribution in stainless steels is expected to be very insignificant.

Pit propagation of carbon steel materials has also been shown to vary with bulk solution pH, manifesting in different pit propagation pathways. The distinct pit propagation profiles also correlate well to the evolution of three different types of corrosion product already discussed in section 11.2.1. Referring to Figure 8-9 (a) and (b), the pit growth process continues linearly at pH of 3.8 (unbuffered), because of the non-protective nature of the 'amorphous' $FeCO_3$ corrosion products while substantial uniform corrosion is still occurring. However, at a higher pH value of 6.6, pit propagation is driven by the local galvanic cell between crystalline $FeCO_3$ covered areas (as the cathode) and locally exposed areas (as the anodes) of the steel surface as a result of attainment of substantial coverage of the corroding surface with a crystalline form of $FeCO_3$ [164]. This effect is shown in Figure 8-9 (a) to occur after 72 hours. With increase coverage by crystalline $FeCO_3$, the cathodic area becomes significantly larger than the localised anodic sites; a scenario that could help to drive pit propagation as shown in Figure 8-9 (c).

At this pH level, thickness loss due to uniform corrosion is also significantly suppressed by the extent of protection from the corrosion product layer as shown in Figure 11-14 after 168 hours. The pitting corrosion scenario at pH value of 6.6 is consistent with the definition of pitting corrosion of carbon steel in scenarios where a protective $FeCO_3$ has been formed by Papavinasam *et al* [38]. The only difference in this case is that no external mechanical or chemical process was required to initiate the pitting corrosion process. Figure 8-9 (c) and (d) also show a trend that supports the potential retardation of pit growth, which can be attributed to the formation of corrosion product across initially active pits. Similar observations have also been reported at 80°C by Han *et al* [164]. This implies that by increasing the pH of an

unbuffered corrosion system starting at a pH of 3.8 to a pH of 6.6, the corrosion rate is significantly reduced, leading to a different pitting corrosion pathway on the surface.

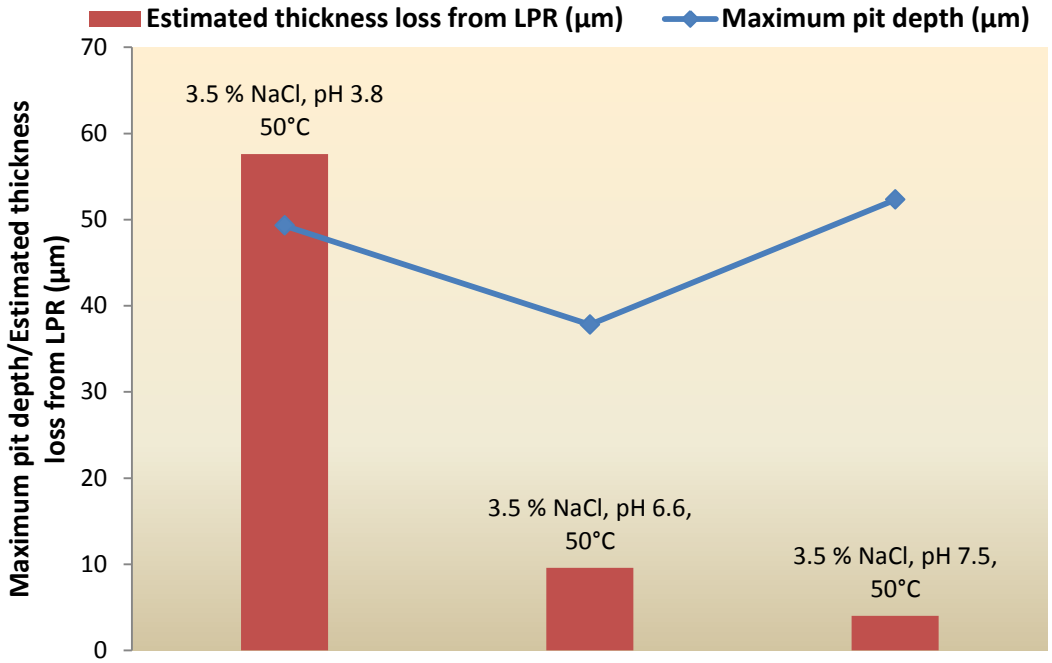

Figure 11-14 Schematic summary of relationship between estimated thickness loss due to uniform corrosion and depth of deepest propagated pit (relative to corroded surface) as a function of bulk solution pH in CO_2-saturated corrosion systems after 168 hours.

Once the pH of the corrosion environment is increased to 7.5, pit propagation after pseudo-passivation is achieved is slow. While the pit morphology after 168 hours is also almost similar to pit morphologies that are characteristics of pitting in stainless steels, the pit growth rate after pseudo-passivation is lower than that recorded at pH 3.8. However, uniform corrosion is significantly suppressed to $\leq$ 0.01 mm/yr after just 20 hours due to the rapid pseudo-passivation process. Just as in the case of pitting in stainless steels, the pit propagation process may also be supported by a large pseudo-passivating corrosion product layer acting as a cathode like a typical passive oxide layer would. The evidence of this scenario is shown by the large area of the corroded surface surrounding the localised pit (see Figure 8-12(c) and (d)) with minimum uniform corrosion. This area was covered by the $FeCO_3$ corrosion product. However, the potential difference obtainable from a passive oxide layer is expected to be far greater than that achieved from the pseudo-passivation effect on carbon steel at pH of 7.5, hence the lower pit growth rate after pseudo-passivation. On the other hand, it is also likely that the pits itself has both anodic and cathodic sites such that the propagation rates may be dependent on the distribution of these sites across the depth profile of the pits. The morphology of pits recorded at

this pH level after 168 hours were also well defined with a narrow base shown in Figure 8-12 (c) and (d).

11.3.1.1 Pit propagation; pseudo-passivation and the bulk pH effect

By considering the change in total penetration depth (the sum of pit depth relative to corroded surface and thickness loss due to uniform corrosion) between each measurement along with the time interval between the removal of each sample, it is possible to determine the total pit penetration or metal penetration rate as a function of time within the 168 hour exposure time. This information has been extracted from Figure 8-10 and the pit penetration rate as a function of time is provided in Figure 11-15 in conjunction with the open circuit measurements for test at pH 7.5 also as a function of time. The results confirm the previous statement that pit growth is exceptionally high (in excess of 10 mm/year) during and in the immediate aftermath of the pseudo-passivation process, but after passivation is complete and the potential stabilises, the pit growth rate is reduced dramatically to below ≈ 0.06 mm/year.

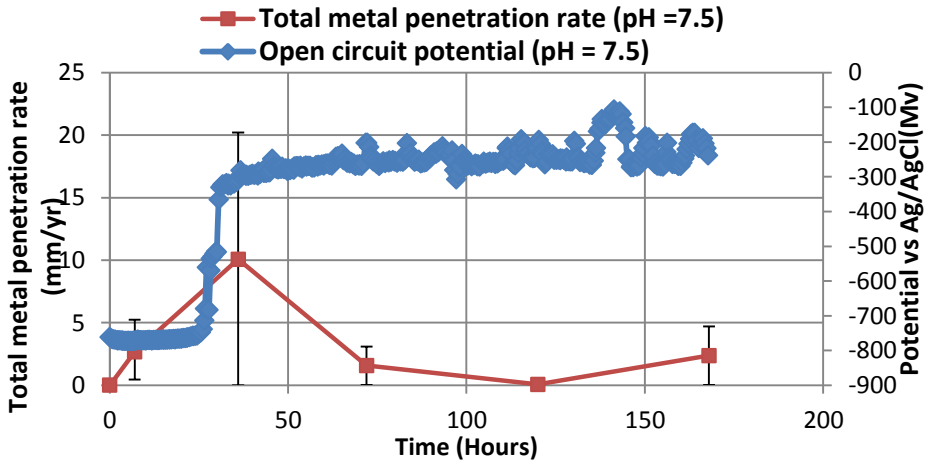

Figure 11-15 Total metal penetration rate and open circuit potential for X65 steel at pH 7.5 as a function of time.

From the forgoing discussions on the effect of pH on pitting corrosion of carbon steel, it is therefore improtant to afford consideration to the uniform corrosion rate of the surrounding area when reviewing the susceptibility of the carbon steel to pitting corrosion when the general corrosion rate is appreciable and vice versa. These have been shown to be an important aspects of corrosion prediction and mitigation as it applies to the infleunce of environmental parameters; temperature, CO_2 partial pressure, chloride ion concentration and *in-situ* pH. For tests performed at pH 6.6 and 7.5, the growth of the pit is not significantly masked by the general corrosion rate and thus shows that increasing solution pH may not necessarily reduce the risk of pitting of carbon steel pipelines.

In order to emphasis the importance of this approach, Figure 11-16 presents a comparison between corrosion rate and maximum pit depth from experiments in this work at pH of 3.8 and 6.6 with that predicted using the NORSOK standard M-506 model. The NORSOK standard M-506 model is known as one of the open source models with significant sensitivity to pH [186]. For the application of the model in the case of experiments at pH 3.8 (unbufferd), the average pH for the whole duration of the test was used and was estimated as ≈ 4.8. The results in Figure 11-16 shows that the NORSOK standard M-506 model predicted almost similar thickness loss due to uniform corrosion at starting pH values of 3.8 and 6.6 to estimated thickness loss from experiments. The results in Figure 11-16 thus confirm that (in comparison to the pitting and uniform corrosion data provided in Figure 8-10) while the NORSOK standard M-506 model may not have been developed to predict pitting corrosion, prediction of thickness loss of pipeline steels based on this model in conditions where pitting is likely to occur may be underestimated especially at higher pH values given the strong sensitivity of this model to pH.

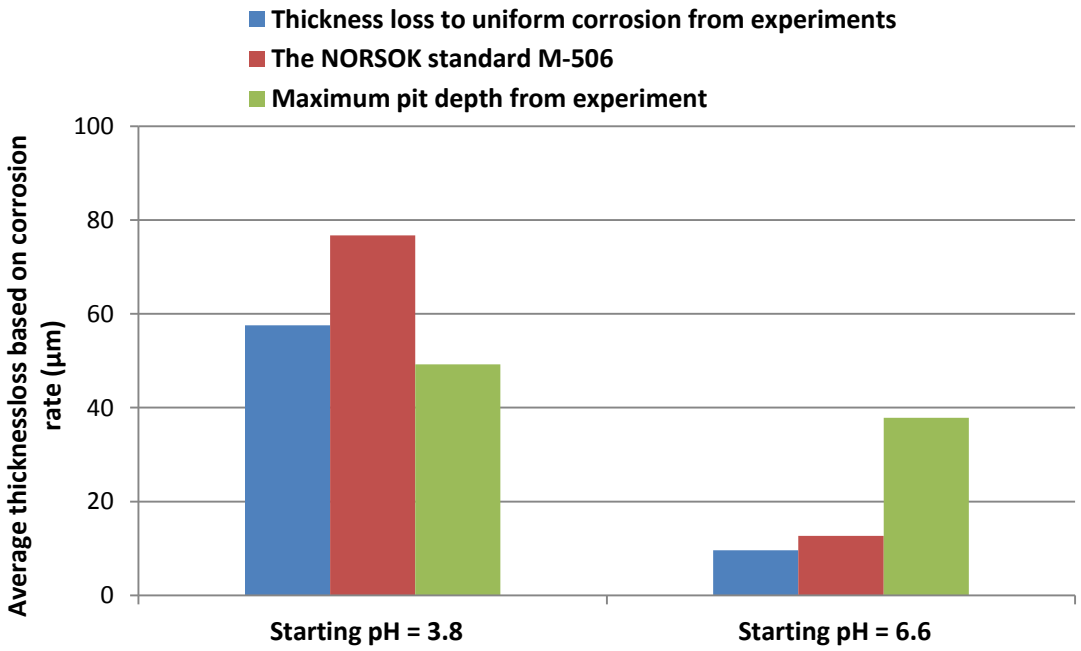

Figure 11-16 Comparison between the thickness loss due to unform corrosion and maximum pit depth from experiments and those predicted using the NORSOK standard M-506 model.

11.3.2 Pitting corrosion of carbon steel in sour corrosion environments

The process of pitting corrosion of carbon steel in H_2S-containing corrosion systems has been established in Chapter 7 of this thesis. In this section, pit initiation and propagation is discussed with reference to pit initiation and propagation in CO_2-saturated corrosion environment. The complex corrosion kinetics that have been shown to characterise both the early and later stage

of corrosion of carbon steels in H_2S-containing corrosion environments may also be influencing the pitting corrosion behaviour; pit initiation and propagation. Ferrite dissolution and FeS (mackinawite) formation from a direct reduction reaction has already been shown in section 11.2.2 to dominate the early stages of sour corrosion, while the process of dissolution and/or transformation of initially FeS (mackinawite) became more influential at the later stages. These processes are also likely to influence the different stages of the pitting process depending on other environmental parameters

11.3.2.1 Pit initiation

As already stated in earlier sections of this Chapter, initial ferrite dissolution is occurring at the same time as FeS formation from solid-state reactions in the early stages of sour corrosion. Both phenomena have been shown in this study and discussed in section 11.2.2 to be influenced by the presence of and/or absence of CO_2 and H_2S gas as well as temperature. Ferrite dissolution process leads to the evolution of Fe_3C to induce some non-uniformity in the coverage of initially formed FeS corrosion products. The Fe_3C rich regions left behind after initial ferrite dissolution usually becomes the preferred sites for the precipitation of FeS corrosion products, having a lower over-potential for cathodic reactions to occur [9, 88]. These FeS covered regions surround small local anodes. The fast process of formation of FeS as shown in Figure 9-15(a) corroborates the assertion of non-uniform coverage of initially formed FeS corrosion products. This scenario is more likely to induce a local galvanic cell at various points across the surface of the steel exposed to sour corrosion environments than in the CO_2-saturated corrosion systems. The cathodic reaction in the galvanic couple is supported by the conductive nature of FeS (mackinawite) corrosion products [24, 132] to promote the oxidation of complexed intermediate species ($(FeHS)^+_{ad}$) drive ferrite dissolution. With the electro-conductive nature of FeS corrosion products, the cathodic process can occur on the film surface without any restriction by diffusion [36]. This is the envisaged precursor to pit initiation from this study and is also almost similar to the local galvanic set-up around initiated pits in stainless steels.

The aforementioned electrochemical processes are collectively considered the main driving force behind the initiation of pits and/or micropits as shown in Figure 9-20 (a), (b) and (c) for tests in H_2S-CO_2-containing corrosion system at 30, 50 and 80°C respectively. Thus, the depth of recorded initiated pits and/or micropits was higher in H_2S-containing corrosion systems than in CO_2-saturated corrosion systems to corroborate the role of the faster rate of initial formation of mackinawite (FeS) corrosion product layer in sour corrosion systems. The effect of cathodic reactions occurring at the FeS layer is the undermining of local ferrite-rich pores underneath

some of the FeS layers. Mackinawite (FeS) formation and breakdown has also been reported to coincide with evidence of localise corrosion [138] to confirm the observed trend in the initial stages of pitting corrosion from this study. A schematic summary of the stages of pit initiation process in H_2S-containing corrosion systems is shown in Figure 11-17. Referring to Figure 9-19(a) and (b), increasing the temperature from 30 to 50°C increases the depth of initiated pits (relative to corroded surface) because of the effect of increasing temperature on the kinetics of FeS formation via solid state reactions to induce the necessary local galvanic cells that helps drive pit initiation. However, with an increase in the temperature of the corroding surface to 80°C, the depth of initiated pit is reduced due to the competition between ferrite dissolution and FeS formation such that the depth of initiated pit is masked.

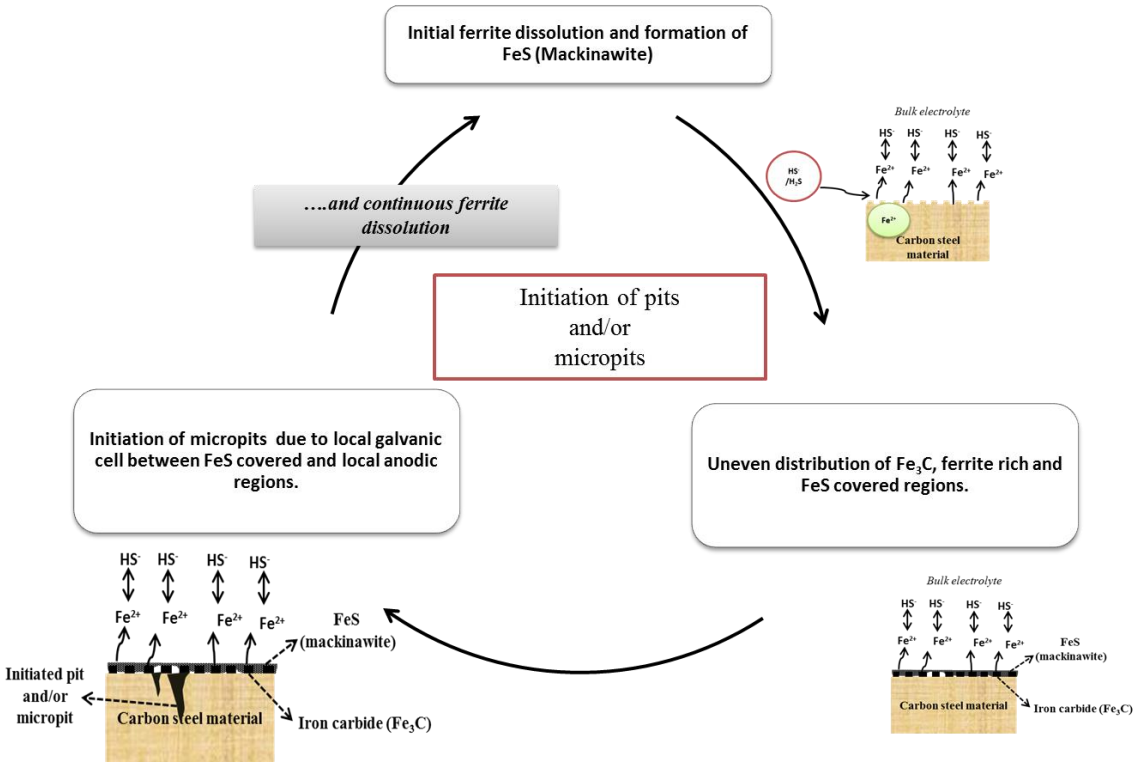

Figure 11-17 Schematic representation of the likely stages of pit initiation of carbon steel in an unbuffered H_2S-containing corrosion system.

One other key observation from this study is the synergy between the presence of CO_2 gas in H_2S-containing corrosion systems and temperature. It is already been established in this study that CO_2-saturated corrosion systems are more aggressive than H_2S-containing corrosion systems in terms of the uniform corrosion component of material loss. The aggressiveness of CO_2-saturated corrosion environments manifests mainly in the form of uniform corrosion due to

the high initial ferrite dissolution that usually precedes $FeCO_3$ formation. Thus, in CO_2-containing sour corrosion environments, the CO_2 corrosion component of the electrochemical process is manifested more in terms of continuous ferrite dissolution in the initial stages and in combination with elevated temperature, increases the contribution of uniform corrosion to metal penetration. A summary to show the effect of the synergy between the presence of and/or absence of CO_2 and/or H_2S gas and temperature on the relationship between pit depth and thickness loss to uniform corrosion is provided in Figure 11-18.

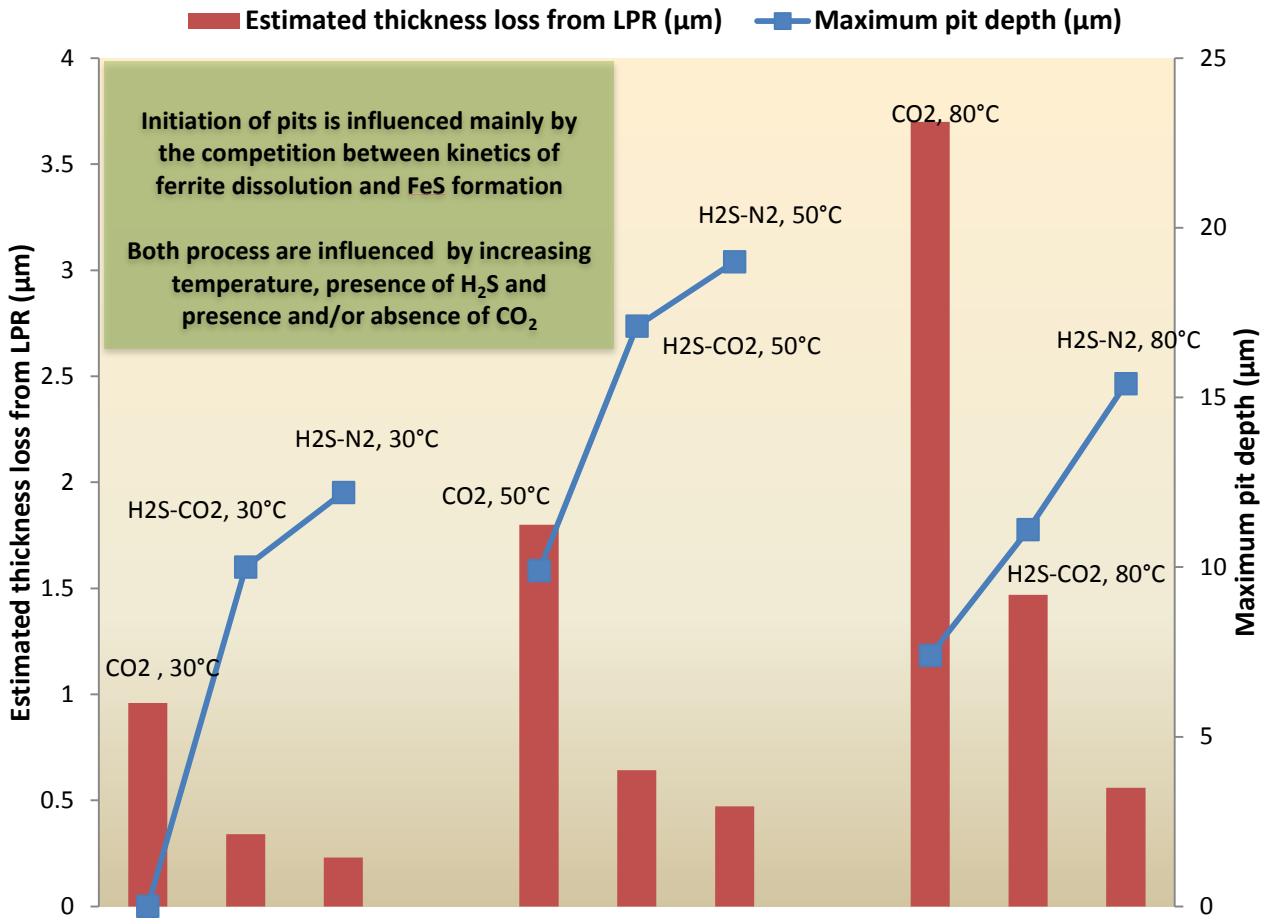

Figure 11-18 Schematic summary of relationship between estimated thickness loss due to uniform corrosion and depth of deepest initiated pit (relative to corroded surface) as a function of environmental parameters in H_2S-containing corrosion systems after 7 hours.

Referring to Figure 11-18, for all conditions, uniform corrosion contribution to metal loss is inversely proportional to (at varying degrees) to the depth of initiated pits (relative to corroded surface). The key inference from this trend is that as the temperature increases, the rate of FeS formation is promoted as well as the rate of ferrite dissolution. However, by increasing the temperature (from 50 to 80°C), the surface recedes further due to the continuous ferrite dissolution, thereby masking the true extent of metal penetration. Figure 11-18 also shows

clearly that the contribution of ferrite dissolution is increased with CO_2 content in the gas phase, such that a clear synergy is seen to exist between CO_2 presence and temperature in the early stages of pitting corrosion of carbon steels in H_2S-containing corrosion systems. The effect of competition between ferrite dissolution and FeS formation on pitting corrosion process is likely to become complex beyond 7 hours, especially with the prospect of precipitation of different forms of corrosion products from bulk solution with time as already discussed in section 11.2.2.

11.3.2.2 Pit propagation

Based on the established complexities associated with overall corrosion behaviour of carbon steel in H_2S-containing corrosion systems in section 11.2.2, it is also likely for such complexities to be transferred into a long term impact on the pitting corrosion of carbon steels in these environments. Experiments conducted as part of this study over a period of 168 hours in H_2S-containing conditions offers a time dependent electrochemical response that could either corroborate or provide novel dimensions to the long term localised corrosion impact as influenced by the process parameters under investigation in this study. Based on the established science of pitting corrosion in passive materials, it is often expected that pit depth would be higher after 168 hours for all the conditions under investigation in the study. However, from the results presented in Figure 10-20(a) and (b), pit depth was highest in H_2S-CO_2-containing system than in CO_2-only and H_2S-N_2-containing systems at all temperatures. Advanced post-experimental analysis was able to show that the mechanisms behind these variations in pit depth relative to corroded surface revolves around three main phenomena; the rate of ferrite dissolution and precipitation of FeS from the bulk solution, the process of dissolution and/or transformation of initially formed FeS and competitive precipitation between FeS and $FeCO_3$ (when the conditions are favourable). These phenomena dominate the pit propagation process to varying degrees at different temperatures and gas phase composition and is summarised in Figure 11-19.

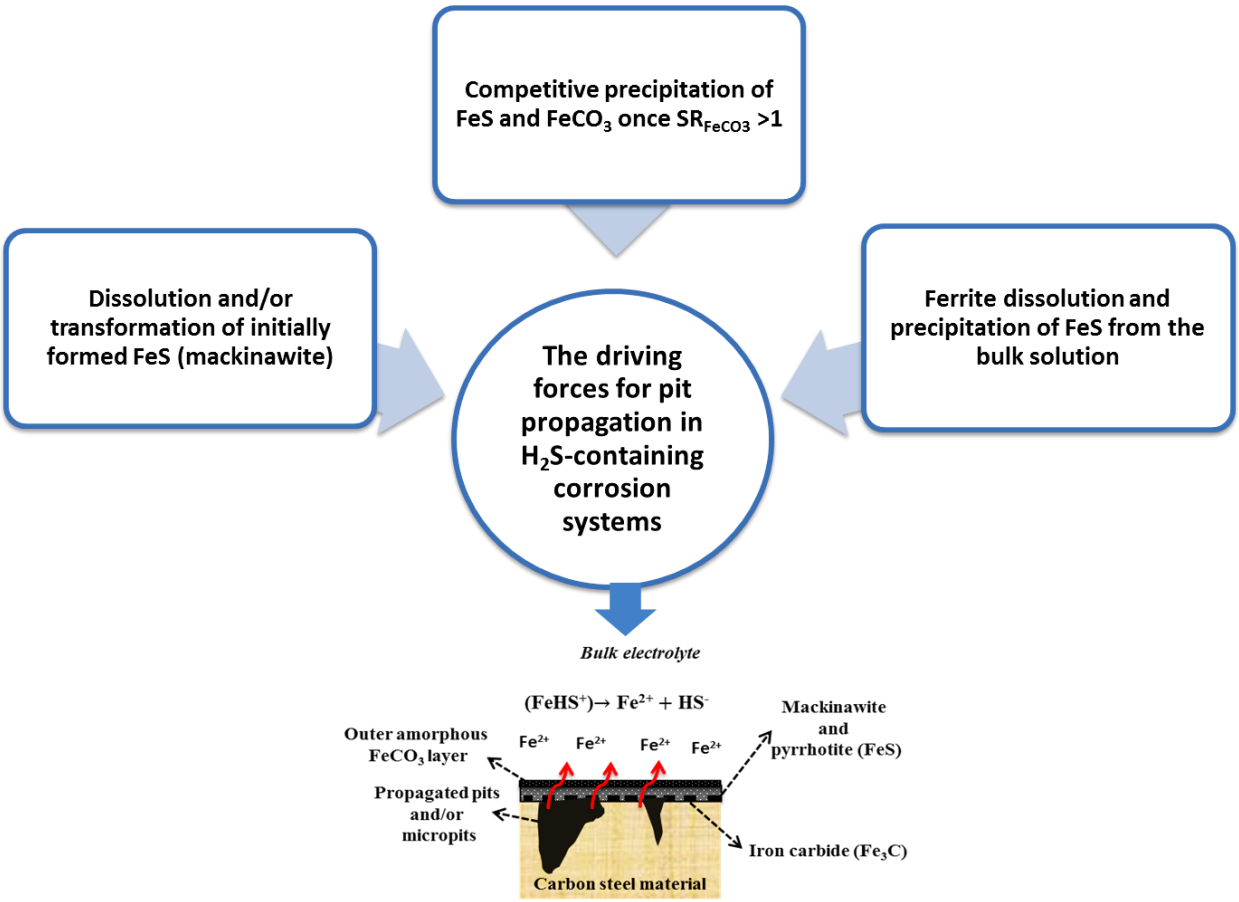

Figure 11-19 Schematic representation of the contributing phenomena to the process of pit propagation on carbon steel exposed to H_2S-containing corrosion systems across different ranges of environmental parameters.

Based the role of FeS on the process of pit initiation, it could also be envisaged that with increasing build-up of FeS corrosion products on the steel surface, the local galvanic cells to drive pit propagation is significantly enhanced. On this premise, it becomes easy to appreciate the reason why the depth of the deepest pit (relative to corroded surface) on the steel surface is higher in H_2S-CO_2 gas system than in H_2S-N_2 gas systems. As already established in previous sections, the presence of CO_2 gas promotes the availability of ferrous ions via ferrite dissolution for the precipitation of FeS from the bulk solution. This enhances the build-up of FeS more in H_2S-CO_2 gas system than in H_2S-N_2 gas systems (albeit with more local deformity) to support the galvanic couple that drives pit propagation. This is one aspect of the pit propagation process that is responsible for higher depth of pits in H_2S-CO_2 gas system than in H_2S-N_2 gas systems for all temperatures after 168 hours as shown in Figure 10-20(a) and (b). However, as the temperature changes, the pit propagation process becomes more complex as the other factors (shown in Figure 11-19) become more dominant.

At 30°C the kinetics of sour corrosion remained almost constant in both H_2S-containing systems to corroborate initial assertions that perhaps the initially formed mackinawite layer had remained intact and only increased in volume to sustain a marginal increase in pit depth over 168 hours especially in the presence of CO_2. In the H_2S-N_2-containing systems the kinetics of FeS precipitation especially from the bulk solution is minimised due to lower rate of ferrite dissolution while in the H_2S-CO_2-containing systems there is probably just enough FeS precipitated from the bulk to induce local galvanic cells and support a steady pit growth (see SEM images provided in Figure 10-3 (b) and (c)). As the temperature increases, the role of CO_2 gas in the gas phase becomes more influential, especially in terms of supersaturating the bulk solution towards precipitating FeS and $FeCO_3$ corrosion products. Just as this process is occurring, so too is the process of dissolution and/or transformation of initially formed mackinawite FeS to other morphology of mackinawite and forms of FeS [128, 138, 175] along with an extensive build- up of FeS. With build-up of FeS corrosion product, the pit propagation process is expected to be sustained due to the galvanic effect of FeS layer.

However, at 50°C, the process of dissolution and/or transformation of initially formed mackinawite FeS are shown in Chapter 7 to completely dominate the corrosion processes for a significant period of the tests such that the pit depth relative to corroded surface is also masked while pit propagation is also being hindered. In H_2S-CO_2-containing systems, the pit depth increased marginally from ≈17 μm after 7 hours to ≈ 24 μm 168 hours, while there were no pits on the steel surface after 168 hours in H_2S-N_2-containing systems at 50°C. This suggests that the mackinawite dissolution may have been more influential in H_2S-N_2-containing systems than in H_2S-CO_2-containing systems at this temperature. It is important to emphasise here that the dissolution of initially formed mackinawite has been shown in section 11.2.2 to correlate to higher ferrite dissolution rate and hence a higher thickness loss due to uniform corrosion in H_2S-CO_2-conataining system than in H_2S-N_2-containing systems as shown in Figure 11-20. However, the kinetics of FeS transformation and/or represipitation from the bulk solution is also expected to be higher in H_2S-CO_2-conataining system than in H_2S-N_2-containing systems. There was also evidence of pyrrhotite as part of the corrosion product after 168 hours at 50°C to support the assertion on dissolution and/or transformation of initially formed FeS film. The dominance of the dissolution process as well as the impact on pit propagation as the temperature increases is also seen in this study as the effect of a synergy between temperature and the presence of CO_2.

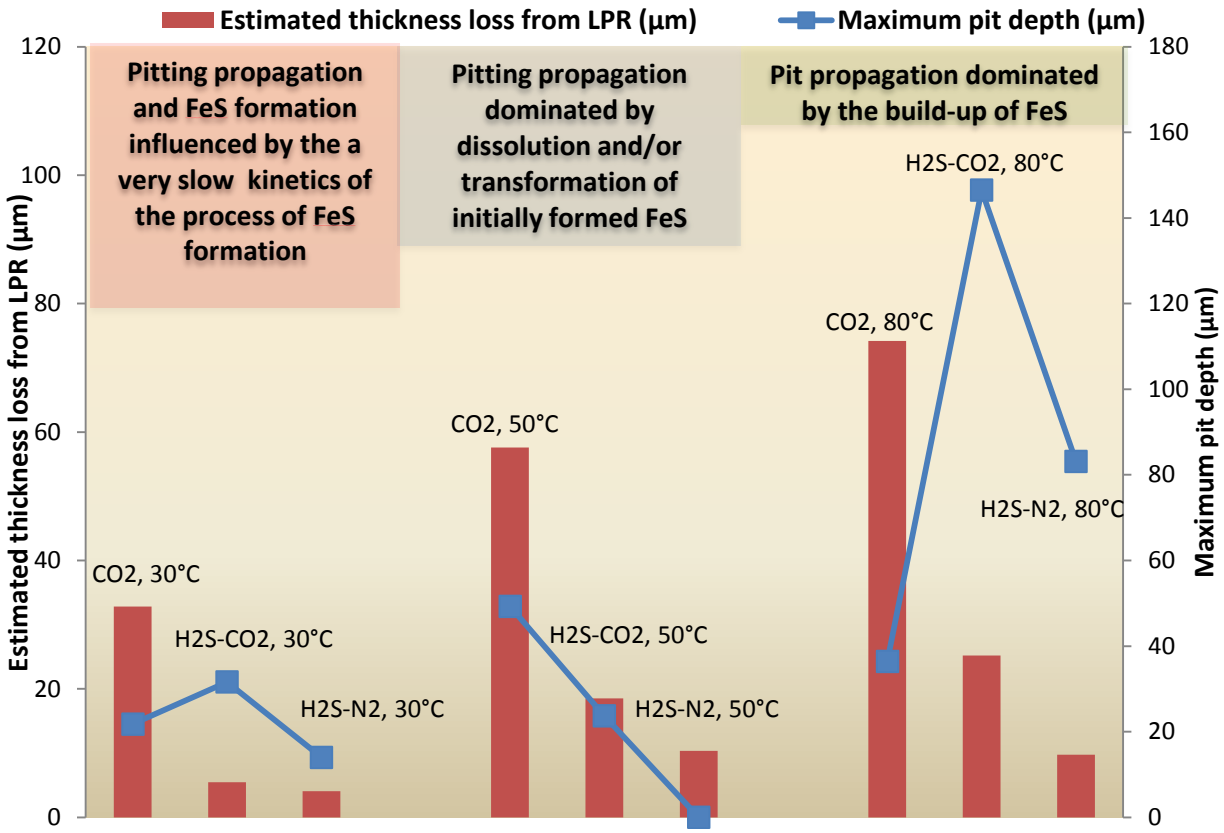

Figure 11-20 Schematic summary of relationship between estimated thickness loss due to uniform corrosion and depth of deepest propagated pit (relative to corroded surface) as a function of environmental parameters in H_2S-containing corrosion systems after 168 hours.

By increasing the temperature further (to 80°C), the role of CO_2 gas in the gas phase in supersaturating the bulk solution to the extent where FeS is precipitated as the inner layer and $FeCO_3$ as an outer layer in H_2S-CO_2-containing systems becomes the most dominant factor to pit propagation. The process of dissolution and/or transformation of initially-formed mackinawite FeS to other morphology of mackinawite and forms of FeS are envisaged to occur rapidly at this temperature. There was also extensive build-up of FeS corrosion product than at lower temperature. All of these chemical and electrochemical processes are considered to be contributing to the manifestation of heavy localised and pitting corrosion in H_2S-CO_2-containing system than in H_2S-N_2-containing system at this temperature.

The presence of CO_2 gas in the gas phase at 80°C also favours the precipitation of FeS (and $FeCO_3$ once supersaturation is attained) from the bulk phase as a result of ferrite dissolution. This means that at some point in the corrosion process, there will be competitive precipitation of $FeCO_3$ and FeS. A combination of competitive precipitation of $FeCO_3$ and FeS, continuous ferrite dissolution, especially during FeS transformation is also likely to create localised anodic

sites. It is important to mention here that the FeS corrosion product formed in H_2S-CO_2-containing systems is shown in this study to be more uneven in terms of coverage than in H_2S-N_2-containing systems to corroborate the role of CO_2 corrosion component on the morphology of FeS corrosion products. These FeS corrosion products will also act to support the charge transfer process (as a cathode) across the FeS layer and promote pit propagation [24, 132], especially as the anode-to-cathode area ratio is set to decrease further with build-up of larger volumes of FeS.

Based on the discussion above relating to the role of CO_2 gas and the $FeCO_3$ formation process in the pitting coroison process at 80°C, it is therefore not surprising to have observed higher pit depth in H_2S-CO_2 corrosion systems than in H_2S-N_2. corrosion systems as well as the relationship between thickness losses to uniform corrosion and pit depth relative to corroded surface as shown in Figure 11-20. Referring to Figure 11-20, the change in the dominance of the three phenomena enlisted in Figure 11-19 over 168 hours as the temperature changes is most likely linked to the irregular relationship between pit depth and thickness loss to uniform corrosion in Figure 11-20. Evidences from electrochemical measurements is also provided for both H_2S-CO_2 and H_2S-N_2-containing systems in Figure 10-9 to support the pitting behaviour at 80°C, where the corrosion potential increased over 168 hours by ≈ 70-100 mV; potentially enough to sustain some form of local galvanic effect [164]. Pitting corrosion as depicted in this case is somewhat similar to pitting in passive alloys I terms of the role of the cathode in the local galvanic cells except that in this case, pit propagation is also likely to be occurring underneath a layer of FeS.

11.3.3 An empirical guideline for forecasting the risk of pitting corrosion of carbon steel in sweet and sour corrosion environments

Exploring and understanding the pitting corrosion initiation process in carbon steel exposed to H_2S-containing corrosion systems has in no doubt been very useful in terms of the providing insights into the electrochemical processes that governs sour corrosion kinetics, the likely influence of some key process parameters and their overall impact on material degradation in the earliest possible exposure time. However, information on pitting corrosion obtained in H_2S-containing corrosion systems based on short term assessment is usually not reliable in making judgements on the long-term integrity of carbon steel materials exposed to such conditions in oilfields. Results from experiments based on 168 hours tests from this study has helped to shape and improve on the understanding of the pitting corrosion behaviour of carbon steel in sweet and sour corrosion systems. A very important parameter that has thus far help to put into

perspective the pitting corrosion behaviour of carbon steels in these environments has been the pitting factor. The pitting factor (P_f) is used to reflect the relative contribution of uniform and pitting corrosion to the overall degradation mechanism for an active material like carbon steels (ASTM standard G46-94 [70]) (see detail description of pitting factor in section 6.6.4). The pitting factor has been plotted as a function of the thickness loss to uniform corrosion to reveal the risk of pitting corrosion over a wide range of parameters in Figure 11-21.

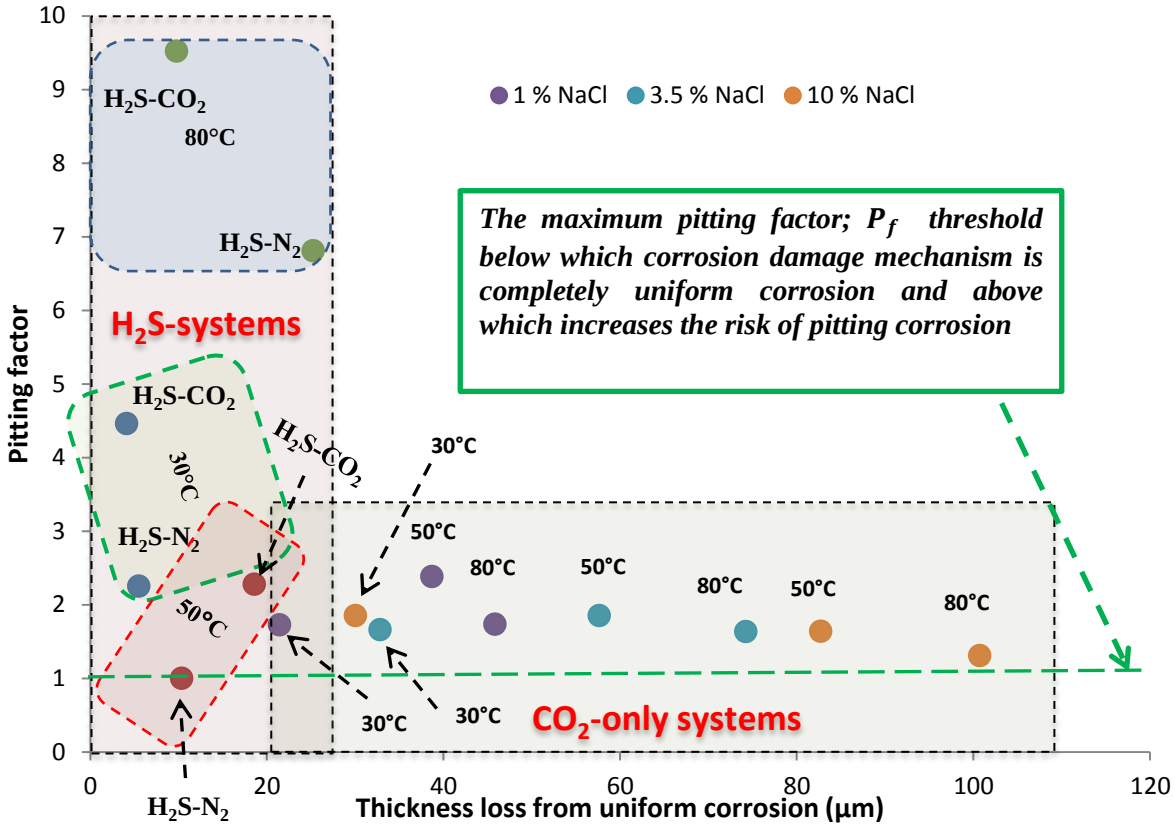

Figure 11-21 Summarised relationship between pitting factor and thickness loss to uniform corrosion across a wide range of parameters in both sweet and sour corrosion environments after 168 hours *(All tests in H_2S-containing environment were carried out in 3.5 wt.% NaCl solution)*.

Referring to Figure 11-21 and according the (ASTM standard G46-94 [70]), a pitting factor of 1 is an indicator that the corrosion damage mechanism for materials is dominated by uniform corrosion with no pitting. A pitting factor of unity (1) has been marked out as a threshold in Figure 11-21. Pitting and uniform corrosion dominates corrosion damage mechanism of carbon steel in CO_2 environments as shown in Figure 11-21. However, the active nature of carbon steel allows for the manifestation of significant uniform corrosion, leading to pitting factors just above unity for all experimental conditions in CO_2-saturated corrosion environments. While the pitting factor in CO_2-saturated corrosion system is just over unity, it can be imagined that the pitting factor for stainless steel material exposed to the same environments will be far greater

than unity. In H_2S-containing systems, the formation of FeS is able to protect and minimise the uniform corrosion aspect of material loss but also increases the risk of pitting corrosion as shown in Figure 11-21. The pitting factor of carbon steels in H_2S-containing systems at 80°C is almost 7-10 times the pitting factor in CO_2-saturated systems and so is the risk of pitting corrosion 7-10 times greater. Figure 11-21 also reflects the complex interaction between CO_2 presence, temperature and the already discussed complex electrochemical processes that characterises the different ranges of these parameters in H_2S-containing systems.

Figure 11-21 offers a clear and concise road map to summarise the likely influence of various environmental parameters on the pitting corrosion behaviour of carbon steels in sweet and sour corrosion environments. It is important to emphasise that the result presented in Figure 11-21 are based on 168 hours tests and does not take into account the potential changes in the pitting corrosion processes after 168 hours.

Chapter 12. Conclusions, industrial relevance of study and recommendation for future study

12.1 Conclusions

A comprehensive and parametric study on the pitting corrosion behaviour of X65 carbon steel in an unbuffered sweet and sour corrosion oilfield conditions was carried out using a combination of electrochemical and post-experiment surface analysis techniques. The key findings from this study are summarised in the following sections.

12.1.1 Corrosion of carbon steel and corrosion product formation in CO_2 saturated environments

- The evolution of corrosion product formation was successfully tracked over 168 hours at different time intervals. The process of corrosion product formation was observed to follow a sequence of; preferential ferrite dissolution, evolution of empty cementite, formation of an inner amorphous form of $FeCO_3$ and finally ends with the formation of an outer crystalline layer of $FeCO_3$.

- $FeCO_3$ corrosion formed in an unbuffered was found to be non-protective. In conditions where crystalline $FeCO_3$ is formed, they were on a nano-scale. The non-protective nature of such corrosion product promoted continuous ferrite dissolution in the presence of $FeCO_3$.

- Temperature was observed to promote the different aspect of corrosion processes; increasing the temperature promoted the rate of preferential ferrite dissolution, evolution of empty cementite, formation of an inner amorphous form of $FeCO_3$ and finally ends with the formation of an outer crystalline layer of $FeCO_3$. At higher temperature, the time intervals for these processes are shorter.

- The effect of chloride ion was observed to be related to the aggressivity of the corrosion environments and the rate of availability of ferrous ions for $FeCO_3$ formation. Increasing the chloride ion concentration was also observed to promote the rate of preferential ferrite dissolution, evolution of empty cementite, formation of an inner amorphous form of $FeCO_3$ and finally ends with the formation of an outer crystalline layer of $FeCO_3$. There was no significant effect of chloride ion concentration on the morphology of $FeCO_3$.

- Changes in *in-situ* pH were observed to influence both the kinetics of corrosion and formation of different morphology of $FeCO_3$ corrosion product. A more acidic corrosion environment promoted the preferential ferrite dissolution, evolution of empty cementite, formation of an inner non-crystalline and/or amorphous form of $FeCO_3$, while a less acidic corrosion environment promoted the formation of crystalline $FeCO_3$ with a unique morphology and capacity to pseudo-passivate the corrosion interface.

12.1.2 Pitting corrosion of carbon steel in CO_2 corrosion environments

- The nature of pitting corrosion of carbon steel in unbuffered CO_2-saturated environment was observed and confirmed to be different from pitting in passive alloys like stainless steels. Initial ferrite dissolution and distribution of iron carbide were very influential in the initiation of pitting corrosion. The propagation of pitting corrosion was sustained by the non-protective and/or non-crystalline nature of $FeCO_3$.

- In carbon steel, there was also substantial uniform corrosion occurring at the same time as pitting corrosion propagation. In conditions where uniform corrosion was significantly high, the pit depths were usually masked.

- The rate of initiation of pitting corrosion was found to increase with increasing temperature in carbon steel materials. However, with increase in exposure time, some of the active pits were observed to stop propagating at 80°C due to the precipitation of a non-crystalline form $FeCO_3$ at the base of the pits in a process termed the "***pit self-healing process***".

- The depth of measure pits was observed in this study to be higher with decreasing chloride ion concentration for all temperatures; pit initiation and propagation stages.

- Pitting corrosion is likely to occur at different solution pH and the pitting corrosion process at different bulk pH correlates the evolution of different forms of corrosion products at each bulk pH.

- In acidic corrosion environments, pitting corrosion process were observed to initiate and propagates steadily due to the formation of porous and non-crystalline (amorphous) form of $FeCO_3$. While at less acidic corrosion environments, pitting corrosion only

occurs once significant protection is attained from precipitated $FeCO_3$ and in some instances, when pseudo-passivation effect is achieved.

12.1.3 Corrosion of carbon steel and corrosion product formation in sour corrosion environments

- The kinetics of sour corrosion and FeS formation was observed in this study to be influenced by a combination of ferrite dissolution and FeS formation from direct reduction reaction in the early stages of corrosion. With the presence of CO_2 gas in H_2S-containing gas phase, the contribution of CO_2/H_2CO_3 corrosion is significant and manifest mainly in the form uniform corrosion, especially at higher temperatures

- FeS forms very quickly on the steel surface depending on other environmental parameters to substantially influence the corrosion process. However, the FeS corrosion product layer was not very protective and uniform, which was also correlated to temperatures and gas phase composition; presence of and/or absence of CO_2 gas.

- After an extended exposure period, the corrosion kinetics becomes mainly influenced by the rate of formation, dissolution and/or transformation of initially formed mackinawite form of FeS to pyrrhotite form of FeS.

- There was evidence of competitive precipitation of $FeCO_3$ and FeS on the steel surface in H_2S-CO_2 containing systems at 80°C. FeS forms first as an inner layer while $FeCO_3$ forms later as an outer layer due to the dependence of $FeCO_3$ precipitation on supersaturation.

- The process of dissolution and/or transformation of a mackinawite were also observed to be dependent on temperatures and gas phase composition; presence of and/or absence of CO_2 gas. Mackinawite dissolution and /transformation process was faster at higher temperature and did not occur at 30°C after 168 hours.

12.1.4 Pitting corrosion of carbon steel in sour corrosion environments

- Pitting corrosion was found to occur and dominate the early stages corrosion damage mechanism at all temperatures (30, 50 and 80°C) with the formation of FeS corrosion (mackinawite) products in H_2S-containing corrosion environments.

- Evolution of pitting corrosion in the early stages of carbon steel corrosion in sour corrosion environments was observed to be governed by ; uniform corrosion (in terms of preferential ferrite dissolution and evolution of iron carbide), localised environments (active local anodes), the corrosion products (FeS), active ionic species in the bulk solution and environmental parameters.

- Over an extended exposure time, pitting corrosion was observed to correlate with the process of dissolution and/or transformation of initially formed mackinawite.

- Pitting corrosion was more dominant in H_2S-CO_2 containing systems at 80°C than in H_2S-N_2 containing systems. H_2S-containing environment, levels of pitting was also higher at 80°C than at lower temperatures.

- The concept of competitive precipitation of $FeCO_3$ and FeS was also observed to correlate with the deepest recorded pits on steel exposed to H_2S-CO_2 containing systems at 80°C and after 168 hours.

12.2 Industrial relevance of study

- This study has been very robust in understanding and clearly defining pitting corrosion process of carbon steel materials exposed to oilfield corrosion environments, as being fundamentally different from pitting in passive alloys.

- This robustness of the systematic approach of this research could also help with testing the efficacy of corrosion inhibitors against pitting corrosion and material penetration.

- Experimental data from this research could be used in making intelligent judgement on the risk of pitting corrosion in different oilfield corrosion scenarios, which also includes being able to decide on the most optimise corrosion and pitting corrosion mitigation strategy.

- Experimental data from this research could also be adopted as a solid foundation upon which a corrosion prediction model capable of predicting the risk of pitting corrosion can be successfully built.

12.3 Recommendation for future research

- Further studies to obtain a mechanistic mechanism of pitting corrosion in sweet and sour corrosion environment is required in order to characterise the distribution of anodic and cathodic sites within the depth profile of an active and/or dormant pit and identify the tendency for pit to grow continuously in carbon steel materials.

- Characterisation of the boundaries of different forms of FeS; mackinawite, pyrrhotite, pyrite in sour corrosion environments in terms of oilfield process parameters such as the partial pressure of H_2S gas, temperature and CO_2:H_2S ratio is also an interesting area of interest. Further investigation needs to be carried out in terms of correlating sour kinetics within these boundaries and the localised corrosion implication of carbon steels exposed to such environments.

- There is also a need to investigate other properties of the different forms of iron sulphide such as the erosion-corrosion resistance, shear resistance and other mechanical properties that could become useful in the process of corrosion mitigation.

- Investigation into the corrosion behaviour; pitting and other forms of localised corrosion at high temperature a high pressure sweet and sour conditions are increasingly becoming more relevant in recent times. This will help understand and provide solution to localised corrosion in carbon steel materials exposed to such conditions during-deep water exploration.

References

1. M.G. Fontana, *Corrosion engineering*. 3rd ed. McGraw-Hill series in materials science and engineering. 1986, New York ; London: McGraw-Hill.

2. P.R. Roberge, *Handbook of corrosion engineering*. 2000, New York ; London: McGraw-Hill. xi, 1139 p.

3. B.D. Craig, *Oilfield metallurgy and corrosion*. 3rd ed. 2004, Denver, Colo.: MetCorr. 282.

4. H. Sun, D.J. Blumer, M. Swidzinski, and J. Davis. "Evaluating corrosion inhibitors for sour gas subsea pipelines", International Petroleum Technology Conference, (Doha, Qatar: IPTC International, 2009).

5. M.S. Günter Schmitt, George F. Hays,, E.-H.H. Wayne Burns, Antoine Pourbaix,, and a.G. Jacobson, *Global needs for knowledge dissemination, research, and development in materials deterioration and corrosion control*, 2009: New York, USA. p. 44.

6. M.P.H. Gerhardus H. Koch and N.G.T. Brongers, Y. Paul Virmani and J.H. Payer, *Corrosion Costs and Preventive Strategies in he United States*, 2002. p. 12.

7. G2MTLaboratory. *Cost of Corrosion Annually in the US Over $1 Trillion*. 2011 25/09/2014]; Available from: http://www.g2mtlabs.com/cost-of-corrosion/.

8. M.B. Kermani and D. Harrop, "The impact of corrosion on oil and gas industry", SPE Production & Operations, 11, 3 (1996): p. 186-190.

9. B.M. Kermani and A. Morshed, "Carbon dioxide corrosion in oil and gas production: A compendium", Corrosion, 59, 08 (2003): p. 659-683.

10. B. Hedges, H.J. Chen, K. Sprague, and T.H. Bieri. "A review of monitoring and inspection techniques for CO_2 and H_2S corrosion in oil & gas production facilities", CORROSION, paper no, 120, (San Diego, CA.: NACE International, Houston, Texas, 2006).

11. J.J. Perdomo, A.J. Lusinchi, A. Viloria, and J.L. Morales. "CO_2 and H_2S corrosion of API 5L-B and 5L-X52 grade steels", CORROSION, paper no.042, (Orlando, FL:NACE International, 2000).

12. H.U. Schutt and F.F. Lyle. "CO_2-H_2S corrosion under wet gas pipeline conditions in the presence if bicarbonate, chloride, and oxygen", CORROSION, pape no. 11, (San Diego, CA:NACE International, 1998).

13. A. Al-Saeed, R. Chandra, N. Al-Mai, M. Al-Awadi, and Q. Dashti. "Corrosion monitoring, root cause analysis and selection criteria for future well completion design in deep HPHT sour wells", SPE International Conference and Exhibition on Oilfield Corrosion, (Aberdeen, UK: SPE International, 2012).

14. A. Al-Hashem and J.A. Carew. "Downhole materials optimization for harsh petroleum production", CORROSION, paper no.346, (San Diego, CA: NACE International, 2003).

15. B. Kermani. "Materials optimization for oil and gas sour production", CORROSION, paper no. 156, (Orlando, FL.: NACE International, Houston, Texas, 2000).

16. K.M. Morsi. "Field experience with production of deep sour gas reservoir", SPE Gas Technology Symposium, (Dallas, Texas: 1989 Copyright 1989, Society of Petroleum Engineers, Inc., 1989).

17. C.I. Ossai, "Advances in asset management techniques: an overview of corrosion mechanisms and mitigation strategies for oil and gas pipelines", International Scholarly Research Notices ISRN Corrosion, 2012, (2012): p. 10.

18. H. Fang, B. Brown, and S. Nešić, "Effects of sodium chloride concentration on mild steel corrosion in slightly sour environments", Corrosion, 67, 1 (2011): p. 015001-1-015001-12.

19. H.A. Videla, Robert, and L.K. Herrera. "An updated overview of SRB induced corrosion and protection of carbon steel", CORROSION, paper no. 488, (Houston, TX:NACE International: NACE International, 2005).

20. M. Girgis. "Challenges in highly sour gas environment containing elemental sulphur", Abu Dhabi International Petroleum Exhibition and Conference, (Abu Dhabi, UAE: SPE International, 2008).

21. D.J. D.Garber, M.V. B.Patil, and M.K.M. Yap. "CO_2, H_2S and bacteria pitting corrosion model", CORROSION, paper no. 257, (Houston, TX: NACE International, 2011).

22. J.N. Al-Hajji and M.R. Reda, "Corrosion behavior of low-residual carbon steels in a sour environment", Corrosion, 49, 05 (1993).

23. J. Moloney, W. Mok, and C. Gamble. "Corrosion and hydrate control in wet sour gas transmission systems", SPE Asia Pacific Oil and Gas Conference and Exhibition, (Perth, Australia: SPE Intenational, 2008).

24. J. Kvarekval. "Morphology of localised corrosion attacks in sour environments", CORROSION, (Nashville, TN.: NACE International, Houston, Texas, 2007).

25. F.A. Ramirez, R. Hill, and S. martinez. "Material assessment for souring subsea systems", Offshore Technology Conference, (Houston, Texas, USA, 2010).

26. R. Evans. "Factors influencing sulphide scale generation associated with waterflood induced reservoir souring", International Symposium on Oilfield Scale, (Aberdeen, United Kingdom: Copyright 2001, Society of Petroleum Engineers Inc., 2001).

27. S.N. Smith. "Discussion of the history and relevance of the CO_2-H_2S ratio", CORROSION, paper no. 65, (Houston, TX : NACE International, 2011).

28. S. Maxwell. "Implications of re-injection of produced water on microbially influenced corrosion (MIC) in offshore water injection systems", CORROSION, paper no. 549, (Houston, TX: NACE International, 2005).

29. J.J.Moloney, W.Y.Mok, and C.G.Gamble. "Compatible corrosion and kinetic hydrate inhibitors for wet sour gas transmission lines", CORROSION, paper no. 350, (Atlanta, GA:NACE International, 2009).

30. G. Wilken. "Effect of environmental factors on downhole sour gas corrosion", CORROSION, paper no. 76, (Denver, CO: NACE International, Houston, Texas, 1996).

31. L. Zhang, W. Zhong, J. Yang, T. Gu, X. Xiao, and M. Lu. "Effects of temperature and partial pressure on H_2S-CO_2 corrosion of pipeline steel in sour conditions", CORROSION, paper no. 79, (Houston, TX :NACE International, 2011).

32. A. Hernández-Espejel, M.A. Domínguez-Crespo, R. Cabrera-Sierra, C. Rodríguez-Meneses, and E.M. Arce-Estrada, "Investigations of corrosion films formed on API-X52 pipeline steel in acid sour media", Corrosion Science, 52, 7 (2010): p. 2258-2267.

33. S. Papavinasam, A. Doiron, J. Li, D.-Y. Park, and P. Liu. "Sour and sweet corrosion of carbon steel: general or pitting or localized or all of the above?", CORROSION, paper no. 332, (San Antonio, TX: NACE International, 2010).

34. G. Svenningsen, A. Palencsár, and J. Kvarekvål. "Investigation of iron sulfide surface layer growth in aqueous H_2S-CO_2 environments", CORROSION, paper no.359, (Atlanta, GA: NACE International, 2009).

35. R.H. Hausler. "Contribution to the understanding of H_2S corrosion", CORROSION, paper no. 732, (New Orleans, LA.: NACE International, Houston, Texas, 2004).

36. G. Dicken, K. Bruce, B. Johnson, and M.J. Al-ghafri. "The use of carbon steel in highly sour oil and gas production systems", SPE International Oilfield Corrosion Conference, (Aberdeen, UK: Society of Petroleum Engineers, 2008).

37. R. Woollam, K. Tummala, J. Vera, and S. Hernandez. "Thermodynamic prediction of $FeCO_3$-FeS corrosion product films", CORROSION, paper no. 076, (Houston, TX.: NACE International, Houston, Texas, 2011).

38. S. Papavinasam, A. Doiron, and R.W. Revie, "Model to predict internal pitting corrosion of oil and gas pipelines", Corrosion, 66, 3 (2010): p. 11.

39. S.N. Smith, B. Brown, and W. Sun. "Corrosion at higher H_2S concentrations and moderate temperatures", CORROSION, paper no. 81, (Houston, TX.: NACE International, Houston, Texas, 2011).

40. K.-M. Yap and S. Srinivasan. "Key factors in development of a CO_2-H_2S corrosion prediction model for multiphase oil-gas production systems", CORROSION, 374, (Houston, TX: NACE International, 2010).

41. H. Hoffmeister. "Modelling the effect of chloride content on H_2S corrosion by coupling of phase and polarization behavior", COROSION, paper no. 501, (Nashville, TN: NACE International, 2007).

42. S.N. Smith and M.W. Joosten. "Corrosion of carbon steel by H_2S in CO_2 containing oilfield environments", CORROSION, paper no. 115, (San Diego, CA: NACE International, 2006).

43. Z. Ahmad, *Principles of Corrosion Engineering and Corrosion Control*. 2006: Elsevier Science.

44. N. Perez, *Electrochemistry and Corrosion Science*. 2004: Springer.

45. E.E. Stansbury and R.A. Buchanan, *Fundamentals of Electrochemical Corrosion*. 2000: Asm International.

46. D.E.J. Talbot and J.D.R. Talbot, *Corrosion science and technology*. 2007: CRC Press.

47. R. Baboian, *Corrosion Tests And Standards: Application And Interpretation*. 2005: Astm International.

48. M. Stern and A.L. Geary, "Electrochemical polarization; I. A theoretical analysis of the shape of polarization curves", Journal of the Electrochemical Society, 104, 1 (1957): p. 56-63.

49. I. Gamry Instruments, "Application Notes; Basics of Electrohemical Impedance Spectroscopy", (20101): p. 17.

50. D.A. Shifler. "Understanding and modelling galvanic corrosion in marine environments", CORROSION, paper no. 283, (San Diego, CA: NACE International, 2006).

51. S.M. Wilhelm, "Galvanic corrosion in oil and gas production; Part 1-Laboratory Studies", Corrosion, 48, 08 (1992).

52. D. Zeng, L. Huang, T. Gu, S. Huo, Y. Lin, Z. Hongjun, and H. Yin. "Evaluation and selection of OCTG and gathering lines for high sour gas fields", International Oil and Gas Conference and Exhibition in China, (Beijing, China: Society of Petroleum Engineers, 2010).

53. A.N. Moosavi, K. Rumash, and M. Kadri. "Material selection for downhole sour environment", Abu Dhabi International Petroleum Exhibition and Conference, (Abu Dhabi, UAE: Society of Petroleum Engineers, 2008).

54. M.B. Kermani and R.G. MacCuish. "Materials assessment for sour service applications", SPE Annual Technical Conference and Exhibition, (New Orleans, Louisiana: 1990 Copyright 1990, Society of Petroleum Engineers, Inc., 1990).

55. B. Kermani, K.A. Esaklul, and J.W. Martin. "Materials design strategy: Effects of H_2S/CO_2 corrosion on materials selection", CORROSION, paper no. 121, (San Diego, CA: NACE International, 2006).

56. B. Kermani, T.E. Perez, C. Morales, G.L. Turconi, and J.C. Gonzales. "Materials optimisation in hydrocarbon production", CORROSION, paper no. 111, (Houston, TX: NACE International, 2005).

57. H. Sun, D. Blumer, and J. Davis. "Pit propagation of carbon steel in sour conditions", CORROSION, paper no. 282, (San Antonio, TX: NACE International, 2010).

58. Z. Zhu, N. Tajallipour, P.J. Teevens, H. Xue, and F.Y.F. Cheng. "A mechanistic model for predicting localized-pitting corrosion in a brine water-CO_2 system", CORROSION, paper no. 256, (Houston, TX:NACE International, 2011).

59. D.J.D. Garber, D.K. Knierim, M.J. Acuna, and M.K.C. Deokar. "Modelling pitting corrosion in a CO_2 system containing bacteria", CORROSION, paper no. 545, (New Orleans, LA: NACE International, 2008).

60. R. Nyborg. "Initiation and growth of mesa corrosion attack during CO_2 corrosion of carbon steel", CORROSION, paper no. 48, (San Diego, CA: NACE International, 1998).

61. R. Nyborg and A. Dugstad. "Understanding and prediction of mesa corrosion attack", CORROSION, paper no. 642, (San Diego, CA: NACE International, 2003).

62. P. Indonesia. *CO_2 Corrosion* 2009 11/05/2015]; Available from: https://pipelinemaster.wordpress.com/category/integrity-management/corrosion-integrity-management/.

63. F. Services. *Corrosion* 2006 11/05/2015]; Available from: http://www.forensic.cc/non-fire/machinery-breakdown/mechanical-&-material/corrosion.

64. GO-TECH. *CO2 corrosion* 2015 11/05/2015]; Available from: http://octane.nmt.edu/waterquality/corrosion/CO2.aspx.

65. A.S.M. International, *Metals Handbook, Ninth Edition: Volume 13-Corrosion (ASM Handbook)*, 1987, ASM International Ohio.

66. P. Roberge, *Corrosion Engineering*. 2008: McGraw-Hill Education.

67. D.W. Hoeppner. *Pitting corrosion: morphology and characterization*. 1985.

68. J.C. Scully, *The fundamentals of corrosion*. 3rd ed. 1990, Oxford: Pergamon. 250 p.

69. M. Schütze, R.W. Cahn, and E.J. Kramer, *Corrosion and Environmental Degradation: A Comprehensive Treatment*. 2000: Wiley-VCH.

70. A.S.T.M. International, *ASTM G46-94 Standard Guide for Examination and Evaluation of Pitting Corrosion*, 2005, ASTM International: West Conshohocken, PA. p. 7.

71. G.S.F.a.N. Sridhar, "Understanding localized corrosion", Materials Today, 11, 10 (2008): p. 38-44.

72. J. Kvarekval. "Corrosion layer breakdown and localized corrosion in H_2S/CO_2 environment ", CORROSION, paper no. 1537, (Salt Lake City, UT: NACE International, 2012).

73. S. Nesic, H. Li, J. Huang, and D. Sormaz. "An open source mechanistic model for CO_2 / H_2S corrosion of carbon steel", CORROSION, paper no. 572, (Atlanta, GA.: NACE International, Houston, Texas, 2009).

74. M.E. Parker, J.P. Meyer, and S.R. Meadows, "Carbon Dioxide Enhanced Oil Recovery Injection Operations Technologies (Poster Presentation)", Energy Procedia, 1, 1 (2009): p. 3141-3148.

75. B.D. Craig and B.D. Craig, *Oilfield metallurgy and corrosion*. 3rd ed. 2004, Denver, Colo.: MetCorr. viii, 282 p.

76. Nordsveen M, Nesic. S, Nyborg. R, and S. A, "A mechanistic model for carbon dioxide corrosion of mild steel in the presence of protective iron carbonate films—Part 1: Theory and Verification", Corrosion, 59, 5 (2003): p. 443-456.

77. C. De Waard and D.E. Milliams, "Carbonic Acid Corrosion of Steel", Corrosion, 31, 5 (1975): p. 177-181.

78. A. Dugstad. "Fundamental Aspects of CO_2 Metal Loss Corrosion - Part 1: Mechanism", CORROSION paper no. 06111, (San Diego, CA.: NACE International, Houston, Texas, 2006).

79. B.R. Linter and G.T. Burstein, "Reactions of pipeline steels in carbon dioxide solutions", Corrosion Science, 41, 1 (1999): p. 117-139.

80. G.I. Ogundele and W.E. White, "Observations on the Influences of Dissolved Hydrocarbon Gases and Variable Water Chemistries on Corrosion of an API-L80 Steel", Corrosion, 43, 11 (1987): p. 665-673.

81. J.O.M. Bockris, D. Drazic, and A.R. Despic, "The electrode kinetics of the deposition and dissolution of iron", Electrochimica Acta, 4, 2–4 (1961): p. 325-361.

82. A. Atkinson and A. Marshall, "Anodic dissolution of iron in acidic chloride solutions", Corrosion Science, 18, 5 (1978): p. 427-439.

83. S. Nešić, "Key issues related to modelling of internal corrosion of oil and gas pipelines – A review", Corrosion Science, 49, 12 (2007): p. 4308-4338.

84. W. Sun, S. Nešić, and R.C. Woollam, "The effect of temperature and ionic strength on iron carbonate ($FeCO_3$) solubility limit", Corrosion Science, 51, 6 (2009): p. 1273-1276.

85. W. Durnie, R. De Marco, A. Jefferson, and B. Kinsella, "Harmonic analysis of carbon dioxide corrosion", Corrosion Science, 44, 6 (2002): p. 1213-1221.

86. F. Farelas, M. Galicia, B. Brown, S. Nesic, and H. Castaneda, "Evolution of dissolution processes at the interface of carbon steel corroding in a CO_2 environment studied by EIS", Corrosion Science, 52, 2 (2010): p. 509-517.

87. A. Dugstad. "Mechanism of protective film formation during CO_2 corrosion of carbon steel", CORROSION, paper no.31, (San Diego, CA: NACE International, Houston, Texas, 1998).

88. J.L. Crolet, N. Thevenot, and S. Nesic, "Role of Conductive Corrosion Products in the Protectiveness of Corrosion Layers", Corrosion, 54, 3 (1998): p. 194-203.

89. S. Al-Hassan, B. Mishra, D.L. Olson, and M.M. Salama, "Effect of microstructure on corrosion of steels in aqueous solutions containing carbon dioxide", Corrosion, 54, 6 (1998): p. 480-491.

90. A. Dugstad, H. Hemmer, and M. Seiersten, "Effect of steel microstructure on corrosion rate and protective iron carbonate film formation", Corrosion, 57, 04 (2001).

91. J. Han, Y. Yang, S. Nesic, and B.N. Brown. "Roles of passivation and galvanic effects in localized CO_2 corrosion of mild steel", CORROSION, paper no. 332, (New Orleans, LA: NACE International, 2008).

92. J. Han, D. Young, H. Colijn, A. Tripathi, and S. Nešić, "Chemistry and structure of the passive film on mild steel in CO_2 corrosion environments", Industrial & Engineering Chemistry Research, 48, 13 (2009): p. 6296-6302.

93. S. Guo, L. Xu, L. Zhang, W. Chang, and M. Lu, "Corrosion of alloy steels containing 2% chromium in CO_2 environments", Corrosion Science, 63, (2012): p. 246-258.

94. W. Sun and S. Nesic. "Basics Revisited: Kinetics of Iron Carbonate Scale Precipitation in CO_2 Corrosion": NACE International, 2006).

95. Z. Xia, K.C. Chou, and Z. Szklarska-Smialowska, "Pitting corrosion of carbon steel in CO_2-containing NaCl brine", Corrosion, 45, 8 (1989): p. 636-642.

96. J.L. Crolet and M.R. Bonis, "pH Measurements in Aqueous CO_2 Solutions under High Pressure and Temperature", Corrosion, 39, 2 (1983): p. 39-46.

97. C. de Waard, U. Lotz, and D.E. Milliams, "Predictive model for CO_2 corrosion engineering in wet natural gas pipelines", Corrosion, 47, 12 (1991): p. 976-985.

98. F.F. Eliyan and A. Alfantazi, "Influence of temperature on the corrosion behavior of API-X100 pipeline steel in 1-bar CO_2-HCO_3^- solutions: An electrochemical study", Materials Chemistry and Physics, 140, 2–3 (2013): p. 508-515.

99. G. Schmitt and M. Horstemeier. "Fundamental Aspects of CO_2 Metal Loss Corrosion - Part II: Influence of Different Parameters on CO_2 Corrosion Mechanisms": NACE International, 2006).

100. R. Nyborg, *Controlling internal corrosion in oil and gas pipelines*, 2005: BUSINESS BRIEFING: EXPLORATION & PRODUCTION: THE OIL & GAS REVIEW 2005.

101. J. Kvarekval and A. Dugstad. "Corrosion mitigation with pH stabilization in slightly sour gas-condensate pipelines", CORROSION, paper no.646, (San Diego, CA: NACE International, 2006).

102. A. Dugstad, L. Lunde, and S. Nesic. "Control of internal corrosion in multi-phase oil and gas pipelines", Prevention of pipeline corrosion conference, (Houston, TX, 1994).

103. S. Nesic, J. Postlethwaite, and S. Olsen, "An electrochemical model for prediction of corrosion of mild steel in aqueous carbon dioxide solutions", Corrosion, 52, 04 (1996): p. 280-294.

104. K.V.a.A. Dugstad, "Corrosion of carbon steel in an aqueous carbon dioxide environment. I: Solution effects", Materials performance, 28, , (1989): p. 5.

105. F.F. Eliyan, F. Mohammadi, and A. Alfantazi, "An electrochemical investigation on the effect of the chloride content on CO_2 corrosion of API-X100 steel", Corrosion Science, 64, 0 (2012): p. 37-43.

106. N. Anselmo, J.E. May, N.A. Mariano, P.A.P. Nascente, and S.E. Kuri, "Corrosion behavior of supermartensitic stainless steel in aerated and CO_2-saturated synthetic seawater", Materials Science and Engineering: A, 428, 1–2 (2006): p. 73-79.

107. X. Gao, B. Brown, and S. Nesic. "Effect of chloride on localized corrosion initiation of carbon steel in a CO_2 aqueous environment", CORROSION, paper no. 3880, (San Antonio, TX: NACE International, 2014).

108. X. Lou and P.M. Singh, "Role of water, acetic acid and chloride on corrosion and pitting behaviour of carbon steel in fuel-grade ethanol", Corrosion Science, 52, 7 (2010): p. 2303-2315.

109. X. Jiang, S. Nešić, B. Kinsella, B. Brown, and D. Young, "Electrochemical investigation of the role of Cl− on localized carbon dioxide corrosion behavior of mild steel", Corrosion, 69, 1 (2012): p. 15-24.

110. G. Schmitt and S. Feinen. "Effect of anions and cations on the pit initiation in CO2 corrosion of iron and steel", CORROSION, paper no.01, (Orlando, FL: NACE International, 2000).

111. J. Soltis, "Passivity breakdown, pit initiation and propagation of pits in metallic materials – Review", Corrosion Science, 0 (2014).

112. G. Wranglen, "Pitting and sulphide inclusions in steel", Corrosion Science, 14, 5 (1974): p. 331-349.

113. J. Stewart and D.E. Williams, "The initiation of pitting corrosion on austenitic stainless steel: on the role and importance of sulphide inclusions", Corrosion Science, 33, 3 (1992): p. 457-474.

114. G. Wranglén, "Review article on the influence of sulphide inclusions on the corrodibility of Fe and steel", Corrosion Science, 9, 8 (1969): p. 585-602.

115. W. Sun, D. V.Pugh, S. N.Smith, S. Ling, J. L.Pacheco, and R. J.Franco. "A parametric study of sour corrosion of carbon steel ", CORROSION, paper no.278, (San Antonio, TX.: NACE International, Houston, Texas, 2010).

116. M.d. Romero. "The mechanism of SRB action in MIC, based on sulfide corrosion and iron sulfide corrosion products", COROSSION, paper no.481, (Houson, TX: NACE International, 2005).

117. *Petroleum and Natural Gas Industries - Materials for Use in H_2S-Containing Environments in Oil and Gas Production: Parts 2 and 3*, 2011, NACE.

118. W. Sun and S. Nesic. "A mechanistic model of H_2S corrosion Of mild steel", CORROSION, paper no.655, (Nashville, TN.: NACE International, Houston, Texas, 2007).

119. Y. Zheng, B. Brown, and S. Nešić, "Electrochemical study and modelling of H_2S corrosion of mild steel", Corrosion, 70, 4 (2013): p. 351-365.

120. M. Singer, B. Brown, A. Camacho, and S. Nešić, "Combined effect of carbon dioxide, hydrogen sulfide, and acetic acid on bottom-of-the-line corrosion", Corrosion, 67, 1 (2011): p. 015004-1-015004-16.

121. J. Kittel, F. Ropital, F. Grosjean, E.M.M. Sutter, and B. Tribollet, "Corrosion mechanisms in aqueous solutions containing dissolved H2S. Part 1: Characterisation of H_2S reduction on a 316L rotating disc electrode", Corrosion Science, 66, 0 (2013): p. 324-329.

122. P.W. Bolmer, "Polarization of iron in H_2S-NaHS buffers", Corrosion, 21, 3 (1965): p. 69-75.

123. G.I. Ogundele and W.E. White, "Some Observations on the Corrosion of Carbon Steel in Sour Gas Environments: Effects of H2S and $H_2S/CO_2/CH_4/C_3H_8$ Mixtures", Corrosion, 42, 7 (1986): p. 398-408.

124. H. Ma, X. Cheng, G. Li, S. Chen, Z. Quan, S. Zhao, and L. Niu, "The influence of hydrogen sulfide on corrosion of iron under different conditions", Corrosion Science, 42, 10 (2000): p. 1669-1683.

125. H. Fang, B. Brown, and S. Nesić. "High salt concentration effects on CO_2 corrosion and H_2S corrosion", CORROSION paper no. 276, (San Antonio, TX: NACE International, 2010).

126. W. Sun, S. Papavinasam, and S. Nesic. "Kinetics of iron sulfide and mixed iron sulfide/carbonate scale precipitation in CO2/H2S corrosion", CORROSION, paper no. 644, (San Diego, CA: NACE International, 2006).

127. S.N. Smith and J.L. Pacheco. "Prediction of corrosion in slightly sour environments", CORROSION, paper no. 241, (Denver, CO: NACE International, 2002).

128. S.N. Smith. "Current understanding of corrosion mechanisms due to H_2S in oil and gas production environments", CORROSION, Paper no. 5485, (Dallas, TX: NACE International 2015, 2015).

129. J. Kvarekval, R. Nyborg, and H. Choi. "Formation of multilayer iron sulfide films during high temperature CO_2/H_2S corrosion of carbon steel", CORROSION, paper no. 339, (San Diego, CA : NACE International, 2003).

130. Y. Li, R.A. van Santen, and T. Weber, "High-temperature FeS–FeS_2 solid-state transitions: Reactions of solid mackinawite with gaseous H2S", Journal of Solid State Chemistry, 181, 11 (2008): p. 3151-3162.

131. J. Tang, Y. Shao, J. Guo, T. Zhang, G. Meng, and F. Wang, "The effect of H_2S concentration on the corrosion behavior of carbon steel at 90°C", Corrosion Science, 52, 6 (2010): p. 2050-2058.

132. H.-H. Huang, W.-T. Tsai, and J.-T. Lee, "Corrosion morphology of A516 carbon steel in H_2S solution", Scripta Metallurgica et Materialia, 31, 7 (1994): p. 825-828.

133. J.-L. Crolet and M.R.Bonis. "Algorithm of the protectiveness of corrosion layers 2 - protectiveness mechanisms and H_2S corrosion prediction", CORROSION, paper no. 365, (San Antonio, TX.: NACE International, Houston, Texas, 2010).

134. B.N. Brown and S. Nesic. "CO_2/H_2S corrosion under Scale forming conditions", CORROSION, paper no. 625, (Houston, TX:NACE International: NACE International, 2005).

135. L. ZHANG, J. YANG, J. Sun, and M. LU. "Effect of pressure on wet H_2S-CO_2 corrosion of pipeline steel", CORROSION, paper no. 565, (Atlanta, GA: NACE International, 2009).

136. S. Nesic, S. Wang, H. Fang, W. Sun, and J.K.-L. Lee. "A new updated model of CO_2-H_2S corrosion in multiphase flow", CORROSION, paper no. 535, (New Orleans, LA: NACE International, 2008).

137. W. Sun, D.V. Pugh, S. Ling, R.V. Reddy, J.L. Pacheco, R.S. Nisbet, N.M. Nor, M.S. Kersey, and L. Morshidi. "Understanding and quantifying corrosion of L80 carbon steel in sour environments", CORROSION, paper no.63, (Houston, TX: NACE International, 2011).

138. B. Brown and S. Nesic. "Aspects of localized corrosion in an H_2S-CO_2 environment", CORROSION, paper no. 1559, (Salt Lake City, UT.: NACE International, Houston, Texas, 2012).

139. K. Videm and J. Kvarekvål, "Corrosion of carbon steel in carbon dioxide-saturated solutions containing small amounts of hydrogen sulfide", Corrosion, 51, 04 (1995): p. 260-269.

140. Y. Zheng, J. Ning, B. Brown, and S. Nešić, "Electrochemical model of mild steel in a mixed H_2S-CO_2 aqueous environment in the absence of protective corrosion product layers", Corrosion, (2014): p. 316-325.

141. J. Kvarekval. "Corrosion Layer breakdown and Localized Corrosion in H_2S-CO_2 Environments", NACE International, (Houston, Texas, 2012).

142. D.R. Lide, *CRC Handbook of Chemistry and Physics: A Ready-reference Book of Chemical and Physical Data*. 2004: CRC Press.

143. J.C. Kotz, P. Treichel, and J.R. Townsend, *Chemistry and Chemical Reactivity*. 2009: Thomson Brooks/Cole.

144. P.G.T. Fogg and W. Gerrard, *Solubility of gases in liquids: a critical evaluation of gas/liquid systems in theory and practice*. 1991: J. Wiley.

145. T.J. Barrett, G.M. Anderson, and J. Lugowski, "The solubility of hydrogen sulphide in 0–5 m NaCl solutions at 25°–95°C and one atmosphere", Geochimica et Cosmochimica Acta, 52, 4 (1988): p. 807-811.

146. O.M. Suleimenov and R.E. Krupp, "Solubility of hydrogen sulfide in pure water and in NaCl solutions, from 20 to 320°C and at saturation pressures", Geochimica et Cosmochimica Acta, 58, 11 (1994): p. 2433-2444.

147. D.-Q. Zheng, T.-M. Guo, and H. Knapp, "Experimental and modeling studies on the solubility of CO_2, $CHClF_2$, CHF_3, $C_2H_2F_4$ and $C_2H_4F_2$ in water and aqueous NaCl solutions under low pressures", Fluid Phase Equilibria, 129, 1–2 (1997): p. 197-209.

148. B. Rumpf, H. Nicolaisen, C. Öcal, and G. Maurer, "Solubility of carbon dioxide in aqueous solutions of sodium chloride: Experimental results and correlation", Journal of Solution Chemistry, 23, 3 (1994): p. 431-448.

149. W. Stumm and J.J. Morgan, *Aquatic chemistry: chemical equilibria and rates in natural waters*. 1996: Wiley.

150. M. Nordsveen, S. Nešić, R. Nyborg, and A. Stangeland, "A Mechanistic Model for Carbon Dioxide Corrosion of Mild Steel in the Presence of Protective Iron Carbonate Films—Part 1: Theory and Verification", Corrosion, 59, 5 (2003): p. 443-456.

151. J. Han, B.N. Brown, and S. Nešić, "Investigation of the Galvanic Mechanism for Localized Carbon Dioxide Corrosion Propagation Using the Artificial Pit Technique", Corrosion, 66, 9 (2010): p. 095003-095003-12.

152. M.B. Tomson, A.T. Kan, G. Fu, and L. Cong. "Measurement of total alkalinity and carboxylic acid and their relation to scaling and corrosion", SPE International

Symposium on Oilfield Scale, (Aberdeen, United Kingdom: Society of Petroleum Engineers, 2004).

153. R. van Eldik and D. Palmer, "Effects of pressure on the kinetics of the dehydration of carbonic acid and the hydrolysis of CO_2 in aqueous solution", Journal of Solution Chemistry, 11, 5 (1982): p. 339-346.

154. J. Li and Z. Duan, "A thermodynamic model for the prediction of phase equilibria and speciation in the H_2O–CO_2–NaCl–$CaCO_3$–$CaSO_4$ system from 0 to 250 °C, 1 to 1000 bar with NaCl concentrations up to halite saturation", Geochimica et Cosmochimica Acta, 75, 15 (2011): p. 4351-4376.

155. A.G. Dickson, "An exact definition of total alkalinity and a procedure for the estimation of alkalinity and total inorganic carbon from titration data", Deep Sea Research Part A. Oceanographic Research Papers, 28, 6 (1981): p. 609-623.

156. J. Goldstein, *Scanning Electron Microscopy and X-Ray Microanalysis*. 2003: Kluwer Academic Pub.

157. D.B. Williams, A.R. Pelton, and R. Gronsky, *Images of materials*. 1991: Oxford University Press.

158. M. Bulletin, *Focused Ion Beam microscopy and Micromachining* C.A.V.a. A.M.Minor, Editor 2007. p. 11

159. R.E. Melchers, "Pitting corrosion of mild steel in marine immersion environment—Part 1; Maximum pit depth", Corrosion, 60, 9 (2004): p. 824-836.

160. A.S.T.M. International, *ASTM G102-89 (2010) Standard practice for calculation of corrosion rates and related information from electrochemical measurements*, 2010, ASTM International: West Conshohocken, PA.

161. W.E. Bronner, O.R. Melroy, and R.P. Buck, "Apparent transfer coefficients for ion transport between water and nitrobenzene", Journal of Electroanalytical Chemistry and Interfacial Electrochemistry, 162, 1–2 (1984): p. 263-274.

162. M. Suzuki, S. Kihara, K. Maeda, K. Ogura, and M. Matsui, "Effect of temperature on ion transfer at the aqueous/organic solution interface studied by current-scan polarography with the electrolyte solution dropping electrode", Journal of Electroanalytical Chemistry and Interfacial Electrochemistry, 292, 1–2 (1990): p. 231-244.

163. E. Makrlík and L.Q. Hung, "Thermodynamics of transfer of some univalent ions from the aqueous phase into the nitrobenzene phase of a two-phase water-nitrobenzene extraction system", Journal of Electroanalytical Chemistry and Interfacial Electrochemistry, 158, 2 (1983): p. 269-276.

164. J. Han, B.N. Brown, and S. Nešić, "Investigation of the galvanic mechanism for localized carbon dioxide corrosion propagation using the artificial pit technique", Corrosion, 66, 9 (2010): p. 12.

165. F. Farelas, B. Brown, and S. Nesic. "Iron carbide and its influence on the formation of protective iron carbonate in CO_2 corrosion of mild steel", CORROSION, paper no. 2291, (Orlando, FL: NACE International, 2013).

166. M. Gao, X. Pang, and K. Gao, "The growth mechanism of CO_2 corrosion product films", Corrosion Science, 53, 2 (2011): p. 557-568.

167. M.M. Antonijevic, S.C. Alagic, M.B. Petrovic, M.B. Radovanovic, and A.T. Stamenkovic, "The Influence of pH on Electrochemical Behavior of Copper in Presence of Chloride Ions", International Journal of Electrochemical Science, 4, (2009): p. 9.

168. I.G. Wood, L. Vocadlo, K.S. Knight, D.P. Dobson, W.G. Marshall, and G.D.B. Price, J., "Thermal expansion and crystal structure of cementite, Fe_3C, between 4 and 600 K determined by time-of-flight neutron powder diffraction Note:T=540 K", Journal of Applied Crystallography, 37, (2004): p. 9.

169. K.M. H. Effenberger, and J. Zemann, "Crystal structure refinements of magnesite, calcite, rhodochrosite, siderite, smithonite, and dolomite, with discussion of some aspects of the stereochemistry of calcite type carbonates", Z. Kristallogr, 156, (1981): p. 11.

170. F. Deganello, L.F. Liotta, A. Longo, M.P. Casaletto, and M. Scopelliti, "Cerium effect on the phase structure, phase stability and redox properties of Ce-doped strontium ferrates", Journal of Solid State Chemistry, 179, 11 (2006): p. 3406-3419.

171. D.B. Langille and D.C. O'Shea, "Raman spectroscopy studies of anti-ferromagnetic $FeCO_3$ and related carbonates", Journal of Physics and Chemistry of Solids, 38, 10 (1977): p. 1161-1171.

172. L. Bellot-Gurlet, D. Neff, S. Reguer, J. Monnier, M. Saheb, and P. Dillmann, "Raman studies of corrosion layers formed on archaeological irons in various media", Journal of Nano Research, 8, (2009): p. 147-156.

173. H.P. Leckie, "Effect of pH on the stable passivity of stainless steels", Corrosion, 24, 3 (1968): p. 70-74.

174. C.O.A. Olsson and D. Landolt, "Passive films on stainless steels—chemistry, structure and growth", Electrochimica Acta, 48, 9 (2003): p. 1093-1104.

175. Y.-S. Choi, S. Nesic, and S. Ling, "Effect of H2S on the CO_2 corrosion of carbon steel in acidic solutions", Electrochimica Acta, 56, 4 (2011): p. 1752-1760.

176. R.C. Woollam, J.R. Vera, C. Mendez, A. Huggins, and W.H. Durnie. "Localized corrosion due to galvanic coupling between FeS-covered and uncovered areas: Another oilfield myth?", CORROSION, paper no. 2715, (Orlando: FL.: NACE International, Houston, Texas, 2013).

177. P. Marcus and E. Protopopoff, "Potential-pH Diagrams for Adsorbed Species: Application to Sulfur Adsorbed on Iron in Water at 25° and 300°C", Journal of The Electrochemical Society, 137, 9 (1990): p. 2709-2712.

178. H.Y. Jeong, J.H. Lee, and K.F. Hayes, "Characterization of synthetic nanocrystalline mackinawite: Crystal structure, particle size, and specific surface area", Geochimica et Cosmochimica Acta, 72, 2 (2008): p. 493-505.

179. A. R. Lennie, S. A. T. Redfern, P. F. Schofield, and D.J. Vaughan, "Synthesis and rietveld crystal structure refinement of mackinawite, tetragonal FeS", Mineralogical Magazine, 59, (1995): p. 6.

180. D.R. Morris, L.P. Sampaleanu, and D.N. Veysey, "The Corrosion of Steel by Aqueous Solutions of Hydrogen Sulfide", Journal of The Electrochemical Society, 127, 6 (1980): p. 1228-1235.

181. M. Mullet, S. Boursiquot, M. Abdelmoula, J.-M. Génin, and J.-J. Ehrhardt, "Surface chemistry and structural properties of mackinawite prepared by reaction of sulfide ions with metallic iron", Geochimica et Cosmochimica Acta, 66, 5 (2002): p. 829-836.

182. F. Xu and A. Navrotsky, "Enthalpies of formation of pyrrhotite Fe1-0.125xS (0 <= x <= 1) solid solutions", American Mineralogist, 95, 5-6 (2010): p. 717-723.

183. W.D. Callister, *Materials Science And Engineering: An Introduction*. 2007: John Wiley & Sons.

184. C.I. Pearce, R.A.D. Pattrick, and D.J. Vaughan, "Electrical and Magnetic Properties of Sulfides", Reviews in Mineralogy and Geochemistry, 61, 1 (2006): p. 127-180.

185. P.H. Tewari and A.B. Campbell, "Dissolution of iron during the initial corrosion of carbon steel in aqueous H2S solutions", Canadian Journal of Chemistry, 57, 2 (1979): p. 188-196.

186. R. Nyborg. "Overview of CO_2 corrosion models for wells and pipelines", CORROSION paper no. 2233, (Denver, CO.: NACE International, Houston, Texas, 2002).

187. M. Clugston and R. Flemming, *Advanced Chemistry*. 2008: Oxford University Press, USA.

188. K. Al-Anezi, C. Somerfield, D. Mee, and N. Hilal, "Parameters affecting the solubility of carbon dioxide in seawater at the conditions encountered in MSF desalination plants", Desalination, 222, 1–3 (2008): p. 548-571.

Appendix

Appendix A. Characterization of solution chemistry and solubility of solute gases

This section discusses the relevant fundamental theories/laws and analytical approach for defining the ionic strength of test solutions, and the solubility of solute gases (H_2S and CO_2) dissolved in the brine phase. These analytical tools help to create a very clear picture and sequence of the science of solute gas solubility and subsequent influence on the corrosiveness of saturated brine in a simulated oilfield corrosion environment. Some of the key theories/concepts deemed relevant in this regard include;

1) Defining Solution Concentration; Molarity and Molality
2) Roault's Law
3) Dalton's Law of partial Pressure
4) Henry's Law of Gas Solubility

A.1 Solution concentration; molarity and molality

Solution Concentration measures how much of a solute is dissolved in a unit volume of solvent. Such concentration could either be defined as molar concentration or mass concentration. Molar concentration (Molarity), measures the amount of moles of solute (gas, liquid or solid) dissolved in a unit volume of solute. Mass concentration is a derivative of molar concentration the measures the mass of solute dissolved in a unit volume of solvent. Molality on the other hand defines the amount of moles of solute (gas, liquid or solid) dissolved in a unit kilogram of solvent[143, 187].

Mathematically,

$$Molarity\ "C_M"\ [(^{mole}/_{dm^3})\ or\ (^{mole}/_{L})]\ =\ \frac{Number\ of\ Moles\ of\ Solute}{Volume\ of\ Solution} = \frac{n}{V} \quad \text{A.1}$$

While,

$$Mass\ Conc.\left[^{\mathrm{Kg}}/_{L}\right] = \frac{Mass\ of\ Solute}{Volume\ of\ Solution} = \frac{m}{V} \quad \text{A.2}$$

$$Mass\ Conc.\ =\ Molar\ Conc.\ (C_M)\ \times Molecular\ weight\ of\ gas \quad \text{A.3}$$

$$Molality\left[{\text{Mole}}/{\text{Kg of Solvent}}\right] = \frac{Number\ of\ moles\ of\ solute}{Unit\ mass\ of\ solvent} = \frac{n}{m} \quad \text{A.4}$$

A.1.1 Statement and implication of Roault's Law

Raoult's Law states that;

"At a particular temperature, the vapour pressure of an ideal solution containing non-volatile solutes is directly proportional to the mole fraction of the pure solvent present in the solution"

Mathematically, this implies that;

$$p = p_i^* x_i \quad \text{A.5}$$

Where,

$p =$ Partial pressure of component i in the solution

$p_i^* =$ Vapour pressure of pure solvent i in solution

$x_i =$ Mole fraction of pure solvent i in the solution

This implies that *at a particular temperature, the vapour pressure of an ideal solution containing non-volatile solutes is dependent on the vapour pressure and mole fraction of the pure solvent at that temperature.* The key significance of Raoult's Law is in defining the relative lowering of the vapour pressure of a solution containing a non-volatile solute from that of a pure solvent., in which case, the vapour pressure of the solution (p) will be equal to the vapour pressure of the solvent (p_i), over the solution,*i.e.*,

$$p = p_i \quad \text{A.6 [143, 144]}$$

Hence, according to Raoult's Law, the vapour pressure of the solvent is given as:

$$p_i = p_i^* x_i \quad \text{Or} \quad p = p_i = p_i^* x_i \quad \text{A.7}$$

Since x_i is always less than one for a solution, the vapour pressure of the solution is always less than p_i^*, *i.e.,* vapour pressure of the pure solvent.

And for a binary solution,

$$\sum x_i = 1 \text{ Or } x_1 = 1 - x_2 \quad \text{A.8}$$

Where

x_2 = Mole fraction of non-volatile solute in solution

Therefore,

$$p_i = p_i^*(1 - x_2) \quad \text{A.9}$$

And

$$\frac{(p_i^* - p_i)}{p_i^*} = x_2 \quad \text{A.10}$$

This equation defines a modified form of Raoult's law and states that "The relative lowering of vapour pressure of a solution containing a non-volatile solute is equal to the mole fraction of the solute in solution"

A.1.2 Henry's Law of Gas Solubility

Henry's Law states that;

> ……."The solubility of gaseous specie in a liquid is directly proportional to the partial pressure of the gaseous specie above the surface of the solution in equilibrium with the aqueous phase" …….

Thus, for a gas $A_{(g)}$ dissolved in solution as $A_{(aq)}$

$$A_{(g)} \leftrightarrow A_{(aq)} \quad \text{A.11}$$

With the equilibrium constant K'_H:

$$K'_H = {[A_{(aq)}]}/{[A_{(g)}]} \quad \text{A.12}$$

Using Henry's law to express the gas concentration in terms of partial pressure using the ideal gas law, we have;

$$PV = nRT \quad \text{A.13}$$

When applied to a gas "A", that gives us:

$$[A_{(g)}] = {n_A}/{V} = \frac{P_A}{RT} \quad \text{A.14}$$

Where

$${n_A}/{V} = c_M\ (Molar\ Concentration) = A_{(aq)}$$

And as a function of $K'_H = RT$,

Therefore,

$$A_{(aq)}\ K'_H = P_A \quad \text{A.15}$$

Or,

$$P_A = K'_H c_M \quad \text{A.16}$$

The Mathematical Statement of Henry's Law!

From the statement of Henry's Law,

$$P_A = K'_H c_i = P_i \quad \text{A.17}$$

Where $P_A = P_i$ is partial pressure of solute gas above the solution

K_H' is Henry's constant on a molar scale and in units of (Pa/ (mol/dm^3 or Pa/ mol/L)

$c_m = c_i$ Is the molar concentration of the dissolved gases in solution

Note:

(1) "Henry's constant (K') for gaseous species dissolved in pure solvents can be obtained from tables of Molar Thermodynamic Values for pure substances and aqueous solutes in handbook of Chemistry and physics[142].

(2) In the application of Henry's law is in dealing with the non-ideality of gaseous species in equilibrium with its aqueous phase. It is assumed that if the partial pressure of the solute gas (P_i) is less than or equal to atmospheric pressure (1.013bar), then the term $P_i V = nRT$ may be sufficiently close to zero to be neglected and then the fugacity f_i, of gaseous species is assumed equal to its partial pressure[144-146].

3) Henry's Law is also strongly temperature dependent since solubility of gaseous species varies inversely with increasing temperature [188].

This means that

$$P_i \approx f_i \quad \text{A.18}$$

And Henry's law can now be re-written as;

$$f_i = K'_H c_i \quad \text{A.19}$$

This implies that the Linearity of the Henry's law equation is limited in application for real gases to low gas pressures[144].

A.1.3 Dalton's Law of Partial Pressure

Dalton's Law of Partial pressures states that;

…. "The pressure of a gas mixture is the sum of the partial pressures of the individual components of the gas mixture"….

This implies that for an individual ideal gas component (i) in a gas mixture, it can be represented as;

$$PV = nRT \quad \text{(Ideal Gas Equation of state)} \tag{A.20}$$

P = Total gas pressure of gas mixtures

$$n_T = \sum n_i \tag{A.21}$$

n_T= Total number of moles in gas mixture)

n_i= number of moles of individual gas components

$$PV = RT \sum n_i = P = \frac{n_1 RT}{V} + \frac{n_2 RT}{V} \tag{A.22}$$

(Ideal gas equation of state as a function of no. of moles of individual component in the gas mixtures)

Therefore,

$$P = P_1 + P_2 = \sum P_i \tag{A.23}$$

Mathematical expression of Dalton's law of partial pressure

Application of Eq. A10, A19, and A23, for Raoult's law, Henry's law and Dalton's law respectively would help characterize the chemistry of corrosive media especially for a system of more than one gas phase dissolved in brine. These theories have been explored in combination with relevant thermodynamic data and experimental results from literatures.

A.1.4 Analysis towards Estimating the H_2S and CO_2 Gas Solubility Gas Bubbled Above NaCl Solution

1) **Estimating the gas phase pressure composition**

Basis of Analysis: Litre of H_2O ≡ 1.0 Kg of H_2O

3.5% NaCl Solution

A 3.5 wt. % NaCl solution will contain; 35g of NaCl and 965g of H_2O in 1.0 Litre of Solution.

Recalling the molecular weight of NaCl and H_2O as 58.44g/mol. and 18g/mol. respectively,

Therefore, No. of Moles (Molarity) of NaCl in 1.0 L of NaCl solution;

$$= \frac{35\text{g}}{58.44\text{gmol}^{-1}} = \frac{0.598\text{moles}}{\text{Litre}} \text{ of solution}$$

No. of moles (Molality) of NaCl per kg of H_2O (mNaCl)

$$= \frac{0.598\text{moles}}{\text{Litre}} \text{ of solution } \times {}^{1}\Big/_{\text{mass of } \frac{\text{water}}{\text{liter}} \text{ of solution}}$$

$$= \frac{0.598}{0.965} = 0.62 \frac{moles}{kg} of\ water$$

No. of Moles of H_2O in 1.0 L Solution

$$= \frac{965\, {}^{g}\!/_{L}}{18 gmol^{-1}} = 53.61\ {}^{moles}\!/_{L}$$

Total No. of Moles in 1.0 L solution of 10 wt. % NaCl in water

From Stoichiometry, $NaCl_{(aq)} \leftrightarrow Na^{+}{}_{aq} + Cl^{-}{}_{aq}$

1mole 1mole 1mole

Therefore,

$$\sum n = 53.61 + 0.598 + 0.598 = 54.806\, moles$$

Moles Fraction (y_i)of H_2O in 10 wt. % NaCl solution $= \frac{53.61}{54.806} = 0.978$

A.1.5 Raoult's Law and vapour pressure of solution

Therefore, according to Raoult's Law, The vapour pressure of a solution containing dissolved solute;

$= \text{Mole fraction of } H_2O \text{ in solution } \times \text{vapour pressure of pure water @ Temp (℃)}$ A.24

Vapour pressure of pure H_2O is a $f(T)$ and is given handbooks of thermodynamic properties for substances (Handbook of Chemistry and Physics CRC[142]).

Estimated vapour pressure data are shown for all temperatures in Table A. 1 and Table A. 2.

Table A. 1 Vapour pressure of pure water

Temperature (Degree C)	Vapour Pressure of Water (mmHg)	Vapour Pressure of Water (Bar)
30	31.8	0.0424
50	92.5	0.1233
80	355.1	0.473

Vapour pressure of pure H_2O @ T(°C) is sourced from Handbook of Chemistry and Physics CRC[142].

A.25

Therefore, the Vapour pressure of 10 wt. % NaCl @ Different (T) °C $= x_i \times P_v^*$

Where $P_v^* =$ vapour pressure of pure water.

Table A. 2 Summary of analysis of gas phase of test solutions based on Molar concentration calculations and Rauolt's law

Temperatures (°C)	30 (°C)	50 (°C)	80 (°C)
Concentration of NaCl Solution (% w/v)	3.5%	3.5%	3.5%
Mole Fraction of pure water (y_i)	0.978	0.978	0.978
Vapour Pressure (p_i^*)of Pure water @ Temperature (bars)	0.0425	0.123	0.47
Vapour Pressure (p_i)of NaCl Solutions (bars)	0.0416	0.120	0.46
Molality of Solution ($^{moles}/_{Kg\ of\ H_2O}$)	0.62	0.62	0.62
Total Partial Pressure PT (bar)	0.97	0.89	0.55

The partial pressure and solubility analysis of the constituent active gases for experimental conditions listed in Chapter 5 of this report were based on the following assumptions;

Assumption (1)

Therefore if the total pressure of gas phase above the brine at any given time of the test is constant at 1.013bar, then

$$P_T = 1.013bar = P_{H_2s-CO_2} + P_{NaCl-H_2O} \quad \text{A.26}$$

$$P_{H_2s-CO_2} = 1.013 - P_{NaCl-H_2O} \quad \text{A.27}$$

Assumption (2)

1) Analysis Based on Dalton's Law

Considering a pre-mixed gas system containing 10 mol. % H_2S and 90 mol. % CO_2, and with molar composition designated as "x_i"

So that from Dalton's law of mixture of gases,

$$P_{T_{H_2S-CO_2}} = P_{H_2S-CO_2} = P_{H_2S} + P_{CO_2} \quad \text{A.28}$$

And A.29

$$P_i = \frac{mol.\%\ of\ gas_{\ i}}{100} \times P_T$$

Therefore, A.30

$$P_{H_2S} = \frac{x_i\%\ of\ H_2S\ gas}{100} \times P_{T_{H_2S-CO_2}}$$

Therefore, as an example, for a total gas phase pressure over a 1 litre of 3.5 wt. % of NaCl solution, and from a gas source of molar composition of 10 mol.% H_2S, The partial pressure of H_2S gas at every point in time is given by;

$$\boldsymbol{P_{H_2S}} = \frac{\mathbf{3.5}}{\mathbf{100}} \times P_T \quad \text{A.31}$$

Based on the abovementioned assumption, the partial pressure of constituent gases in different test conditions is presented in Table A. 3.

Table A. 3 Summary of detail gas phase analysis of gas phase of 100 mol. % CO_2, 10 mol. % H_2S-90 mol. % CO_2 and 10 mol. % H_2S-90 mol. % N_2 above a 3.5% NaCl Solution

Temperature (°C)	Partial pressure of combining gases					
	Vapour Pressure of 3.5% NaCl Solution (Bar)	100% CO_2	90% CO_2-10% H_2S		10% H_2S-90% N_2	
		P-CO_2	P-H_2S	P-CO_2	P-H_2S	P-N_2
30	0.042	0.971	0.097	0.874	0.097	0.874
50	0.120	0.893	0.089	0.8037	0.089	0.804
80	0.460	0.553	0.055	0.498	0.055	0.498

From Eq. A.31, we now have the exact partial pressure of H_2S gas for estimating the Concentration of dissolved H_2S gas in Brine Using Henry's Law assuming a total gas pressure of 1.0 atmosphere

$$P_{H_2S} = k_H C_{H_2S} \quad \text{A.32}$$

Where, $k_H = Henry's\ Constant\ of\ gas\ solubility$ &
$C_{H_2S} = Concentration\ of\ H_2S\ gas\ dissolved\ in\ Brine$

Assumptions (3); From the Assumptions of (1) and (2) above,

The analysis up until Eq. A.31 for estimating $\boldsymbol{P_{H_2S}}$, is such that $\boldsymbol{P_{H_2S}}$ is assumed as equal to the fugacity of H_2S gas in the solution [145, 146]**.**

Estimating Henry's Law Constant for H_2S Gas in NaCl Solution at different Temperatures

According to experiments conducted by Barrett, *et al*[145], at atmospheric pressure (1.013bar) in variable concentration of NaCl Solutions, the following values in Table A. 4 were collated at 30,50 and 80°C.

Table A. 4 Molar solubility of H_2S gas (mol/kg of H_2O) @ different temperatures (°C) and NaCl Concentration at atmospheric pressure in a steady state gas flow system

mNaCl (mol/kgH_2O)	Henry's law solubility (H_2S (mol/kg)		
	30°C	50°C	80°C
0	0.0899	0.0579	0.0215
1	0.0778	0.0504	0.0190
2	0.0667	0.0436	0.0171
3	0.0588	0.0385	0.0153
4	0.0525	0.0347	0.0142
5	0.0468	0.0310	0.0130

The data in Table A. 4 is plotted in Figure A. 1 and used to estimate the solubility constant for H_2S gas in 3.5 wt. % NaCl solutions at different temperatures.

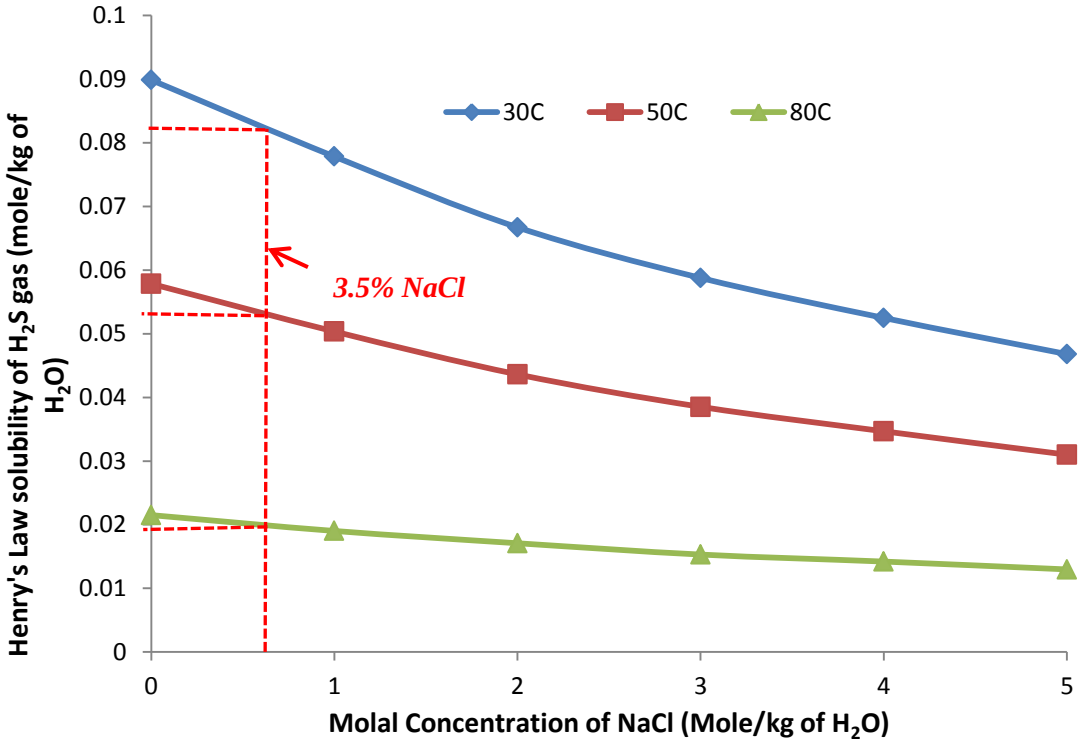

Figure A. 1 Generated plot of solubility of H_2S vs Molality of NaCl from Table A.1 (Data plotted here are from experiments by Barrett, *et al*,[145]**.**

From Figure A. 1, the solubility of H_2S gas in any concentration of NaCl (expressed in Mole/Kg of water) can be estimated at temperatures of 30, 50 and 80℃ as shown in Table A. 5. These data can therefore be applied towards defining the concentration of $H_2S_{(aq)}$ available for cathodic reduction during corrosion of carbon steel in H_2S - CO_2 corrosion environments.

Table A. 5 Summary of solubility data for H_2S gas in 3.5 wt. % NaCl solution

Temperature (°C)	H_2S Gas Solubility (mole/Kg of H_2O)
30	0.082
50	0.053
80	0.020

Similar analysis is also carried out for CO_2 gas solubility as it applies to this study and provided in the section below.

For a 100% Mole Fraction of CO_2 gas source, Raoult's law approximation of eq. A.5-A.10 is applied by assuming

$$P_{H_2s-CO_2} \approx P_{CO_2} \quad \text{A.33}$$

And the Dalton's law of partial pressure is not applied since it is assumed that the total gas pressure above the brine will be restricted to 1.013 bars.

Table A. 6 Summary of detail gas phase analysis of gas phase of 100 mole % CO2 above 3.5% NaCl

Temperature (℃)	Vapour Pressure of 3.5% NaCl Solution (Bar)	P_{T-CO_2} (Bar)	P_{CO_2} (psi)
30	0.0416	0.9714	14.1000
50	0.1200	0.8930	12.9500
80	0.4600	0.5530	8.0200

Solubility data plotted in Figure A.1 were extrapolated data from curve fitting on experimental results of experiment conducted by Zheng, *et al* [147]. The data presented here in Fig 4.7 represented an average of two repeated tests at chosen temperatures. These data were confirmed to be accurate by comparing with the results of Y. Yasunishi and F. Yoshida, 1979 at 35℃ cited in Rumpf, *et al* [148] and that of distilled water at 30℃ repoted by Stumm. W and Morgan, J.J[149]. A table of the Raw data and curve fitted plots for each temperature is shown in the appendix B.

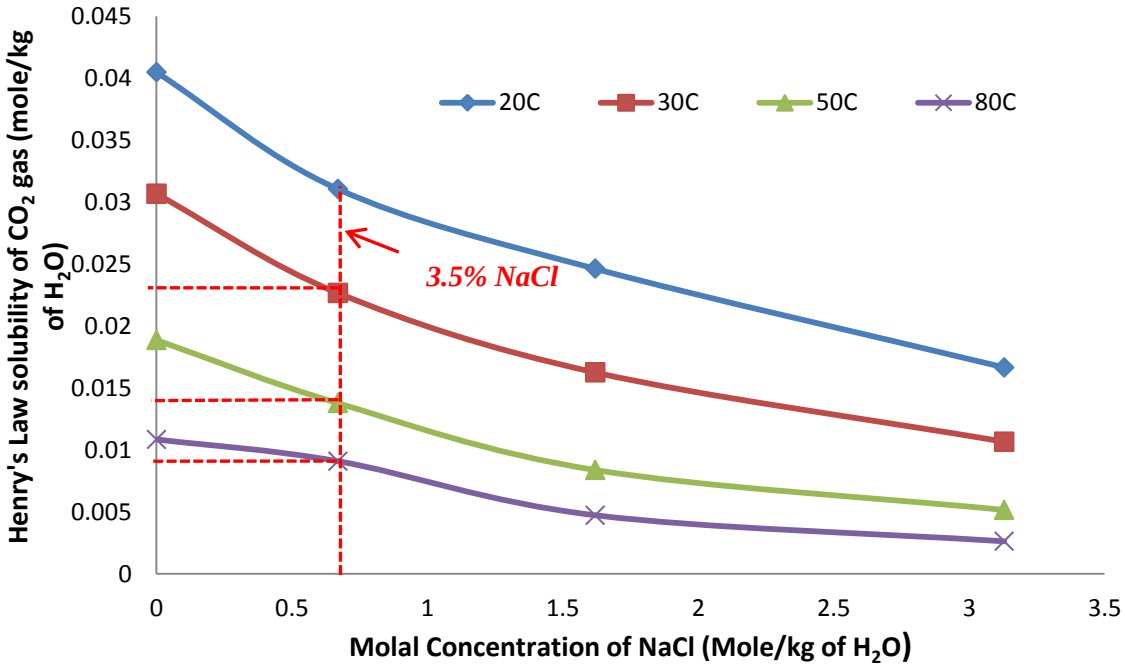

Figure A. 2 Generated plot of solubility of CO_2 vs Molality of NaCl from Experimental data found in literatures [147]

Table A. 7 Summary of solubility data for CO_2 Gas at all chosen test conditions

Temperature (℃)	CO_2 Gas Solubility (mole/Kg of H_2O		
	1% NaCl	3.5% NaCl	10% NaCl
30	0.0285	0.0230	0.0150
50	0.0175	0.0140	0.0075
80	0.0105	0.0090	0.0040

From values presented in Table A. 4 and Table A. 7 for solubility of H_2S and CO_2 and the Henry's Law analysis,

$$P_{H_2S_{(g)}} = K_H{}'C_{H_2S_{(aq)}} \text{ and } P_{H_2S_{(g)}} \approx f_{H_2S}$$

And $$P_{CO_{2(g)}} = K_H{}'C_{CO_{2(aq)}} \text{ And } P_{CO_{2(g)}} \approx f_{CO_2}$$

Therefore, at different concentration of NaCl and Temperature, the Molar Concentration of dissolved gas is calculated using the expression;

$$= x\ {}^{moles}/_{Kg\ of\ water} \times {}^{wt\ of\ water}/_{L\ of\ Solution} \quad \text{A.34}$$

The results are tabulated for different concentration of NaCl for CO_2 and H_2S gas based on a total gas pressure of 1 atmosphere (1.013 bars)

Table A. 8 Molar Concentration of H_2S and CO_2 gas dissolved in 3.5% NaCl Solution

Temperature (℃)	Solubility of H_2S Gas (mole/Kg of water)	Solubility of CO_2 Gas (mole/Kg of water)	Solubility of H_2S Gas (Moles/L of solution)	Solubility of CO_2 Gas (Moles/L of solution)
30	0.0820	0.0230	0.0791	0.0222
50	0.0530	0.0140	0.0511	0.0135
80	0.0200	0.0090	0.0193	0.0087

From the values obtained in table 4.12-4.14, the value of Henry's Law constant is estimated for each temperature, NaCl concentration and partial pressure of the solute gas (Provided the pressure is $\leq$ 1.013 bars)

Therefore;

$$K_H = \frac{f_{H_2S}}{C_{H_2S_{(aq)}}} = (bar/mole/L) \quad \text{A.35}$$

And converting to ppm as follows

$$Mass\ Conc.\ (C_m) \quad \left\{\frac{g}{vol}.\right\} = \ Molar\ Conc.(C_M)\ \times Molecular\ weight\ of\ gas$$

From the Heny's law approximation,

$$f_i = \ K'_H c_i \quad \text{A.36}$$

As implied from the Henry's solubility data above, Henry's law constant $K'_H = f(T)$. This implies that at constant temperature,

$\frac{f_i}{c_i} = K'_H = cont.$ Therefore, $\frac{f_1}{c_1} = \frac{f_2}{c_2} = K'_H = cont$

The solubility data presented for the gases (H_2S and CO_2) dissolved in brine were estimated at a total gas phase pressure of 1.013 bars and based on a single gas component as the solute gas dissolved in the liquid phase.

Therefore, the partial pressures used in the solubility calculation were based on;

$P_{gas} = 1.013\ bar - P_v^*$ For each temperature and salt concentration

If ($P_{gas} \approx f_1$) and the corresponding solubility (c_1), therefore, $P_{gas\ (actual)} \approx f_2$ and the corresponding solubility (c_2).

Therefore

$$c_2 = \frac{f_2 \times c_1}{f_1} \quad \text{A.37}$$

Note; Solubility data for conditions of interest to this research are plotted in Figure 5-7 **of Chapter 5.**

Appendix B.
Procedure for unbuffered CO_2 corrosion experiments

1) The electrolyte is sparged with CO_2 gas for a minimum of 12 hours in order to de-aerate the solution down to 20ppb and saturate it with CO_2 gas. A completely CO_2 saturated solution of 10 wt.% NaCl at 25°C will be at a pH of 3.64. This data is also provided for all other concentrations of NaCl solutions in Crolet and Bonis [96] and were used for checking that solutions are fully saturated before commencement of test.

2) Fill the test vessel with brine solution (2 litres) and to an appropriate volume and place on the hot plate.

3) The temperature regulator is switched on and temperature probe immersed into the test cell to activate the regulating system to the desired experiment temperature.

4) pH probe/pH meter is calibrated prior to every tests.

5) The pH probe is inserted into the electrolyte to record the pH of the electrolyte before immersing the samples.

6) Prior to commencement of test, the working electrodes (10 samples) are polished, degreased with acetone, rinsed with distilled water and dried with compressed air before immersion into the test cell, along with the reference and counter electrode.

7) All components and parts of the bubble test set-up are checked to ensure they are all in good working condition. This includes the electrochemical connections, good seal to prevent oxygen ingress.

8) The assembled test cell is sparged with CO_2 gas for another 30 minutes at a gas flow rate of 0.1L/min.

9) Ensure that all electrical connection between working electrode, reference electrode and potentiostat is made.

10) Check must be carried out to ensure that the point of insertion of probes/electrodes and sample/sample holder assembly are sufficiently sealed to minimise oxygen ingress.

11) Start electrochemistry measurements. Electrochemical response is recorded for two samples from each of the twin bubble cell.

12) In the course of the experiments, samples not connected to the potentiostat are removed at experimental sampling time intervals (a detail of experimental sampling time is provided later on in this chapter).

13) The pH of the test solution is also monitored throughout the duration of the experiments and recorded at chosen time intervals.

At the end of every sampling time and after each tests;

14) Two of the sample from each of the twin bubble cell are washed, air dried, and carefully stored in a de-aerated chamber to avoid oxidation of corrosion products prior to surface analysis

15) Some samples are also cleaned with Clark's solution to remove all corrosion products prior to pitting corrosion analysis.

Appendix C. Logistics for operation of the sour corrosion test rig and for conducting H_2S gas based experiments

C.1.1 Logistics of Operation and Emergency Health and Safety Measures prior to running H_2S based experiments

1) Standard Laboratory procedure should be observed whilst working in the laboratory at all times.
2) Prior to the start of any experiment involving H_2S gas, a notice must be given to the project supervisor, laboratory technician and one other member of the research group, this to ensure that an appropriate and immediate response be taken should in case the H_2S alarm goes off.
3) Extreme care must be taken and a personal H_2S safety alarm must be carried and switched on when entering the laboratory.
4) The alarm should be set to activate when the H_2S concentration inside the fume cupboard is more than 10ppm of if the H_2S concentration is more than 5ppm in the laboratory area.
5) A sign "H_2S Test in progress" must be displayed on the laboratory entrance and exit doors throughout the duration of the test.
6) When the H_2S alarm is activated, the laboratory should be evacuated immediately. The cause of the alarm should be determined by checking the information displayed on the control box mounted outside the laboratory.
7) A shut down valve should be automatically activated to cut off the H2S supply when the set limit or the alarm is reached.
8) It is considered safe to re-enter the laboratory when the control box outside the laboratory registers the H_2S levels as being less than 1ppm.
9) The "Reset" button on the control box is pressed once to deactivate the alarm.
10) Pressing the "Reset" button a second time re-energises the automatic shutdown valve to allow gas to pass through.
11) The H_2S gas supply is turned off using the valve on top of the cylinder.
12) All leaks should be made good if it is safe to do so.

C.1.2 General procedure for sour corrosion experiments

1) All components and parts of the sour rig/bubble test set-up **must** be checked to ensure they are all in good working condition and are safe and ready to use.

2) The gas lines (piping) and components of the sour rig must be pressure tested at 0.8 bars with Nitrogen (N_2) and held at this pressure for five minutes to check all connection point

for any leakages.

Note; this pressure testing exercise must be carried out without the bubble test vessels.

3) The blow off valve on every component of the sour corrosion rig/scrubbing system must be checked to ensure it is working properly by increasing the pressure in step two (2) to the designated differential pressure rating.

4) Pressure testing operations with N_2 ends when the pressure is released down to zero.

5) Fill the test vessel with brine solution and to an appropriate volume and place on the hot plate.

6) Brine solution is sparged with Nitrogen overnight for a minimum of 12 hours to de-aerate the test cell down to 20ppb of oxygen that is typical of oilfield environments.

7) Carefully mount sample-sample holder assembly on the lid of the test vessel and ensure that the sample-sample holder assembly sits firmly within the cavity created for it.

8) Assemble the bubble cell-lid (this includes immersion of reference electrode, temperature probes and pH electrode along with the sample/sample holder assembly) and activate the temperature regulating system to the desired experiment temperature. This is done while still sparing with Nitrogen.

9) Check must be carried out to ensure that the point of insertion of probes/electrodes and sample/sample holder assembly are completely sealed.

10) Seal the whole vessels using the customised sealing screw assembly that holds beaker cover firmly in place.

11) Start the test with Nitrogen (N_2). This is carried out by allowing the flow of Nitrogen (N_2) through the sour rig system (from In-let to out-let) for 15 minutes. All valves must be open to allow the gas to flow through the scrubbing units before exiting the fume chamber.

12) All tendencies for leakage of gas and test fluid at possible hotspots must be checked at this stage using Nitrogen gas and leak detector. This should also be carried out at all times in the course of the experiment. The pressure gauge must be regularly checked at these times to ensure that there is no trapped pressure along the gas transporting lines.

Following completion of sparging with H_2S base gas, start the electrochemistry test

C.1.3 Procedure for long-term sour corrosion experiments

In the event of the need for long-term experiment which in most cases will be required to run overnight, and for up to seven (7) days, the following procedure should be followed;

1) Once its 4:40 pm every week day, the H_2S supply must be shut in at exactly the same time as the in-let to and out-let line for H_2S gas from the test vessel. The H_2S based gas mixture is shut-in in the test vessel at 1.5 psi above atmospheric pressure. This is to maintain constant concentration of H_2S gas for test over-night.

2) Once this is done, the Nitrogen (N_2) gas supply is turned on to flush the rig for 10-15 minutes. The flushing nitrogen is made to by-pass the test vessel into the scrubbing system.

3) In-case of pressure build-up in the test vessel, the pressure released valve (rated at 0.13 bar above atmospheric pressure) will be activated to release excess pressure into the scrubbing system.

4) By 8:00 am the next day, the exhaust line of the test vessel is opened.

5) This is followed by opening the H_2S gas supply line to continue sparging while the experiment is running.

6) This cycle of events is repeated until the test is finished.

C.1.4 Procedure following the completion of sour corrosion experiments

1) Turn off the H_2S as supply line.
2) The heating and stirring control on the hotplate should be turned off first.

3) The test vessels must then be purged with nitrogen gas (N_2) and outlet gas should be routed

to the scrubber unit for a minimum combined duration of two (2) hours.

4) Then allow the test vessel to cool down to temperatures below 50℃.

5) Slightly open the vent valve on top of the cover of test vessel.

6) Engage the H_2S detector to check for the presence of any residual H_2S gas by placing the detector close to the slightly opened vent valve.

7) Note: If the alarm sounds in response to any significant amount of H_2S gas in excess of the acceptable 5ppm threshold, close the valve and repeat purging process in step (3).

8) Loosen the screws that firmly hold the cover of the vessel against the flange edge of the beaker.

9) Carefully lift the beaker cover off the test vessel.

10) Carefully remove the sample from the sample holder assembly.

11) Clean sample using the set out procedure for cleaning, drying and storage after experiments (see section 5.4.1).

12) Empty the test vessel by disposing the test solution into a designated container. (Note: the solutions in the container should be treated with additional potassium permanganate to remove any remaining H_2S prior to final disposal)

C.1.5 Procedure for Cleaning the Scrubber system of the Sour corrosion rig

1) Switch on the heater and stirrer unit.

2) Allow the Vessel to heat to 30°C.

3) Purge vessel with Nitrogen and the outlet gas should be routed to the scrubber unit for at least 60 minutes.

4) Stop the N_2 purging and slightly open the vent valve on top of the vessel lid and inject the H_2S Scavenger and close back the valve.

5) Purge the vessel with N_2 again for another 15 minutes.

6) Stop purging and carefully check the presence of any residual H_2S in the vessel using the H_2S detector. If any appreciable amount of H_2S (more than 5pm) is present, close the valve and return to step 4.

7) Loosen the sealing clip.

8) Lift the lid carefully from the vessel.

9) Empty the vessel. Dispose of the solution into a designated container. (The solution in the container should be treated with additional H_2S Scavenger and mixed with water to remove any H_2S in the solution prior to final disposal.

Appendix D.

Repeated Tafel polarisation curves for experiment in CO_2-conatining corrosion environment

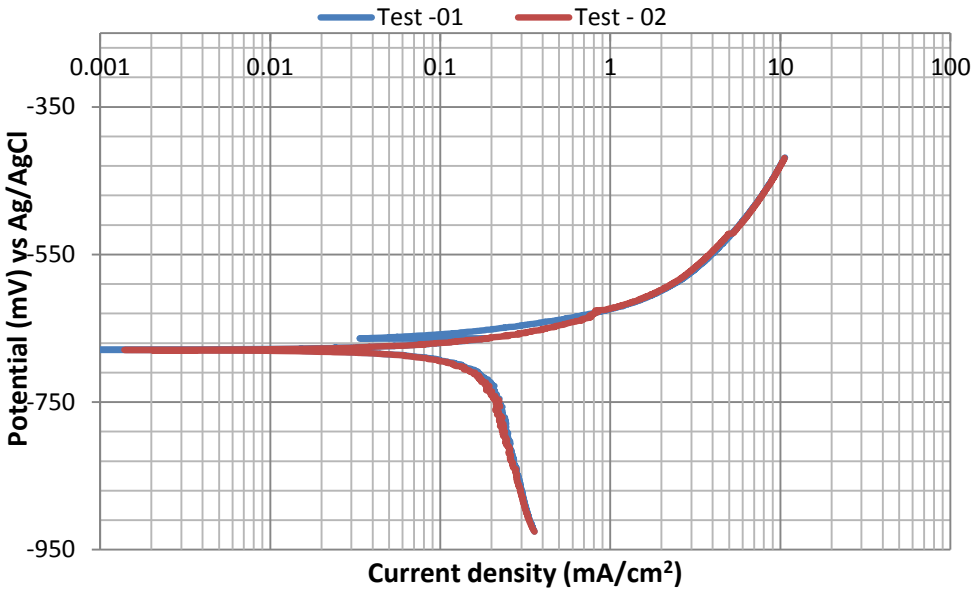

(a)

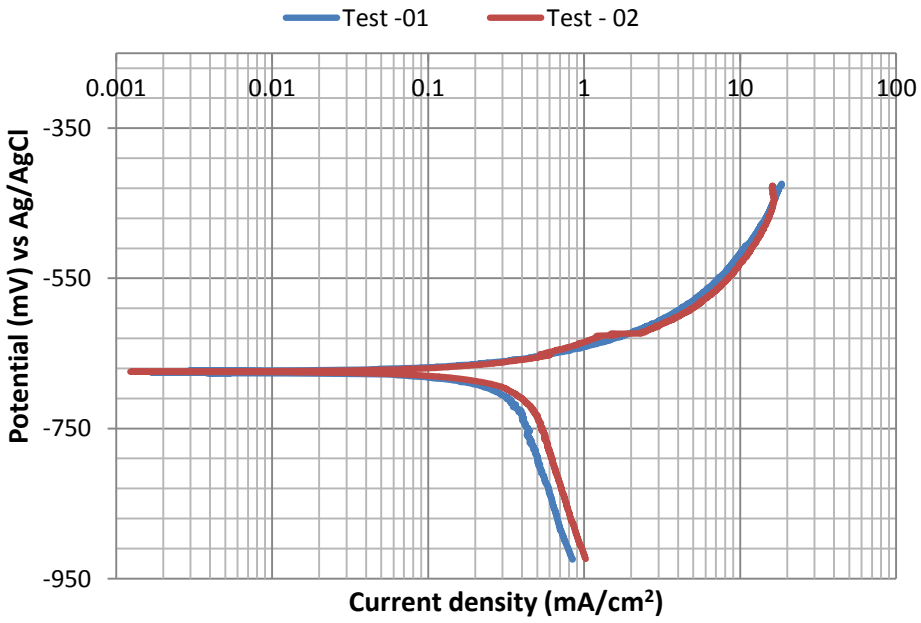

(b)

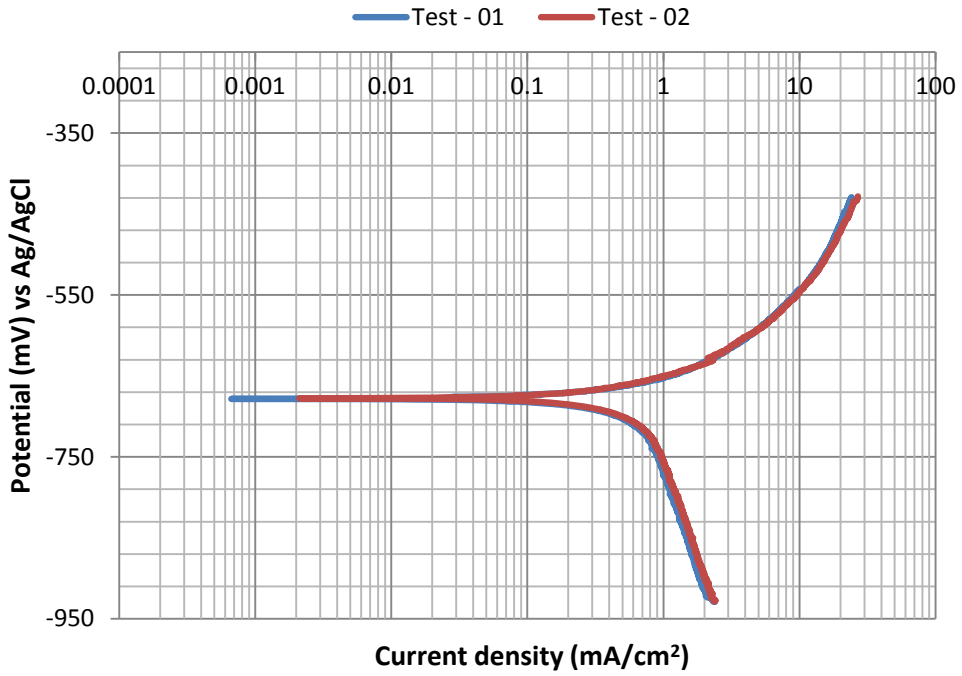

(c)

Figure D. 1 Repeatable Tafel polarisation curves for test solution system of 3.5 wt. % NaCl for (a) 30°C, (b) 50°C and (c) 80°C under a CO_2 gas atmosphere